西安电子科技大学
XIDIAN UNIVERSITY

14th International conference

Laser-light and Interactions with Particles (LIP2024)

September 18th-22nd, 2024

Xi'an, China

www.lip-conference.org

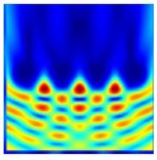
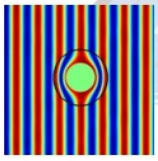
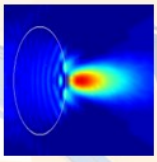
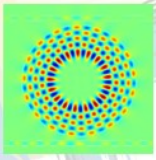
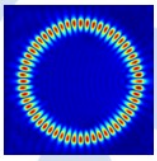
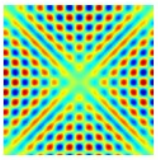

Beam shape description of laser/electromagnetic wave

Optical forces and other mechanical effects of light

Light/laser/electromagnetic scattering of complex particles and aggregates

Optical particle sizing and characterization methods

Light/electromagnetic wave propagation in complex media

Optical imaging with structured illumination (tissue, particles,...)

AI-assisted analysis in light/electromagnetic scattering

Applications of light scattering methods in biology and biomedicine

Applications of light scattering methods in multiphase flow, nanoscience, plasma and soft matter physics, aerosol science and atmospheric environment




SCIENTIFIC COMMITTEE

L.A. AMBROSIO, *University of São Paulo, São Paulo, USP, Brazil*

X.S. CAI, *University of Shanghai for Science and Technology, Shanghai, China*

G. GOUESBET, *CORIA, National Institute of Applied Sciences, Rouen, France*

D. GRIER, *Depart. of Physics and Center for Soft Matter Research, New-York University, NY, USA.*

Y.P. HAN, *School of Physics, Xidian University, Xidian, China*

J.A. LOCK, *Cleveland State University, Cleveland, OH, USA.*

P.L. MARSTON , *Depart. Physics & Astronomy, Washington State University, Pullman, USA*

F.R.A. ONOFRI, *IUSTI, National Center for Scientific Research, Marseille, France*

K. F. REN, *Optics & Lasers, CORIA, Normandy University, Rouen, France*

G. VIDEEN, *Army Research Laboratory, Adelphi, MD, USA*

J.J. WANG, *School of Physics, Xidian University, Xidian, China*

T. WRIEDT, *ITW, University of Bremen, Bremen, Germany*

P. YANG, *Dept. Atmospheric Sciences, Texas A&M University, College Station, TX, USA*

M. YURKIN, *CORIA, University of Rouen Normandy, Rouen, France*

ADVISORY COMMITTEE

Y. AIZU, *Muroran Institute of Technology, Muroran, Japan*

M. BERG, *Kansas State University, USP, Manhattan, KS, USA*

P. BRIARD, *School of Physics, Xidian University, Xidian, China*

M. BRUNEL, *Laser/particle(s) interaction, CORIA, Normandy University, Rouen, France*

Y.E. GEINTS, *Zuev Institute of Atmospheric Optics, Russian Academy of Sciences, Tomsk, Russia*

D. JAKUBCZYK, *Institut of Physics, Polish Academy of Sciences, Warsaw, Poland*

F. LAMADIE, *Atomic Energy and Alternative Energies Commission, Marcoule, France*

R. LI, *School of Physics, Xidian University, Xidian, China*

I. V. MININ,*Tomsk Polytechnic University, Tomsk,Russia*

O. MARAGÒ, *IPCF, National Research Council, Messina, Italy*

F. G. MITRI, *Schlumberger–Doll Research Center, Cambridge, Massachusetts 02139, USA*

A.A.R. NEVES, *Federal University of ABC, Santo André, Brazil*

T. NIEMINEN , *Dept. of Physics, University of QueenslandBrisbane, Australia*

ORGANIZING COMMITTEE

Conveners

LIXIN GUO, *School of Physics, Xidian University, China*

YIPING HAN, *School of Physics, Xidian University, China*

F. ONOFRI, *IUSTI, CNRS, Marseille France*

G. GOUESBET, *CORIA, INSA de Rouen, Saint-Etienne du Rouvray, France*

Conference co-chairs

LIXIN GUO, *School of Physics, Xidian University, China*

YIPING HAN, *School of Physics, Xidian University, China*

Organizing Committee

HUIXIN ZHOU, *Vice Dean of School of Physics, Xidian University, China*

BING WEI, *Vice-Dean of School of Physics, Xidian - University, China*

XIANG'E HAN, *Professor, School of Physics, Xidian University, China*

LU BAI, *Professor, School of Physics, Xidian University, China*

PENG GAO, *Professor, School of Physics, Xidian University, China*

JIANGTING LI, *Professor, School of Physics, Xidian University, China*

YULONG SHEN, *Director of Division of International Cooperation and Exchange, Xidian University, China*

ZHIWEI CUI, *A/Professor, School of Physics, Xidian University, China*

P. BRIARD, *A/Professor, School of Physics, Xidian University, China*

KE LIN, *A/Professor, School of Physics, Xidian University, China*

HAIYING LI, *A/Professor, School of Physics, Xidian University, China*

ZHENGJUN LI, *A/Professor, School of Physics, Xidian University, China*

Conference secretaries

JIAJIE WANG, *School of Physics, Xidian University*

RENXIAN LI, *School of Physics, Xidian University*

MINGJIAN CHENG, *School of Physics, Xidian University*

QINGWEI DUAN, *School of Physics, Xidian University*

HOSTS, PARTNERS & SPONSORS

Hosts

School of Physics, Xidian University

International Academic Platform for Science and Technology of Optoelectronic Perception under Complex Environment (OPCE)

Key Laboratory of Optoelectronic Imaging and Detection

Key Laboratory of Radio Physics

Division of International Cooperation and Exchange

Collaborative Innovation Center of Information Sensing Technology

List of partners & sponsors

Shaanxi Provincial Physical Society

CORIA, UMR 6614, CNRS, INSA Rouen & Normandy University

IUSTI, UMR 7343, CNRS & Aix-Marseille University

Xi'an Institute of Optics and Precision Mechanics of CAS

Zhejiang University

University of Shanghai for Science and Technology

Contact Information:

EMAIL: contact@lip-conference.org or lip2024_contact@163.com

JIAJIE WANG: E-mail: wangjiajie@xidian.edu.cn Tel: (+86)13992831154

RENXIAN LI: E-mail: rxli@mail.xidian.edu.cn Tel: (+86) 13772021733

MINGJIAN CHENG: E-mail: mjcheng@xidian.edu.cn Tel:(+86) 15291578113

QINGWEI DUAN: E-mail: qwduan@xidian.edu.cn Tel:(+86) 15591847672

WECHAT GROUP:

LIST of CONTENTS

(O17) Forward scattering model for spherical particles: refraction and diffraction ring effects

(O18) Light Scattering by Multilayer and Homogenized Curvilinear Systems

(O19) Single non-spherical particle far-field scattering simulation based on FDTD method

(O20) Light scattering by a buried circular cylinder

(O21) Particle size measurement using the laser diffraction model based on Monte Carlo method

(O22) Soot sizing in laminar diffusion flames: impact of self absorption

OPTICAL PARTICLE SIZING AND CHARACTERIZATION METHODS

(O23) Motional and removable characteristics of lunar dust particles in electrostatic field

(O24) On the effective-medium approach for monolayers of small particles and its relationship with multiple scattering models

(O25) Simulation of the light scattering properties of interstellar tholins

REPORTS FROM YOUNG SCHOLARS FROM XIDIAN UNIVERSITY

(O26) A self-adaptive network based on free space optical communication

(O27) Spectral prediction of composite structured metasurfaces based on convolutional neural network

(O28) Use of an iterative generalized regression neural network to determine the particle shape distribution of nanorods by depolarized dynamic light scattering

(O29) Transmission characteristics of Laguerre-Gaussian beams in dusty environments

(O30) Large-field optimized optical sectioning structured illumination microscopy

(O31) Calibration of space dust detection system onboard tianwen-2 mission

(O32) Blood cell characterization based on deep learning and diffraction phase microscopy

OPTICAL IMAGING WITH STRUCTURED ILLUMINATION

(O33) Quantitative measurement of extinction, scattering, and absorption spectra from metallic nanoparticles

(O34) Image analysis method for liquid-gas interface area disturbed by ultrasonic cavitation for evaluation of optimum influence modes

(O35) Preliminary derivation of second-order rainbow scattering by cam theory and

experimental verification

(O36) Optimizing structured light therapy for 3d melanoma models: a Monte Carlo and machine learning approach

AI ASSISTED ANALYSIS IN LIGHT/ELECTROMAGNETIC SCAT

(O37) Convolutional neural network for particle's shape reconstruction in interferometric particle imaging

(O38) Convolutional neural network can track the radius evolution of levitating evaporating microdroplets

(O39) Property of plasmon-polaritons in nanorings assisted by lemniscateordered emitters

RELATED APPLICATIONS

(O40) Analysing the reconstructed phase maps of digital in-line holograms: application to the characterization of viscoelastic fluids

(O41) Near field distribution on the surface of spherical particles forming a two dimensional array in light-absorbing medium

(O42) Parameters of differential equations in four-flux and two-flux models approximated for wo3-nio inorganic electrochromic devices

(O43) Interferometry laser imaging for droplet sizing (ILIDS) with not fully defocused images

(O44) Samarium-based complex salt micro-/nanoparticles: from synthesis to laser excitation fluorescence lifetime dynamics

(O45) Sum-rules methods for spectral response functions

(O46) Fano-resonance assisted optical pulling force on plasmonic nanoparticles under femtosecond pulsed excitation

POSTER PAPERS

(P1) Size-mediated photophoresis of a core-shell microparticle

(P2) The super-resolution image distortion and correction of microsphere nanoscopy

(P3) Higher-order optical force theory and their application in manipulating particles

(P4) Tunable optical force on a gold nanosphere by coating hybrid organic-inorganic perovskite

(P5) Analysis of photonic nanojet based on finite difference frequency domain

(P6) The internal - field distributions of chiral particle by dual Hermite Gaussian

beams

(P7) Scattering by a plasma anisotropic coated sphere located in an off-axis zero-order Bessel beam

(P8) Tunable terajets formed by microsphere compound lenses

(P9) Scattering of Gaussian beams by a rotating dielectric cylinder

(P10) Combination of vectorial complex ray model and equivalent current method for the scattering field near rainbow caustics

(P11) Research on holographic focusing schlieren imaging for three dimensional inhomogeneous flow field visualization

(P12) Accuracy of the anomalous diffraction approximation in modelling scattering patterns of biological cells

(P13) Magnetic resonance generated by a rotating dielectric cylinder

(P14) A theoretical scattering model of the rain–wind–sea wave interactions at high winds

(P15) Reflection and refraction of Gaussian beam by a biaxial anisotropic slab

(P16) Light scattering by a metal sphere using physics informed neural network

(P17) The optical fiber coupling efficiency in the near-sea atmosphere is optimized by using a focusing mirror

(P18) On-axis average intensity of radially polarized Anomalous vortex beams in maritiem turbulent atmosphere

(P19) Light scattering by anisotropic objects using physics-informed neural network

(P20) A line-by-line calculation model of the radiation characteristics of high temperature gases

Keynote Lecture:

Optical forces and torques in structured light

Speaker:

Baoli Yao, Xiaohao Xu (Xi'an Institute of Optics and Precision Mechanics, Chinese Academy of Sciences, China)

Abstract:

The discovery of novel optical forces and torques has triggered the revolution in optical manipulation. The birth of this subject is marked by the observation of radiation pressure in 1901, which was subsequently used for atom cooling, awarded a Nobel Prize for Chu, Cohen-Tannoudki & Phillips in 1997. The finding of gradient force directly led to the advent of optical tweezers, which earned Ashkin a share of the 2018 Nobel Prize in Physics. Recent progress concerning the discovery of curl force and nontrivial optomechanical manifestations, including the negative optical forces and lateral optical forces, has breathed new life into this flourishing subject. In this talk, we report the observation of a novel type of optical force, which originates from the imaginary Poynting momentum of light. We will also uncover the existence of optical gradient and curl torques, which represent the rotational analogs of the gradient and curl forces. By utilizing the two fundamental torque components and sculpting light fields, we achieved the negative optical torques and the lateral optical torques. This work highlights an important and previously overlooked connection among optomechanics, light structure and Mie-tronics, and is expected to have far-reaching consequences in life science, modern physics and nanotechnology.

Biography:

Prof. Dr. Baoli Yao received the B.S. degree in Applied Physics at Xi'an Jiaotong University, China in 1990, and the Ph.D. degree in Optics at Xi'an Institute of Optics and Precision Mechanics (XIOPM), CAS in 1997. He pursued the postdoc at Institute for Physical Chemistry, Technical University of Munich, Germany during 1997-1998. He obtained the professorship at XIOPM in 1999. He is a senior member of OSA, and the director of State Key Laboratory of Transient Optics and Photonics, China. His research fields include: super-resolution and 3D optical microscopy, digital holographic microscopy, imaging through scattering medium, optical micro-manipulation and photomechanics. He has published more than 330 papers in peer-reviewed journals and 7 book's chapters, and owned 25China & 1 US invention patents. He obtained the High-speed Imaging Award of Japan in 2015.

Keynote Lecture:

Electromagnetic Forces in Continuous Media

Speaker:

Vadim Markel, University of Pennsylvania, USA

Abstract:

Electromagnetic forces acting on continuous media has been subject to much research and controversy. At the root of all difficulties is the fact that the expression for the Lorentz force does not contain a magnetic moment directly. Therefore, when computing the force acting on magnetized matter, one needs a model for magnetization (either Amperian current loops or displacement of imaginary magnetic monopoles). The two models result in two different force densities, but the differences are subtle. In spite of some claims to the contrary, both expressions are consistent with the laws of conservation of energy and momentum. However, a more delicate question is whether the correct form of electromagnetic force density can be established by the so-called Balazs thought experiment, which examines the motion of the center of energy of the system ``electromagnetic pulse + object''. I will show that a careful analysis of the experiment reveals that both models for the force density are consistent with linear motion of the center of energy, which is expected or any closed system. Consequently, the model in which magnetization is represented by Amperian current loops is fully consistent with all conservation laws, and one can abandon the model of magnetic monopoles, which have not been observed in nature. This conclusion has also an implication for the form of the Poynting vector in magnetized media

Biography:

Vadim Markel earned an undergraduate degree in Physics with specialization in Quantum Optics from Novosibirsk State University in 1987. From 1987 through 1993, he worked at the Institute of Automation and Electrometry of the Siberian Branch of the Russian Academy of Sciences conducting research in nonlinear and statistical optics. He received PhD in Physics (Optics) from New Mexico State University in 1996 and continued with postdoctoral studies in quantum many-body theory at the University of Georgia (1998-1999) and in inverse problems and imaging at the Washington University – St. Louis (1999-2001). He is currently an Associate Professor of Radiology at the University of Pennsylvania. Dr. Markel has spent two years (2015-2017) as an A*MIDEX Excellence Chair at the University of Aix-Marseille and Institut Fresnel in France and a year (2018-2019) as a visiting scholar at the University of Michigan. He was selected as an Outstanding Referee by the APS (2016) and by the IoP (2018). Dr. Markel's research spans optical physics and electromagnetic theory with applications to photonics and biomedical imaging.

Keynote Lecture:

Make the beam shape coefficient evaluation easy by using scalar spherical wave expansion and addition theorem

Speaker:

Jianqi Shen, University of Shanghai for Science and Technology, China

Abstract:

The calculation of beam shape coefficients (BSCs) is crucial in investigating the interaction between shaped beams and spherical particles. Different techniques have been developed in the framework of generalized Lorenz-Mie theory (GLMT). Even though, it is still hard in formulating the analytical expressions of the BSCs, especially for off-axis located beams, and also in coding. In some circumstances numerical computation for the BSCs is time-consuming. The work presents an indirect method for formulating and evaluating the BSCs. Based on the spherical wave expansion of scalar functions and the addition theorem, the indirect method simplifies the analytical work and speeds up the BSC computation.

Biography:

Prof. Jianqi Shen got his doctor degree from university of Shanghai for Science and Technology in 1999 and 4 years late he got his second doctor degree in Brandenburg university of Cottbus. Now he is working in university of Shanghai for Science and Technology. He is on the board of Chinese Society of Particuology. His research interest covers particle size analysis and electromagnetic scattering.

Keynote Lecture:

Digital holography for particle characterization: hologram modeling, refractive index measurement, and optical compression

Speaker:

Fabrice R.A. Onofri, Lilian Chabrol, Paul Bresson, Fabrice Lamadie, Aix-Marseille Université, CNRS, IUSTI, UMR 7343, France

Abstract:

Digital In-Line Holography is a highly attractive optical method for the simultaneous determination of the three dimensional positions and velocities, the shape and size of particles (drops, bubbles, bacteria, etc.) dispersed in a fluid. In this keynote, after a summary of the basics of the DIH, the authors review their latest contributions to further enhance its capabilities, and most notably on the asymptotic modelling and understanding of hologram formation, refractive index measurements and reduction of the sensor filling rate.

Biography:

Fabrice Onofri is a research director at the French National Center for Scientific Research (CNRS). He earned his Ph.D. degree at the University of Rouen and his habilitation degree at Aix-Marseille University, France. His research mainly focuses on the optical and electromagnetic characterization of particle and particle systems. Over the years, his research has found applications in various fields ranging from aerosols and multiphase flows to soft matter and plasma physics, in the frame of national and international projects as well as industrial granted projects.

Keynote Lecture:

Super-resolution Fluorescence and Quantitative Phase Microscopy Visualize Live Cells in 3D

Speaker:

Peng Gao, School of Physics, Xi'dian University, Xi'an 710071, China

Abstract:

Optical three-dimensional (3D) microscopy is of great importance in many fields, especially in biology. Due to the transparency of biological samples (such as biological cells) under visible light, optical 3D microscopy is often implemented with fluorescence imaging, phase contrast imaging, or other nonlinear processes to enhance the contrast of intracellular structures. In this talk, two 3D optical microscopic technique, namely, sparse scanning structured illumination microscopy (SS-SIM) and quantitative phase contrast tomography (QPCT), will be presented. In SS-SIM, structured patterns of different orientations and different phase shifts are generated by resonantly scanning a focused light and modulating its intensity sinusoidally. As a consequence, super-resolution and optical-sectioned fluorescence imaging with a penetration depth of ~300 micrometers can be performed, implying a great potential for deep tissue imaging. In QPCT, 24 LEDs distributed on a ring are lighted up one by one sequentially to generate oblique illuminations at different angles, and quantitative phase contrast imaging for each illumination is carried out by retardering the dc term for four different phase shifts with an ultra-fast SLM. A 3D tomographic phase map is reconstructed from the complex amplitudes obtained at different illumination angles. Both the SS-SIM and QPCT were utilized to obtain 3D subcellular organelles inside live COS7 cells. The comparison of the two imaging modalities tells that SS-SIM enables visualization of specific subcellular organelles in virtue of fluorescence tagging. While, QPCT can visualize up to ten types of subcellular organelles once for all, for that nearly all the subcellular organelles have different refractive index above the cytosol. The combination of the 3D fluorescence and phase images provide complementary information for the same sample, contributing to revealing the mechanisms of many life events.

Biography:

Prof. Dr. Peng Gao, studied Physics and received his Ph.D. at the Xi'an Institute of Optics and Precision Mechanics (XIOPM), CAS, in 2011. He was a "Humboldt Fellow" in University Stuttgart (2012-2014) and Marie-Curie Fellow (IEF) in KIT (2014-2018). He is currently a PI at Xidian University and the director of Super-resolution Optical Microscopy Engineering Research Center at Xi' an city. His group focuses on developing super-resolution optical microscopy and quantitative phase microscopy techniques for biology. So far, he has authored over 100 peer-reviewed papers published in journals, including Nat. Photonics, Adv. Opt. Photon. Some of his publications were

highlighted by tens of international media, such as Science Daily, Physics News, and so on. He is currently one of the associate editors of Optics and Laser Technology (OLT) and Frontiers in Physics.

Keynote Lecture:

The discrete dipole approximation for light-scattering simulations

Speaker:

Maxim A. Yurkin, CORIA, University of Rouen Normandy

Abstract:

Light scattering is widely used in remote sensing of various objects ranging from metal nanoparticles and macromolecules to atmospheric aerosols and interstellar dust, being in some cases the only available approach to characterize their geometric or optical properties. All these applications require accurate simulations, which are not trivial for particles of arbitrary shape and internal structure. The discrete dipole approximation (DDA) is one of the general methods to handle such problems. In this talk I will start with an introduction to the DDA, including both the basic underlying physical picture and rigorous derivation starting from the integral form of Maxwell's equation for the electric field. The latter shows that the DDA is a numerically exact method and a special case of volume-discretization method of moments. Importantly, the DDA applies to almost any electromagnetic problem involving non-magnetic particles. It can handle arbitrary shaped beams, particles in complicated environments (e.g., on a multi-layered substrate), and simulate a broad range of quasi-classical electromagnetic phenomena (such as emission enhancement, near-field radiative heat transfer, and electron energy-loss spectroscopy). I will also discuss computational aspects, including the latest efficiency improvements, and the existing open-source DDA codes that largely explain the method's popularity. Finally, I will highlight current capabilities and limitations (open questions) of the DDA.

Biography:

Maxim A. Yurkin received his BS and MS degrees in physics from the Novosibirsk State University (NSU) with honors (2002, 2004), and dual PhD in computer science and biophysics from the University of Amsterdam and Voevodsky Institute of Chemical Kinetics and Combustion (ICKC, Novosibirsk), respectively (2007). Currently, he is a CNRS researcher (Chair of Excellence by Normandy Region) at CORIA, University of Rouen Normandy. His research interests include the theory and simulations of electromagnetic scattering, the discrete dipole approximation (DDA), and inverse light-scattering problems. Specifically, he has made multiple important contributions to the theory and numerical efficiency of the DDA, and is the main developer of the open-source ADDA code. He received inaugural Young Scientist's Award in electromagnetic and light scattering from Elsevier (2007) and two Prizes of the Academia Europaea for Russian young scientists (2010, 2016).

Keynote Lecture:

Wave scattering by many small particles, creating materials with a desired refraction coefficient and other applications

Speaker:

Alexander G. Ramm, Kansas State University

Abstract:

The theory of wave scattering by many small impedance particles of arbitrary shapes is developed. The basic assumptions are: $a \ll d \ll \lambda$, where a is the characteristic size of particles, d is the smallest distance between the neighboring particles, λ is the wavelength. This theory allows one to give a recipe for creating materials with a desired refraction coefficient. One can create material with negative refraction: the group velocity in this material is directed opposite to the phase velocity. One can create a material with a desired wave focusing property. Quantum-mechanical scattering by many potentials with small supports is considered. Equation is derived for the EM field in the medium in which many small impedance particles are embedded. Similar results are obtained in [6] for heat transfer in the media in which many small particles are distributed. The theory presented in this talk is developed in the author's monographs and in papers. Practical realizations of this theory are discussed. The problem of creating material with a desired refraction coefficient is discussed in the case when the material is located inside a bounded closed connected surface on which the Dirichlet boundary condition is imposed.

Biography:

Alexander G. Ramm was born in Russia, emigrated to USA in 1979 and is a US citizen. He is Professor Emeritus of Mathematics with broad interests in analysis, scattering theory, inverse problems, theoretical physics, engineering, signal estimation, tomography, theoretical numerical analysis and applied mathematics. He is an author of 725 research papers, 23 research monographs and an editor of 3 books. He has lectured at many Universities throughout the world, gave more than 155 invited and plenary talks at various Conferences and had supervised 11 Ph.D students. He was Fulbright Research Professor in Israel and Ukraine; distinguished isiting professor in Mexico and Egypt; Mercator Professor in Germany; Research Professor in France; invited plenary speaker at the 7-th PACOM; he won Khwarizmi international award in 2004 and received other honors. A.G.Ramm was the first to prove uniqueness of the solution to inverse scattering problems with fixed-energy scattering data; the first to prove uniqueness of the solution to inverse scattering problems with non-over-determined scattering data and the first to study inverse scattering problems with under-determined scattering data. He solved many-body wave scattering problem when the bodies are small particles of arbitrary shapes. He gave formulas for the scattering

amplitude for scalar and electromagnetic waves by small bodies of arbitrary shapes and analytical formulas for the polarizability tensors for these bodies. He gave a solution to the Pompeiu problem, proved the Schifier's conjecture and gave many results about symmetry problems for PDE, including first symmetry results in harmonic analysis. He has developed the Dynamical Systems Method (DSM) for solving linear and nonlinear operator equations, especially ill-posed. He developed random fields estimation theory for a wide class of random fields. He has developed a theory of convolution equations with hyper-singular integrals and solved analytically integral equations with hyper-singular kernels. He has introduced a wide class of domains with non-compact boundaries. He developed the theory of local, pseudolocal and geometrical tomography.

The 14th International Conference on
Laser-light and Interactions with Particles (LIP2024)
September 18-22nd, 2024, Xi'an, Shaanxi, China

Transmission of Gaussian pulses Light in low visibility haze

Xinyu WEI, Qiang XU*, Yiping HAN, Zhensen WU

School of Physics, Xidian University, Xi'an 710071, P.R.China
Corresponding author:qxu@xidian.edu.cn

Abstract

In wireless optical communication, aerosol particles such as rain, fog, smoke, and haze are the main sources of interference for pulse signals. Through the absorption and scattering of lasers, these interference sources can cause intensity attenuation and waveform distortion of pulse signals, seriously affecting the quality and bandwidth of information transmission Studying the scattering and transmission characteristics of aerosol particles on different types of pulsed lasers has important scientific significance and application value, which will provide key basis for laser communication, laser detection, laser fuse anti smoke interference, etc.

1 Gaussian pulse scattering characteristics

Unlike continuous lasers, ultra short pulse lasers have many characteristics such as narrow pulse width, wide spectrum, and high peak power, which have made them widely used [1-3] In recent years, with the rapid development of mode locking and chirped pulse amplification technology [4], researchers have achieved the generation of ultra short pulses with different pulse widths (picosecond [6], femtosecond [7]) in multiple frequency bands (such as optical band, mid infrared band [5]). Mees et al. analyzed the temporal changes of the scattering field and internal field spatial distribution of spherical particles under Gaussian pulse incidence [8,9]

The difference between pulse waves and continuous waves lies in their waveform discontinuity and amplitude fluctuation. Due to the differences between the two types of incident waves, the scattering characteristics of particles under pulse wave incidence may differ from those under continuous wave incidence. Therefore, the study of pulse transmission needs to first consider the scattering characteristics of particles in pulse waves.

Assuming a pulse expression is:

$$\vec{E}_i = \vec{E}_0 g(t_e)\exp(i\omega_0 t_e) \tag{1}$$

In the formula, $\vec{E}_0$ is the initial electric field vector, $g(t_e)$ is the pulse envelope function, $\exp(i\omega_0 t_e)$ is the carrier wave with frequency ω_0, $t_e = t - z/c + \psi$ is the phase time shift factor, and ψ is the initial phase.

By representing equation (1) using the spectral function $G(\omega)$ of the pulse envelope $g(t_e)$, we obtain

$$\vec{E}_i = \vec{E}_0\left[\int_0^\infty G(\omega-\omega_0)\exp(i\omega t_e)\mathrm{d}\omega + \int_0^\infty G^*(\omega+\omega_0)\exp(-i\omega t_e)\mathrm{d}\omega\right] \tag{2}$$

In the formula, $G^*(\Omega)=G(-\Omega)$, asterisks represent complex conjugation.

Within a certain spectral range, the electric field component of scattered pulses can be expressed as:

$$E_{s\theta} = -iE_{s2}\cos\varphi \tag{3}$$

$$E_{s\varphi} = iE_{s1}\sin\varphi \tag{4}$$

and,

$$E_{sk} = E_0\frac{c}{r}\left[\int_0^\infty G(\omega-\omega_0)\frac{1}{\omega}S_k(\theta,\omega)\exp(i\omega t_e)\mathrm{d}\omega + \int_0^\infty G^*(\omega+\omega_0)\frac{1}{\omega}S_k^*(\theta,\omega)\exp(i\omega t_e)\mathrm{d}\omega\right] \quad k=1,2 \tag{5}$$

Among them, $S_k(\theta,\omega)$ is the amplitude function of Mie scattering.

Let the input pulse function be

$$u_i(i) = \exp(-t^2/T^2)\cos\omega_0 t \tag{6}$$

If the Gaussian envelope pulse width T is given, it can be concluded that when $t_1 = t_2 = t$ the output pulse envelope is

$$\left\langle |u(t)|^2 \right\rangle = \left[T/(2\pi)^{1/2}\right]\int_0^\infty \exp\left[-(T^2/8)\omega_d^2\right]A(\omega_d)\cdot\cos\left[\omega_d t_e - \phi(\omega_d)\right]\mathrm{d}\omega_d \tag{7}$$

In the formula, $t_e = t - z/c$.

2 the simulation results

The formula derived from the above theory can accurately calculate the transmission characteristics of envelope Gaussian pulses. Take the input pulse width as T=1ns,10ns , transmission distance $z = 5\mathrm{km}$, light wavelength $\lambda = 0.6943\mu\mathrm{m}$, scattering particle diameter $D = 9\mu\mathrm{m}$, and particle scattering cross-section $\sigma_s = 1.272\times10^{-10}\,\mathrm{m}^2$. The theoretical derivation of the pulse transmission formula was simulated using these parameters, and the simulation results are shown in Figure 1.

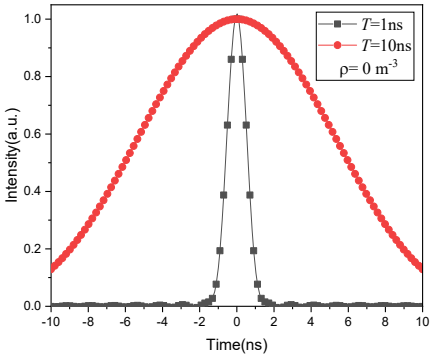

(a)

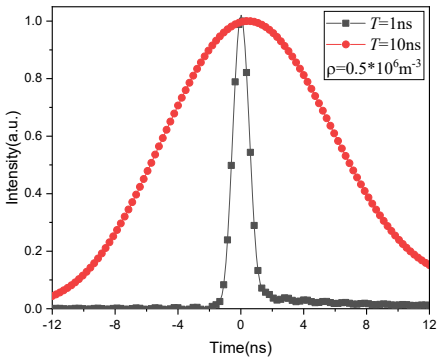

(b)

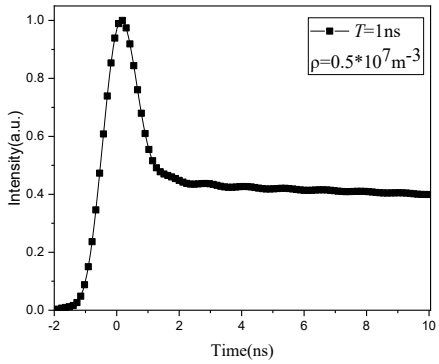

(c)

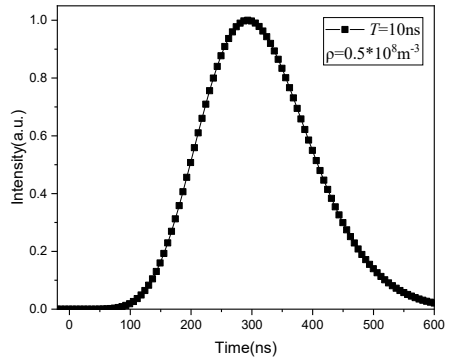

(d)

Figure1 Transmission of Gaussian envelope pulses under different conditions

The transmission and reception waveforms of Gaussian envelope pulses under the above parameter conditions are shown in Figure 1. Figure (a) shows the received waveform of Gaussian envelope pulses transmitted in free space; Figure (b) shows the received waveforms of pulse transmission with two different pulse widths at medium concentrations; Figure (c) shows the received waveform of pulse transmission with pulse width at medium concentration; The received waveform of pulse transmission with pulse width at medium concentration is shown in Figure (d).

3 Acknowledgement

This work was supported by the National Natural Science Foundation of China (Grant no. 61975158) and Aeronautical Science Foundation (Grant no.2023M073081004).

4 Reference

[1] [Wang X L , Zhai H C , Wang Y ,et al.Spatially angular multiplexing in ultra-short pulsed digital holography[J].Acta Physica Sinica, 2006, 55(3):1137-1142.DOI:10.1016/S0379-4172(06)60105-4.

[2] Leburn C G .Unifying ultrafast laser imaging and spectroscopy: Pioneering technology demonstrates how ultrafast laser sources can enable 3D imaging of cells at high resolution and in real time[J].PhotonicsViews, 2021, 18(3):96-99.DOI:10.1002/phvs.202100043.

[3] Kejin Z , Lei L , Qingwei Z ,et al.Influence of different scattering medium on propagation characteristics to femtosecond laser pulses[J]. *Acta Phys. Sin.*, 2019, 68(19). 194207

[4] Xiaonong Zhu, Wenxia Bao. Fundamentals of Ultrashort Pulse Laser and Its Applications[J]. Chinese Journal of Lasers, 2019, 46(12): 1200001

[5] Qi W S , Ying D , Liang Z Y ,et al.Theoretical study on generating mid-infrared ultrashort pulse in mode-locked Er~(3+):ZBLAN fiber laser[J].Acta Physica Sinica, 2016.DOI:10.7498/aps.65.044206.

[6] Chunmei O , Lu C , Hui Z ,et al.Experimental study on all-normal-dispersion mode-locked fiber laser with optimal spectral filtering position[J].Acta Physica Sinica - Chinese Edition-, 2010, 59(6):3936-3941.DOI:10.3724/SP.J.1077.2010.01263.

[7] Chen X , Minglie H , Dapeng Z ,et al.High energy dissipative soliton mode-locked fiber oscillator based on a multipass cell [J]. *Acta Phys. Sin*. 2013, 62(5):54203-054203.DOI:10.7498/aps.62.054203.

[8] Mees L ,G. Gréhan, Gouesbet G .Time-resolved scattering diagrams for a sphere illuminated by plane wave and focused short pulses[J].Optics Communications, 2001, 194(1-3):59-65.DOI:10.1016/S0030-4018(01)01268-8.

[9] Mees L , Gouesbet G ,Gréhan, Gerard.Scattering of laser pulses (plane wave and focused Gaussian beam) by spheres[J].Applied Optics, 2001,

40(15):2546.DOI:10.1364/AO.40.002546.

The 14th International Conference on
Laser-light and Interactions with Particles (LIP2024)
September 18-22nd, 2024, Xi'an, Shaanxi, China

COMPLEX CHARACTERISTICS OF BESSEL BEAMS

Guoxia Han*, Yihan Tian, Shiru Song, Qihui Zhao and Yunzhen Xing

College of Science, China University of Petroleum (East China), Qingdao 266580, China
Corresponding author: gxhan@upc.edu.cn

Abstract

We conduct a comprehensive investigation and research on the scattering, focusing and self-accelerating characteristics of Bessel beams based on the generalized Lorenz-Mie theory(GLMT), scalar diffraction theory and Richards-Wolf vector diffraction theory and the angular spectrum propagation theory. The research presented in this paper offers significant guidance for important applications such as communication, national defense, medicine and micro/nano processing.

1 Introduction

In 1987, Durnin proposed a special solution for the scalar wave equation in free space [1]. Through experiments, it has been proven that the field described by this special solution has non-diffracting characteristics and the field distribution in the transverse cross-section remains unchanged and exhibits the form of the first type of Bessel function. Durnin calls this type of beam as "non-diffracting beam", known as the Bessel beam [9].

In recent years, the research on Bessel beams in particle scattering, analysis of focusing characteristics, and superposition of Bessel beam has regained the attention of many scientists [2-4]. In addition, due to the correlation between vortex phase and orbital angular momentum (OAM) of high-order Bessel beams, they are used as ideal light sources for particle rotation and atomic control [5-7]. By utilizing the vortex phase of high-order Bessel beams, optical tweezers can also be devised that possess the capability to simultaneously manipulate multiple particles [8].

In this work, firstly, the scattering characteristics of the beam are investigated and the influence of Bessel beam parameters on the generation of "photonic nanojets" with spherical particle is explored. Secondly, based on scalar diffraction theory and Richards-Wolf vector diffraction theory, we explore the focusing characteristics of vector Bessel beam under high and low Numerical Aperture(NA) lenses and the Perfect Optical Vortex (POV) beams, double POV beams (DR-POV) and POV beams' arrays under paraxial and non-paraxial conditions are obtained. Finally, based on the theory of angular spectrum modulation and trajectory modulation, a series of Bessel beams with a symmetrical spot distribution and self-accelerating along a desirable trajectory are achieved.

2 Scattering characteristics of Bessel beams

We compute the intensity of the scattering field resulting from the interaction between Bessel beams and spherical particles and the influence of the parameters (polarization state, cone angle, spatial topological charge and beam center) on scattering characteristics is analyzed.

The results in figure 1 show that the cone angle of Bessel beams affects the length of the "photonic nanojets" and the intensity of focused field. As the half-cone angle increases, the primary lobe of the Bessel beam undergoes a narrowing process, and simultaneously, the dielectric particles' focusing effect on the beam weakens. As a result, the intensity of the light field after being scattered and focused by spherical particles gradually decreases, and the length of the "jets" formed is constantly decreasing. Additionally, the shape of the scattering field is changed with different spatial topological charges and the petal-shaped focal plane can be obtained.

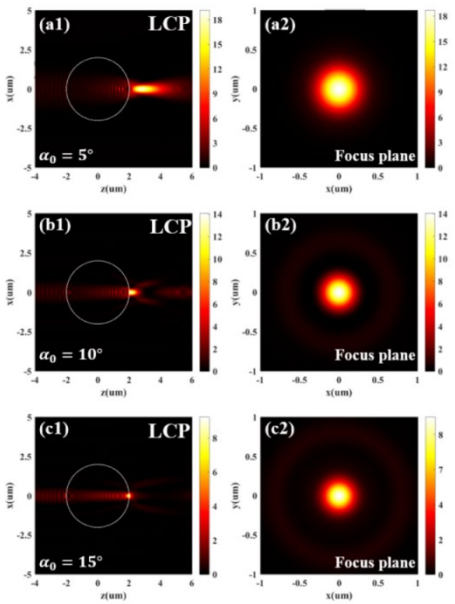

Figure 1 *Intensity distribution of left-handed circularly polarized Bessel beams with different half-cone angles incident on spherical particles, (a1)- (c1) y=0 planes and (a2)- (c2) focusing planes.*

3 Focusing characteristics of Bessel beams

Based on the Richards-Wolf vector diffraction theory, the tightly focused field distribution of Bessel beams under different polarization is calculated. As shown in figure 2, the tightly focused field of radially polarized Bessel beam is weaker than circularly polarized counterpart. And as the topological charge increases up to 35, the difference gradually diminishes. Moreover, the tight focusing characteristics of double Bessel beam and multi-focal Bessel beam were also studied, and at the tightly focused field, DR-POV beams and POV beam arrays are formed, respectively.

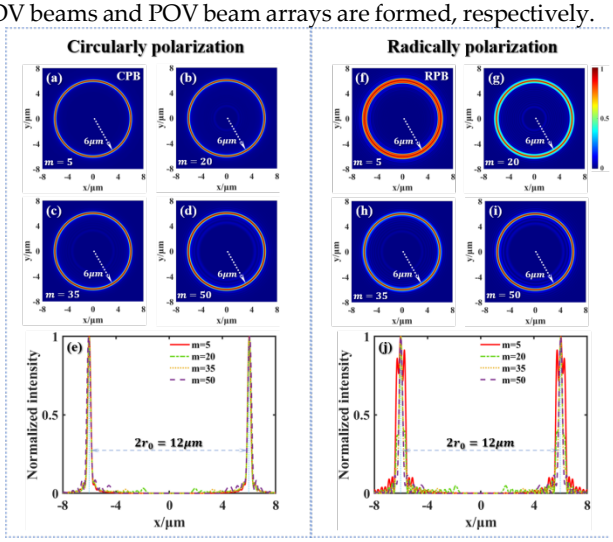

Figure 2 *Intensity distribution in the focal plane of (a)-(e) circularly polarization Bessel beam and (f)-(j) radically polarization Bessel beam with topological charge m=5, 20, 35, 50. (e), (j) the one-dimensional intensity distribution of the focal point along the x-axis.*

4 Self-accelerating characteristics of Bessel beams

Mathematical transformations of angular spectrum propagation theory are employed to derive the formula for calculating arbitrary propagation intensity and trajectory control. For propagation intensity modulation, the resultant angular spectrum is obtained by applying an amplitude factor $\mathrm{I}(\mathrm{z})$,

$$A(\sqrt{k^2-k_z^2}) = \frac{2}{\mathrm{rect}(\frac{k_z}{2k})k_z}\int_{-\infty}^{+\infty}\sqrt{I(z)}e^{ik_{z0}z}e^{-ikz}dz$$

Based on the Fourier translation theorem, the angular spectrum of propagation trajectory modulation at the position $(\mathrm{z}, \mathrm{z}+\Delta\mathrm{z})$ is derived,

$$A(\sqrt{k^2-k_z^2}) = \frac{2}{\mathrm{rect}(\frac{k_z}{2k})k_z}\int_{-\infty}^{+\infty}e^{-ik_x f(z)-ik_y g(z)+ik_{z0}z}e^{-ikz}dz$$

We have implemented self-accelerating Bessel Beams using angular spectrum propagation and trajectory modulation. Figure 3 shows Bessel beams propagating along parabola, hyperbolic secant curves, cosine curves and spatial spiral trajectories, respectively. The intensity distribution of the transverse cross-section light field at different propagation positions of the beam is not deformed by the periodic fluctuations of the beam. That is, the beam has maintained non-diffracting characteristics. Therefore, we generate Bessel beams with a circularly symmetrical spot structure, non-diffracting and desirable trajectories.

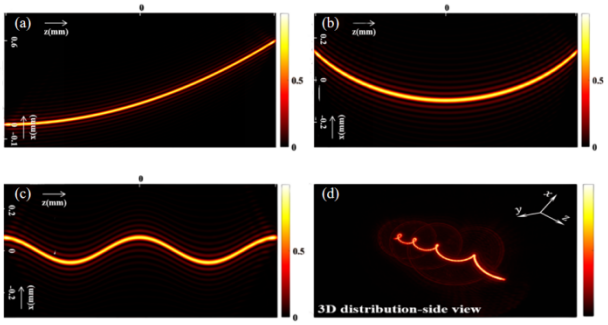

Figure 3 *Intensity distribution of self-accelerating Bessel beams at y=0 plane along (a)parabola (b)hyperbolic secant curves (c)cosine curves (d) spatial spiral trajectories.*

5 Conclusion

The characteristics of Bessel beams — scattering characteristics, focusing characteristics, and self-acceleration characteristics—are studied, which deepen the understanding of Bessel beams and lay the foundation for their application in various fields.

6 References

[1] Durnin J., Exact solutions for non-diffracting beams. I. The scalar theory[J]. JOSA A, 1987, 4(4): 651-654.

[2] Bai J., Gao Y., Ge X C., et al., Scattering properties of dual Bessel beams on chiral layered particle[J]. Journal of Quantitative Spectroscopy and Radiative Transfer, 2024,323109049.

[3] Ding Z., Yu Y., Li S., Hou C., Focusing property of auto-focusing Bessel beams[J]. Optics express, 2023, 31(20): 33228-33240.

[4] Vasilyeu R., Dudley A., Khilo N., et al., Generating superpositions of higher–order Bessel beams[J]. Optics Express, 2009, 17(26): 23389-23395.

[5] Č,ižmár T., Kollárová V.,et al., Generation and control of multiple Bessel beams for optical micro-manipulation[J]. Univ. of St. Andrews (United Kingdom); Palacky Univ. (Czech Republic), 2008, 703870380Q-70380Q-7.

[6] Rhodes D.P., Lancaster G.P.T., Livesey J., et al., Guiding a cold atomic beam along a co-propagating and oblique hollow light guide[J]. Optics Communications, 2002, 214(1-6): 247-254.

[7] Florjańczyk M., Tremblay R., Guiding of atoms in a travelling-wave laser trap formed by the axicon [J]. Optics Communications, 1989, 73(6): 448-450.

[8] Kamath P.P., Sil S., Truong G.V., et al., Particle trapping with optical nanofibers: a review [Invited]. [J].Biomedical optics express,2023,14(12):6172-6189.

[9] Durnin J., Miceli Jr.J.J, Eberly J.H., Diffraction-free beams[J]. Physical Review Letters, 1987, 58(15): 1499.

The 14th International Conference on
Laser-light and Interactions with Particles (LIP2024)
September 18-22nd, 2024, Xi'an, Shaanxi, China

POLYCHROMATIC GENERALIZED LORENZ-MIE THEORY

Leonardo André Ambrosio[1], Jhonas Olivati de Sarro[1], Gérard Gouesbet[2]

[1] Department of Electrical and Computer Engineering, University of São Paulo, São Carlos, SP, 13566-590, Brazil.
[2] Coria, Normandie University, Saint-Etienne du Rouvray, 76800, France.

Corresponding author: leo@sc.usp.br

Abstract

A theoretical framework for a polychromatic generalized Lorenz-Mie theory (PGLMT) is presented. Such an approach relies on an extension of the monochromatic generalized Lorenz-Mie theory *stricto sensu* (GLMT), which deals with the interaction between a homogeneous spherical particle and a monochromatic arbitrary-shaped beam, through time-averaging the fields and physical quantities. The concept of Field Shape Spectra (FSS) is introduced and a connection is established with the beam shape coefficients (BSCs) in the GLMT. An example of field description is given based on the superposition of three (red, green and blue) Gaussian-like laser beams, for which the FSS becomes simple weighted sums of BSCs. The theoretical work here presented, although direct and intuitive, is important whenever light-matter interactions with spherical scatterers and polychromatic optical fields must be considered and is a first step towards a more general approach for arbitrary-shaped particles.

1 Introduction

The (monochromatic) GLMT here considered has its theoretical roots on Bromwich potentials in accordance with the notations presented by Gouesbet and Gréhan in Ref. [1] and assuming a time-harmonic factor exp(+$i\omega t$), where ω is an arbitrary but fixed angular frequency. In this framework, such scalar auxiliary potentials are at the core of a partial wave expansion in spherical coordinates (r,θ,ϕ), from which the electric and magnetic fields for the incident, scattered and internal waves are found through Maxwell's equations. These fields are subsequently used to derive important physical quantities in light-matter interactions and electromagnetic scattering, such as scattered intensities and phase angles, radiation pressure, extinction and scattering cross sections, among others.

Successfully as it stands, the GLMT *stricto sensu* has several intrinsic restrictions: (i) the particle must be spherical; (ii) the particle must be homogeneous; (iii) the incident field is assumed to be a monochromatic laser beam. While the first two restrictions have been largely explored and overcome during the past decades, see for instance database provided by in Refs. [2-5], the latter has not been yet addressed in the literature. In order to assess a secure route to those willing to perform computational simulations and investigate physical phenomena with polychromatic waves, a PGLMT is welcome and deserves a dedicated study [6].

Let us consider a Bromwich scalar potential of the form $U^i_{TX}(\mathbf{r},t)=U^i_{TX}(\mathbf{r},\omega)\exp(i\omega t)$, where TX = TM (Transverse Magnetic) or TE (Transverse Electric). This represents the instantaneous complex potential of an incident monochromatic wave in the GLMT and is written as:

$$U^i_{TX}(\mathbf{r},t)=\sum_{n=1}^{\infty}\sum_{m=-n}^{n}c_n^{pw}(\omega)G^m_{n,TX}(\omega)\frac{\psi_n[k(\omega)r]}{k(\omega)}P_n^{|m|}(\cos\theta)e^{im\phi}e^{i\omega t}, \tag{1}$$

In Eq. (1), the frequency dependence is explicitly taken into account. Besides, $\psi_n(.)$ is a Ricatti-Bessel function associated with spherical Bessel functions of the first kind, $P_n^m(.)$ are associated Legendre functions in Robin's notation [7], and $k(\omega)$ is the wave number. Notice that $c_n^{pw}(\omega)$ is the usual plane wave constant from the GLMT.

Instead of the usual BSCs $g^m_{n,TX}$, here we have introduced frequency dependent quantities $G^m_{n,TX}(\omega)$. For continuous frequency dependent quantities, $G^m_{n,TX}(\omega)$ is a function of a continuous variable and represents a field shape spectrum. For incident fields composed of a set of j beams with discrete frequencies wj, $G^m_{n,TX}(\omega)$ becomes a distribution proportional to the BSCs and weighted by their corresponding electric or magnetic field strengths E_{0j} and H_{0j}, respectively. In this way, the field strengths E_0 and H_0 in the GLMT are absorbed by the FSS $G^m_{n,TX}(\omega)$.

In this way, it can be shown from (1) and remembering that $E_{r,TE}$ = $H_{r,TM}$ = 0, $E^i_{r,TM}=\partial_r^2U^i_{TM}-\mu\varepsilon\partial_t^2U^i_{TM}$ and $H^i_{r,TE}=\partial_r^2U^i_{TE}-\mu\varepsilon\partial_t^2U^i_{TE}$ in the GLMT, that the incident electric radial field component in the PGLMT can be expressed as:

$$\begin{aligned}E^i_r(\mathbf{r},t)&=\int_{-\infty}^{\infty}E^i_{r,TM}(\mathbf{r},\omega)e^{i\omega t}d\omega\\&=\int_{-\infty}^{\infty}\left\{\sum_{n=1}^{\infty}\sum_{m=-n}^{n}n(n+1)c_n^{pw}(\omega)G^m_{n,TM}(\omega)\right.\\&\left.\times\frac{\psi_n[k(\omega)r]}{k(\omega)r^2}P_n^{|m|}(\cos\theta)e^{im\phi}e^{i\omega t}\right\}d\omega\end{aligned} \tag{2}$$

A similar expression for $H^i_r(\mathbf{r},t)$ can be written from (2) by replacing $G^m_{n,TM}(\omega)$ by $G^m_{n,TE}(\omega)$. Notice that the permeability μ and permittivity ε can also be frequency dependent quantities.

Introducing orthogonality relations for the ϕ-dependent exponentials and similarly for associated Legendre functions of the same order m but different degrees n [8], the FSS $G^m_{n,TM}(\omega)$ can be isolated in (2) and in the expression for $H^i_r(\mathbf{r},t)$. They will read as:

$$\begin{Bmatrix} G^m_{n,TM}(\omega) \\ G^m_{n,TE}(\omega) \end{Bmatrix} = \frac{1}{4\pi c_n^{pw}(\omega)} \frac{2n+1}{n(n+1)} \frac{(n-|m|)!}{(n+|m|)!} \frac{k(\omega)r^2}{\psi_n[k(\omega)r]} \times \int_0^{\pi}\int_0^{2\pi} \begin{Bmatrix} E^i_r(\mathbf{r},\omega) \\ H^i_r(\mathbf{r},\omega) \end{Bmatrix} P_n^{|m|}(\cos\theta) e^{-im\phi} \sin\theta d\phi d\theta \quad (3)$$

In deriving (3), we have followed the convention that

$$X(\mathbf{r},t) = \int_{-\infty}^{\infty} X(\mathbf{r},\omega)\exp(i\omega t)d\omega$$

$$X(\mathbf{r},\omega) = \frac{1}{2\pi}\int_{-\infty}^{\infty} X(\mathbf{r},t)\exp(-i\omega t)d\omega$$

Suppose the incident field is now a multichromatic wave represented by the sum of J monochromatic fields, each of which operating at a frequency ω_j as follows:

$$E^i_r(\mathbf{r},t) = \sum_{j=1}^{J} E^i_r(\mathbf{r},\omega_j)e^{i\omega_j t}$$
$$H^i_r(\mathbf{r},\omega) = \sum_{j=1}^{J} H^i_r(\mathbf{r},\omega_j)e^{i\omega_j t} \quad (4)$$

The fields in (4) can represent, for instance, the red, green and blue lasers (J = 3) in an RGB laser system, with $E^i_r(\mathbf{r},\omega)$ and $H^i_r(\mathbf{r},\omega)$ being exactly the radial incident field components of the monochromatic GLMT. The new multichromatic fields in (4) have the following FSS, which are a simplification of (3):

$$\begin{aligned} \begin{Bmatrix} G^m_{n,TM}(\omega) \\ G^m_{n,TE}(\omega) \end{Bmatrix} &= \sum_{j=1}^{J} \frac{1}{4\pi c_n^{pw}(\omega)} \frac{2n+1}{n(n+1)} \frac{(n-|m|)!}{(n+|m|)!} \frac{k(\omega)r^2}{\psi_n[k(\omega)r]} \\ &\times \int_0^{\pi}\int_0^{2\pi} \begin{Bmatrix} E^i_r(\mathbf{r},\omega_j) \\ H^i_r(\mathbf{r},\omega_j) \end{Bmatrix} P_n^{|m|}(\cos\theta) e^{-im\phi} \sin\theta d\phi d\theta \delta(\omega-\omega_j) \\ &= \sum_{j=1}^{J} \begin{Bmatrix} G^m_{n,TM}(\omega_j) \\ G^m_{n,TE}(\omega_j) \end{Bmatrix} \delta(\omega-\omega_j) \\ &= \sum_{j=1}^{J} \begin{Bmatrix} E_0(\omega_j) g^m_{n,TM}(\omega_j) \\ H_0(\omega_j) g^m_{n,TE}(\omega_j) \end{Bmatrix} \delta(\omega-\omega_j) \end{aligned} \quad (5)$$

where, as stated, $g^m_{n,TM}(\omega_j)$ and $g^m_{n,TE}(\omega_j)$ are the BSCs for the j-th beam oscillating at ω_j, and $E_0(\omega_j)$ and $H_0(\omega_j)$ are normalization factors corresponding to the field strengths for the j-th beam. The expression for the FSS in (5) must be used in the context of (2) in order to recover (4). Expressions for all the incident, scattered and internal field components, as well as physical quantities of interest such as scattered intensities, phase angles, extinction, scattering and absorption cross sections and radiation pressure cross sections can be found, for instance, in Ref. [9], together with details of calculation.

2 Numerical results and disscussion

As an example of computation of (2) and (5), we consider the time-average incident electric field intensity $|\mathbf{E}|^2$ of a set of red, green and blue +z-propagating Bessel beams [J = 3 in (4)] in air, with operating wavelengths frequencies λ_1 = 632.8 nm (He-Ne laser), λ_2 = 532 nm (Nd:YAG laser) and λ_3 = 441.6 nm (He-Cd laser). All three beams have the same order v = 0 and the same polarization [circularly symmetric (1,0)]. The axicon angles are α_1 = 10°, α_2 = 12° and α_3 = 14°, respectively. Finally, the analytical expressions for the electric field components and the BSCs for an off-axis displacement (x_0,y_0,z_0) are given by (1), (10) and (11) of Ref. [9] using a Cartesian coordinate system (x,y,z) attached to the spherical system. In the (P)GLMT, the off-axis position is taken with respect to a spherical scatterer whose center is located at the origin.

To calculate $<|\mathbf{E}|^2> = <|E_r|^2 + |E_\theta|^2 + |E_\phi|^2>$ we proceed as follows. First, notice from (2) that

$$\left\langle \left|E^i_r(\mathbf{r},t)\right|^2 \right\rangle = \lim_{T\to\infty} \frac{1}{T}\int_{-T/2}^{T/2} \left(\int_{-\infty}^{\infty}\int_{-\infty}^{\infty} E^i_r(\mathbf{r},\omega) \times E^{i*}_r(\mathbf{r},\omega') e^{i(\omega-\omega')t} d\omega d\omega' \right) dt \quad (6)$$

Now, since

$$\lim_{T\to\infty} \frac{1}{T}\int_{-T/2}^{T/2} e^{i(\omega-\omega')t} dt = \begin{cases} 1, & \omega = \omega' \\ 0, & \text{otherwise} \end{cases} \quad (7)$$

It follows from (5), (6) and (7) that, for the multichromatic field composed of three Bessel beams,

$$\left\langle \left|E^i_r(\mathbf{r},t)\right|^2 \right\rangle = \sum_{j=1}^{3} \left|E^i_r(\mathbf{r},\omega_j)\right|^2 \quad (8)$$

Figures 1(a)-(c) show the total time-averaged electric field intensities in the x_0-y_0 plane using the analytical expressions available in Ref. [9]. The fields have been calculated at r = 0, that is, at the origin. The corresponding RGB composition is seen in Fig. 1(d).

Similarly, Figs. 1(e)-(h) show the reconstructed PGLMT fields computed with the FSS in (5). The accurateness of the reconstruction can be inferred from Fig. 2, where the logarithm of the percent error, which is given by $100(<|\mathbf{E}^{exa}|^2> - <|\mathbf{E}^{GLMT}|^2>)/<|\mathbf{E}^{exa}|^2>$. Truncation of the infinite sums over n have been taken into account in accordance with Wiscombe's criterion [10]. An excellent agreement has been achieved, with very low error.

3 Acknowledgement

L. A. Ambrosio thanks CNPq (309201/2021-7) and FAPESP (2020/05280-5) for supporting this work.

4 Conclusions and perspectives

In this work we have shown that the PGLMT can accurately reproduce the polychromatic fields composed of discrete sums of monochromatic beams. To do so, circularly symmetric Bessel beams were considered, and the reconstructed electric fields compared to those available in the literature and that exactly satisfies Maxwell's equations. The next steps include considering distinct amplitudes for the RGB beams, a larger range of discrete frequencies and other types of monochromatic beams. Also, it is important for the PGLMT to be tested with field shape spectra of pulses, since ultimately this is the most appealing application of the present theory. This is currently in progress.

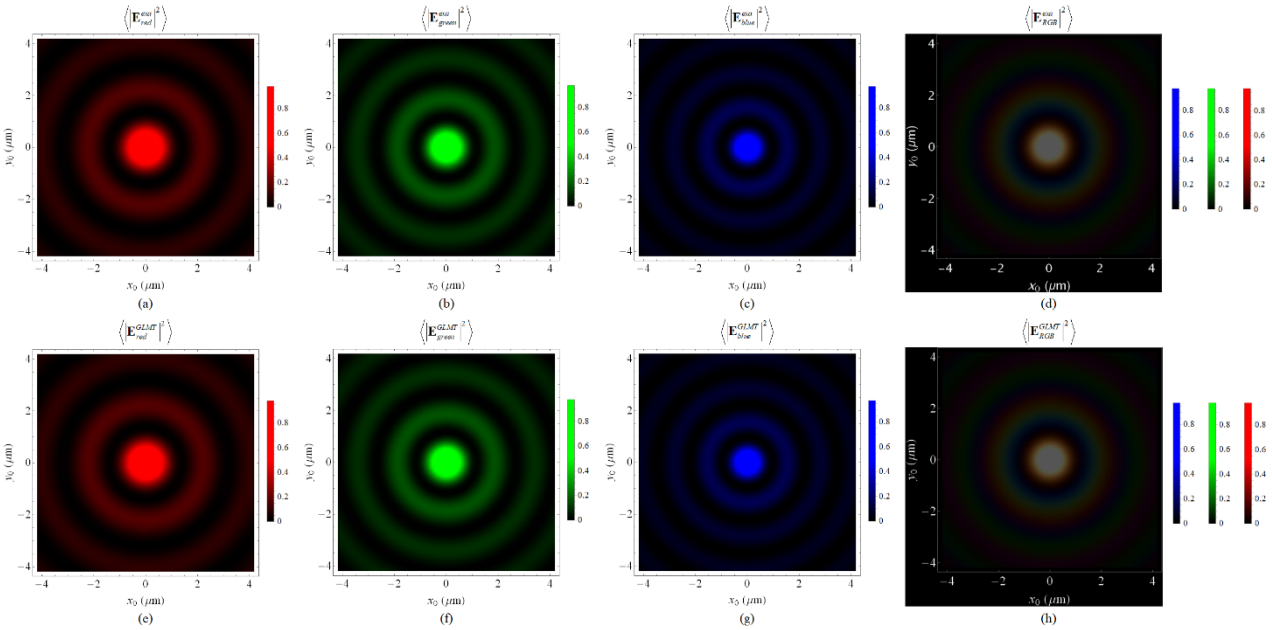

Figure 1 *(a)-(c) Exact total time-averaged electric field intensities for the red, green and blue Bessel beams, respectively, in the x_0-y_0- plane. (d) RGB composition for (a)-(c), using Wolfram Mathematica's function "ColorCombine". (e)-(h) Same as (a)-(d), now for the fields reconstructed using the PGLMT.*

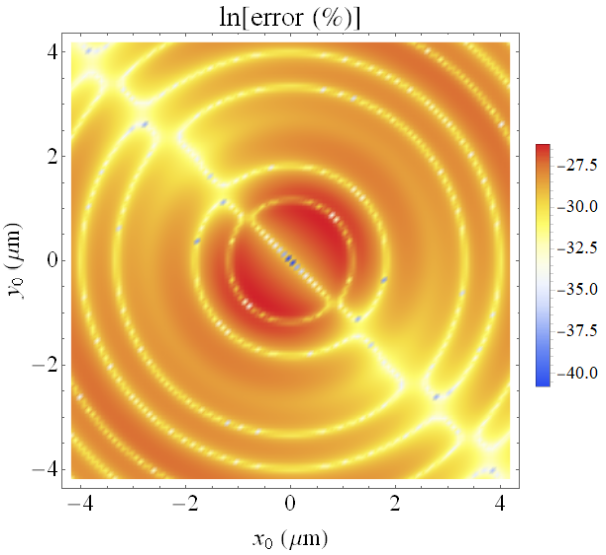

Figure 2 *Logarithm of the percent error for the fields given in Figs. 1(d) and (h). The PGLMT here presented and detailed in Ref. [6] is accurate enough to reconstruct polychromatic fields, thus representing a robust approach for the calculation of physical quantities in polychromatic light-matter interactions.*

5 References

[1] G. Gouesbet, and G. Gréhan, *Generalized Lorenz-Mie Theories* (Springer, 2nd. Ed., 2017).

[2] G. Gouesbet, T-matrix formulation and generalized Lorenz–Mie theories in spherical coordinates, Opt. Communications 283(4):517-521 (2010).

[3] G. Gouesbet, J. Lock, List of problems for future research in generalized Lorenz–Mie theories and related topics, review and prospectus [Invited], Appl. Opt. 52(5):897-916 (2013).

[4] G. Gouesbet, Latest achievements in generalized Lorenz-Mie theories: A commented reference database, Annal. Phys. 526(11-12):461-489 (2014).

[5] G. Gouesbet, T-matrix methods for electromagnetic structured beams: A commented reference database for the period 2014–2018, J. Quant. Spectrosc. Radiat. Transfer 230:247-281 (2019).

[6] L. A. Ambrosio, J. O. de Sarro, G. Gouesbet, An approach for a polychromatic generalized Lorenz-Mie theory, J. Quant. Spectrosc. Radiat. Transfer 312:108824 (2024).

[7] L. Robin, *Fonctions sphériques de Legendre et fonctions sphéroidales* (Gauthier-Villars, Paris, Volumes 1, 2, 3, 1957).

[8] G. B. Arfken GB, H. J. Weber. *Mathematical methods for physicists* (Harcourt/Academic Press, 2001).

[9] J. J. Wang, T. Wriedt, L. Mädler, Y. P. Han, and P. hartmann, Multipole expansion of circularly symmetric Bessel beams of arbitrary order for scattering calculations, Opt. Communications 387, 102-109 (2017).

[10] Wiscombe W.J., Improved Mie scattering algorithms, Appl. Opt. 19(9):1505-1509 (1980).

The 14th International Conference on
Laser-light and Interactions with Particles (LIP2024)
September 18-22nd, 2024, Xi'an, Shaanxi, China

DESCRIPTION OF THE BSCS OF 1D FWS AFTER TWO PAIRS OF LENSES

Jhonas O. DE SARRO [1,*], Beatriz H. D. ROCHA [1], Leonardo A. AMBROSIO [1] and Gerárd GOUESBET [2]

[1] Department of Electrical and Computer Engineering, University of São Paulo, São Carlos, SP, 13566-590, Brazil
[2] Coria, Normandie University, Saint-Etienne du Rouvray, 76800, France

Corresponding author: jodesarro@usp.br, jodesarro@gmail.com

Abstract

We present, for the first time, a work that effectively deals with a more realistic description of a Frozen Wave (FW) in electromagnetic scattering. Based on the generalized Lorenz–Mie theory (GLMT), we mathematically describe a FW beam that actually interacts with a scatterer after passing through two optical 4f systems, each one composed of a pair of convex lenses. The considered FW is linearly polarized and composed of zero-order Bessel beams (BBs). Applications encompass optical trapping and micromanipulation, volumetric displays, and so on.

1 Introduction

Frozen Wave (FW) is a technique capable of engineering the intensity shape of non-diffracting beams along the propagation axis, having many potential applications, among others, in optical trapping and micromanipulation of particles [1,2]. The theoretical description of the interaction between spherical particles and electromagnetic FW fields (which leads to the prediction of forces, torques, and so on) is commonly undertaken upon the generalized Lorenz–Mie theory (GLMT) [3,4,5,6]. In the context of the GLMT, the fields are characterized by means of two expansion coefficients named the beam shape coefficients (BSCs) and the Mie (internal and scattered) coefficients, the first carrying geometrical information concerning the incident beam and the latter being related to geometrical and electromagnetic properties of the particle [7].

When a FW is experimentally generated for some specific purposes (e.g., optical tweezers and 2D or 3D image reconstruction), a pre-treatment of the beam is essential if it is desired to reach some degree of proportion between its transverse and longitudinal dimensions—its spot size is very small when compared to its depth of field [8,9]. The referred proportion may be experimentally achieved with the aid of $4f$ optical systems. Such technique may be analytically described for paraxial FWs, for one and two $4f$ systems, using the Fresnel diffraction integral [8,10].

In this work, we shall express the scalar field of a paraxial FW after it had crossed two $4f$ systems and then write the expressions of the BSCs for a linearly polarized beam by considering the scalar solution as a transverse component of the electric field. Finally, we shall present numerical simulations for the intensity of the field components which, as will be seen, are closer to that observed in recent experiments in optical micromanipulation [8].

2 Frozen Waves after two pair of lenses

Let us consider a paraxial, scalar FW-type beam as the incident field, made by a discrete superposition of $2N+1$ zero order BBs of same angular frequency ω_0 ($k=2\pi/\lambda=\omega_0/c$, where λ is the wavelength and c the light-speed in vacuum), with distinct longitudinal and transverse wave numbers given respectively by $\beta_q=Q+2\pi q/L\geq 0$ and $h_q=[2k(k-\beta_q)]^{1/2}$, and with origin at O of a $O_{\xi\eta\zeta}$ Cartesian coordinate system, such an origin coinciding with the location of the center of the first lens L_1', of focal length f_1', of a $4f$ system, as shown in Fig. 1(a).

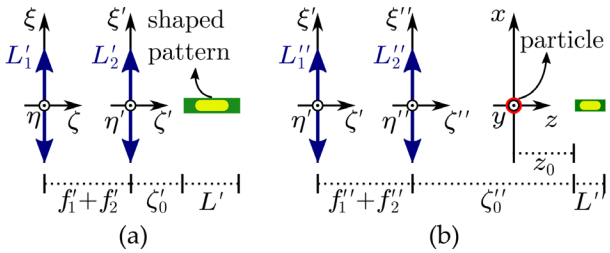

Figure 1 *(a) FW (indicated as shaped pattern) after one $4f$ system, the origin of $O_{\xi\eta\zeta}$ and $O'_{\xi'\eta'\zeta'}$ coincide respectively with the center of the first and the second lenses. (b) Same as in (a) but now after a second $4f$ system. The O^P_{xyz} system is placed at the scatterer (the red dot) and the pattern is shaped at a longitudinal distance z_0 from it.*

The intensity of such incident field is intended to mimic, inside a longitudinal interval $[0,L]$ (in the $O_{\xi\eta\zeta}$ system), and around the axis, any longitudinal intensity profile $|F(z)|^2$ freely chosen *a priori*, so that the complex coefficients that weight amplitudes and phases in the superposition can be analytically extracted, in the $e^{i\omega t}$ convention, as $A_q=(1/L)\int_0^L F(z)\exp(i2\pi q\zeta/L)d\zeta$ [1,2].

After a longitudinal distance $f_1'+f_2'$, the beam emerges from the origin O' of the $O'_{\xi'\eta'\zeta'}$ system, where a lens L_2' of focal length f_2' is placed. According to [10], the

emerging field can be mathematically described in the $O'_{\xi'\eta'\zeta'}$ system by

$$\psi'(\xi',\eta',\zeta') = \sum_{q=-N}^{N} A'_q J_0\left(h'_q\sqrt{\xi'^2+\eta'^2}\right)e^{-i\beta'_q(\zeta'-\zeta'_0)}, \quad (1)$$

in which $A'_q = -(f'_1/f'_2)\exp(-ikg')A_q$, $\beta'_q = k - h'^2_q/2k$, $h'_q = -h_q f'_1/f'_2$, $g' = (f'_1+f'_2)(1+f'_1/f'_2)+\zeta'_0[1-(f'_1/f'_2)^2]$, and $\zeta'_0 = (f'_1+f'_2)f'_2/f'_1$. Therefore, the beam is transverse and longitudinally deformed by $|h'^{-1}_0|/|h^{-1}_0| = f'_2/f'_1$ and $L'/L = (f'_2/f'_1)^2$ [10], respectively, and its structuring occurs inside the interval $[\zeta'_0, \zeta'_0+L']$ with respect to the $O'_{\xi'\eta'\zeta'}$ system.

After a second pair of lenses L'_1 and L'_2 of focal lengths f'_1 and f'_2, see Fig. 1(b), the beam can be mathematically described with relation to a $O''_{\xi''\eta''\zeta''}$ Cartesian coordinate system, with origin O'' at the axial center of lens L'_2, by simply duplicating the prime symbols in Eq. (1) and in the definitions related to it, except for the longitudinal displacement, $\zeta''_0 = \zeta'_0(f''_2/f''_1)^2 + (f''_1+f''_2)f''_2/f''_1$. Therefore, after this second $4f$ system, the resulting beam is longitudinally structured inside the interval $[\zeta''_0, \zeta''_0+L'']$ with respect to the $O''_{\xi''\eta''\zeta''}$ reference system, and its deformations are given by $|h''^{-1}_0|/|h^{-1}_0| = f''_2 f'_2/f''_1 f'_1$ and $L''/L = (f''_2 f'_2/f''_1 f'_1)^2$ in the transverse and longitudinal directions, respectively.

3 The beam shape coefficients

In the GLMT framework, it is of common practice to consider a spherical particle centered at the origin O^P of a O^P_{xyz} Cartesian coordinate system [red particle in Fig. 1(b)], and so to describe the BSCs and other physical quantities at a given distance from this scatterer [7]. From such consideration, with the z axis being colinear to the propagation axes ζ, ζ' and ζ'', and the axes x parallel to the axes ξ, ξ' and ξ'' (and so, y parallel to η, η' and η''), we can write the expression of the scalar field for an on-axis FW after two $4f$ systems, in the O^P_{xyz} coordinate system, by duplicating the primes of Eq. (1), that is:

$$\psi''(x,y,z) = \sum_{q=-N}^{N} A''_q J_0\left(h''_q\sqrt{x^2+y^2}\right)e^{-i\beta''_q(z-z_0)}, \quad (2)$$

where z_0 is the longitudinal distance from the particle to the beginning of the shaped beam.

The BSCs of monochromatic, on-axis arbitrary-order FWs are known for a wide variety of polarizations [3,4,5,6]. For the representative particular case of on-axis, zero-order x polarized FW, with Eq. (2) being the component in x of the electric field (and other components calculated through Gauss' law), it is direct the rewriting of the BSCs for TM modes [6]:

$$g^m_{n,TM} = \frac{1}{2}i^{m+1}(-1)^{(m-|m|)/2}\frac{(n-m)!}{(n+|m|)!}\sum_{q=-N}^{N}A''_q e^{i\beta''_q z_0} \times\left\{J_{m-1}(0)e^0\left[m\pi^m_n\left(\frac{\beta''_q}{k}\right)+\frac{k}{\beta''_q}\tau^m_n\left(\frac{\beta''_q}{k}\right)\right]\right. \quad (3)$$
$$\left. + J_{m+1}(0)e^0\left[m\pi^m_n\left(\frac{\beta''_q}{k}\right)-\frac{k}{\beta''_q}\tau^m_n\left(\frac{\beta''_q}{k}\right)\right]\right\},$$

and also for TE modes [6]:

$$g^m_{n,TE} = -\frac{i}{2}i^{m+1}(-1)^{(m-|m|)/2}\frac{(n-m)!}{(n+|m|)!}\sum_{q=-N}^{N}A''_q e^{i\beta''_q z_0} \times\left\{J_{m-1}(0)e^0\left[m\frac{k}{\beta''_q}\pi^m_n\left(\frac{\beta''_q}{k}\right)+\tau^m_n\left(\frac{\beta''_q}{k}\right)\right]\right. \quad (4)$$
$$\left. - J_{m+1}(0)e^0\left[m\frac{k}{\beta''_q}\pi^m_n\left(\frac{\beta''_q}{k}\right)-\tau^m_n\left(\frac{\beta''_q}{k}\right)\right]\right\}.$$

For the case of only one $4f$ system, it suffices to remove one prime of the double-primed symbols in Eqs. (2)–(4).

4 Numerical simulation

As an example, let us consider similar parameters as those used by Suarez et al. to generate the scalar FW [8]: $\lambda = 514\,\text{nm}$, $Q = 0.999993k$, $N = 27$, $L = 2\,\text{m}$, $f_1 = f_3 = 150\,\text{mm}$, $f_2 = 50\,\text{mm}$, $f_4 = 25\,\text{mm}$, and

$$F(z) = \begin{cases} 1, & 0.10\,\text{m} \le z \le 0.15\,\text{m} \\ 1, & 0.20\,\text{m} \le z \le 0.25\,\text{m} \\ 0, & \text{elsewhere.} \end{cases} \quad (5)$$

Following the presented background, the scalar field and the x component of the electric field are calculated through Eq. (2). The electric field is assumed x polarized and the remaining y and z components are evaluated via Gauss' law. The results are presented in Fig 2.

In Fig. 2(a), we have comparison plots between the intensities of the scalar field ψ and the component x of the electric field, at the origin of the O^P_{xyz} system. In Figs. 2(b) and 2(c), we have the same, but for now for ψ' and ψ'', respectively. Their transverse and longitudinal deformations can be evaluated resulting respectively in 0.333 and 0.111, after the first $4f$ system, and in 0.056 and 0.031, after the two $4f$ systems, as can be also visualized in the plots. The others components can be appreciated in Figs. 2(d)–2(f).

5 Conclusions and perspectives

In the present work, using the GLMT, we show a method to describe the BSCs of a paraxial FW after two $4f$ systems. We presented an example of a x polarized FW indicating that the resulting field is indeed deformed in both longitudinal and transverse dimensions. Future works may consider the generalization of the method by the inclusion of an arbitrary number of $4f$ systems, the analysis and description of other kinds of polarization, and also the inclusion of several FW beams aiming to describe longitudinally-structured light-

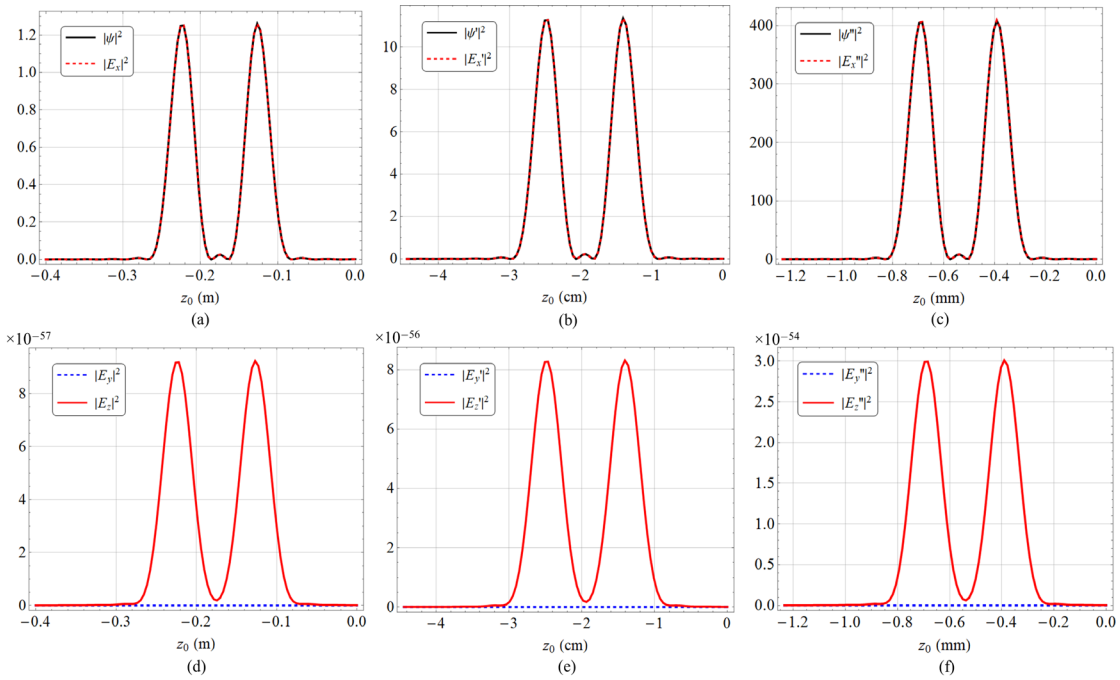

Figure 2 *(a) Original scalar field ψ and GLMT-remodeled x component field E_x intensities at the origin of the O_{xyz} system, as a function of the axial displacement z_0. (b) and (c) Same as (a), but now for ψ' and ψ'', respectively. (d)-(f) y and z components of the electric field as calculated from the GLMT and associated with the scalar fields ψ' and ψ'', respectively. The scalar field is assumed to generate a x polarized FW.*

sheets after 4f systems (this requires the analysis of off-axis FWs, which is already under development by the authors). We envision many possible applications such as optical trapping and micromanipulation of multiple particles, volumetric and holographic displays, optical scalpels, and so on.

6 Acknowledgement

L. A. A. thanks CNPq (309201/2021-7) and FAPESP (2020/05280-5) for supporting this work.

7 References

[1] M. Zamboni-Rached, "Stationary optical wave fields with arbitrary longitudinal shape by superposing equal frequency Bessel beams: Frozen Waves," *Opt. Express*, vol. 12, no. 17, pp. 4001–4006, Aug. 2004, doi: 10.1364/OPEX.12.004001.

[2] M. Zamboni-Rached, E. Recami, and H. E. Hernández-Figueroa, "Theory of 'frozen waves': modeling the shape of stationary wave fields," *J. Opt. Soc. Am. A*, vol. 22, no. 11, pp. 2465–2475, Nov. 2005, doi: 10.1364/JOSAA.22.002465.

[3] L. A. Ambrosio and M. Zamboni-Rached, "Analytical approach of ordinary frozen waves for optical trapping and micromanipulation," *Appl. Opt.*, vol. 54, no. 10, pp. 2584–2593, Jan. 2015, doi: 10.1364/AO.54.002584.

[4] N. L. Valdivia and L. A. Ambrosio, "On Analytical Descriptions of Finite-Energy Paraxial Frozen Waves in Generalized Lorenz-Mie Theory," in *2017 SBMO/IEEE MTT-S International Microwave and Optoelectronics Conference (IMOC)*, Aguas de Lindoia, Brazil: IEEE, Nov. 2017, pp. 1–5. doi: 10.1109/IMOC.2017.8121078.

[5] L. A. Ambrosio, "Circularly symmetric frozen waves: Vector approach for light scattering calculations," *J. Quant. Spectrosc. Radiat. Transf.*, vol. 204, pp. 112–119, Jan. 2018, doi: 10.1016/j.jqsrt.2017.09.007.

[6] L. A. Ambrosio, M. Z. Rached, and G. Gouesbet, "Discrete vector frozen waves in generalized Lorenz–Mie theory: linear, azimuthal, and radial polarizations," *Appl. Opt.*, vol. 57, no. 12, pp. 3293–3300, Apr. 2018, doi: 10.1364/AO.57.003293.

[7] G. Gouesbet and G. Gréhan, *Generalized Lorenz-Mie Theories*. Springer-Verlag Berlin Heidelberg, 3rd ed., 2023.

[8] R. A. B. Suarez, L. A. Ambrosio, A. A. R. Neves, M. Zamboni-Rached, and M. R. R. Gesualdi, "Experimental optical trapping with frozen waves," *Opt. Lett.*, vol. 45, no. 9, p. 2514, Apr. 2020, doi: 10.1364/OL.390909.

[9] A. H. Dorrah *et al.*, "Light sheets for continuous-depth holography and three-dimensional volumetric displays," *Nat. Photonics*, vol. 17, no. 5, pp. 427–434, May 2023, doi: 10.1038/s41566-023-01188-y.

[10] M. Zamboni-Rached, G. de A. Lourenço-Vittorino, T. V. de Sousa, J. A. V. Mendonça, J. N. Pereira, and E. Recami, "Mathematical description of a Frozen Wave beam after passing through a pair of convex lenses with different focal distance." arXiv, Sep. 24, 2019. doi: https://doi.org/10.48550/arXiv.1907.08202.

The 14th International Conference on
Laser-light and Interactions with Particles (LIP2024)
September 18-22nd, 2024, Xi'an, Shaanxi, China

ON A RELATIONSHIP BETWEEN ELECTROMAGNETIC AND ACOUSTICAL BEAM SHAPE COEFFICIENTS

Gouesbet Gérard[1],Leonardo A. Ambrosio[2]

And Jianqi Shen[3]

1. CORIA-UMR6614, Normandie Université, CNRS-Université et INSA de Rouen, Campus universitaire du Madrillet, 76800, Saint-Etienne du Rouvray, France
2. Department of Electrical and Computer Engineering, São Carlos School of Engineering, University of São Paulo, 400 Trabalhador São-Carlense Ave., São Carlos, SP 13566-590, Brazil
3. College of Science, University of Shanghai for Science and Technology, 516 Jungong Road, Shanghai, 200093, China

Corresponding author: gouesbet@coria.fr

Abstract

In both some T-matrix theories (namely Generalized Lorenz-Mie Theory and Extended Boundary Condition Method) and in acoustics, incident fields may be expressed in terms of expansions over basic functions with expansion coefficients expressed in terms of beam shape coefficients. Although electromagnetic scattering is a vectorial scattering and acoustical scattering is a scalar scattering, it is possible to provide relationships between electromagnetic and acoustical beam shape coefficients, as examined in the present work.

1 Introduction

The strong analogy between electromagnetic and acoustical scatterings allows one to transfer the arsenal to the evaluation of beam shape coefficients (BSCs), available for Generalized Lorenz-Mie Theory (GLMT) and Extended Boundary Condition Method (EBCM) for structured beams, to the field of acoustical scatterings. See [1]-[4] for the localized approximation, [5] for the finite series, and all of them for quadratures.

Another question is to ask whether there would not be any direct relationship between electromagnetic and acoustical BSCs. This question is addressed in the present work.

2 Background and motivation

The approach used is motivated by the electromagnetic Davis scheme of approximations to the description of Gaussian beams [6]-[8]. This approximation relies on a x-polarized potential vector $\mathbf{A} = (A_x,0,0)$ for a Gaussian beam propagating in the z-direction (with the use of a time dependence factor of the form $\exp(i\omega t)$. The x-component of the potential vector is searched under the form of a series involving even powers of the beam confinement factor, leading to a series of successive approximations depending on the number of the terms retained in the series, and electric and magnetic fields successive approximations are afterward obtained using the Lorenz gauge.

In the present work, we use the same scheme but with the x-polarized component of the potential vector expressed in spherical coordinates r, θ and φ using the form of an acoustical field, satisfying Helmholtz equation, in a lossless medium and neglecting nonlinear effects, reading as [9]-[12]:

$$\psi_A = \psi_{A0} \sum_{n=0}^{\infty} \sum_{m=-n}^{+n} c_{n,A}^{pw} g_{n,A}^{m} X_n^m(r,\theta,\varphi) \qquad (1)$$

in which ψ_{A0} is an acoustical force strength, $c_{n,A}^{pw}$ is an acoustical plane wave coefficient (superscript pw) whose expression can be omitted here, $g_{n,A}^{m}$ denotes acoustical BSCs, and X_n^m are basic functions whose expression can as well be omitted here.

The analogy with electromagnetic scattering may be shown with the somewhat similar expression for the radial magnetic field reading as:

$$H_r = H_0 \sum_{n=0}^{\infty} \sum_{m=-n}^{+n} c_n^{pw} g_{n,TE}^{m} X_n^m(r,\theta,\varphi) \qquad (2)$$

in which H_0 is an electromagnetic force strength, c_n^{pw} denotes electromagnetic plane wave coefficients (superscript pw), $g_{n,TE}^{m}$ denotes electromagnetic Transverse Electric (TE) BSCs, and X_n^m are the same basic functions than in Eq. (1). We have a quite similar approach for the Transverse Magnetic (TM) BSCs associated with the radial component of the electric field.

3 Relation between acoustical and electromagntic BSCs

Let $A_x = \psi_A$ be taken as the x-component of a potential vector and proceed in the same way than in the electromagnetic Davis scheme of approximation. The magnetic field is obtained in the Lorenz gauge using, e.g. Eq.(1.110) in [13]:

$$\mathbf{H} = \nabla \times \mathbf{A}/\mu \quad (3)$$

in which μ is the permeability of the medium in which the wave is propagating. We then use the expression of the curl in spherical coordinates, particularly the expression for the r-coordinate reading as:

$$(\nabla \times \boldsymbol{A})_r = (\partial A_\varphi \sin\theta/\partial\theta - \partial A_\theta/\partial\varphi)/(r\sin\theta) \quad (4)$$

in which we implement the expressions of A_θ and A_φ to eventually obtain an expression of H_r in terms of the derivatives of A_x with respect to θ and φ.

The rest of the calculation is afterward carried out as follows: (i) the expression for H_r so obtained is equated with the expression of H_r given by Eq. (2), (ii) the derivatives of $A_x = \psi_A$ are evaluated using Eq. (1), (iii) the $\varphi -$ terms are eliminated by using classical relations of orthogon ality involving $\exp[i(m\text{-}m')\varphi]$ leading to an expression containing only a summation over n, (iv) to obtain a solution it is sufficient to remove the summation and finally (v) we get rid of the coordinate θ by setting $\theta = \pi/2$. The result obtained, after having implemented the expressions for the acoustical and electromagnetic plane wave coefficients, then reads as:

$$g_{n,TE}^{m} = P_1[g_{n,A}^{m+1}\tau_n^{|m+1|}(0) - g_{n,A}^{m-1}\tau_n^{|m-1|}(0)]/P_n^{|m|}(0) \quad (5)$$

in which P_1 is a prefactor irrelevant in the present context and τ_n^m denotes generalized Legendre functions with a classical notation. Since $P_n^{|m|}(0)$ is 0 for $(n - m)$ odd, Eq. (5) holds for $(n - m)$ even.

For $(n - m)$ odd, we derive the expression of H_r, expressed in terms of derivatives of A_x with respect to θ, proceed afterward in a way similar to the case $(n - m)$ even, eventually setting $\theta = \pi/2$, and obtain:

$$g_{n,TE}^{m} = P_1\{g_{n,A}^{m+1}\left[\tau'^{|m+1|}_n(0) + (m+1)\pi_n^{|m+1|}(0)\right] - g_{n,A}^{m-1}[\left[\tau'^{|m-1|}_n(0) - (m-1)\pi_n^{|m-1|}(0)\right]\}/D \quad (6)$$

in which a prime denotes a derivative with respect to the argument $\cos\theta$, π_n^m denotes generalized Legendre functions using again a classical notation, and in which D is a short-hand notation for the derivative of $P_n^{|m|}(\cos\theta)$ with respect to the argument, taken at $\theta = \pi/2$.

The fact that we consider separately the cases $(n - m)$ even and $(n - m)$ odd is reminiscent of a procedure used when the BSCs are evaluated by using the finite series technique, invented decades ago for electromagnetic BSCs [14]-[15], with a recent renewal in electromagnetism, e.g. [16] and references therein, and with an application to acoustical waves [17].

The electric field is treated similarly, although with an increased need of algebra, using either, e.g. Eq. (1.120) in [13]:

$$\mathbf{E} = (\nabla \times \nabla \times \mathbf{A})/(i\omega\mu\varepsilon) \quad (7)$$

in which ε is the permittivity of the medium in which the wave is propagating, or; e.g. Eqs. (1.117) and (1.120) in [13]:

$$\mathbf{E} = [\nabla(\nabla \cdot \mathbf{A}) - \nabla^2\mathbf{A}]/(i\omega\mu\varepsilon) \quad (8)$$

After a significant amount of algebra, it is found that, both for $(n - m)$ even and $(n - m)$ odd, the TM-BSCs associated with the electric field are obtained.

4. Localized approximations and on-axis beams

The results obtained in Eqs. (5) and (6) allow one to build a bridge between the localized approximation procedures used for both electromagnetic and acoustical waves, although under slightly different forms.

Let us consider an electromagnetic arbitrary shaped beam, in particular an electromagnetic on-axis Gaussian beam. The localized approximation $g_{n,TE}^{m,LA}$ (in which "LA" stands for "Localized Approximation") to the BSCs $g_{n,TE}^{m}$ reads as [18]:

$$g_{n,TE}^{m,LA} = (-i/Q)^{|m|-1}X\ (Q, \pi/2) \quad (9)$$

in which X is an operator and Q a function of n and m which do not need to be specified in the present context.

This is to be compared with the expression for the localized approximation $g_{n,A}^{m,LA}$ to the BSCs $g_{n,A}^{m}$ derived for on-axis Gaussian acoustical waves reading as [1]:

$$g_{n,A}^{m,LA} = (-i/Q)^{|m|}Y\ (Q, \pi/2) \quad (10)$$

in which Y is an operator which do not need to be specified in the present context.

Now, assume $m = \pm 1$ in Eq. (9), it corresponds to $m = 0$ in Eq. (10). This is in agreement with the fact, valid for both localized and non-localized on-axis BSCs, that the non-zero electromagnetic BSCs are for $m = \pm 1$ and that the non-zero acoustical BSCs are for $m = 0$.

Similarly, let us consider Eqs. (5) and (6). In both of these equations, non-zero m = ±1 coefficients for the electromagnetic BSCs agree with non-zero $m = 0$ coefficients for the acoustical wave.

5. Conclusion

This work pertains to a study which investigates the relationship between electromagnetic and acoustical scatterings. It demonstrates that electromagnetic beam shape coefficients may be expressed in terms of acoustical beam shape coefficients. The relationship between the present work and the work published in [19] is certainly worthwhile to be elucidated and clarified. This is currently under examination.

6. References

[1] G. Gouesbet and L.A. Ambrosio. Rigorous justification of a localized approximation to encode on-axis Gaussian acoustical waves. Journal of the Acoustical Society of America, 154 (2), 1062-1072, 2023.

[2] G. Gouesbet and L.A. Ambrosio. Description of acoustical Gaussian beams from the electromagnetic scheme of approximations and the on-axis localized approximation. Journal of the Acoustical Society of America, 155 (2), 1583-1592, 2024.

[3] G. Gouesbet and L.A. Ambrosio. Rigorous justification of a localized approximation to encode off-axis Gaussian acoustical beams. To be published in the Journal of Acoustical Society of America, 2024.

[4] L.A. Ambrosio and G. Gouesbet. A localized approximation approach for the calculation of beam shape coefficients of acoustic and ultrasonic Bessel beams. To be published in Acta Acustica, 2024.

[5] L.A. Ambrosio and G. Gouesbet. Finite series approach for the calculation of beam shape coefficients in ultrasonic and other acoustic scattering. Journal of Sound and Vibration., 585, 118461, 2024.

[6] L.W. Davis. Theory of electromagnetic beams. Physical Review, 19, 3, 1177-1179, 1979.

[7] G. Gouesbet, J.A. Lock and G. Gréhan. Partial wave representations of laser beams for use in light scattering calculations. Applied Optics, 34, 12, 2133-2143, 1995.

[8] G. Gouesbet, H. Shen and L.A. Ambrosio. Diverging and converging schemes of approximations to describe fundamental EM Gaussian beams beyond the paraxial approximation. Journal of Quantitative Spectroscopy and Radiative Transfer, 291, 108344, 2022.

[9] T.S. Bart and M.F. Hamilton. Nonlinear effects in focused sound beams. The Journal of the Acoustical Society of America, 84, 1488-1496, 1988.

[10] A.D. Pierce. Acoustics: An introduction to its physical principles and applications. Springer, Third Edition, 2019.

[11] D. Baresch, J.L. Thomas and R. Marchiano. Three-dimensional acoustic radiation force on an arbitrarily located elastic sphere. Journal of the Acoustical Society of America, 133, 1, 25-36, 2013.

[12] D. Blackstock. Fundamentals of Physical Acoustics. Joh, Wiley & Sons, 2000.

[13] G. Gouesbet and G. Gréhan. Generalized Lorenz-Mie theories. 3rd edition. Springer. 2023.

[14] G. Gouesbet, G. Gréhan and B. Maheu. Expressions to compute the coefficients g_n^m in the generalized Lorenz-Mie theory, using finite series. Journal of Optics (Paris), 19, 1, 35-48, 1988.

[15] G. Gouesbet, G. Gréhan and B. Maheu. Computations of the g_n coefficients in the generalized Lorenz-Mie theory using three different methods. Applied Optics, 27, 23, 4874-4883, 1988.

[16] L.F.M. Votto, G. Gouesbet and L.A. Ambrosio. A framework for the finite series method of the generalized Lorenz-Mie theory and its application to freely propagating Laguerre-Gaussian beams. Journal of Quantitative Spectroscopy and Radiative Transfer, 309, 108706, 2023.

[17] L.A. Ambrosio and G. Gouesbet. Finite series approach for the calculation of beam shape coefficients in ultrasonic and other acoustic scattering. Journal of Sound and Vibration, 585, 118461, 2024.

[18] G. Gouesbet. Validity of the localized approximation for arbitrary shaped beams in the generalized Lorenz-Mie theory for spheres. Journal of the Optical Society of America, 16, 7, 1841-1850, 1999.

[19] J. Shen, S. Zhong and J. Lin. Formulation of beam shape coefficients based on spherical expansion of the scalar function. Journal of Quantitative Spectroscopy and Radiative Transfer, 309, 108705.

The 14th International Conference on
Laser-light and Interactions with Particles (LIP2024)
September 18-22nd, 2024, Xi'an, Shaanxi, China

OPTICAL ENANTIOSELECTIVE MANIPULATION OF CHIRAL PARTICLES

Manman LI, Shaohui YAN, Yanan ZHANG, and Baoli YAO*

Xi'an Institute of Optics and Precision Mechanics, Chinese Academy of Sciences, Xi'an 710119, China
*Corresponding author: yaobl@opt.ac.cn

Abstract

The chirality-dependent forces can offer new possibilities for passive optical separation and identification of chiral particles, which opens great opportunities to develop the technologies of pharmaceutics, chemicals, and biomedicine. Chiral optical fields are attracting increasing attention due to their potential applications in chiral light-matter interaction. Here, based on the vectorial diffraction theory and T-matrix method, considering the polarization and phase characteristics of the light beams, we realize the optical manipulation such as optical enantioselective trap and rotation of chiral particles. Tightly focusing two tailored vector beams, we demonstrate the generation of a chiral optical field which with multiple spots carrying switchable handedness. The results provide insight into the optical separation and identification of chiral objects, may find applications in chiral detection and sensing.

1 Introduction

Light beam carries linear momentum, when it is scatted or absorbed by a particle, the transfer of momentum can cause the motion of the particle. So, light beam can be used to manipulate particles, known as optical manipulation [1], which has been widely used in modern scientific researches due to its unique advantages of noncontact and noninvasive operation capability. Chirality describes the nonsuperimposable property of an object with its mirror image, pervading in nature from subatomic to galactic scales, and is also an intrinsic feature of a light beam [2]. Chiral particles which with the same chemical composition but opposite chirality, called enantiomers, can have completely different chemical properties and biological functions [3]. Therefore, the separation and identification of chiral substances consist of an active, interdisciplinary, and meaningful research topic.

In recent years, the study of chirality-dependent optical forces has attracted tremendous attention not only for the optical separation of enantiomers but also for the further chiral identification of single particles. Most of these studies adopt nonparaxial beams with linear or circular polarization state as illumination [4-6]. Here, based on the vectorial diffraction theory and T-matrix method, we realize enantioselective manipulation of chiral particles by tightly focused light beams with spatially inhomogeneous states of polarization and with helical wave front. Most the generation of chiral optical fields carry only one handedness or local two handedness of optical chirality [7, 8]. Here we demonstrate a strategy to realize a controllable chiral optical field carrying one or two handedness simultaneously in a 4π optical microscopic system.

2 Theoretical Model

According to the Richards-Wolf vectorial diffraction [9], the focused field in the vicinity of the focus can be expressed as

$$\mathbf{E}_{\mathrm{inc}}(\mathbf{r}) = \frac{-ikf}{2\pi}\int_0^{\theta_m}\int_0^{2\pi}\sqrt{\cos\theta}\,\mathbf{A}_0(\theta,\phi)\exp(i\mathbf{k}\cdot\mathbf{r})\sin\theta\, d\phi\, d\theta\,, \quad (1)$$

where f is the focal length, θ_m is the maximal converging angular determined by the NA, $\mathbf{k}$ is the wave vector in the image space, and $\mathbf{A}_0(\theta, \phi)$ is the input field.

In the T-matrix method, the incident and scattered fields are expanded as a series of suitable vector spherical wave functions (VSWFs),

$$\mathbf{E}_{\mathrm{inc}}(\mathbf{r}) = \sum_{n=1}^{\infty}\sum_{m=-n}^{n}\left[a_{mn}\mathbf{M}^1_{mn}(k\mathbf{r}) + b_{mn}\mathbf{N}^1_{mn}(k\mathbf{r})\right], \quad (2)$$

$$\mathbf{E}_{\mathrm{sca}}(\mathbf{r}) = \sum_{n=1}^{\infty}\sum_{m=-n}^{n}\left[p_{mn}\mathbf{M}^3_{mn}(k\mathbf{r}) + q_{mn}\mathbf{N}^3_{mn}(k\mathbf{r})\right], \quad (3)$$

where $\mathbf{M}^{1,3}_{mn}(k\mathbf{r})$ and $\mathbf{N}^{1,3}_{mn}(k\mathbf{r})$ are VSWFs of the first and third kinds, (a_{mn}, b_{mn}) and (p_{mn}, q_{mn}) respectively are the expansion coefficients of incident and scattered fields and which can be obtained by the T-matrix as [10]

$$\begin{bmatrix} p_{mn} \\ q_{mn} \end{bmatrix} = \begin{bmatrix} T^{11}_{mnm'n'} & T^{12}_{mnm'n'} \\ T^{21}_{mnm'n'} & T^{22}_{mnm'n'} \end{bmatrix}\begin{bmatrix} a_{m'n'} \\ b_{m'n'} \end{bmatrix}. \quad (4)$$

The T-matrix here is non-diagonal with respect to the parity index since parity in not conserved for a chiral spherical particle, which with elements

$$\begin{aligned} T^{11}_{mnm'n'} &= -\delta_{mm'}\delta_{nn'}b_n\,, \quad T^{22}_{mnm'n'} = -\delta_{mm'}\delta_{nn'}a_n\,, \\ T^{12}_{mnm'n'} &= -\delta_{mm'}\delta_{nn'}c_n\,, \quad T^{21}_{mnm'n'} = T^{12}_{mnm'n'}\,, \end{aligned} \quad (5)$$

where a_n, b_n, and c_n are the Mie scattering coefficients.

3 Numerical Results and Discussion

3.1 Optical manipulation of chiral particles in the vector beams

Polarization is one of the fundamental properties of light beam and plays an important role in light-matter interactions. It is found that a focused cylindrical vector beam composed of radial and azimuthal components with a π/2 phase difference can selectively trap and rotate

particles with different chiral parameters via the chirality-tailored optical forces. A focused vector beam with radially varied polarizations exhibiting bifocal spots intensity distribution can stably trap one enantiomer in one focal spot meanwhile the other enantiomer in the other spot. The focused azimuthally polarized beam carries neither optical orbital angular momentum nor optical chirality, but can drive orbital rotation of the left- and right-handed enantiomers in opposite directions. Moreover, a focused hybrid polarized beam which combining properties of the m^{th}-order cylindrical and circular polarizations exhibits multiple local optical chirality of opposite signs in the focal plane, as shown in Figure 1, can trap multiple pairs of enantiomers and the number as well as the positions of trapped enantiomers can be changed by altering the value and sign of polarization orders.

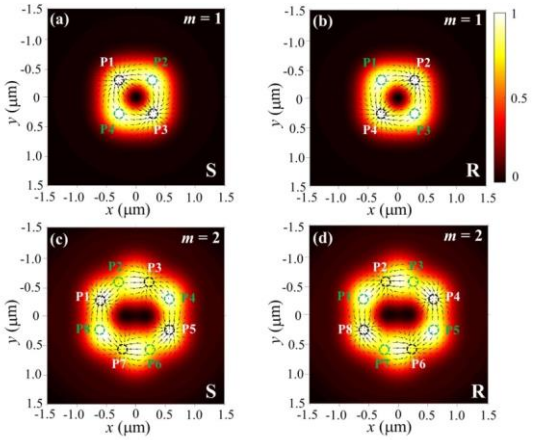

Figure 1 *Transverse optical force distributions experienced by the left-handed (S) and right-handed (R) enantiomers in the focal plane illuminated by the focused hybrid polarized beam with polarization orders (a,b) m = 1 and (c,d) m = 2.*

3.2 Optical manipulation of chiral particles in the vortex beams

Light carrying orbital angular momentum is inherently chiral due to the helical wave front. The focused azimuthally polarized beam with orbital angular momentum carrying radial-splitting optical chirality, as shown in Figure 2, can selectively trap one enantiomer inside or outside the intensity maxima depending on the sign of the orbital angular momentum. And the identification and separation of chiral dipolar particles by a focused circularly polarized vortex beam are also demonstrated, left- and right-handed circular polarizations lead to opposite effects on the particle of trapping and rotating, while the sign of topological charge will change the particle's rotation direction.

3.3 Generation of the chiral optical fields

Chiral optical fields have drawn significant attention not only due to their potential as probes of chiral matter but also due to their applications in chiral light-matter interaction. By modulating the wavefronts of the incident vector beams with appropriately designed phase masks in a 4π optical microscopic system, a chiral optical field with multiple spots carrying switchable handedness can be generated. The location, the number and the handedness of such chiral spots can be arbitrarily adjusted depending on the actual application requirements.

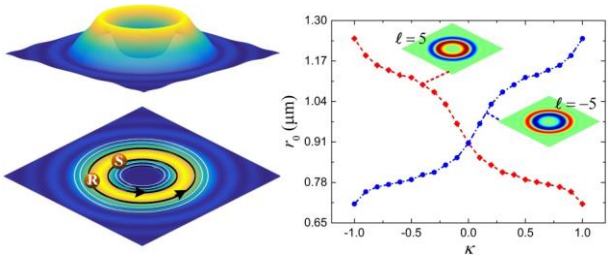

Figure 2 *(a) A sketch map of the optical separation and discrimination of chiral particles, (b) normalized optical chirality density distributions and the stable orbit r_0 as functions of particle's chirality parameter κ, under the focused vortex beam illumination.*

4 Acknowledgments

This research is supported by the National Natural Science Foundation of China (NSFC) under Grant Nos. 11904395 and 11974417, and the Key Research Program of Frontier Sciences, CAS, Grant No. ZDBS-LY-JSC035.

5 References

[1] D. G. Grier, "A revolution in optical manipulation," Nature **424**, 810-816 (2003).

[2] A. Guijarro and M. Yus, *The origin of chirality in the molecules of life: a revision from awareness to the current theories and perspectives of this unsolved problem* (Royal Society of Chemistry, 2008).

[3] L. A. Nguyen, H. He, and C. Pham-Huy, "Chiral drugs: an overview," Int. J. Biomed. Sci. **2**, 85 (2006).

[4] S. B. Wang and C. T. Chan, "Lateral optical force on chiral particles near a surface," Nat. Commun. **5**, 3307 (2014).

[5] T. Zhang, M. R. C. Mahdy, Y. Liu, J. H. Teng, C. T. Lim, Z. Wang, and C.-W. Qiu, "All-optical chirality-sensitive sorting via reversible lateral forces in interference fields," ACS Nano **11**, 4292-4300 (2017).

[6] R. Ali, F. A. Pinheiro, R. S. Dutra, F. S. S. Rosa, and P. A. Maia Neto, "Enantioselective manipulation of single chiral nanoparticles using optical tweezers," Nanoscale **12**, 5031-5037 (2020).

[7] K. C. van Kruining, R. P. Cameron, and J. B. Götte, "Superpositions of up to six plane waves without electric-field interference," Optica **5**, 1091-1098 (2018).

[8] D. Ayuso, O. Neufeld, A. F. Ordonez, P. Decleva, G. Lerner, O. Cohen, M. Ivanov, and O. Smirnova, "Synthetic chiral light for efficient control of chiral light-matter interaction," Nat. Photonics **13**, 866-871 (2019).

[9] B. Richards and E. Wolf, "Electromagnetic diffraction in optical systems. II. Structure of the image field in an aplanatic system," Proc. R. Soc. A **253**, 358-379 (1959).

[10] M. I. Mishchenko, L. D. Travis, and A. A. Lacis, *Scattering, absorption, and emission of light by small particles* (Cambridge university press, 2002).

The 14th International Conference on
Laser-light and Interactions with Particles (LIP2024)
September 18-22nd, 2024, Xi'an, Shaanxi, China

OPTICAL TRAPPING EFFICIENCIES OF DARK-HOLLOW GAUSSIAN BEAM AND ANNULAR BEAM

Sumit YADAV[1], Abdul ALIM[1] and Arijit K DE[2,*]

[1] Condensed phase dynamics group, Department of Physical Sciences, Indian Institute of Science Education and Research (IISER) Mohali, Knowledge City, Sector 81, SAS Nagar, Punjab 140306, India
[2] Condensed phase dynamics group, Department of Chemical Sciences, Indian Institute of Science Education and Research (IISER) Mohali, Knowledge City, Sector 81, SAS Nagar, Punjab 140306, India

*Corresponding author: akde@iisermohali.ac.in

Abstract

Here, we present the beam focusing properties and trapping efficiencies of beams with null intensity at the center: the dark hollow Gaussian beam and the annular beam generated by a spatial light modulator. We discuss how the trapping efficiency is influenced by the focusing angle and the beam's power compared with the Gaussian beam.

Optical tweezers are a tool employed to manipulate particles of different sizes ranging from micrometers to nanometers using light from a single laser beam only [1]. Commonly, the laser beam has a Gaussian transverse intensity profile, and under tight focus it leads to a 3D optical trap which, in the geometric optics limit, is explained based on the bending of light rays [2-3]. Using the advanced beam-shaping technique, one can alter the optical beam structure which increases the potential applications of optical tweezers. The employment of an obstructed beam is expected to increase the gradient force, by enhancing the contributions from the outer rays of a beam and suppressing the contributions from the central rays responsible for axial scattering forces. The trapping efficiency was investigated using various obstructed Gaussian beams, such as Laguerre Gaussian beams and higher-order Bessel beams [4]. It was demonstrated that the dark hollow Gaussian (DHG) beam, in the dipole regime, results in high trapping forces due to the tight focusing characteristics [4]. In the Mie regime, stable axial trapping was shown for the metallic particles using a centrally obstructed Gaussian beam, and an increase in trapping efficiency was observed with obstruction size [5]. However, for dielectric particles, it was shown that there is no enhancement in trapping efficiency for doughnut (Laguerre-Gaussian) beams and obstructed Gaussian beams, using vector diffraction theory [6]. On the other hand, in the ray optics regime, a long axial confinement was observed using an obstructed Gaussian beam [7] and stable trapping using a low numerical aperture (NA) objective [8]. As the trapping efficiency relies on the focusing properties of the rays, our group proposed two different methodologies presenting the focusing of the beam considering the 2D distribution of light rays [9] and the 3D distribution of light cones [10]. Here, we present the focusing properties and trapping efficiency of beams that have null intensity at the center: the dark hollow Gaussian beam and annular-shaped beam, generated by using a liquid crystal on silicon-spatial light modulator (LCOS-SLM) with the aid of computer-generated holograms (CHGs).

Our custom optical tweezers setup is based on an inverted microscope with a high NA (1.3) oil immersion objective and a linearly polarised (along the y-axis) Gaussian beam centered at 800 nm wavelength is used [11]. As a sample, we used polystyrene particles of 1 μm diameter dispersed in ultrapure water. To detect the trapping, we used bright field microscopy and point detection of backscatter signals simultaneously [12]. A CMOS camera is used in bright microscopy, and video micrographs are recorded at 100 frames per second (fps) in the cropped mode of the camera. In point detection, a 200 μm pinhole is placed at the conjugate focal plane to improve the signal-to-noise ratio of the backscatter signal is captured using a photomultiplier (PMT) at a 50 μs time interval.

Different types of CGHs are used to generate DHG and annular beams using LCOS-SLM as shown in the first row of Figure. 1. A blazed diffraction grating in CGH is used to separate the generated beam in the first order of diffraction. The CGH contains blazed diffraction grating along with an obstruction and an annular amplitude mask, which generates an obstructed Gaussian beam and an annular beam respectively. First-order diffraction is separated using a spatial filter and lens arrangement, and the conjugate plane is aligned with the objective's back focal plane using a 4f geometry setup. The dark hollow or an obstructed Gaussian beam is represented by the obstruction size (ε) which is defined by the ratio of the radius of obstruction (r_a), and the maximum beam diameter (w_0) that passes through the objective. An annular beam is defined by the inner (r_1) and outer radii

(r_2) of the annulus, and the width of the annulus is ($r_2 - r_1$). The radial intensity distribution of the generated (red curve) DHG and annular beam and fitted with analytical function (blue curve) are shown in the second row of Figure. 1. The third row of Figure. 1 shows the intensity distribution of DHG and annular beam at the focal plane (Fourier transform of the generated and the fitted analytical functions). At the focal plane, the intensity distribution of the obstructed beam follows the sinc type intensity distribution where the annular beam exhibits the Bessel-kind intensity distribution.

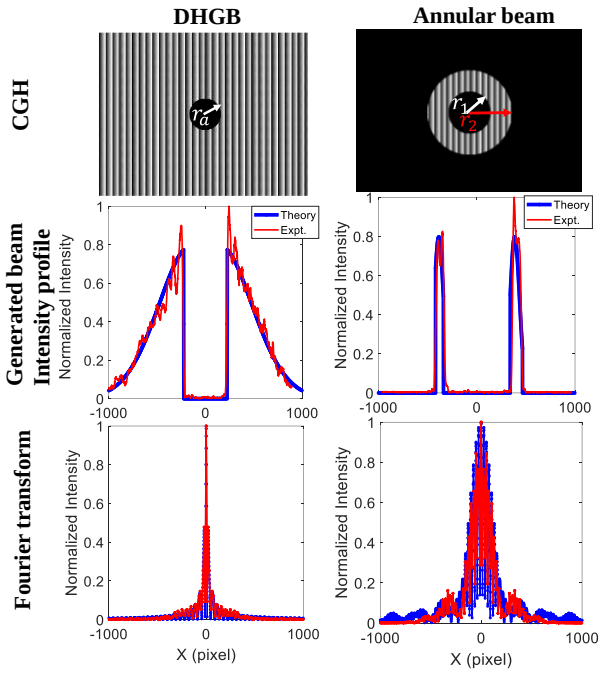

Figure 1 *First row) The computer-generated hologram, second row) the radial intensity distribution of the experimentally generated beam (red curve) and fitted with analytic function (blue curve), third row) the intensity distribution at focal plane (Fourier transform) of the obstructed and annular beam respectively.*

To compare the trapping efficiency of the obstructed beam with the Gaussian beam, we kept the same power at the trapping position for each beam [13]. The lateral trap stiffness is determined from the particle's trajectory extracted from the transmitted wide-field microscopy. Figures. 2a, b shows the trap stiffness along the x- and y-direction with power for the Gaussian (ε=0) and obstructed beams. The trap stiffness increases with power, while the trend is different for different obstruction-sized beams. Further, to compare the trap stiffness for obstructed and Gaussian beams, we fit the trap stiffness with power for each beam. The trap stiffness is found to decrease with obstruction size.

As discussed, the focusing properties annular beam are different than the obstructed beam. The trapping efficiency also shows distinct behavior for this type of beam with annular size [14]. To generate the annular beam, we have divided the full Gaussian beam into 6 annular rings of equal width along with the increasing outer diameter and the numbering of rings is from center to radially outward. The central pencil beam or the 1st and 2nd beams does not show any stable trapping, the particle is being dragged while due to the dominating scattering force, the particle is pushed out along the axial direction. The condition of

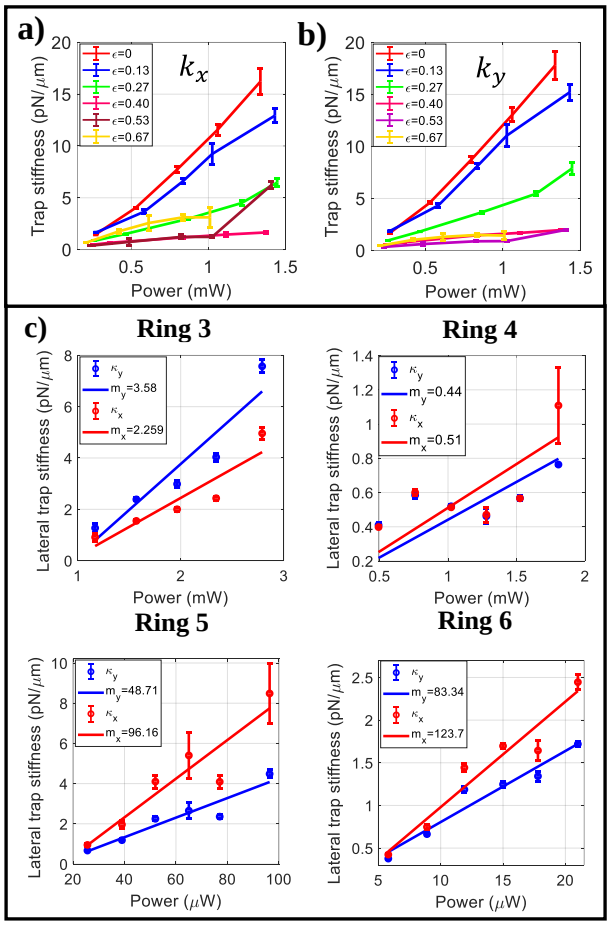

Figure 2 *a, b) Trap stiffness of an obstructed Gaussian beam along x and y direction respectively, c) trap stiffness of the different annular beam.*

dominating scattering force over gradient force is due to the shallow focusing of the central beams. On the other hand, the outer rings show stable trapping, and the trapping efficiency is evaluated at different powers, which is shown in Figure. 2c. The trap stiffness increases linearly with power. The trap's stability depends on the beam's power as well as the bending angle of the ray, and the bending angle is maximum for the outermost ring beam. However, the carrying power is maximum for an intermediate ring beam [10]. Due to a balanced contribution of power and focusing angle, an intermediate ring gives better trapping efficiency.

Similar to the previous studies in the Mie regime [6], we observed a less trapping efficiency of the DHG beam compared to the Gaussian beam. Also, the annular beam exhibits different focusing properties than the DHG beam, and depending on the focusing angle and power carried by each ring beam corresponding to the input Gaussian beam an intermediate ring beam provided a better trapping efficiency which is other than the ring carrying maximum power.

References

[1] Ashkin A., Optical trapping and manipulation of neutral particles using lasers: A reprint volume with commentaries, World Scientific (2006).

[2] Ashkin A., Forces of a single-beam gradient laser trap on a dielectric sphere in the ray optics regime, Biophys. J. 61: 569-582 (1992).

[3] Callegari A., Mijalkov M., Gököz A. B., Volpe G., Computational toolbox for optical tweezers in geometrical optics, J. Opt. Soc. Am. B 32: B11-B19 (2015).

[4] Liu Z., Wang X., Huang K., Propagation characteristics and optical forces exerted upon a Rayleigh dielectric sphere for a controllable dark-hollow beam, Opt. Laser Technol. 117: 105-109 (2019).

[5] Gu M., Morrish D., Three-dimensional trapping of Mie metallic particles by the use of obstructed laser beams, J. Appl. Phys. 91: 1606-1612 (2002).

[6] Ganic D., Gan X., Gu M., Optical trapping force with annular and doughnut laser beams based on vectorial diffraction, Opt. Express 13:1260-1265 (2005).

[7] Lei M., Li Z., Yan S., Yao B., Dan D., Qi Y., Qian J., Yang Y., Gao P., Ye T., Long-distance axial trapping with focused annular laser beams, PloS One 8, e57984 (2013).

[8] Alinezhad H. G., Meydanloo S., Nader S. Reihani S., Enhancement of axial force of optical tweezers by utilizing a circular stop at the back focal plane of the objective, J. Opt. Soc. Am. B 35, 2654-2660 (2018).

[9] Devi A., De A. K., Theoretical investigation on optical Kerr effect in femtosecond laser trapping of dielectric micro-particles, J. Opt. 19, 0655041-0655046 (2017).

[10] Devi A., De A. K., An alternate analytic formulation of optical force on a dielectric sphere in the ray optics limit, J. Opt. Soc. Am. B 35:244-250 (2018).

[11] Devi A., De A. K., A table-top compact multimodal nonlinear laser tweezer, Opt. Commun. 482: 126440 (2021).

[12] Devi A., Yadav S., De A. K., Deciphering single- and multi-particle trapping dynamics under femtosecond pulsed excitation with simultaneous spatial and temporal resolution, Sci. Rep. 12: 5373 (1-6) (2022).

[13] Yadav S., Alim A., De A. K., Optical trapping of dielectric microparticles with the focused annular beam, *Proc. SPIE 12198, Optical Trapping and Optical Micromanipulation XIX*, 121980H (3 October 2022).

[14] Yadav S., Alim A., De A. K., Testing the 'light-cone' model to assess trapping efficiency using annular beams in geometric optics limit, *Biophotonics Congress: Optics in the Life Sciences 2023 (OMA, NTM, BODA, OMP, BRAIN)*, Technical Digest Series (Optica Publishing Group, 2023), paper ATu3D.3.

The 14th International Conference on
Laser-light and Interactions with Particles (LIP2024)
September 18-22nd, 2024, Xi'an, Shaanxi, China

PROGRESS ON THE LIGHT SCATTERING PATTERNS OF NON-SPHERICAL DROPS SIMULATED BY VECTORIAL COMPLEX RAY MODEL

Qingwei DUAN [1,*], Xiang'e HAN [1,*], Qinyao LI [1], and Kuanfang REN [1-2,*]

[1] School of Physics, Xidian University, Xi'an 710071, China
[2] CORIA-UMR 6614, Normandie Université, CNRS, Saint-Etienne du Rouvray 76801, France
Corresponding authors: qwduan@xidian.edu.cn; xehan@mail.xidian.edu.cn; fang.ren@coria.fr

Abstract

The study on the light scattering by drops has led to several measurement techniques which have played important roles in characterizing the size, temperature and even evaporation rate of drops. Nevertheless, the current measurement techniques are usually limited to spherical drops, since the calculation and simulation for the light scattering by non-spherical drops pose great challenges for conventional light scattering models. The vectorial complex ray model (VCRM) provides a powerful tool to deal with the interaction of light with large non-spherical objects of smooth surface. In this communication, we will present our recent progress on simulating the light scattering patterns of non-spherical drops. Experimental results are also presented for the validations.

1 Introduction

Drops are widely encountered in industrial processes (inkjet printing, atomization and combustion), environmental sciences (precipitation), biological and chemical processes. Intensive researches have been carried out to characterize the parameters of drops such as the size, shape, temperature and even evaporation rate. The optical methods based on light scattering, such as rainbow refractometry, are attracting more and more attentions for their advantages in measurement precision, efficiency and being non-intrusive. Nevertheless, these methods are generally applicable only to spherical drops.

Small drops can maintain spherical shape due to surface tension. However, as the size increases, the drop's shape may be deformed under the gravity, air resistance or other forces. The scattering patterns of oblate spheroidal drops have been observed in experiments nearly forty years ago [1]. However, the prediction for those complex patterns is still a challenge for conventional light scattering models. On the one hand, analytical models such as the Mie theory [2] are limited to particles of very simple shape such as spheres or infinite circular cylinders. on the other hand, the numerical methods [3], though applicable to non-spherical particles in principle, are severely limited by the particle size in practice. Unfortunately, the size of a non-spherical drop is usually much greater than the wavelength of light. Some literature used ray methods or geometric optics [4, 5] to predict the scattering of a non-spherical drop. However, these methods encountered difficulties to calculate the divergence factor and the phase shift due to focal lines.

In this context, Ren et al. [6] proposed the vectorial complex ray model (VCRM). In VCRM, the wavefront curvature is introduced as an intrinsic property of rays. The divergence factor and the phase shift due to focal lines can then be deduced directly from the wavefront curvatures. It is thus very suitable for the light scattering by a large nonspherical particle of smooth surface. The VCRM has been validated by experimental measurement and numerical method respectively by Onofri et al. [7] and Yang et al. [8] in the case of scattering in a symmetric plane. Nevertheless, the numerical implementations of VCRM have been restricted to the scattering in a symmetric plane [6-8]. Until recently, the bottleneck problem of VCRM in calculating the light scattering in three-dimensional (3D) space has been solved [9, 10], thereby providing a powerful tool to calculate and interpret the 3D light scattering of non-spherical particles. In this communication, we will present our recent progress of VCRM in simulating the light scattering patterns of non-spherical drops.

2 VCRM for light scattering in 3D space

In the framework of VCRM, the incident light wave is described by bundles of rays, and each ray possesses the properties of direction, polarization, phase, amplitude and a crucial one -- the curvature of wavefront [6, 10]. The electric vector of an emergent ray can be expressed as

$$\begin{pmatrix} E_{\perp}^{e} e^{i\Phi_{\perp}^{e}} \\ E_{\parallel}^{e} e^{i\Phi_{\parallel}^{e}} \end{pmatrix} = k\sqrt{D} \begin{pmatrix} E_{\perp} e^{i\Phi_{\perp}} \\ E_{\parallel} e^{i\Phi_{\parallel}} \end{pmatrix} e^{i(\Phi_P + \Phi_F)} \qquad (1)$$

where subscripts $\perp$ and $\parallel$ stand for the components perpendicular and parallel to the scattering plane, respectively. $k = 2\pi/\lambda$ is the wavenumber and λ is the wavelength. The divergence factor D, which counts the intensity variation due to the divergence or convergence of a wave, is determined in VCRM by the Gaussian curvature of the wavefront. Figure 1 shows an example of the wavefront variation for a light ray scattered by an oblate drop [10]. The variations of the amplitude and phase due to reflection, refraction, and cross polarization are counted for the two polarizations by $(E_{\perp}, E_{\parallel})$ and $(\Phi_{\perp}, \Phi_{\parallel})$, respectively. They are calculated by the coordinate transformation matrix between two successive interaction points and the Fresnel formulas at the interaction point.

Φ_P and Φ_F, independent of polarization are respectively the phase shifts due to the optical path difference and the focal lines [6, 10].

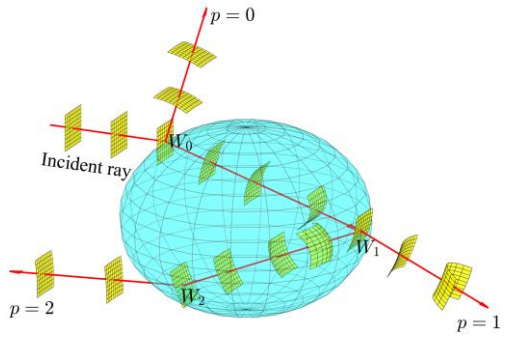

Figure 1. *Evolution of wavefront for a light ray scattered by a non-spherical drop [10]. p denotes the order of a scattered ray.*

After the amplitudes and phases of all emergent rays are calculated, the following task is to calculate the scattered intensity in the given directions. To address this problem, we have developed an interpolation algorithm based on line-by-line triangulation. The detail can be found in [10] and will not be repeated here.

3 Results for the light scattering patterns of non-spherical drops

In the following parts, we will present the results simulated with VCRM for the light scattering patterns of two groups of non-spherical drops: ellipsoidal drops and pendant drops. Codes were written in Python and run on a PC (Intel i9-13900ks, RAM 64 GB).

3.1 Ellipsoidal drops

For an ellipsoidal drop, its surface function is in form of $x^2/a^2 + y^2/b^2 + z^2/c^2 = 1$. The direction of incident plane wave is set as the x-axis. For a scattered ray, its direction in 3D space is characterized by the azimuth angle φ and the elevation angle ψ.

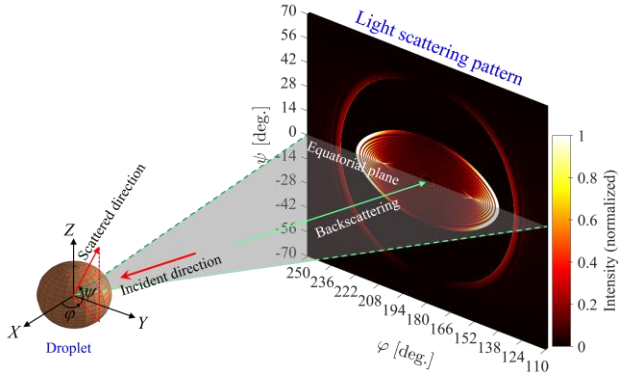

Figure 2. *Configuration of the light scattering pattern formed by an ellipsoidal drop [10]. Color coding: light intensity.*

We present firstly the configuration of the scattering in Figure 2. It illustrates a typical light scattering pattern near the primary and secondary rainbows of an oblate water drop $(a = b = 100\ \mu m;\ c = 85\ \mu m)$ simulated with VCRM. The relative index of refraction m=1.333, and the wavelength $\lambda = 632.8$ nm. The observation region is in backscattering region with φ= [110°, 250°] and ψ=[−70°, 70°].

Figure 3 shows the comparisons between the experimental results [7] and the corresponding simulated results by VCRM [10]. In each inset, the upper half is the result by experiment, while the lower half is by simulation. We find that the agreement is quite good. It should be noted that in the simulated patterns an abrupt variation of intensity is observed along the caustics. This is an intrinsic default of ray models and may be remedied by combining VCRM with physical optics [11].

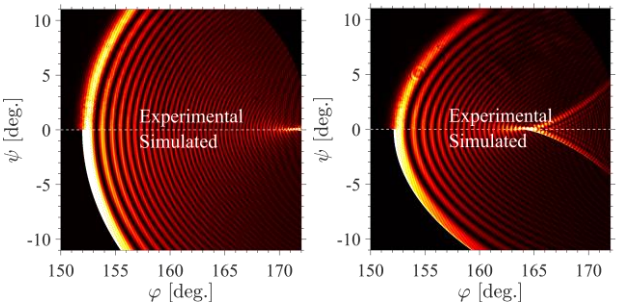

Figure 3. *Comparison of with experimental results [7] in the primary rainbow region of two oblate drops with increased aspect ratios [10].*

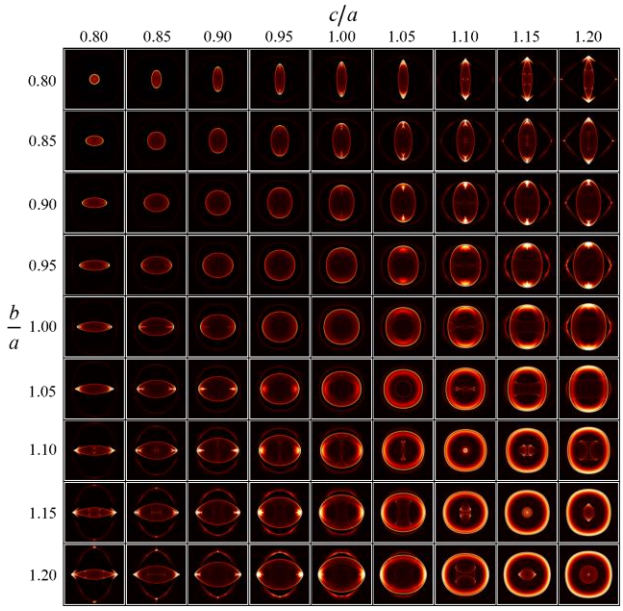

Figure 4. *A part of the database for the light scattering patterns of ellipsoidal drops.*

For different aspect ratios b/a and c/a, we have established a database with VCRM for the light scattering patterns of ellipsoidal drops. Figure 4 shows a part of the database which covers a wide range of aspect ratios (from 0.8 to 1.2). a is a constant of 100 μm, m = 1.333 and λ = 0.6328 μm. Unpolarized incident light is used here to focus on the effect of the drop shape on the scattering pattern.

Furthermore, we have also studied how scattering pattern respond to the orientation of an ellipsoidal drop. The drop's orientation relative to the laboratory frame of reference X, Y, Z is described by Euler angles α, β, γ.

Figure 5 shows the scattering patterns of an oblate drop with two different orientations. For an oblate drop, the angle γ (rotation about the symmetric axis of the drop) does not affect the orientation, thus is set as 0 for clarity. The other parameters are the same with those in Figure 1.

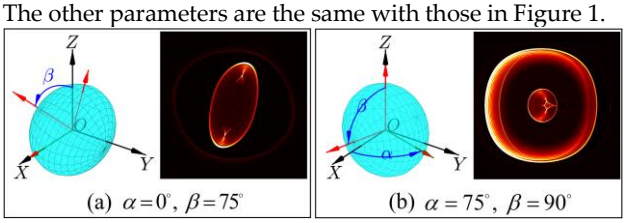

(a) $\alpha = 0^\circ$, $\beta = 75^\circ$ (b) $\alpha = 75^\circ$, $\beta = 90^\circ$

Figure 5. *Light scattering patterns of an oblate drop of different orientations.*

3.2 Pendant drops

A pendant drop sustain on a needle is commonly used to measure the surface tension of a fluid. For the perspective of light scattering in characterizing simultaneously the size, shape, temperature and even their transient variation of a pendent drop, in the following part we present our recent progress on simulating the light scattering patterns of pendent drops. Due to the limitation of paper pages, here we only present the results.

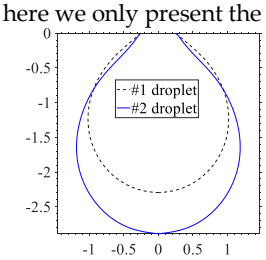

(a) profiles of the two pendant drops

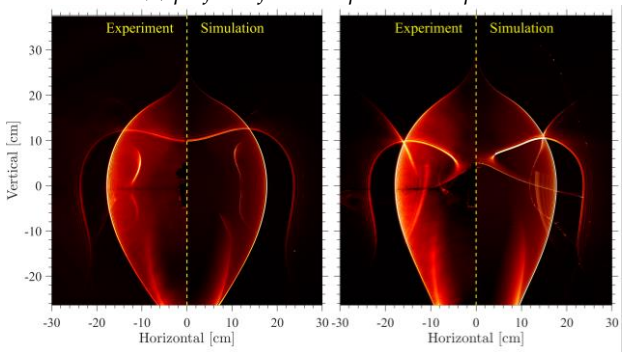

(b) scattering of #1 drop; (c) scattering of #2 drop

Figure 6. *Comparison of the light scattering patterns simulated by VCRM with experiments for two pendant drops of different sizes.*

Figure 6(a) shows the profiles of the two drops. The #1 drop is smaller, while the #2 drop is relatively larger and consequently is deformed more significantly. Figures 6(b) and (c) are the light scattering patterns observed on a screen placed in the primary and secondary region. The width and height of the screen are 60 and 64 cm, respectively, and the distance away from the drop is 19.05 cm. In each of (b) and (c), the left half is the result by experiment, while the right half is the simulated result by VCRM.

4 Conclusion

We presented our recent progress on simulating the light scattering patterns of non-spherical drops based on VCRM. The simulations for ellipsoidal drops and pendant drops have been compared with corresponding experimental results, and the agreements are quite satisfying. The extension to drops or bubbles of other shapes should not be too difficult. The determination of the parameters of non-spherical drops through light scattering patterns are to be investigated.

5 Funding

National Natural Science Foundation of China (62205262); Overseas Expertise Introduction Project for Discipline Innovation (B17035).

6 References

[1] P. L. Marston and E. H. Trinh, Hyperbolic umbilic diffraction catastrophe and rainbow scattering from spheroidal drops, Nature 312(5994), 529–531 (1984).

[2] H. C. van de Hulst, Light scattering by small particles (Dover Publications, 1981).

[3] M. I. Mishchenko, J. W. Hovenier, and L. D. Travis, eds., Light Scattering by Nonspherical Particles: Theory, Measurements, and Applications (Academic Press, 2000).

[4] J. F. Nye, Rainbow scattering from spheroidal drops—an explanation of the hyperbolic umbilic foci, Nature 312(5994), 531–532 (1984).

[5] H. Yu, F. Xu, and C. Tropea, Optical caustics associated with the primary rainbow of oblate drops: simulation and application in non-sphericity measurement, Optics Express 21(22), 25761–25771 (2013).

[6] K. F. Ren, F. Onofri, C. Rozé, and T. Girasole, Vectorial complex ray model and application to two-dimensional scattering of plane wave by a spheroidal particle, Optics Letters 36(3), 370–372 (2011).

[7] F. R. Onofri, K. F. Ren, M. Sentis, Q. Gaubert, and C. Pelcé, Experimental validation of the vectorial complex ray model on the inter-caustics scattering of oblate drops, Optics Express 23(12), 15768–15773 (2015).

[8] M. Yang, Y. Wu, X. Sheng, and K. F. Ren, Comparison of scattering diagrams of large non-spherical particles calculated by VCRM and MLFMA, J. Quant. Spectrosc. Radiat. Transfer 162, 143–153 (2015).

[9] Q. Duan, F. R. Onofri, XE Han, and K. F. Ren, Generalized rainbow patterns of oblate drops simulated by a ray model in three dimensions, Optics Letters 46, 4585-4588 (2021).

[10] Q. Duan, F. R. Onofri, XE Han, and K. F. Ren, Numerical implementation of three-dimensional vectorial complex ray model and application to rainbow scattering of spheroidal drops, Optics Express 31, 34980-35002 (2023).

[11] C. Zhang, C.Rozé, and K. F. Ren, Airy theory revisited with the method combining vectorial complex ray model and physical optics, Optics Letters 47, 2149-2152 (2022).

The 14th International Conference on
Laser-light and Interactions with Particles (LIP2024)
September 18-22nd, 2024, Xi'an, Shaanxi, China

ON THE Q FACTOR OF MIE MODES

Xavier ZAMBRANA-PUYALTO[1,*] and Søren RAZA[1]

[1] Department of Physics, Technical University of Denmark, Fysikvej, DK-2800 Kongens Lyngby, Denmark

*Corresponding author: xavislow@protonmail.ch

Abstract

We show a series of analytical calculations and numerical simulations that have led us to approximately determine the Q factor of any Mie mode as a function of its complex refractive index. Our analytical approximation gets increasingly better for greater refractive indices and multipolar orders. In particular, we note that, for each refractive index and multipolar order, it predicts a singular gain value which makes the Q factor diverge. Numerical simulations show the predictions to be correct.

1 Introduction

The Q factor is one of the most important properties of an optical cavity as it quantifies how long light can get trapped in cavity without leaking out. For homogeneous spheres, we can compute the analytical response of the sphere using the Generalized Lorenz-Mie Theory (GLMT) [1]. The eigenmodes of a sphere are the multipolar fields, and GLMT shows us that we can compute the Q factor associated to each of these modes using the so-called Mie coefficients. To compute the Q factor, we will need to know the complex refractive index of the particle, which we will denote as $n + ik$, with n being the refractive index and k the extinction coefficient.

2 Analytical results

First, we assume that a spherical optical cavity embedded in air is lossless and it is entirely defined by its refractive index n, with no losses ($k=0$). We will also assume that n is large. For this case, it can be demonstrated that the Q factor associated to a multipolar mode is [2]:

$$\begin{aligned} Q_j^\tau &= K_j^\tau n^{2(j+1)+\tau} \\ K_j^\tau &= \frac{2}{\pi}\frac{(2j-1)!!(2j+1)!!}{2j+1}\left(\frac{j(\tau+1)}{2}\right)^2 r_{(2j+\tau-1)/2}^{-2j-\tau} \end{aligned} \quad (1)$$

where (j, τ) are the multipolar order and parity of the resonant mode, and r_j is the first zero of the Riccati-Bessel function, which makes K^τ_j be a different constant for each multipolar mode. In Figure 1a) we show this relation for the dipolar magnetic mode, which yields a simple relation of the kind $Q(n) = 0.16\, n^3$. Then, we numerically study how material losses (via the imaginary part of the refractive index k) affect the Q factor. We discover that the behaviour is:

$$Q_j^\tau(n,k) = \frac{Q_{j,0}^\tau(n)}{|1 + B_j^\tau n^{2(j+1/2)+\tau} k|} \quad (2)$$

with $Q^\tau_{j,0}(n)$ being the Q factor for a lossless n obtained with eq.(1), and B^τ_j being a different constant for each multipolar mode. In Figure 1b), we display $Q^\tau_j(n,k)$ for $n=20$. For this case, B^τ_j becomes equal to 0.32.

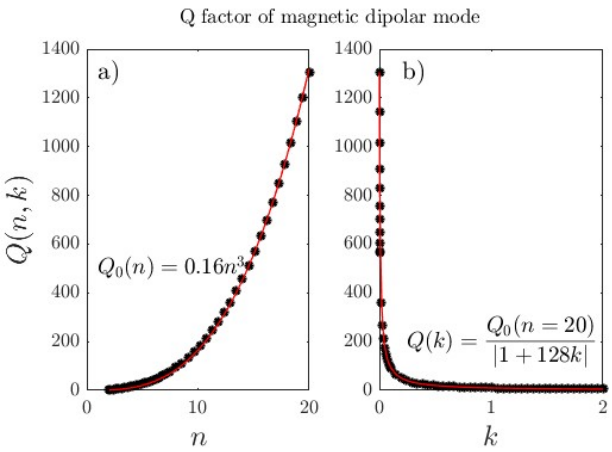

Figure 1 *Q factor of the magnetic dipolar mode as a function of its complex refractive index n+ik. On the left, a lossless Mie resonator is simulated, i.e k=0. On the right, a Mie resonator with n=20 is chosen, and the effect of losses is simulated.*

Our formulas (eq.(1-2)) are general, and apply to all Mie modes which are calculated under the GLMT assumptions [2], i.e. a sphere made of a linear, homogeneous and isotropic material embedded in a non-absorbing, linear, homogeneous and isotropic medium.

Also, notice that the denominator of eq.(2) can go to zero if we allow the sphere to have optical gain (k<0). That means that given multipolar order, there is a unique value of gain that makes the Q factor diverge. This singular value gain is completely determined by the coefficient B^τ_j, which is the term that determines how losses affect the Q factor.

3 Acknowledgement

This work was supported by a research grant (VIL50376) from VILLUM FONDEN.

4 References

[1] Gérard Gouesbet and Gérard Gréhan, Generalized Lorenz-Mie Theories. Vol 31. Berlin: Springer, 2011.

[2] Xavier Zambrana-Puyalto and Søren Raza, arXiv:2403.09360 (2024).

The 14th International Conference on
Laser-light and Interactions with Particles (LIP2024)
September 18-22nd, 2024, Xi'an, Shaanxi, China

FORWARD SCATTERING MODEL FOR SPHERICAL PARTICLES: REFRACTION AND DIFFRACTION RING EFFECTS

Lilian CHABROL[1*] and FABRICE ONOFRI[1*]

[1] Laboratoire IUSTI - UMR n°7343 CNRS/Aix-Marseille Université, Marseille, 13453, France

Corresponding authors: lilian.chabrol@proton.me, fabrice.onofri@univ-amu.fr

Abstract

We propose an asymptotic model for the forward scattering of spherical particles. The contributions of pure diffraction, specular reflection and surface waves are described by an approximation of the first two terms of the Debye expansion derived by Nussensweig [1]. It is shown that these terms can be rewritten, using Fraunhofer or Rayleigh-Sommerfeld integrals, as a diffraction problem involving an opaque disc and a thin concentric ring with a complex outer radius. The latter allows us to consider part of the effects associated with the refractive index of the particle in the forward domain. The other part, induced by rays hitting the surface of the particle, is introduced using a Geometric Optics Approximation (GOA) valid in the near- and far-field. Numerical results confirms that this complete model provides fast and accurate predictions in the small angle and large particle size limits, opening up large prospects for computationally intensive applications such as on-line digital holography notably.

1 Introduction

When considering the scattering of light by spherical particles, the Lorenz-Mie Theory (LMT) [2] and Debye series expansion [3] are the reference. However, they both require large computational resources or data storage capacities that are not always compatible with the development of fast and accurate inverse analyses [4-8]. This is especially true when change in the particle refractive index has to be considered as well as for particles with a large size parameter, i.e. $\alpha = ka \gg 1$ where a is the particle radius, $k = 2\pi/\lambda$ the wave number and λ the wavelength of the incident light. This explains the renewed interest in the development of asymptotic models, whether for the analysis of far-field diffraction patterns [9-11], holograms [12-18], interferometric images [19-21], critical [22-24] or rainbows patterns [8, 25-29] for instance.

The forward scattering part of the scattering, which is what we are most interested in here, is often obtained by considering the scalar diffraction by a disc (or hole in a plane) with the same radius as the particle [30]. The Franhoffer, Fresnel or Rayleigh-Sommerfeld (RS) approximations are numerically very effective, especially when computed using a Fourier transform algorithm [30, 31]. However, a drawback of this approach is that any information about the particle's refractive index is lost, whereas estimation of this parameter is highly desirable in many applications where particle material recognition or analysis is required [14, 18, 32, 33].

In this work, we propose an approximation for the forward scattering of a spherical particle that considers the refractive index of the particle m>1. Based on a derivation by Nussensweig [34] from Debye series, it is valid in the high-frequency regime and in the small-angle limit, with a computational efficiency comparable to the above-mentioned approximations of scalar diffraction.

2 Debye expansion and LMT theory and

The Debye expansion of Mie's series provides a better understanding of the scattering mechanisms with respect to the Geometric and Physical Optics Approximations (GOA, POA)[3, 35]. With the expansion parameter $p = 0,1,2,...,+\infty$, it is possible to separate the refraction processes $p \geq 1$ exiting from the particle after $p-1$ internal reflections, with $p = 1$ for single refraction, $p = 2$ for rays responsible for the first rainbow, etc. The case $p = 0$ (hereafter referred to as $p = 0_{All}^{Deb}$) is more complex since it accounts for several mechanisms : pure diffraction (independent from the particle refractive index, noted $p = 0_{d}^{Deb}$), specular reflection ($p = 0_{r}^{Deb}$) and surface waves ($p = 0_{sw}^{Deb}$).

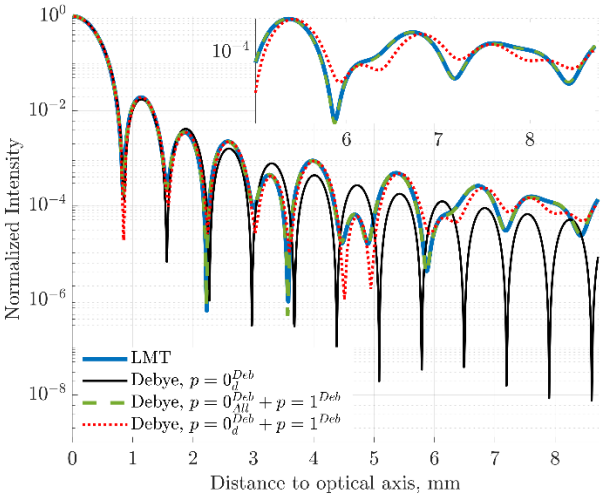

Figure 1 *Normalised forward scattering patterns according to the LMT and Debye series, for a particle with relative refractive index* $m = 1.33$ *and radius 45μm, a particle-screen distance of 10cm.*

Numerical analyses have shown [36] that for the forward scattering, the main two contributing mechanisms are $p = 0_{All}^{Deb}$ and $p = 1^{Deb}$ (apart from possible rainbows or some specific resonances). As an illustration, Figure 1 shows , on a screen placed at 0.10 m, the scattering intensity of the corresponding pure or interfering mechanisms of a water droplet with a radius of 45µm.

It is clear from Figure 1 that pure diffraction does not provide a proper description of the forward scattering pattern. A better approximation is obtained by combining pure diffraction ($p = 0_d^{Deb}$) and single refraction ($p = 1^{Deb}$). However, and quite generally, only the combination of the scattering mechanisms included in the term $p = 0_{All}^{Deb}$ and $p = 1^{Deb}$ match satisfactorily with LMT's predictions. In the next sections, we discuss how to approximate these two terms more rapidly than by a direct calculation from Debye series.

3 Refraction of light by a homogeneous sphere

We approximate the term $\boldsymbol{p = 1^{Deb}}$ with a GOA where, basically, a pencil of light undergoes two refractions through the surface of the sphere. Our approach is quite similar with those provided by van de Hulst [37] – with two important differences. First, it is valid whatever is the observation distance (while in Ref [37] a remote sensing approximation is used). The intensity variation of the curvature matrix upon propagation of light path is taken into account [38]. Second, the phase shifts due to focal lines are tracked by counting the sign shifts of the curvature radii upon light propagation, as well as crossing of the optical axis. Nonetheless, the expressions obtained are too complicated to be given in this abstract but, basically, they allow to express formally the associated complex field

$$\boldsymbol{U_{\chi,p=1^{GO}}^{GOA} = f(a,m,\chi,x,y,z)} \quad (1)$$

where $\boldsymbol{\chi}$ stands for the cross-polarization state.

4 Surface waves, specular reflection, and diffracting ring

To describe properly the $p = 0_{All}^{Deb}$ term, we start with an approximation derived by Nussenzveig from the two first term of a Watson transformation of Debye expansion series [3]. It is valid in the high-frequency limit with minor restriction on the refractive index :

$$\alpha^{1/3} \gg 1 \text{ and } |m-1|^{1/2}\alpha^{1/3} \gg 1$$

This approximation can be reformulated as follows:

$$U_{Nus}(\alpha,\theta,m) = \left(\frac{\theta}{\sin(\theta)}\right)^{1/2}\begin{bmatrix} \dfrac{J_1(\alpha\theta)}{\alpha\theta} \\ +C_1(\alpha,m)J_0(\alpha\theta) \\ -C_2(\alpha,m)\theta J_1(\alpha\theta)\end{bmatrix} \quad (2)$$

whith $C_1(\alpha,m)$ and $C_2(\alpha,m)$ two functions that are size parameter and refractive index dependent. J_0 and J_1 are the Bessel functions. Looking at Eq. (2), Nussenzveig perceived that the first term in the bracket resembles to the Fraunhofer approximation of diffraction.

However, what Nussenzveig did not noticed (or reported) is that the second and third terms in Eq. (2) can be obtained using a series expansion of the Bessel function J_1. Having this in mind, we rewrote Eq. (2) as a sum of two diffraction contributions: the diffraction by a circular aperture of radius a, plus the diffraction by an annular ring of interior and external radiuses a and $\tilde{a}(a,m)$:

$$U_{Nus} \cong U_{Fra}\{Disc_a\} + K(a,m)U_{Fra}\{Ring_{a,\tilde{a}}\} \quad (3)$$

$\tilde{a}$ being a complex number, the integration of Fraunhofer diffraction must be made in the complex plane between a and $\tilde{a}$. Physically, all is like the forward scattering is the result of the diffraction of an opaque disc (i.e. no refraction coming out from this area) and the one of a thin corona $|\tilde{a}|/a = 1+\varepsilon$, with $\varepsilon \ll 1$, accounting for some refractive and/or surface wave effects from for rays (or partial waves) that do not hit the particle surface.

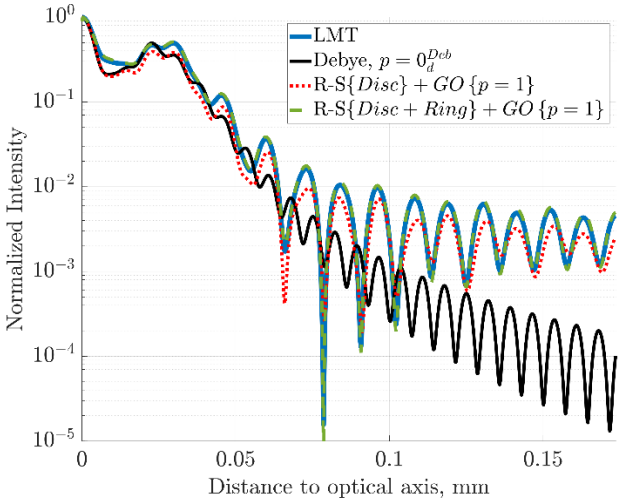

Figure 2 *Comparison of normalised intensities from LMT and our model. Relative refractive index m = 1.33. Distance particle-screen: 1mm.*

The validity of the previous model, expressed in term of Fraunhofer diffraction of two objects, hold only if the related hypothesizes are verified: small angle and far field limits. Any generalization should allow, in these limits, to retrieve the results provided by Eq. (3). A natural attempt to extend the scope of the previous equation is to employ the Rayleigh-Sommerfeld (R-S) diffraction integral rather than the Fraunhofer one:

$$U_{p=0_{All}^{Deb}} \cong U_{R-S}\{Disc_a\} + K(a,m)U_{R-S}\{Ring_{a,\tilde{a}}\} \quad (4)$$

Figure 2 compare the exact solution (LMT), with predictions from Rayleigh-Sommerfeld's diffraction coupled to $p = 1$ from GO, as well as our R-S based model depicted by Eq. (4) coupled to $p = 1$ from GOA. We again consider a droplet with radius 45µm but observed at very short distance, z=1mm. Visually, our model expressed in term of R-S integral, Eq. (4), provides a far better description than

the one simply coupling pure diffraction with the Geometrical contribution p=1.

5 Conclusion

The contribution of the first two terms of the Debye expansion to forward scattering is reformulated as a diffraction problem involving an opaque disc and a thin annular ring. This allows fast calculations using Fraunhofer or Rayleigh-Sommerfeld integrals, when compared to calculations with LMT. Adding to this model the contribution of simple refraction, modelled with a GOA, further improves its accuracy without significantly increasing the computational time. This model should open up great prospects for optical particle sizing techniques such as laser diffraction or digital holography requiring intensive calculations.

This work was supported by a French government grant managed by the Agence Nationale de la Recherche, reference ANR-23-CE51-0023.

6 References

[1] Nussenzveig, H.M., High-Frequency Scattering by a Transparent Sphere. I. Direct Reflection and Transmission. Journal of Mathematical Physics, 1969. **10**(1): p. 82-124.

[2] Bohren, C.F. and D.R. Huffman, Absorption and scattering of light by small particles. 1998, New york: Wiley & Sons.

[3] Hovenac, E.A. and J.A. Lock, Assessing the contribution of surface waves and complex rays to far-field scattering by use of the Debye series. J. Opt. Soc. Am. A, 1992. **9**(5): p. 781-795.

[4] Świrniak, G., G. Głomb, and J. Mroczka, Inverse analysis of the rainbow for the case of low-coherent incident light to determine the diameter of a glass fiber. Applied Optics, 2014. **53**(19): p. 4239-4247.

[5] Saengkaew, S., et al., Rainbow refractrometry: On the validity domain of Airy's and Nussenzveig's theories. Opt. Commun., 2006. **259**(1): p. 7-13.

[6] Rosebrock, C.D., et al., Time-resolved detection of diffusion limited temperature gradients inside single isolated burning droplets using Rainbow Refractometry. Combustion and Flame, 2016. **168**: p. 255-269.

[7] Soulez, F., et al., Inverse problem approach in particle digital holography: out-of-field particle detection made possible. Journal of the Optical Society of America A, 2007. **24**(12): p. 3708-3716.

[8] Ouattara, M., et al., Droplet sizing and mixture fraction measurement in liquid flows with rainbow-angle diffractometry. Applied Optics, 2017. **56**(29): p. 8109-8120.

[9] Nascov, V. and P.C. Logofătu, Fast computation algorithm for the Rayleigh-Sommerfeld diffraction formula using a type of scaled convolution. Applied Optics, 2009. **48**(22): p. 4310-4319.

[10] Dwivedi, G., et al., Comparison of numerical reconstruction of digital holograms using angular spectrum method and Fresnel diffraction method. Journal of Optics, 2017.

[11] Onofri, F., et al., High-resolution laser diffractometry for the on-line sizing of small transparent fibres. Optics Communications, 2004. **234**(1–6): p. 183-191.

[12] Berg, M.J., Tutorial: Aerosol characterization with digital in-line holography. Journal of Aerosol Science, 2022. **165**: p. 106023.

[13] Shao, S., K. Mallery, and J. Hong, Machine learning holography for measuring 3D particle distribution. Chemical Engineering Science, 2020: p. 115830.

[14] Sentis, M.P.L., F.R.A. Onofri, and F. Lamadie, Bubbles, drops, and solid particles recognition from real or virtual photonic jets reconstructed by digital in-line holography. Optics Letters, 2018. **43**(12): p. 2945-2948.

[15] Sentis, M.P.L., F.R.A. Onofri, and F. Lamadie, Photonic jet reconstruction for particle refractive index measurement by digital in-line holography. Optics Express, 2017. **25**(2): p. 867-873.

[16] Sentis, M.P.L., et al., Digital in-line holography for the characterization of flowing particles in astigmatic optical systems. Optics and Lasers in Engineering, 2017. **88**: p. 184-196.

[17] Méès, L., et al., Evaporating droplet hologram simulation for digital in-line holography setup with divergent beam. Journal of the Optical Society of America A, 2013. **30**(10): p. 2021-2028.

[18] Tian, L., et al., Quantitative measurement of size and three-dimensional position of fast-moving bubbles in air-water mixture flows using digital holography. Applied Optics, 2010. **49**(9): p. 1549-1554.

[19] Qieni, L., et al., Simultaneous retrieval of particle size and refractive index by extended interferometric particle imaging technique. Optics Express, 2020. **28**(2): p. 2192-2200.

[20] Brunel, M., et al., Interferometric out-of-focus imaging of freezing droplets. Optics Communications, 2019. **433**: p. 173-182.

[21] Glover, A.R., S.M. Skippon, and R.D. Boyle, Interferometric laser imaging for droplet sizing: a method for droplet-size measurement in sparse spray systems. Applied Optics, 1995. **34**(36): p. 8409-8421.

[22] Onofri, F.R.A., et al., Near-critical-angle scattering for the characterization of bubbly flows: spheroidal bubbles, , in 8th International Conference on Multiphase Flow (ICMF 2013). 2013: Jeju, Korea.

[23] Onofri, F.A., et al., Optical characterization of bubbly flows with a near-critical-angle scattering technique. Exp. in Fluids, 2009. **47**(4-5): p. 721-732.

[24] Marston, P.L. and D.L. Kingsbury, Scattering by a bubble in water near the critical angle: interference effects. Journal of the Optical Society of America, 1981. **71**(2): p. 192-196.

[25] Yu, H., F. Xu, and C. Tropea, Spheroidal droplet measurements based on generalized rainbow patterns. Journal of Quantitative Spectroscopy and Radiative Transfer, 2013. **126**: p. 105-112.

[26] Xiang'e, H., et al., On rainbows of inhomogeneous spherical droplets. Optics Communications, 2007. **269**(2): p. 291-298.

[27] Wang, X., et al., Synthetic aperture rainbow refractometry. Optics Letters, 2022. **47**(20): p. 5272-5275.

[28] Onofri, F.R.A., et al., Experimental validation of the vectorial complex ray model on the inter-caustics scattering of oblate droplets. Optics Express, 2015. **23**(12): p. 15768-15773.

[29] Duan, Q., et al., Generalized rainbow patterns of oblate drops simulated by a ray model in three dimensions. Optics Letters, 2021. **46**(18): p. 4585-4588.

[30] Goodman, J.W., Introduction to Fourier Optic. Mac. Graw-Hill, New York, 1960.

[31] Voelz, D., Computational Fourier Optics: A MATLAB Tutorial. SPIE Tutorial Texts. 2011: SPIE Press, Bellingham.

[32] Lee, S.-H., et al., Characterizing and tracking single colloidal particles with video holographic microscopy. Optics Express, 2007. **15**(26): p. 18275-18282.

[33] 33. Onofri, F.R.A., et al. Analysis of the Rainbow Scattering by Homogeneous and Inhomogeneous Droplets in Liquid–Liquid Systems. in Laser-light and Interaction with Particle (LIP) and Electromagnetic Light-Scattering (ELS) conferences 2018. College Station, TX, USA.

[34] Nussenzveig, H.M., High-frequency scattering by an impenetrable sphere. Annals of Physics, 1965. **34**(1): p. 23-95.

[35] Nussenzveig, H.M., Diffraction effects in semiclassical scattering. 1992, Cambridge: Cambridge University Press.

[36] Onofri, F., Assessment of Non Diffractive Contributions in the Formation and Analysis of Digital Holograms, in 13th international conference series on Laser-light and Interactions with Particles (LIP) K.M. Jakubczyk D., Onofri F, Gouesbet G., Editor. 2022, Institute of Physics, Polish Academy of Sciences: Warsaw, Poland.

[37] van de Hulst, H.C., Light Scattering by Small Particles. 1957, New-York: Dover Publications.

[38] Deschamps, G.A., Ray Techniques in Electromagnetics. Proc IEEE 1972. **60**(9): p. 1022- 1035

The 14th International Conference on
Laser-light and Interactions with Particles (LIP2024)
September 18-22nd, 2024, Xi'an, Shaanxi, China

LIGHT SCATTERING BY MULTILAYER AND HOMOGENIZED CURVILINEAR SYSTEMS

Milena RAMANOVICH[1,*], Denis V. NOVITSKY[1] and Andrey NOVITSKY[2]

[1] Nanophotonics Center, B.I. Stepanov Institute of Physics, National Academy of Sciences, Minsk, 220072, Belarus
[2] Department of Physical Optics and Applied Informatics, Belarusian State University, Minsk, 220030, Belarus
Corresponding author: milenaromanovitch@yandex.by

Abstract

We propose a new avenue to homogenize multilayer curvilinear systems using an operator effective medium approximation. We derive local effective material parameters and characterize the performance of approximation though comparing scattering cross sections of the multilayer and homogenized counterparts. We expect that our results can be useful for metamaterial and nanophotonics engineering.

1 Introduction

Light scattering by artificial metamaterials is extremely important for their design and characterization [1]. A complex periodic system can be treated as a uniform material, if a procedure of homogenization is feasible. A continuous medium approximation allows distinguishing metamaterial's properties using material parameters as permittivity and permeability tensors [2]. Perhaps, the most simple and popular approach is the effective medium theory widely used for description of composite materials. However, its applicability is still under discussion, especially for systems of nonplanar geometry.

Here, we consider multilayer metamaterials of planar, cylindrical and spherical symmetry as well as corresponding homogenized systems and compare their scattering cross sections. We use the so-called operator effective medium approximation, which well suits for analysis of inhomogeneous and curvilinear media and provides nonlocal correction to the effective material parameters.

2 Operator effective medium approximation

Operator effective medium approximation first proposed in Ref. [3] for planar multilayer structures uses equivalence of evolution operators of metamaterial's unit cell shown in Fig. 1(a) and homogenized layer depicted in Fig. 1(b) as

$$\left(\Omega_a^b\right)_{eff} = \Omega_c^b \Omega_a^c . \tag{1}$$

Evolution operator for a planar homogeneous slab can be written as an exponent of the matrix, however, in general, for cylindrical and spherical multilayer systems, one has to exploit the Born series of the form [4]

$$\Omega_a^b = 1 + ik_0 \int_a^b M(r)dr + \ldots , \tag{2}$$

where k_0 is the wavenumber in vacuum and M is a characteristic matrix governing the fields $\mathbf{W}$ through the differential equation

$$d\mathbf{W}/dr = ik_0 M(r)\mathbf{W} . \tag{3}$$

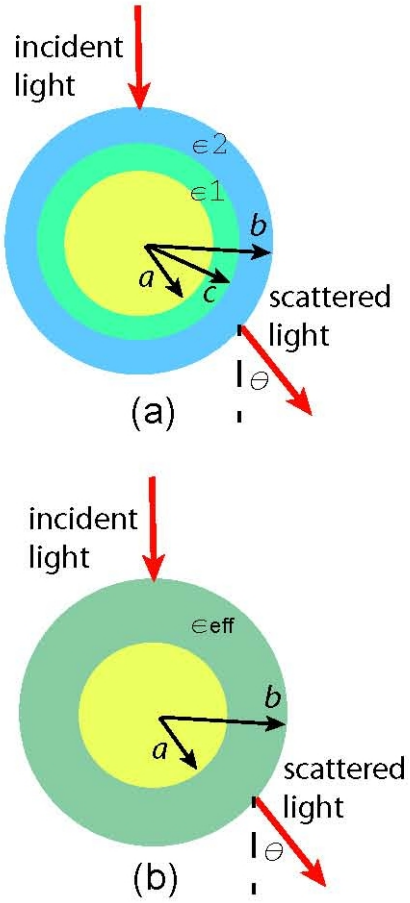

Figure 1 *Light scattering by (a) multilayer and (b) homogenized spherical particle*

Applying Eq. (1) to spherically symmetric couple of layers results in the anisotropic effective medium permittivity $\varepsilon = \mathrm{diag}(\varepsilon_r, \varepsilon_t, \varepsilon_t)$ with

$$\varepsilon_t = \rho_1 \varepsilon_1 + \rho_2 \varepsilon_2 , \qquad \varepsilon_r = \left(\frac{\rho'_1}{\varepsilon_1} + \frac{\rho'_2}{\varepsilon_2} \right)^{-1} , \tag{4}$$

where $\rho_1 = (c-a)/(b-a)$, $\rho_2 = (b-c)/(b-a)$, $\rho'_1 = (c^{-1}-a^{-1})/(b^{-1}-a^{-1})$ and $\rho'_2 = (b^{-1}-c^{-1})/(b^{-1}-a^{-1})$. Dielectric permittivity tensor (4) can be used for the effective cylindrical media only if electromagnetic waves propagate in the plane orthogonal to the cylinder axis. Otherwise, the permittivity is not enough and effective magnetic permeability tensor should be involved.

3 Results

Our results show that the proposed consistent effective medium theory is applicable to a wide range of media including inhomogeneous planar, cylindrically and spherically symmetric media. We have calculated differential and total scattering cross sections to reveal the effectiveness of our homogenization approach. The near-field scattering patterns confirm viability of the operator effective medium theory as well.

In particular, for the spherical particles, we have shown that the effective medium theory operates well for greater radii of particles. We have introduced the new applicability condition of this approximation imposed on the curvature of the particle: it should be smaller than the inverse wavelength. The effective medium approach is also shown to work better for all-dielectric than for metal-dielectric systems.

For the cylindrical particles, we have clearly demonstrated that the larger the number of cylindrical layers, the better agreement between exact and homogenized solutions. We have also compared magnetic and non-magnetic effective medium approximations and observed that the non-magnetic approximation works better.

Finally, we turn to the non-Hermitian generalization of the planar and spherical media to show how to balance loss and gain, so that the homogenized parameters are real-valued. In particular, the application of our effective medium approach allows to obtain the position of the interface between the layers with loss and gain necessary to reach this balance.

4 Conclusion

To sum up, the operator effective medium theory is a powerful tool for analysis of the material properties that can be proved using the electromagnetic wave scattering calculations. Our results might be attracting for metamaterials and nanooptics communities. The details of our research can be found in Ref. [4].

Acknowledgement

A.N. acknowledges the support of the State Program for Scientific Research "Convergence-2025" (Task 2.1.02.1). M.R. and D.V.N. were supported by the State Program of Scientific Research ``Photonics and Electronics for Innovations'' (Task 1.5).

References

[1] Kadic M., Milton G.W., van Hecke M., Wegener M., 3D metamaterials, Nature Reviews Physics 1: 198–210 (2019).

[2] Maslova E.E., Rybin M.V., On homogenization approaches for manipulation with fields inside and outside metamaterials, J. Appl. Phys. 134: 063103 (2023).

[3] Popov V., Lavrinenko A. V., Novitsky A., Operator approach to effective medium theory to overcome a breakdown of Maxwell Garnett approximation, Phys. Rev. B 94: 085428 (2016).

[4] Novitsky A., Ramanovich M., Novitsky D.V., Operator effective medium approximation for inhomogeneous and curvilinear media, Phys. Rev. B 94: 085428 (2016).

The 14th International Conference on
Laser-light and Interactions with Particles (LIP2024)
September 18-22nd, 2024, Xi'an, Shaanxi, China

SINGLE NON-SPHERICAL PARTICLE FAR-FIELD SCATTERING SIMULATION BASED ON FDTD METHOD

Hong HUA[1], Tianyi CAI[1,*] Zeqi LIU[2], Wu ZHOU[1], and Xiaoshu CAI[1,2]

[1] School of Energy and Power Engineering, Shanghai Key Laboratory of Multiphase Flow and Heat Transfer in Power Engineering, University of Shanghai for Science and Technology, Shanghai, 200093, China
[2] Jiaxing MeaParTech Instrument Technology Co., Ltd, Zhejiang, 314000, China

**Corresponding author: tycai@usst.edu.cn*

Abstract

The morphology of nanoparticles significantly influences their performance in applications including catalysis, sensing, and biomedicine. Utilizing polarized imaging dynamic light scattering (PIDLS) technology, the authors introduce the concept of optical sphericity, a rapid assessment tool for nanoparticle morphology. To further delineate the applicability of optical sphericity and to propose new particle morphology descriptors based on polarized light scattering characteristics, this paper employs the Finite-Difference Time-Domain (FDTD) method. Through simulations of the far-field scattering of individual non-spherical particles, it explores how variations in shape, size, and material affect the polarized scattering properties of nanoparticles. This study provides a dataset for subsequent ensemble simulations of nanoparticles, facilitating a comparison between simulated and experimental results of PIDLS thereby advancing nanoparticle morphology measurement techniques.

1. Research background

The morphology of nanoparticles directly influences their physical properties such as surface area, crystal structure, and crystal defects, thereby affecting their optical, electrical, and magnetic characteristics. Currently, non-spherical nanoparticles demonstrate unique potential applications in fields such as catalysis, energy storage, sensing, and biomedicine.Cylindrical nanoparticles, due to their large aspect ratio and residual magnetization characteristics, can control their self-assembly in weak magnetic fields, which is crucial for cell assembly. They are prepared by using nano porous aluminum templates in metal electrodeposition, which can widely adjust their structure and magnetic properties.[1]The Cu_2O pyramid shaped nanoparticles can significantly improve the efficiency of photocatalytic reactions and exhibit excellent photo stability. [2]Polarized imaging dynamic light scattering (PIDLS) technology allows for the acquisition of far-field polarized scattering images of nanoparticles, facilitating rapid assessment of nanoparticle morphology using optical sphericity. Preliminary validation of this method's feasibility has been demonstrated through morphological measurements of seven non-spherical particles by Wang and his colleagues.[3] However, the generality and applicability of this method still lack theoretical support. Therefore, this study aims to simulate the far-field scattering spatial distribution of individual non-spherical nanoparticles using the Finite-Difference Time-Domain (FDTD) method, exploring the regularities in the polarized scattering characteristics of nanoparticles of different shapes, sizes, and materials.

1.1. Basic Principles of PIDLS

The measurement principle of PIDLS is depicted in Figure 1. This technique builds upon the foundation of image-based dynamic light scattering (IDLS) by incorporating the acquisition of polarization signals. An incident laser beam, after passing through a polarizer for correction, illuminates the sample pool. The scattered light is then captured at four different polarization angles—0°, 45°, 90°, and 135°—using a polarized camera, which records the light intensity in grayscale images. The obtained far-field scattering signals are subsequently processed and analyzed using a computer. Figure 2 illustrates the schematic principle of the image sensor in the polarized camera.

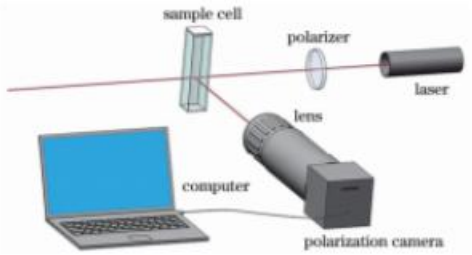

Figure 1 *Principle diagram of polarization image dynamic light scattering measurement*

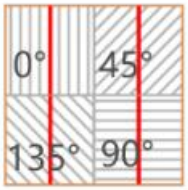

Figure 2 *Schematic diagram of polarization camera image sensor principle*

Figure 3 shows the grayscale images representing the scattered light intensity in four polarization directions obtained from the shooting of polystyrene ellipsoidal particles.

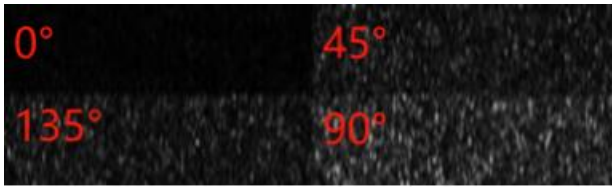

Figure 3 *Speckle images of ellipsoidal particles captured by a polarization camera in 0 °, 45 °, 90 °, and 135 ° polarization directions*

1.2. Optical sphericity

Define the degree of linear polarization (DoLP) as the optical sphericity Φ， Criterion for the degree of deviation of nanoparticles from the sphere. [4] Its expression is as follows:

$$DoLP = \frac{\sqrt{S_1^2 + S_2^2}}{S_0} \quad (1)$$

$$\Phi = Dolp \quad (2)$$

S0: One of the Stokes parameters, with a value of I0 ° +I90 ° .

S1: One of the Stokes parameters, with values ranging from I0 ° + I90 ° .

S2: One of the Stokes parameters, with a value of I45 ° - I135 ° .

The optical sphericity and related scattering data of several nanoparticles obtained by the author's team in the preliminary experiments, including PS spheres, MOF-199A, MOF-199B, MOF-199C, silver nanosheets, gold nanorods, silver nanowires, etc., are shown in Table 1.

Table 1 *Experimental results of dynamic light scattering measurement of polarization images of different particles*

Code Number	*I0/S0*	*I45/S0*	*I90/S0*	*I135/S0*	*S0*	*S1*	*S2*	*DoLP*
PS 球	*0.9962*	*0.4922*	*0.0038*	*0.5016*	*1.0000*	*0.9924*	*-0.0094*	*0.9924*
MOF-199A	*0.9927*	*0.4734*	*0.0073*	*0.5250*	*1.0000*	*0.9854*	*-0.0516*	*0.9868*
MOF-199B	*0.9926*	*0.4706*	*0.0074*	*0.5284*	*1.0000*	*0.9852*	*-0.0578*	*0.9869*
MOF-199C	*0.9895*	*0.4801*	*0.0105*	*0.5165*	*1.0000*	*0.9790*	*-0.0364*	*0.9797*
Silver nanosheets	*0.7648*	*0.5025*	*0.2352*	*0.5105*	*1.0000*	*0.5296*	*-0.0080*	*0.5297*
Gold nanorods	*0.7428*	*0.4999*	*0.2572*	*0.5163*	*1.0000*	*0.4856*	*-0.0164*	*0.4859*
Silver nanorods	*0.6745*	*0.4236*	*0.3255*	*0.5880*	*1.0000*	*0.3490*	*-0.1644*	*0.3858*

To verify the feasibility of evaluating particle morphology using optical sphericity, a comparative parameter, Wadell sphericity Ω, is introduced. Its expression is as follows:

$$\Omega = \frac{Sn}{S} \quad (3)$$

S_n: surface area of the equivalent sphere;
S: The actual surface area of the particles.

As shown in Figure 5, the changes in optical sphericity and Wadell sphericity of particles with different morphologies are consistent. Therefore, we believe that optical sphericity as a descriptor for nanoparticle morphology is feasible.

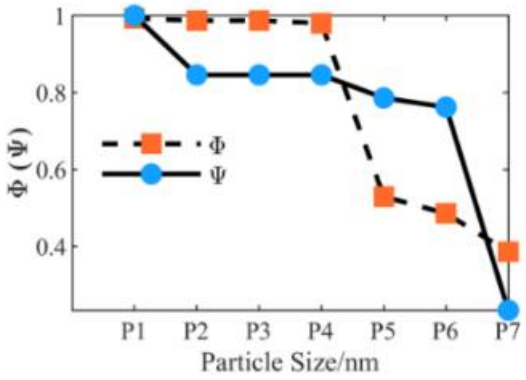

Figure 5 *Comparison between optical and Wadell sphericity*[5]

The following figure shows our electron microscopy images of ellipsoid, double ring, gourd shaped, and fat emulsion particles, as well as the distribution of optical sphericity.

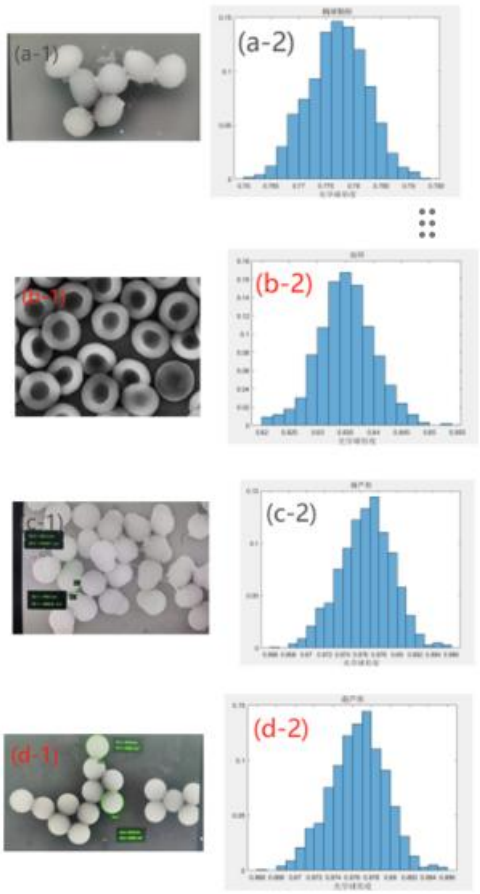

Figure 6 *Electron microscopy images of ellipsoid, double ring, gourd shaped, and fat emulsion particles, as well as the distribution of optical sphericity (a-1) Ellipsoid electron microscopy images (a-2) Ellipsoidal sphericity distribution images (b-1) Double ring electron microscopy images (b-2) Double ring ellipsoidal sphericity distribution images (c-1) gourd shaped electron microscopy images (c-2) Hulu shaped ellipsoidal sphericity distribution images (d-1) Fat emulsion electron microscopy images (d-2) Fat emulsion ellipsoidal sphericity distribution images*

The study reveals that the concept of optical sphericity faces a multi-valued problem, meaning that particles of different sizes, materials, and shapes can exhibit the same optical sphericity. Additionally, in the setup for polarized image dynamic light scattering, the camera's receiving surface is placed on a horizontal plane at a scattering angle of 90°, as shown in Figure 1. Altering the position of the receiving surface could potentially enhance the sensitivity to particle morphology. Thus, the research incorporates simulations of particles with various shapes, sizes, and materials to explore their far-field scattering polarization characteristics. This approach aims to evaluate the applicability of optical sphericity and may lead to the development of improved measurement system configurations or enhanced morphological descriptors based on polarized light scattering characteristics.

2. Methodology

This paper employs the FDTD method to simulate the far-field scattering characteristics of various non-spherical particles.

The principle of PIDLS, as introduced in Figure 1, involves placing the receiver screen on a horizontal plane at a 90° scattering angle to capture the scattering intensity and polarization information from the observation face. Essentially, this involves decomposing the light vectors in the observation plane into components parallel to the plane at angles of 0°, 45°, 90°, and 135°. The FDTD method solves Maxwell's equations to compute the light field, consistent with the theoretical basis of scattering. In FDTD, the three-dimensional far-field monitors can acquire the intensity information of light around a sphere and the decomposed components of the electric field strengths in the x, y, and z directions, where the square of the electric field strength corresponds to the light intensity. Thus, theoretically, it is feasible to synthesize and decompose vectors to obtain specific information about light intensity and polarization at I0°, I45°, I90°, and I135°. From a theoretical perspective, FDTD can capture far-field light intensity and polarization information about particles.

The simulation technique pathway is shown in the following diagram.

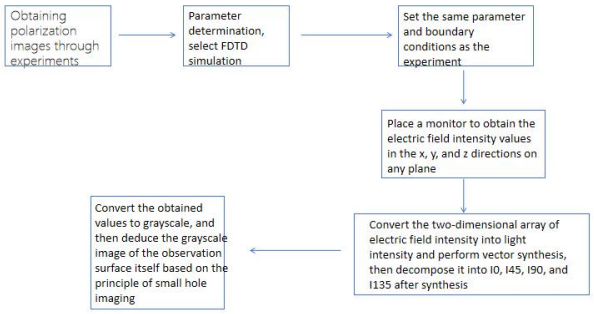

Figure 7 *Feasibility Analysis Diagram*

The specific steps include: initially setting the size of the three-dimensional simulation area and dividing it into a grid, then setting boundary conditions for each direction. The medium within the three-dimensional area (simulation environment) is also configured. As the simulation targets a single particle, direct settings for the particle's volume, shape, material, and position are established. Regarding the light source setup, linearly polarized light polarized in the z-direction and incident in the x-direction is selected. Once the fundamental light path information is configured, three-dimensional far-field monitors and three-dimensional scattering surface monitors are set up within the space to acquire the required polarization information and light intensity data.

3. Results and Discussion

In the study, linearly polarized light with a wavelength of 500 nm, polarized along the z-axis and incident in the x-

direction, is used as the simulation's incident light. The simulations are performed in a water medium for single particles, specifically focusing on gold and diamond particles. This setup is chosen to enable a comparison with experimental data. The far-field simulations address various scenarios: a) particles of equal volume but different shapes, b) particles of the same shape but different volumes, c) particles of the same volume and shape but made from different materials, and d) particles with different aspect ratios, specifically rectangular prisms, and cylinders.

Monitors are positioned in the simulation environment as per the setup in Figure 1, allowing the simulation to capture the x-component and z-component of the field, representing the electric field strengths at 90° and 0°, respectively. The results provide detailed polar diagrams of the far-field scattering light intensity and the electric field strength information at 0° and 90°, which are illustrated in the corresponding figures.

As shown in Figure 8, the basic operating conditions of simulation Figure 9 and Figure 10 are presented. The incident light is incident along the x-axis direction and polarized in the z-axis direction. The observation plane in our experiment is the xz plane, so the obtained electric field strengths in the 0 ° and 90 ° directions are derived from the vector decomposition of the xz plane.

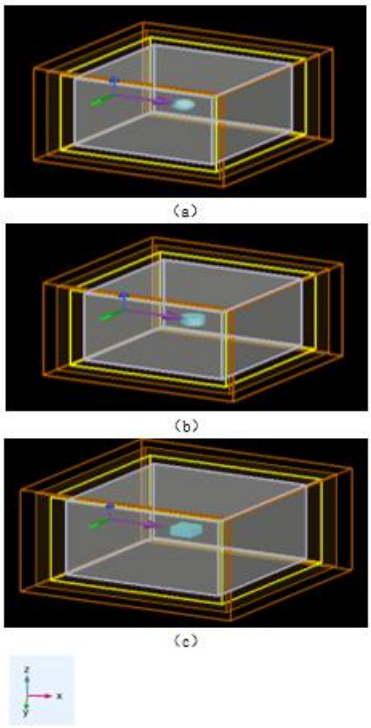

Figure 8 *Simulation diagram (x direction is long, y direction is wide, and z direction is high) (a) The radius of gold spherical particles is 60nm, (b) The bottom radius of gold cylindrical particles is 60nm, and the height is 90nm, (c) The length of gold rectangular particles is 106nm, the width is 106nm, and the height is 90nm*

As illustrated in Figure 9, smaller particles exhibit similar far-field light intensity distributions, with subtle differences dependent on the particles' morphology. Figure 10 shows that particles of similar volumes, specifically spheres and cylinders, present highly consistent electric field strength distributions at 0° and 90° directions because the surfaces where light is incident are curved. In contrast, rectangular particles, having flat incident surfaces, display distinctly different electric field distributions at the 0° direction compared to spherical and cylindrical particles. Due to the limited data available from simulations of different particle morphologies, more definitive patterns could be discerned with further research.

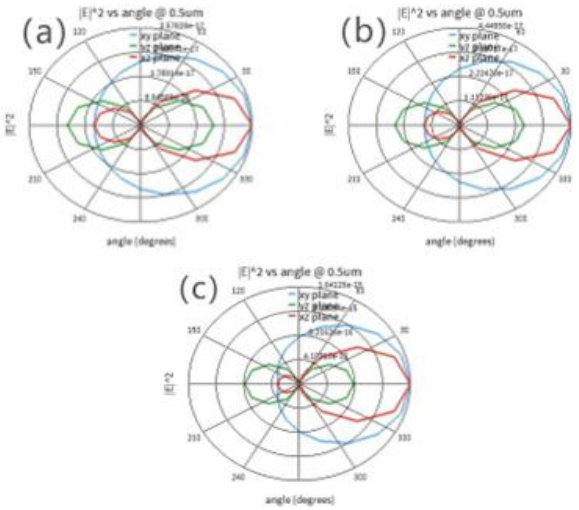

Figure 9 *Far-field scattering vector pole diagram of particles with different shapes and equal volumes (a) Gold spherical particles with a radius of 60nm (b) Gold cylindrical particles with a bottom radius of 60nm and a height of 90nm (c) Gold rectangular particles with a length of 106nm, a width of 106nm, and a height of 90nm*

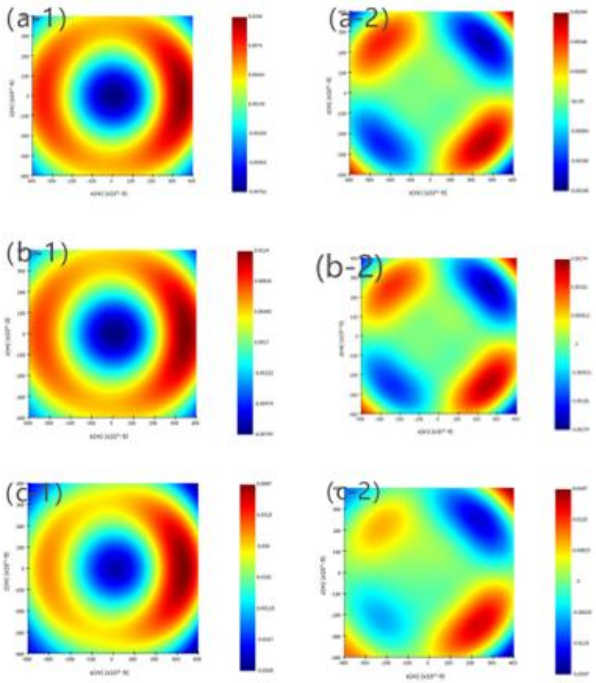

Figure 10 *Distribution of Electric Field Intensity in the 0 ° and 90 ° Directions of Particles with Similar Volumes and Different Shapes (a-1) Gold Spherical Particle Radii 60nm E0 ° (a-2) Gold Spherical Particle Radii 60nm E90 ° (b-1) Gold Cylindrical Particle Bottom Radii 60nm High 90nm E0 ° (b-2) Gold Cylindrical Particle Bottom Radii 60nm High 90nm E0 ° (c-1) Gold Rectangular Particle Lengths 106nm Wide 106nm High 90nm E0 ° (c-2) Gold Rectangular Particle Lengths 106nm Wide 106nm High 90nm E90 °*

As depicted in Figure 11, for very small test particles, both the forward and backward scattering intensities are typically high. In simulations involving rectangular and cylindrical particles with aspect ratios close to 1, even larger particles do not exhibit significant changes in scattering intensity.

Figure 12 illustrates that for particles of the same shape but different volumes, as the volume increases while maintaining a similar aspect ratio, and with the incident light striking the particle as shown in Figure 8 without any rotation of the particle configuration, the results observed on the same viewing plane do not deviate significantly. This consistency suggests that the physical shape and orientation of the particles critically influence the scattering patterns observed, regardless of size changes under constant aspect ratios.

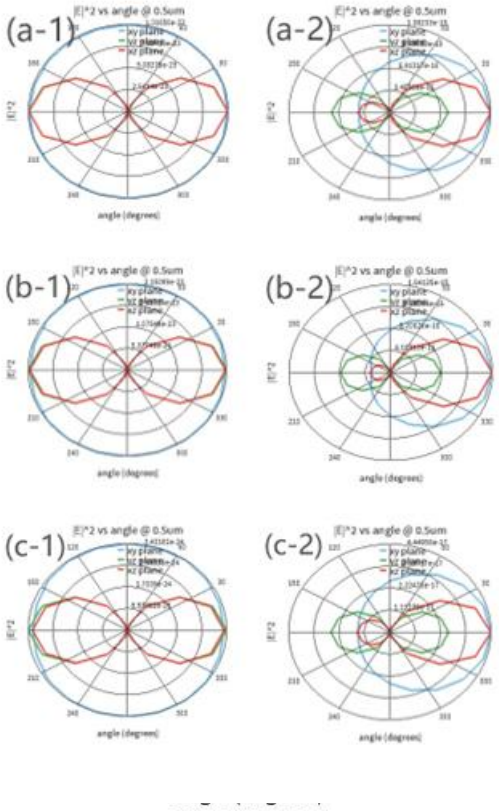

Figure 11 *Far-field scattering vector pole diagram of particles of the same shape but different volumes (a-1) Gold spherical particle radius 5nm (a-2) Gold spherical particle radius 60nm (b-1) Gold rectangular particle length 5nm, width 5nm, height 7nm (b-2) Gold rectangular particle length 106nm, width 106nm, height 90nm (c-1) Gold cylindrical particle bottom radius 5nm, height 7nm (c-2) Gold cylindrical particle bottom radius 60nm, height 90nm*

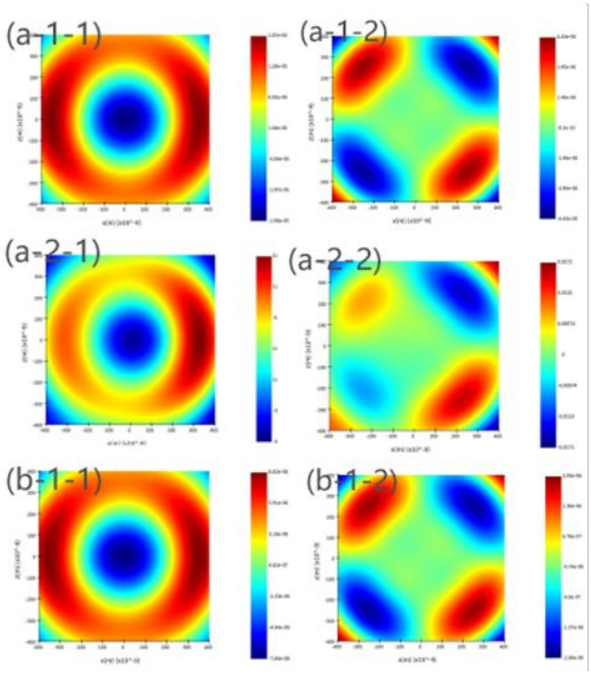

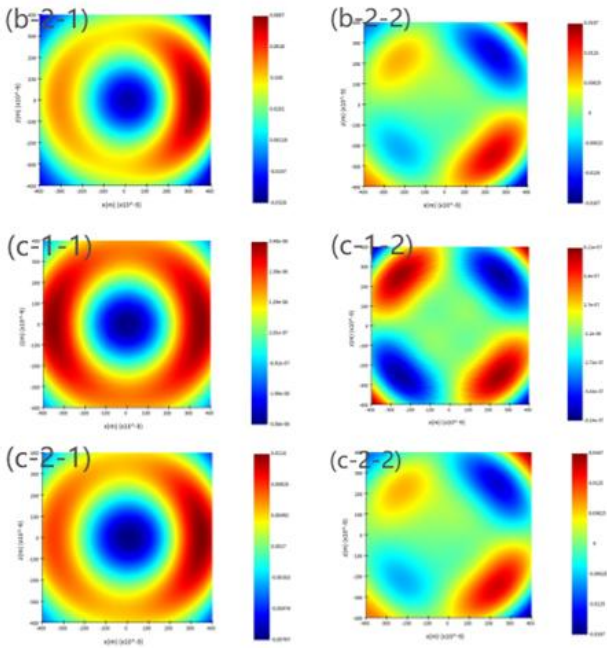

Figure 12 *Distribution of electric field intensity in the 0 ° and 90 ° directions for particles of the same shape but different volumes (a-1-1) Spherical particle radius 5nm E0 ° (a-1-2) Spherical particle radius 5nm E90 ° (a-2-1) Spherical particle radius 60nm E0 ° (a-2-2) Gold spherical particle radius 60nm E90 ° (b-1-1) Gold rectangular particle length 5nm wide 5nm high 7nm E0 ° (b-1-2) Gold rectangular particle length 5nm wide 5nm high 7nm E90 ° (b-2-1) Gold rectangular particle length 106nm wide 106nm high 90nm E0 ° (b-2-2) Gold rectangular particles with a length of 106nm, width of 106nm, height of 90nm, E90 ° (c-1-1-1) Gold cylindrical particles with a bottom radius of 5nm, height of 7nm, E0 ° (c-1-2) Gold cylindrical particles with a bottom radius of 5nm, height of 7nm, E90 ° (c-2-1) Gold cylindrical particles with a bottom radius of 60nm, height of 90nm, E0 ° (c-2-2) Gold cylindrical particles with a bottom radius of 60nm, height of 90nm, E90 ° (c-2-2)*

In Figures 13 and 14, a distinct response is observed in spherical particles when materials with significantly different refractive indices are used. However, the response in simulated rectangular and cylindrical particles is less pronounced. This suggests that further simulations with various materials could help establish more definitive patterns regarding the impact of material properties on scattering behaviors.

Due to the large volume of the particles, their polar diagrams of light intensity show weaker backward scattering, and therefore, these diagrams are not presented. For ease of comparison between different shaped particles' polarization signals, simulations were conducted for both rectangular and cylindrical particles. The rectangular particles have a square base, and the aspect ratio for the cylinders is defined by the ratio of radius to height, while for rectangular particles, it is defined by the ratio of half the base length to height. The distributions of electric field strength at 0° and 90° for particles with different aspect ratios are as follows:

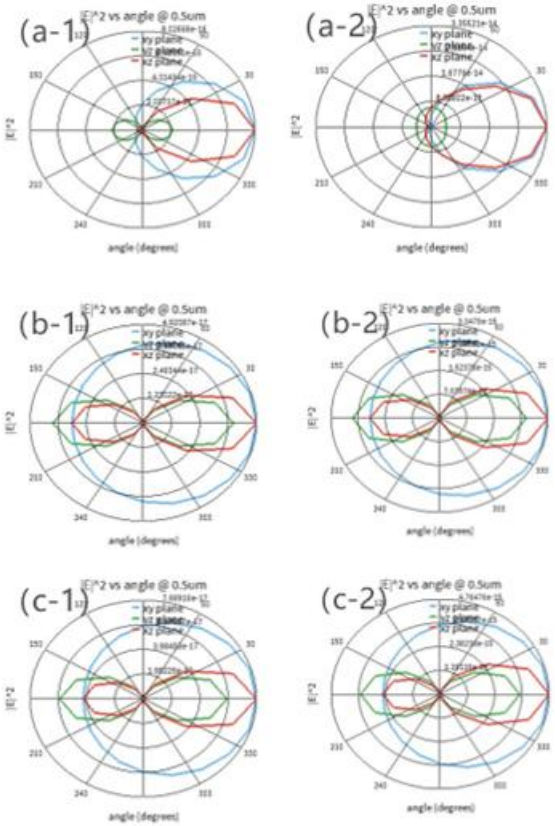

Figure 13 *Far-field scattering vector pole diagram of particles of the same volume, shape, and different materials (a-1) Gold spherical particle radius of 100nm (a-2) Diamond spherical particle radius of 100nm (b-1) Gold rectangular particle length of 80nm, width of 80nm, height of 200nm (b-2) Diamond rectangular particle length of 80nm, width of 80nm, height of 200nm (c-1) Gold cylindrical particle bottom radius of 40nm, height of 200nm (c-2) Diamond cylindrical particle bottom radius of 40nm, height of 200nm*

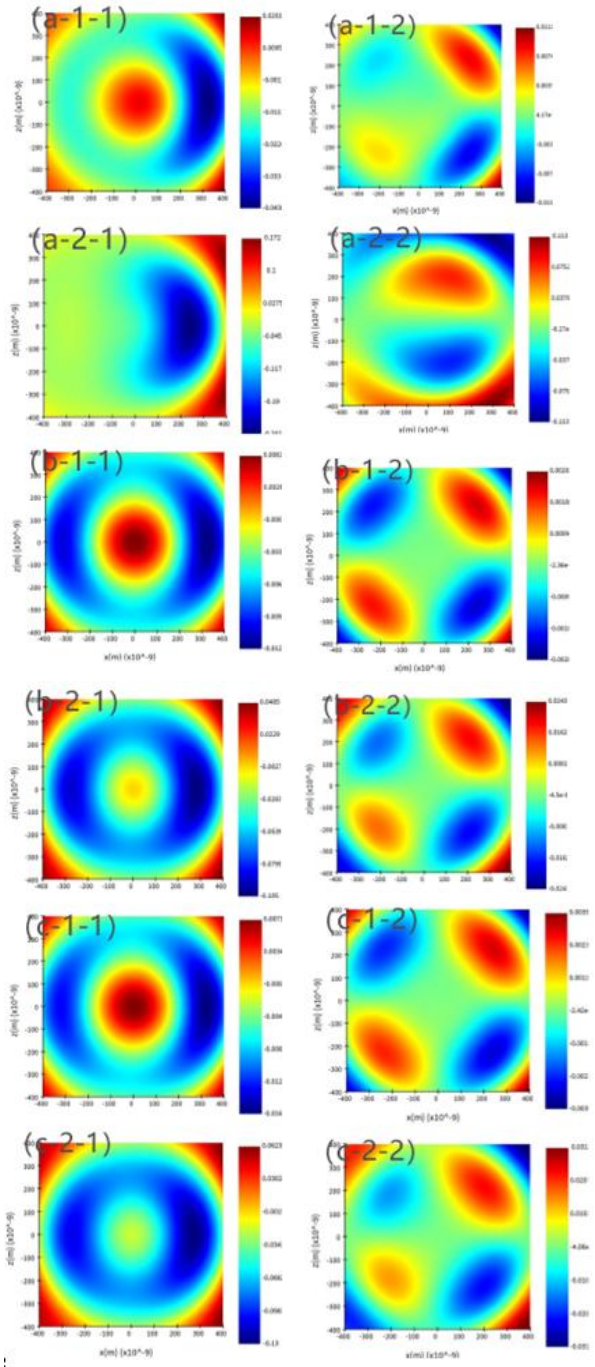

Figure 14 *Distribution of electric field intensity in the 0 ° and 90 ° directions for particles of the same volume, shape, and different materials (a-1-1-1) Gold spherical particle radius 100nm E0 ° (a-1-2) Gold spherical particle radius 100nm E90 ° (a-2-1) Diamond spherical particle radius 100nm (a-2-2) Diamond spherical particle radius 100nm E90 ° (b-1-1) Gold rectangular particle length 80nm, width 80nm, height 200nm E0 ° (b-1-2) Gold rectangular particle length 80nm, width 80nm, height 200nm E90 ° (b-2-1) Diamond rectangular particle length 80nm, width 80nm, height 200nm E0 ° (b-2-1) 2-2) Diamond rectangular particles with a length of 80nm, a width of 80nm, and a height of 200nm E90 ° (c-1-1) Gold cylindrical particles with a bottom radius of 40nm and a height of 200nm E0 ° (c-1-2) Gold cylindrical particles with a bottom radius of 40nm and a height of 200nm E90 ° (c-2-1) Diamond cylindrical particles with a bottom radius of 40nm and a height of 200nm E0 ° (c-2-2) Diamond cylindrical particles with a bottom radius of 40nm and a height of 200nm E90 °*

Figures 15 and 16 illustrate the variations in the electric field intensity at 0° and 90° directions for gold rectangular and cylindrical particles, respectively, as their aspect ratios change. These figures show a clear trend: as the aspect ratio increases, the electric field intensity at the 0° direction undergoes significant changes. Comparing these two figures highlights that different particle shapes develop more distinctive structural features in the 0° direction's electric field strength as their aspect ratios increase. This observation suggests that the shape and proportion of particles critically influence their electromagnetic responses under polarized light conditions.

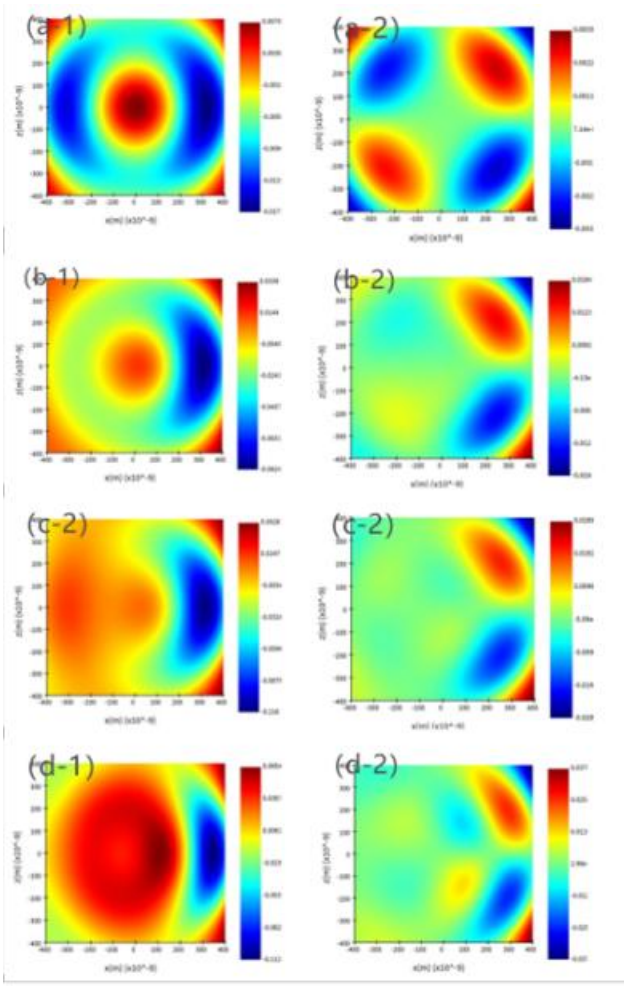

Figure 15 *Distribution of electric field intensity at 0 ° and 90 ° for gold rectangular particles with different aspect ratios (a-1). The aspect ratio of gold rectangular particles is 0.148 E0 ° (a-*

2). The aspect ratio of gold rectangular particles is 0.148 E90 ° (b-1). The aspect ratio of gold rectangular particles is 0.37 E0 ° (b-2). The aspect ratio of gold rectangular particles is 0.37 E90 ° (c-1). The aspect ratio of gold rectangular particles is 0.5 E0 ° (c-2). The aspect ratio of gold rectangular particles is 0.5 E90 ° (d-1). The aspect ratio of gold rectangular particles is 0.75 E0 ° (d-2). Diameter ratio 0.75 E90 °

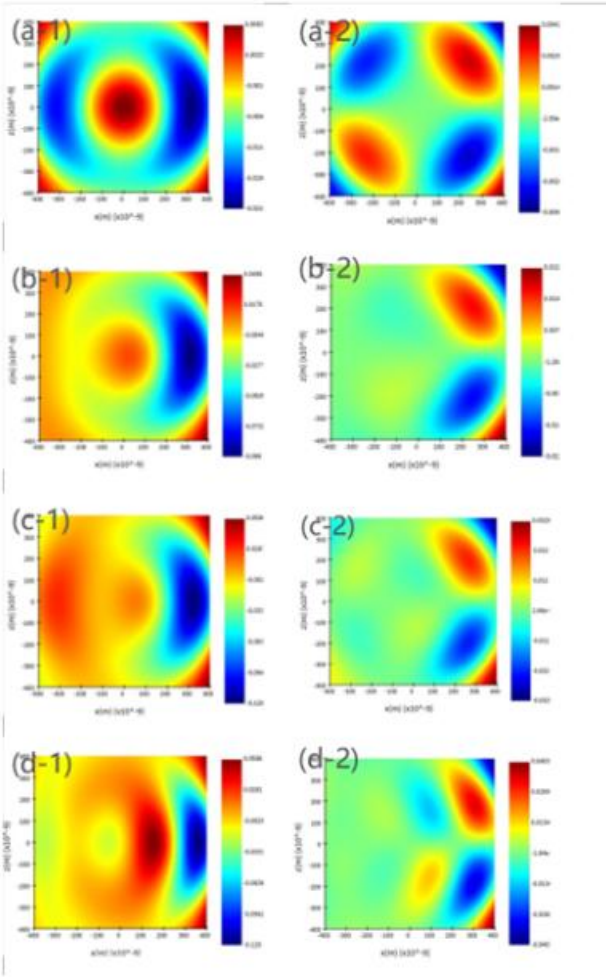

Figure 16 *Distribution of electric field intensity at 0 ° and 90 ° for gold cylindrical particles with different aspect ratios (a-1) Length to diameter ratio of gold cylindrical particles 0.148 E0 ° (a-2) Length to diameter ratio of gold cylindrical particles 0.148 E90 ° (b-1) Length to diameter ratio of gold cylindrical particles 0.37 E0 ° (b-2) Length to diameter ratio of gold cylindrical particles 0.37 E90 ° (c-1) Length to diameter ratio of gold cylindrical particles 0.5 E0 ° (c-2) Length to diameter ratio of gold cylindrical particles 0.5 E90 ° (d-1) Length to diameter ratio of gold cylindrical particles 0.75 E0 ° (d-2) Length to diameter ratio of gold cylindrical particles 0.75 E90 °*

4. Summary

The current implementation of the Finite-Difference Time-Domain (FDTD) method provides a basic analysis, showing that smaller particles like rectangles, spheres, and cylinders exhibit similar polarization information at 0° and 90° directions. As the aspect ratio of these particles increases, their polarization characteristics at these angles start to exhibit distinct features. This observation indicates that optical sphericity has a specific applicable range. Therefore, future work will focus on assessing the applicability of optical sphericity across different scales and shapes. In addition to examining optical sphericity, our simulations have initially used a horizontal plane at a 90° scattering angle as the signal reception surface. Future simulations will need to consider choosing reception surfaces at various angles to potentially enhance results for different particle types on different reception surfaces.

[1] Flores-Rojas G G, López-Saucedo F, Vera-Graziano R, et al. Magnetic nanoparticles for medical applications: Updated review[J]. Macromol, 2022, 2(3): 374-390.

[2] .Su Q, Zuo C, Liu M, Tai X. A Review on Cu2O-Based Composites in Photocatalysis: Synthesis, Modification, and Applications. Molecules. 2023; 28(14):5576.

[3] Wang B, Cai T, Cai X, et al. Polarized imaging dynamic light scattering for simultaneous measurement of nanoparticle size and morphology[J]. Particuology, 2024, 85: 213-223.

[4] Wang B, Cai T, Cai X, et al. Polarized imaging dynamic light scattering for simultaneous measurement of nanoparticle size and morphology[J]. Particuology, 2024, 85: 213-223.

[5] Wang B, Cai T, Cai X, et al. Polarized imaging dynamic light scattering for simultaneous measurement of nanoparticle size and morphology[J]. Particuology, 2024, 85: 213-223.

The 14th International Conference on
Laser-light and Interactions with Particles (LIP2024)
September 18-22nd, 2024, Xi'an, Shaanxi, China

LIGHT SCATTERING BY A BURIED CIRCULAR CYLINDER

Huayong ZHANG[1*], Zhenzhen CHEN[2]

[1] Information Materials and Intelligent Sensing Laboratory of Anhui province, Anhui University, Hefei, Anhui 230601, P. R. China
[2] Institute of advanced manufacture technology engineering, Hefei University, Hefei, Anhui 230601, P. R. China
Corresponding author: hyzhang0905@163.com

Abstract

For an incident electromagnetic plane wave, its scattering by an infinitely long circular cylinder beneath a plane interface is investigated. The electromagnetic fields within different regions are expanded over appropriate rectangular or cylindrical vector wave functions, and the unknown expansion coefficients are determined by the boundary conditions. To analyse the coupling scattering between the circular cylinder and plane interface, the transformations of rectangular and cylindrical vector wave functions are applied. Mueller matrix elements are calculated, and the scattering features are discussed briefly.

Formulation

As illustrated in Fig.1 (a), an infinitely long circular cylinder of radius r_0 is attached to the Cartesian coordinate system $O'x'y'z'$, with the axis $O'z'$ parallel with and $O'y'$ normal to a plane interface between free space and medium 1. An accessory system $O''x''y''z''$ is introduced, which is parallel with $O'x'y'z'$. The coordinates of origin O' in $O''x''y''z''$ are $(0,d,0)$, i.e., origin O' located at a distance d beneath the plane interface. An electromagnetic (EM) plane wave propagates in the plane xOz of the system $Oxyz$, and its propagation direction has an angle $\pi-\zeta$ with respect to the axis Oz which is normal to the plane interface. To describe an EM plane wave with arbitrary illumination, an angle ψ is set between the axes Ox and $O''z''$ in the plane interface, i.e., $Oxyz$ obtained by rotations of $O''x''y''z''$ through Euler angles $(\frac{\pi}{2},-\frac{\pi}{2},\psi)$.

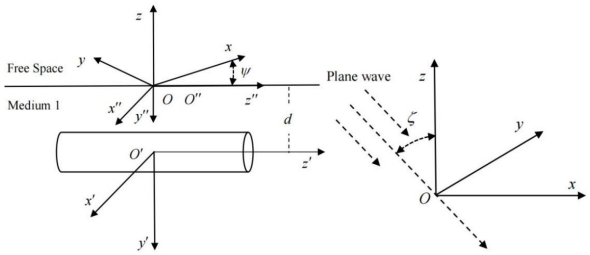

Fig. 1 *(a) A circular cylinder beneath a plane interface. (b) The propagating direction of an EM plane wave.*

The 14th International Conference on
Laser-light and Interactions with Particles (LIP2024)
September 18-22nd, 2024, Xi'an, Shaanxi, China

PARTICLE SIZE MEASUREMENT USING THE LASER DIFFRACTION MODEL BASED ON MONTE CARLO METHOD

Geyi Su, Minglei Guan and Mingxu Su *

Institute of Particle and Two-phase Flow Measurement, University of Shanghai for Science and Technology, Shanghai, 200093, China

Corresponding author: sumx@usst.edu.cn

Abstract

A laser scattering model based on the Monte Carlo method (MCM) is developed to investigate the light scattering and extinction characteristics of the non-parallel incident beams, the high-concentration particles, and the mixed particles, which are challenging by the conventional method. Meanwhile, a set of online measurement test systems for acquiring scattered light energy distribution is constructed to verify the model's accuracy, which yields the maximum root mean square errors (RMSE) between the MCM and the conventional model and the experimental results of 0.006 and 0.011, respectively. Afterward, the differential evolution (DE) algorithm is introduced to invert particle size based on the spectral content. The inversion results show that the MCM model can effectively correct the measurement errors caused by the non-parallel incident beams and multiple scattering effects due to high concentrations. Thus, the absolute relative errors compared with the set values have been reduced from 13.08% and 11.50% in the conventional model to within 3.00%. Additionally, two distinct sizes and mixing ratios of the mixed particle system have been successfully inverted with maximum absolute relative errors of 8.64%, 9.55%, and 4.38%, respectively, in comparison with the set values.

1 Introduction

Particle size analyzers (PSAs) based on static light scattering or laser diffraction (LD) have been widely used for particle size distribution (PSD) characterization of various suspensions or emulsions due to their non-contact and high-precision characteristics [1,2]. Several recent studies have already implemented the PSAs for determining particle size and concentration [3], studying the sensitivity of laser light scattering particle sizing to refractive index and irregularity [4], and investigating the optical properties of different irregularly shaped particles [5]. Nevertheless, it is extremely important to devote sufficient attention to the scattered light energy distribution in non-parallel beam incidence, highly concentrated particle systems, and mixed particle systems. Specifically, the conventional model employed to estimate the PSD relies on parallel incident beams and a single scattering approximation. An essential requirement for using LD-PSAs is the strict alignment of the detector with the incident light. Additionally, the turbidity levels of most objects in industrial processes may exceed the acceptable range for laser scattering. Multiple scattering can happen when the light scattered by one particle encounters another before reaching the detector, elevating the apparent scattering angle [6] and leading to an underestimation of particle size. Also, a mixed particle system tends to introduce more complexity than a single-type particle system, while the characterization of composite particle parameters is widely needed in many fields, such as crystallization, materials science, aerosols, and hybrid nanofluids [7, 8]. Hence, it is crucial to quantify and evaluate the impact of non-parallel beams and multiple scattering effects, offer potential corrections, for the accurate characterization of the particle size and mixing ratios with the LD principle. The MCM employs reproducible random sampling to estimate the probability of a range of outcomes that can be effectively utilized to simulate light scattering and trace the behaviour of the photons involved [9]. Hence, improving the model based on the MCM provides an expectable way of expanding the potential use of the LD PSAs.

2 Principle

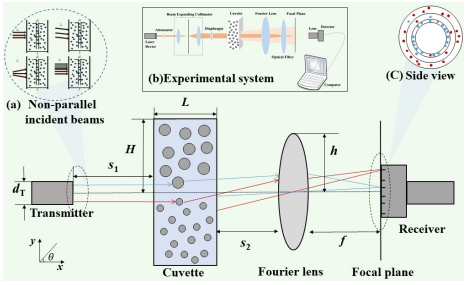

Fig. 1 *Schematic diagram of MCM with photon propagation process in a dispersion.*

As shown in Fig. 1, the MCM interprets the continuous incident light beam as a set of photons. A receiver is positioned at the focal plane of a Fourier lens to detect the light beam, as per the guidelines of Fresnel diffraction. According to the properties of Fourier lenses, rays that are parallel to the secondary optical axis converge on a common point located on the focal plane. Assuming a photon passes through the particle system and leaves the cuvette after last colliding with a particle (where light

scattering occurs and is explained by Mie's theory), the direction of photon motion falls within the range of the two scattering angles ($\theta_{i,1}$, $\theta_{i,2}$) corresponding to the inner and outer diameter of an assumed ring on the detector. The photon, carrying information about particle size, is then classified and counted correspondingly.

The resting events of the photon are determined according to the following conditions:

$$\begin{cases} (\varepsilon_1 > a) \cap (n \geq 1) & \text{absorbed} \\ (x > S_1 + L) \cap (n < 1) & \text{transmission} \\ (x > S_1 + L) \cap (|y| < h) \cap (\theta_{i,1} < |\theta_n| < \theta_{i,2}) \cap (n = 1) & \text{single scattering} \\ (x > S_1 + L) \cap (|y| < h) \cap (\theta_{i,1} < |\theta_n| < \theta_{i,2}) \cap (n > 1) & \text{multiple scattering} \\ \text{others} & \text{escape} \end{cases} \quad (1)$$

Where ε_1 is a random number obeying a uniform distribution in the interval [0, 1], a is the albedo [10], and n indicates the number of occurrences of light scatterings.

The scattered light energy distribution E_i is calculated as:

$$N_i = N_{r,i}(\theta_{i,1} + \theta_{i,2})/2 \quad (2)$$

$$E_i = \sum_i \left[N_i / \left(\sum_{\theta_{i,1}}^{\theta_{i,2}} N_i \right) \right] \quad (3)$$

Where $N_{r,i}$ is the number of scattered photons received within the ith ring between $\theta_{i,1}$ and $\theta_{i,2}$.

3 Results and discussion

3.1 Model and algorithm validation

With the developed MCM, numerical simulations were performed, given the particle sizes D of 2.6, 9.4, and 15 μm, respectively. Fig. 2(a) shows the scattered light energy distribution when only a single scattering is considered. The MCM simulation has a maximum RMSE of 0.006 and 0.011 compared with the conventional model and experimental results.

The Differential Evolution (DE) algorithm [11] has been used for the inversion of PSD, in which four critical parameters of the DE algorithm were optimized to set the population size of 1000, the upper and lower limits of the scaling factor set at 0.3 and 0.5, and the crossover factor of 0.85. The PSD is determined by globally minimizing the objective function, which is defined according to the RMSE between the experimental and theoretical scattered light energy distribution:

$$RMSE = \sqrt{\frac{1}{N}\sum_{j=1}^{N}(\alpha_s - \alpha_e)^2} \quad (4)$$

where α_s and α_e are the simulated and experimental scattered light energy distribution, respectively.

To minimize the number of undetermined parameters in the optimization process, the PSD is assumed to follow a certain functional form, such as the Rosin-Rammler (R-R) distribution. It provides the following expression:

$$f(D) = \frac{K}{D}\left(\frac{D}{\overline{D}}\right)^{K-1} \exp\left(-\left(\frac{D}{\overline{D}}\right)^{K}\right) \quad (5)$$

where $\overline{D}$ is the modal diameter, and K is the distribution width.

As shown in Fig. 2(b), the DE algorithm was used to determine the median particle diameter D_{50} of different cases, and the absolute relative errors between the inversion results and the set values were less than 5%.

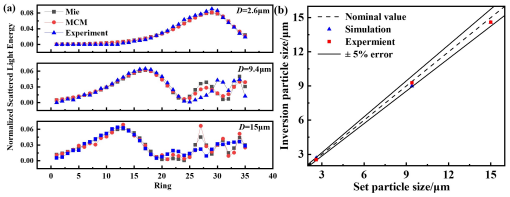

Fig. 2 Scattered light energy and inversion results.

3.2 Non-parallel incident beams

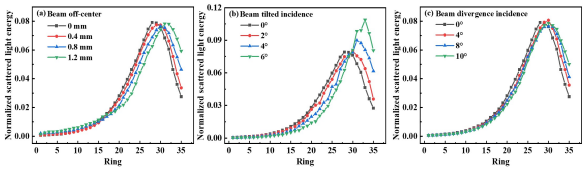

Fig. 3 Scattered light energy distribution in particle systems incident on a non-parallel beam (D = 2.6 μm).

Table 1 *Particle size inversion and correction results (D_{50}).*

	Conventional		MCM	
Divergence angle /°	Inversion value /μm	Relative error /%	Inversion value /μm	Relative error /%
4	2.44	6.15	2.53	2.69
8	2.35	9.62	2.53	2.69
10	2.26	13.08	2.62	0.70

As shown in Fig. 3, we simulated the scattered light energy distributions of three non-parallel beams incident on the particle system: incident beam diverging from the center of the detector, tilted incidence, and divergent incidence. As the offset distance, tilted incidence angle, and divergence angle increase, the scattered light energy distribution curves all deviate compared to the scattered light energy distribution of the parallel beam. As shown in Table 1, when the divergence angle increases, the conventional model D_{50} gradually decreases compared to the set value, and the inversion relative error gradually increases. When the divergence angle was increased to 10°, the inversion relative error reached 13.08% compared with the set value. Then, the MCM was used to calculate the scattered light energy distribution at different divergence angles to construct the coefficient matrix instead of the scattered light energy coefficient matrix calculated by the Mie theory, and the relative error of the inversion for particle size at different divergence angles was within 3.00%.

3.3 High-concentration particle systems

As shown in Fig. 4, with the increase of concentration, the collision probability of photons and particles gradually becomes more prominent, and the number of scattered and escaped photons gradually increases, resulting in the off-axis photons moving to a larger angle, corresponding

to the outer ring of the detector. When the concentration is 5×10^{-5}, the number of multiple-scattered photons has been more than 25% of the total number of scattered photons, and the peak of the total scattered photon number moves correspondingly toward the outer ring, from the 25-ring to the 27-ring. Therefore, the scattered light energy curve is shifted to the outer ring (rightward). We generated an improved coefficient matrix for the subsequent inversion, which yielded the inversion results as shown in Fig. 4(d), including PSD before (using the conventional model) and after correction (using the Monte Carlo model). After correction, the relative error for the particles with a set size of 2.6 μm for different concentrations remains within 3.0%.

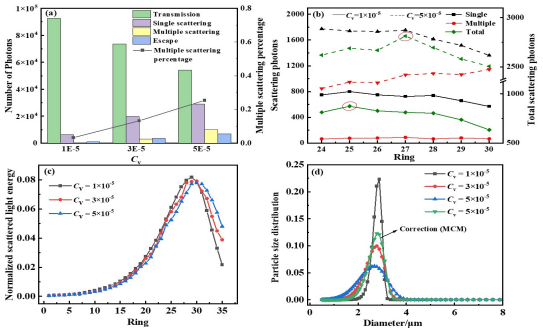

Fig. 4 *Numerical simulation results of the MCM model at different concentrations (D = 2.6 μm).*

3.4 Mixed particle systems

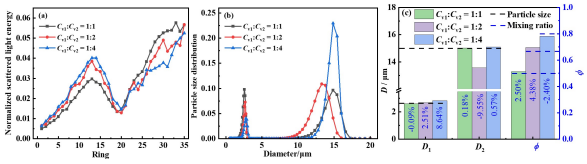

Figure 5 *Numerical simulation results of the MCM model at mixed particle systems (D_1 = 2.6 μm, D_2 = 15 μm).*

Fig. 5(a) shows the scattered light energy distribution of the mixed particles under different mixing ratios. As the proportion of component II (D_2 = 15 μm) in the mixed particle system increases, the corresponding scattered light energy increases on inner ring, and decreases on outer ring, indicating that the scattered light energy is very sensitive to the particle size and mixing ratio. Figs. 5(b) and (c) show that the peaks of the inverted particle sizes correspond well at different mixing ratios, and the maximum absolute relative errors for the two particle sizes and mixing ratios of the mixed particle systems are 8.64%, 9.55%, and 4.38%, respectively.

4 Conclusions

This letter proposes a laser scattering model based on the Monte Carlo method, and a set of online particle size measurement test systems is constructed to verify the model's accuracy. The maximum root means square error between the MCM and the conventional model, and the measurement results are 0.006 and 0.011. Then, by combining the Differential Evolution algorithm and improved coefficient matrix, the MCM model can effectively correct the measurement errors caused by the non-parallel incident beams and multiple scattering effects at high concentrations in the conventional model, and the absolute relative errors compared with the set values are reduced to within 3.00%. Furthermore, two different particle sizes and mixing ratios of the mixed particle system are successfully inverted with maximum absolute relative errors of 9.55% compared with the set values.

Acknowledgement

This work was supported by the National Natural Science Foundation of China (Nos. 52376162).

References

[1] X. Cai, M. Su, J. Shen, "*Particle Size Measurement Technology and Application*," (Chemical Industry Press, Beijing, 2022).

[2] R. Xu, Light scattering: A review of particle characterization applications, Particuology 18:11-21 (2015).

[3] A.S. Lokhov, M.D. Kravchishina, A.A Klyuvitkin, et al., In situ measurements of the characteristics of suspended particles in the barents sea by the LISST-Deep laser diffractometer, Oceanology 60(5):650-663 (2020).

[4] JCG Martín, D. Guirado, E. Zubko, et al., Computational study of the sensitivity of laser light scattering particle sizing to refractive index and irregularity, Journal of Quantitative Spectroscopy and Radiative Transfer 241:106745 (2019).

[5] Z. Evgenij, Modeling the optical properties of forsterite particles using different irregularly shaped particles, Journal of Quantitative Spectroscopy and Radiative Transfer 323:109053 (2024).

[6] R. Hussain, M. Noyan, G. Woyessa, et al., An ultra-compact particle size analyser using a CMOS image sensor and machine learning, Light, science & applications 9: 21 (2020).

[7] R. Lenin, P. A. Joy, C. Bera, A review of the recent progress on thermal conductivity of nanofluid, Journal of Molecular Liquids 338(15): 116929 (2021).

[8] Li Z, Liu J, Ning Z, Xu H, et al., Compact gas cell for simultaneous detection of atmospheric aerosol optical properties based on photoacoustic spectroscopy and integrating sphere scattering enhancement, Photoacoustics 36: 100591 (2024).

[9] S. Dap, D. Lacroix, R. Hugon, et al., Retrieving particle size and density from extinction measurement in dusty plasma, Monte Carlo inversion and Ray-tracing comparison, Journal of Quantitative Spectroscopy and Radiative Transfer 128: 18-26 (2013).

[10] G. Su, Q. Huang, C. Sun, et al., A study on light extinction model and inversion of mixed particle system based on Monte Carlo method, Powder Technology 430: 119023 (2023).

[11] X. Zhang, X. Zhang, and Z. Wu, Spectrum allocation by wave based adaptive differential evolution algorithm, Ad Hoc Networks 94: 101969 (2019).

The 14th International Conference on
Laser-light and Interactions with Particles (LIP2024)
September 18-22nd, 2024, Xi'an, Shaanxi, China

SOOT SIZING IN LAMINAR DIFFUSION FLAMES : IMPACT OF SELF ABSORPTION

Mijail Littin[1], Guillaume Lefevre[1], Marek Mazur[1], Andrés Fuentes[2] and Jérôme Yon[1,*]

[1] INSA Rouen Normandie, Univ. Rouen Normandie, CNRS, Normandie Univ., CORIA UMR 6614, F-76000, Rouen France

[2] Departamento de Industrias, Universidad Técnica Federico Santa María, Av. España 1680, Valparaíso, Chile

Corresponding author: jerome.yon@insa-rouen.fr

Abstract

Experimental characterization of soot is recognized as essential for enhancing the understanding of aggregation and oxidation mechanisms occurring directly in flames. Laser Induced Incandescence and Line of Sight Attenuation provide information concerning soot volume fraction but only Angular Light Scattering can inform us of the aggregate size by an in-situ approach. In this work, we aim at improving the spatial resolution and the quality of the size and forward scattering coefficient determination. Indeed, the aggregate size is of interest for the understanding of the formation/oxidation processes whereas the forward scattering contains interesting information on the aggregate volume and optical properties. In particular, we aim at investigating the influence of light self-absorption (or trapping) which is suspected to be the cause of the observed dissymmetry of the scattered signal.

1 Introduction

Soot particles, resulting from the incomplete combustion of fossil fuels, are recognized as the second most significant anthropogenic contributor to global warming [1]. Additionally, their adverse health effects continue to be documented [2]. Although the literature provides information on the soot volume fraction, temperature, and primary sphere diameter [3-5], data on soot aggregates are still scarce, despite their relevance in validating aggregation and oxidation mechanisms. Consequently, the need to provide high spatial resolution data concerning the sizes of soot aggregates emerges as a crucial research question.

In the quest to characterize soot particles, significant efforts have been made to develop in-situ optical techniques. For instance, recent advancements allow the determination of soot volume fraction, temperature, and maturity through multiwavelength line-of-sight attenuation (MW-LOSA) and Emission [6]. The characterization of the aggregate size, number and diameter of primary spheres as well as number density has been recently achieved with a high spatial resolution thanks to the coupling of MW-LOSA and Horizontal Planar Angular Light Scattering (HPALS) [7].

Such optical techniques lead to inversion problems where a specific radial property of soot in axisymmetric flames needs to be reconstructed from the projection that is captured by the optical detection (Abel transform). A critical consideration in this inversion process is the correction for a phenomenon known as signal trapping. Indeed, soot particles can scatter and absorb light. Therefore, as photons travel from their source, pass through the flame, and reach the detector, they experience attenuation along the line of sight. There have been several attempts to correct this effect for emission measurements which is often used to determine the soot temperature [8-9]. However, to the best of the authors' knowledge, this effect has never been considered for angular light scattering measurements.

In the current study, extinction and angular light scattering measurements at a wavelength of 520 nm are presented. A significant signal trapping effect, indicated by pronounced dissymmetry of the scattered profile, is observed in these measurements. To address this, a methodology employing extinction reconstructions is introduced for an accurate reconstruction of the radial property associated with the scattering. We finally evaluate the impact of trapping on the size determination as well as for the determination of the forward scattering coefficient.

2 Methodology

2.1 Experimental Setup

The current investigation examines an axisymmetric laminar ethylene-air diffusion co-flow flame using a Gülder-type burner operating at atmospheric pressure. The burner comprises a 10.9 mm inner diameter central tube for fuel injection and a 90 mm inner diameter co-annular tube for co-flow air supply. To maintain consistent flow rates, two mass flow controllers were employed to supply pure ethylene at 0.194 splm and air at 150 slpm.

In order to capture images of extinction and angular and spectral scattering of the flame, an experimental campaign was conducted using the device illustrated in Figure 1. A continuous laser source (CELESTA) is operated at 520 nm. The light is collimated with the aid of an achromatic lens (f = 300 mm) positioned between the light source and the flame. For LOSA measurements (extinction) and angular

scattering measurements, the light is filtered and captured with a CCD camera (Thorlabs) with an objective lens (Canon 200 mm). The LOSA measurements were performed in-line (0°), while the scattering measurements were taken at 110.2°.

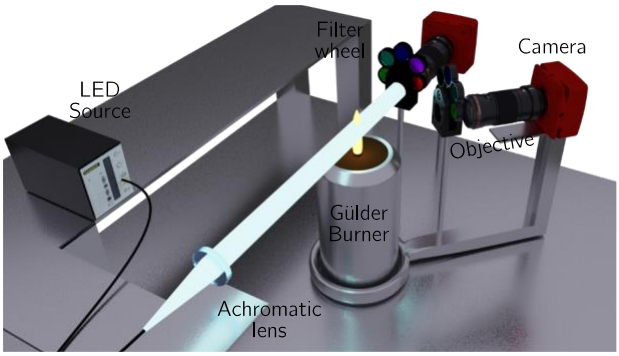

Figure 1 Experimental setup used for extinction, emission and light scattering measurements

2.2 Signal inversion considering self-absorption

Soot particles possess the capability to scatter and absorb light. As a result, when photons travel toward the detector, their intensity is reduced along the line of sight (LoS), a phenomenon known as signal trapping. Therefore, the Abel transform of the measured profiles must be corrected from this effect:

$$P_{sca}(x_s) = 2\int_x^{\infty} \frac{K_{sca}(r)F(x_s,r)r}{\sqrt{r^2-x^2}}dr \qquad (1)$$

In this equation, $P_{sca}(x_s)$ is the collected profile on the detector at position x_s, $K_{sca}(r)$ is the researched radial scattering coefficient and $F(x,r)$ is the trapping correction factor introduced in this work.

This factor is evaluated by considering the local extinction coefficient κ_{ext} retrieved from LOSA measurements at same wavelength as well as the trapping occurring from the light source to the particles at a given position D in the flame (green line in Figure 2) and from the particles to the detector (cyan line in the figure):

$$F(x_s,y_s) = \exp\left[-\left(\int_{-\infty}^{D}\kappa_{ext}(r)\,dl + \int_{D}^{\infty}\kappa_{ext}(r)\,dy\right)\right] \qquad (2)$$

Figure 2-a represents a top view of the flame at a chosen height above burner (HAB); the colours are representative of the degree of attenuation (F) for each position in the flame. The brighter corresponds to stronger trapping. The effect of the trapping consideration is then modelled in the direct way by application of equation 1 to synthetic signals (Figure 2-b). The blue dashed curve is the Abel transform without trapping correction whereas the orange curve considers this effect. We clearly observe the dissymmetry induced by the trapping on the collected signal. We will now apply this model in the opposite way in order to determine the scattering coefficient profile $K_{sca}(r)$ by inverting P_{sca}. In order to reduce the noise propagation during this inversion process, a novel piecewise Spline-based Abel Transform (SAT) technique is adopted (not presented here). Therefore, the radial profile of $K_{sca}(r)$ made of pieces of spline functions is adapted in order to make its Abel transform (P_{sca}) matching the measurement.

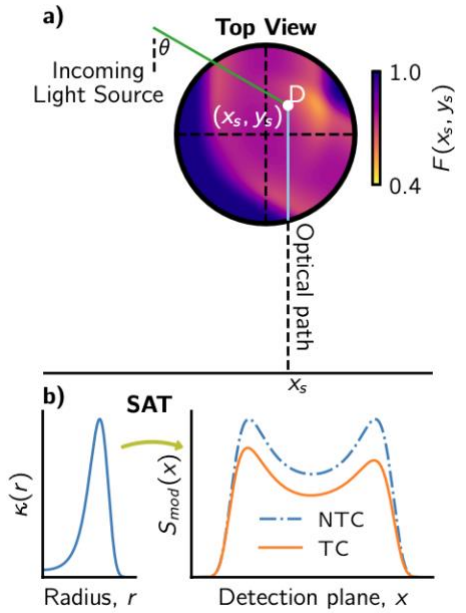

Figure 2 *a) Schematic of angular light scattering signal trapping effect. b) Graphic representation of the Spline-based Abel Transform (SAT) method. Starting from a known profile, SAT is applied in the direct way and the modelled measured profile is obtained. It is also shown how the signal is attenuated in the presence of trapping, emphasizing the changes in signal behaviour. The notations TC and NTC indicates when trapping is corrected or not, respectively.*

3 Results

Figure 3 reports the measured profile in blue obtained at 30 mm height above the burner and for the scattering angle of 110° and the result of the fitting process by considering (TC) or not (NTC, $F = 1$) the self-absorption.

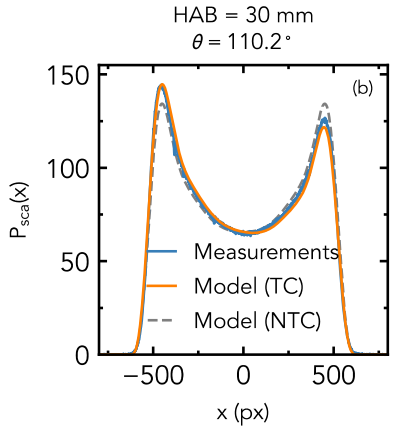

Figure 3 Measured and modelled scattering signals considering (TC) or not (NTC) the trapping of the light.

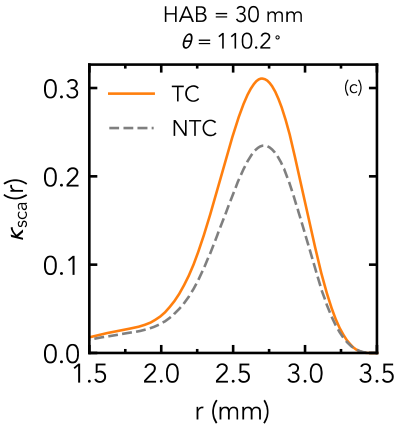

Figure 4 Result of the Abel inversion by considering (TC) or not (NTC) the trapping of the light.

The model enables a good capture of the observed dissymmetry. The corresponding radial profiles of scattering coefficient are reported in Figure 4 by considering or not the trapping correction. We clearly observe, for this flame, wavelength and specific height above the burner a strong influence of the trapping correction, especially in terms of signal amplitude near the wings of the flame.

This operation is then repeated for different scattering angles. We report in Figure 5 the angular profiles obtained at two radial positions respectively $r = 2.1$ and 2.8 mm.

The angular dependence is fitted by an exponential decrease corresponding to a Guinier regime providing the monodisperse equivalent gyration radius R_g^* and the forward scattering coefficient $k_{vv}(0°)$. We observe that R_g^* is not affected strongly by trapping. In turns, the forward scattering is strongly impacted in soot-laden areas of the flame.

4 Conclusion

In this study, a model has been developed for correcting signal trapping in angular light scattering measurements of soot, conducted in a laminar co-flow diffusion flame using a Gülder burner. A significant dissymmetry in scattering profiles, indicative of a pronounced signal trapping effect, has been observed experimentally and well captured by the proposed model. It is found that when signal trapping is neglected, there is an underestimation reaching 40% in the maximum value for the studied case. Therefore, the inclusion of this correction when performing light scattering measurements is recommended even if the repercussion on the soot size determination is shown to be small.

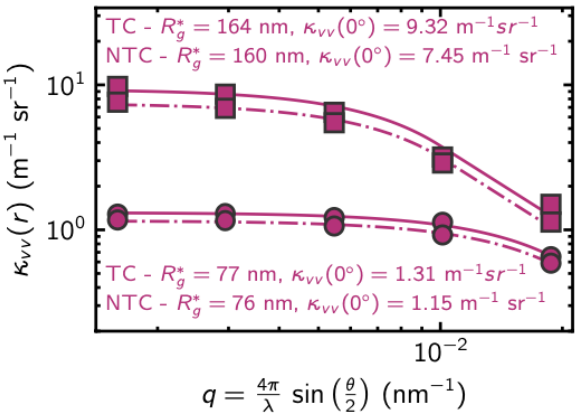

Figure 5 Impact of the trapping correction on the angular scattering dependence and corresponding extracted parameters (gyration radius and forward scattering coefficient).

5 References

[1] J. Tollefson, Soot a major contributor to climate change. Nature, 15, 15 (2013)

[2] L. Rasking, P. Koshy, E. Bongaerts, H. Bové, M. Ameloot, M. Plusquin, . . . T. S. Nawrot, Ambient Black Carbon reaches the Kidneys. Environment International, 107997 (2023)

[3] D. Cortés, J. Morán, F. Liu, F. Escudero, J.-L. Consalvi, A. Fuentes, Effect of fuels and oxygen indices on the morphology of soot generated in laminar coflow diffusion flames, Energy & fuels, 32(11): 11802-11813 (2018).

[4] R. Hadef, K. P. Geigle, W. Meier, M. Aigner, Soot characterization with laser-induced incandescence applied to a laminar premixed ethylene–air flame. International Journal of Thermal Sciences, 49(8), 1457-1467 (2010)

[5] H. Michelsen, C. Schulz, G. J. Smallwood, S. Will, Laser-induced incandescence: Particulate diagnostics for combustion, atmospheric, and

industrial applications. Progress in Energy and Combustion Science, 51, 2-48 (2015)

[6] J. Yon, J. J. Cruz, F. Escudero, J. Morán, F. Liu, A. Fuentes, Revealing soot maturity based on multi-wavelength absorption/emission measurements in laminar axisymmetric coflow ethylene diffusion flames. Combustion and Flame, 227, 147-161 (2021)

[7] J. Yon, J. Morán, F. Lespinasse, F. Escudero, G. Godard, M. Mazur, A. Fuentes, Horizontal Planar Angular Light Scattering (HPALS) characterization of soot produced in a laminar axisymmetric coflow ethylene diffusion flame. Combustion and Flame, 232, 111539 (2021)

[8] F. Escudero, A. Fuentes, J.-L. Consalvi, F. Liu, R. Demarco, Unified behavior of soot production and radiative heat transfer in ethylene, propane and butane axisymmetric laminar diffusion flames at different oxygen indices, Fuel, 183, 668-679 (2016)

[9] G. Legros, Q. Wang, J. Bonnety, M. Kashif, C. Morin, J.-L. Consalvi, F. Liu, Simultaneous soot temperature and volume fraction measurements in axis-symmetric flames by a two-dimensional modulated absorption/emission technique. Combustion and Flame, 162(6), 2705-2719 (2015)

The 14th International Conference on
Laser-light and Interactions with Particles (LIP2024)
September 18-22nd, 2024, Xi'an, Shaanxi, China

MOTIONAL AND REMOVABLE CHARACTERISTICS OF LUNAR DUST PARTICLES IN ELECTROSTATIC FIELD

Haiyan ZHANG[1], Wei ZHANG[2], Siyuan CHANG[1], Fugang WANG[1], Zhendong ZHAO[1], Chao ZONG[1] , Yi WANG[1], Cunhui LI[1]

[1] Science and Technology on Vacuum Technology and Physics Laboratory, Lanzhou Institute of Physics, Lanzhou 730000, China
[2] Beijing Institute of Spacecraft System Engineering, Beijing 100094, China;

Corresponding author: zhy_zhanghaiyan@163.com

Abstract

Lunar dust consists of particles with an average particle size of 70 μm, which is the number one environmental problem for lunar exploration missions. When these dust particles adhere to the lunar exploration equipment, they will damage the equipment or even make it fail. Thus, this thesis proposes a method to mitigate the adhered lunar dust particles through the electrostatic principle based on the shared charge model, aiming to mitigate dust pollution. Firstly, the force model of a single lunar dust particle is established. The main adhesive force of a lunar dust particle is the electrostatic force and the van der Waals force. Then, the lunar dust particles' kinematic characteristics are obtained when they escape from the adhesive surface. It is observed that when a particle's electrostatic force is larger than the sum of van der Waals force and gravity, the particle will escape from the adhesive surface, and then arrive at the upper electrode. Finally, the phenomenon is verified through experiments, and the number of escaped particles at different voltages, the threshold potential upon particle moving, and the spacing between the two parallel electrode plates.

1 Introduction

Lunar dust poses a major operational hazard to human explorations on the lunar surface and to the support systems, and exploration instruments. In Apollo missions, it has been found that the lofted lunar dust particles are highly adhesive and can easily adhere to the exposed lunar exploring instruments, such as solar cell surface, thermal radiator, lunar vehicle, and so on[1-3]. When these particles adhere to their surface, they always cause performance degradation or failure. Thus, to guarantee lunar exploration instruments work well on the lunar surface, it is essential to mitigate these adhesive particles away from instrument surfaces.

At present, there are two ways can remove lunar dust particles from the adhesive surface, including the passive method and the active method[4]. The passive method means that the lunar dust particles are removed from the adhesive surface without any external force, mainly including surface modification and coating[5-6]. Although the passive method has the advantage of energy saving and operation simple on the lunar surface, the high adhesive properties of lunar dust particles make this method has relatively low efficiency. However, the active method can overcome the above shortcomings, thus it has become the first choice for future lunar exploration missions[7]. The active method mainly includes fluidal, mechanical, and electrostatic/electrodynamic methods[8]. Fluidal and mechanical methods have been applied in early Apollo missions, but they can cause protective surface damage[9].

Compared with fluidal and mechanical methods, electrodynamic/electrostatic methods use electrostatic forces to remove dust, which has attracted more attention in recent years because of its high efficiency and protected surface-friendliness. Based on this, this thesis designs a lunar dust rehoming system using electrostatic forces.

2 Numerical simulation method and prediction

The lunar dust particle removal system is shown in Figure 1. It mainly includes high voltage and two electrodes. The high voltage is used to supply power to electrodes, making the upper electrode own positive electricity but the bottom electrode own negative electricity. One thing to note is that the upper electrode and the bottom electrode has the same voltage.

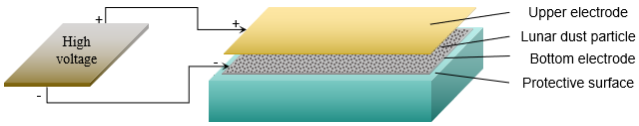

Figure 1 *The diagram of particle removal system composition*

From Figure 1, it also can be seen that the bottom electrode is above the protective surface, when the two electrodes are powered up, adhesive dust particles will be charged. Figure 2 shows the force diagram of a dust particle when it located in Figure 1 system. The loft dust particles always are charged. When it adheres to the bottom electrode, it will be charged with negative electricity, and then escape from the bottom electrode and move along the electric field line, finally, these particles

arrive at upper electrode. In the whole removal process, the force on a particle is electrical force, van der Waals force, and gravity. If the electrical force is larger than the sum of van der Waals force and gravity, dust particles will escape from adhered surface.

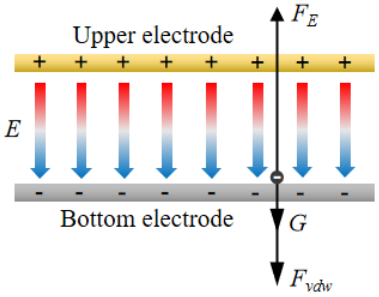

Figure 2 *The force diagram of a dust particle*

To obtain lunar dust particles' trajectories and other moving characteristics, the simulation of charged dust particles between the two parallel electrodes is done based on COMSOL software. The physical field adopts an electrostatic module and particle tracking module. The grid division of the established model is shown in Figure 3.

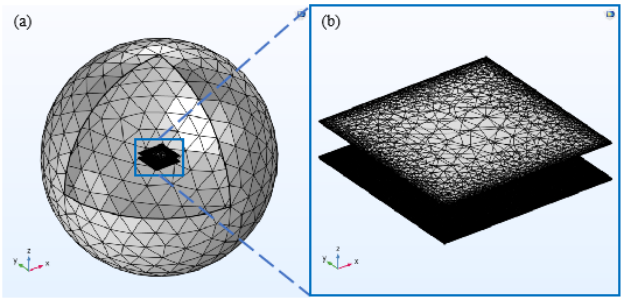

Figure 3 *The force diagram of a dust particle*

The whole simulation region is spherical, the size of the two electrodes is 5 mm × 5 mm. The properties of the simulated dust particles include particle number, density, diameter, and quantity of electric charge. These properties are set according to lunar dust particles' actual value. The quantity of the electric charge can be calculated through equation (1),

$$Z = \frac{Q_{\max}}{e} = \frac{4\pi\varepsilon_0\varepsilon_r R_p^2 E}{e} \tag{1}$$

Where, e denotes elementary charge, its value is 1.602×10^{-19}C.

The relevant simulation results of the electrical field property are shown in Figure 4. The voltage of the upper electrode and bottom electrode is 2 kV and -2 kV, respectively. The distance of the two electrodes is 10 mm. Figure 4(a)~Figure 4(c) illustrates the potential distribution cloud of the whole simulation region, frontal region, and local region in order. The fluid lines in Figure 4 represent the distribution of electric potential or electric fields. In Figure 4, it can be seen that the electric field not only exists between the electrodes but also extends some distance, which is called the edge field effect.

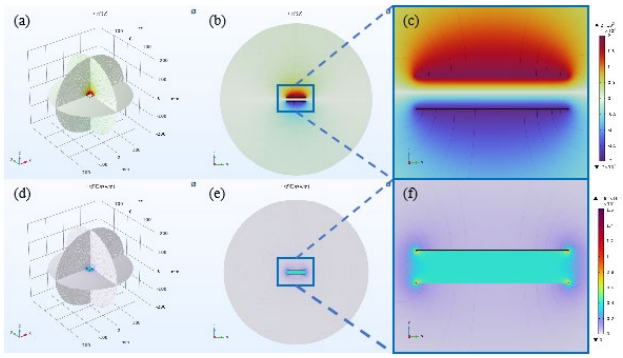

Figure 4 *The distribution cloud of potential and electric field intensityof parallel plate*

In order to observe this phenomenon more directly, this study also selected the field intensity distribution diagram at the upper surface heights of 0.1 mm, 0.5mm, and 1.0 mm from the lower plate, as shown in Figure 5. Since the potential difference between the upper and lower plates is 4 kV and the distance between the plates is 10 mm, the theoretical value of the field strength between the plates can be calculated as 4×10^5 V/m according to theoretical calculaion. As shown in Figure 5, the maximum field strength near the electrode edge at the upper surface height of 0.1mm at the lower distance reaches 3.16×10^6 V /m, which is about 8 times higher than the theoretical value. By observing Figure 5, it is easily found that the electric field intensity at the edge of the electrode will gradually decrease with the higher the distance from the upper surface of the lower plate, and the lowest electric field intensity is the calculated theoretical value of field intensity, that is, 4×10^5 V/m. However, since the particle size of the lunar dust particles is basically distributed in the micron order, it is only necessary to care about the electric field intensity of the surface height of the lower plate no more than 1 mm.

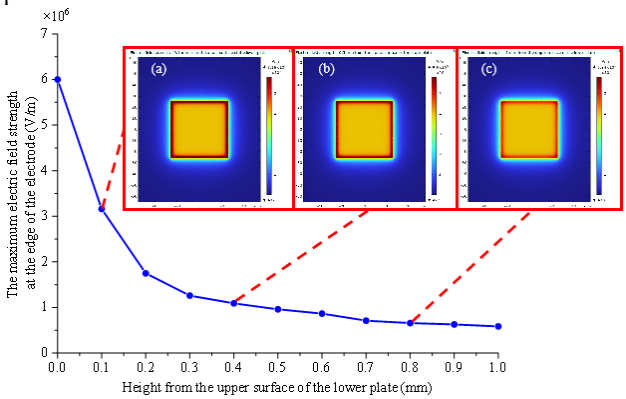

Figure 5 *The distribution of electric field intensity near the bottom plate varies with the height of the section*

Figure 6 shows the front view of the lunar dust particles' trajectories. In this simulation , the diameter of the lunar dust particles is ranged from 10 μm~325 μm. It can be obviously seen that the particles as a whole will form a "U" shaped trajectory with high sides and low middle, that

is, for particles of the same particle size, the particles located at the edge of the plate will be more easily removed.

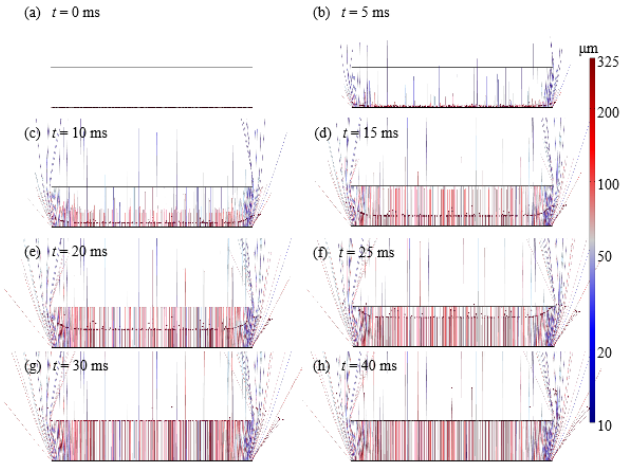

Figure 6 *The simulated dust particles' trajectories*

3 Experiment setup and results

The expriment may further reveal the lunar dust particles' kinematic dynamic characteristics. The expriement system is shown in Figure 7.

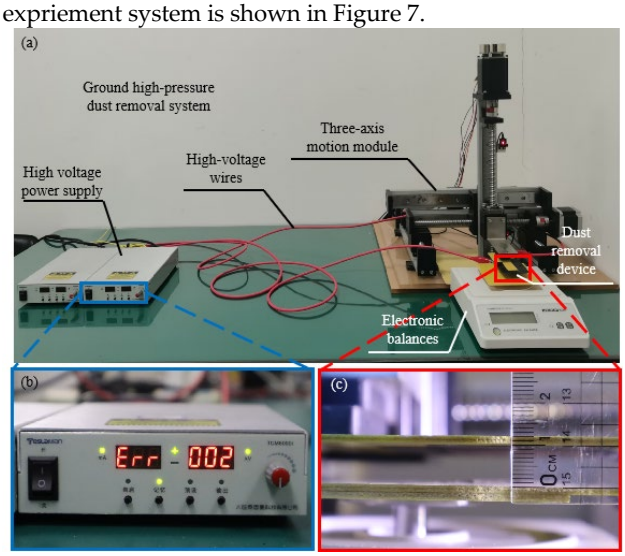

Figure 7 *The experiment system*

In experiment, the CAS-1 simulated lunar dust particles are adopted, Figure 8 shows the SEM image of the sample. There are 6 kinds of lunar dust particle diameters are used in experiment, including 10±2μm, 20±3μm, 50±5μm, 75±10μm, 100±15μm, and 325±25μm.

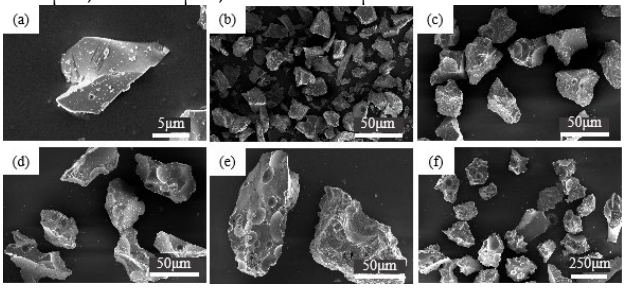

Figure 8 *The SEM images of the sample*

Figure 9 shows the lunar dust particle motion process. In this experiment, the lunar dust diameter is 300±25 μm, the distance of the two electrodes is 10 mm, and the voltage of the upper electrode and the bottom electrode is +3.6kV and -3.6kV, respectively. At 0 ms, all dust particles deposite the bottom electrode, upon powering on, these dust partilces are charged by the bottom electrode. When they obtain negative electricity, they will be repelled by the bottom electrode. Then, these particles will escape from the adhesive electrode. At 27 ms, part of the particles start moving towards the top electrode plate. When the time is at 55 ms, most of the moving particles are attracted by the upper electrode plate.

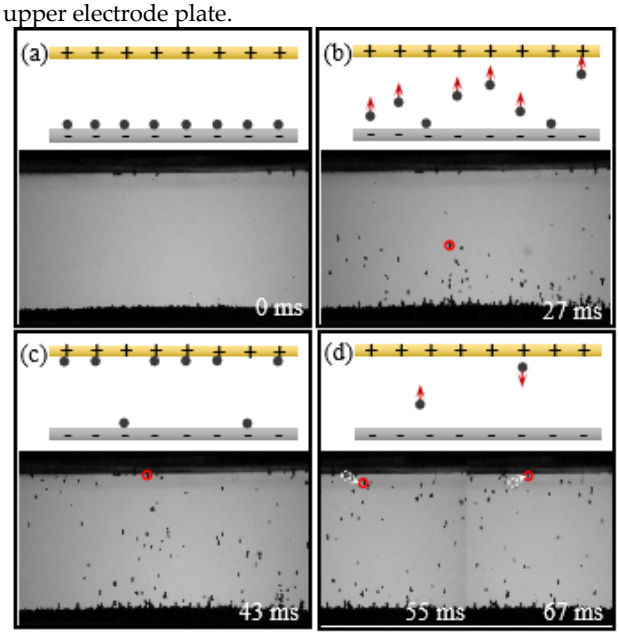

Figure 9 *Lunar dust particle trajectories at different time*

4 Conclusion.

This abstract briefly introduces lunar dust particle mitigation by adopting the electrostatic method. The main system contains high voltage, dust removal device, a three-axis motion module, electrodes, and simulated lunar dust particles. Through COMSOL simuation, the electrical field and electric field intensity distribution are predicted, the edge field effect is found. When particles move away from the adhesive electrode, they will form a "U" shape. Through experiment, the particle trajectories have been verified, and the results show that particles move in an almost straight line trajectory toward the top plate, and the amount of dust particles are moved through this method.

5 References

[1] Zakharov A. V., Zelenyi L. M., and Popel S. I. Lunar dust: Properties and potential hazards[J]. Solar System Research, 2020, 54: 455-476.

[2] Pohlen M., Carroll D., Prisk G. K.. Overview of lunar dust toxicity risk[J]. npj Microgravity, 2022, 8(1): 55.

[3] Horányi M., Szalay J. R., and Wang X. The lunar dust environment: concerns for Moon-based astronomy[J]. Philosophical Transactions of the Royal Society A, 2022, 382(2271): 20230075.

[4] Afshar-Mohajer N., Wu C. Y., Curtis, J. S., and et al. Review of dust transport and mitigation technologies in lunar and Martian atmospheres[J]. Advances in Space Research, 2015, 56(6): 1222-1241.

[5] Zanon, P., Dunn, M., and Brooks, G.. Current Lunar dust mitigation techniques and future directions[J]. Acta Astronautica, 2023, 213: 627-644.

[6] Dove A., Devaud G., Wang, X., and et al.. Mitigation of lunar dust adhesion by surface modification[J]. Planetary and space science, 2011, 59(14): 1784-1790.

[7] Hirabayashi M., Hartzell C. M., Bellan, P. M., and et al. Electrostatic dust remediation for future exploration of the Moon[J]. Acta Astronautica, 2023, 207: 392-402.

[8] Farr B., Wang X., Goree J., and et al. Dust removal from a variety of surface materials with multiple electron beams[J]. Acta astronautica, 200: 42-47.

[9] Huh D., Fujioka H., Tung Y. C., and et al. Acoustically detectable cellular-level lung injury induced by fluid mechanical stresses in microfluidic airway systems[J]. Proceedings of the National Academy of Sciences, 2007, 104(48): 18886-18891.

The 14th International Conference on
Laser-light and Interactions with Particles (LIP2024)
September 18-22nd, 2024, Xi'an, Shaanxi, China

On the Effective-Medium Approach for Monolayers of Small Particles and its Relationship with Multiple Scattering Models

Augusto García-Valenzuela [1*], Omar Vázquez-Estrada [2], Anays Acevedo-Barrera [1] and Rubén G. Barrera [3]

[1] Instituto de Ciencias Aplicadas y Tecnología, Universidad Nacional Autónoma de México, Apartado Postal 70-186, Ciudad de México, 04510 Mexico

[2] Tecnológico Nacional de México / ITS de Tantoyuca, Desviación Lindero Tametate S/N, La Morita, Tantoyuca, Veracruz, Mexico

[3] Instituto de Física, Universidad Nacional Autónoma de México, Apartado Postal 20-364, Ciudad de México, 01000, Mexico

Corresponding author: augusto.garcia@icat.unam.mx

Abstract

We examine the effective-medium approach to calculate the reflectivity and transmissivity of monolayers of small particles. We consider cases where particles are smaller than the wavelength of the incident radiation but still large enough to scatter light significantly. We present comparisons between effective-medium, multiple-scattering and finite-element simulations of the reflectivity spectra of free-standing, ordered monolayers of gold particles. We aim to provide some insight into the applicability of the effective-medium approach and its limitations to calculate the reflectivity and transmissivity of disordered and ordered monolayers of particles.

1 Introduction

A monolayer of particles consisting of particles with all their centres lying on a plane will reflect part of the incident light specularly. It may reflect some diffuse light in all directions in the case of a disordered monolayer or one or more diffracted beams in case of ordered monolayers. For some years now, it has been known that the specular reflection of ordered and disordered monolayers of very small particles (compared to the wavelength of incident radiation) can be modelled as the reflection of a thin homogeneous layer with an effective Refractive Index (RI). In the limit of small particles, an Effective-Medium Approach (EMA) for monolayers of particles can be used in the quasi-electrostatic approximation [1]. However, within that approximation, scattering losses will not be considered, thus in the case of a monolayer of transparent—non absorbing—particles, where the only losses are due to scattering, will yield zero reflectivity.

Recently [2], we found experimentally that the reflectivity of a sparse and dense monolayer of particles that are not very small compared to the incident wavelength of light and scatter light significantly, follows closely that of an equivalent uniform layer with an effective RI. This was found for monolayers of non-absorbing particles (made of PMMA) adsorbed at the base of an optical prism and for the reflectivity measured from the glass side (internal reflection configuration) as a function of the angle of incidence. One finds that it is possible to adjust, very well, the reflectivity data for all angles of incidence, by assuming that there is an effective medium with a complex refractive index whose imaginary part takes account of the scattering losses. It is surprising to notice that this two-parameter fit (real and imaginary parts of an effective RI assuming the film's thickness is one particle's diameter) works well not only for all incidence angles below the critical angle but also for angles well beyond this angle. This means that an effective-medium model holds well even when light penetrates just a small fraction of the effective film (of thickness equal to one particle's diameter) [2].

The mentioned experimental observation means that the EMA can be used for monolayers of particles beyond what is currently accepted. It makes apparent that, currently, the fundamental limits of the EMA for monolayers of particles are not well understood. Since an EMA is generally very useful in studying the optical properties of granular materials, we find it necessary to delineate the limits of an EMA for a monolayer in terms of the size and RI of the particles, as well as their surface coverage, to have physical insight into the fundamental limitations of the EMA.

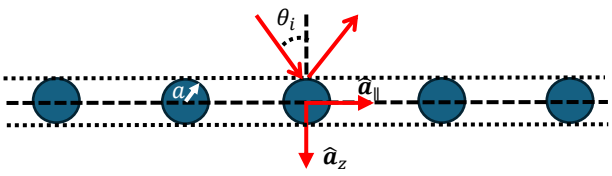

***Figure 1**. Schematic of an ordered monolayer of particles.*

In this work we start studying the applicability and limitations of the EMA in the quasi-static approximation to model the optical reflectivity of monolayers of particles that scatter light significantly. We will consider only free-standing sparse monolayers where the problem we want to address is more manageable.

2 Reflectivity: its meaning and modelling

Let us start by defining what we mean by reflectivity. From an experimental point of view, we call reflectivity to the collimated-to-collimated reflectance. However, the reflectance of a sufficiently well collimated beam approaches that of a plane wave. Thus, for the purpose of this work, reflectivity is the plane wave- to-plane wave reflectance, which is obtained by dividing the intensity of the reflected plane wave by the intensity of the incident plane wave.

2.1 Effective-medium approximation to the reflectivity

If we were to model a free-standing monolayer of particles within an Effective-Medium Approach (EMA), one will consider an equivalent thin and homogenous film of thickness d embedded within a transparent boundless medium. Thus, to calculate the reflectivity, one would use the following well-known expression for the plane-wave reflectance of a thin homogenous film of thickness d when the incident and transmission medium are the same,

$$R_{EMA} = |r_{121}|^2 = \left| \frac{r_{12} + r_{21} \exp[2ik_{z2}d]}{1 + r_{12}r_{21} \exp[2ik_{z2}d]} \right|^2, \qquad (1)$$

where the subscript EMA stands for effective-medium approach, r_{121} is the plane-wave reflection coefficient, relating the amplitudes of the incident and reflected plane waves, of a three-medium configuration (two interfaces), where medium 2 is a uniform layer with RI n_2, lying between two half-spaces of RI n_1 (medium 1). $r_{12} = -r_{21}$ are the Fresnel reflection coefficients for the corresponding s- or p-polarization, of the interface between medium 1 and 2, and the interface between medium 2 and 1, respectively. k_{z2} is the component of the wave-vector within the layer of medium 2, along the direction perpendicular to the interfaces (z-axis) given by,

$$k_{z2} = k_0 \sqrt{n_2^2 - n_1^2 \sin^2 \theta_i}, \qquad (2)$$

where k_0 is the wave number in vacuum of the incident light and θ_i is the angle of incidence.

If an isotropic EMA is valid for a monolayer, then, Eq. (2) with $n_2 = n_{eff} = n'_{eff} + in''_{eff}$ will fit the reflectivity of the monolayer for all angles of incidence using a single value for n_{eff}, being a constant that might be a complex number.

2.2 Multiple scattering model for the reflectivity of sparse monolayers of particles

The most direct way to solve for the reflectivity of a monolayer is to set up a system of multiple scattering equations and solve for the scattered fields in the reflection hemisphere. Then, extracting the specularly reflected field and dividing by the amplitude of the incident wave yields the reflection coefficient and its squared modulus is the reflectivity.

In a sparse monolayer of spherical particles, whether ordered or disordered, the Single Scattering Approximation (SSA) to the reflectivity for s (TE) or p (TM) polarization is found to be given as,

$$r^{s(p)} = -2 \frac{\Theta}{\cos \theta_i} \frac{S_{1(2)}(\pi - 2\theta_i)}{x^2} \qquad (3)$$

where $S_1(\theta)$ and $S_2(\theta)$ are diagonal elements of the amplitude scattering matrix as defined in the book by Bohren and Huffman [3], θ being the scattering angle with respect to the incidence direction, Θ is the surface coverage fraction by the particles, $x = k_0 n_m a$ is the particles size parameter in the medium surrounding the particles, and θ_i is the angle of incidence to the plane of the monolayer (see Fig. 1). For spherical particles $\Theta = \rho_s(\pi a^2)$, where ρ_s is the surface number-density of particles.

A simple improvement to the SSA is to suppose that the field exciting the particles is the transmitted field [4]. In this case the reflectance is given by,

$$\left| r^{s(p)} \right|^2 = \left| -\frac{\alpha S_{1(2)}(\pi - 2\theta_i)}{1 - \alpha S(0)} \right|^2, \qquad (4)$$

where we defined $\alpha = 2\Theta/(x^2 \cos \theta_i)$, and $r^{s(p)}$ is the reflection coefficient of the specularly reflected plane wave for $s(p)$ polarization.

3 Comparison with numerical simulations

We are interested in comparing Eqs. (1) with (4) and with numerical simulations to see when they match each other.

In Fig. 2(a) we present an example of the mentioned comparison. R_{EMA} in this case was calculated with n_2 given by the Maxwell Garnett (MG) effective-medium theory and taking the film's thickness as one particle's diameter, $d = 2a$. The numerical simulation curve was calculated using the Finite Element Method (FEM) assuming a square array of particles. The example is for gold nanoparticles of 20 nm radius and a surface coverage of $\Theta = 15\%$. The RI of gold was taken to be that of Johnson and Christy in Ref. [5]. In Fig. 2(b) we plot the same curves as in Fig. 2(a) but for particles of 30 nm radius and a surface coverage of 10%.

We can appreciate in Fig. 2(a) that the three curves follow each other closely. This result is not obvious since the particle radius is 20 nm (40 nm diameter) and scattering is already significant. However, in Fig. 2(b) we can see that the EMA curve using MG underestimates the reflectivity for all wavelengths considered. Other examples will be studied

and presented at the conference, exploring the validity of different approximations within the EMA, including some extension to the standard MG EMA, as a function of the particles size and the surface coverage. Also, the validity the multiple-scattering model in Eq. (4) will be studied. We will study as well, cases for oblique angles of incidence, including grazing incidence for which the intrinsic anisotropy of a monolayer of particles [1] may play an important role.

We believe that the current work, together with the recent experimental observation that the EMA is still valid for transparent particles as large as 100 nm in radius of RI close to 1.6 and immersed in air, makes it appealing to extend EMAs for monolayers. The main application we foresee is the optical characterization of nano and submicron particles.

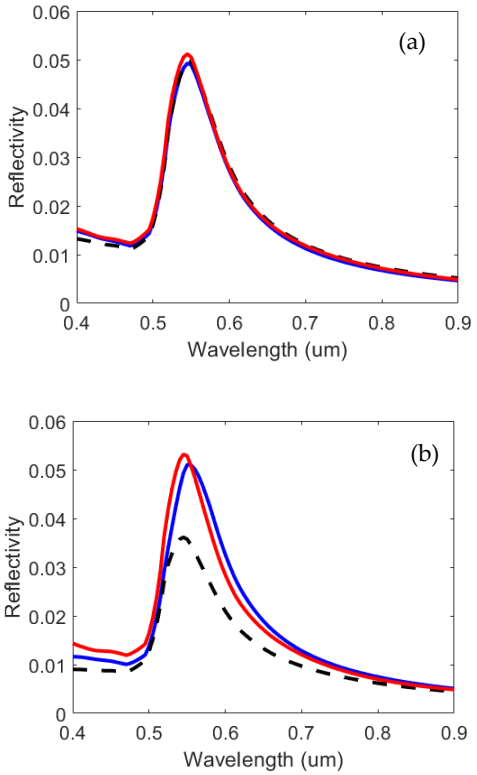

***Figure 2**. Plot of the reflectivity versus the wavelength of light (in μm) for normal incidence ($\theta_i = 0°$) for a monolayer of gold nanoparticles of (a) 20 nm radius and a surface coverage of $\Theta = 15\%$, and (b) 30 nm radius and a surface coverage of $\Theta = 10\%$. Red curve is the numerical simulation, blue curve was obtained with Eq. (4) and black dashed curve with Eq. (1) using the Maxwell Garnett EMA.*

4 Some insights into the validity of EMAs for monolayers

We expect to gain physical insight into the applicability of the EMA to model the reflectivity of monolayers of particles. Even though some specific approximations used within the EMA, such as the MG approximation or some of its extensions, are limited, it does not necessarily mean that improved approximations could not be used with this problem. Nevertheless, there will be some restrictions due to the fundamental limitations of the EMA. It should be convenient to understand when there are opportunities to use new approximations within the EMA and when it is not possible, and one should resort to multiple-scattering models and/or numerical simulations only.

5 Conclusions

We are in the process of delineating the limits of validity of some established approximations used in with the EMA to model the reflectivity of monolayers of particles small compared to the wavelength. We are particularly interested in cases when particles scatter light significantly. This work should offer some new knowledge that may have important applications into the optical characterization of submicron particles.

6 Acknowledgement

We acknowledge financial support by Dirección General de Asuntos del Personal Académico from Universidad Nacional Autónoma de México through grant PAPIIT IN-105824. AAB is also grateful to CONAHCYT (México) for a postdoctoral fellowship.

7 References

[1] Barrera RG, del Castillo-Mussot M, Monsivais G, Villaseñor P, Mochán WL. Optical properties of two-dimensional disordered systems on a substrate. Phys Rev B Condens Matter. 1991 Jun 15;43(17):13819-13826.

[2] A. Acevedo-Barrera, R. Méndez-Fragoso and A. García-Valenzuela, Experimental assessment of the effective-medium approximation for disordered monolayers of particles with high scattering losses, submitted.

[3] C.F. Bohren, and D.R. Huffman, *Absorption and scattering of light by small particles* (Wiley, New-York, 1983).

[4] Augusto García-Valenzuela, Edahí Gutiérrez-Reyes, and Rubén G. Barrera, "Multiple-scattering model for the coherent reflection and transmission of light from a disordered monolayer of particles," J. Opt. Soc. Am. A 29, 1161-1179 (2012).

[5] Johnson, P. B.; Christy, R. W. Optical Constants of the Noble Metals. Phys. Rev. B 1972, 6, 4370–4379.

The 14th International Conference on
Laser-light and Interactions with Particles (LIP2024)
September 18-22nd, 2024, Xi'an, Shaanxi, China

SIMULATION OF THE LIGHT SCATTERING PROPERTIES OF INTERSTELLAR THOLINS

Ankur GOGOI

Department of Physics, Jagannath Barooah University, Jorhat, Assam 785001, India

*Corresponding author: ankurgogoi@gmail.com

Abstract

The interaction of light with tholin particles of varying shapes and sizes, using simulations with realistic optical constants are investigated at 500 nm and 700 nm incident wavelengths to analyze their scattering efficiencies, phase functions, and albedo variations. Our comparative analysis highlights the wavelength and size dependence of tholins on their scattering behaviour.

1 Introduction

Tholins, intricate organic aerosols found throughout the solar system, inhabit the atmospheres of celestial bodies such as Pluto, Titan, Kuiper Belt objects, comets, and the surfaces of asteroids [1,2]. These particles act as heterogeneous media, scattering solar and stellar light, thus significantly influencing the distribution of electromagnetic radiation throughout the galaxy. The light scattering behavior of tholins depends on their physical characteristics (e.g., size, shape, composition, porosity, density) and optical properties (e.g., refractive index, dielectric constant), giving them distinct signatures. Analyzing the light scattered by tholins is essential as it provides crucial insights into the composition, structure, and dynamics of their environments, aiding in remote sensing and detection. Furthermore, tholins have substantial astrobiological significance, potentially serving as precursors to life and offering valuable insights into the chemical evolution of organic molecules in extraterrestrial settings. Therefore, investigations into the properties of terrestrial interstellar dust analogues are paramount, as they share similarities with planetary regolith and cometary dust, facilitating a deeper understanding of celestial processes and environments.

In this study, we present a comprehensive simulation of the light scattering properties of interstellar tholins using the discrete dipole approximation (DDA) code DDSCAT 7.3.0, jointly developed by B. T. Draine and P. J. Flatau [3].

2 Results and Discussion

Computational models of tholins were developed on the basis of the six standard irregular shapes suggested by Zubko et al. [4], and simulated their scattering properties at 500 nm, 700 nm, and 900 nm incident wavelengths using the discrete dipole approximation (DDA). The refractive indices used in the calculations are tabulated in table 1.

Table 1 *Refractive index of tholins used in the calculations*

Wavelength (nm)	Real part	Imaginary part
500	1.61	0.00213
700	1.58	0.00175
900	1.57	0.00195

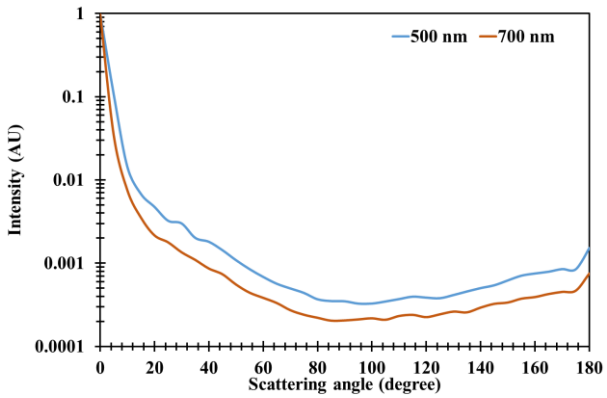

Figure 1 *Scattering properties of tholins for target geometry 2 at 500 nm and 700 nm incident wavelengths*

We modelled the interaction of light with tholin particles of various shapes and sizes, spanning from nanometers to micrometers. Figure 1 depicts the representative results calculated by of the light scattering calculations for incident wavelengths 500 nm and 700 nm. Our simulations incorporate realistic optical constants, allowing a detailed analysis of scattering efficiencies, phase functions, and albedo variations. A comparative analysis of theoretical calculations with other reported measurements is performed, including the wavelength and size dependence of tholins on their scattering behaviour. This study offers critical insights into the role of tholins in the interstellar environment and emphasizes the importance of accurate scattering models in analyzing cosmic dust and planetary atmospheres.

3 References

[1] Frattin, E., Muñoz, O., Moreno, F., Nava, J., Escobar-Cerezo, J., Gómez Martín, J.C., Guirado, D., Cellino, A., Coll, P., Raulin, F. and Bertini, I., 2019. Experimental phase function and degree of linear polarization of cometary dust analogues. *Monthly Notices of the Royal Astronomical Society*, *484*(2), pp.2198-2211.

[2] Hadamcik, E., Renard, J.B., Alcouffe, G., Cernogora, G., Levasseur-Regourd, A.C. and Szopa, C., 2009. Laboratory light-scattering measurements with Titan's aerosols analogues produced by a dusty plasma. *Planetary and Space Science*, *57*(13), pp.1631-1641.

[3] Draine, B.T. and Flatau, P.J., 1994. Discrete-dipole approximation for scattering calculations. *Josa a*, *11*(4), pp.1491-1499.

[4] Zubko, E., Muinonen, K., Shkuratov, Y., Videen, G. and Nousiainen, T., 2007. Scattering of light by roughened Gaussian random particles. *Journal of Quantitative Spectroscopy and Radiative Transfer*, *106*(1-3), pp.604-615.

The 14th International Conference on
Laser-light and Interactions with Particles (LIP2024)
September 18-22nd, 2024, Xi'an, Shaanxi, China

A SELF-ADAPTIVE NETWORK BASED ON FREE SPACE OPTICAL COMMUNICATION

Ruike YANG[1,*], Ran TAN[1]

[1] *School of Physics, Xidian University, Xi'an, Shaanxi 710071, China*

**Corresponding author: yrk18687@163.com*

Abstract

To get the effective control of Unmanned Aerial Vehicles (UAV) clusters under changing complex weather, a self-adaptive UAV network with long range and excellent performance is considered as a potential solution. In this paper, based on the performance analysis of free-space optical (FSO) communication links under foggy weather, a transmission strategy is designed to adaptively adjust the transmission strategy according to the change of fog and turbulence intensity with collaborative communication and optimized modulation parameters. The scheme incorporates the residual energy of the UAV network and the link performance into the transmission decision to form a self-adaptive capability. After simulation verification, the lifetime and transmission performance of the optimized self-adaptive network are significantly better than those of the network using the open shortest path routing transmission strategy, which is a successful UAV adaptive network design scheme.

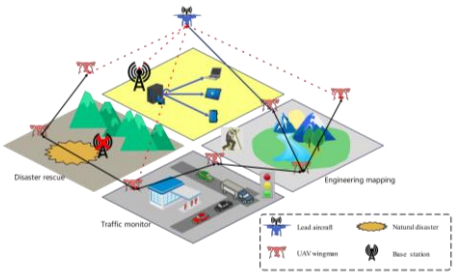

Figure 1 *Self-adaptive network and applications*

1 Main theory and calculation

For UAV networks, transmission efficiency and energy distribution are extremely important performance. In this paper, based on the analysis of the performance of free-space optical communication link in fog environment, a networking process and routing protocol are designed combining the two constraints of transmission performance and node energy.

1.1 Model of the FSO link in fog

Combining the Malaga model with the pointing error brought by the UAV, we derive a closed expression for the signal-to-noise ratio and outage probability of the FSO link in foggy weather.

1.2 Self-adaptive transmission strategy

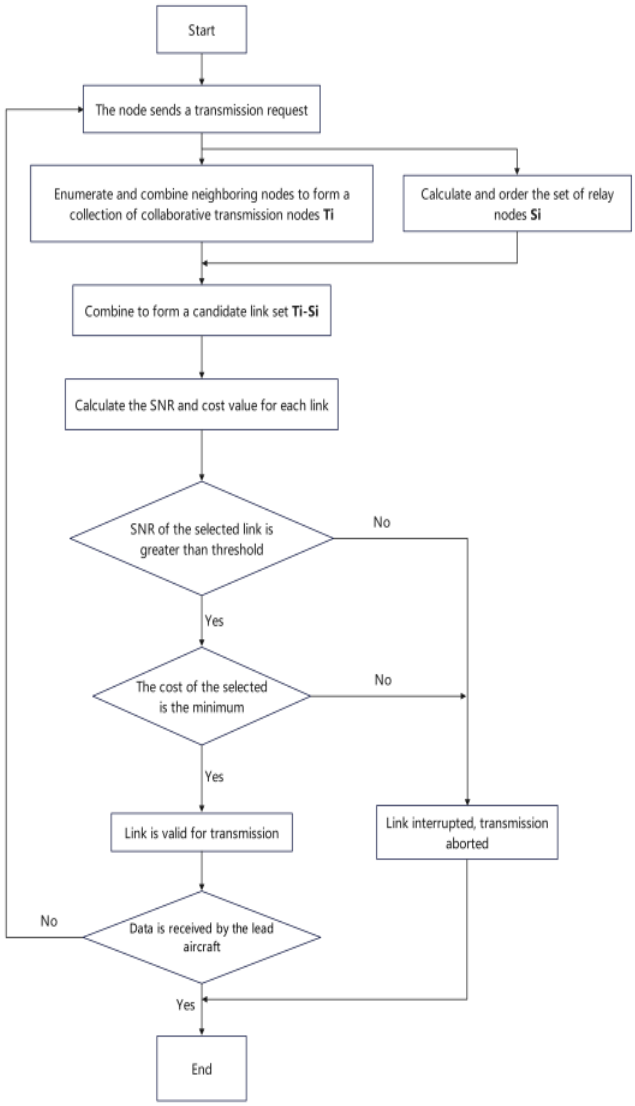

Figure 2 *Flow chart of the transmission strategy*

2 The optimized modulation parameters

After several simulations using the OPNET platform, we give optimized modulation parameters for different kinds of fogs to better achieve network performance under foggy conditions.

Table 1 *The optimized modulation parameters*

	Light	Moderate	Dense
K1	1.27	1.13	0.96
K2	0.97	1.18	1.46
K3	1.51	1.76	2.01

3 Smulation and calculations

The variation of network lifetime with the number of UAVs under different routing schemes in the case of moderate fog is shown in Figure 3(a). When the number of UAVs is less than 50, the network lifetime is slightly lower than that of the UAV network applying the open shortest path routing algorithm (OSPF) because the self-adaptive network proposed in this paper requires the UAVs to periodically receive information from the leader aircraft. As the number of UAVs increases, the topology of the network becomes progressively more complex, the number of candidate collaborative links which meet the performance requirements increases, and the advantages of collaborative communication begin to emerge. Self-adaptive networks can realize longer link transmissions with limited energy cost, and the network lifetime increases significantly. In an adaptive network consisting of 150 UAVs, the optimized adaptive network lifetime can be extended up to 2.5 times. Figure 3(b) shows the real-time proportion of surviving nodes over time in an adaptive network consisting of 150 UAVs. The active point rate is the ratio of the number of UAVs in the network with non-zero residual energy to the total number of nodes in the network, which is used to measure the average residual energy of the nodes and the node survival time. The simulation results show that the adaptive network avoids continuous loading of the same node for a short period of time due to the continuous adjustment of candidate relay nodes. The survival of the network nodes is effectively achieved and the creation of hollow areas in the network is avoided.

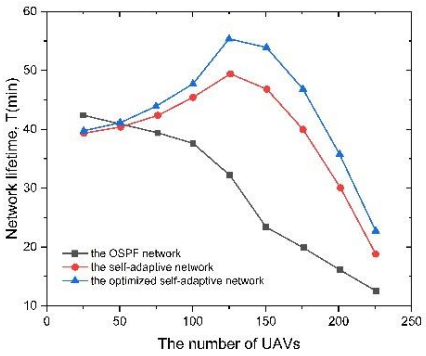

Figure 3(a) The variation of network lifetime with the number of UAVs

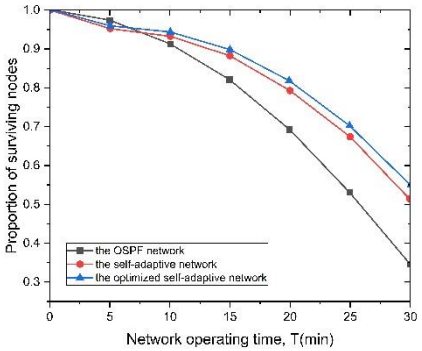

Figure 3(b) *The real-time proportion of surviving nodes*

The transmission performance of a network consisting of 150 UAVs is computed in this paper under moderate fog. Figure 4(a) shows the transmission outage probability versus the number of relays for UAV networks using different routing algorithms. As the number of relays increases, the advantage of collaborative communication becomes more obvious. And the optimized modulation parameters can make the network transmission decision more focused on the link performance according to the atmospheric environment, and the optimized self-adaptive network decreases the interruption probability by nearly half when the number of relays is high compared with the UAV network applying the open shortest route transmission, which effectively improves the reliability of the link. Figure 4(b) shows the variation of data packet transmission rate with network operating time for UAV networks applying different transmission strategies. The data packet transmission rate is the ratio of the number of data packets received at the receiving end to the number of data packets at the sending end, which reflects the network reliability on the one hand and the data processing efficiency of the routing algorithm on the other. As the network operates, the data packet rate gradually decreases. This is due to the reduced energy of the UAVs as the network proceeds, the number of active nodes decreases and hollow areas appear. However, the adaptive network considers the UAV residual energy and network energy equalization during link selection, and its transmission performance is significantly better than the UAV network applying the shortest routing algorithm in the mid and late stages. On the other hand, the optimized adaptive network has a data transmission efficiency of up to 1.1 times due to the fact that the collaborative communication enables transmission across the void region and the diversity gain reduces the probability of data loss.

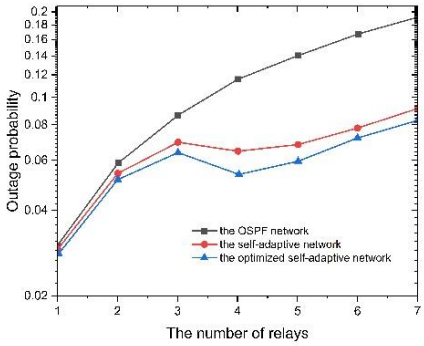

Figure 4(a) *The variation of outage probability with the number of relays*

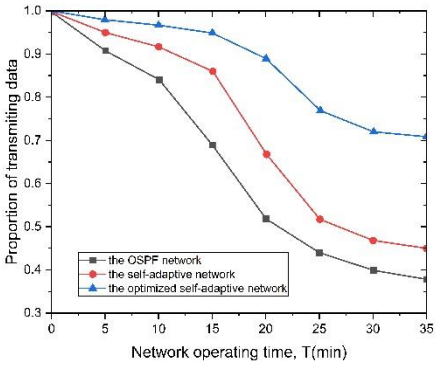

Figure 4(a) *The real-time proportion of transmiting date*

References

[1] US Department of Defense. Unmanned system integrated roadmap 2013-2038 [R].Washington: DoD, 2013.

[2] North Atlantic Treaty Organization(NATO). Develop UAV roadmap[R]. Washington: DoD, 2007.

[3] R. Kovalchukov et al., "Analyzing effects of directionality and random heights in drone-based mmWave communication," IEEE Trans. VehicTechnol., vol. 67, no. 10, pp. 10064–10069, Oct. 2018.

[4] Jacquet P, Muhlethaler P, Clausen T, et al. Optimized link state routing protocol for ad hoc networks[C]. 2001.

[5] Forsmann J H, Hiromoto R E, Svoboda J. A time-slotted on-demand routing protocol for mobile ad hoc unmanned vehicle systems[C].Unmanned Systems Technology IX. International Society for Optics and Photonics, 2007, 6561: 65611P

[6] Shirani R. Reactive-greedy-reactive in unmanned aeronautical ad-hoc networks: A combinational routing mechanism[D]. Ottawa: Carleton University, 2011.

[7] Rosati S, Krużelecki K, Traynard L, et al. Speed-aware routing for UAV ad-hoc networks[C].2013 IEEE Globecom Workshops (GC Wkshps). IEEE, 2013: 1367-1373.

[8] Zheng Y, Wang Y, Li Z, et al. A Mobility and Load aware OLSR routing protocol for UAV mobile ad-hoc networks[J]. 2014.

[9] Forsmann J H, Hiromoto R E, Svoboda J. A time-slotted on-demand routing protocol for mobile ad hoc unmanned vehicle systems[C].Unmanned Systems Technology IX. International Society for Optics and Photonics, 2007, 6561: 65611P

[10] Mahmoud, Haitham HM, Tawfik Ismail, and M. Saeed Darweesh. "Dynamic traffic model with optimal gateways placement in IP cloud heterogeneous CRAN." IEEE Access 8 (2020): 119062-119070.

[11] Erdogan, Eylem, et al. "A cognitive radio enabled RF/FSO communication model for aerial relay networks: Possible configurations and opportunities." IEEE Open Journal of Vehicular Technology 2 (2020): 45-53.

[12] Jung K J, Nam S S, Alouini M S, et al. Ergodic Capacity Analysis of UAV-based FSO Links over Foggy Channels[J]. IEEE Wireless Communications Letters, 2022.

[13] A. J. Navas, J. M. G. Balsells, J. F. Paris, and A. P. Notario, "A unifying statistical model for atmospheric optical scintillation," Numerical Simulations of Physical and Engineering Processes, J. Awrejcewicz, Ed. Intech, 2011, ch.8.

[14] Alouini, Mohamed-Slim, Ansari, et al. Performance Analysis of Free-Space Optical Links Over Malaga (M) Turbulence Channels With Pointing Errors[J]. IEEE transactions on wireless communications, 2016, 15(1):91-102.

[15] Dehghan, Mostafa, Majid Ghaderi, and Dennis Goeckel. "Minimum-energy cooperative routing in wireless networks with channel variations." IEEE Transactions on Wireless Communications 10.11 (2011): 3813-3823.

[16] Himsoon, Thanongsak, et al. "Lifetime maximization via cooperative nodes and relay deployment in wireless networks." IEEE journal on selected areas in communications 25.2 (2007): 306-317.

The 14th International Conference on
Laser-light and Interactions with Particles (LIP2024)
September 18-22nd, 2024, Xi'an, Shaanxi, China

SPECTRAL PREDICTION OF COMPOSITE STRUCTURED METASURFACES BASED ON CONVOLUTIONAL NEURAL NETWORK

Tan QU[1,*], Jing ZHANG[1] and Zhensen WU[2]

[1] School of Electronic Engineering, Xidian University, Xi'an, Shaanxi 710071, China.
[2] School of Physics, Xidian University, Xi'an, Shaanxi 710071, China.

Corresponding author: tqu@xidian.edu.cn

Abstract

The metasurface can achieve flexible regulation of phase, amplitude and polarization within the sub-wavelength scale. Combined with deep learning algorithms, the paper proposes a spectral response prediction method for composite structure metasurface based on convolutional neural network (CNN). Taking the elliptical cylindrical structure as an example, the effects of the long and short axes and the height of the metasurface units on the amplitude and phase changes are analysed, and the optical response laws of the composite structured metasurface with two different unit arrangement combinations are investigated. Comparing with deep neural network (DNN) and radial basis function neural network (RBFNN) for spectral prediction of composite structure metasurface, the experimental results show that the CNN model constructed in this paper performs better in terms of accuracy and efficiency. It is further investigated to design a linear-linear polarization converter in the visible range by controlling the arrangement of the unit structure by selecting two kinds of units with excellent performance and complementary tendency each. The research will provide basis for the inverse design of metasurface and its applications in nanophotonics.

1 Introduction

Metamaterials are unique man-made structures or composites that possess physical properties unmatched by natural materials, while electromagnetic metasurfaces are special two-dimensional metamaterials that can be maximised by carefully designed periodic structures or combinations of multiple materials. Metasurface can realize new properties and functions that are difficult to be achieved with natural materials and composites, such as negative refractive index[1], stealth[2-3], frequency selection[4], and optical field modulation.[5]

Traditional simulation of electromagnetic modulation of metasurface mostly adopts the method of moments, the finite element method, and the finite difference time-domain method which requires a complex modelling process and a large amount of computational resources. Focused on the structure-function mapping relationship in inverse design of metasurface, a CNN-based optical spectrum response prediction method is investigated.

2 Methods

2.1 Composite structure metasurface model

Composite-structure controls metasurface properties by combining geometries and alignments. The use of alignment combinations of two or more unit structures is expected to achieve better modulation. In this paper, we study the combination of two different structural units to investigate the effect of different arrangement combinations on the spectrum response of the metasurface.

Similar to the monostructured metasurface, the metasurface consists of a three-layer structure of Au-SiO_2-Au, with a dielectric spacer SiO_2 layer of 150 nm in thickness and a substrate gold layer of 450 nm. The difference lies in the two different cells, cell A and cell B, which were selected taking into account the influence of the long and short axes and height on the amplitude and phase variations. Here the long, short, and height dimensions of the elliptical metal A and B cell are optimised with $a_1 = 315\text{nm}, b_1 = 105\text{nm}, c_1 = 60\text{nm}$, and $a_2 = 275\text{nm}, b_2 = 80\text{nm}, c_2 = 80\text{nm}$, respectively.

2.2 Network model

In constructing the network, the first convolutional layer collects 8*8 input information and uses a 3*3 convolutional kernel so as to obtain more information about the structural features of the metasurface. Then a 2*2 pooling layer is used to aggregate the collected information efficiently and make it more accurate. A 3-layer convolutional network and 7-layer fully connected layer is constructed to transform the 8*8 format input into 1*128.

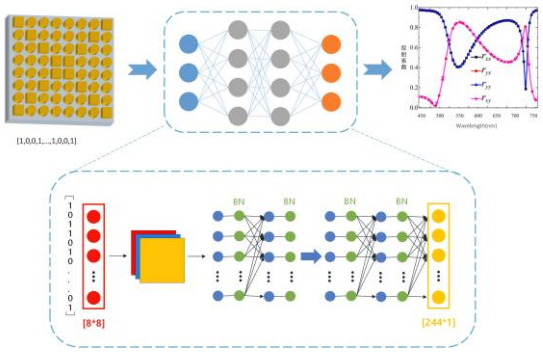

Figure 1 The diagram of convolutional neural networks for spectrum response prediction

3 Results and discussions

In order to demonstrate the effectiveness of the CNN proposed here in dealing with the problem of metasurface spectral prediction of composite structures, we conducted comparative experiments between CNN, DNN and RBFNN.

The experimental data are the 20,000 composite structural data sets collected in Section 2.1, the input is the 01 representation of the 8*8 structural arrangement, and the output is their reflectance spectra r_{ij} in the wavelength range (450nm~750nm), and each set of data consists of four reflectance spectra, and each reflectance spectrum is taken at 61 points.

In order to better evaluate the performance of the network, this paper selects Mean absolute error (MAE), Mean Absolute Percentage Error (MAPE), R-Squared and average computing time to evaluate the performance of the constructed network model.

Method / Index	MAE	MAPE	R-Squared	Average Time
DNN	0.034	8.67%	0.959	3.89s
RBFNN	0.051	12.34%	0.923	**1.63s**
CNN(Ours)	**0.028**	**6.23%**	**0.986**	2.26s

Table 1 *Comparison on spectral prediction between different methods*

From the comparison of the results of different methods in Table 1, it can be seen that the CNN used in this paper fits the best in solving the composite metasurface spectral prediction problem, and performs better than the DNN and second to the RBFNN in terms of the speed. But the RBFNN is not very efficient in determining the radial basis function related parameters, which makes the RBFNN fit the worst in this spectral prediction. The fitting effect of DNN is the second best, but due to the computational amount of the fully-connected network is too large, its inference speed is also the slowest. It is shown that our approach balances speed and accuracy in spectral response prediction to some extent.

4 Conclusion

In this paper, a CNN-based method for the prediction of metasurface spectra of composite structures is proposed. By constructing a CNN consisting of three convolutional pooling layers and seven fully connected layers, the spectral prediction of complex structural metasurfaces is accomplished. The experiment show that most of the predicted results are relatively similar to the waveforms of the desired results. The research has good application value in structure-function prediction and inverse design of metasurfaces.

5 Acknowledgement

This work was supported by the National Natural Science Foundation of China (No. 62071359).

6 References

[1] SMITH D R, PADILLA W J, VIER D C, et al. Composite medium with simultaneously negative permeability and permittivity, Physical Review Letters 84(18): 4184-4187 (2000).

[2] Ulf Leonhardt, Tomáš Tyc, Broadband Invisibility by Non-Euclidean Cloaking, Science 323:110-112 (2009).

[3] Chen, P.Y., Soric, J. and Alù, A. Invisibility and Cloaking Based on Scattering Cancellation. Adv. Mater., 24: OP281-OP304 (2012).

[4] Jeong H , Le D H , Lim D ,et al. Reconfigurable metasurfaces for frequency selective absorption, Advanced Optical Materials 1902182 (2020).

[5] H. He, H. Yang, Z. Xie, and X. Yuan, Dynamic polarization rotation and vector field steering based on phase change metasurface, Frontier of physics 18:12303 (2023).

The 14th International Conference on
Laser-light and Interactions with Particles (LIP2024)
September 18-22nd, 2024, Xi'an, Shaanxi, China

USE OF AN ITERATIVE GENERALIZED REGRESSION NEURAL NETWORK TO DETERMINE THE PARTICLE SHAPE DISTRIBUTION OF NANORODS BY DEPOLARIZED DYNAMIC LIGHT SCATTERING

Hameed AKHTAR, Zhao ZHANG, Jia Jie WANG, Yi Ping HAN, Huan YANG and Paul BRIARD*

[1] School of Physics, Xidian University, Xi'an, 710071, P. R. China

Corresponding author: paulbriard@outlook.com

Abstract

In this extended abstract, we discuss the possibility of determining the bivariate probability density function (PDF) of the diameters and lengths of a polydisperse distribution of cylindrical nanorods using an iterative generalized regression neural network (GRNN) in a depolarized dynamic light scattering (DDLS) setup. The predictors of the GRNN are the normalized electric field autocorrelation functions (EACFs), called depolarized signals, which are recorded in vertical-horizontal (VH) polarization geometry at multiple scattering angles. The response of the GRNN gives the parameters of the PDF that describes the distributions of the diameters and lengths of the nanorods in the sample. In our simulations, the PDFs of the nanorods in the 'experimental' sample and the samples used to train the GRNN are Gaussian and unimodal. The possibility of experimental validation of our approach is also discussed.

1 Introduction

In a conventional dynamic light scattering (DLS) setup, nanoparticles that are undergoing Brownian motion and are illuminated by a laser beam scatter the light toward a photodetector. The relationship between the translational Brownian motion of the particles and the fluctuation in the scattered light permits the estimation of the particle size distribution (PSD). The size is equal to the Stokes radius if the particles are non-spherical. Many ways of estimating a PSD based on DLS have been investigated, such as the information-weighted constrained regularized least-squares method, among other least-squares approaches [1]. The use of a GRNN is another approach that has been successfully used to estimate unimodal and bimodal lognormal PSDs of nanoparticles by conventional DLS, using predictors such as the z-average size estimated by cumulant at multiple scattering angles, or the normalized EACF recorded at a single scattering angle [2]. Unlike conventional DLS, DDLS permits the estimation of characteristic information about the shape of the particles, as the rotational diffusion coefficient of a nanoparticle is related to its shape (rotational diffusion is ignored in conventional DLS). The main issue with the use of DDLS is the mixing of the relaxation decays of the depolarized signals of the translational and rotational diffusion. The majority of efforts to develop DDLS have involved the estimation of the average rotational and translational diffusion coefficients of the nanorods [3], their average diameter and average length [4], and their average aspect ratio [5]; however, these works have not investigated the dispersion around their average values. A depolarized-polarized ultrafast image-based DLS (DUIDLS), in which an ultrafast camera is used instead of a photodetector to record the light fluctuations [6], can estimate the distribution of equivalent cylindrical particles (monodisperse cylindrical particles that scatter the same light fluctuations as the polydisperse particles in the sample between times t and t+τ). The distribution of equivalent cylindrical particles and the distribution of the particles in the sample are not the same, but they are related to each other. A method of estimating the average nanorods of each mode of a bimodal Gaussian distribution of nanorods using a DUIDLS approach was proposed in [7], but no information was estimated about how the diameters and lengths were dispersed around these average nanorods, again due to the mixing of information about translational and rotational diffusion in the light fluctuations. A GRNN has the potential to estimate the dispersion of the diameters and lengths around their average values.

2 Normalized electric field autocorrelation

The DDLS experimental setup is illustrated in the Figure 1.

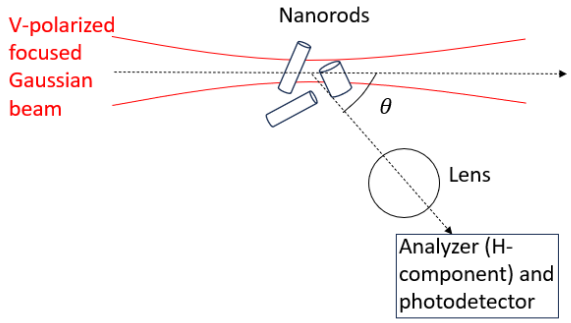

Figure 1 *DDLS experimental setup in VH polarization geometry at scattering angle θ*

The analyzer is a polarizer that can be used to select the horizontal component of the light scattered by the nanorods in the sample (with VH polarization geometry, where the incident light is vertically (V) polarized with respect to the scattering plane, and the scattered light recorded by the photodetector is horizontally (H) polarized with respect to the scattering plane). The lens positioned between the nanoparticles and the photodetector is used to select the scattering volume (the volume in which the illuminated particles scatter the light toward the photodetector). The vertical-vertical polarization geometry is ignored in the present work. The photodetector records the scattered light intensity, and the fluctuations in the light intensity are characterized by a normalized intensity autocorrelation function from which the normalized EACF is obtained. The expression for the EACFs of polydisperse nanorods is as follows (as derived from the non-normalized EACFs of monodisperse symmetric-top particles [8, pp. 129]):

$$g_{VH}^{(1)}(q,\tau) = \sum_{d}\sum_{L} f(d,L) C_{\beta} e^{-\Gamma\tau} + \delta\varepsilon \quad (1)$$

where τ is the time interval between two records of light intensity by the photodetector, q is the magnitude of the scattering vector (a vector representing the change in the wave vector between the incident wave and the scattered wave), f(d,L) is the PDF (of diameters and lengths) of the nanorods in the sample (where we use the approximation that all nanorods in a class with diameter [d_i d_{i+1}]), and a class with length [L_j L_{j+1}] have diameter d_i and length L_j), and C_β is a coefficient proportional to $|\beta|^2$, where β is the anisotropic polarizability of a nanorod [8, pp. 129] of diameter d_i and length L_j . We describe the polarizability tensor of a cylindrical nanorod using a spheroidal model [9, pp. 71]. A noise term $\delta\varepsilon$ is added to the normalized EACFs of the 'experimental' sample (where δ is the noise level, and ε is a normal random number). $\Gamma = q^2 D_t + 6D_r$ is the relaxation decay, where D_t is the translational diffusion coefficient, and D_r is the rotational diffusion coefficient perpendicular to the axis of the nanorod (both diffusion coefficients are computed using the bead-shell model [10]). We use the term 'experimental' to distinguish this sample from those used to train the GRNN (as the present work involves only a numerical simulation of the DDLS experiment).

3 Training samples and structure of the GRNN

The GRNN requires a description of the training samples, i.e., a description of their PDFs $f_v(d,L)$, which permits their EACFs to be computed (we use the same method as for computing the normalized EACFs of the experimental sample in Eq. (1), but without noise added to the EACFs). The PDFs of the experimental sample and the training samples are Gaussian and unimodal in this work. We use a least-squares approach to estimate the distributions of the relaxation decays $f_\beta(q,\Gamma)$, in a similar way to Wang et al. [2], in order to calculate the average relaxation decays at multiple scattering angles. When the average relaxation decays have been obtained, the bead-shell model is used to estimate the diameter and length of a characteristic nanorod of the distribution (in the same way as in [11]). It is worth mentioning that $f_\beta(q,\Gamma)$ is not the percentage frequency of particles that have relaxation decay Γ, due to the involvement of the anisotropic polarizability of the nanorods in the light fluctuations. However, we use the characteristic nanorod estimated by the least-squares method as an initial guess for the average nanorod, to describe the training samples. Similarly to Wang et al., our GRNN is composed of four layers of neurons: an input layer, a pattern layer, a summation layer, and an output layer. In the input layer, the predictors of our GRNN are the EACFs of the training samples and the experimental sample. The summation layer and the pattern layer apply a smoothing parameter and calculate the Euclidian distance between the EACFs of the experimental sample and the EACFs of the training samples, following Wang et al. The output layer is a vector containing the characteristic parameters of the PDF of the experimental sample, as estimated by the GRNN, consisting of the diameter and length of the average nanorod, and the covariance matrix. For a unimodal Gaussian PDF, the covariance matrix is characterized by two standard deviations, σ_d and σ_L, which describe the dispersion in the diameters and lengths around their average values. Rather than using a single GRNN, we apply an iterative approach where, except in the first iteration, the output of the GRNN is used as the initial guess for the next iteration.

4 Example of numerical results.

The parameters of the simulation are as follows. The nanoparticles are gold nanorods in water at a temperature of 298K (where the dielectric permittivity of water and gold have the same values as in [5]), under a free-space wavelength of 632.8 nm. The scattering angles are computed from 10º to 170º at increments of 10º. The PDF for the experimental sample has an average diameter of 20 nm and an average length of 120 nm. The parameters of the covariance matrix are σ_d^2 = 30 nm² and σ_L^2 = 60 nm². We use 1000 random training samples with covariance matrix elements such that $\sigma_d^2 \in$ [10 nm² 50 nm²] and $\sigma_L^2 \in$ [50 nm² 100 nm²]. The average nanorod in the training samples has a diameter $d \in [0.5d_{IG}\ 1.5d_{IG}]$ and a length $L \in [0.5L_{IG}\ 1.5L_{IG}]$, where d_{IG} and L_{IG} are the diameter and length of the average nanorod in the initial guess. The smoothing parameter for the GRNN is 0.01, and the noise level is $\delta = 10^{-3}$. In the last iteration, the training samples have the same average nanorod, and differ only in terms of their covariance matrix (100 training samples, with 10 values of σ_d^2 and 10 values of σ_L^2, linearly spaced). Figure 2 shows the PDF for the experimental sample set in the

simulation and the PDF estimated using our iterative GRNN, after three iterations. The differences between the PDFs depend on the noise in the experimental EACFs and the way the training samples have been described. Instead of describing a unimodal Gaussian PDF, more parameters of the PDF can be used to describe multimodal Gaussian PDFs, i.e., mixing the proportions of the Gaussian modes, the average diameters and lengths of each Gaussian mode and the covariance matrix.

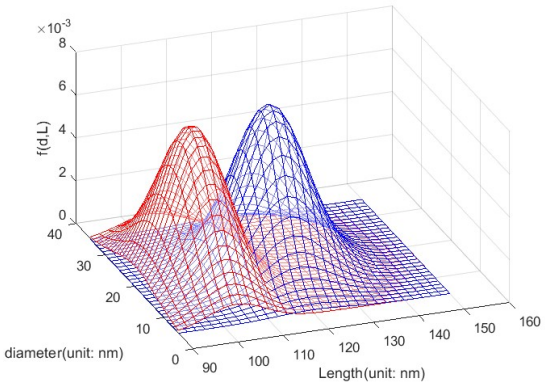

Figure 2 *Comparison between the PDF of the "experimental sample" (blue lines) and the estimated PDF using an iterative GRNN (red lines), after three iterations.*

An iterative GRNN has the potential to estimate these multimodal PDFs. Experimental validation of the measurements of diameter and length (or the diffusion coefficients from which the diameter and length can be estimated) obtained via electron microscopy is usually done via comparison with measurements made with DDLS [3-6,11]. Electron microscopy gives information about the few particles in the electron microscopy image, whereas the GRNN returns a PDF that represents statistical information about the distribution of nanorods in the whole sample. It may be convenient to record the depolarized signals of a mixture of unimodal samples and to compare the measurements from an electron microscopy image with those estimated by the GRNN for the average nanorods for each Gaussian mode; however, this approach does not permit validation of the estimates of the dispersion in the diameters and lengths around the average nanorods of each Gaussian mode. Another possibility is to record as many electron microscopy images as necessary to retrieve statistical information about the dispersion of diameters and lengths in the sample: this method could be used to validate the use of an iterative GRNN to estimate the dispersion of the diameters and lengths around their average values in the sample, to complement the numerical simulations.

5 Conclusion.

We have discussed the possibility of using an iterative GRNN to estimate a unimodal Gaussian PDF for a sample of nanorods based on depolarized signals recorded at multiple scattering angles in a DDLS setup. Avenues for future work involve a more accurate estimation of the average nanorod of the unimodal Gaussian PDF, to allow our approach to be extended to multimodal Gaussian PDFs, and the experimental validation of this approach.

6 References

[1] Xu M., Shen J., Thomas J. C., Huang Y., Zhu Xinjun, Clementi L. A., Vega J. R., Information-weighted constrained regularization for particle size distribution recovery in multiangle dynamic light scattering. Optics Express 26(1): 15-31 (2018) To write to write to write to write to write to write to write to write to write to write)

[2] Wang Z., Wang Y., Shen J., Liu W , Yuan X, Fu X, Zhang G. Dynamic light scattering inversion based on Tikhonov regularization and parameter-optimized generalized regression neural network. Powder Technology 409:117802 (2022)

[3] Nixon-Luke R., Bryant G., A depolarized dynamic light scattering method to calculate translational and rotational diffusion coefficients of Nanorods. Particle & Particle Systems Characterization 36(2): 1800388 (2019)

[4] Khouri S., Shams M., Tam K. C. Determination and prediction of physical properties of cellulose nanocrystals from dynamic light scattering measurements. Journal of Nanoparticle Research 16: 2499 (2014)

[5] Rodríguez-Fernandez J., Perez–Juste J., Liz–Marzan L. M., Lang P. R. Dynamic Light Scattering of Short Au Rods with Low Aspect Ratios. Journal of Physical Chemistry C 111(13): 5020–5025 (2007)

[6] Liu Z., Cai X., Briard P., Dimension Measurement of Nanorods Based on Depolarized-Polarized Image-Based Dynamic Light Scattering. Acta Optica Sinica 41(21): 2129001 (2021)

[7] Zhao A. Y., Wang J. J., Han Y. P., Aihoon F., Yang H., Briard P. Statistical numerical investigation of translational-rotational ultrafast image-based dynamic light scattering to measure a bimodal Gaussian sample of cylindrical nanoparticles. Journal of Physics: Conference Series 2353: 012007 (2022)

[8] B. J. Berne and R. Pecora. *Dynamic light scattering with applications to chemistry, biology, physics* (Dover, 2000)

[9] Van De Hulst H. C., *Light Scattering by small particles* (Wiley, New-York , 1956)

[10] Ortega A., Garcıa de la Torre J. Hydrodynamic properties of rodlike and disklike particles in dilute solution. Journal of chemical physics 119(18): 9914-9919 (2003)

[11] Briard P., Liu Z., Cai X., Measurement of the mean aspect ratio and two characteristic dimensions of polydisperse arbitrary shaped nanoparticles, using translational-rotational ultrafast image-based dynamic light scattering. Nanotechnology 31(39): 395709 (2020)

The 14th International Conference on
Laser-light and Interactions with Particles (LIP2024)
September 18-22nd, 2024, Xi'an, Shaanxi, China

TRANSMISSION CHARACTERISTICS OF LAGUERRE-GAUSSIAN BEAMS IN DUSTY ENVIRONMENTS

Yuancong CAO[1,*], Wenjie JIANG[1], Bowen Tao[1] and Mingjian CHENG[1]

[1] School of Physics, Xidian University, Xi'an, 710071, China

Corresponding author: yccao_xd@163.com

Abstract

Complex multi-particle environments (such as dust and haze) have significant effects on laser transmission. Vortex beams carrying orbital angular momentum, such as Laguerre-Gaussian beams, have important applications in optical communications and optical remote sensing. In this paper, we utilize a simulation method with random particle screens to simulate the transmission of Laguerre-Gaussian beams in dusty environments. Dust particles with sizes following a certain distribution are randomly generated on scattering screens, and multiple particle screens are placed along the transmission link to simulate a multi-particle system. We investigate the transmission characteristics of LG beams with different transmission distances, particle sizes, orbital angular momenta, and wavelengths in dusty particle scattering screens.

1 INTRODUCTION

Structured beams, due to their unique spatial intensity distribution and phase structure, hold significant promise in fields such as optical communications, optical remote sensing, and optical imaging[1]. However, in turbulent, dusty, or hazy transmission media, the characteristics of structured beams are significantly affected. Laguerre-Gaussian beams, with their helical phase distribution and carrying orbital angular momentum, offer advantages in information encoding. The Generalized Lorenz-Mie Theory (GLMT) proposed by G. Gouesbet et al[2]. In the 1990s provides an accurate framework for calculating the scattering of structured beams by spherical particles. Over the past three decades, various particle scattering models for structured beams, including Laguerre-Gaussian beams, Bessel-Gaussian beams[3],Hermite-Gaussian beams[4], etc., have been developed, considering different types of particles such as homogeneous medium spheres, charged spheres, aerosol spheres, and multi-layer spheres. Dust particles, a typical example, have garnered attention in studies on the scattering of structured beams[5,6]. However, for multi-particle systems like those found in haze or dust environments, single-particle scattering models are inadequate. Many studies on the scattering of beams by agglomerative particle systems are based on models such as GLMT and DDA.

For situations where there's a significant difference between beam and particle sizes, these single-scattering models lack accuracy. In this study, we propose a simulation approach using random particle screens placed along the beam transmission path to simulate beam transmission in multi-particle systems (as shown in Figure 1) [7]. The particles are randomly distributed and follow the size distribution model of haze particles. Since the particle size relative to the beam size is small, each particle on the screen is treated as an obstruction model, resulting in diffraction at the particle edges and creating a distribution similar to Airy patterns behind the screen[8]. A particle scattering screen is placed every *dz* m along the path. We investigate the effects of particle size, transmission distance, and different OAM modes of the beam on transmission. Additionally, we simulate the intensity distribution of the beam after passing through the particle screens under different conditions to explore the influence of particle screen systems on beam transmission attenuation.

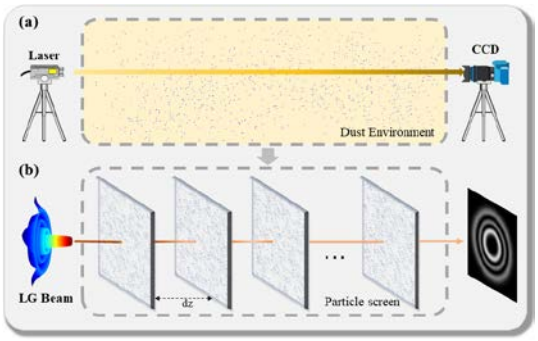

Figure1 *Schematic representation of Laguerre-Gaussian (LG) beam transmission in a dusty environment equivalent to a particle screen.*

2 Simulation results

In the dusty environment according to the size distribution function of dust particles, we randomly generated screens with a number of particles that satisfy this distribution. These screens are placed every 5m along the transmission path of the beam. The waist radius of the beam is 0.01m, and the particle sizes range from 30μm to 50μm. We calculated the phase distribution and intensity distribution of 0th order and 4th order topological Laguerre-Gaussian beams after transmitting 25m (5 screens), 50m, and 75m. As shown in Figure 2, it is evident that particle scattering significantly affects the intensity and phase distributions of the beam, causing a noticeable decrease in intensity and blurring of the phase boundary. The results presented in Figure 2 are similar to those in reference [8], validating the validity of our particle screen model. This demonstrates how the particle scattering

screens model affects the intensity and phase distributions of Laguerre-Gaussian beams under varying distances in a dusty environment, confirming the consistency with existing literature findings.

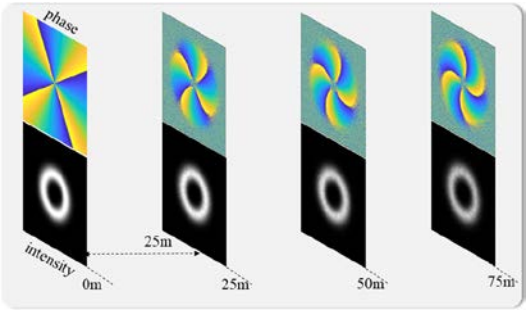

Figure 2 *The phase and intensity distributions of 0th and 4th order topological Laguerre-Gaussian (LG) beams at different distances (25m, 50m, 75m) in a dusty environment.*

Different intensities of dust storms also have varying impacts on laser transmission attenuation. The intensity of a dust storm depends on the number of dust particles per unit volume. To simulate this, we randomly generated dust models with different numbers of particles on screens. As shown in Figure 3, we calculated the field distribution and phase distribution of LG beams passing through 10 screens with 5000, 10000, and 20000 particles on each screen. With increasing particle concentration, the beam's spot field distribution becomes more diffused and its intensity weaker, resembling the trend observed in Figure 2 with increased transmission distance. However, the overall annular beam pattern and its topological distribution remain unaffected. Furthermore, as shown in Figure 4, LG beams of different topologies and orders may exhibit varying attenuation characteristics in a dusty environment.

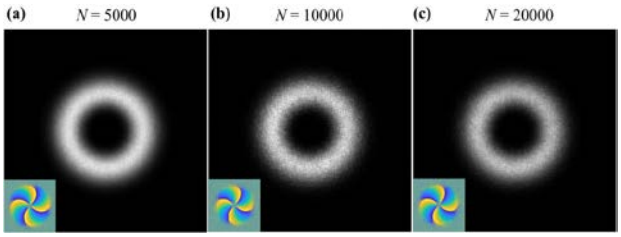

Figure 3 *The impact of 10 screens with different particle concentrations (N=5000, 10000, 20000) on the transmission* of LG beams.

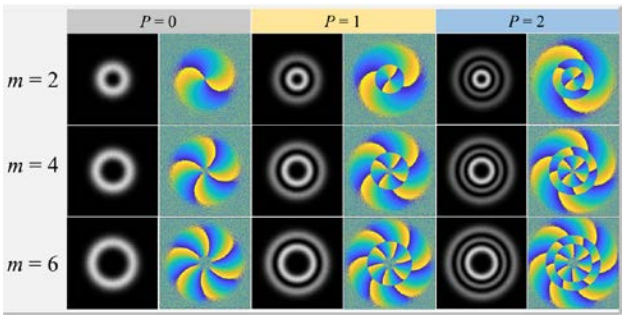

Figure 4 *The transmission results of LG beams with different topologies and orders through screens with dust particles.*

In addition, lasers of different wavelengths exhibit varying transmission characteristics in complex environments. Therefore, we also simulated and computed the field distribution and phase distribution of LG beams with different wavelengths over a 50m transmission through dust environments (as shown in Figure 5). In comparison, the LG beam with a wavelength of 1550nm exhibits a more split beam profile after passing through the particle screen. This is due to the greater diffraction of longer wavelengths, resulting in a more dispersed field distribution.

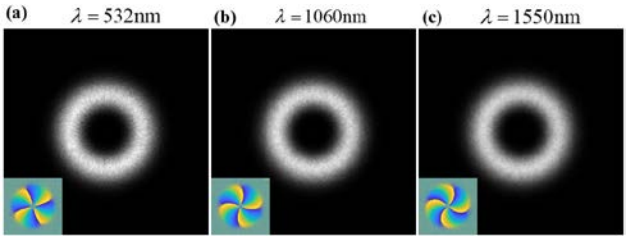

Figure 5 *The results of different wavelengths (532nm, 1060nm, 1550nm) passing through the particle screen.*

3 Conclusion

We simulated a sand-dust environment by randomly generating a fixed number of particles on a flat plane that satisfy certain size distributions. Treating these particles as occlusion models, we studied the field distribution and phase distribution of LG beams at different distances, particle densities, topologies, and wavelengths. The study found that as the transmission distance and particle density increase, the beam spot becomes more diffused and its intensity decreases, although the overall annular structure remains unchanged. Additionally, when treating particles as occlusion models, diffraction occurs at the edges of particles, causing longer-wavelength LG beams to exhibit more pronounced diffraction effects, resulting in a denser distribution of beam spots.

4 References

[1] Cheng M, Guo L, Li J, et al. Channel capacity of the OAM-based free-space optical communication links with Bessel-Gauss beams in turbulent ocean [J].IEEE Photonics Journal, 2016,8(1):1-11.

[2] Gouesbet, G., Maheu, B., & Gréhan, G. (1988). Light scattering from a sphere arbitrarily located in a Gaussian beam, using a Bromwich formulation. JOSA A, 5(9), 1427-1443.

[3] Shi, C., Guo, L., Cheng, M., et al. (2020). Aerosol scattering of vortex beams transmission in hazy atmosphere. Optics Express, 28(19), 28072-28084.

[4] Qingqing, H., Mingjian, C., Lixin, G., Jiangting, L., Xu, Y., and Songhua, L. (2017). Scattering of aerosol particles by a hermite–gaussian beam in marine atmosphere. Applied Optics, 56(19), 5329.

[5] Zhou, Y. H., Shu He, Q., & Jing Zheng, X. (2005). Attenuation of electromagnetic wave propagation in sandstorms incorporating charged sand particles. The European Physical Journal E, 17, 181-187.
[6] Gill, E. W. B. (1948). Frictional Electrification of Sand. Nature, 162(4119).
[7] Ahmed A. S. Role of particle-size distributions on millimetre-wave propagation in sand/duststorms[C]. IEE Proceedings H (Microwaves, Antennas and Propagation), 1987.
[8] Viola S, Chen Z, Yao A M, et al. Degradation of light carrying orbital angular momentum by ballistic scattering[J]. Physical Review Research, 2020, 2(3): 033093.

The 14th International Conference on
Laser-light and Interactions with Particles (LIP2024)
September 18-22nd, 2024, Xi'an, Shaanxi, China

LARGE-FIELD OPTIMIZED OPTICAL SECTIONING STRUCTURED ILLUMINATION MICROSCOPY

Xiaofei CHEN [1-3], Kai WEN [1-3], Yunze LEI [1-3], Sha AN [1-3], Hongfei SUO [1-3] and Peng GAO [1-3,*]

[1] School of Physics, Xi'dian University, Xi'an 710071, China
[2] Key Laboratory of Optoelectronic Perception of Complex Environment, Ministry of Education, Xi'an 710071, China
[3] Engineering Research Center of Information Nanomaterials, Universities of Shaanxi Province, Xi'an 710071, China

Corresponding author: peng.gao@xidian.edu.cn

Abstract

Optical-sectioning structured illumination microscopy (OS-SIM) is one type of three-dimensional (3D) fluorescence microscopic techniques, featuring quick imaging speed and low photobleaching. However, conventional OS-SIM generates fringe patterns through a spatial light modulator (SLM), which limits the imaging full-of-field (FOV). Therefore, this work proposed a novel method that has a large-field and good sectioning capability by combining 1D grating for stripe projection and an SLM for phase-shifting to break the fringes limitation imposed by the pixel number and size of the digital projection devices. Meanwhile, the illumination was optimized to improve the sectioning ability of OS-SIM. Eventually, three-dimensional imaging of OS-SIM within a large FOV of 780×1030 μm^2 under a 20×/0.75*NA* micro-objective was demonstrated.

1 Introduction

Optical-sectioning structured illumination microscopy (OS-SIM) [1-3] is one of the fast, minimally invasive, 3D imaging technique. The optical sectioning capability of OS-SIM is due to the contribution of the fast decay of the fluorescence signal (modulated by the illumination fringes) with the defocusing distance. One phase-shifting operation along an arbitray orientation is applied, the defocus portion of the sample can be eliminated, yielding an optical sectioned image with a clear background. Compared to other three-dimensional imaging techniques, OS-SIM has a faster imaging speed and lower phototoxicity [4, 5]. However, the field of view (FOV) of conventional OS-SIM is constrained by the pixel count and size limitations of SLM or DMD, making it unable to image a large sample [6, 7]. Conventional wide-field OS-SIM can collect data from multiple fields of view by mechanically moving the sample and then reconstruct the data using stitching algorithms [8, 9], but this method is rather time consuming and suffers from the image discontinuities between two neighbouring images.

Furthermore, current OS-SIM techniques typically utilize commercial LEDs or mechanically oscillating longer optical fibers (at least 10 meters) as illumination sources to suppress speckle noise [10]. However, their small divergence angle and large axial modulation region result in slow axial stripe decay and weak slicing capability, failing to meet the high-precision measurement requirements for biological samples.

In this work, we present a large-field, optimized OS-SIM. Employing grating projection and spatial light modulator spectrum modulation, we overcome the limitations of the screen size on the field of view and the limitations of mechanical movement on imaging. In the end, the 3D imaging with the space bandwidth product (SBP) 4.7 times above the traditional technology was obtained. Furthermore, we combined a rotating ground glass with coherent illumination to optimize the optical sectioning strength of OS-SIM. With a larger divergence angle and a smaller axial modulation region, it exhibits superior axial optical sectioning capability.

2 Methods

2.1 Experimental setup

The LF-OS-SIM setup proposed is illustrated in Fig. 1. A 488 nm, narrow linewidth laser is used as the light source. Polarizer P2, oriented horizontally, is positioned along the beam path to convert the illumination into horizontally polarized light, ensuring maximum modulation efficiency of the SLM. The intensity of the illumination can be controlled by adjusting the angle between the polarization directions of P1 and P2. The beam passes through L1, where it is collimated into parallel light, uniformly illuminating a 22 × 22 mm^2 grating.

The illumination light is diffracted into multiple parallel beams with different propagation directions by the grating, among which the efficiency of the ±1st orders is highest. After passing through lens L3 for Fourier transformation, the spectrum of the ±1st order diffraction appears on a plane at a certain distance from SLM. It is important to note that firstly, this distance ensures that the dispersed spectra of various diffraction orders falling on the SLM cover multiple SLM pixels. This ensures accurate phase modulation while also avoiding damage

to the SLM caused by illumination intensity. Secondly, the combination of TIR prism and tilted SLM ensures that the reflected beam modulated by the SLM propagates strictly along the optical axis.

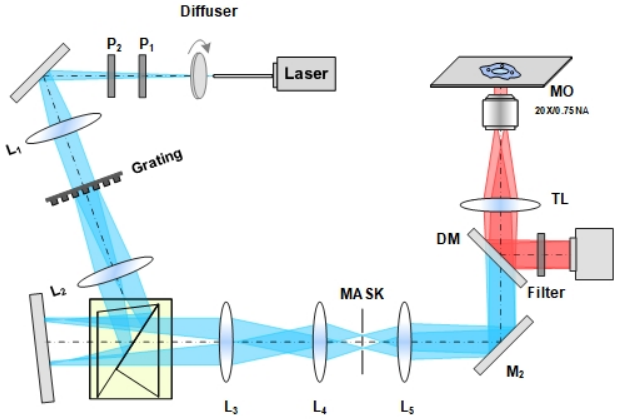

Figure 1 *The schematic setup of large-field OS-SIM.*

After modulation of phase shifts by the spatial light modulator, the spectra of various diffraction orders are imaged again onto a spatial filter mask through the 4f system composed of lenses L4 and L5. The selected diffracted light is transformed by the L5 Fourier transform to produce fringe patterns, and then imaged on the sample plane by the 4f system composed of TL-MO. Finally, the information on the sample plane is imaged on a COMS camera by a 4f system MO-TL.

2.2 Optimization of the illumiantion of OS-SIM for better axial sectioning capability

To further illustrate the advantages of coherence optimization in improving the axial sectioning capability of LF-OS-SIM, the effects of illumination with the range of divergence angles of 0 rad, 0.24 rad, 0.49 rad, and 0.99 rad on optical sectioning were tested, respectively. The results are shown in Fig. 2. Three-dimensional distributions of the fringe patterns were obtained by placing a mirror on the sample plane and scanning the objective along the axial direction. For each axial plane, three phase-shifted patterns were captured by loading binary patterns onto the SLM with phase shifts of 0, 2π/3, and 4π/3. Subsequently, the optical-sectioning image for each axial plane was obtained using the RMS algorithm [4]. Figure 2(a) shows the X-Z sections of the fringe pattern distribution and Fig. 2(b) shows X-Z sections of the optical-sectioned images for different beam divergence angles of 0 rad, 0.24 rad, 0.49 rad, and 0.99 rad respectively. It is evident that as the range of the beam divergence angle increases, the axial modulation region of the fringes becomes smaller (defined with FWHM and it decreases from 30.0 μm to 7.3 μm) (Fig. 2(b) and Fig. 2(c)). The results confirm that the illumination angle span of the illumination has a significant effect on both the axial distribution of fringe patterns and the optical-sectioning capability of LF-OS-SIM. It's worth mentioning that as the axial extension of the fringe patterns narrows, the contrast of the fringes also decreases, as shown in Fig. 2(d). Insufficient fringe contrast might impair the reconstruction efficacy of LF-OS-SIM. In practical applications, there needs to be a balance between the contrast of the fringes and the axial extension of the fringe patterns.

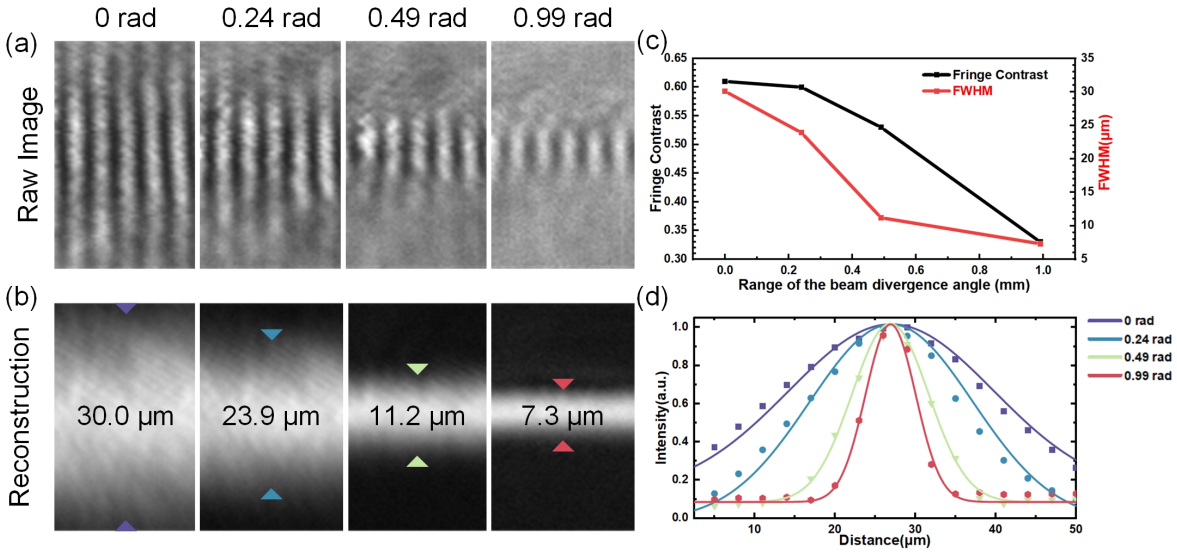

Figure 2 *Effect of illumination extension on the axial range of structured illumination and optical sectioning.*

2.3 3D imaging of OS-SIM

In the second experiment, LF-OS-SIM was used to perform large-field three-dimensional imaging of a one-euro coin sample. In this experiment, LF-OS-SIM is equipped with a low magnification objective (20×/0.75), enabling a FOV of 1030×780×300 μm², as shown in Fig. 1. Subsequently, layer-by-layer data acquisition of the sample is performed using a piezoelectric displacement stage controlled electronically. WF images are obtained by averaging the data acquired at phase shifts of 0, 2π/3,

and 4π/3, while OS images are generated using the RMS algorithm[4]. Figure 3(a) respectively presents the X-Y section of the sample under wide-field illumination, illumination with a beam divergence angle of 0.24 rad, and illumination with a beam divergence angle of 0.61 rad, using different color gradients to represent information from various depths of the sample. Figure 3(b) respectively illustrates the three-dimensional morphology of the sample under wide-field illumination, illumination divergence angle of 0.24 rad, and illumination divergence angle of 0.61 rad. Figure 3(c) shows the X-Z section of the sample along the dashed line in Fig. 3(b). It is evident that under wide-field illumination conditions, it is nearly impossible to distinguish information from different depths of the sample, whereas the optical sectioning capability is stronger when the illumination beam divergence angle is 0.61 rad compared to 0.24 rad.

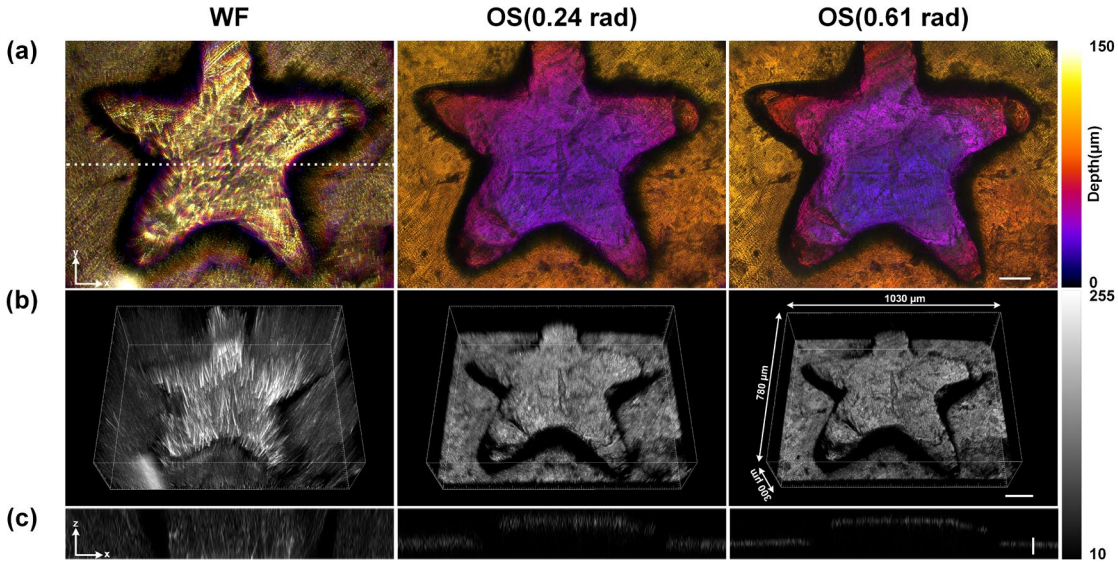

Figure 3 *Three-dimensional images of large-field three-dimensional imaging of a one-euro coin using large-field OS-SIM with different illumination condition.*

3 Conclusion

In this work, we present a scheme of large-field OS-SIM technique. High-throughput imaging was achieved by combining grating projection with phase modulation using the SLM, thereby eliminating errors associated with mechanical movement. Additionally, adjusting the illumination beam divergence angle enhanced the optical sectioning capability of the OS-SIM. As a result, we achieved optical sectioning images with a space-bandwidth product 3.7 times higher than traditional SIM. We anticipate that the proposed large-field OS-SIM method will play a significant role in industrial inspection and the observation of biological structures and functions.

4 References

1. M. A. A. Neil, et al., "Method of obtaining optical sectioning by using structured light in a conventional microscope," Optics letters **22**, 1905-1907 (1997).
2. D. R. Mason, et al., "Enhanced resolution beyond the Abbe diffraction limit with wavelength-scale solid immersion lenses," Optics letters **35**, 2007-2009 (2010).
3. D. Dan, et al., "Structured illumination microscopy for super-resolution and optical sectioning," Chinese Science Bulletin **59**, 1291-1307 (2014).
4. X. Chen, et al., "Superresolution structured illumination microscopy reconstruction algorithms: a review," Light: Science & Applications **12**, 172 (2023).
5. J. R. Allen, et al., "Structured illumination microscopy for superresolution," Chemphyschem **15**, 566-576 (2014).
6. K. Wen, et al., "Large-field structured illumination microscopy based on 2D grating and a spatial light modulator," Optics Letters **47**, 2666-2669 (2022).
7. J. Zheng, et al., "Large-field lattice structured illumination microscopy," Optics Express **30**, 27951-27966 (2022).
8. Z. Li, et al., "Fast widefield imaging of neuronal structure and function with optical sectioning in vivo," Science advances **6**, eaaz3870 (2020).
9. Q. Zhong, et al., "High-throughput optical sectioning via line-scanning imaging with digital structured modulation," Optics Letters **46**, 504-507 (2021).
10. C. Chen and H. Li, "Advanced Wide-Field Fluorescent Microscopy for Biomedicine," Biomedical Photonic Technologies, 1-30 (2023).

The 14th International Conference on
Laser-light and Interactions with Particles (LIP2024)
September 18-22nd, 2024, Xi'an, Shaanxi, China

CALIBRATION OF SPACE DUST DETECTION SYSTEM ONBOARD TIANWEN-2 MISSION

Zecheng CUI, Miaomiao Qi, Ting Zhang and Jiajie WANG*

School of Physics, Xidian University, Xi'an, 710071, China

Corresponding author: wangjiajie@xidian.edu.cn

Abstract

The *Dust Detection System* (DDS) represents the optical component of the Tianwen-2 payload *Dust Multi-properties Analyzer* (DMA), which has been designed with the objective of investigating the properties of space dust, including the size and speed. The mission targets the near-Earth asteroid 2016 HO3 and an active asteroid 311P/PanSTARRS. This paper focuses on ground calibration experiments for the DDS. The Standard spherical silicon dioxide (SiO_2) particles are employed for the determination of the fitting factor between engineering parameters and the theoretical scattered flux. Subsequently, the accuracy of particle size measurements on particles of other materials will be verified. Two numerical models of the F-D (scattered flux and diameter) curve calculated by light scattering theory are provided by numerical fitting and regression method to serve as reference for the inverse calculation of particle size for actual on-orbit particle events.

1 Introduction

Space dust refers to small particles in cosmos that range in size from submicron to millimeters [1]. The investigation of space dust presents a significant opportunity to gain insight into the origin of the universe and the evolution of planetary systems [2-4]. Moreover, the assessment of space dust concentration and size within and surrounding the capsule can inform the implementation of protective measures, which may assist in the mitigation of potential risks to astronauts and spacecraft during on-orbit operations [5, 6]. Consequently, a comprehensive understanding of space dust is essential for the planning exploration of deep space. In recent years, an increasing number of space detection missions have incorporated the detection of space dust as a scientific objective. These missions focus on the physical properties, including material, size, charge, shape, concentration, velocity, and others [6-12]. Among these, ESA's *Rosetta* mission which investigated the space dust in the vicinity of 67P/Churyumov-Gerasimenko concluded in 2016 as scheduled [13]. Following the success of the Rosetta payload GIADA, the light scattering method, which represents a revolutionary approach, emerged as a highly promising new technique for detecting the size, material, and velocity of space dust [14]. For the non-contact, no disruption advantages, light scattering is a well-established method for measuring particle diameter and concentration in dispersed media such as aerogels and colloids. Furthermore, the method has been demonstrated to be effective in the detection of marine particles [15-17], aerosol particles [18-20], and cells [21].

The *Tianwen-2* mission, which is designed to investigate the near-Earth asteroid 2016 HO3 and an active asteroid 311P/PanSTARRS, is scheduled for launch in 2025 [22]. The payload *Dust Multi-properties Analyzer* (DMA) contains a structure designated the *Dust Detection System* (DDS), which has been specifically designed to detect the particle size and velocity of incoming particles by employing light scattering techniques. In conjunction with other components, the density, diameter, mass, velocity and composition of space dust can be determined in situ.

This paper will primarily focus on the calibration of the DDS device, through which the measurements of standard spherical particles. Section 2 will introduce the DDS device briefly, and reveal the measurement principle. The calibration experiment and data processing will be investigated in Section 3. The result is subjected to numerical fitting and regression method. Finally, a conclusion will be presented in Section 4.

2 The design and measurement principle of DDS

2.1 Confugration of DDS

The general schematic diagram of the DDS is presented in Figure. 1. A semiconductor laser chip emits an elliptical Gaussian beam with a wavelength of 976 nm. Subsequently, the beam is transformed into a 40 mm-width, equal energy distribution, and quasi-collimated detection light curtain through the use of a customized Powell lens and a cylinder lens. As the particle traverses through the detection light curtain, it interacts with the light curtain and scatters light in all directions. A proportion of the scattered light with a specific angle is collected by a compound parabolic concentrator (CPC) [23] and transferred to current signal by a photodiode located behind it. Subsequently, the scattered light signals are then amplified, denoised, and recorded by circuit. This enables the retrieval of the scattering cross-section and the geometry diameter through the application of light scattering theory. The structure of DDS ensures that the acceptance angle of the scattered light and the intensity of the incident light are equal regardless of where the particles pass through the detector light curtain, which benefits the calculation of particles' diameter.

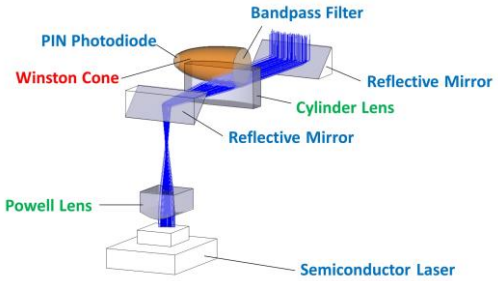

Figure 1 *DDS schematic diagram.*

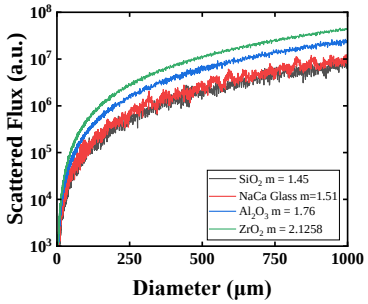

Figure 2 *The scattered flux vs. diameter curves of spherical particles with different materials.*

2.2 Scattered flux calculation

We commence with an examination of the most fundamental case: spherical particle scattering. The Lorenz-Mie theory represents a well-established methodology for calculating the scattering properties of spherical particles [24]. Suppose a particle of diameter *D* located at the origin, the refractive index m_1 is illuminated by a polarized plane electromagnetic wave $\vec{E} = x\exp(i\vec{k}\cdot\vec{r})$, where k is the wave number $k = 2\pi/\lambda$ and λ is the wavelength, ignoring the time factor $\vec{E} = x\exp(i\omega t)$. The medium in which the light is transformed has the refractive index m_2. The spatial distribution of scattered light is described as:

$$I = \frac{\lambda^2 I_0}{4\pi^2 r^2}\left(i_1 \sin^2\varphi + i_2 \cos^2\varphi\right), \quad (1)$$

where I_0 is the intensity of the incident light and *r* is the distance between the origin (where the scattered sphere is located) and the target position. The variables i_1 and i_2 are proportional to the amplitude function $|S_1|^2$ and $|S_2|^2$, respectively:

$$|S_1|^2 = \sum_{n=1}^{\infty}\frac{2n+1}{n(n+1)}\left[a_n\pi_n(\cos\theta) + b_n\tau_n(\cos\theta)\right], \quad (2)$$

$$|S_2|^2 = \sum_{n=1}^{\infty}\frac{2n+1}{n(n+1)}\left[a_n\tau_n(\cos\theta) + b_n\pi_n(\cos\theta)\right], \quad (3)$$

where π_n, τ_n are related with associated Legendre functions, scattering coefficients a_n, b_n can be obtained by Lorenz-Mie theory [25].

The detection of scattered light from all directions represents a significant challenge in the context of compact scattering measurement systems. In general, it is more convenient to collect light from a significant angular range. In the context of Figure. 1, the scattered flux can be calculated as follows:

$$F = \frac{\lambda^2 I_0}{2\pi^2}\int_{\theta_1}^{\theta_2}\left[i_1(\theta) + i_2(\theta)\right]\sin\theta\cdot\cos^{-1}\left[\frac{\cos\frac{\theta_2-\theta_1}{2}}{\sin\theta}\right]d\theta, \quad (4)$$

where $[\theta_1, \theta_2]$ is the acceptance angle range of the DDS.

In accordance with the aforementioned principle, the scattered flux versus diameter (F-D) curves of spherical particles comprising disparate materials have been calculated and are presented in Figure. 2. The calculated scattering angle has been a range of [70.5°, 109.5°], which aligns with the configuration depicted in Figure. 1. The figure illustrates the favourable monotonicity of the F-D curves when an appropriate acceptance angle selected. This serves as the foundation for the sizing of particles through light scattering techniques.

3 Experiment calibration and data processing

In order to evaluate the detection capabilities of the DDS, a series of essential calibration experiments have been conducted. In this section, the engineering parameters will be correlated with the actual scattered flux in accordance with the principles of light scattering theory. The results will be verified experimentally through the measurement of particle size in a variety of materials.

The initial calibration experiments employ silicon dioxide (SiO_2) standard spherical particles as the event particles. A variety of particle sizes are selected and measured using a microscope. The diameter of each particle ranges from 1 to 1,000 μm. Subsequently, the particles are released by gravity into the detection light curtain of the DDS, while the processed scattered light flux from the PIN photodiode is recorded. Given to the linearity of the signal processing system, a comparison is made between the experimental F-D curve to theoretical one, with the ratio obtained by means of a linear fitting method. The calibration ratio, or calibration factor, was determined to be 83. A selection of representative results is presented in Table. 1. Furthermore, the detection size range of SiO_2 particles is 9 to 1,000 μm in ground laboratory conditions.

Diameter /μm	Theoretical Scattered Flux	Engineering Parameters	Ratio
22.1	6939	84	82.6
28.5	9766	114	85.7
80.0	78832	853	92.4
158.1	21532	2615	82.3
253.0	539229	7217	74.7
500.0	1816267	22908	79.3
800.0	4154215	59287	70.1

Table 1 *A part of the comparison experiment data and theoretical scattering result.*

In light of the aforementioned conclusion, a series of scattering experiments were conducted, involving the interaction of standard spherical particles with a range of materials, including soda-lime glass and zirconium oxide (ZrO_2). Figure 3 illustrates the investigation of the F-D curve of experimental data and the theoretical result, employing the calibration ratio. Given to the disparity in refractive indices, the detection size range of soda-lime glass and ZrO_2 particles are 8 to 1000μm and 4 to 420μm, respectively. Furthermore, the theoretical and experimental results for the remaining two materials demonstrate good coupling, thereby corroborating the accuracy of the calibration factor.

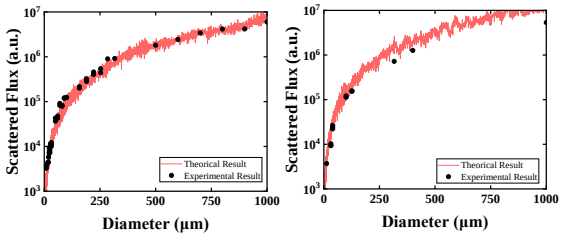

(a) SiO_2 (b) Soda-lime glass

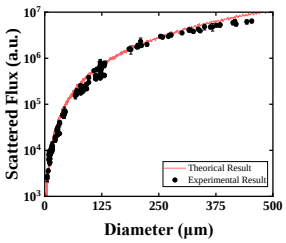

(c) ZrO_2

Figure 3 *The comparison between experimental result and theoretical F-D curve, after processed by calibration ratio.*

However, it is not appropriate for F-D curves employed in engineering applications due to their oscillatory. It is preferable to provide a definitive function (or model) to characterise the F-D relationship. The following section will present two methods.

Numerical fitting represents a convenient method for describing a monotonic functional relationship. The most crucial stage in numerical fitting is the selection of an appropriate objective function. Furthermore, in the context of this problem, it is also crucial to consider the physical meaning. In accordance with the tenets of light scattering theory, the scattered light flux is proportional to the differential scattering cross section, which in turn is proportional to the square of the particle diameter. Accordingly, the F-D relationship can be fitted by the following equation:

$$F = a(m)D^2 + b, \tag{5}$$

where D and m are the diameter and refractive index of particle, respectively. $a(m)$ is the fitting factor which related to the refractive index. b is the noise of device in experiment.

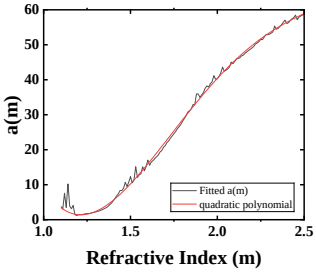

Figure 4 *The comparison between fitted result and final polynomial equation of a(m)*

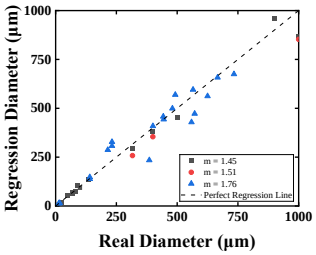

Figure 5 *The regression projection result in test set.*

The initial step is to perform a numericalisation of the F-D curves. The F-D curves for the refractive index in the range of 1.2 to 2.5 are calculated using the principles of light scattering theory. The calculated curves are employed to fit the value of $a(m)$ in Eq.(5). It should be noted that the b value in this fitting is set to zero given that no noise is present in theoretical calculations. Subsequently, a quadratic polynomial is utilized to fit the $a(m)$, m relationship, which follows:

$$a(m) = 33.3m^4 - 287.3m^3 + 893.5m^2 - 1137.2m + 506.9. \tag{6}$$

The comparison between the fitted result and the final polynomial equation of a(m) is shown in illustrated. 4. Finally, experimental results are compared with the objective of verifying the fitting equation Eq. (5) and (6). The calculated results indicate that the mean discrepancy between the experimental and fitted particle sizes for SiO_2, soda-lime glass, and ZrO_2 are 17.8%, 11.0%, and 9.8%, respectively.

Non-linear regression represents an additional method employed in numerical processing. In essence, it is a supervised learning process, whereby input-output mappings are learned from empirical data (training dataset). The experimental data set is divided into two distinct subsets: the training set, which comprises 80% of the data, and the test set, which contains the remaining 20%. Each data set comprises three variables: diameter, refractive index and the scattered flux. The latter two are treated as input vector, and the former is output value. The inputs and outputs from the training set are employed to construct the regression model. The reliability of the model is subsequently evaluated by comparing the outputs from the test set with the values obtained after inputting the model. The comparison is illustrated in Figure. 5. The mean discrepancy between the experimental and fitted particle sizes is 16.51%.

4 Conclusion

Calibration activities on the DDS are of critical importance in the context of data processing for actual on-orbit particle events. Furthermore, it provides a correlation between the engineering parameters and the actual scattered flux, as well as a prediction of the particle size discrepancy associated with the particle events obtained through different data processing methods. It is evident that the calibration experiment serves to validate the reliability of the DDS for the sizing of spherical particles. This will provide unique and valuable data for the in-situ detection of space dust in Tianwen-2 mission.

5 Acknowledgement

6 References

[1] Yan, Z., et al. Micro-dust Detection in deep space. in 7th Annual Conference of the Committee on Deep Space Exploration Technology of the Chinese Academy of Astronautics. Harbin, China, 2010.

[2] Zuo, W., et al., Design and implementation of space dust database. Chinese Journal of Geochemistry **23**(2): 135-140(2004)

[3] Rietmeijer, F.J.M., The Earliest Chemical Dust Evolution in the Solar Nebula. Geochemistry **62**(1): 1-45(2002)

[4] Grün, E., H. Krüger, and R. Srama, The Dawn of Dust Astronomy. Space Science Reviews **215**(7): 46(2019)

[5] Cain, J.R., Lunar dust: The Hazard and Astronaut Exposure Risks. Earth, Moon, and Planets **107**(1): 107-125(2010)

[6] Horányi, M., et al., The Lunar Dust Experiment (LDEX) Onboard the Lunar Atmosphere and Dust Environment Explorer (LADEE) Mission. Space Science Reviews **185**(1): 93-113(2014)

[7] Auer, S., et al., The charge and velocity detector of the cosmic dust analyzer on Cassini. Planetary and Space Science **50**(7): 773-779(2002)

[8] Brownlee, D.E., et al., Stardust: Comet and interstellar dust sample return mission. Journal of Geophysical Research: Planets **108**(E10)(2003)

[9] Tuzzolino, A.J., et al., Dust Flux Monitor Instrument for the Stardust mission to comet Wild 2. Journal of Geophysical Research: Planets **108**(E10)(2003)

[10] Fujiwara, A., et al., The Rubble-Pile Asteroid Itokawa as Observed by Hayabusa. Science **312**(5778): 1330-1334(2006)

[11] Li, D., et al., In Situ Measurements of Lunar Dust at the Chang'E-3 Landing Site in the Northern Mare Imbrium. Journal of Geophysical Research: Planets **124**(8): 2168-2177(2019)

[12] Zhao, C.X., et al., A design of dust analyzer for future Main Belt Comet exploration mission. Advances in Space Research **69**(10): 3880-3890(2022)

[13] Accomazzo, A., et al., The final year of the Rosetta mission. Acta Astronautica **136**: 354-359(2017)

[14] Sordini, R., et al., GIADA performance during Rosetta mission scientific operations at comet 67P. Advances in Space Research **62**: 1987-1997(2018)

[15] Ackleson, S.G. and R.W. Spinrad, Size and refractive index of individual marine particulates: a flow cytometric approach. Applied Optics **27**(7): 1270-1277(1988)

[16] Stramski, D. and M. Sedlák, Application of dynamic light scattering to the study of small marine particles. Applied Optics **33**(21): 4825-4834(1994)

[17] Babin, M., et al., Light scattering properties of marine particles in coastal and open ocean waters as related to the particle mass concentration. Limnology and Oceanography **48**(2): 843-859(2003)

[18] Aptowicz, K.B., et al., Decomposition of atmospheric aerosol phase function by particle size and asphericity from measurements of single particle optical scattering patterns. Journal of Quantitative Spectroscopy and Radiative Transfer **131**: 13-23(2013)

[19] Cross, E.S., et al., Single particle characterization using a light scattering module coupled to a time-of-flight aerosol mass spectrometer. Atmos. Chem. Phys. **9**(20): 7769-7793(2009)

[20] Muñoz, O., et al., Experimental determination of scattering matrices of randomly oriented fly ash and clay particles at 442 and 633 nm. Journal of Geophysical Research: Atmospheres **106**(D19): 22833-22844(2001)

[21] Loiko, V.A., et al., Morphometric model of lymphocyte as applied to scanning flow cytometry. Journal of Quantitative Spectroscopy and Radiative Transfer **102**(1): 73-84(2006)

[22] Li, C., et al., Scientific Issues and Detection Schemes on the Dust Characteristics Of Main Belt Comets. Journal of Deep Space Exploration: 1-8(2024)

[23] Winston, R., Light Collection within the Framework of Geometrical Optics*. Journal of the Optical Society of America **60**(2): 245-247(1970)

[24] Mie, G., Beiträge zur Optik trüber Medien, speziell kolloidaler Metallösungen. Annalen der Physik **330**(3): 377-445(1908)

[25] Yang, W., Improved recursive algorithm for light scattering by a multilayered sphere. Applied Optics **42**(9): 1710-1720(2003)

The 14th International Conference on
Laser-light and Interactions with Particles (LIP2024)
September 18-22nd, 2024, Xi'an, Shaanxi, China

BLOOD CELL CHARACTERIZATION BASED ON DEEP LEARNING AND DIFFRACTION PHASE MICROSCOPY

Nauman ALI[1,2,3], Xin LIU[1,2,3], Wenjian WANG[1,2,3], Ruihua LIU[1,2,3], Kequn ZHOU[1,2,3], Ying MA[1,2,3*], Peng GAO[1,2,3*]

[1] Advanced imaging and spectroscopy Lab, Xidian University, Xi'an, 717701, China
[2] Key Laboratory of Optoelectronic Perception of Complex Environment, Xi'an, 717701, China
[3] Engineering Research Centre of Information Nanomaterials, City, Xi'an, 717701, China

Corresponding author: yingma@xidian.edu.cn , peng.gao@xidian.edu.cn.

Abstract

Quantitative characterization of blood cells is very important for medical diagnosis and life science research. This study presents a novel label-free and high-throughput approach for analysing flowing blood cells in a microfluidic channel by combining deep learning with partially coherent illumination-based diffraction phase microscopy (PCI-DPM). Diluted blood was injected into a microchannel and imaged with PCI-DPM, yielding high-contrast phase images for the blood cells. A modified YOLOv5-s neural network was used to perform automatic identification and analysis of blood cells in the phase image of PCI-DPM, revealing the diameter, dry mass, volumetric density, and speed of blood cells precisely. The proposed approach allows quick and accurate assessment of blood samples, providing valuable insights for patients in different pathological states, such as haematological disorders and infections.

1 Introduction

Inspection of blood cells on their shape, motility, and dry mass can help us identify potential diseases1, even in the absence of evident symptoms at the early stages of a disease. For instance, the dry mass density of blood cells acts as an essential parameter in haematology and cancer diagnostics. However, high-throughput inspection of blood cells is a challenging task. At an earlier time, blood cells were inspected by manually counting under a microscope2. This process was rather time-consuming and tedious. With recent advancements in computer science, automated analysis of blood cells has become possible and widely applied in different medical fields3,4. The automated analysis approaches often require fluorescent labelling of cells to render the cells with high contrast. Yet, the extraneous fluorescent labelling raises the cost of blood inspection and will also potentially change the natural state of blood cells. Therefore, people desire a label-free technique that can inspect blood cells in a low-cost and automated way.

In this paper, we propose and demonstrate the combination of Deep Learning and partially coherent illumination-based diffraction phase microscopy (PCI-DPM) with statistical analysis for label-free characterization of flowing blood cells in a microfluidic channel. The DL-based analysis approach identifies the diameter, concentration, and the dry mass of blood cells together with the flow speed of the flowing blood cells in a microfluidic device, providing essential parameters including the cell diameter, concentration, dry mass, and the flow speed.

2 Methods

2.1 Setup of PCI-DPM phase microscopy

In this research, we use partially coherent illumination-based diffraction phase microscopy (PCI-DPM) to acquire the quantitative phase images. The schematic diagram of PCI-DPM is shown in Fig. 1. The illumination source of PCI-DPM is a solid-state crystal laser with a wavelength of 532 nm (1875-5321L, Laserland, Wuhan, China). The output laser having a diameter of 4 mm is focused by a microscope objective MO1 (20×/0.4, Nanjing, China) on a glass diffuser (diffusing angle is 15°). The diffuser is rotated by a motor (KN335714, Huatong Electronics, Co., Ltd., China) at 200 revolutions per second (RPS). The light, after being scattered by the diffuser, is collimated by a lens L1 (f = 75 mm). Then, the lens L2 (f = 75 mm) is used to refocus the light into a multi-mode fibre (MMF) with a diameter of 60 μm. At the other end of the multi-mode fibre, the output light is collimated by a CCTV lens (f= 12 mm, HM1214MP5, China), resulting in a partially coherent illumination (PCI) for PCI-DPM. After being reflected by mirror M1, the illumination beam is converted into a linear polarized light by a polarizer P1 with its polarization along the horizontal direction. To adjust/optimize the fringe contrast for different samples, a quarter-wave plate (QW) is placed on the illumination beam. Fresh blood was extracted from a rat and diluted with PBS by a ratio of 1:10, and then solution was pumped through a microfluidic channel. The microfluidic channel was fabricated using the following steps: first, two rectangular strips of double-sided adhesive tape were adhered to a glass substrate (25×75 mm microscope slide), having a 1 mm-width gap between the two strips. Second, the two strips were covered with a microscope cover glass on the top, forming a channel with a depth of ~100 μm. Third, the two ends of the channel were connected with two microfluidic tubes, acting as the inlet and outlet. The100 μm depth of the channel was designed to be smaller than the depth of field of the DHM system, so

that it prevents DHM imaging from defocusing. The blood cells flowing in a microfluidic device are limited to a in focus layer and imaged by a telescope system consisting of a microscopic objective MO2 (10×/0.45, CFI Plan Apochromat, Nikon, Japan) and a tube lens L3. An object wave is formed when the illumination beam passes vertically through a microfluidic channel. A polarizing grating G (#12-677, 159 grooves/mm, Edmund Optics, New Jersey, America) is placed in the image plane of the sample to split the object wave into different copies along with the diffraction orders. Among these, the ±1st diffraction orders have around 42.5% the total intensity for each. In the PCI-DPM system, the -1st order is filtered by a pinhole PH (diameter-50 m, GCO-P50A, Daheng Optics, Beijing, China) and used as the reference wave, as shown in Fig. 1. While the +1st order passes through the large hole on the filter mask with its spectrum unaffected, still acting as the object wave. Due to the polarization-dependent diffraction of the grating, the object and reference waves are elliptically polarized along two orthogonal directions. Finally, the object and reference light are converted to the same polarized wave by a linear polarizer P2 and interfere with each other in the plane of the CCD. The CCD camera (4,000 3,000, pixel size 1.85 m, DMK 33UX226, The Imaging Source Asia Co., Ltd., China) records the generated off-axis hologram between the object and reference waves. Both the amplitude and phase images of the sample can be reconstructed using conventional off-axis hologram reconstruction algorithm18, 39

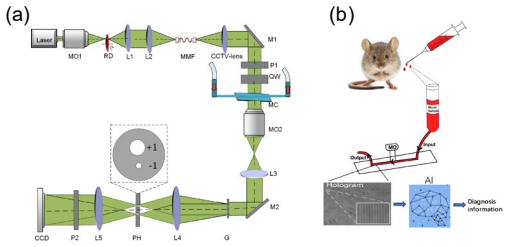

Figure 1 *Schematic diagram of partially coherent illumination-based diffraction phase microscopy (PCI-DPM). (a) Schematic of PCI-DPM. (b) Flowchart of blood inspection. CCD, charge-coupled devices; G, polarization grating; L1-L5, achromatic lens; MC, microchannel; M1 and M2, Mirrors; MMF, multi-mode fiber; MO1 and MO2, microscopic objectives; P1-P2, polarizers; PH, pinhole; QW, quarter-wave plate; RD, rotating diffuser.*

2.2 Deep learning architecture and training

This research will utilize the YOLOv5 network to detect and count the blood cells in the phase image, as shown in Fig.2. YOLOv5 is a CNN-based algorithm that allows for object detection, localization, and image classification. In general, YOLOv5 divides the input image into subregions during the forward propagation and predicts bounding boxes and probabilities for each region. The YOLOv5 network has four variations, including YOLOv5-s, YOLOv5-m, YOLOv5-l, and YOLOv5-x. In this study, YOLOv5-s is chosen because it has two benefits: a short detection time and a manageably small weight size for the model that YOLOv5-s trains. A model with smaller weight offers a faster process speed since the high-throughput blood cell detection is often overwhelming task for embedded hardware. The network architecture of YOLOv5-s is divided into three parts: Backbone, Neck, and Head/Detect.

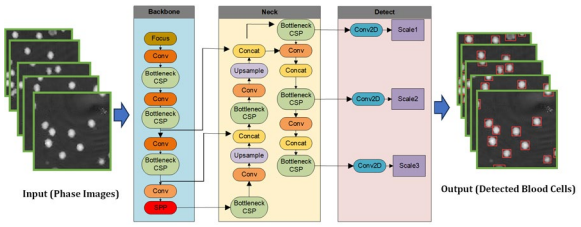

Figure 2 *Schematics and architecture of YOLOv-5. Conv, convolutional layer; CSP, cross stage partial network; Concat, concatenate; SPP, spatial pyramid pooling.*

3 Results

We trained YOLOv5-s using the phase images of blood cells. The model was trained for 150 epochs on the training dataset, model completed its learning in 1.79hours, and after every epoch, it was evaluated on the validation set. The mean Precision (mAP50) between the network output and the ground-truth was 0.923, and the mAP50-95 (average of multiple Intersection over Union (IoU) thresholds) was 0.493, reflecting a comprehensive performance across varying levels of detection thresholds. During testing, the pre-processing stage, which prepares the image for later analysis, took only 6.0 milliseconds to complete. This rapid preparation step permitted a quick transition to the inference stage, where blood cell identification occurred, with the network interpreting the image and identifying the blood cells inside it in 671.8 milliseconds. The detection of blood cells for different concentrations is shown in Fig. 3.

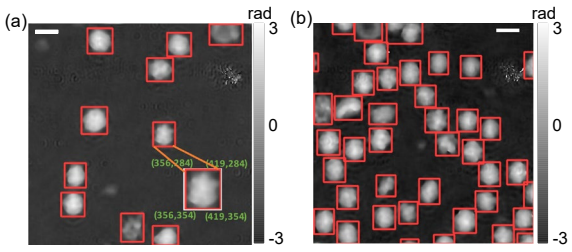

Figure 3 *Blood cell detection in phase image by YOLOv5 network. Detection of blood cells in a low-concentration environment (a) and high-concentration environment (b). Scale bar in (a) and (b) represents 5μm*

After the detection of blood cells, the model gives us the total number of blood cells in an image and bounding box coordinates of every blood cell as shown in Fig. 3(a). Thus, to obtain a complete picture of blood cell characteristics, we calculated the diameter of the blood cell by using the bounding box coordinates given by our model's predictions. Specifically, the average diameter of the blood cells was calculated by averaging the length and width of each bounding box. At the same time, we conducted the high-throughput analysis of the blood cell concentration when they were flowing in a microchannel.

We also used the bounding box coordinates given by the model to identify the territory of each individual blood cell. The phase values of all the pixels (the Gray value divided by 255 and multiplied by 2π) within the cell territory were subtracted by the mean background value identified from the area outside the cells. Eventually, the phase values of the pixels within the cell territory were integrated and the statistics of the integrated phase values are calculated. Further, the dry mass of each isolated cell was determined by using these integrated phase values. In the last experiment, we demonstrate that the proposed technique can be used to monitor the flowing speed of the cells within the microchannel, exploring the dynamic behaviour of the sample. First, our model identifies an individual cell at two adjacent phase images recorded at the time of t1 and t2, and registers the coordinates of the centres of the cell in the two-phase images. Then, the travelled distance $\Delta x=(x2-x1).\delta$ of a blood cell between two time points can be calculated using the centre coordinates of a cell measured at two neighbouring time points t1 and t2.

4 Conclusions

In this work, we demonstrated that the combination of deep learning with partially coherent illumination-based diffraction phase microscopy (PCI-DPM) provides a versatile way for automatic counting and analysing blood cells. A trained YOLOv5 neural network allows for detecting the concentration, diameter, dry mass of the blood cells. Using the proposed technique, we also investigated the variation of the flow speed of the blood cells in the microchannel, providing a dynamic view of cellular motion within microchannels.

5 References

1. Buttarello, M., & Plebani, M. (2008). Automated blood cell counts: state of the art. *American Journal of Clinical Pathology*, *130*(1), 104–116.
2. LEHMANN, T. (2004). Content-based image retrieval in medical application. *Methods of Information in Medicine*, *43*(4), 354–361. https://cir.nii.ac.jp/crid/1571980075536184960.bib?lang=en
3. Lin, Z. (2011). The cell image segmentation based on the KL transform and OTSU method. *2011 International Conference on Multimedia and Signal Processing*, *1*, 25–28.
4. Lloyd, A. C. (2013). The Regulation of Cell Size. *Cell*, *154*(6), 1194–1205. https://doi.org/10.1016/J.CELL.2013.08.053

The 14th International Conference on
Laser-light and Interactions with Particles (LIP2024)
September 18-22nd, 2024, Xi'an, Shaanxi, China

QUANTITATIVE MEASUREMENT OF EXTINCTION, SCATTERING, AND ABSORPTION SPECTRA FROM METALLIC NANOPARTICLES

Alla GISICH[1,2,3*], Baptiste AUGUIÉ[1,2,3] and Eric C. LE RU[1,2]

[1] School of Chemical and Physical Sciences, Victoria University of Wellington, Wellington, 6012, New Zealand
[2] The MacDiarmid Institute for Advanced Materials and Nanotechnology Wellington, 6012, New Zealand
[3] The Dodd-Walls Centre for Photonic and Quantum Technologies, University of Otago, Dunedin 9054, New Zealand

Corresponding author: alla.gisich@vuw.ac.nz

Abstract

Metallic nanoparticles are used in many applications, relying on either scattering or absorption of light. Unfortunately, their optical characterisation using traditional UV–vis spectroscopy cannot distinguish between absorption and scattering contributions to extinction. Recent progress has been made with an integrating sphere technique [1,2] enabling the collection of pure absorption spectra to complement standard extinction measurements. Scattering can also be measured independently, in a 90-degree configuration, although it is more difficult to obtain quantitative results with this method. In this study, we apply these three techniques to characterise solutions of Au nanospheres with diameters in the range of 20–100 nm, check the consistency of extinction as the sum of absorption and scattering, and validate the results against theoretical results from Mie theory.

1 Introduction

As light passes through a turbid medium, its intensity decays exponentially, and the extinction E measured by traditional UV–vis spectrometers characterises the combined contribution of both absorbance A and scattering S [3, 4].

$$E = A + S \quad (1)$$

Traditional UV–vis spectroscopy cannot distinguish between both contributions, but in some applications such as photothermal therapy or photocatalysis, one is interested in the absorption component, while in others, such as display technologies or nano-antennas, it may be the scattering contribution that is most relevant.

While pure absorption can be accurately measured using an integrating sphere, determining scattering from such measurements is indirect, as it involves subtracting absorption from extinction [1,2]. This approach faces challenges when dealing with weakly scattering samples, as extinction closely resembles absorption, resulting in noisy and unreliable scattering signals.

Scattering measurements can alternatively be performed directly using a 90-degree configuration. However, the measurement is non-trivial, and careful corrections are necessary to interpret the data accurately. Indeed, as light propagates in the solution, it is both absorbed and scattered, modifying the spectrum of the incident light along the beam path. To account for this effect, a correction factor has been proposed to describe the spectral modification of the incident light due to extinction in the incident beam's path length [5].

We note that both scattering and absorption must also affect the scattered light exiting the solution, on its way to the 90-degree detector, which poses a greater challenge as the light path is more complicated.

Figure 1 illustrates a typical 90–degree configuration for measuring scattering from colloidal solutions. The scattering signal collected at 90 degrees is denoted I_s, and the path length inside the medium is decomposed as $L = l_1 + l_2$.

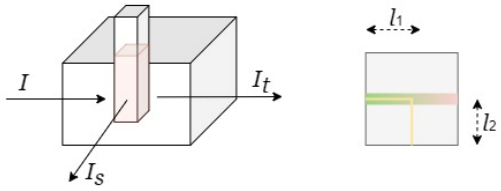

Figure 1. *Left: 90 – degree configuration for measuring scattering at 90 degrees. Right: top view of the cuvette.*

The total scattering contribution can formally be defined as the integral over all angles of the scattering amplitude Q, which is a function of wavelength λ and polarization of the radiation and the observation angles θ and φ (where θ is the scattering angle, and φ is the azimuthal angle). Our approach to relate Q quantitatively to the measured signal I_s relies on the possibility of factoring the function $Q(\lambda,\theta,\varphi)$ into a product $Q(\lambda)F(\theta,\varphi)$, where the two factors are evaluated separately. In practice, this assumption requires that the angular profile of scattering does not vary with wavelength in the spectral range of interest. For small subwavelength particles with an essentially Rayleigh-like phase function, as considered in this work, Mie simulations confirm that this approximation is valid. Under this hypothesis, it is possible to define a scaling factor K, that accounts for the integral of $F(\theta,\varphi)$ over the solid angle of collection, and scattering can be calculated as:

$$S = Q_{90}\, K, \quad (2)$$

where Q_{90} is the scattering at $\theta = 90$ degrees, measured with a restricted solid angle [5].

To account for the "inner-filter" effect described above, whereby extinction affects the spectrum along the incident beam and after scattering, we introduce another factor, F(E), which depends only on extinction at a given wavelength:

$$S = K\, I_s / I_o \,/ F(E), \quad (3)$$

where

$$E = -\log_{10}(I_t / I_o), \quad (4)$$

where I_t, I_0 are the transmission signals for sample and reference (water) respectively, I_s is the scattering of the sample measured at 90 degrees, and E is the extinction of the sample.

In previous studies, F(E) was assumed to be of the form 10^{-EL} [5]. However, our analysis demonstrates that this representation is an approximation with limited applicability, and we propose an alternative method to obtain this factor experimentally with a reference measurement.

The factors K and F(E) should be the same for all scattering measurements performed under the same conditions since they account for the setup's configuration (numerical aperture and other geometrical parameters), and shouldn't depend on nanoparticle characteristics, as long as their angular response remains Rayleigh-like.

In other words, once those parameters have been characterised with reference samples, the setup can be used to characterise nanoparticles with different diameters and concentrations.

2 Methods

Our setup (Figure 2) used for extraction of absorption and scattering contributions of metallic nanoparticles includes a Laser-Driven Light Source (EQ-99X-QZ-S, Energetiq Technology), a Square One Cuvette Holder (Ocean Insight), and Spectrometer Flame-S (FLMS15991).

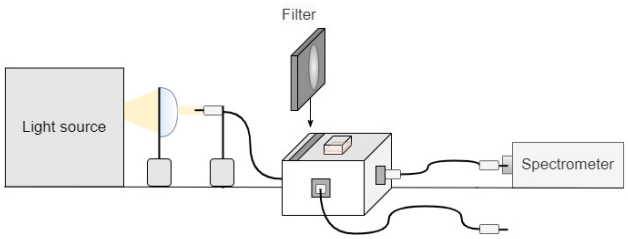

Figure 2. *Setup with a 90-degree adapter. Light is focused into a multimode fibre (diameter 800µm), and sent through the cuvette with a collimating lens. A neutral density filter (ND1.5) is used to attenuate the light in transmission, to avoid saturation. Both transmission and 90-degree scattering outputs are connected to the spectrometer via a 600µm core multimode fibre.*

In the experiment, I_0 was obtained by measuring transmission through a reference water sample. The solution of nanoparticles was then inserted to measure I_t. The scattering spectrum, I_s, was collected from the 90-degree port. Due to the limited numerical aperture of the collecting lens, the measured scattering is only a small proportion of the total scattered light, and the signal intensity I_s was very weak in comparison to I_t, requiring full light intensity (no ND filter), and longer integration times.

For measurements with the integrating sphere technique that can measure both extinction and absorption in turbid samples, we used the spectrophotometer Cloudspec (MaramaLabs) [1,2].

The samples consisted of gold nanoparticles in solution (diameters ranging from 20 to 100 nm, used as-is from Nanocomposix), and non-absorbing silica nanospheres (diameter 50nm, Nanocomposix) in water were used to calibrate K and F(E), as described below.

3 Results

Example results are shown in Figure 3, together with theoretical predictions as an ideal scenario for scattering from a 90-degree setup.

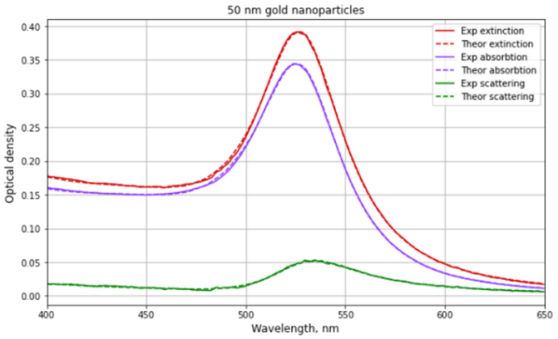

Figure 3. *Extinction, absorption, and scattering spectra alongside Mie theory predictions for 50 nm gold nanoparticles.*

Employing the correction factor F(E) as 10^{-EL} in our initial experiments leads to a reasonably good agreement for the scattering of 60 nm gold nanoparticles at different concentrations (dilution factors of 2, 4, and 8), as depicted in Figure 4. The comparison between scattering spectra acquired from the 90-degree setup and Mie theory shows good agreement. However, this approach consistently failed for other diameters of gold nanoparticles, as illustrated in Figure 5, when comparing scattering spectra with those obtained indirectly from CloudSpec as the difference between extinction and absorption.

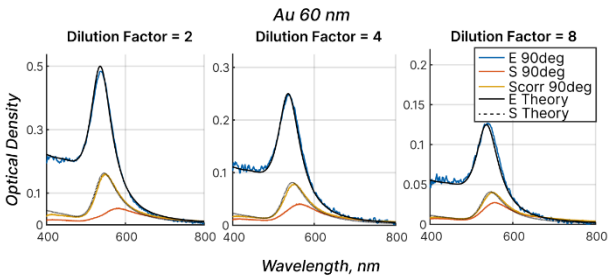

Figure 4. *Extinction and scattering spectra of Au 60 nm nanoparticles obtained from the 90-degree setup, compared with theoretical predictions from Mie theory.*

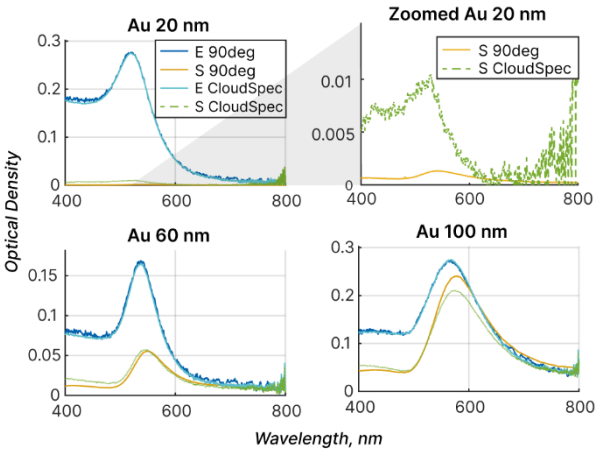

Figure 5. *Extinction and scattering spectra of Au nanoparticles (diameters from 20 to 100 nm) obtained from the 90-degree setup and CloudSpec.*

The discrepancy in scattering measurements may arise from several factors such as stray light in the 90-degree setup, potential imperfections in the ND filter's response, or an inaccurate model for F(E). Indeed, the exponential factor 10^{EL} oversimplifies the light path in solution, as the incident beam is spread out by scattering, and the 90-degree port collects light from a non-trivial scattering volume inside the solution. Further experiments conducted with silica nanoparticles of different concentrations, where scattering and extinction spectra should be identical, have confirmed that modelling F(E) as 10^{EL} does not fully capture the system's response in the 90-degree configuration.

Our proposed alternative is to use such silica samples as a calibration measurement, and to determine F(E) experimentally with a simple polynomial fit. This calibrated factor can subsequently be used for unknown scattering samples, which yields superior results (Figure 6).

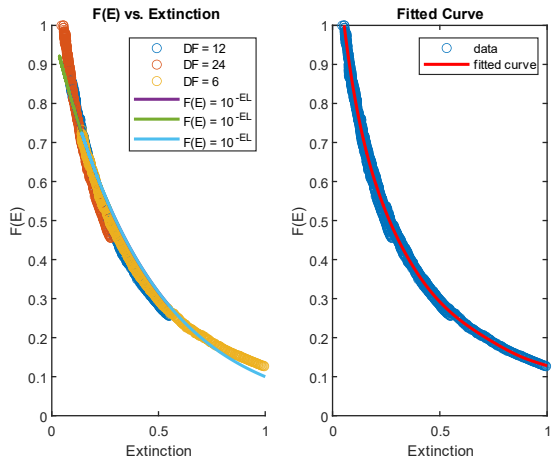

Figure 6. *F(E) for silica nanoparticles (dilution factors of 6, 12, 24) comparing with F(E) as 10^{-EL}, with extinction from CloudSpec measurement and L equal to 1 (Left), and using a polynomial fit (Right).*

4 Conclusion

Experimental access to all three types of spectra, rather than only extinction as in standard UV–vis spectroscopy, provides a much richer characterisation tool and offers therefore a more stringent test of the parameters used in a theoretical fit. Notably, good agreement with Mie theory could only be obtained by considering the size polydispersity of the colloids and choosing the correct, non-trivial factor F(E) and dielectric function for the metal [1].

These findings are crucial to improve measurement reliability using UV–vis and integrating sphere techniques, across their broad range of applications. Direct measurement of scattering is also advantageous for the smaller particle sizes, where subtraction between extinction and absorption is unreliable.

5 Acknowledgement

The authors thank the Royal Society Te Apārangi for support through Marsden grants MFP-VUW2204 and MFP-VUW2118.

6 References

[1] A. Djorović, S. J. Oldenburg, J. Grand, and E. C. Le Ru, "Extinction-to-Absorption Ratio for Sensitive Determination of the Size and Dielectric Function of Gold Nanoparticles," *ACS Nano*, vol. 14, no. 12, pp. 17597–17605, Dec. 2020, doi: 10.1021/acsnano.0c08431.

[2] J. Grand, B. Auguié, and E. C. Le Ru, "Combined Extinction and Absorption UV–Visible Spectroscopy as a Method for Revealing Shape Imperfections of Metallic Nanoparticles," *Anal. Chem.*, vol. 91, no. 22, pp. 14639–14648, Nov. 2019, doi: 10.1021/acs.analchem.9b03798.

[3] H. C. Hulst and H. C. van de Hulst, *Light Scattering by Small Particles*. Courier Corporation, 1981.

[4] *Absorption and Scattering of Light by Small Particles*, 1st ed. John Wiley & Sons, Ltd, 1998. doi: 10.1002/9783527618156.

[5] N. Micali, F. Mallamace, M. Castriciano, A. Romeo, and L. Monsú Scolaro, "Separation of Scattering and Absorption Contributions in UV/Visible Spectra of Resonant Systems," *Anal. Chem.*, vol. 73, no. 20, pp. 4958–4963, Oct. 2001, doi: 10.1021/ac010379n.

Image analysis method for liquid-gas interface area disturbed by ultrasonic cavitation for evaluation of optimum influence modes

Authors: Varvara Yu. Gordeeva[1], Jean-Bastien Carrat[2], Roman N. Golykh[1]

[1] Biysk Technological Institute (branch) of Polzunov Altai State Technical University, Biysk, Altai region, Russia
[2] Lavrentyev Institute of Hydrodynamics of SB RAS, Novosibirsk, Russia

The mass transfer between liquids and gases play crucial role in water purification process, chemical technology, food production and other industry (for example, water purification with ozone aeration, radon absorption in healing bath, new materials obtaining by chemical reactions between gas and liquid, sparkling drinks produced with CO2 absorption, degassing of melts for solid materials strength increasing, absorption of CO2 from atmosphere to prevent changes of global climate) [1,2,3]. The rate of mass transfer is very limited by diffusion coefficient of gas in liquid [4] (diffusion of gas in liquid is weaker in more than 10,000 times in comparison of gas diffusion in gas).

One of most efficient physical principles of diffusion acceleration is ultrasonic cavitation influence of liquid with large (aeration) bubbles [5]. The cavitation micro bubbles (less than 100 micron) initiate surface waves in aeration bubbles (1...5 mm) walls.

In this work, we would like to introduce our method of evaluation of the large bubble surface area from the 2D-image received experimentally by high-speed imaging. We found in frame of the ray optics that the brightness of a 2D-image pixel depends on slope of the surface projected on the pixel so that the grayscale level in the image corresponds to cosine of angle between the refracted ray and photosensor screen normal vector. Then, finding brightness of the bubble image pixels, we assign each pixel with the corresponding slope and receive a slope map of the bubble. From the slope map, we calculate the surface area. The algorithm is based on Taylor series expansion of the light intensity and solving the reverse problem of finding the surface wave profile for amplitude of each harmonics (with using Fourier's and wavelet transformation). In this way, we receive the wave profile.

The pure reflection at the visual border of bubble is considered in the problem by assumption that average increasing of the surface area is the same on every part of the surface because effects acting on the surface like micro-bubbles concentration, their collapse pressure waves, etc, are the same in volume around the bubble investigated. The assumption is based on the fact that macroscopic parameters are same for the cavitation bubbles when the airlift bubble size is much less than US wave length in cavitating liquid [6,7].

In order to prove the area evaluation method, we used it with non-disturbed bubbles in the same visualization system. The bubble was considered as semi-sphere with the mean radius of the bubble image, so we can calculate the area analytically and compare result with that achieved in present algorithm. The check showed good coincidence between the area calculation methods.

The method allows finding an optimal mode of ultrasonification for optically transparent fluids.

Acknowledgement

This study was supported by the Russian Science Foundation, grant No. 23-12-00278, https://rscf.ru/en/project/23-12-00278/

References

1. Yong Gu, Yu Li, Fang Yuan, Qiang Yang. Optimization and control strategies of aeration in WWTPs: A review // Journal of Cleaner Production, Volume 418, 15 September 2023, 138008
2. Anthony L. Morrison, Vladimir Strezov, Robert K. Niven, Mark P. Taylor, Scott P. Wilson, Jianlong Wang, David J. Burns, Peter J. C. Murphy. Impact of Salinity and Temperature on Removal of PFAS Species from Water by Aeration in the Absence of Additional Surfactants:

A Novel Application of Green Chemistry Using Adsorptive Bubble Fractionation // I*ndustrial & Engineering Chemistry Research* **2023** *62* (13), 5635-5645
3. Pahija E., Golshan S., Blais B., Boffito D.C. Perspectives on the process intensification of CO2 capture and utilization // Chemical Engineering and Processing - Process Intensification, V. 176, 2022, 108958
4. Novosiolov A.G., Duzhii A.B., Golikova E.Y. Molecular diffusion of gases in liquid. Coefficients of molecular diffusion for carbon dioxide in water // ITMO: Series “Processes and Food Production Equipment”, 2014, No. 2. In Russian.
5. Golykh R.N., Carrat J.B., Khmelev V.N., Manyakhin I.A., Minakov V.D., Genne D.V., Barsukov A.R. Influence of ultrasonic cavitaiton influence on interphase surface “gas-liquid” at forced aeration // Journal of Applied Mechanics and Technical Physics, 2024
6. Golykh R.N. Increasing of efficiency of ultrasound on processes in systems with liquid phase // Extended abstract of Dr. Sci. Dissertation, Biysk, 2020. In Russian.
7. Golykh R., Shalunov A., Khmelev V., Lopatin R., Minakov V., Shakura V. Evaluation of Optimum Modes and Conditions Providing IncreasingUltrasonic Cavitation Area in High-Viscous and Non-Newtonian Fluids // Romanian Journal of Acoustics and Vibration. 2020. No. 2 – P. 101–108.

The 14th International Conference on
Laser-light and Interactions with Particles (LIP2024)
September 18-22nd, 2024, Xi'an, Shaanxi, China

PRELIMINARY DERIVATION OF SECOND-ORDER RAINBOW SCATTERING BY CAM THEORY AND EXPERIMENTAL VERIFICATION

Zhenyu WANG [1], Yingchun WU [1,*], Xinhao WANG [1] and Xuecheng WU [1]

[1] State Key Laboratory of Clean Energy Utilization, Zhejiang University, Hangzhou, 310027, China

Corresponding author: wuyingchun@zju.edu.cn

Abstract

Based on the theory of high-frequency scattering from homogeneous spherical droplets, the scattering amplitude and differential cross-section expressions for second-order rainbow scattering from transparent water droplets are derived and experimentally verified. Starting from the Mie electromagnetic solution, the Poisson summation formula is used to transform the level summation of the scattering amplitude to the complex domain integral, and then the Debye series is used to decompose the scattering amplitude into the infinite term representing the continuous internal reflection of the light ray, and what is to be deduced in this paper is the fourth term of Debye's series, and the deformation of the integration path of the complex function is utilized to make the integration path go through the saddle point [1] of the integrand and to analyse the distribution of Regge poles [2], then use stable phase method [1] and residue theorem [3] to calculate the integral, finally obtain the scattering intensity distribution formula.

1 Introduction

The problem of high-frequency scattering by a homogeneous sphere has many important applications, and it presents considerable interest in connection with optical-model, eikonal, and Regge-pole approaches to atomic, molecular, and nuclear scattering [4]. Although Mie series solutions based on electromagnetic plane waves scattered by a uniform sphere are exact, for large particles the series converge so slowly that they become practically useless. To understand and gain physical insight into the vast amount of information buried in the Mie solution, it is necessary to extract this information in a sufficiently simple form. Debye series and Complex angular momentum (CAM) method has led to an accurate quantitative theory of the rainbow scattering, which appears in the third term of the Debye series [5].

This article deals with the second-order rainbow scattering of water droplets (N=1.33), and gives quantitative expressions for the scattering amplitude and scattering differential cross section, through semiclassical scattering theory, Mie electromagnetic theory, Debye series and CAM theory. Experiments with second-order rainbow has been done to verify the correctness of the theory.

2 Derivation process

Similar critical effects exist in both classical and semiclassical scattering theories: rainbow scattering, Glory scattering, Forward diffractive scattering, Orbiting and resonance scattering [6]. Differential scattering cross sections diverge at these singularities, producing critical effects that require other models which can be solved exactly to explain them.

2.1 Mie electromagnetic solution

In spherical coordinates, the components of the scattered electric field at large distances are of the form [7]

$$E_\phi = \frac{e^{ikr}}{ikr}\sin\phi S_1(\beta,\theta), E_\theta = \frac{e^{ikr}}{-ikr}\cos\phi S_2(\beta,\theta), (r\to\infty) \quad (1)$$

where $\beta = ka$ is the size parameter and the complex quantities

$$S_j(\beta,\theta), (j=1,2) \quad (2)$$

are the scattering amplitudes associated with the two independent polarizations.

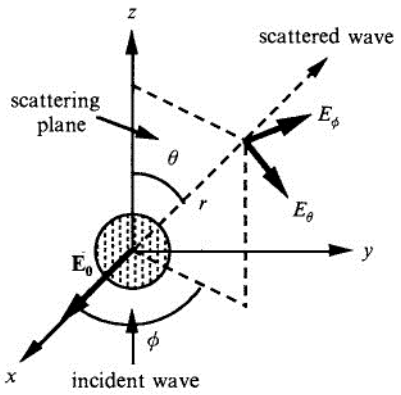

Figure 1 *Coordinate and scattered electric field components* [6]

The exact solution for S_j was given by Mie (1908) in the form of a partial-wave expansion [7]

$$S_j(\beta,\theta) = \frac{1}{2}\sum_{l=1}^{\infty}\left\{\left[1-S_l^{(j)}(\beta)\right]t_l(\cos\theta)+\left[1-S_l^{(i)}(\beta)\right]p_l(\cos\theta)\right\},$$
$$(i,j=1,2;i\neq j) \quad (3)$$
$$p_\nu(x)\equiv\frac{P_{\nu-1}(x)-P_{\nu+1}(x)}{1-x^2}, t_\nu(x)\equiv -xp_\nu(x)+(2\nu+1)P_\nu(x)$$

Where $P_v(x)$ is the Legendre function of the first kind, which becomes a Legendre polynomial when $v = l$ is an integer.

The functions $S_l(\beta)$ are S-matrix elements associated with magnetic (j=1) and electric (j=2) multipoles, respectively. They are given by [7]

$$S_i^{(j)}(\beta) = -\frac{\zeta_i^{(2)}(\beta)}{\zeta_i^{(1)}(\beta)}\left[\frac{\ln'\zeta_i^{(2)}(\beta) - Ne_j \ln'\psi_j(\alpha)}{\ln'\zeta_i^{(1)}(\beta) - Ne_j \ln'\psi_j(\alpha)}\right] \quad (4)$$

$$e_1 = 1, e_2 = N^{-2}, \alpha = N\beta$$

and ψ_l and $\zeta_l^{(1,2)}$ are the Ricatti-Bessel and Ricatti-Hankel functions, respectively defined in terms of spherical Bessel and Hankel functions by [8]

$$\psi_l(z) = zj_l(z), \zeta_l^{(j)}(z) = zh_l^{(j)}(z) \quad (5)$$

2.2 Poisson summation formula

By Poisson summation formula [9]

$$\sum_{\ell=0}^{\infty}\phi(l+\frac{1}{2},x) = \sum_{m=-\infty}^{\infty}(-)^m\int_0^{\infty}\phi(\lambda,x)\exp(2im\pi\lambda)\mathrm{d}\lambda \quad (6)$$

where the interpolating function $\phi(\lambda,x)$ duces to $\phi(l+1/2,x)$ at the physical points $\lambda = l+1/2$ (l = 0, 1, 2, ...), and x denotes a set of parameters. The interpolating function $S(\lambda,\beta)$ simplifies to $S_l(\beta)$ physical points, λ is called the complex angular momentum and will be extended to complex values later.

2.3 Debye expansion

A preliminary transformation of the scattering amplitude is required before applying the Poisson representation to obtain fast convergence. Similar to the geometrical optics, the scattering amplitude is decomposed into an infinitesimal number of terms representing continuous internal reflection effects.The corresponding Debye expansion of the S-function is of the form [4]

$$S^{(j)}(\lambda,\beta) = S_0^{(j)}(\lambda,\beta) + \sum_{p=1}^{p} S_p^{(j)}(\lambda,\beta) + \Delta S_p^{(j)}(\lambda,\beta), j = 1,2 \quad (7)$$

where P is the order of the last term that one wants to retain.

Debye expansion of the total scattering amplitude is

$$S_j(\beta,\theta) = S_{j0}(\beta,\theta) + \sum_{p=1}^{p} S_{jp}(\beta,\theta) + \Delta S_{jp}(\beta,\theta) \quad (8)$$

where S_{j0} is the direct reflection term, S_{j1} is the direct transmission term, and S_{jp} ($p \geqslant 2$) corresponds to transmission following (p - 1) internal reflections.

The fourth term of the Debye expansion, $S_{j3}(\beta,\theta)$, is related to the transmission through the sphere with two internal reflections. That is, the term corresponding to second-order rainbow scattering.

2.4 Complex angular momentum method

In order to make the asymptotic approximation more efficient, the key step is to transfer the Poisson summation to the complex λ-plane [10]

$$\sum_{l=0}^{\infty}\phi(l+\frac{1}{2},x) = \frac{1}{2}\int_C \phi(\lambda,x)\frac{\exp(-\mathrm{i}\pi\lambda)}{\cos(\pi\lambda)}\mathrm{d}\lambda \quad (9)$$

where C denotes the contour shown in Figure 1.

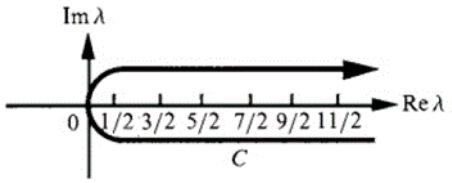

Figure 2 *Contour of integration C for Watson's transformation* [4]

The basic idea of CAM approximations is to concentrate the dominant asymptotic contributions to the amplitude (by taking advantage of the freedom of path deformation) within the neighbourhood of a small number of points in the complex λ plane, to obtain rapidly converging asymptotic expansions. The amplitude of the Poisson transform is usually dominated by the contribution of the saddle point, plus the sum of the residue of the Regge-Debye poles.

3 Results and discussions

The theoretical derivation of second-order rainbow is still in progress and specific theoretical formulas remain to be derived and comparatively verified. By the Lorenz-Mie theory, inversion algorithm of the second-order rainbow can be used through processing the second-order rainbow signals to get accurate measurement of droplet size, temperature and refractive index in sprays [11]. But this new second-order rainbow scattering theory by the CAM theory can not only ensure accuracy, but reduce time-consuming.

4 Acknowledgement

The authors gratefully acknowledge the support from project supported by Natural Science Foundation of Zhejiang Province for Distinguished Young Scholars (LR24E060002) and National Science and Technology Major Project of China (J2019-III-0010-0054).

5 References

[1] Chester C, Friedman B, Ursell F. An extension of the method of steepest descents[J]. Mathematical Proceedings of the Cambridge Philosophical Society, 1957, 53(3): 599–611.

[2] Nussenzveig H M. The poles of the S-matrix of a rectangular potential well of barrier[J]. Nuclear Physics, 1959, 11: 499-521.

[3] Ould El Hadj M, Stratton T, Dolan S R. Scattering from compact objects: Regge poles and the complex angular momentum method[J]. Phys. Rev. D, 2020, 101 , issue = 10: 104035 , numpages = 18.

[4] Nussenzveig H M. High-Frequency Scattering by a Transparent Sphere. I. Direct Reflection and Transmission[J]. Journal of Mathematical Physics, 1969, 10(1): 82-124.

[5] Nussenzveig H M. High-Frequency Scattering by a Transparent Sphere. II. Theory of the Rainbow and the Glory[J]. Journal of Mathematical Physics, 1969, 10(1): 125-176.

[6] Hulst H C V D. Light scattering by small particles[J]. Quarterly Journal of the Royal Meteorological Society, 1958, 84(360): 198-199.

[7] Mie G. Beiträge zur Optik trüber Medien, speziell kolloidaler Metallösungen[J]. Annalen der Physik, 1908, 330(3): 377-445.

[8] Frank O, Daniel L, Ronald B, et al. The NIST Handbook of Mathematical Functions[M]. Cambridge University Press New York NY, 2010.

[9] Nussenzveig H M. Uniform approximation in scattering by spheres[J]. Journal of Physics A: Mathematical and General, 1988, 21(1): 81.

[10] Nussenzveig H M. Complex angular momentum theory of the rainbow and the glory[J]. J. Opt. Soc. Am., 1979, 69(8): 1068--1079.

[11] Xinhao W, Yingchun W, Qimeng L, et al. Secondary rainbow refractometry for droplet refractive index and size measurement[J]. Optics and Lasers in Engineering, 2022, 149: 106831.

The 14th International Conference on
Laser-light and Interactions with Particles (LIP2024)
September 18-22nd, 2024, Xi'an, Shaanxi, China

Optimizing Structured Light therapy for 3D Melanoma Models: A Monte Carlo and Machine Learning Approach

Elena Vasilieva[1], Alexander Doronin[1,*], Vladislav V. Yakovlev[2,3] and Vanderlei S. Bagnato[3,4]

[1] School of Engineering and Computer Science, Victoria University of Wellington, Wellington, 6140, New Zealand
[2] Department of Physics and Astronomy, Texas A&M University, College Station, USA
[3] Department of Biomedical Engineering, Texas A&M University, College Station, USA
[4] Institute of Physics, São Carlos, São Paulo University, Brazil

Corresponding author: alex.doronin@vuw.ac.nz

Abstract

In this report, we introduce a cutting-edge strategy for photodynamic melanoma treatment that aims to address the challenges of excessive absorption and heat generation. Central to our approach is a novel structured illumination technique specifically designed to enhance light delivery to melanoma-infected tissues, utilizing 3D tomography for precise targeting and Machine Learning based detection of melanoma optical properties. We developed a sophisticated optical model of human skin incorporating melanoma characteristics and employed advanced simulation of photon transport in this complex, turbid medium. To evaluate the efficacy of our method, we employed a cost function that quantifies both the volume irradiated and the absorption of optical radiation within the melanoma. This function allows us to fine-tune the illumination parameters to maximize the effectiveness of the photodynamic therapy, as demonstrated by our computational simulations. These simulations suggest a significant potential for enhancing treatment outcomes and minimizing side effects. However, experimental validation is crucial to confirm these theoretical predictions and to advance the application of this innovative strategy in transforming melanoma photodynamic treatments.

1 Introduction

Melanoma stands as one of the most severe types of skin cancer, originating from pigment-producing melanocytes. This cancer is marked by the uncontrolled proliferation of these cells, predominantly affecting the skin, though it can also manifest in the eyes and, on rare occasions, internal organs. The primary danger of melanoma stems from its propensity for metastasis—the spread of cancer cells to other parts of the body. This trait makes melanoma notoriously difficult to manage with conventional cancer treatments [1]. Over recent decades, the incidence of melanoma has been on a steady incline globally. Despite constituting only a small fraction of all skin cancer cases, melanoma is responsible for the majority of skin cancer deaths, attributed to its high metastatic potential and resistance to existing treatments. The treatment landscape for melanoma has significantly evolved over the past decades, transitioning from traditional surgery and chemotherapy to incorporate advanced therapies such as immunotherapy, targeted therapy, radiation therapy, and notably, photodynamic therapy (PDT). While surgery remains the primary treatment for early-stage melanoma, aiming to remove the tumour and surrounding healthy tissue to prevent cancer spread, accurately achieving clean surgical margins is a persisting challenge. Meanwhile, PDT has garnered attention for its innovative use of a photosensitizing agent activated by light to produce reactive oxygen species that destroy cancer cells and tumour-supporting blood vessels, and potentially trigger an immune response against the cancer. Despite its advantages of being non-invasive and having fewer side effects, PDT's effectiveness hinges on the optimal selection and application of photosensitizers, light sources, and tissue properties, with melanin's light absorption posing a significant challenge. Ongoing research is crucial to optimize these variables and fully ascertain the long-term efficacy and safety of PDT in melanoma treatment, enhancing prospects for improving patient outcomes in this aggressive cancer.

2 Structured light illumination

In this report, we delve into a critical aspect of photodynamic therapy (PDT) for melanoma: the effect of melanoma cell absorption leading to overheating and a reduced photodynamic response. Overheating and suboptimal photodynamic action can result in necrosis—an uncontrolled form of cell death. During necrosis, cell contents, including harmful substances, are released into the surrounding tissue, which can trigger inflammation and, in some cases, foster conditions conducive to tumour recurrence and spread.

To address these complexities, we utilize in silico investigations to assess the impact of structured optical illumination on melanoma and adjacent tissues, leveraging 3D structures obtained from tomography combined with machine learning predictions of chromophore distributions, see Figure 1.

In this study, we leverage our newly developed, open-source, and power-efficient Monte Carlo (MC) method, named Neu(t)ralMC, designed in-house to explore

complex light-tissue interactions in photodynamic therapy (PDT) for melanoma [2,3]. Despite the inherent computational challenges associated with the statistical nature of MC solutions, such as inefficiencies, the method supports effective parallelization strategies that have significantly improved computational efficiency, accuracy in tissue modelling, and broadened applications in biomedical optics—including spectrum analysis, polarization, coherence properties, and the angular momentum of light.

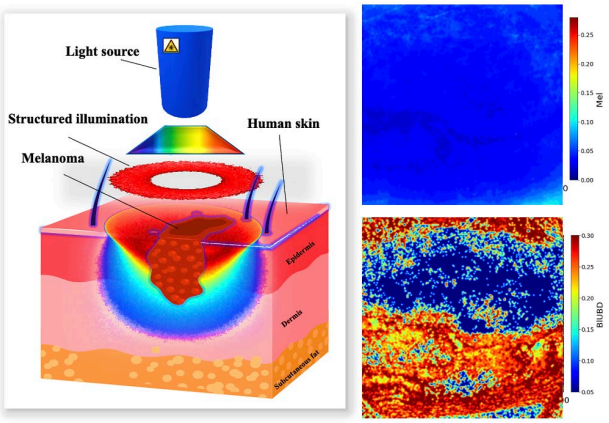

Figure 1 *Conceptual visualization of structured light illumination (left) combined with machine learning based prediction of skin optical properties (right).*

Building on this foundation, we have enhanced our simulations by integrating optical detection of skin properties through tomography, enriching the mathematical representations of melanoma and surrounding tissues. These tissues are modelled as distinct 3D volumetric regions each with unique optical characteristics, enabling a nuanced simulation of their interactions with structured illumination. This detailed modelling allows us to visualize and quantify the spatial distribution of light with high precision, particularly focusing on the malformation site and its immediate environment [3-7].

Further, we introduced a ML-based optimization within our MC framework to fine-tune the parameters of offset illumination. This function is designed to adjust the light's incidence angles and intensities to reduce the risk of overheating the melanoma cells while ensuring effective light delivery to the surrounding tissue.

3 Conclusions and Future work

The results from our simulations confirm that offset illumination can be optimized to deliver therapeutic light efficiently, minimizing thermal damage to melanoma cells. These findings underscore the potential of our MC method in improving both the efficacy and safety of PDT. The integration of machine learning for estimating chromophore concentrations and other advanced optical detection techniques further enhances our ability to tailor and optimize PDT. The insights gained from this study hold substantial promise for advancing targeted phototherapy strategies in melanoma treatment, potentially leading to more personalized and effective therapeutic approaches.

4 References

[1] *Guy, G.P., Thomas, C.C., Thompson, T.D., Watson, M., Massetti, G.M., & Richardson, L.C. (2015). Vital Signs: Melanoma Incidence and Mortality Trends and Projections — United States, 1982–2030. Morbidity and Mortality Weekly Report, 64, 591 - 596.*

[2] *Nguyen, V., Clennell, A., Yakovlev, V., & Doronin, A. (2024). An open-source energy efficient hybrid Monte Carlo and machine learning algorithm for assessing light transport in turbid scattering media. Dynamics and Fluctuations in Biomedical Photonics XXI.*

[3] *Doronin, A., Yakovlev, V., & Bagnato, V. (2024). Photodynamic treatment of malignant melanoma with structured light: in silico Monte Carlo modeling. Biomedical Optics Express, 15, 1682 - 1693.*

[4] *Clennell, A., Nguyen, V., Yakovlev, V.S., & Doronin, A. (2023). Neu(t)ralMC: energy-efficient open-source Monte Carlo algorithm for assessing photon transport in turbid media. Optics express, 31 19, 30921-30931 .*

[5] Zherebtsov, E.A., Dremin, V.V., Popov, A.P., Doronin, A., Kurakina, D.A., Kirillin, M.Y., Meglinski, I.V., & Bykov, A.V. (2019). Hyperspectral imaging of human skin aided by artificial neural networks. Biomedical optics express, 10 7, 3545-3559 .

[6] https://www.lighttransport.net/

[7] https://github.com/aledoronin

The 14th International Conference on
Laser-light and Interactions with Particles (LIP2024)
September 18-22nd, 2024, Xi'an, Shaanxi, China

CONVOLUTIONAL NEURAL NETWORK FOR PARTICLE'S SHAPE RECONSTRUCTION IN INTERFEROMETRIC PARTICLE IMAGING

Alexis ABAD[1], Alexandre POUX[1] and Marc BRUNEL[1,*]

[1] UMR CNRS 6614 CORIA, Avenue de l'Université, BP 12, 76801 Saint-Etienne du Rouvray cedex, France

Corresponding author: marc.brunel@coria.fr

Abstract

A Convolutional Neural Network has been developed to reconstruct the shape of irregular rough particles from their interferometric images. Reconstructions can be done for different sizes and any orientation of the particles. The network can work either with centrosymmetric or non-centrosymmetric particles. The experimental database has been build using a set-up involving a Digital MicroMirrors Device.

1 Introduction

Interferometric Particle Imaging (IPI) enables the characterization of particles in flows. It is a single-shot technique that uses nanosecond laser pulses. It has been initially developed to measure the size of spherical droplets, taking advantage of the angular dependency of the scattered field in the Mie regime [1-4]. But the technique can be extended to the analysis of rough particles. In this case, the interferometric images of the particles are speckle patterns whose structure is directly linked to the shape and size of the rough particle [5]. More precisely, the 2 dimensional (2D) Fourier transform of the speckle pattern is linked to the 2D autocorrelation of the original particle's shape. The consequence is that the particle's size and shape of a rough particle can be determined from its interferometric out-of-focus image obtained under coherent laser light. Phase retrieval algorithms can be used to reconstruct the shape of the particle [6]. Another possibility is to use deep learning methods [7]. In this paper, we present the development of a Convolutional Neural Network (CNN) that is able to reconstruct the shape of a rough particle from its interferometric speckle-like image. Domains of applications cover meteorology, aviation security and nuclear safety, air quality measurements, disease transmission, combustion, cosmetics… [1-9].

2 Construction of the database

The realization of a CNN requires the construction of a database. The goal is to reconstruct the 2D-shape of a particle from its 2D-interferometric image. A significant number of pairs of images {particle's shape, corresponding interferometric image} is thus necessary in order to train the CNN. In a flow, the exact orientation of an irregular particle is never perfectly known. The recording of such a database with real rough particles would thus require the use of a multi-camera set-up, one sensor recording the in-focus image, another sensor recording simultaneously the interferometric image. The acquisition of thousands of pairs of this type would represent a very important time for only one experimental configuration. A second possibility is to use "programmable" particles [10], and for each particle's shape programmed to record the interferometric image. This is possible programming rough particles on a Digital Micromirror Device, this latter being illuminated by a coherent laser beam, as described in reference 10. Sources of noise can be further added numerically. In our case we add a gaussian noise and modify randomly the contrast and the brightness of the interferometric images. A database composed of tens of thousands of pairs of images has been constructed using this set-up. The particles can exhibit various shapes: sticks, crosses, dendrites, L-, Y- or T-shapes, ellipsoids. The size of the particles programmed is random (from 400 micrometers to 1.2 millimeters), the width of the branches, and the 3D-orientation of the particles are random too. To illustrate this, figure 1 shows a dendrite-like particle programmed on the DMD and its interferometric image. Note that the particle's shapes stored in the database are filled images: the dark spaces between bright asperities are filled. The database that we have constructed is actually composed of 18000 pairs of such images. The acquisition of the whole database took approximately 100 hours. The set-up has been automated for this application.

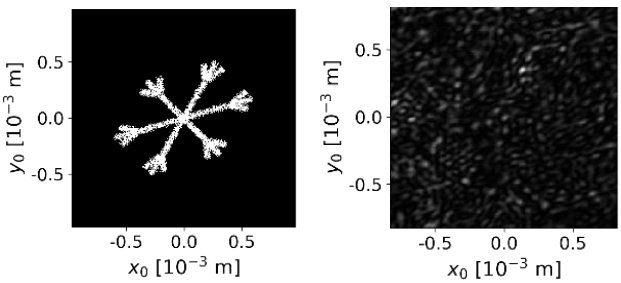

Figure 1 *Dendrite-like particle programmed on a DMD (left), and its interferometric image recorded on a CCD sensor (right).*

3 Architecture of the network developed

The neural network developed is a Convolutional Neural Network (CNN) based on a symmetric Unet architecture with residual block modules [7]. The encoder part contains four stages composed of a simple convolution, a residual block, a dropout and a maxpooling operation. The decoder part contains four stages composed of an up-convolution, simple convolution a residual block and a dropout operation. Each residual block is composed of blocks of batch-normalization + ReLU block + convolution. Only the center of the interferometric images is retained, with dimensions of 256×256 pixels in grayscale. The choice of image size is a balance between computation time (for network training), GPU memory capacity, and sampling conditions of the speckle pattern. Training is done on 90% of images of the database. Test operation is performed on the last 10%.

4 Shape's reconstructions using the CNN

Let us now present some particle's shapes reconstructions using the CNN with images reserved for the test operation (and thus not used for training). Figures 2, 3, 4, 5, 6 and 7 show different exemples for different particle's shapes. On the left appear the filled original particles (programmed on the DMD). On the right appear the reconstructed shapes obtained using the CNN applied to the interferometric images recorded on the CCD sensor. These reconstructions are neither the best, nor the worse. They have been chosen randomly within the 1800 reconstructions performed from the test database. We can observe that the CNN is not perturbed by the presence of non-centrosymmetric particles. Such cases were a problem encountered using phase-retrieval algorithms. The CNN can reconstruct either big or small particles, although the number of bright spots in the speckle patterns can be significantly different. The quality of reconstructions is estimated quantitatively using Jaccard index and Multi Scale – Structural SIMilarity that show a good accuracy.

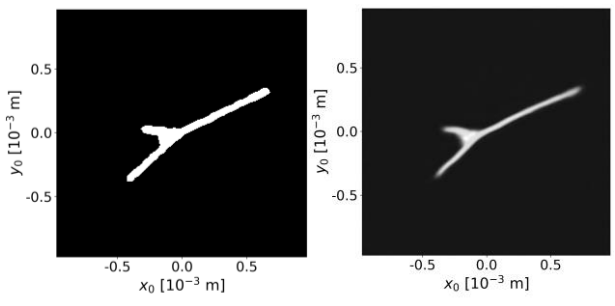

Figure 2 *Filled program object (left) and its reconstruction by the CNN (right)*

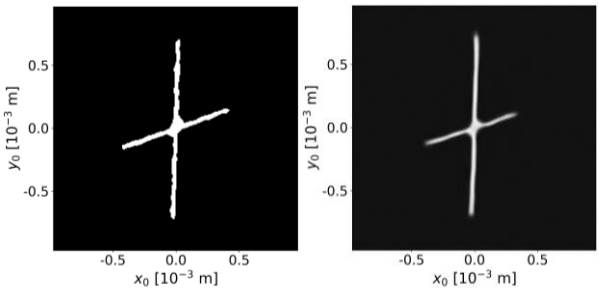

Figure 3 *Filled program object (left) and its reconstruction by the CNN (right)*

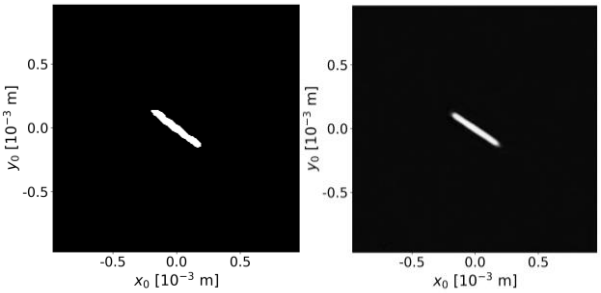

Figure 4 *Filled program object (left) and its reconstruction by the CNN (right)*

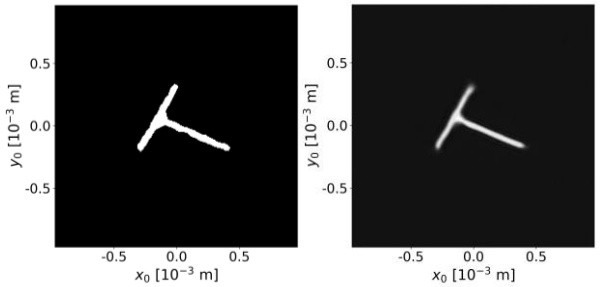

Figure 5 *Filled program object (left) and its reconstruction by the CNN (right)*

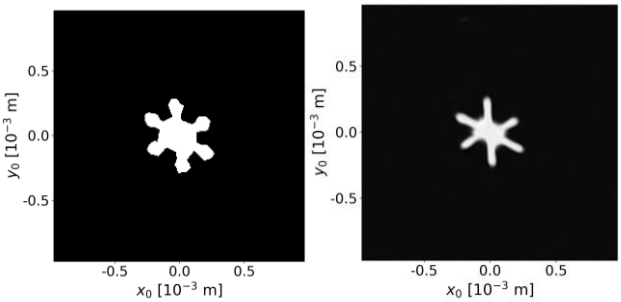

Figure 6 *Filled program object (left) and its reconstruction by the CNN (right)*

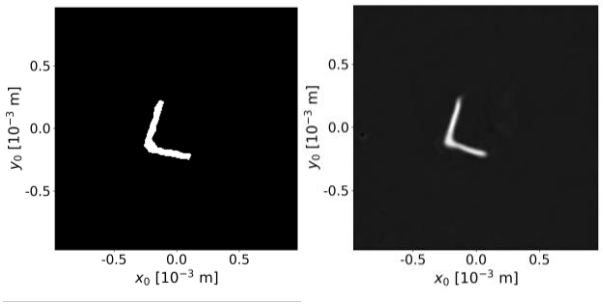

Figure 7 *Filled program object (left) and its reconstruction by the CNN (right)*

5 Conclusion

A Convolutional Neural Network has been developed to reconstruct the shape of irregular rough particles from their interferometric images. It shows very promising performances. Next works will consist of enlarging progressively the database to a wide variety of cases and configurations, The CNN should become an important tool to perform high-quality particle's reconstructions in Interferometric Particle Imaging experiments.

.

6 References

[1] Glover A.R., Skippon S.M., and Boyle R.D., Interferometric laser imaging for droplet sizing: a method for droplet-size measurement in sparse spray systems, Appl. Opt. 34, 8409 (1995).

[2] Mounaïm-Rousselle C., and Pajot O., Droplet sizing by Mie scattering interferometry in a spark ignition engine, Part. Part. Syst. Charact. 16, 160 (1999).

[3] Kawaguchi T., Akasaka Y., Maeda M. Size measurements of droplets and bubbles by advanced interferometric laser imaging technique. Meas. Sci. Technol. 13, 308 (2002).

[4] Damaschke, N., Nobach H., Tropea, C. Optical limits of particle concentration for multi-dimensional particle sizing techniques in fluid mechanics. Exp. Fluids 32, 143 (2002).

[5] Brunel M., Shen H., Coëtmellec S., Gréhan G., Delobel T. Determination of the size of irregular particles using interferometric out-of-focus imaging. Int. J. Opt. 2014, 143904 (2014).

[6] Delestre B., Abad A., Talbi M., Fromager M., Brunel M., Experimental particle's shapes reconstructions from their interferometric images using the Error-Reduction algorithm, Opt. Commun. 498, 127229 (2021).

[7] Zhang H., Li Z., Sun J., Fu Y., Jia D., Liu T.. Characterization of particle size and shape by an IPI system through deep learning. J. Quant. Spectrosc. Radiat. Transf. 268, 107642 (2021).

[8] Parent G., Zimmer L., Renaud A., and Richecoeur F., Adaptation of a PTV method for droplets evaporating in vicinity of a flame, Exp. Fluids 63, 100 (2022).

[9] Grandoni L., Méès L., Grosjean N., Leuzzi G., Monti P., Pelliccioni A., and Salizzoni P., Interferometric laser imaging for respiratory droplets sizing, Exp. Fluids 64, 80 (2023)

[10] Fromager, M; Aït Ameur, K; Brunel, M Digital micromirror device as programmable rough particle in interferometric particle imaging Appl. Opt., 56, 3594 (2017).

The 14th International Conference on
Laser-light and Interactions with Particles (LIP2024)
September 18-22nd, 2024, Xi'an, Shaanxi, China

CONVOLUTIONAL NEURAL NETWORK CAN TRACK THE RADIUS EVOLUTION OF LEVITATING-EVAPORATING MICRODROPLETS

Kwasi NYANDEY[1, 2,*], Gennadiy DERKACHOV[1] and Daniel JAKUBCZYK[1]

[1] Institute of Physics, Polish Academy of Sciences, Al. Lotników 32/46, 02-668 Warsaw, Poland
[2] Laser and Fibre Optics Centre, Department of Physics, School of Physical Sciences, College of Agriculture and Natural Sciences, University of Cape Coast, Cape Coast, Ghana

Corresponding author: kwasi.nyandey@ucc.edu.gh/nyandey@ifpan.edu.pl

Abstract

We have used convolutional neural network in a classification task to track the radius evolution of levitating evaporating microdroplets of pure diethylene glycol and diethylene glycol-nanoparticles suspensions. The technique has the potential to distinguish droplet size differences of ±10 nm, and we expect it to be applicable for online/real-time tracking of droplet evaporation.

1 Introduction

Evaporation of microdroplets has been already fairly well studied (see e.g. [1, 2] and references therein), droplet size (radius) being, of course, the primary parameter of interest. Numerous sizing methods have been proposed, which can be divided into two major groups: online and off-line. Off-line methods can be quite accurate – for example in our laboratory we have previously combined electrodynamic trapping and several optical methods [3, 4] for sizing of evaporating microdroplets of pure liquids and liquid suspensions of nanoparticles. For example, comparing experimental light scattering patterns to a library of similar patterns generated from Mie theory in favourable cases enables measuring the droplet radius with the accuracy of ± 10 nm for pure droplets. Online sizing with optical methods reported earlier in literature, is usually less accurate. E.g. Phase-Doppler particle sizing method [5], which was derived from the Laser Doppler Velocimetry method (LDV) [6], Interferometric techniques (with setup identical to LDV) [7, 8], Fast-Fourier-Transform method [9] and a combination of light scattering and aerodynamics for particle size measurements [10].

On the contrary, neural networks have been trained to learn image/data features for various tasks. For example, in classification tasks, learned features from data are used to classify unseen data into appropriate classes among several, while in detection tasks, specific shapes, objects or trends are detected within images or data with very high accuracy and precision. It is important to emphasize that in classification it is required that an image or parameter of interest belongs to exactly one class while in detection an image or the dataset may contain no object/parameter of interest or several of different kind. In literature, several tasks have been accomplished by a combination of different network design ideas, a careful increase in depth and width of the network and improved optimization of computing resources, with accompanied higher performances [11].

We have also (previously) successfully applied neural networks to recognize and classify complex suspensions, (e.g. nanoparticles [12], varying milk fat contents [13]), illuminated by a laser beam. In spite of these advancements mentioned above, the instantaneous or online optical study of microdroplets' evaporation still remains a challenge. Consequently, we have proposed a technique – as a first-approach – for characterizing the size of evaporating microdroplets into small radii ranges of 10 nm leading to the tracking of their evaporation rates. Thus, our primary goal is to train a convolutional neural network on images generated from a wider range of droplet radius. This approach is novel, because we require the classification to track evaporation scenarios, which are contrary to the conventional classification tasks in which the correctly classified data lies on the main diagonal in the confusion matrix. Therefore, for the first time, we aim to classify experimental data by tracking droplet evaporation models, such as the radius-square-law for isothermal evolution [14].

2 Experiment

As it is well known, an operational method of droplet tracking must be robust and devoid of experimental uncertainties associated with the detector, misalignment of trapping field and geometrical imperfections of the setup in relation to the illumination beam. In view of this, we have modified the variant of quadrupole electrodynamic trap that we developed previously in our laboratory (see [3]), making it suitable for wider-angle-resolved elastic light scattering measurements.

The field of view was centred at the azimuth angle of 90 ± 0.1° to the illumination direction. Hence, the

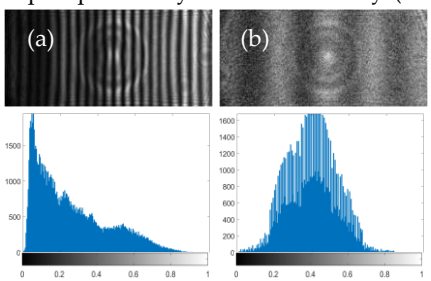

Figure 2: *Light scattering patterns recorded at the beginning (a) and end (b) of evolution of a levitated microdroplet of pure diethylene glycol, 99.99%. Their corresponding histograms are presented in the bottom panels.*

effective field of view determined from the ROI covered an angular span of ± (15.37 ± 0.01°) in opposite directions and an angle of elevation of 5 ± 0.01°.

For each trapped droplet we recorded movies (@ 75 fps) of the light scattering patterns over the entire evolution of the evaporation. The scattering patterns within a rectangular ROI were then cropped out into 221x501 images (Figure 2) before normalizing to a 0 – 1 range. As can be inferred from the scattering patterns, the signal-to-noise ratio is very high at the beginning of the evolution of the droplet due to the size of the droplet. Then, as the droplet evaporates and reduces in size, the signal-to-noise ratio reduces and the noise begins to manifest.

We used the scattering patterns recorded from a microdroplet of pure diethylene glycol (DEG), 99.99% and established a good fit (Figure 3) between the measured pattern and the generated Mie scattering pattern. We adopted a two-stage classification approach. In the first stage (Stage 1), the radii range –1 to 30 μm – was divided into 967 classes with a class interval of 30 nm. While in the second stage (Stage 2) the same radii range was divided into two subsets (1 – 15 and 15 – 30 μm). For convenience and in relation to evaporating droplet, we reverse this order and label the subsets as Stage 2_1 (30 – 15 μm) and Stage 2_2 (15 – 1 μm). These subsets enabled us to reduce the class intervals to 10 nm, resulting in 1501 and 1401 classes respectively. The radii within each class (for both stages 1 and 2) were randomly generated independently using the Matlab random generator (rand) (and sorted in descending order). Then theoretical light scattering patterns were generated according to Mie theory, using the measured angular span (azimuthal), wave properties (wavelength and polarization), a constant refractive index of 1.4444 + 0.0i (corresponding to DEG at 658 nm and 21°C) and varying radius. Each generated pattern was composed into a 221x501 image (corresponding to the angular elevation and azimuth in the ROI) with brightness values normalized to a 0 – 1 range.

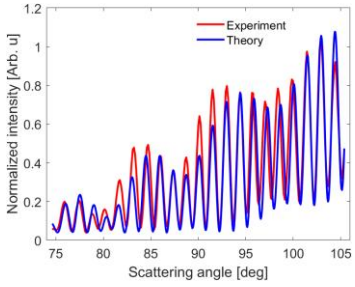

Figure 3: *A fit of theory to the pattern presented in Figure 2(a) (radius = 12723.3 nm). The slight discrepancies are caused primarily by distortions of the image, though the deviation of the droplet from sphericity may also contribute.*

This normalization ensures that the network is not susceptible to brightness differences between theoretical and experimental data as well as variations within experimental data due to changing droplet size. It also ensures that more emphasis is placed on the width and positions of the peaks in the scattering pattern. We generated 2000 images within each class for Stage1 and 1000 images in Stage2 and divided the data into training and validation sets for training the convolutional neural network.

We further generated test set over the radii range 2 – 13 μm, using the radius-square-law [14] to a total of 3000 images. In this case we varied the time linearly from 0 to 3000 seconds. The dataset was neither subdivided nor labelled into classes. The data was generated in Matlab (2023a) environment on a PC equipped with two GPUs (NVIDIA GeForce RTX 3090)

After generation, each image was multiplied by uniformly distributed random noise (with double-precision floating-point values within the range 0 – 0.9) (Figure 4). Each noise was generated independently and elementwise-multiplication was performed before normalizing the resulting image to 0 – 1 range (compare Figure 2 and 4).

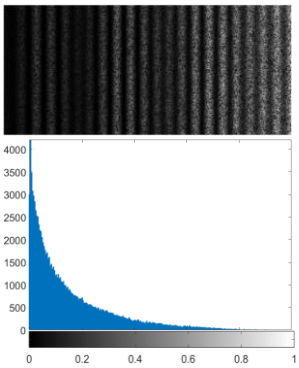

Figure 4: *Theoretically generated light scattering pattern multiplied by uniformly distributed noise (top). The respective histogram has been presented below.*

In Stage 1, we trained the network on the training set (90%) and cross-validated (during training) with the validation set (10%). While in Stage 2, we trained the network on each subset separately with the same proportion of training and validation sets. We set the cross-validation to be cried out at the end of every epoch and training to stop automatically when the validation loss stops decreasing. The training was carried out using both GPUs. Training lasted ~ 13hr with a validation accuracy of 99.01%.

3 Results and discussion

3.1 Testing on theoretical data

For testing, we used the network trained in Stage 1 to consecutively predict the class of each image in the test set (generated with the radius-square-law). The predicted class-labels were obtained and their individual class-average-radius was calculated from the lower- and upper-class-limits of the training data set. The class-average-radius was plotted against time (Figure 5). As can be clearly seen, the network almost completely classified the images into their appropriate classes revealing the trend in the data. This result is very important in the sense that it reveals the

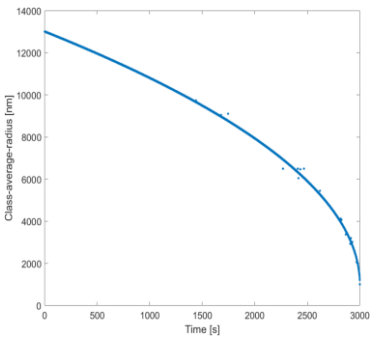

Figure 5: *Classification of theoretical images corresponding to time-varying radius of evaporating microdroplet. Images were obtained from generated radii using radius-square-law.*

network's ability to reproduce complex trends in data, even in classification tasks.

3.2 Testing on experimental data

As presented above, we classified the experimentally recorded light scattering patterns from pure microdroplet of DEG. Here again, the images were not labelled and the classification was done consecutively (Figure 6(top panel)). The main branch of evaporation is clearly visible. In Figure 6 (bottom panel) we present a plot of the classification of similar patterns recorded from a microdroplet of suspension of polystyrene (diameter 1.1 μm) in DEG.

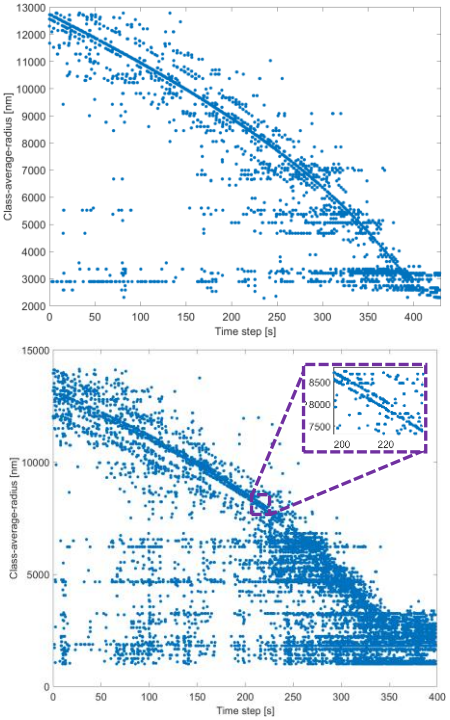

Figure 6: *Classification of experimental light scattering patterns recorded from a pure microdroplet (top panel) and suspension of polystyrene microspheres (diameter 1.1 μm) in DEG (bottom panel).*

It is worth mentioning that due to the large class interval (30 nm) in the Stage 1 network, there were several misclassified images and poor performance when getting to the end of evolution (see Figure 6 (top panel)). The Stage 2 network was used to minimize these problems (Figure 7). On the other hand, when the fit is not unique or the droplet contains enough nanoparticles to distort the Mie scattering patterns, the deduced evaporation progresses with several discontinuous branches until the entire scattering patterns become speckled (compare Figure 6 (top panel) with inset in bottom panel).

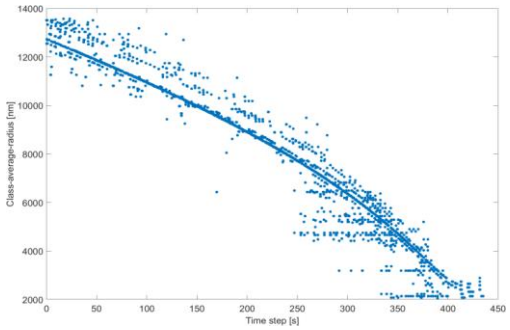

Figure 7*: A reclassification of Figure 6 (top panel) data using Stage 2₂ network with 10nm class-interval. Compare the end of evolution to Figure 6*

4 Conclusion

As a classification, we have successfully employed a 41-layer convolutional neural network to track the radius evolution of levitating, evaporating microdroplets of pure DEG, as well as microdroplets containing a suspension of polystyrene particles in DEG. This result is very promising for the future online/real-time tracking of evaporation rate of microdroplets.

5 References

[1] Xue, H., Moyle, A. M., Magee, N., Harrington, J. Y., & Lamb, D. (2005). Experimental studies of droplet evaporation kinetics: Validation of models for binary and ternary aqueous solutions. Journal of the atmospheric sciences, 62(12), 4310-4326.

[2] Zang, D., Tarafdar, S., Tarasevich, Y. Y., Choudhury, M. D., & Dutta, T. (2019). Evaporation of a Droplet: From physics to applications. Physics Reports, 804, 1-56.

[3] Jakubczyk, D., Derkachov, G., Kolwas, M., & Kolwas, K. (2013). Combining weighting and scatterometry: application to a levitated droplet of suspension. Journal of Quantitative Spectroscopy and Radiative Transfer, 126, 99-104.

[4] Hołyst, R., Litniewski, M., Jakubczyk, D., Kolwas, K., Kolwas, M., Kowalski, K., ... & Zientara, M. (2013). Evaporation of freely suspended single droplets: experimental, theoretical and computational simulations. Reports on progress in physics, 76(3), 034601.

[5] Bachalo, W. D., & Houser, M. J. (1984). Phase/Doppler spray analyzer for simultaneous measurements of drop size and velocity distributions. Optical engineering, 23(5), 583-590.

[6] Yeh, Y., & Cummins, H. Z. (1964). Localized fluid flow measurements with an He-Ne laser spectrometer. Appl. Phys. Lett, 4(10), 176-178.

[7] Farmer, W. M. (1972). Measurement of particle size, number density, and velocity using a laser interferometer. Applied Optics, 11(11), 2603-2612.

[8] Bachalo, W. D. (1980). Method for measuring the size and velocity of spheres by dual-beam light-scatter interferometry. Applied optics, 19(3), 363-370.

[9] Steiner, B., Berge, B., Gausmann, R., Rohmann, J., & Rühl, E. (1999). Fast in situ sizing technique for single levitated liquid aerosols. Applied optics, 38(9), 1523-1529.)

[10] Davis, E. J., & Periasamy, R. (1985). Light-scattering and aerodynamic size measurements for homogeneous and inhomogeneous microspheres. Langmuir, 1(3), 373-379.

[11] Szegedy, C., Liu, W., Jia, Y., Sermanet, P., Reed, S., Anguelov, D., & Rabinovich, A. (2015). Going deeper with convolutions. In Proceedings of the IEEE conference on computer vision and pattern recognition (pp. 1-9).

[12] Jakubczyk, T., Jakubczyk, D., & Stachurski, A. (2021). Assessing the properties of a colloidal suspension with the aid of deep learning. Journal of Quantitative Spectroscopy and Radiative Transfer, 261, 107496. Journal of Quantitative Spectroscopy and Radiative Transfer, 261, 107496.

[13] Nyandey, K., & Jakubczyk, D. (2024). Combining transmission speckle photography and convolutional neural network for determination of fat content in cow milk: an exercise in classification of parameters of a complex suspension. The European Physical Journal Plus, 139(2), 123.

[14] Jakubczyk, D., Kolwas, M., Derkachov, G., Kolwas, K., & Zientara, M. (2012). Evaporation of micro-droplets: the" radius-square-law" revisited. Acta Physica Polonica A, 122(4), 709-716.

The 14th International Conference on
Laser-light and Interactions with Particles (LIP2024)
September 18-22nd, 2024, Xi'an, Shaanxi, China

PROPERTY OF PLASMON-POLARITONS IN NANORINGS ASSISTED BY LEMNISCATE-ORDERED EMITTERS

Gennadiy BURLAK[1,*] and Gustavo MEDINA-ÁNGEL [1-2]

[1] CIICAp, Universidad Autonoma del Estado de Morelos, Av. Universidad 1001, Cuernavaca, Morelos 62209, México
[2] FCAeI, Universidad Autónoma del Estado de Morelos, Av. Universidad 1001, Cuernavaca, Morelos 62209, México

Corresponding author: gburlak@uaem.mx

Abstract

The property of plasmon-polaritons (PP) in a periodic lattice of conducting nanorings (NR) in the presence of quantum nanoemitters (NE) arranged according to Bernoulli lemniscate (LB) is investigated. The coupling between the PP and the NE leads to that the field dynamics of the NE become dependent on the properties of the PP in NR. If the intersection point of the LB branches is located inside the gaps of the NR lattice, there is a significant enhancement of the field. This effect may enable new types of radiating devices using dispersive nanoobjects in modern nanoelectronics.

1 Introduction

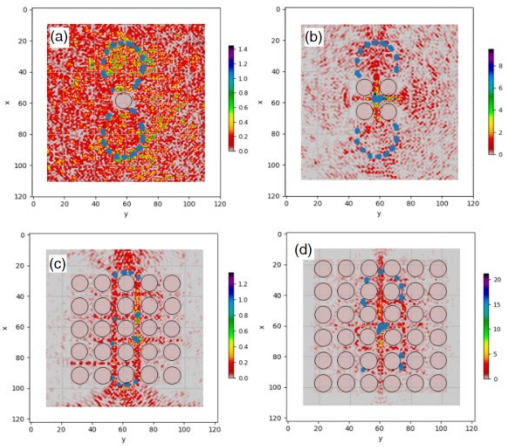

Figure 1 *Structure of optical field (the red) at NR plasma frequency $\omega_p = 2.3$ THz and different number of NRs (black circles) in the lattice with the embedded NEs (blue points) with (a)NR = 1, (b)NR = 4(2 × 2), (c)NR = 25(5 × 5), and (d) NR = 36(6 × 6).*

The use of inhomogeneous nanostructures with non-trivial topology is currently attracting of considerable scientific attention and wide applications. [1-8]. An important property of NEs is their nonlinearity and the possibility of laser emission. By tuning the parameters of the hybrid system, one can significantly change its properties. Such factors lead to a resonant change in the field shape associated with PP generation in NR. In this report, we study case of a periodic system of conducting nanorings with embedded Bernoulli lemniscate NEs. We show that the latter leads to a resonant change in the field shape associated with PP generation in NR. In the case of conducting particles, the frequency of longitudinal oscillations tends to ω_p, and the coupling of localized surface plasmons results in significant hybridization of plasmon excitations already in the case of the dimmer [9]. In this study, we explore a periodic system of conducting NR with embedded Bernoulli lemniscate NEs, where PP interactions assisted with reconnection of the optical PP fields can occur.

2 Basic equations

Figure.1 shows a sketch of the structure of considered system at small times. To study such a hybrid system, we deal with Maxwell's equations in the lattice of 2D nanorings, coupled the rate equations of electron population (within a semiclassical theory) for NE. The dynamics of such an advanced system does not allow a simple analytical description. Therefore FDTD (finite-difference time-domain) technique is used to investigate the dynamic properties of field in such a periodic media with gain and the use $J = \sum_k J_k(R_k^r, t)\delta_r R_k^r$ is the electrical current of PP in NR placed in different positions, and $P = \sum_k P_k(R_k^s, t)\delta_r R_k^s$ is the polarization of electrons in the embedded NE placed in R_k^r. In the above the sums run for all the number of NR (k=1), N_r and NE (k=1 N_s) respectively. For semiclassical approximation in the single electron case, the equation for P_k in the vicinity of the embedded NE reads [10, 11]

$$\frac{\partial^2 \mathrm{P_k}}{\partial \mathrm{t}^2} + \Delta\omega_a \frac{\partial \mathrm{P_k}}{\partial \mathrm{t}} + \omega_a^2 \mathrm{P_k} = \frac{6\pi\varepsilon}{\tau_{21}\omega_a^2}(\mathrm{N_{1,k}} - \mathrm{N_{2,k}})\mathrm{E_k}. \qquad (1)$$

To complete the model, we add the rate equations for the occupation levels of emitters $N_{i,j} = N_i(R_k^s, t)$ (we consider that the NEs are four-level quantum dots).

In what follows we use the dimensionless time t re-normalized as $t \rightarrow tc/l0$, where $l0=100\ \mu m$ is the typical spatial scale and c is the light velocity in the vacuum.

3 Lasing of NE in the system with NR

We consider the system, which combines the Maxwell's equations containing the PP field with semiclassical optical emission from laser emitters. We apply FDTD technique to study the field dynamics in the NR lattice and incorporated NE with the field gain.

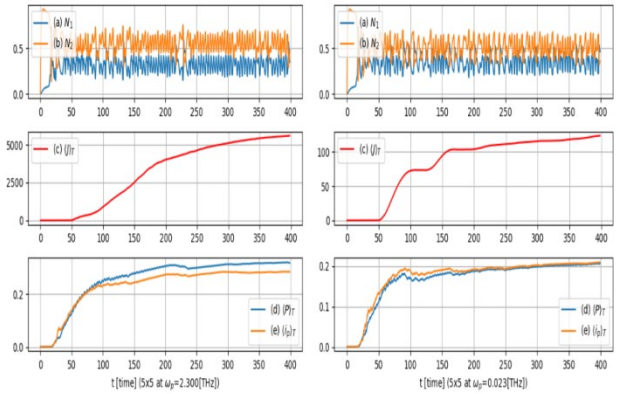

Figure 2 *Temporal dynamics of the system at different* ω_p. **Left panel**. *Dynamics for the 5 × 5 lattice at and* ω_p *=2.3 THz, where (a),(b) show the dynamics of the lasering levels* $N_{1,2}$ *of NE.* **Right panel**. *The same as the left but for much smaller* ω_p *=2.3×10*$^{-2}$ *THz. We observe that in both cases the dynamics of quantum subsystem NE for* $|P|$ *and* $i_p = \partial|P|/\partial t$ *considerably depend on the* ω_p *value of NR.*

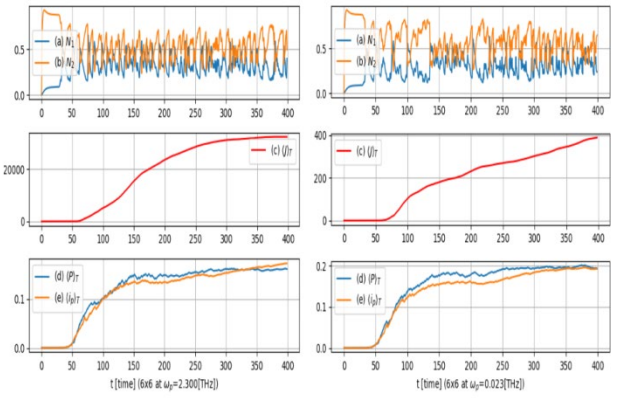

Figure 3 *The same as Fig. 2 but for 6×6 lattice.*

Fig.2 shows the temporal dynamics of the system (1) for the 5×5 lattice at ω_p *=2.3 THz* , where (a),(b) show the dynamics of the lasering levels $N_{1,2}$ of NE, respectively (the dynamics of $N_{0,3}$ levels is not displayed here); (c) average current in NR 〈J〉 and (d, e) are the average quantum polarization $|P|$ and photocurrent $i_p = \partial|P|/\partial t$ respectively. Our simulations show that only $E_{||}$ (corresponding to TM field mode) mainly contributes to the field dynamics in such a system. Figures 2 and 3 shows that the time dynamics of average current 〈J〉 in NRs drastically differs for different values of ω_p. At ω_p *=2.3 THz* the amplitude of 〈J〉 is in 5 times larger with respect of 〈J〉 for case ω_p *=0.0023 THz*. One can see that when time increases such a dynamics acquires an ordered spatial shape and at long times it weakly dependents on the details of the NE distribution. As Fig. 4 shows, at time *t>100* the energy exchange between the NE and the surface PP takes place mainly in the gaps of the NR lattice. The latter indicates the nonlinear dynamics (lasing instability) of such an interaction in the subsystem of NE. Since for PP in the NR subsystem there is the important parameter is the plasma frequency ω_p of PP, we should expect that the dynamics of the coupling with all the NEs will significantly depend on the plasma frequency ω_p too. To insight into the time dynamics, it is useful to study the properties of the average current in the NR lattice, which read

(2)

Where $I_{i,j}$ is the current in I, i,j nanoring, and N are the numbers of NR in x,y directions respectively (we used $N_{x,y}=N$) Corresponding time dynamics is presented in Fig. 2 and Fig. 3, where the time dependencies of (c) average current 〈J〉 in the lattice of nanorings, and (a) the dynamics of populations of lasing levels $N_{1,2}$ of NEs are shown. We observe that at t≈100 there is a rapid growth of 〈J〉 because of the instability (laser generation) in the NE. The latter indicates begin of coupling of NE with PP in the NR. Fig. 4 show the spatial distribution of the average field energy at long-time simulations and ω_p *=2.3 THz* for different number of NRs in the lattice with embedded NEs (cf. Fig. 1.): (a) NR =1 (b) NR = 4(2×2), (c) NR=25(5×5), and (d) NR=36(6×6). In Fig. 4(a), the single NR occupies the center of the lattice, so the field structure reproduces well the overall shape of the LB, except in the region where the intersection point of the LB branches is located, near this point the NE field emission is small. In panel (c) of, a significant interference contribution of the PP field in periodic NRs is added, which leads to an ordering of the field along the LB. When the number of NRs is even (see panels (b) and (d)), the center of the LB is inside the NR lattice slit, so the NE density here is significant, which leads to the appearance of field peaks along the x—axis of the LB.

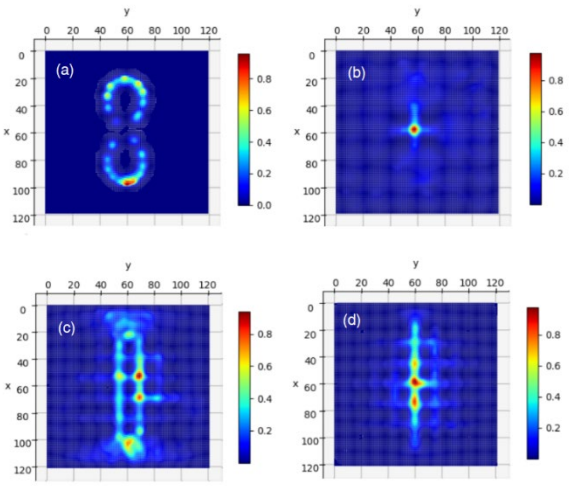

Figure 4 *Spatial distribution of the average field energy at long-times and ωp =2.3 THz for different number of NRs in the lattice with embedded NEs (cf. Fig. 1.): (a) NR=1, (b) NR = 4(2×2), (c) NR = 25(5×5), and (d) NR = 36(6×6)*

4 Discussion

We have considered the field dynamics in a periodic NR lattice with PP assisted by the emission of NEs, which are arranged in the form of LB. From Fig. 1, we can see that the NE density increases near the intersection of the LB branches. Therefore, the cases where NRs occupy the center in Fig.1(a),(c) (and prevent the increase of NE density) will be quite different from the situations in Fig.1(b),(d). In the latter case, the NE density is large, which leads to the appearance of local field peaks at large times, see Fig.4(b),(d). Our simulations show that the PPs with frequency ω_p are excited in the NR lattice, and the coupling of PP to NE via the common optical field takes place in all NRs. The latter leads that the dynamics of the NE quantum system is perturbed by the PP field, which leads to the dependence of the quantum polarization P on the plasma frequency ω_P of PPs in the NRs. This effect is demonstrated in Figs. 2 and 3 for different lattices. In the case of the odd lattice (without NR in the center) the amplitude of the average quantum polarization *P* for case large ω_p =2.3 *THz* , (PP field is large) significantly exceeds the *P* comparing to case of smaller case ω_P =0.0023 *THz* . value (see Fig. 2 (d, e)). This exhibits the strength of the studied coupling of the PP and NE subsystems. Besides, such a coupling significantly changes the average current in the NR (see Fig.2(c)). It is worth noting that the described dynamics takes place in a significantly nonlinear regime when a developed laser emission appeases in the NE (see Fig. 2(a)).

5 Acknowledgement

This work was supported in part by CONAHCYT (Mexico) under the grant No. A1-S-9201. G. M-A. acknowledges a fellowship provided by the CONAHCYT-Mexico

6 References

[1] Chen X., Zhang A., Liu J., Xie Z., Su M., He Y., Zhou X., Chen Y., Li Y., Chen S., Fan D. Orbital angular momentum modes identification of optical vortices using binaural circular aperture. *Journal of Optics*, 21(6): 065603 (2019)

[2] Veer S.D., Goswami T., Ravindranathan S., Gonnade R., Kharbanda N., Ghosh H.N., Babu S.S., A donor strapped perylene bisimide macrocycle and its lemniscate dimer with extended charge separation, *Organic Chemistry Frontiers*, 10(20): 5099-5107 (2023)

[3] Sugic D., Dennis M.R., Singular knot bundle in light. *J. Opt. Soc. Am. A*, 35(12): 1987-1999 (2018)

[4] Lucherelli M.A., Stiegler L.M., Steiger F., Åhlgren E.H., Requena-Ramírez J., Castro E., Abellán G., Carbon nano-onions: Individualization and enhanced water dispersibility. *Carbon*, 218:118760 (2024)

[5] Šlevas P., Orlov S., Creating an Array of Parallel Vortical Optical Needles. *In Photonics*, 11(3):203 (2024)

[6] Subramaniam N.K.K., Trabelsi Y., Azarkaman A., Farmani H., Advanced nanostructures plasmonics noninvasive sensors for type 1 diabetes. *Optical and Quantum Electronics*, 54(8):515 (2022)

[7] Wang Y., Luong H., Zhang Z., Zhao Y., Coupling between plasmonic nanohole array and nanorod array: the emerging of a new extraordinary optical transmission mode and epsilon-near-zero property. *Journal of Physics D: Applied Physics*, 53(27):275202 (2020)

[8] Dehghan N., D'Errico A., Jaouni T., Karimi E., Effects of aberrations on 3D optical topologies. *Communications Physics*, 6(1):357 (2023)

[9] Ch. Downing, G. Weick, Plasmonic modes in cylindrical nanoparticles and dimmers, Proc. R. Soc. A.47620200530 (2020)

[10] Siegman, A.E. *Lasers* (Mill Valley, California, 1986).

[11] Burlak, G., Rubo, Y.G. Mirrorless lasing from light emitters in percolating clusters. *Phys. Rev. A*, 92:013812 (2015).

The 14th International Conference on
Laser-light and Interactions with Particles (LIP2024)
September 18-22nd, 2024, Xi'an, Shaanxi, China

ANALYSING THE RECONSTRUCTED PHASE MAPS OF DIGITAL IN-LINE HOLOGRAMS : APPLICATION TO THE CHARACTERIZATION OF VISCOELASTIC FLUIDS

Denis LEBRUN, Robin NOURY, Gilles GODARD and Marie-Charlotte RENOULT

[1] UMR 6614 CORIA, Av. De l'Université, University and INSA of Rouen Normandy,
76801 Saint-Etienne du Rouvray, France

*Corresponding author: denis.lebrun@coria.fr

Abstract

The phase maps of Digital-In-line holograms are reconstructed for the 3D localization of beads moving on a thin filament of a viscoelastic fluid. We show that the asymptotic shape of the reconstructed phase of the wave along the optical axis leads to an accurate measurement of the depth of particles and filaments. This method works, even when the filament is destabilized by a pulsed air flow.

1 Hologram recoding and reconstruction

The hologram recording system is shown in Fig. 1.

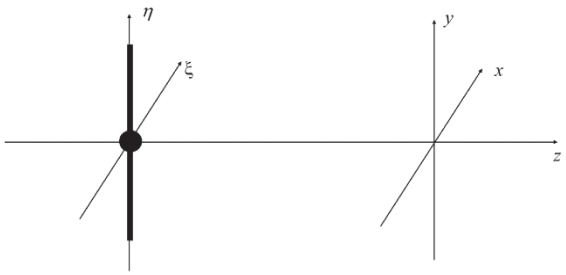

Figure 1 *Hologram recording, axes systems.*

Considering an opaque object $[1 - O(\xi,\eta)]$ illuminated by a monochromatic plane wave of wavelength λ and located at a distance z_e from an image sensor plane (x,y), the complex amplitude distribution in the quadratic sensor plane is obtained by the Huygens-Fresnel integral [1]:

$$A_{z_e}(x,y) = \frac{e^{\frac{2i\pi z_e}{\lambda}}}{i\lambda z_e}\int_{-\infty}^{+\infty}\int_{-\infty}^{+\infty}[1 - O(\xi,\eta)] \times e^{i\pi\frac{(x-\xi)^2+(y-\eta)^2}{\lambda z_e}}\,d\xi d\eta \quad (1)$$

Omitting a constant phase term, this integral is usefully rewritten as the following convolution operation:

$$A_{z_e}(x,y) = [1 - O(x,y)] ** h_{z_e}(x,y) \quad (2)$$

where $h_z(x,y) = \frac{1}{i\lambda z}e^{i\pi\frac{x^2+y^2}{\lambda z}}$ is the so-called Fresnel kernel. The intensity distribution $\left(I_{z_e}(x,y) = \left|A_{z_e}(x,y)\right|^2\right)$ recorded in the (x,y) plane is used to reconstruct the complex amplitude at a given distance z by using again a convolution operation:

$$R_z(x,y) = I_{z_e}(x,y) ** h_z(x,y) \quad (3)$$

After some simplifications described in [2], we find that the complex amplitude at a given reconstruction distance z from the camera can be approximated to:

$$R(x,y,z) = 1 - O * h_{z-z_e}(x,y) - O * h_{z+z_e}(x,y) \quad (4)$$

2 Searching for the best focusing plane

Numerous papers deal about an automatic method for the determination of the z coordinate of a given object recorded by digital holography [3]. Several approaches use the properties of the real part or the modulus of the reconstructed wave and others the complex values. Here, as proposed, only the phase of the reconstructed wave

$$\Phi(x,y,z) = atan2\left\{\frac{Im[R(x,y,z)]}{Re[R(x,y,z)]}\right\} mod(2\pi) \quad (5)$$

is used. Here, $atan2(\,)$ is the four-quadrant inverse tangent function.

2.1 Theoretical phase variations

Figure 2 shows an example of reconstruction of the phase map for a bead of diameter $d = 50\,\mu m$ recorded at a distance $z_e = 100\,mm$ from a 2D quadratic image sensor.

As shown on Fig. 2b, the phase variations are very high around the best focusing plane, thus, as early proposed by Yang *et al.* [4], we have only modelized the theoretical variations of the phase function along the optical axis at the center ot the particle image as a function of the defocus amount Δz (i.e. $\Phi(0,0,\Delta z)$ where $\Delta z = z - z_e$).

After having applied the developments that can be found in Ref. [2], the solutions of integrals (4) are:

$$R_{sphere}(0,0,\Delta z) = e^{i\pi\frac{d^2}{4\lambda\Delta z}} + e^{i\pi\frac{d^2}{4\lambda(\Delta z+2z_e)}} - 1 \quad (6)$$

for the case of a sphere. For the case of an infinite vertical cylinder, we obtain:

$$\begin{aligned} R_{cylind}(0,\Delta z) = {} & 1 - C(\alpha_{\Delta z}) - S(\alpha_{\Delta z}) + i[C(\alpha_{\Delta z}) - S(\alpha_{\Delta z})]sign(\Delta z) \\ & -C(\alpha_{\Delta z+2z_e}) - S(\alpha_{\Delta z+2z_e}) + i\left[C(\alpha_{\Delta z+2z_e}) - S(\alpha_{\Delta z+2z_e})\right] \end{aligned} \quad (7)$$

Where $C(\alpha)$ and $S(\alpha)$ are the normalized Fresnel integrals and

$$\alpha_z = \sqrt{\frac{d^2}{2\lambda|z|}}$$

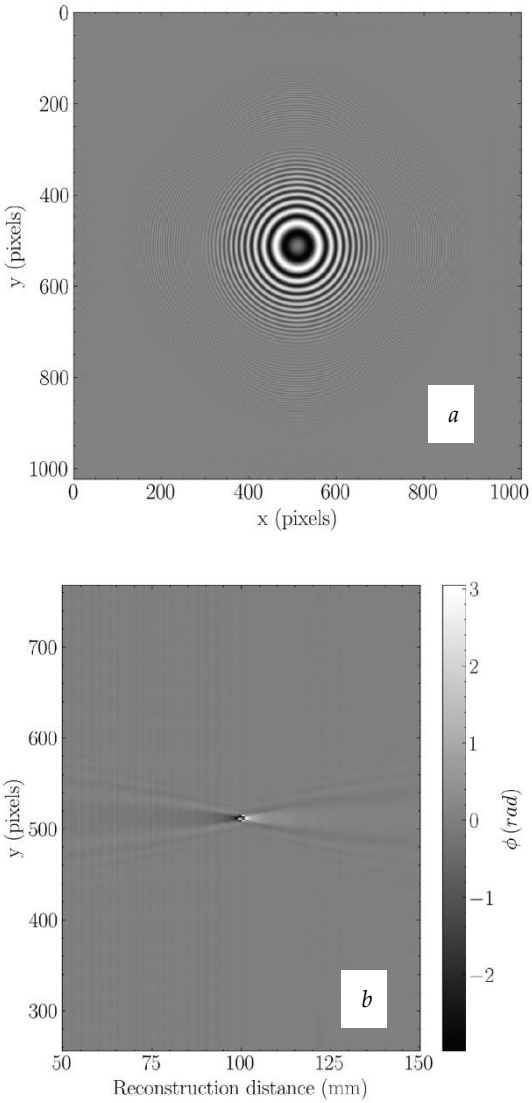

Figure 2 *Phase reconstruction of a spherical particle (bead) hologram.* $d = 50\ \mu m, z_e = 100\ mm$. *a) Intensity distribution of a simulated hologram in the (x,y) plane. b) Reconstructed phase in the (y, z) plane.*

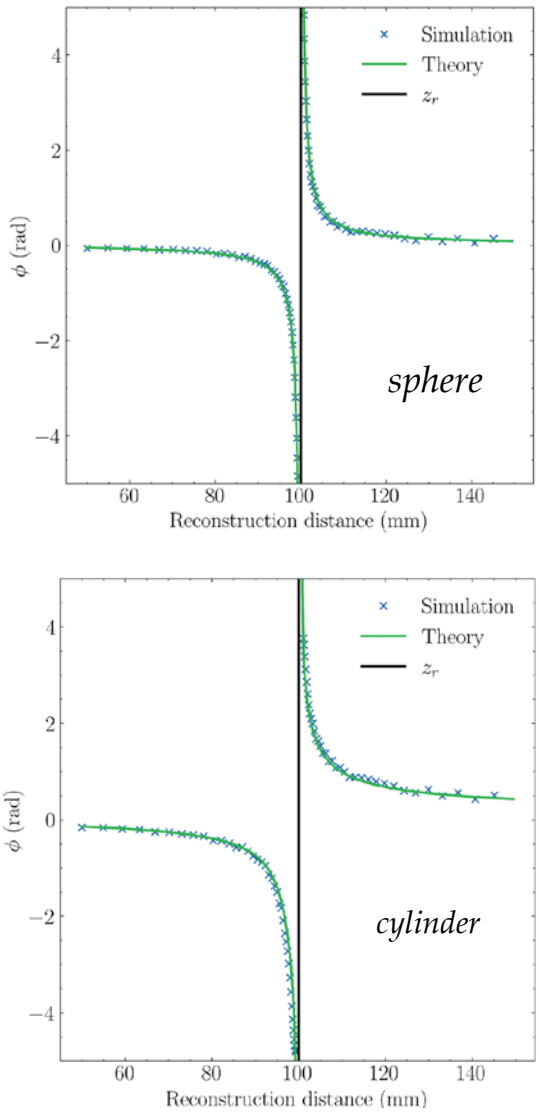

Figure 3 *Unwrapped phase evolution of the reconstructed hologram along the optical axis. Comparison of a spherical particle (bead) and a cylindrical particle (filament) of diameters* $d = 50\ \mu m$ *recorded at a distance* $z_e = 100\ mm$ *from the 2-D detector.*

2.2 Theoretical phase signatures

Equations (6) and (7) have been used to plot the theoretical variations of phase along the optical axis. Note that the phase information obtained by the $atan2()$ function of equation (5) is wrapped in the range of $[-\pi, \pi]$ with 2π discontinuities. Therefore, an unwrapping process has to be used in order to retrieve a continuous phase information.

Figure 3 shows the unwrapped phase evolutions of sphere and a cylinder of diameters 50 µm. Although the phase signatures are different, the asymptotic behaviour of the phase value around the best focusing plane is quite identical and can be used for both geometrical structures.

3 Application to the study of the elongation of a viscoelastic filament

Note that the phase variations are very sensitive to other objects that can be recorded around the sample volume. Thus, this approach is very efficient when few objects are present in the field. We have tested this method on viscoelastic fluids stretched by a controlled device. At some concentrations, the controlled stretching leads to the formation of a Beads-On-A-String (BOAS), i.e. attached drops on a filament. Figure 4 shows an example of hologram recorded during the elongation of the viscoelastic filament.

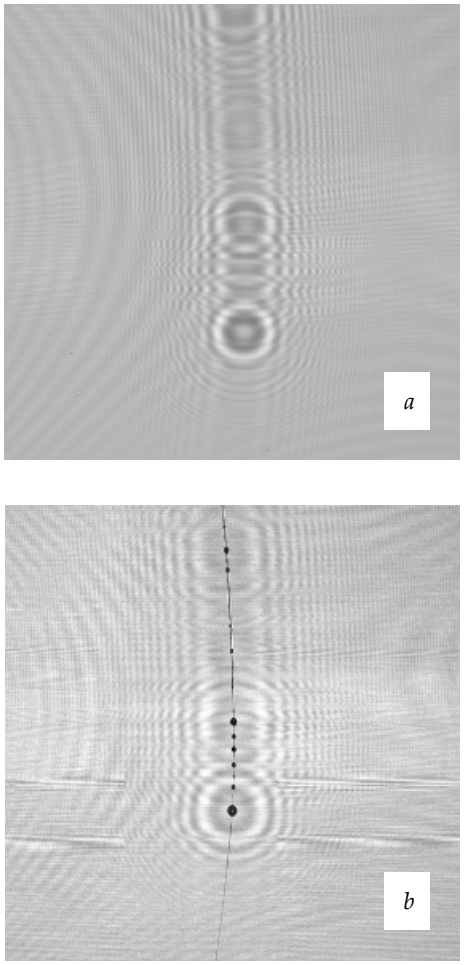

Figure 4 *Application of the method on a viscoelastic filament. a) Hologram, b) reconstructed hologram at z=335 mm, c) phase variations for a given bead.*

The holograms are automatically processed and the 3D coordinates of the fluid filament can be studied. As shown by the 3-D representation of Fig. 5, the filament is not straight. This deformation corresponds to a stress caused by a pulsed transverse air jet applied at the center of the filament.

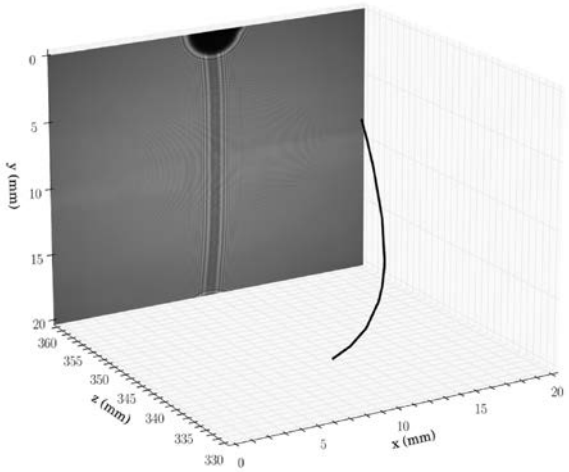

Figure 5 *Three-dimensional representation of the reconstructed hologram of a viscoelastic filament disturbed by a pulsed transverse air jet during its elongation.*

4 Conclusion

Digital in-line holography is used for the characterization of a viscoelastic filament during the stretching operation. When the filament is destabilized by a pulsed air jet for example, we show that we are able to localize the beads the appear along the filament. It must be emphasized that the phase signature method is used for the crucial stage of the focusing process. This approach has demonstrated its high reliability and reproducibility. Future studies are being considered for size measurements of micrometric beads and cylinders from the reconstructed phase distribution along the optical axis.

5 References

[1] J.W. Goodman, Introduction to Fourier Optics (Roberts and Company, 2005)

[2] R. Noury, MC Renoult, G. and D. Lebrun, "Phase analysis for focus plane detection in digital inline holography: application to three-dimensional locations of drops and threads in a beads-on-a-string structure," Appl. Opt. 62, 6241-6252 (2023), https://doi.org/10.1364/AO.494647

[3] S Mohammed, L Bouamama, D Bahloul, and P Picart, "Quality assessment of refocus criteria for particle imaging in digital off-axis holography," Appl. Opt. **56**, F158-F166 (2017)

[4] W. Yang, A. Kostinski, and R. Shaw, "Phase signature for particle detection with digital in-line holography," Opt. Lett. 31, 1399-1401 (2006).

The 14th International Conference on
Laser-light and Interactions with Particles (LIP2024)
September 18-22nd, 2024, Xi'an, Shaanxi, China

NEAR FIELD DISTRIBUTION ON THE SURFACE OF SPHERICAL PARTICLES FORMING A TWO-DIMENSIONAL ARRAY IN LIGHT-ABSORBING MEDIUM

Valery LOIKO*, Alexander MISKEVICH, and Natalia LOIKO

Institute of Physics, National Academy of Sciences of Belarus, Minsk, 220072, Belarus

*Corresponding author: loiko@ifanbel.bas-net.by

Abstract

The statistical semi-analytical method has been developed to describe distribution of electric and magnetic fields on the surface of spherical particles forming 2D array. It is based on the multipole expansions of waves and the Green's function in terms of vector spherical wave functions and takes into account multiple scattering of waves in the quasicrystalline approximation (QCA). The equations are derived to describe (i) ensemble-averaged and (ii) ensemble- and surface-averaged energy densities of electric and magnetic fields on the surface of spherical particles embedded in a light-absorbing medium.

1 Introduction

In the last decades, the ensembles of spherical particles are objects of intensive investigations. The interest is caused by unique possibilities given by such structures in optics, optoelectronics, photonics, chemistry, etc. The majority of studies devoted to these structures consider far-field characteristics of scattered light and imply that absorbing or nonabsorbing particles are located in a nonabsorbing host medium. However, some applications require consideration of local (near) fields which are formed on the surface and in the vicinity of particles located in light-absorbing environment, e.g. solar cells, photochemical reactors, etc. There are publications considering far-field properties of particulate layers [1] in an absorbing host medium, or near-field characteristics of isolated particles [2]. But we are not aware of publications in which the near-field characteristics of densely packed 2D arrays of particles in an absorbing medium is studied.

We present a brief summary of the method we are developed for determining the (i) ensemble-averaged and (ii) ensemble- and surface-averaged energy densities of electric and magnetic fields on the surface of 2D array's spherical particles embedded in a light-absorbing medium.

2 Theoretical model

We consider the array of N identical spherical particles centered at the points $\mathbf{R}_1$, $\mathbf{R}_2$, …, $\mathbf{R}_N$ in the monolayer plane (x,y). The coordinate origin is in the center of arbitrarily chosen particle. The monolayer stands in an absorbing medium. The EM plane wave with the electric vector $\mathbf{E}_0$ impinges upon the array:

$$\mathbf{E}_0(\mathbf{r}) = E_0\hat{\boldsymbol{\varepsilon}}_0 e^{ik_h\hat{\mathbf{r}}_0\cdot\mathbf{r}}e^{-i\omega t}, \qquad (1)$$

Here $\hat{\boldsymbol{\varepsilon}}_0 = \varepsilon_\theta\hat{\boldsymbol{\theta}}_0 + i\varepsilon_\varphi\hat{\boldsymbol{\varphi}}_0$ is the unit vector of polarization, $\hat{\mathbf{r}}_0$, $\hat{\boldsymbol{\theta}}_0$, $\hat{\boldsymbol{\varphi}}_0$ are unit vectors determined by the direction of the wavevector of incident wave ($\hat{\mathbf{r}}_0 = \hat{\boldsymbol{\theta}}_0 \times \hat{\boldsymbol{\varphi}}_0$), $k_h = 2\pi m_h/\lambda$ is complex wavenumber, $m_h = n_h + i\kappa_h$, n_h and κ_h are refractive and absorption indices of host medium, λ is the wavelength of incident wave in vacuum, E_0 is the amplitude of incident wave in the monolayer plane (z=0).

The field $\mathbf{E}(\mathbf{r})$ in some point $\mathbf{r}$ is the sum of fields of incident wave and waves scattered by the given configuration of an ensemble:

$$\mathbf{E}(\mathbf{r}) = \mathbf{E}_0(\mathbf{r}) + \sum_{j=1}^{N}\mathbf{F}_j(\mathbf{r},\mathbf{R}_j) = \\ = \frac{(k_p^{\,2}-k_h^{\,2})}{4\pi}\int_{V_p} d\mathbf{r}'\ddot{G}(\mathbf{r},\mathbf{R}_j+\mathbf{r}')\cdot\mathbf{E}(\mathbf{R}_j+\mathbf{r}') \qquad (2)$$

Here $\mathbf{F}_j(\mathbf{r}, \mathbf{R}_j)$ is the field created in point $\mathbf{r}$ by the particle centred at point $\mathbf{R}_j$, $k_p = 2\pi m_p/\lambda$ is complex wavenumber, $m_p = n_p + i\kappa_p$, n_p and κ_p are refractive and absorption indices of particle, V_p is the particle volume, $0 \le |\mathbf{r}'| \le D/2$, D is the particle diameter, $\mathbf{E}(\mathbf{R}_j+\mathbf{r}')$ is the field in point $\mathbf{R}_j+\mathbf{r}'$ within the particle (internal field), $\ddot{G}$ is the dyadic (tensor) Green's function. To find the field on the external surface of the particles of an ensemble with a given distribution statistics, the fields and Green's function are averaged over possible configurations of the ensemble in the QCA [3]. As a result, we obtain the equation for the averaged field $\langle\mathbf{E}_{NF}(\mathbf{r}_s)\rangle$ on the surface of the particle

$$\langle\mathbf{E}_{NF}(\mathbf{r}_s)\rangle = \mathbf{E}_0(\mathbf{r}_s) + \frac{(k_p^{\,2}-k_h^{\,2})}{4\pi}\int_{V_p} d\mathbf{r}'\ddot{G}(\mathbf{r}_s,\mathbf{r}')\cdot\langle\mathbf{E}_{in}(\mathbf{r}')\rangle + \\ + \frac{(k_p^{\,2}-k_h^{\,2})}{4\pi}\rho_0\int d\mathbf{R}g(R)\int_{V_p} d\mathbf{r}'\ddot{G}(\mathbf{r}_s,\mathbf{R}+\mathbf{r}')\cdot\langle\mathbf{E}_{in}(\mathbf{r}')\rangle e^{ik\hat{\mathbf{r}}_0\cdot\mathbf{R}}, \qquad (3)$$

and equation for the averaged field in particle centred at the coordinate origin:

$$\langle\mathbf{E}_{in}(\mathbf{r}')\rangle = \mathbf{E}_0(\mathbf{r}') + \frac{(k_p^{\,2}-k_h^{\,2})}{4\pi}\int_{V_p} d\mathbf{r}''\ddot{G}(\mathbf{r}',\mathbf{r}'')\cdot\langle\mathbf{E}_{in}(\mathbf{r}'')\rangle + \\ + \frac{(k_p^{\,2}-k_h^{\,2})}{4\pi}\rho_0\int d\mathbf{R}g(R)\int_{V_p} d\mathbf{r}''\ddot{G}(\mathbf{r}',\mathbf{R}+\mathbf{r}'')\cdot\langle\mathbf{E}_{in}(\mathbf{r}'')\rangle e^{ik_h\hat{\mathbf{r}}_0\cdot\mathbf{R}}. \qquad (4)$$

Here ρ_0 is the average number density of particles, $g(R)$ is the radial distribution function, describing the probability to find particle center at the distance R relative to coordinate origin, $R = |\mathbf{R}|$. Eq. (4) is an integral equation for the field $\langle\mathbf{E}_{in}(\mathbf{r}')\rangle$. The first integral describes the contribution to the field $\langle\mathbf{E}_{in}(\mathbf{r}')\rangle$ of elementary volumes of the same particle. The second one describes the

contribution of the fields from the remaining particles. This equation is solved by expanding all fields and the Green's function in terms of vector spherical wave functions (VSWF) [4]. Integration of (4) leads to two independent systems of algebraic equations for expansion coefficients $d_{mlM,E}^{(e),(o)}$ [5]. Using this coefficients, we obtained the equations to describe the distributions of electric, $\langle w_{NF}^{E}(\mathbf{r}_s)\rangle$, and magnetic, $\langle w_{NF}^{M}(\mathbf{r}_s)\rangle$, field energy densities on the surface of array's particle, averaged over the ensemble configurations, and equations for field energy densities, $\langle w_{NF}^{E}(r_s)\rangle$ and $\langle w_{NF}^{M}(r_s)\rangle$, averaged over both the ensemble configurations and particle surface in solid angle 4π:

$$\begin{aligned}\langle w_{NF}^{E}(\mathbf{r}_s)\rangle &= \frac{\mathrm{Re}\,\varepsilon_h}{2}\langle \mathbf{E}_{NF}(\mathbf{r}_s)\rangle\cdot\langle \mathbf{E}_{NF}^{*}(\mathbf{r}_s)\rangle \\ &= \frac{8\pi^2 E_0^2\,\mathrm{Re}\,\varepsilon_h}{x^2(1+\beta_h^2)}\left[\left|\sum_{l=1}^{\infty}\sum_{m=0}^{l} i^{l+1}\alpha_{ml}E_{rml}\right|^2\right. \\ &\left.+\left|\sum_{l=1}^{\infty}\sum_{m=0}^{l} i^{l+1}\alpha_{ml}E_{\theta ml}\right|^2+\left|\sum_{l=1}^{\infty}\sum_{m=0}^{l} i^{l+1}\alpha_{ml}E_{\varphi ml}\right|^2\right],\end{aligned} \tag{5}$$

$$\begin{aligned}E_{rml} &= \frac{l(l+1)}{x(1+i\beta_h)}\pi_l^{(m)}(\mu)\sin\theta(c_{lE}\chi_l-\psi_l) \\ &\times\left(\varepsilon_\theta\frac{d_{mlE}^{(e)}}{c_{lE}}\cos m\varphi+i\varepsilon_\varphi\frac{d_{mlE}^{(o)}}{c_{lE}}\sin m\varphi\right),\end{aligned} \tag{6}$$

$$\begin{aligned}E_{\theta ml} &= \tau_l^{(m)}(\mu)(c_{lE}\chi_l'-\psi_l')\left(\varepsilon_\theta\frac{d_{mlE}^{(e)}}{c_{lE}}\cos m\varphi+i\varepsilon_\varphi\frac{d_{mlE}^{(o)}}{c_{lE}}\sin m\varphi\right) \\ &+im\pi_l^{(m)}(\mu)(c_{lM}\chi_l-\psi_l)\left(\varepsilon_\theta\frac{d_{mlM}^{(o)}}{c_{lM}}\cos m\varphi+i\varepsilon_\varphi\frac{d_{mlM}^{(e)}}{c_{lM}}\sin m\varphi\right),\end{aligned} \tag{7}$$

$$\begin{aligned}E_{\varphi ml} &= im\pi_l^{(m)}(\mu)(c_{lE}\chi_l'-\psi_l')\left(\varepsilon_\varphi\frac{d_{mlE}^{(o)}}{c_{lE}}\cos m\varphi+i\varepsilon_\theta\frac{d_{mlE}^{(e)}}{c_{lE}}\sin m\varphi\right) \\ &-\tau_l^{(m)}(\mu)(c_{lM}\chi_l-\psi_l)\left(\varepsilon_\varphi\frac{d_{mlM}^{(e)}}{c_{lM}}\cos m\varphi+i\varepsilon_\theta\frac{d_{mlM}^{(o)}}{c_{lM}}\sin m\varphi\right),\end{aligned} \tag{8}$$

$$\begin{aligned}\langle w_{NF}^{M}(\mathbf{r}_s)\rangle &= \frac{\mu_h}{2}\langle \mathbf{H}_{NF}(\mathbf{r}_s)\rangle\cdot\langle \mathbf{H}_{NF}^{*}(\mathbf{r}_s)\rangle \\ &= \frac{8\pi^2 E_0^2|\varepsilon_h|}{x^2(1+\beta_h^2)}\left[\left|\sum_{l=1}^{\infty}\sum_{m=0}^{l} i^{l+1}\alpha_{ml}H_{rml}\right|^2\right. \\ &\left.+\left|\sum_{l=1}^{\infty}\sum_{m=0}^{l} i^{l+1}\alpha_{ml}H_{\theta ml}\right|^2+\left|\sum_{l=1}^{\infty}\sum_{m=0}^{l} i^{l+1}\alpha_{ml}H_{\varphi ml}\right|^2\right],\end{aligned} \tag{9}$$

$$\begin{aligned}H_{rml} &= \frac{l(l+1)}{x(1+i\beta_h)}\pi_l^{(m)}(\mu)\sin\theta(c_{lM}\chi_l-\psi_l) \\ &\times\left(\varepsilon_\theta\frac{d_{mlM}^{(o)}}{c_{lM}}\sin m\varphi-i\varepsilon_\varphi\frac{d_{mlM}^{(e)}}{c_{lM}}\cos m\varphi\right),\end{aligned} \tag{10}$$

$$\begin{aligned}H_{\theta ml} &= \tau_l^{(m)}(\mu)(c_{lM}\chi_l'-\psi_l')\left(\varepsilon_\theta\frac{d_{mlM}^{(o)}}{c_{lM}}\sin m\varphi-i\varepsilon_\varphi\frac{d_{mlM}^{(e)}}{c_{lM}}\cos m\varphi\right) \\ &+im\pi_l^{(m)}(\mu)(c_{lE}\chi_l-\psi_l)\left(\varepsilon_\theta\frac{d_{mlE}^{(e)}}{c_{lE}}\sin m\varphi-i\varepsilon_\varphi\frac{d_{mlE}^{(o)}}{c_{lE}}\cos m\varphi\right),\end{aligned} \tag{11}$$

$$\begin{aligned}H_{\varphi ml} &= im\pi_l^{(m)}(\mu)(c_{lM}\chi_l'-\psi_l')\left(\varepsilon_\varphi\frac{d_{mlM}^{(e)}}{c_{lM}}\sin m\varphi-i\varepsilon_\theta\frac{d_{mlM}^{(o)}}{c_{lM}}\cos m\varphi\right) \\ &-\tau_l^{(m)}(\mu)(c_{lE}\chi_l-\psi_l)\left(\varepsilon_\varphi\frac{d_{mlE}^{(o)}}{c_{lE}}\sin m\varphi-i\varepsilon_\theta\frac{d_{mlE}^{(e)}}{c_{lE}}\cos m\varphi\right),\end{aligned} \tag{12}$$

$$\begin{aligned}\langle w_{NF}^{E}(r_s)\rangle &= \frac{\mathrm{Re}\,\varepsilon_h}{8\pi}\int_0^{2\pi}\mathrm{d}\varphi\int_0^{\pi}\langle \mathbf{E}_{NF}(\mathbf{r}_s)\rangle\cdot\langle \mathbf{E}_{NF}^{*}(\mathbf{r}_s)\rangle\sin\theta\,\mathrm{d}\theta \\ &= \frac{2\pi E_0^2\,\mathrm{Re}\,\varepsilon_h}{x^2(1+\beta_h^2)}\sum_{l=1}^{\infty}\sum_{m=0}^{l}\alpha_{ml}\left[\left(\left|\varepsilon_\theta\frac{d_{mlM}^{(o)}}{c_{lM}}\right|^2+\left|\varepsilon_\varphi\frac{d_{mlM}^{(e)}}{c_{lM}}\right|^2\right)A_{lM}\right. \\ &\left.+\left(\left|\varepsilon_\varphi\frac{d_{mlE}^{(o)}}{c_{lE}}\right|^2+\left|\varepsilon_\theta\frac{d_{mlE}^{(e)}}{c_{lE}}\right|^2\right)(B_{lE}+C_{lE})\right],\end{aligned} \tag{13}$$

$$\begin{aligned}A_{lM} &= |c_{lM}\chi_l|^2-2\,\mathrm{Re}\left[c_{lM}\chi_l\psi_l^{*}\right]+|\psi_l|^2, \\ B_{lE} &= \frac{l(l+1)}{x^2(1+\beta_h^2)}\left(|c_{lE}\chi_l|^2-2\,\mathrm{Re}\left[c_{lE}\chi_l\psi_l^{*}\right]+|\psi_l|^2\right), \\ C_{lE} &= |c_{lE}\chi_l'|^2-2\,\mathrm{Re}\left[c_{lE}\chi_l'\psi_l'^{*}\right]+|\psi_l'|^2,\end{aligned} \tag{14}$$

$$\begin{aligned}\langle w_{NF}^{M}(r_s)\rangle &= \frac{\mu}{8\pi}\int_0^{2\pi}\mathrm{d}\varphi\int_0^{\pi}\langle \mathbf{H}_{NF}(\mathbf{r}_s)\rangle\cdot\langle \mathbf{H}_{NF}^{*}(\mathbf{r}_s)\rangle\sin\theta\,\mathrm{d}\theta \\ &= \frac{2\pi E_0^2|\varepsilon_h|}{x^2(1+\beta_h^2)}\sum_{l=1}^{\infty}\sum_{m=0}^{l}\alpha_{ml}\left[\left(\left|\varepsilon_\theta\frac{d_{mlM}^{(o)}}{c_{lM}}\right|^2+\left|\varepsilon_\varphi\frac{d_{mlM}^{(e)}}{c_{lM}}\right|^2\right)(B_{lM}+C_{lM})\right. \\ &\left.+\left(\left|\varepsilon_\varphi\frac{d_{mlE}^{(o)}}{c_{lE}}d_{mlE}^{(o)}\right|^2+\left|\varepsilon_\theta\frac{d_{mlE}^{(e)}}{c_{lE}}\right|^2\right)A_{lE}\right],\end{aligned} \tag{15}$$

$$\begin{aligned}A_{lE} &= |c_{lE}\chi_l|^2-2\,\mathrm{Re}\left[c_{lE}\chi_l\psi_l^{*}\right]+|\psi_l|^2, \\ B_{lM} &= \frac{l(l+1)}{x^2(1+\beta_h^2)}\left(|c_{lM}\chi_l|^2-2\,\mathrm{Re}\left[c_{lM}\chi_l\psi_l^{*}\right]+|\psi_l|^2\right), \\ C_{lM} &= |c_{lM}\chi_l'|^2-2\,\mathrm{Re}\left[c_{lM}\chi_l'\psi_l'^{*}\right]+|\psi_l'|^2.\end{aligned} \tag{16}$$

In (5)-(16) ε_h is the dielectric constant of the host medium, $\beta_h=\kappa_h/n_h$, $x=\pi D n_h/\lambda$ is the size parameter of particle, $r_s=|\mathbf{r}_s|$, $\pi_l^{(1)}$, $\tau_l^{(1)}$ are angular functions, χ_l, ψ_l, $\tilde{\psi}_l$ are Riccati-Bessel, c_{lM}, c_{lE} are Mie coefficients [5].

3 Calculation results

Using the developed method, we analysed the dependences of $\langle w_{NF}^{E}(r_s)\rangle$, $\langle w_{NF}^{M}(r_s)\rangle$, $\langle w_{NF}^{E}(\mathbf{r}_s)\rangle$, and $\langle w_{NF}^{E}(\mathbf{r}_s)\rangle$ at normal incidence of wave. Fig. 1 shows the spectra of coefficients of coherent transmission, T_c, and reflection, R_c, incoherent scattering, F_{inc}, and absorption, A, for a layer of medium with thickness $L=D$ with an embedded array of spherical wavelength-sized silver (Ag) particles with filling factor $\eta=0.5$ [5]. Data are also given for the absorption coefficients of the particles, A_p, and the medium, $A_h=A-A_p$, for different values of the imaginary part of the refractive index of the medium, κ_h [6]. The thick dashed lines represent the normalized dependences of electric, $w_n^E(r_s)=\langle w_{NF}^{E}(r_s)\rangle/w_0$, and magnetic, $w_n^M(r_s)=\langle w_{NF}^{M}(r_s)\rangle/w_0$, field energy densities ($w_0=E_0^2\,\mathrm{Re}[\varepsilon_h]/2$) averaged over the ensemble configurations and polar and azimuthal scattering angles. It can be seen that $w_n^E(r_s)$ and $w_n^M(r_s)$ correlate with the far-field characteristics: T_c, R_c, F_{inc}, and $A=1-(T_c+R_c+F_{inc})$. If

the medium is lossless [Fig. 1(a)], the total absorption is determined only by the absorption of particles. The spectral positions of the larger peaks of $w_n^E(r_s)$ and $w_n^M(r_s)$ practically coincide with the spectral position of the lattice-induced peak of resonant absorption A=A_p (0.525 μm<λ<0.54 μm). Here, only coherent scattering of light occurs (F_{inc}=0). Wider and smaller peaks are observed in the spectral range, where the incoherent scattering coefficient changes sharply (0.46 μm<λ<0.48 μm). The presence of absorption in a medium [Fig. 1(b)] leads to a decrease and some blurring of these peaks. A further increase in κ_h [Fig. 1(c, d)] leads to smoothing the dependences. For a large value of κ_h=0.5 there is a maximum for $w_n^E(r_s)$ (at λ≈0.33 μm) and a minimum for $w_n^M(r_s)$ (at λ≈0.325 μm), which are mainly determined by the refractive and absorption indices of the particles (n_{Ag} and k_{Ag}). They are presented in Fig. 1(d). for different filling factors of an array.

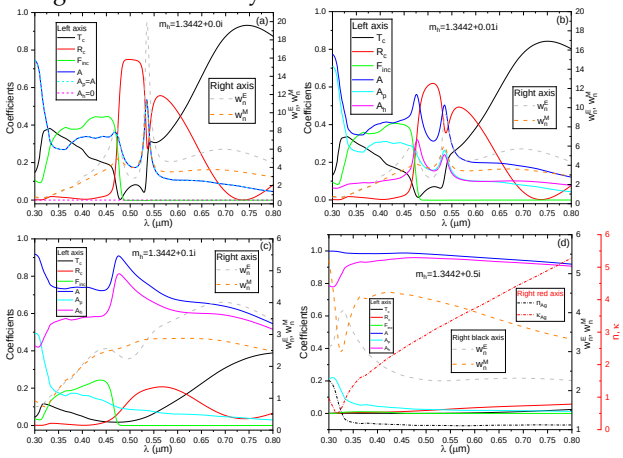

Figure 1 *Spectra of (left axes) T_c, R_c, F_{inc}, and A_p coefficients of Ag particle array with an imperfect triangular lattice, absorption coefficients of the matrix, A_h, and a selected layer, A, with a thickness L=D [5], containing the array located in the host medium with the refractive index n_h=1.3442 at different values of κ_h. (Right black axes) spectra of $w_n^E(r_s)$ and $w_n^M(r_s)$. (d, right red axis) $n_{Ag}(\lambda)$ and $\kappa_{Ag}(\lambda)$ [7]. D=0.3 μm, η=0.5.*

Maps of angular distributions of $w_n^E(\mathbf{r}_s)=\langle w_{NF}^E(\mathbf{r}_s)\rangle/w_0$ and $w_n^M(\mathbf{r}_s)=\langle w_{NF}^M(\mathbf{r}_s)\rangle/w_0$ in the ranges 0°<θ<180° and 0°<φ<360° are shown in Fig. 2 for a nonabsorbing medium at wavelengths λ=0.57 μm and 0.49 μm. At λ=0.57 μm, a maximum of lattice-induced peak of $w_n^E(r_s)$ occurs for the array of spherical Ag particles with the diameter D=0.3 μm and the array filling factor η=0.4. At λ=0.57 μm, the local minimum near this peak takes place. One ca see that for such a system, the highest concentration of the magnetic field energy density occurs in the region of small polar angles (0°<θ<15°, Fig. 2 (right column)), and the energy density of the electric field is mainly concentrated in 4 spots (Fig. 2 (left column)).

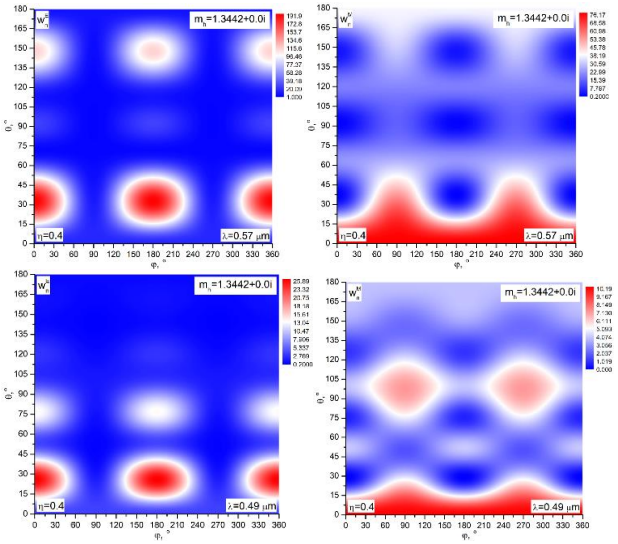

Figure 2 *Maps of angular distributions of $w_n^E(\mathbf{r}_s)$ and $w_n^M(\mathbf{r}_s)$ on the surface of Ag particle in the array with the imperfect triangular lattice for the wavelengths (top row) λ=0.57 μm and (bottom row) λ=0.49 μm. D=0.3 μm, η=0.4.*

4 Conclusions

The statistical method has been developed to describe the distribution of the near field on the surface of spherical particles forming the 2D array. It is shown that the spectral position of the lattice-induced resonant peaks of electric and magnetic field energy densities, averaged over the ensemble configurations and the particle surface, practically coincide with the lattice-induced resonant peaks of far-field characteristics. The differences are shown in the angular distribution of fields formed on the surfaces of particles at the wavelengths of maximum of lattice-induced resonant peak and local minimum near this peak.

5 References

[1] Mishchenko M.I., Dlugach J.M., Multiple scattering of polarized light by particles in an absorbing medium, Appl. Opt. 58:4871–7 (2019).

[2] Xu H., Electromagnetic energy flow near nanoparticles—I: single spheres, JQSRT 87:53–67 (2004).

[3] Lax M., Multiple Scattering of Waves. II. The Effective Field in Dense Systems, Phys. Rev. **85**, 621-629 (1952).

[4] Loiko N.A., Miskevich A.A., Loiko V.A., Scattering and absorption of light by a monolayer of spherical particles under oblique illumination, J. Exp. Theor. Phys. **131**, 227–243 (2020).

[5] Loiko N.A., Miskevich A.A., Loiko V. A., Optical characteristics of a monolayer of identical spherical particles in an absorbing host medium, J. Opt. Soc. Am. A **40**, 682–691 (2023).

[6] N. A. Loiko, A. A. Miskevich, and V. A. Loiko, "Light absorption by a planar array of spherical particles and a matrix in which they are embedded: statistical approach," J. Opt. Soc. Am A. **41**, 1-10 (2024).

[7] E. D. Palik, ed., *Handbook of Optical Constants of Solids* (Academic, 1985), Vol. 1.

The 14th International Conference on
Laser-light and Interactions with Particles (LIP2024)
September 18-22nd, 2024, Xi'an, Shaanxi, China

PARAMETERS OF DIFFERENTIAL EQUATIONS IN FOUR-FLUX AND TWO-FLUX MODELS APPROXIMATED FOR WO_3-NiO INORGANIC ELECTROCHROMIC DEVICES

David BARRIOS*

Universidad Carlos III de Madrid, Escuela Politécnica Superior, Leganés, Madrid, Spain

*Corresponding author: dbarriosp76@gmail.com

Abstract

A new recent procedure developed for determining the extinction coefficients of a suspended particle device (SPD) and a polymer dispersed liquid crystals (PDLC) smart windows −approximated considering a three-substrate layers sandwich structure (TSLSS), with glass (G) outer layers− was used in this work for four WO_3-NiO inorganic electrochromic devices (ECD), switching from bleached-off to colored-on optical states. WO_3 varies from uncolored to bluish and NiO varies from uncolored to brownish, leading to a neutral greyish colored state of the whole ECD. The four ECDs have the four combinations of single and double thicknesses of the WO_3 and NiO active layers (i.e., 11, 12, 21 and 22). Considering four forward scattering ratios (FSR) and two average crossing parameters (ACP), new equations of intrinsic and extrinsic scattering and absorption coefficients of four-flux model (4FM) and two-flux model (2FM) were accurately determined recently for the electrolyte (E) substrate layer (used for WO_3-NiO ECDs) in a TSLSS G-E-G sample. Approximated later for the SPD and PDLC samples, due to the consideration of TSLSS, here they are now approximated for the four ECDs.

1 Introduction

The inverse problem of absorption and scattering of light by small particles [1] can be aborded by means of 4FM [2,3] and 2FM [4] radiative transfer models. The three-extinction matching requirement (TEMR) [5] is a phenomenon observed when the same extinction (ε) coefficients are obtained using optical constants (n & κ) $\varepsilon = 4\pi\kappa/\lambda_n = 4\pi\kappa n/\lambda$ (compressed wavelength $\lambda_n = \lambda/n$) and with the forward (ε_i) and backward (ε_j) 4FM [2,3] collimated differential equations (CDE) of Eq. (1) and (2), once the collimated forward and backward intensities of light (I_c & J_c) at front and back inner interfaces (at $z = \delta$ and $z = 0$, in Fig. 1) have been properly determined from collimated interface reflectance (r_c, multiplying Fresnel reflection coefficients by its conjugated, using n^G & κ^G) and from collimated layer attenuation ($\tau_c = e^{-\varepsilon \cdot dz}$), from n & κ [5] (being asterisked intensities starting at the interface, i.e., computed as the sum of transmitted and reflected intensities reaching to the interface). The same external and internal diffuse interface reflectance ($r_d = r_d^i = r_d^\delta$) were computed integrating r_c up to the critical angle of total internal reflection, required to compute diffuse light intensities. Then, intrinsic scattering (α) and absorption (β) coefficients are obtained from the 4FM diffuse differential equations (DDE) of Eq. (3) and Eq. (4) [2,3] thanks to four intuitive proposed relations for ACP (ξ) and FSR (σ) parameters multiplying diffuse light intensities (I_d & J_d) (i.e., $\xi^i = 1 + I_d^\delta/(I_c^0 + I_d^0)$ and $\sigma_d^i = I_d^0/(I_d^0 + J_d^\delta)$, and $\xi^j = 1 + J_d^\delta/(J_c^\delta + J_d^\delta)$ and $\sigma_d^j = J_d^\delta/(I_d^0 + J_d^\delta)$. The solutions for α and σ_c^i are given in [5,6], being $\beta = \varepsilon - \alpha$ and $\sigma_c^j = 1 - \sigma_c^i$. Then, Eq. (5) and (6) of the 2FM [4] are considered as the total differential equations (TDE), equalizing them to CDE plus DDE and solving for extrinsic scattering (S) and absorption (K) coefficients [5,7].

$$\frac{dI_c}{dz} = \frac{(I_c^\delta)^* - (I_c^0)}{dz^X} = \varepsilon_i \cdot (I_c^\delta)^* \quad (1)$$

$$\frac{dJ_c}{dz} = \frac{(J_c^\delta) - (J_c^0)^*}{dz^X} = -\varepsilon_j \cdot J_c^\delta \quad (2)$$

$$\frac{dI_d}{dz} = \frac{(I_d^\delta)^* - (I_d^0)}{dz^X} = \quad (3)$$
$$= -(I_c^\delta)^* \sigma_c^j \alpha - J_c^\delta \sigma_c^i \alpha - J_d^\delta \xi^j \sigma_d^i \alpha + (I_d^\delta)^* (\xi^i \beta + \xi^i \sigma_d^j \alpha)$$

$$\frac{dJ_d}{dz} = \frac{(J_d^\delta) - (J_d^0)^*}{dz^X} = \quad (4)$$
$$= J_c^\delta \sigma_c^i \alpha + (I_c^\delta)^* \sigma_c^j \alpha + (I_d^\delta)^* \xi^i \sigma_d^j - J_d^\delta (\xi^j \beta + \xi^j \sigma_d^i \alpha)$$

$$\frac{dI}{dz} = \frac{(I_c^\delta)^* - (I_c^0)}{dz^X} + \frac{(I_d^\delta)^* - (I_d^0)}{dz^X} = \quad (5)$$
$$= -(S + K) \cdot (I_c^0 + I_d^0) + S \cdot ((I_c^\delta)^* + (I_d^\delta)^*)$$

$$\frac{dJ}{dz} = \frac{(J_c^\delta) - (J_c^0)^*}{dz^X} + \frac{(J_d^\delta) - (J_d^0)^*}{dz^X} = \quad (6)$$
$$= (S + K) \cdot (J_c^\delta + J_d^\delta) - S \cdot ((J_c^0)^* + (J_d^0)^*)$$

When the sandwich structure of the sample is not accurate but approximated, considering the TSLSS (Fig. 1) such as in [6,7] for the SPD and PDLC samples −neglecting transparent conductor (TC) thin film layers− a recent new procedure [6], based in the system of Eq. (7) to (10), −solved for I_c^0, J_c^δ, τ_c and r_c in Eq. (11) to (14)− must be used in order to force the TEMR (i.e., $\varepsilon = \varepsilon_i = \varepsilon_j$).

$$I_c^0 = \tau_c [(1 - r_c) \cdot I_c^\delta + r_c \cdot J_c^\delta] \quad (7)$$

$$J_c^\delta = \tau_c [(1 - r_c) \cdot J_c^0 + r_c \cdot I_c^0] \quad (8)$$

$$J_c^{\delta\delta} = \tau_c^G [(1 - r_c) \cdot J_c^\delta + r_c \cdot I_c^\delta] \quad (9)$$

$$I_c^{00} = \tau_c^G [(1 - r_c) \cdot I_c^0 + r_c \cdot J_c^0] \quad (10)$$

$$r_c = -\left|\Sigma + (J_c^0)^2 - (I_c^\delta)^2 + \Xi \cdot (\Psi + \Phi) \cdot \Lambda^{-1}\right| \cdot \Theta^{-1} \quad (11)$$

$$\tau_c = (\Psi + \Phi) \cdot \Lambda^{-1} \quad (12)$$

$$I_c^0 = [\Omega - \Delta \cdot (\Psi + \Phi) \cdot \Lambda^{-1}] \cdot \Sigma^{-1} \quad (13)$$

$$J_c^\delta = [\Upsilon - \Pi \cdot (\Psi + \Phi) \cdot \Lambda^{-1}] \cdot \Sigma^{-1} \quad (14)$$

$$\Psi = 2 I_c^\delta (J_c^\delta)^* - 2 (I_c^0)^* J_c^0 + (I_c^0)^* (I_c^0)^* + J_c^0 J_c^0 - I_c^\delta I_c^\delta - (J_c^\delta)^* (J_c^\delta)^*$$

$$\Phi = \sqrt{\Phi_1 + \Phi_2 + \Phi_3 + \Phi_4 + \Phi_5}$$

$$\Phi_1 = (I_c^0)^*(I_c^0)^* \cdot [(I_c^0)^*(I_c^0)^* - 4 \cdot (I_c^0)^* J_c^0 + 2 I_c^\delta I_c^\delta + 4 I_c^\delta (J_c^\delta)^*]$$
$$\Phi_2 = (I_c^0)^* \cdot [6 (I_c^0)^* J_c^0 J_c^0 - 2 (I_c^0)^* (J_c^\delta)^* (J_c^\delta)^* + 4 I_c^\delta I_c^\delta J_c^0]$$
$$\Phi_3 = -4 (I_c^0)^* \cdot [4 I_c^\delta J_c^0 (J_c^\delta)^* + J_c^0 J_c^0 J_c^0 - J_c^0 (J_c^\delta)^* (J_c^\delta)^*]$$
$$\Phi_4 = I_c^\delta I_c^\delta \cdot [I_c^\delta I_c^\delta - 4 I_c^\delta (J_c^\delta)^* - 2 J_c^0 J_c^0 + 6 (J_c^\delta)^* (J_c^\delta)^*]$$
$$\Phi_5 = (J_c^\delta)^* [4 I_c^\delta J_c^0 J_c^0 + (J_c^\delta)^* \{2 J_c^0 J_c^0 - (J_c^\delta)^* (J_c^\delta)^* (4 I_c^\delta (J_c^\delta)^* + (J_c^\delta)^*)\}] + J_c^0 J_c^0 J_c^0$$
$$\Lambda = 2[(I_c^0)^* I_c^\delta - J_c^0 (J_c^\delta)^*] \qquad \Xi = (I_c^0)^* I_c^\delta - J_c^0 (J_c^\delta)^*$$
$$\Theta = 2 (I_c^\delta)^2 - I_c^\delta (J_c^\delta)^* - 2 (J_c^0)^2 + (I_c^0)^* J_c^0$$
$$\Sigma = (I_c^0)^* [2 J_c^0 - (I_c^0)^*] + (J_c^\delta)^* [(J_c^\delta)^* - 2 I_c^\delta] + (I_c^\delta)^2 - (J_c^0)^2$$
$$\Omega = (I_c^0)^* (I_c^\delta)^2 + (J_c^\delta)^* [J_c^0 (J_c^\delta)^* - \{(I_c^0)^* + J_c^0\} I_c^\delta]$$
$$\Delta = (I_c^0)^* J_c^0 [I_c^\delta + (J_c^\delta)^*] - [(I_c^0)^*]^2 I_c^\delta - (J_c^0)^2 (J_c^\delta)^*$$
$$\Upsilon = (I_c^0)^* (I_c^0)^* I_c^\delta + (J_c^0)^2 (J_c^\delta)^* - [I_c^\delta + (J_c^\delta)^*] (I_c^0)^* J_c^0$$
$$\Pi = [(I_c^0)^* + J_c^0] I_c^\delta (J_c^\delta)^* - (I_c^0)^* (I_c^\delta)^2 - J_c^0 (J_c^\delta)^* (J_c^\delta)^*$$

2 Devices and experimental set-up

The sandwich structure of WO_3-NiO inorganic ECDs is G-TC-WO_3-E-NiO-TC-G [8], with fluorine-doped tin oxide (FTO), as TC thin film layers and E substrate layer [5] in the four ECDs, being the inner active multilayer X (Fig. 1) approximated to the TSLSS as X=FTO-WO_3-E-NiO-FTO (x1: colored states 3 V, x2: bleached states -3 V, 0 V or high impedance, Fig. 2). Total and diffuse transmittance (T) and reflectance (R) were measured in the solar wavelength range, with 5 nm steps, using the Perkin Elmer Lambda 950 spectrometer, equipped with an integrating sphere. Regular T and specular R are computed subtracting them.

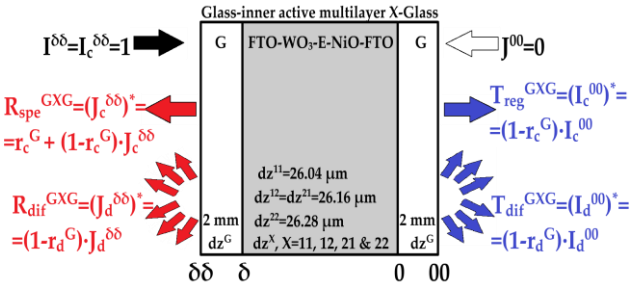

Figure 1 *Approximated three-substrate layers sandwich structure (TSLSS) for the WO_3-NiO ECDs 11, 12, 21 and 22.*

3 Results

3.1 Parameters from 4FM differential equations

From CDE, Fig. 3 shows n & κ obtained fitting to r_c from Eq. (11) –using n^G & κ^G, previously computed from a single-layer G sample– and to τ_c from Eq. (12). From DDE, Fig. 4 shows intrinsic α & β obtained using the solutions of DDE [5,6], derived from the two ACP and four FSR intuitive relations. Low haze of ECDs causes $\beta > \alpha$ ($\sim\forall\lambda$).

3.2 Parameters from 2FM differential equations

Fig. 5 shows extrinsic S & K obtained using the solutions of TDE [5,7], from relation $TDE = CDE + DDE$.

4 Conclusions

Extinction κ and absorption β & K show the higher differences for ECDs 11, 12, 21 and 22 at colored states (as ideally expected in ECDs, $\varepsilon \approx \beta > \alpha \approx 0$). As in previous samples $S < \alpha$ [5-7]. Thickness gradients of light intensities for the ECDs such as in [5-7] are now possible to plot. Future works would be separate WO_3 & NiO results.

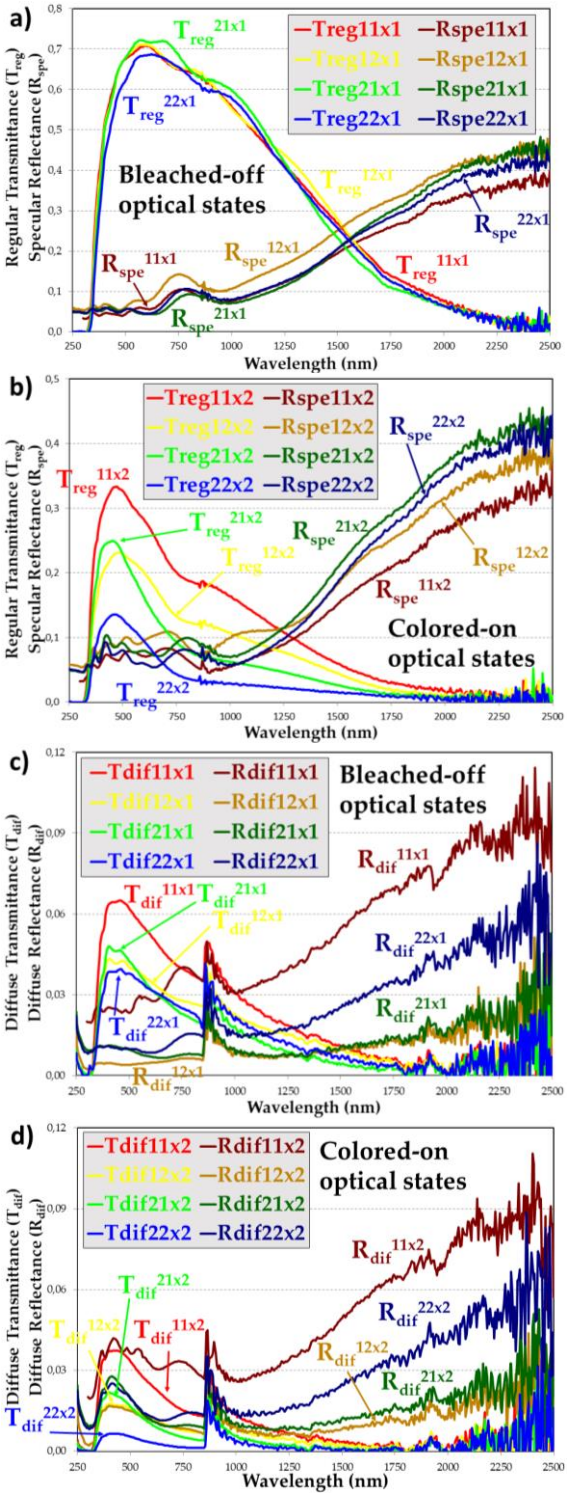

Figure 2 *Optical measurements of the ECDs samples, with single-single (11), single-double (12), double-single (21) and double-double (22) combinations of the thicknesses of WO_3 and NiO thin films active layers (single: 120 nm and double: 240 nm, being FTO: 400 nm, electrolyte: 0.025 mm and glass: 2 mm).*

4 Conclusions

Extinction κ and absorption β & K show the higher differences for ECDs 11, 12, 21 and 22 at colored states (as ideally expected in ECDs, $\varepsilon \approx \beta > \alpha \approx 0$). As in previous

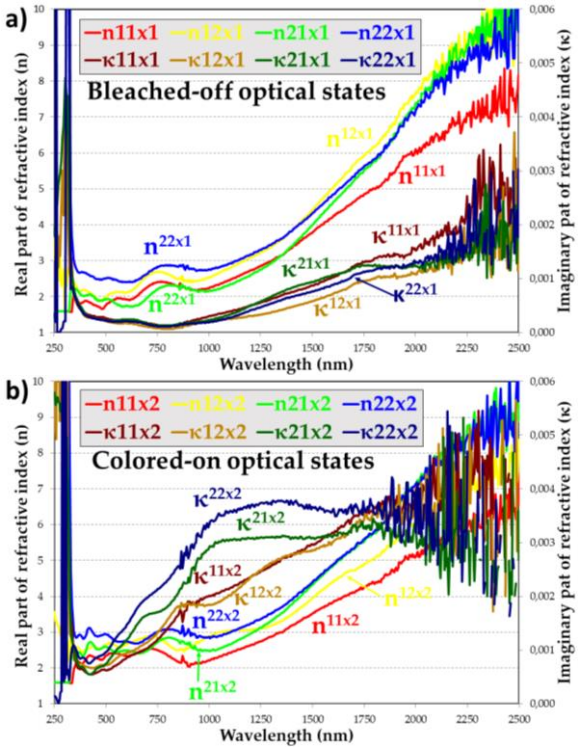

Figure 3 *Optical constants of ECDs.*

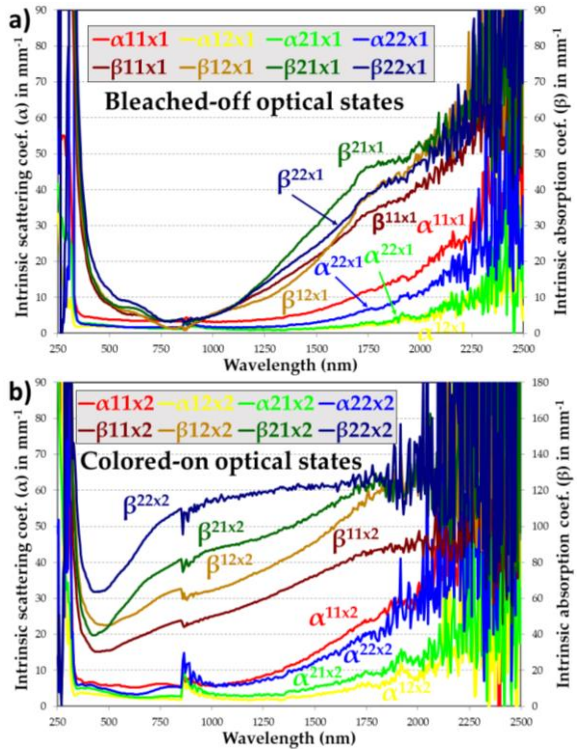

Figure 4 *Intrinsic scattering and absorption coef. of ECDs.*

5 Acknowledgement

The author is grateful to Laboratory for Spectroscopy of Materials (National Institute of Chemistry, Ljubljana), and to the mobility grants of Universidad Carlos III de Madrid.

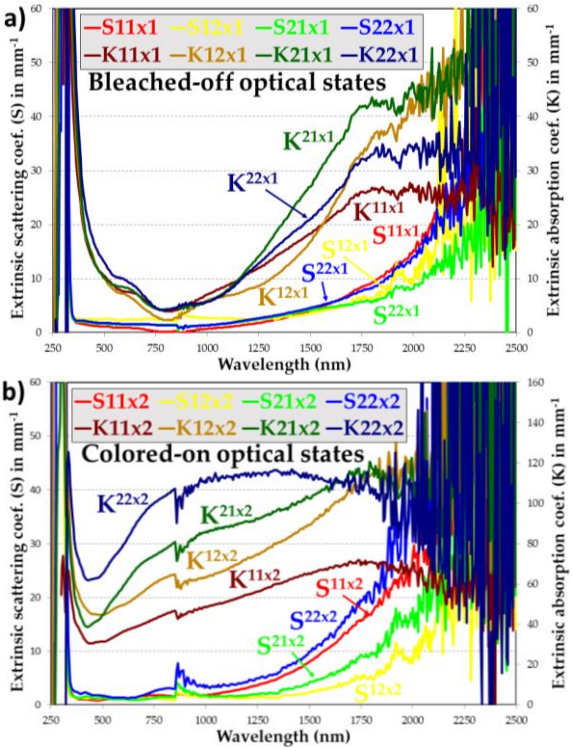

Figure 5 *Extrinsic scattering and absorption coef. of ECDs.*

6 References

[1] C.F. Bohren, and D.R. Huffman, *Absorption and scattering of light by small particles* (Wiley, New-York, 1983).

[2] Beasley J.K., Atkins J.T., Billmeyer Jr F.W., Scattering and absorption of light in turbid media, in Electromagnetic Scattering, R. L. Rowell and R. S. Stein, (Gordon and Breach, New York, 1967).

[3] Maheu B., Letoulouzan J.N., Gouesbet G., Four-flux models to solve the scattering transfer equation in terms of Lorenz–Mie parameters, Applied Optics 23: 3353-62 (1984).

[4] Kubelka P., New contributions to the optics of intensely light-scattering materials. Part I, Journal of Optical Society of America 38: 448–57 (1948).

[5] Barrios D., Intrinsic and Extrinsic Scattering and Absorption Coefficients New Equations in Four-flux and Two-flux Models Used for Determining Light Intensity Gradients, Journal of Optics and Photonics Research (2024).

[6] Barrios D., Parameters of differential equations in four-flux models approximated for multilayers samples showing scattering and absorption, Journal of Quantitative Spectroscopy and Radiative Transfer (2024, sent), *XX ELS Electromagnetic Light Scattering (ELS2023).*

[7] Barrios D., Parameters of differential equations in two-flux models approximated for multilayers samples showing scattering and absorption, Journal of Quantitative Spectroscopy and Radiative Transfer (2024, sent), *XX ELS Electromagnetic Light Scattering (ELS2023).*

[8] Niklasson G.A., Granqvist C.G., Electrochromics for smart windows: thin films of tungsten oxide and nickel oxide, and devices based on these, Journal of Materials Chemistry 17(2): 127-56 (2007).

The 14th International Conference on
Laser-light and Interactions with Particles (LIP2024)
September 18-22nd, 2024, Xi'an, Shaanxi, China

INTERFEROMETRY LASER IMAGING FOR DROPEL SIZING (ILIDS) WITH NOT FULLY DEFOUSED IMAGES

Adelaida GARCIA-MAGARIÑO[1,*], Suthyvann SOR[1], Rafael BARDERA[1] and Javier MUÑOZ-CAMPILLEJO[1]

[1] Instituto Nacional de Tecnica Aeroespacial "Esteban Terradas (INTA), Madrid, 28840, Spain

Corresponding author: garciamga@inta.es

Abstract

In naval and aeronautical fluid dynamics experiments, tests are typically carried out in wind tunnels or water channels. During these tests, the instrumentation is often placed outside the testing area, necessitating the use of instrumentation with a long-range measurements. When implementing the ILIDS technique in these facilities, challenges arise related to the minimum object distance required and the degree of overlapping between droplets' interferograms. The first challenge involves meeting the Nyquist criterion for successful droplet size measurements, which demands very high resolution. To address the second challenge of minimizing the overlap issue, the authors have devised a new approach. By ensuring that droplets are not fully defocused, the image size is reduced, thereby mitigating the overlap problem. This results in the appearance of two complete overlapping circles instead of the usual circular ILIDS interferogram, with the fringe pattern emerging within the overlap region. Furthermore, the authors have developed novel image processing software and conducted experimental studies in the laboratory to evaluate the limitations of this approach. In this work the evaluation of the application of the image processing method to horizontally overlapped patterns is shown. This technique could be applied to analyse the interaction of biphasic flows on surfaces, such as measuring the bubbles produced to reduce drag on ships.

1 Introduction

The ILIDS technique, also known as Interferometric Particle Imaging (IPI) or Mie Scattering Imaging (MSI) in the literature, is an optical method that can provide immediate measurements of sizes and spatial distributions of transparent spherical particles like water droplets or bubbles within a specified field of view without invasive procedures. Originating from earlier research, the ILIDS technique relies on interference patterns created by the scattered light from a transparent, spherical particle under coherent illumination. At specific scattering angles, when the incident wave's polarization relative to the observation plane is considered, the reflected and refracted light dominate over other scattered orders, resulting in the appearance of two distinct glare points in the focal plane. Although theoretically, measuring the distance between these points could determine the droplet size accurately, achieving the necessary resolution for this measurement is challenging. However, by observing the glare points in an out-of-focus plane, interference between reflected and refracted light generates a fringe pattern. In the far-field, the number of fringes or fringe frequency is directly correlated to the droplet diameter, and through geometric optics principles, an expression can be derived. Adequate defocusing is essential to capture the entire fringe pattern effectively and prevent measurement inaccuracies. The accuracy of this geometric analysis has been extensively examined, ensuring that all required conditions are met for reliable results.

An evaluation of the challenges encountered when implementing the ILIDS technique in a wind tunnel with a 3×2 m² open elliptical test section has been carried out by the authors [2]. The primary challenge lies in the minimum object distance required and the limited defocus due to the overlap between droplets' interferograms. To address these challenges, high resolution is necessary to meet the Nyquist criteria. Consequently, instead of the usual single circle in the ILIDS technique, two complete overlapping circles with fringe patterns appearing in the overlap region are observed. The presentation will include the results of this work together with a new application of the image processing method to horizontally overlapped pattern

1.1 Theoretical Backgroud

The droplet diameter is directly related to the angular inter-fringe spacing, that is, to the number of fringes of the interferogram. That relationship can be determined via a geometrical optics analysis by obtaining the phase difference between the reflected and refracted ray paths and is given by the following expression, put forth by [22,23]:

$$d_p = \frac{2\lambda N}{\alpha}\left[\cos\left(\frac{\theta}{2}\right) + \frac{n\sin\left(\frac{\theta}{2}\right)}{\sqrt{n^2+1-2n}}\right]^{-1} \quad (1)$$

where d_p is the particle diameter, N is the number of fringes, λ is the wavelength of the laser sheet, α is the collecting angle of the optical arrangement, θ is the scattering or off-axis angle and n is the relative refractive index corresponding to a water droplet in air.

1.2 Experimental Setup

An experimental study was conducted in the laboratory using three streams of droplets of varying sizes at different object distances relevant to the wind tunnel scenario. Specifically, object distances of 1.6 m for larger droplets and 2.29 m for medium-sized and smaller droplets were chosen, resulting in field of views of 11.9 x 7.9 cm^2 and 22.7 x 15.8 cm^2, respectively.

The study utilized an off-axis angle of approximately 67° and characterized the droplet streams using shadowgraph imaging techniques, with mean diameters and uncertainties of 363±40 μm, 658±49 μm, and 844±22 μm obtained for the smaller, medium-sized, and larger droplets, respectively. The uncertainties stemmed from camera resolution limitations, uneven background illumination, and inherent algorithm uncertainties in droplet sizing. The experimental setup is shown in Fig. 1.

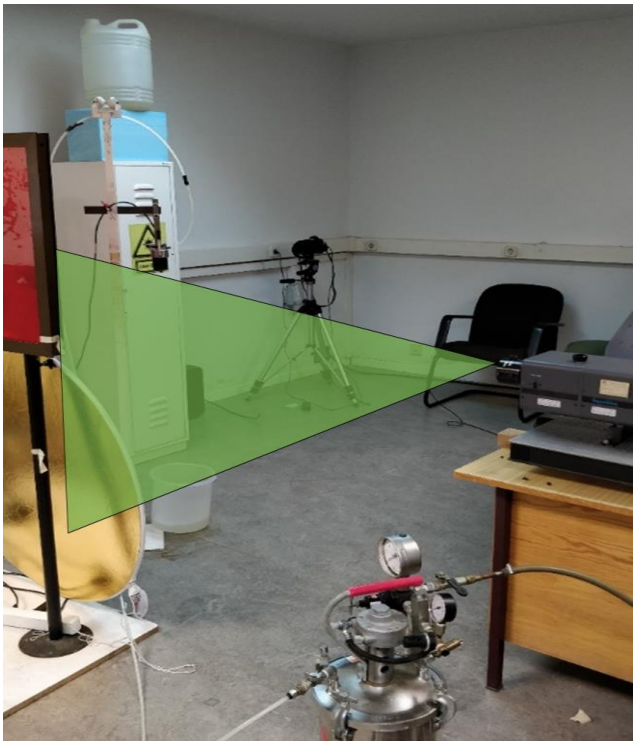

Figure 1 *Experimental Setup*

1.3 Method to isolite the finge pattern

To accurately detect and isolate these circles and fringe patterns, two new image processing methods along with one based on existing literature have been proposed. An example of the results for the three methods can be found in Fig. 2.

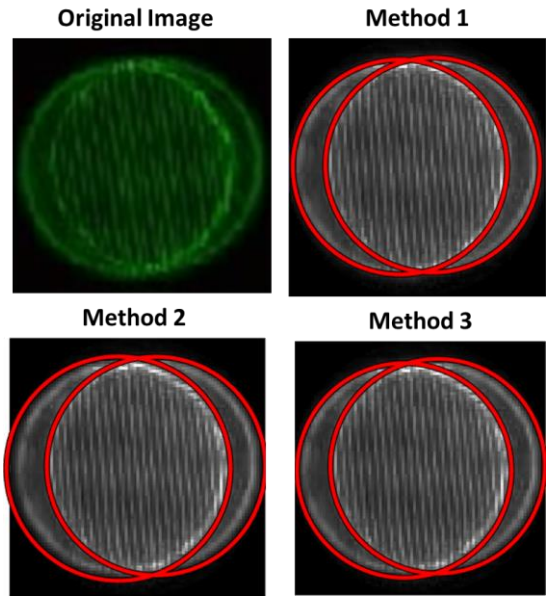

Figure 2 *An example of the results of the three methods.*

2 Application of the image processing method to horizontally overlapped pattern.

To further prove the robustness of the method, it will be implemented to locate, isolate and process a couple of horizontally overlapped interferograms. Such an overlapping has been artificially made by simply overlapping two existing interferograms just to demonstrate the capabilities of the image processing software here presented. The location and isolation of the interferograms is presented in Fig. 3.

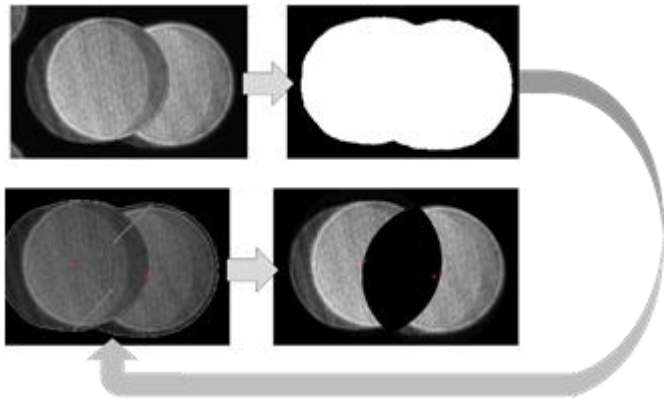

Figure 3 *Implementation to locate and isolate horizontally overlapped interferograms*

In order to assess the best out of the proposed methods, a comparative between them when isolating the fringe pattern an example is shown in Fig 4. As can be seen, both the first and third methods accurately find the desired circles inside the overlapped interferogram, whereas the second method struggles a bit more in doing so. Since the Fourier transform will extrapolate the detected fringe

frequencies in both axis to the whole height and width of the overlapping region, maximum accuracy is needed.

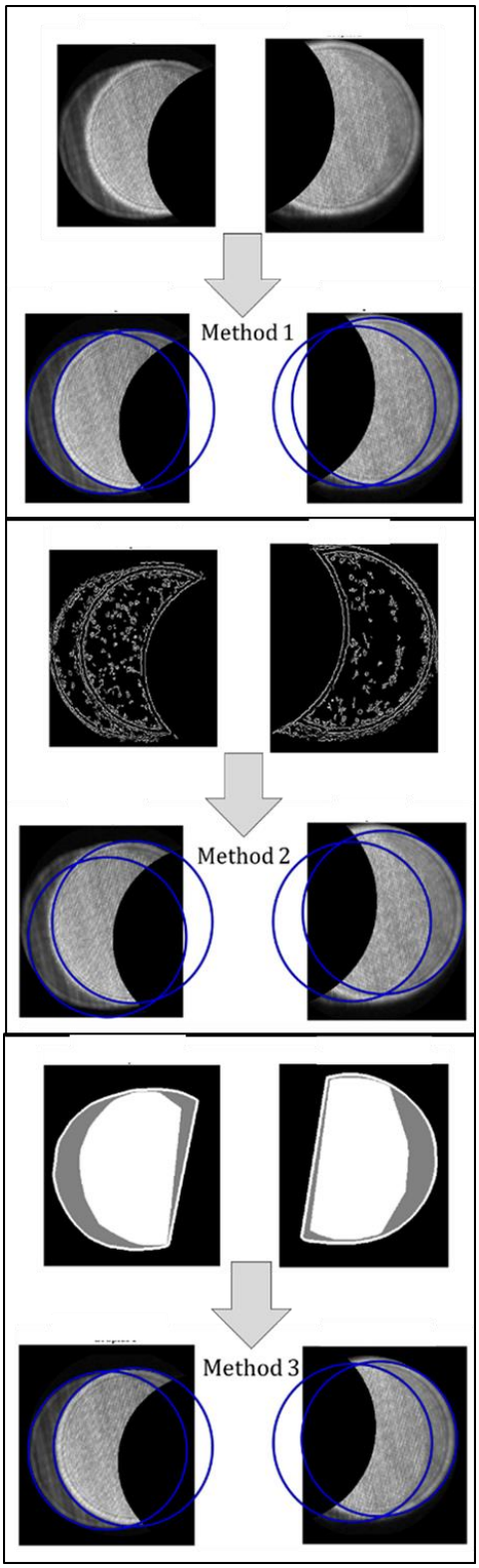

Figure 4 *Comparison between the three presented methods when isolating horizontally overlapped fringe patterns*

3 Conclusions

Comparing the ILIDS results to shadowgraph imaging, the proposed new methods demonstrated excellent performance, even with combinations of high and low intensity rings. In contrast, the method primarily based on literature struggled with detecting circles in the interferograms. Despite studying only a limited number of droplets, the uncertainties in the ILIDS results, arising from image processing software or inherent uncertainties in monodispersed droplet streams, were lower than those in shadowgraph imaging.

4 Acknowledgement

Please avoid the expression, "One of us (X. Y. Z.) thanks" Use instead "X. Y. Z. thanks…".

5 References

[1] Style: LIP references

[2] C.F. Bohren, and D.R. Huffman, *Absorption and scattering of light by small particles* (Wiley, New-York, 1983).

[3] Onofri F.R.A, Radev St. , Sentis M., Barbosa S., A physical-optics approximation of the near-critical-angle scattering by spheroidal bubbles, Optics Letters 37(22):4780-82 (2012)

[4] Barbosa S., Onofri F.R.A., Wozniak M., Touré O., Grisolia C., Optical characterization of highly ordered aggregates of colloidal nanobeads, *Int. Conf. on Lasers and Interactions with Particles (LIP2012)*, paper 7.2, 26- 30 March., Rouen, France, 2012.

The 14th International Conference on
Laser-light and Interactions with Particles (LIP2024)
September 18-22nd, 2024, Xi'an, Shaanxi, China

SAMARIUM-BASED COMPLEX SALT MICRO-/NANOPARTICLES: FROM SYNTHESIS TO LASER EXCITATION FLUORESCENCE LIFETIME DYNAMICS

Nicoleta TOSA[1,*], Alexandra FALAMAS[1], Gheorghe BORODI[1] and Lucian BARBU-TUDORAN[1,2]

[1] Molecular and Biomolecular Physics Department, National Institute for R&D of Isotopic and Molecular Technologies, 67-103 Donat, Cluj-Napoca, 400293, Romania

[2] Electron Microscopy Center, Babes-Bolyai University, 5-7 Clinicilor Street, Cluj-Napoca 400006, Romania

Corresponding author: nicoleta.tosa@itim-cj.ro

Abstract

This work reports on a high yield synthesis of micro-/nanoparticles of samarium-based complex salt through a one-pot pH controlled liquid phase process carried out in friendly conditions, starting from samarium oxide. The synthetic route reproducibility was confirmed by X-Ray diffraction (XRD) patterns of the fabricated samarium-based salt batches. Scanning Electron Microscopy (SEM) images of the samarium-based complex salt micro-/nanoparticles displayed a fractal distribution of "rod" like crystallites with average length of 150 nm, and 30-80 nm width, in agreement with the sizes calculated from XRD. Time-resolved fluorescence measurements of samarium complex salt revealed two fluorescence decay lifetimes of 0.46 ns and 3.72 ns.

1 Introduction

Rare-earth (RE) elements are of great interest due to their special magnetic, electronic and optical properties [1]. Particularly, sodium rare-earth fluorides possess low phonon energy and are known as excellent host matrixes for performing luminescence [2], up-conversion properties [3] and fluorescence imaging [4]. Complex fluorides have been obtained by solid-state reactions and liquid phase synthesis at elevated temperatures and ambient pressure using mixed organic solvents, mixed hydrophilic solvents or high-boiling solvents within inert atmosphere thermolysis. Hydrothermal method was used to synthesize complex fluorides, then lanthanide complex fluorides with different phases or prismatic sodium and samarium tetrafluorides ($NaSmF_4$) nanotube but it needed expensive autoclaves, and did not allow the observation during the crystal growth.

Sodium RE complex fluorides can also be obtained as crystalline powder through a two-step synthesis and used for further doping with lanthanide to obtain pure monocrystals for lasers through the hydrothermal method. This work reports on a high yield synthesis of complex samarium-based particles through a one-pot pH controlled liquid phase process carried out, in aqueous medium at ambient pressure, starting from samarium oxide. The one-pot procedure allowed to improve the synthesis yield, control the crystallites size, and therefore their lifetime fluorescence dynamics.

2 Experimental

2.1 Synthesis

All chemicals used were of analytical grade and used without purification. Samarium oxide (Sm_2O_3) of 99.99% purity was purchased from Sigma Aldrich. Ethylenediaminetetraacetic acid (Complexon II), sodium fluoride (NaF), hydrochloric acid (HCl) and absolute ethanol (C_2H_5OH) were purchased from Merck. Double-distilled water was obtained in the laboratory.

A mixture of samarium oxide (Sm_2O_3) (12.526 mmol), concentrated HCl (36.5% mass fraction, density 1.18 g/mL) and water was refluxed at ambient pressure at controlled pH in a two-neck round-bottom flask for 10 to 14 hours to prepare samarium chloride ($SmCl_3$) intermediate. The $SmCl_3$ solution concentration was adjusted to 0.2 mol/L, then an equal volume of Complexon II solution 0.2 mol/L (25.052 mmol) and a large excess of NaF powder (0.25052 mol) were added. The reaction mixture was left under magnetically stirring at room temperature for over 24 hours and then it was worked up by centrifugation at 10000 rpm for several times. The $NaSmF_4$ crude precipitate was washed with double-distilled water and absolute ethanol, then dried under reduced pressure to obtain 4.59482 g $NaSmF_4$ with a 92% yield.

2.2 Microstructure characterization

XRD patterns of the samples were obtained by using a Bruker D8 Advanced X-ray diffractometer equipped with a Ge (111) monochromator in the incident beam (to obtain only Cu Kα1 radiation, λ = 1.54056 Å) and LynxEye super speed detector. The diffraction data were recorded for 2θ between 10° and 80° with a step of 0.02°. SEM images were obtained using a cold field emission Hitachi SU8230 system operating at accelerating voltage of 30 kV and magnifications from 5000x to 150000x. All samples were coated before viewing with a 5-nm conductive gold layer to increase the contrast level in the secondary electron images.

2.3 Fluorescence measurements

Fluorescence decays in the time domain of micro-/nanoparticles of samarium complex salt were investigated at ambient temperature by time-correlated single photon counting (TCSPC) technique using for pumping an

Yb:KGW laser (Pharos, Light Conversion) with emission at 1030 nm wavelength and 6 W average power. Pulses of 170 fs duration are emitted at 80 kHz repetition rate and 75 μJ energy per pulse. The main part of the laser pulse is used for pumping a collinear optical parametric amplifier (Orpheus, Light Conversion) yielding tuneable output between 200-2600 nm.

The TCSPC measurements were performed using Chimera module (Light Conversion) to obtain high-accuracy kinetic traces in the 200 ps – 5 μs domain. The samples were excited at 403 nm with 16 mW at the sample place. The TCSPC fluorescence signal was recorded in the 550-700 nm spectral range with 1 nm step size and an integration time of 10 s at each point. The instrument response function (IRF) had a duration of ~630 ps.

2.4 Data analysis

For data analysis was employed both Global Target Analysis (GTA), which considers discreet compartments connected by rate equation and fitting of the kinetic curves, using double exponential functions to study the electron dynamics. Shortly, when using GTA the pump pulse excites the population in one or several compartments and it is transferred from one compartment to another according to the chosen connectivity scheme. It was assumed that the pump pulse I(t), a quantity proportional to the instrument response function, excited the population to a first compartment. From the first compartment, the population (c_1) was transferred to a second one with the characteristic time τ_1. The population (c_2) returned to the ground state with the characteristic time τ_2, as shown in Eq. (1):

$$\frac{dc_1(t)}{dt} = I(t)\frac{1}{\tau_1}c_1(t)$$
$$\frac{dc_2(t)}{dt} = \frac{1}{\tau_1}c_1(t) - \frac{1}{\tau_2}c_2(t) \quad (1).$$

The fitting of the kinetic traces using a double exponential function was performed using Eq. (2):

$$y = y_0 + A_1 \exp(-x/t_1) + A_2 \exp(-x/t_2) \quad (2),$$

where A_1 and A_2 are the amplitudes (the number of excited particles), t_1 and t_2 are the decay constants, and y_0 is the offset.

3 Results and discussion

The synthesis was conducted for three batches (B1, B2 and B3) at increased refluxing periods in the first stage to optimize the process. The yield of $NaSmF_4$ (related to Sm_2O_3 transformation) was 92% for B1(10H), 94.7% for B2(12H) and 95% for B3(14H). Thus, the increase of the refluxing time in the first stage of the process determined the increase of the $NaSmF_4$ yield in the second stage.

In Figure 1 are shown the XRD patterns for Sm_2O_3 and for the three batches of $NaSmF_4$ (Fig. 1), the Miller Indices being assigned in each case [6].

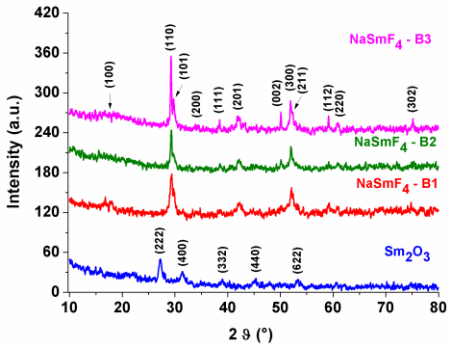

Figure 1 *Comparative XRD patterns recorded in powder for Sm_2O_3 and the three $NaSmF_4$ batches after 10, 12 and 14 hours, respectively.*

The XRD patterns of $NaSmF_4$ displayed a series of well resolved peaks with high intensities (110), (101), (112), (002), and (300). The Sm_2O_3 crystallizes in cubic system space group I_{a-3} having the lattice parameter a=10.915Å, while $NaSmF_4$ belongs to hexagonal system with cell parameters a=6.051Å and c=3.64Å. $NaSmF_4$ crystallite size of has been determined using Scherrer relationship [6] as follows: D=185Å (B1); D=328Å (B2); D=475Å (B3). Figure. 1 shows that the characteristic peaks of the starting material (Sm_2O_3) disappeared and new peaks emerged, proving its conversion into the $NaSmF_4$. The increase of the refluxing time for the Sm_2O_3 determined a better resolution and higher intensities of the $NaSmF_4$ characteristic peaks. The XRD patterns of the $NaSmF_4$ batches are very similar, emphasizing the synthetic route's high reproducibility.

SEM images of Sm_2O_3 showed a multiple flat layer morphology with uneven surfaces but homogeneous as structural aspect (Fig. 2a):

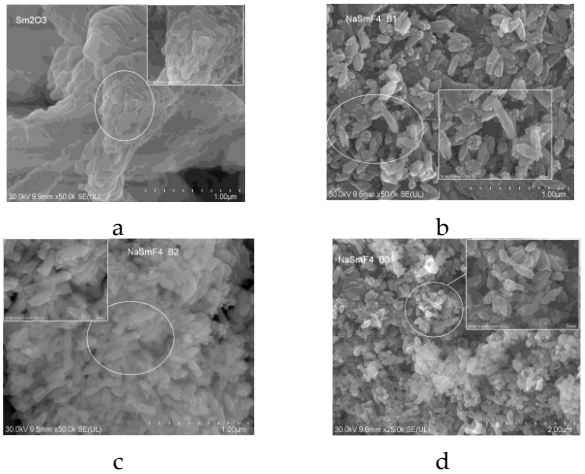

Figure 2 *SEM images recorded in powder for: a. Sm_2O_3; b. $NaSmF_4$-first batch (10 H, B1); c. $NaSmF_4$-second batch (12 H, B2); d. $NaSmF_4$-third batch (14 H, B3).*

SEM images of $NaSmF_4$ (Figure 2b-d) showed the presence of multiple small crystallites with similar "rod" like shapes with average size of 150 nm length and 30-80

nm width. The height of the crystallites was estimated to 30-80 nm, in agreement with the hexagonal system characteristics determined by XRD. The crystallites sizes became larger when the Sm_2O_3 refluxing time increased. SEM images recorded on Sm_2O_3 and $NaSmF_4$ powders showed fractal structures with distinct morphologies.

Time-resolved fluorescence data have been recorded on a $NaSmF_4$ spot dropped on a quartz plate. Pumping with 403 nm, the fluorescence response showed a maximum at 575 nm and a smaller peak around 650 nm (Fig. 3).

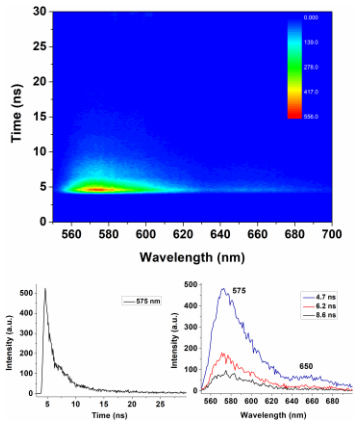

Figure 3 *The dataset carpet showing the kinetics of the $NaSmF_4$ (above), a kinetic curve at 575 nm (bottom left), and the fluorescence spectra recorded at different time moments (bottom right). Pump beam was set at 403 nm.*

The data set was fit using GTA (Eq. (2)) and two decay times were obtained: τ_1=0.46±0.18 ns and τ_2=3.72±0.81 ns. Next, successive drops of the samarium salt were added on the glass quartz, one above the other, and the TCSPC signal at 575 nm after each spot addition was measured. The fluorescence signal decreased of with the $NaSmF_4$ concentration increase, until one point when the signal started to increase again. The normalized fluorescence TCSPC signal at each concentration is shown in Figure 4.

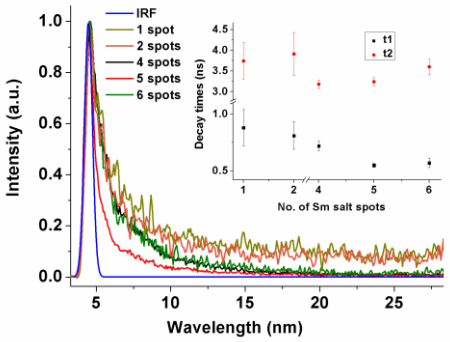

Figure 4 *TCSPC normalized kinetic curves of $NaSmF_4$ showing its dependency on the concentration and instrument response function. Pump beam was set at 403 nm. The inset shows the decay times obtained for each curve after fitting with a double exponential function.*

A decrease is observed when going from one spot of salt to 4 and 5 spots, respectively. Due to a local thinning of the $NaSmF_4$ layer, when adding one more spot to the sample, the fluorescence trace followed the same decay as for 4 spots. The decay of the samarium salt is multiexponential and the best fit was obtained using two decay times. Figure 4 (inset) shows the decay times for each curve using a double exponential function shown by Eq. (2). The resulted times are comparable to the ones obtained using GTA. Both, the short and the longer times decreased with increasing the sample concentration. OK

4 Conclusions

Micro-/nanoparticles of samarium-based complex salt were synthesized through a one-pot pH controlled liquid phase process carried out in aqueous medium at ambient pressure, starting from samarium oxide. The prolongation of the refluxing period increased the synthesis yield and the size of the crystallites. The XRD patterns of the obtained batches of samarium complex salt are very similar, emphasizing the high reproducibility of the synthetic route. SEM images of the particles in all samarium complex salt batches displayed a fractal distribution of "rod" like crystallites with average size of 150 nm length, and 30-80 nm width, in fair agreement with the XRD calculated sizes. Time-resolved fluorescence data analysis showed the best fit for two decay times at 0.46 ns and 3.72 ns, both decreasing with increasing the sample concentration.

5 Acknowledgement

The authors acknowledge the financial support of the Romanian Ministry of Research, Innovation and Digitization (MCID) through the "Nucleu" Program within the National Plan for Research, Development and Innovation 2022-2027, project code PN 23 24 01 02.

6 References

[1] Tan C., Xu D., Zhang K., Tian X., Cai W., Electronic and Magnetic Properties of Rare-Earth Metals Doped ZnO Monolayer, J Nanomater 2015: 329570, 1-8 (2015).

[2] Stouwdam J.-W., Hebbink G.A., Huskens J., van Veggel F.C.J.M., Lanthanide-Doped Nanoparticles with Excellent Luminescent Properties in Organic Media, Chem Mater. 15(24):4604–16 (2003)

[3] Gai S., Yang G., Li X., Li C., Dai Y., He F., Yang P., Facile synthesis and up-conversion properties of monodisperse rare earth fluoride nanocrystals. Dalton Trans. 41:11716-24 (2012)

[4] Chen J.Y., Selvin P.R., Lifetime- and color-tailored fluorophores in the micro- to millisecond time regime. J Am Chem Soc. 122:657-60 (2000)

[5] H.P. Klug, I.E. Alexander, X-Ray Diffraction Procedure for Polycrystalline and Amorphous Materials (Wiley, New-York, 1974), 618.

SUM-RULES METHODS FOR SPECTRAL RESPONSE FUNCTIONS

Brian Stout[1]

[1] *Aix-Marseille Université, CNRS, Centrale Marseille, Institut Fresnel, 13397 Marseille, France*

brian.stout@fresnel.fr

RÉSUMÉ

Recent progress in modeling light-matter interaction in terms of Resonant/QNM interactions is reviewed. It is argued that such descriptions can be refined by formulating them in terms of scattering response functions like S and T-matrices. This methodology allows the derivation of sum rules, which in turn can be used to formulate approximations that satisfy underlying conservation laws. This discussion is demonstrated in the concrete case of a simple, solvable, scattering system, with applications to more complex geometries also discussed.

MOTS-CLEFS : *Scattering , Spectral expansions, Quasi-Normal Modes, dispersion*

1. INTRODUCTION

It has been repeatedly demonstrated that Resonant State or (also known as Quasi-normal modes) can be used to describe the response functions of systems when the excitation frequency is near a resonance. Although the complex eigen-frequencies of the modes in these expansions can be determined with numerical solvers and even the '*coupling constants*' of these modes can be determined via adequate 'normalization', the use of these expansions to make quantitative predictions still requires the addition of 'non-resonant' contributions that vary smoothly as functions of frequency. These 'non-resonant' contributions are typically added heuristically, but we demonstrate in the case of simple (dispersionless and dispersive) scattering systems that Resonant State (QNM) eigenvalues must obey sum rules which can be used to determine the non-resonant contributions analytically.

In the interest of simplicity, we illustrate our demonstrations in a concrete setting by considering the S-matrix of a solvable 1D scatterer at arbitrary incidence angles as shown in the schematic of fig. 1 Despite its relative simplicity, this system is found to exhibit essentially all of the characteristic behaviors

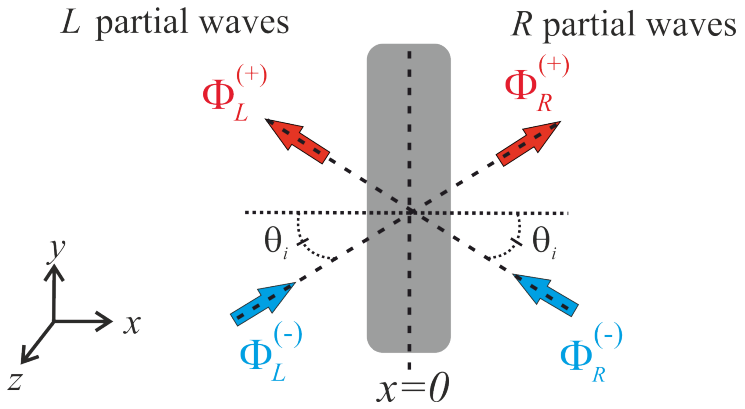

FIGURE 1 : Schematic of an S-matrix representation for a mirror symmetric 1D infinite 'slab' of thickness d immersed in a background medium with incoming partial waves impinging on the surface at an incident angle θ_i from the left(L) or right(R).

of more complex systems and higher dimensionalities.

A pedagogical advantage of this system is that its response can be expressed as a '2×2' S-matrix acting on the coefficients, $C_{L,R}^{(\pm)}$, of a two component partial wave basis :

$$C_{p,\alpha}^{(+)}(\omega) \equiv \begin{bmatrix} C_{p,\alpha,L}^{(+)} \\ C_{p,\alpha,R}^{(+)} \end{bmatrix} = \begin{bmatrix} r_{p,\alpha} & t_{p,\alpha} \\ t_{p,\alpha} & r_{p,\alpha} \end{bmatrix} \begin{bmatrix} C_{p,\alpha,L}^{(-)} \\ C_{p,\alpha,R}^{(-)} \end{bmatrix} \equiv \bar{\bar{S}}(\omega).C_{p,\alpha}^{(-)}(\omega) \,, \tag{1}$$

where, $r_{p,\alpha}$ and $t_{p,\alpha}$ are respectively the reflection and transmission coefficients, with the index p designating the polarization states (TE,TM).

The frequency dependent spectral reflection and transmission coefficients of this S-matrix can be written entirely in the form of a RS spectral expansion on electromagnetic eigenvalue information to obtain :

$$\begin{aligned} r_{p,\alpha}(\omega) &= e^{-i\beta kd}\left[r_{p,\alpha}^{(\text{n.r.})}(\omega) + \sum_{\ell=-\infty}^{\infty}\left(\frac{\mathscr{R}_{p,\alpha}}{kd-\kappa_q^{(+)}d} + \frac{\mathscr{R}_{p,\alpha}}{kd-\kappa_q^{(+)}d}\right)\right] \\ t_{p,\alpha}(\omega) &= e^{-i\beta kd}\sum_{\ell=-\infty}^{\infty}\left(\frac{\mathscr{R}_{p,\alpha}}{kd-\kappa_q^{(+)}d} - \frac{\mathscr{R}_{p,\alpha}}{kd-\kappa_q^{(+)}d}\right) \,, \end{aligned} \tag{2}$$

where for brevity the index $q(p,\alpha,j,\ell)$ combines multipole indices (p,α,j) with an additional discrete RS index, ℓ, for designating the complete set of eigenfrequencies. The terms $\kappa_q^{(+)}$ and $\mathscr{R}_p$ are respectively RS eigenvalues and their residues (coupling constants). The eigenfrequencies $\kappa_q^{(+)}$ can be determined by numerical solvers, while the residues $\mathscr{R}_p$ can also be determined numerically (and analytically in special cases like this one).

A key observation is that non-resonant contributions, $r_{p,\alpha}^{(\text{n.r.})}(\omega)$, are a general feature of response functions, and they can be deduced from the sum rules of the RS eigenvalues. The addition of such slowly varying functions to RS expansions, like in eq. (2), are crucial for enabling them to produce quantitative predictions. Finally, we show how sum-rules can be exploited in order to enable truncated RS expansions to produce approximations that satisfy underlying conservation laws.

RÉFÉRENCES

[1] Stout *et al*, New Journal of Physics **23**, 083004, (2021)

[2] Ben Soltane *et al*, Laser & Photonics Reviews, 2200141, (2022).

The 14th International Conference on
Laser-light and Interactions with Particles (LIP2024)
September 18-22nd, 2024, Xi'an, Shaanxi, China

FANO-RESONANCE ASSISTED OPTICAL PULLING FORCE ON PLASMONIC NANOPARTICLES UNDER FEMTOSECOND PULSED EXCITATION

Sumit YADAV[1], Anita DEVI[1,#] and Arijit K DE[2,*]

[1] Condensed phase dynamics group, Department of Physical Sciences, Indian Institute of Science Education and Research (IISER) Mohali, Knowledge City, Sector 81, SAS Nagar, Punjab 140306, India
[2] Condensed phase dynamics group, Department of Chemical Sciences, Indian Institute of Science Education and Research (IISER) Mohali, Knowledge City, Sector 81, SAS Nagar, Punjab 140306, India
[#] Present affiliation: University of Alberta, Edmonton, AB T6G 2R3, Canada

*Corresponding author: akde@iisermohali.ac.in

Abstract

Here, we present the effects of optical nonlinearity on the trapping force and potential of silver and silver-polystyrene core-shell type nanoparticles under femtosecond pulsed excitation using generalized Lorenz-Mie theory. Depending on the particle-size and core:shell size contribution in core-shell type particle, the Fano-resonance induces an optical pulling force on particle which is further controlled by the nonlinear optical effects under femtosecond pulsed excitation.

Based on the concept of radiation pressure, laser tweezers facilitate spatial confinement and a controlled manipulation of nano-/micron-sized particles [1]. A harmonic potential governed by the gradient force, termed by the gradient of intensity field, confines the particles at the focus of the laser beam. Opposes to gradient force, an asymmetric nature of scattering force (and absorption force, particularly in metallic particles) pushes the particles along the propagation direction of the laser beam. Therefore, the overall trapping potential is asymmetric in nature along the axial direction. Metallic nanoparticles are challenging to stably trap because of their high scattering and absorption forces, however, these particles are also interesting to explore owing to their intriguing plasmonic properties such as surface plasmon plaritons or localized surface plasmon resonance, depending on the particle-size. Due to their plasmonic properties, the magnitude as well as the directionality of the trapping forces are very much dependent on particle-size [2-3]. For instance, an alteration in direction of scattering force (opposite to the direction of beam propagation) was shown because of the enhanced forward scattering force over backward scattering force due to the presence of Fano-resonance [4]. Recently, utilizing the femtosecond pulsed laser instead of continuous wave (CW) laser, tunability in the trapping efficiency was presented for dielectric [5], metallic [6-7] and hybrid nanoparticles [8], owing to the effects of optical nonlinearity, induced by the peak intensity of ultrashort pulses. Using localized approximation of generalized Lorenz-Mie theory (GLMT), the appearance of Fano-resonance for silver nanoparticles with particle-size was demonstrated along with the effect of optical nonlinearity under pulsed excitation [7], which was not explicitly observed in an earlier study using dipole approximation [6]. The presence of Fano-resonance *i.e.* the interference of sharp dipole resonance band with the broadband continuum, enhances the forward scattering force over backward scattering force which results to a switch in the direction of scattering force towards the light source (opposite to the beam propagation) also known as pulling force [4, 9-10]. Thus, Fano-resonance can switch the directionality of trapping forces depending on the particle-size. Here, we present the effects of optical nonlinearity, under pulsed excitation, on the appearance of Fano-resonance and consequently on the trapping efficiency of silver nanoparticles [7]. The discussion further extends to the tunability of appearance of Fano-resonance in silver-polystyrene core-shell type nanoparticles by the variation of contribution of core and shell size along with the effect of optical nonlinearity under pulsed excitation [11].

To numerically calculate the trapping force and potential, the localized approximation of GLMT [12-14] is used and the optical nonlinearity is introduced in refractive index of particle upto seventh order of polarizability [8]. We used the parameters of commercially available Ti:sapphire oscillator (800 nm central wavelength, 76 MHz repetition rate, and 120 fs pulse duration).

Figure 1 shows a comparison of trapping forces and corresponding potentials for 10 nm and 20 nm silver nanoparticles under CW and pulsed excitation. The trapping potential is asymmetric in nature along the axial direction because of the contribution of scattering and absorption forces. The red or blue double headed arrows in figure 1c represent the quantity 'escape potential (i.e. height of potential barrier to escape the particle from trap)' and dashed black double-headed arrow represents the quantity 'absolute potential (i.e. absolute depth of the

potential well)' [5]. Usually, the direction of escape of particle or escape potential is along the direction of beam propagation because of the dominating backward scattering force over forward scattering force. The pulsed excitation provides an enhancement in the trapping force and potential over CW excitation, owing to the effect of optical nonlinearity. Notably, for 10 nm silver nanoparticle

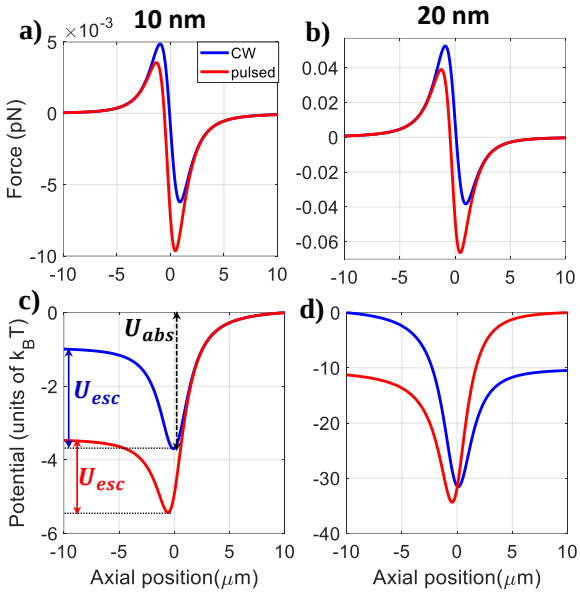

Figure 1 *(a, b) Trapping force and (c, d) corresponding potential for 10 nm and 20 nm sized silver nanoparticles under CW (blue curves) and pulsed (red curve) excitation at 100 mW average power. Red and blue double-headed arrows represent escape potential and dashed double-headed black arrow represent the absolute potential.*

the direction of asymmetric nature of potential (or direction of escape potential) is opposite to the beam propagation (-z to +z) under both CW and pulsed excitations because of the presence of Fano-resonance which enhances the negative optical scattering force or the forward scattering force over backward scattering force. Interestingly, for 20 nm particle-size the direction of escape potential is along the beam propagation under CW excitation, which is due to the enhancement in the backward scattering force with increase in particle-size. However, under pulsed excitation, the direction of escape potential is opposite to the beam propagation, which represents the dominance of forward scattering force over backward scattering force. Therefore, the appearance of Fano-resonance depends on particle-size only under CW excitation, however, under pulsed excitation it depends on particle-size as well as the excitation laser power because of the contribution optical nonlinearity.

Considering the dependence of Fano-resonance on the particle-size, we are further interested to explore the presence of Fano-resonance in core-shell type of nanoparticles and the effects of optical nonlinearity under pulsed excitation.

Figure 2 shows the trapping force and corresponding potential for polystyrene-silver core-shell type nanoparticles under CW and pulsed excitation. The representation of contribution of core and shell size in particle is as, 13-20 nm where, 13 nm is core radius of polystyrene embedded in silver shell of thickness 7 nm (or the outer radius of 20 nm). Under CW excitation, the transition in the direction of escape potential from +z to –z is observed with increase in core size from 13 nm to 14 nm in a fixed particle-size of 20 nm, as shown in figure 2c. The trapping potential of bare type silver nanoparticle of 20 nm size exhibits the direction of escape potential along the +z because of the dominating backward scattering, as shown in figure 1d. However, the forward scattering can be enhanced by using a core-shell type structure of particle owing to the presence of Fano-resonance, as presented by the 14-20 nm polystyrene-silver nanoparticle in figure 2c. Thus, the Fano-resonance can be tuned by the size contribution of core and shell in a fixed size of particle [16-18].

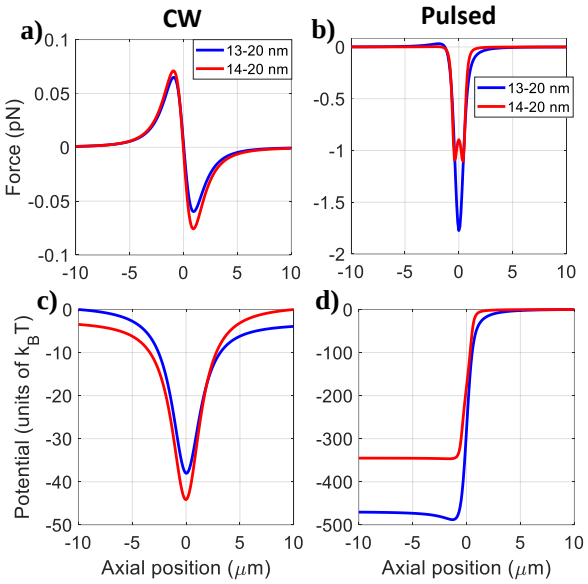

Figure 2 *(a, b) Trapping force and (c, d) corresponding potential for 13-20 nm (blue curve) and 14-20 nm (red curve) polystyrene-silver core-shell nanoparticles under (a, c) CW and (b, d) pulsed excitation (data of 14-20 nm particle is factored by 10 for a clear comparison with 13-20 nm particle) at 100 mW average power.*

Under pulsed excitation, the optical nonlinearity is incorporated for both the materials (polystyrene and silver). As the optical nonlinearity is intensity dependent, therefore its contribution depends on the axial position which results in a splitting in the trapping forces, as shown in figure 2b for 13-20 nm particle. Interestingly, a sharp enhancement in trapping force and corresponding

potential is observed for 14-20 nm particle, which is attributed to the field enhancement at the metal-dielectric interface owing to the size-dependent plasmonic properties of metal layer [19-20].

Moreover, we discuss how the switching of material of outer layer affects the trapping force and potential because of the presence of Fano-resonance and the effects of optical nonlinearity under pulsed excitation with the power variation. The spatial confinement and controlled manipulation of plasmonic nanoparticles can have potential applications in the field of nanotechnology and biomedical science.

References

[1] Ashkin A., Optical trapping and manipulation of neutral particles using lasers: A reprint volume with commentaries, World Scientific (2006).

[2] Kolbow J. D., Lindquist N. C., Ertsgaard C. T., Yoo D., and Oh S.-H., Nano-Optical Tweezers: Methods and Applications for Trapping Single Molecules and Nanoparticles, Chem. Phys. Chem. 22: 1409 (2021).

[3] Hu Y., Nieminen T. A., Heckenberg N. R., and Rubinsztein-Dunlop H., Antireflection coating for improved optical trapping, J. Appl. Phys. 103: 093119 (2008).

[4] Chen H., Liu S., Zi J., and Lin Z., Fano Resonance-Induced Negative Optical Scattering Force on Plasmonic Nanoparticles, ACS Nano 9: 1926-1935 (2015).

[5] Devi A., and De A. K., Theoretical investigation on nonlinear optical effects in laser trapping of dielectric nanoparticles with ultrafast pulsed excitation, Opt. Express 24: 21485–21496 (2016).

[6] Devi A., Nair S. S., and De A. K., Disappearance and reappearance of an optical trap for silver nanoparticles under femtosecond pulsed excitation: A theoretical investigation, EPL 126: 28002 (2019).

[7] Yadav S., Devi A., and De A. K., Synergistic effect of Fano resonance and optical nonlinearity in laser trapping of silver nanoparticles, Phys. Rev. A 102: 043511 (2020).

[8] Devi A., Nair S. S., Yadav S., and De A. K., Controlling optical trapping of metal–dielectric hybrid nanoparticles under ultrafast pulsed excitation: a theoretical investigation, Nanoscale Adv. 3: 3288–3297 (2021).

[9] Yang Y., Li J., and Li Z.-Y., Fano resonance of the ultrasensitve optical force excited by Gaussian evanescent field, J. Opt. 17: 075004 (2015).

[10] Chen J., Ng J., Lin Z., and Chan C. T., Optical pulling force, Nat. Photonics 5: 531–534 (2011).

[11] Yadav S., Devi A., and De A. K., Generalized Lorenz-Mie theory of nonlinear optical trapping of core/shell hybrid nanoparticles, *Proc. SPIE 12017, Complex Light and Optical Forces XVI*, 120170D (2022).

[12] Gouesbet G., Maheu B., and Gréhan G., Light scattering from a sphere arbitrarily located in a Gaussian beam, using a Bromwich formulation, JOSA A 5: 1427–1443 (1988).

[13] Gouesbet G., Grehan G., and Maheu B., Computations of the gn coefficients in the generalized Lorenz-Mie theory using three different methods, Appl. Opt. 27: 4874–4883 (1988).

[14] Gouesbet G., Gréhan G., and Maheu B., Localized interpretation to compute all the coefficients gnm in the generalized Lorenz–Mie theory, JOSA A 7: 998–1007 (1990).

[15] Gouesbet G., and Gréhan G., Generalized Lorenz-Mie Theories, Springer Berlin Heidelberg (2011).

[16] Yang Z.-J., Wang Q.-Q., and Lin H.-Q., Tunable two types of Fano resonances in metal–dielectric core–shell nanoparticle clusters, Appl. Phys. Lett. 103: 111115 (2013).

[17] Hayashi S., Nesterenko D. V., Rahmouni A., Ishitobi H., Inouye Y., Kawata S., and Sekkat Z., Light-tunable Fano resonance in metal-dielectric multilayer structures, Sci. Rep. 6: 33144 (2016).

[18] Rajput N. S., Shao-Horn Y., Li X.-H., Kim S.-G., and Jouiad M., Investigation of plasmon resonance in metal/dielectric nanocavities for high-efficiency photocatalytic device, Phys. Chem. Chem. Phys. 19: 16989–16999 (2017).

[19] Miroshnichenko A. E., Off-resonance field enhancement by spherical nanoshells, Phys. Rev. A 81: 053818 (2010).

[20] Yu P., Yao Y., Wu J., Niu X., Rogach A. L., and Wang Z., Effects of Plasmonic Metal Core -Dielectric Shell Nanoparticles on the Broadband Light Absorption Enhancement in Thin Film Solar Cells, Sci. Rep. 7: 7696 (2017).

The 14th International Conference on
Laser-light and Interactions with Particles (LIP2024)
September 18-22nd, 2024, Xi'an, Shaanxi, China

SIZE-MEDIATED PHOTOPHORESIS OF A CORE-SHELL MICROPARTICLE

Yury GEINTS[1,*], Ekaterina PANINA[1]

[1] NOI Lab., V.E. Zuev Institute of Atmospheric Optics SB RAS, Zuev Square 1, 634021, Tomsk, Russia

Corresponding author: ygeints@iao.ru

Abstract

Multilayer microparticles with a liquid core and a polycomposite light-absorbing shell (microcapsules) are important components of modern bio- and medical technologies, in particular, as transport microcontainers in the system of targeted drug delivery. The opening of microcapsule shell and payload release can be performed by the optical radiation. Photophoretic forces, as well as radiation pressure forces, are mechanical forces by their nature and can cause the movement of microcapsules during the opening cycle. We present the numerical model of photophoresis of a microcapsule illuminated by an intense laser pulse. The numerical simulation of the temperature field in a spherical microcapsule surrounded by auxiliary nanoparticles serving for boosting capsule heating is carried out. The spatial distribution of the absorbed radiation power as well as the temporal dynamics of heating of microcapsules with different absorption are investigated in detail. We show that under the action of net optical force, the microcapsule can move along the laser radiation both forward and backward, depending on the conditions of radiation absorption.

1 INTRODUCTION

Currently, the technology of microencapsulation of various substances is increasingly developed for use in numerous branches of industry, science and technology [1]. The multifunctionality of a microcapsule as a transport microcontainer implies its active targeted transportation to the desired point of a biological or other substance. When illuminated by an optical radiation, a small suspended particle experiences a light pressure force and a photophoretic force, which arises due to the unevenly heated particle surface. In this contribution, we numerically simulate the temporal dynamics of the spatial distribution of capsule temperature and calculate the forces arising from the gradient thermal phoresis and direct light pressure.

1.1 Photophoresis in an absorbing spherical microparticle: Formulation

The force due to the radiation-stimulated thermal gradient ($F_{\Delta T}$) arises from the inhomogeneity of the particle temperature. The molecules of the medium surrounding the particle leave its hotter surface with more energy on average than molecules leaving the colder part, thus creating an effective mechanical force directed from the hot to the cold side of the particle. Meanwhile, under the action of the phoretic force $F_{\Delta T}$ the particle moves along the axis of laser radiation action (both forward and backward), which with a proper configuration of the microsystem can balance the force of gravity and lead to levitation of the particle with respect to Earth's gravitation.

In the continuous medium approximation, which is valid at small Knudsen numbers (Kn<<1) the following expression can be used for photophoresis force $F_{\Delta T}$ calculation [2]:

$$F_{\Delta T} = D\left(p^*/p\right)R\Delta T \ . \qquad (1)$$

Here, the coefficient D is determined only by the properties of the environment surrounding the particle, p is environmental pressure, and p^* is some reference pressure value depending among other things on the radius R of the particle. The parameter ΔT defines the average temperature difference between the illuminated and shadow parts of the particle. It can be seen that depending on the sign of this value photophoresis can be omnidirectional, i.e. both along and against the action of optical radiation. Despite the rather simple form of Eq. (1), the main difficulty in its use in practical calculations of photophoresis is the calculation of the value ΔT since it requires solving the complete problem of particle heating by optical radiation.

The corresponding thermophysical problem is considered in the isobaric approximation supplemented by the optical scattering problem based on the Helmholtz equation for the electromagnetic field.

1.2 Numerical model, results and discussion

For the numerical calculations we employ COMSOL Multiphysics software, which implements the finite element method (FEM) for the solution of differential equations of physics. Structurally, the microcapsule is represented by a core-shell microsphere with a non-absorbing aqueous core and a strongly light-absorbing solid-phase shell (Fig. 1a). A silicone doped with gold nanorods is assumed as the shell material, which provides the desired optical absorption spectrum. According to the assessments of [3], the gold nanorods demonstrate enhanced optical absorption in NIR region of the spectrum, approximately from 700 nm to 900 nm (Fig. 1b). In the simulations, the capsule radius R_c is fixed to 500 nm with a shell thickness h = 65 nm. The gold nanorods inside the capsule shell produce an absorption peak at 755 nm

corresponding to the excitation of the longitudinal plasmonic mode.

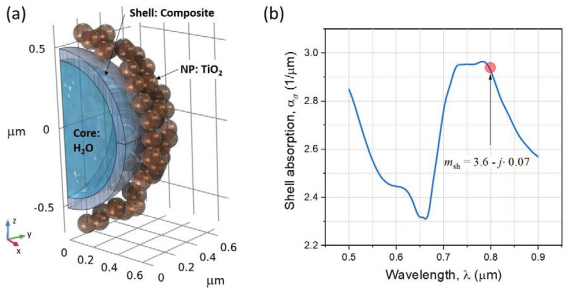

Figure 1 *(a) 3D-model of a capsule with an absorbing nanocomposite shell and an aqueous core surrounded by an ensemble of aux-NPs (TiO2). (b) Optical absorption spectrum of microcapsule with 10% fraction of gold nanorods.*

According to our previous work [4], the best way for improving the opening of microcapsule by the optical radiation is increasing the optical field concentration on its shell. To this end, an auxiliary aerosol consisting of dielectric nanoparticles (NPs) randomly distributed near the microcapsule is considered. This leads to substantial growth of capsule optical absorption that is related both to the focusing of the optical field by a transparent nanoparticle on the nanoscale with the formation of a "photonic nanojet" and to the collective oscillations of electrons on the surface of plasmonic nanoparticles.

A Gaussian optical pulse with typical parameters of ultrashort Ti:Sapphire-laser, λ =800 nm and duration t_p = 1 ps, is directed to the microcapsule. The optical radiation is focused into an 8 μm diameter waist with the total pulse energy being constant and equal to 2 nJ giving a peak pulse intensity I_0 of about 1 GW/cm^2.

Figs. 2(a-d) show the distribution of normalized optical intensity I/I_0 and volume density of heat release sources Q in the principal cross-section of a spherical microcapsule to the end of laser pulse. In addition, for clarity in (a) and (b), the streamlines of the Poynting vector **S** showing the direction of optical energy fluxes inside the capsule are plotted.

Two situations are considered, (a) when the microcapsule is in "clean" conditions, i.e., in a homogeneous medium (water) without additional nanoscatterers, and (b) when the capsule is surrounded by an ensemble of dielectric NPs fabricated of titanium dioxide with a diameter of 120 nm and refractive index 2. In both cases, due to focusing of light by the capsule in its shadow hemisphere a maximum of field intensity is formed, which leads to a corresponding increase in heat generation in this region. Placing the auxiliary nano-aerosol in the vicinity of the capsule changes the structure of energy flows, forcing the optical field to be additionally concentrated in the regions of microfocusing on NPs.

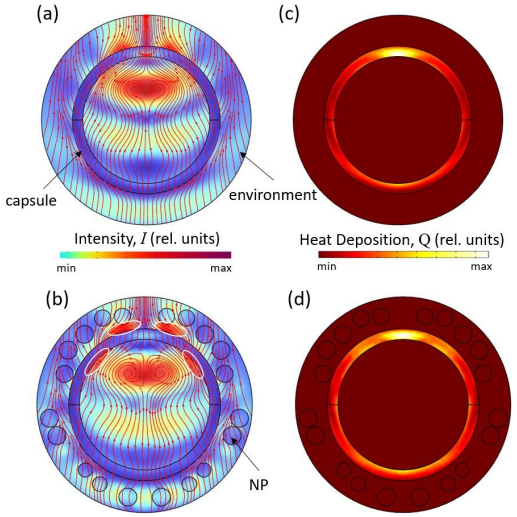

Figure 2 *(a,b) Spatial distribution of optical intensity I and (c,d) power of heat release Q near the microcapsule without (a,c) and with (b,d) auxiliary NPs.*

An example of the spatial distribution of optical intensity and temperature in different regions of the capsule and surrounding dispersed medium is shown in Figs. 3(a) and (b).

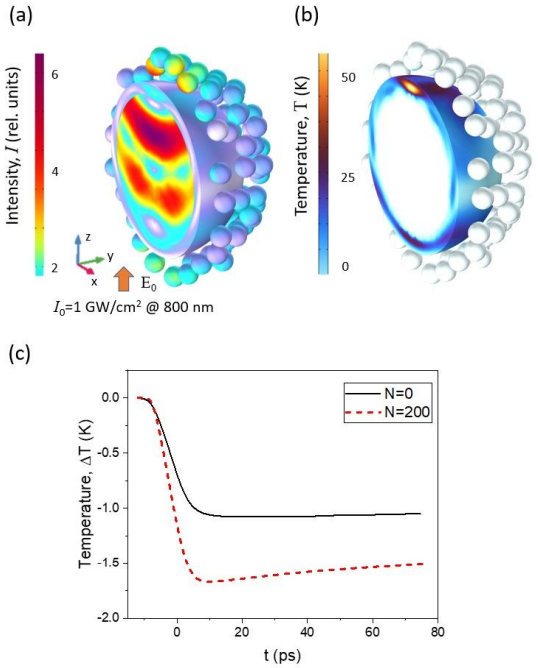

Figure 3 *3D-distribution of (a) optical intensity I and (b) temperature T in the vicinity of microcapsule with auxiliary NPs. (c) Temporal dynamics of the averaged temperature difference ΔT between lower and upper capsule hemispheres versus NP number (N).*

As seen, with the chosen parameters of the photonic microstructure, the maximum of the field intensity is located inside the capsule core, which is considered to be

non-absorbing. However, due to the lensing effect, the optical field intensity rises on the surface of the shadow hemisphere, in the absorbing capsule shell. In this case, the NPs which surround the capsule scatter the optical wave and create additional areas of light focusing on the capsule shell. As a result, the shadow region of the microcapsule becomes more heated than its illuminated part.

Worthwhile recalling, the particle illuminated by an intense optical radiation is also subjected to the optical pressure force F_{opt} arising due to compensation of the net momentum of photons during their scattering and absorption on particle surface. In the absence of a longitudinal gradient of the background optical field, the light pressure force acts along the wave vector of optical radiation and tends to push the microparticle along the direction of light propagation. Thus, to determine the resultant displacement of heated microcapsule one should consider the resultant (net) optical force: $F_{net} = F_{\Delta T} + F_{opt}$.

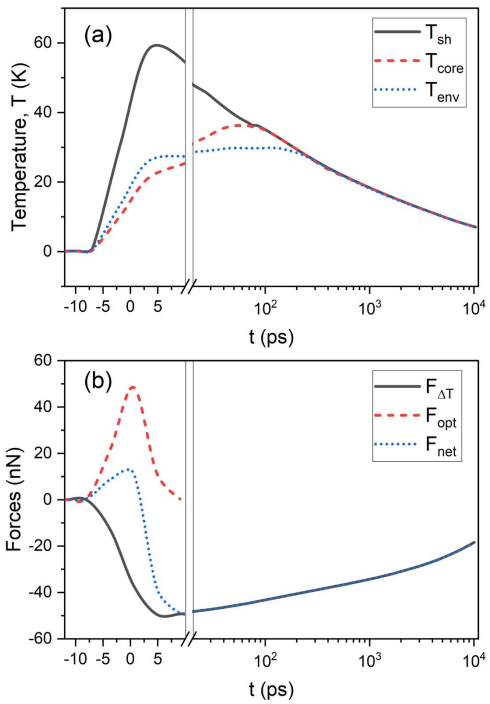

Figure 4 *(a) Temporal dynamics of maximal temperature in shell T_{sh}, core T_{core} and surrounding fluid T_{env}. (b) Amplitude of heat-induced photophoretic force $F_{\Delta T}$, optical pressure F_{opt} and resultant force F_{net} for a capsule with R_c = 500 nm exposed to a 1 ps pulse with the intensity of 1 GW/cm².*

The temporal dependence of the maximum values of the temperature increment in different regions of the capsule and the environment, as well as the dynamics of the optical field forces are shown in Figs. 4(a) and (b). Here, similar to Fig. 3(c), two physical processes corresponding to different time scales are clearly visible. The first one is the laser heating of the core-shell particle during the laser pulse acting interval of approximately 10 ps. The second process describes the cooling of a non-uniformly heated particle due to heat diffusion into the cold capsule core and the environment.

As seen, at the first stage (heating) when the laser radiation is still acting, the temperature of capsule shell T_{sh} considerably exceeds the core temperature T_{core} and the temperature of the surrounding liquid T_{env}. Meanwhile, at this stage the optical pressure F_{opt} prevails over the photophoresis $F_{\Delta T}$ and the net optical force F_{net} is directed along the incident wave vector. Contrarily, after the end of the laser heating stage when the thermal relaxation of capsule takes place, the force of direct light pressure disappears, the temperature in all capsule regions gradually equalizes, and the resultant of forces F_{net} changes its direction to the opposite pulling the microparticle in the opposite direction of the light beam incidence.

To calculate the magnitude of possible displacement of the microcapsule under the action of optical forces we use the equation of motion of a tiny solid particle with mass m exposed to an external force which is governed by the Newton's law of motion. It turns out, that the action of light pressure forces practically does not affect capsule displacement and the whole particle dynamics is determined by more "long-playing" photophoretic forces, which become increasing in the time interval t ~ 10 ns in accordance with the temperature dynamics (Fig. 4b). The maximum distance that a microcapsule can move under the action of a single pulse is of the order of 10 nm, and this distance is accumulated within about 30 ns. This obtained capsule displacement although small needs to be considered, since common ultrashort laser source operates in the pulse-periodic mode with pulse repetition rates typically of the tens kHz. As a result, the final distance of a microcapsule displacement, e.g., for one second of laser irradiation can be already about a millimeter. Obviously, this fact should be taken into account when designing laser-stimulated transportation microcontainers.

2 Acknowledgement

Russian Science Foundation (23-21-00018).

3 References

[1] A.S. Timin, et al., Inorganic/organic multilayer capsule composition for improved functionality and external triggering, Adv. Mater. Interfaces, 1600338 (2016).

[2] H. Rohatschek, Levitation of stratospheric and mesospheric aerosols by gravito-photophoresis, J. Aerosol Sci. 27, 467-475 (1996).

[3] Y.E. Geints, E.K. Panina, A.A. Zemlyanov, Shape-mediated light absorption by spherical microcapsule with gold-nanoparticles-dope, JQSRT 236, 106595 (2019).

[4] Y.E. Geints, E.K. Panina, Boosting light absorption of a therapeutic microcapsule by means of auxiliary solid nanoparticles, Opt. Commun. 537, 129444 (2023).

The 14th International Conference on
Laser-light and Interactions with Particles (LIP2024)
September 18-22nd, 2024, Xi'an, Shaanxi, China

THE SUPER-RESOLUTION IMAGE DISTORTION AND CORRECTION OF MICROSPHERE NANOSCOPY

Wenxuan SHI[1,*], Mingjin ZHANG [2*]

1 School of Aerospace Science and Technology, Xidian University, Xi'an, 710071, China
[2] School of Telecommunications Engineering, Xidian University, Xi'an, 710071, China
Corresponding author: mjinzhang@xidian.edu.cn

Abstract

Super-resolution optical microscopes have emerged as powerful and enabling microscopic imaging tools available today. This technique uses a dielectric microsphere as a "magnifying lens" creating a virtual image of an object located at the surface of the structure. But the images distortion formed by microsphere have been found due to the image magnification varies with the distance from the optical axis. In this paper, the approach of correcting distortion for microsphere nanoscopy is discussed.

1. Introduction

Microscopic imaging has traditionally been constrained by the diffraction limit, which for visible light restricts spatial resolution to several hundred nanometers. Many researchers have worked on improving this limit and obtained major successes in recent years [1-8]. The microsphere optical nanoscopy (MONS) technique recently presented by Li and his team [2-4], which demonstrated the capability to break the optical diffraction limit with a microsphere. This technique uses a dielectric microsphere as a "magnifying lens", the illumination light can be highly focused by the microsphere into an extremely small region, i.e. a photonic nanojet. The virtual image of an object located at the surface of the structure are created. The imaging capability of a microsphere depends on parameters, including the refractive index ratio of the microsphere and its surrounding medium, the illumination wavelength, and its size[9-12]. In this paper, we study methods of recovering and correcting for the radial distortion of microsphere nanoscopy

2. The super-resolution Image Distortion in experiment of Microsphere-based Microscopy

Experimental images are observed through microspheres, which are placed on different sample. The sample is printed circuit board (PCB) with different separation of patterns and spacing. The experiment demonstrates that a microsphere was able to focus light down to sub-diffraction-limited dimensions。But the images are characterized by a strong pincushion distortion which bends the straight lines in near edge of microsphere. This image distortion will affect measurement precision.

3. Reduction of Distortion Aberration for Microsphere Image

The distortion of the microspheres is radial distortion. The way to model this effect is with a shift to the pixel coordinates. The radial shift of coordinates modifies the distance of every pixel from the image center. The image of microsphere can introduce a pincushion distortion in measurements due to the image magnification increases with the distance from the optical axis. Each point in the undistorted image corresponds to a point in the distorted image. The points of the desired image are obtained from corresponding points of the distorted image. The procedure for correcting radial distortion is written. we assume that the distortion image has square shape and is symmetrical along the center line, the center coordinates of radial distortion is suppose the center of the image. This square shape assumption is satisfied, in practice, for most images. The value of radial distortion parameter is predicted at the beginning of the calculation, and modified according to the effect of distortion correction. Then the undistorted image is mapped corresponds to the distorted image. The polynomial model provides a way to correct microsphere distortion, which achieves an accuracy of about 0:1 pixels in image space. The amended image can also be used to calibrate the actual magnification and length values of the microsphere, provided highly measurement accuracy.

4. Conclusion

The microsphere optical nanoscopy imaging produces a pincushion distortion, which has a significant impact on the image geometry. In this paper, the experimental images of microsphere are obtained which show pincushion distortion clearly. A radial distortion model is discussed and applied to correct the pincushion distortion of images. We perform numerical experiments using model to demonstrate the effectiveness of reduction for distortion aberration in microsphere image. The microspheres distortion of the edge lines is strongly reduced and the pincushion distortion is properly removed. The procedure may be helpful in applications of image correction microsphere optical nanoscopy, for instance while performing accurate magnification and

parameter determination for images of microsphere nanoscopy.

References

[1] Hell, S. W. and Wichmann, J., Breaking the diffraction resolution limit by stimulated emission: stimulated-emission-depletion fluorescence microscopy, Optics Letters, 19(11): p.780–782, (1994).

[2] Lin Li, Wei Guo, Yinzhou Yan, Seoungjun Lee1 and Tao Wang, Label-free super-resolution imaging of adenoviruses by submerged microsphere optical nanoscopy Light: Science & Applications, 2: p104, (2013).

[3] Z. Wang, W. Guo, L. Li, B. Luk'yanchuk, A. Khan, Z. Liu, Z. Chen, and M.Hong, Optical virtual imaging at 50 nm lateral resolution with a white-light nanoscope, Nature Communications, 2 (218): (2011).

[4] Seoungjun Lee, LinLi, Rapid super-resolution imaging of sub-surface nanostructures beyond diffraction limit by high refractive index microsphere optical nanoscopy , Optics Communications, 334, 253–257, (2015).

[5] Xiang Hao, Cuifang Kuang, Xu Liu, Haijun Zhang, and Yanghui Li, Microsphere based microscope with optical super-resolution capability, Applied Physics Letters, 99: p.203102, (2011).

[6] X. Zhang and Z. Liu, Superlenses to overcome the diffraction limit, Nature Materials, 7(6), 435-441, (2008).

[7] J. Y. Lee, B. H. Hong, et al., Near-field focusing and magnification through self-assembled nanoscale spherical lenses, Nature, 460(7254), 498-501,(2009).

[8] S. T. Hess, T. P. K. Girirajan, and M. D. Mason, Ultra-high resolution imaging by fluorescence photoactivation localization microscopy, Biophysical journal, 91: p. 4258–72, (2006).

[9] Sylvain Lecler, Properties of a three-dimensional photonic jet ,Optics Letters, 30(19):(2005).

[10] Z. Chen, A. Taflove, and V. Backman, Photonic nanojet enhancement of backscattering of light by nanoparticles: a potential novel visible-light ultramicroscopy technique, Optics Express, 12(7), 1214-1220,(2004).

[11] Alexander Heifetz, Kevin Huang, Experimental confirmation of backscattering enhancement induced by a photonic jet, Applied Physics Letters 89: p.221118, (2006).

[12] Alexis Devilez, Brian Stout, Nicolas Bonod, Evgeny Popov, Spectral analysis of three-dimensional photonic jets, Optics Express, 16(18): p.14200-14212, (2008).

The 14th International Conference on
Laser-light and Interactions with Particles (LIP2024)
September 18-22nd, 2024, Xi'an, Shaanxi, China

HIGHER-ORDER OPTICAL FORCE THEORY AND THEIR APPLICATION IN MANIPULATING PARTICLES

Yuan Zhou [1,2†], Yanan Zhang [1,2†], Xiaohao Xu[1], Shaohui Yan [1,*] and Baoli Yao [1,2*]

[1] State Key Laboratory of Transient Optics and Photonics, Xi'an Institute of Optics and Precision Mechanics, Chinese Academy of Sciences, Xi'an 710119, China
[2] University of Chinese Academy of Sciences, Beijing 100049, China

Corresponding author: shaohuiyan@opt.ac.cn

Abstract

Light possesses energy and it also carries momentum, which can exert optical forces on physical objects. Usually, the optical force on the particle can be calculated within strong approximations based on limiting size regimes, including the dipole approximation, the ray optics, and electromagnetic scattering theory. However, the above three models for calculating the optical force cannot provide a direct relationship between the optical force and the field for the size of the particle that is comparable to the optical wavelength. According to multipole expansion theory, we develop a higher-order optical force theory model, which not only presents the relationship between the optical force and the field moment of incident beam but also illustrates the origin of the optical force on the particle. Based on this optical force model, we have theoretically investigated the azimuthal force generate by IPM (Imaginary Poynting momentum, IPM) of the optical field on metallic microparticles, and have experimentally generated an annular optical field with only IPM in the azimuthal direction for the fist time, realizing an IPM-based optical micromanipulation experiment. In addition, we extended the concept of BSM (Belinfante Spin Momentum, BSM) optical force established in the dipole approximation theory to the multipole moment theory, providing an approach to calculating the BSM optical force on Mie particles. By constructing a BSM vortex optical field without spiral, we realized a bidirectional orbital motion of Mie metallic microparticles by BSM. Our higher-order optical force theory provides an approach to studying the novel optical forces like IPM force, BSM force, orbital momentum force, etc, may facilitate additional progress in optomechanics, optical manipulation, and Mie-tronics.

1 Higher-order optical force theory

Our theory is developed based on the optical force model established by Lin et al. [1-3]. In this model, the optical force on a generic sphere is described by a set of incident field moments [4]:

$$\mathbf{F}^{(N)}=\sum_{l=1}^{N}\left\{\begin{array}{c}A_{N,l}\,\mathrm{Im}\,\mathbf{S}_{\mathrm{em}}^{(l)}+B_{N,l}\nabla D_{\mathrm{e}}^{(l)}+C_{N,l}\nabla D_{\mathrm{m}}^{(l)}+\\ D_{N,l}\,\mathrm{Re}\,\mathbf{S}_{\mathrm{em}}^{(l)}+E_{N,l}\mathbf{P}_{\mathrm{e}}^{(l)}+F_{N,l}\mathbf{P}_{\mathrm{m}}^{(l)}\end{array}\right\}. \tag{1}$$

Using the k-space procedure [4], the Eq. (1) can be written as

$$\begin{aligned}\mathbf{F}^{(N)}&=\mathbf{F}_{\mathrm{IPM}}^{(N)}+\mathbf{F}_{\mathrm{G}}^{(N)}+\mathbf{F}_{\mathrm{RP}}^{(N)}+\mathbf{F}_{\mathrm{CRP}}^{(N)},\\ \mathbf{F}_{\mathrm{IPM}}^{(N)}&=\sum_{l=1}^{N}A_{N,l}\left(k^2+\frac{\Delta}{2}\right)^{l-1}\mathrm{Im}\,\mathbf{S}_{\mathrm{em}}^{(1)},\\ \mathbf{F}_{\mathrm{G}}^{(N)}&=\sum_{l=1}^{N}\left(k^2+\frac{\Delta}{2}\right)^{l-1}\left[B_{N,l}\nabla D_{\mathrm{e}}^{(1)}+C_{N,l}\nabla D_{\mathrm{m}}^{(1)}\right],\\ \mathbf{F}_{\mathrm{RP}}^{(N)}&=\sum_{l=1}^{N}D_{N,l}\left(k^2+\frac{\Delta}{2}\right)^{l-1}\mathrm{Re}\left[\mathbf{S}_{\mathrm{em}}^{(1)}\right],\\ \mathbf{F}_{\mathrm{CRP}}^{(N)}&=\sum_{l=1}^{N}\left(k^2+\frac{\Delta}{2}\right)^{l-1}\left[E_{N,l}\mathbf{P}_{\mathrm{e}}^{(1)}+F_{N,l}\mathbf{P}_{\mathrm{m}}^{(1)}\right],\end{aligned} \tag{2}$$

with $D_{\mathrm{e}}^{(1)}=|\mathbf{E}|^2$ (electric intensity); $D_{\mathrm{m}}^{(1)}=|\mathbf{H}|^2$ (magnetic intensity); $\mathbf{P}_{\mathrm{e}}^{(1)}=\mathrm{Im}[\mathbf{E}^*\cdot(\nabla)\mathbf{E}]$ (electric orbital momentum); $\mathbf{P}_{\mathrm{m}}^{(1)}=\mathrm{Im}[\mathbf{H}^*\cdot(\nabla)\mathbf{H}]$ (magnetic orbital momentum); $\mathbf{S}_{\mathrm{em}}^{(1)}=\mathbf{E}^*\times\mathbf{H}$ (complex Poynting vector). In Eq. (2), the first term $\mathbf{F}_{\mathrm{IPM}}^{(N)}$ is the generalized IPM force as it originates from the IPM of illumination; The second term $\mathbf{F}_{\mathrm{G}}^{(N)}$ is the generalized intensity-gradient force induced by the optical intensity inhomogeneity; The third $\mathbf{F}_{\mathrm{RP}}^{(N)}$ and last $\mathbf{F}_{\mathrm{CRP}}^{(N)}$ terms are the generalized radiation pressure and canonical radiation pressure, generated by the momentum and orbital momentum. When N = 1, all terms in Eq. (2) reduce to their dipolar counterparts. The coefficients $A_{N,l}$~$F_{N,l}$ are determined by the particle properties.

2 Optical Forces on metallic microparticles induced by higher-order IPM and BSM

2.1 Higher-order IPM force

We adopt the Minkowski's form of the time-averaged Poynting momentum, $\mathbf{P}$ = Re($\mathbf{E}^*\times\mathbf{H}$)/(2$c^2$), and the imaginary Poynting momentum (IPM), $\mathbf{II}$ = Im($\mathbf{E}^*\times\mathbf{H}$)/(2 c^2), where c is the speed of light in the background medium. For those particles that can support multipolar responses, the force associated with the IPM can be formulated, by Eq. (2) as [5]

$$\mathbf{F}_{\mathrm{IPM}}^{(N)}=\sum_{l=1}^{N}A_{N,l}\left(k^2+\frac{\Delta}{2}\right)^{l-1}\mathrm{Im}\left(\mathbf{E}^*\times\mathbf{H}\right). \tag{3}$$

For dipolar particles (N = 1), it reproduces Eq. (3) that is directly proportional to the IPM. However, the Laplacian Δ involved in the case of N >1 indicates that the proportionality is invalid in the presence of multipoles. The force thus depends on derivatives of the IPM with respect to space, so that the particle is able to feel not only the local field, but its neighborhood.

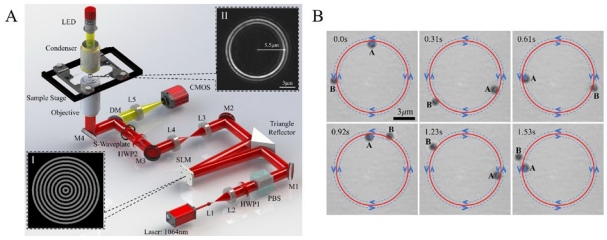

Figure 1 *Particle rotation in the focused IPM vortex beam. A, Schematics of experimental set-ups. L, Lens; HWP, half-wave plate; PBS, polarizing beam splitter; M, mirror; SLM, spatial light modular; DM, dichroic mirror; CMOS, complementary metal oxide semiconductor camera. The polarization parameter α is controlled by S-Waveplate. Insets I and II show the phase mask profile on the SLM and the measured intensity profile at the focal plane, respectively. B, Successive images showing two Au particles trapped and rotated by the IPM vortex beam with polarization parameter* $\alpha = -45^\circ$*. Red circles with a radius of 5.5 μm illustrate the beam profile. The rotation direction of the spheres is indicated by arrows.*

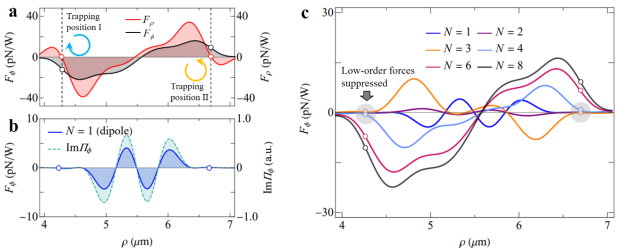

Figure 2 *Numerical results of optical forces for* $\alpha = -45^\circ$ *(the IPM vortex condition). a, Radial and azimuthal forces,* F_ρ *and* F_ϕ *,versus the radial displacement of the gold sphere. The truncation index in these calculations is N = 11, which is large enough to ensure the convergence of the Mie series. Hollow dots mark the values at radial equilibrium positions, where the radial force vanishes with a negative derivative. b, Comparision of the dipolar component of* F_ϕ *with incident IPM. c, Azimuthal force for different N showing that low-order contributions are small at the equilibrium positions.*

2.2 Higher-order BSM force

It is well known that in a source-free homogeneous isotropic medium **P** can be decomposed into its orbital and spin parts:

$$\begin{aligned}\mathbf{P} &= \mathbf{P}^O + \mathbf{P}^S,\\ \mathbf{P}^O &= (1/4\omega)\,\mathrm{Im}\left[\varepsilon\nabla\mathbf{E}\cdot\mathbf{E}^* + \mu\nabla\mathbf{H}\cdot\mathbf{H}^*\right],\\ \mathbf{P}^S &= (1/8\omega)\nabla\times\mathrm{Im}\left(\varepsilon\mathbf{E}^*\times\mathbf{E} + \mu\mathbf{H}^*\times\mathbf{H}\right),\end{aligned} \tag{4}$$

$\mathbf{P}^O$ and $\mathbf{P}^S$ stand for the densities of orbital momentum (OM) and BSM. According to Eqs. (2) and (4), the higher-order BSM force can be written as

$$\begin{aligned}\mathbf{F}_{\mathrm{BSM}}^{(N)} &= \sum_{l=1}^{N}\left(D_{N,l}^{\mathrm{e}} + D_{N,l}^{\mathrm{m}} + D_{N,l}^{\mathrm{x}}\right)\left(k^2 + \frac{\Delta}{2}\right)^{l-1}\mathbf{P}^S\\ &= \mathbf{F}_{\mathrm{BSM}}^{\mathrm{e}(N)} + \mathbf{F}_{\mathrm{BSM}}^{\mathrm{m}(N)} + \mathbf{F}_{\mathrm{BSM}}^{\mathrm{x}(N)}\end{aligned} \tag{5}$$

Specifically, $\mathbf{F}_{\mathrm{BSM}}^{\mathrm{e}(N)}$ and $\mathbf{F}_{\mathrm{BSM}}^{\mathrm{m}(N)}$ are the components due to the interference of electric and magnetic multipoles of adjacent orders, respectively; $\mathbf{F}_{\mathrm{BSM}}^{\mathrm{x}(N)}$ is a hybrid component resulting from the interference between electric and magnetic multipoles of the same order.

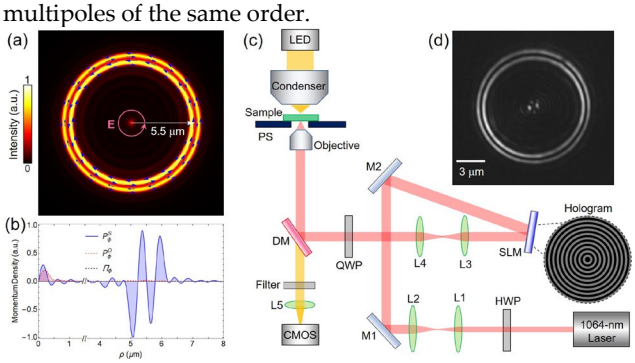

Figure 3 *Property and generation of the BSM vortex beam. (a) Simulated intensity distribution and BSM density (blue arrows) at the focal plane, for the left-handed circularly polarized (LCP) incident beam. (b) Line-scan results across the radial direction, for the azimuthal spin, orbital, and imaginary Poynting momentum density. (c) Schematics of the experimental set-up for the BSM vortex beam generation. L, Lens; HWP, half-wave plate; M, mirror; SLM, spatial light modular; QWP, quarter-wave plate; DM, dichroic mirror; CMOS, complementary metal oxide semiconductor camera. (d) Intensity profile of the beam experimentally measured at the focal plane for the LCP incidence.*

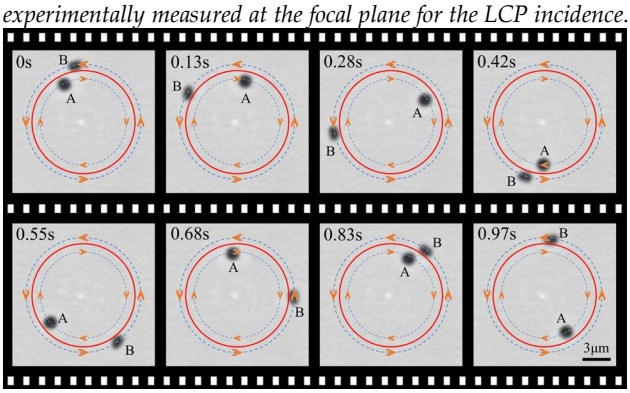

Figure 4 *Particle rotation powered by multipolar BSM forces. Successive images of two gold microparticles A and B (radius a ~ 0.8 μm) simultaneously trapped and rotated at the two sides of the focused ring field intensity shown in Fig. 3d.*

3 Acknowledgement

We gratefully acknowledge support from National Natural Science Foundation of China grants 12274181, 11974417, 62135005, 11904395, 12127805, and 11804119; Key Research Program of Frontier Sciences, CAS grant ZDBS-LY-JSC035; and Ministerio de Ciencia e Innovacion of Spain grant PGC2018-095777-B-C21. We thank Prof. Zhifang Lin for useful early discussions.

4 References

[1] Chen J., Ng J., Lin Z., Chan C. T., Optical pulling force, Nat. Photon. 5, 531-534 (2011).

[2] 28. Jiang Y., Chen J., Ng J., Lin Z., Decomposition of optical force into conservative and nonconservative components, arXiv:1604.05138.

[3] Zheng H., Yu X., Lu W., Ng J., Lin Z, GCforce: decomposition of optical force into gradient and scattering parts, Comput. Phys. Commun. 237, 188-198 (2019).

[4] Zhou Y., Xu X., Zhang Y., Li M., Yan S., Nieto-Vesperinas M., Li B., Qiu C-W., Yao B., Observation of high-order imaginary Poynting momentum optomechanics in structured light, Proceedings of the National Academy of Sciences, 119, e2209721119 (2022).

[5] Zhou Y., Zhang Y., Xu X., Nieto-Vesperinas M., Yan S., Li M., Gao W., Zhang Y., Yao B., Optical forces on multipoles induced by the belinfante spin momentum, Laser & Photonics Reviews, 17, 2300245 (2023).

The 14th International Conference on
Laser-light and Interactions with Particles (LIP2024)
September 18-22nd, 2024, Xi'an, Shaanxi, China

TUNABLE OPTICAL FORCE ON A GOLD NANOSPHERE BY COATING HYBRID ORGANIC-INORGANIC PEROVSKITE

Ping Li [1], Yiping Han [1,*], Haojie Wang [1], Xikang Zhou [1], and Chunmei Long [1]

[1] School of Physics, Xidian University, Xi'an 710071, China

Corresponding author: yphan@xidian.edu.cn

Abstract

Optically controlled gold nanoparticles can enhance the trapping strength by engineering the size and shape of the particles, and the quality of optical force can be improved by tuning the optical properties of gold nanoparticles such as localized surface plasmon resonance (LSPR). The strength and quality of optical force can be further improved by coating 2D Hybrid organic-inorganic perovskite (2D HOIP). In this paper, the optical force on a 2D HOIP gold nanosphere illuminated by a polarized Bessel beam is calculated in the framework of the generalized Lorenz-Mie theory (GLMT). The axial optical force F_z are numerically calculated, and the magnitude of the force is tuned by changing the order l and half-cone angle α_0. The resonance wavelength (frequency) is tuned by changing the thickness of the coating 2D HOIP. Double optical force peaks can be produced, and the positions of both peaks are mainly determined by the thickness of the coating. The numerical results have potential applications involving the trapped perovskite gold nanosphere.

1 Introduction

In biomedical engineering, laser-generated optical tweezers[1,2] have been widely studied and applied in the microscale field in recent years. Optical tweezers can be used as a non-contact, high-precision, controllable manipulation to precisely locate and manipulate tiny biological particles, such as cells, nanoparticles, and molecules. Previous optical tweezers mainly rely on microscope objectives with high numerical aperture to achieve accurate focusing and produce highly localized light field gradients to gain control of tiny objects. However, through the introduction of gold nanoparticles[3] and other metal nanostructures, optical tweezer technology ushered in new development opportunities. As an important part of optical tweezer technology, gold nanoparticles can significantly improve the sensitivity and accuracy of optical capture due to their superior polarizability and light scattering characteristics. In addition, the local surface plasmon resonance (LSPR) effect on the surface of metal nanoparticles is also widely used for optical manipulation to achieve more efficient capture and manipulation effects[4-6]. Its unique manipulation ability and cytocompatibility have attracted much attention.

Many methods and strategies have been used to study the optical manipulation of gold nanoparticles. One important approach is to enhance the electric field gradient by designing metal nanostructures, such as plasma structures, nanoholes, and nanodisks. Another method is to achieve the generation of strong light by adjusting the characteristics of the incident beam, for example by using a special beam mode, such as the Bezier beam.

Bessel beam[7-9] has the characteristics of self-healing and non-diffraction, and has a wide application prospect in micro - and nano-scale light manipulation. Research has shown that Bessel beams can trap and manipulate nanoparticles. The optical forces on dielectric and magnetic medium nanoparticles are studied. The vector angle spectrum method is used to describe the vector Bessel beam, and the Rayleigh model is used to calculate the optical force. The effects of beam parameters (beam order, half-cone angle, polarization, etc.) on optical force are analyzed. The optical forces on a charged sphere are studied using the generalized Lorenz-Mie theory (GLMT)[10], with emphasis on the influence of surface charge on the optical forces. 2D Hybrid organic-inorganic perovskite (2D HOIP) is a new two-dimensional material with many unique properties. In this paper, the theory is extended to study the optical forces on 2D HOIP-coated gold particles, and the effects of beam order, polarization, half-cone angle, and material layer on the optical forces are analyzed. The optical properties of perovskite-coated gold nanospheres are studied in this paper.

We present the theoretical framework for the optical force acting on a HOIP-coated gold nanosphere, and discuss the dielectric function of gold and the refractive index of the perovskite material. The analytical expression for the optical force is derived using the GLMT. We present the numerical results of the optical force on a HOIP-coated gold nanosphere, and investigate the influence of beam parameters, including order and polarization, as well as the effects of different thicknesses of perovskite coatings. Finally, we discuss the potential of HOIP-coated gold nanospheres for precise optical manipulation and suggest future research directions.

2 Theoretical background

Consider a HOIP -coated gold nanosphere illuminated by a vector Bessel beam, as shown in Fig. 1. The center of the particle is located at O, which is the origin of the coordinate system $O-xyz$. The center of the beam is located at O', which is the origin of the coordinate system $O'-x'y'z'$. The coordinates of the beam center O' in

$O-xyz$ are (x_0, y_0, z_0) . The refractive index of the surrounding media is m_3, which is assumed to be 1 in our calculation.

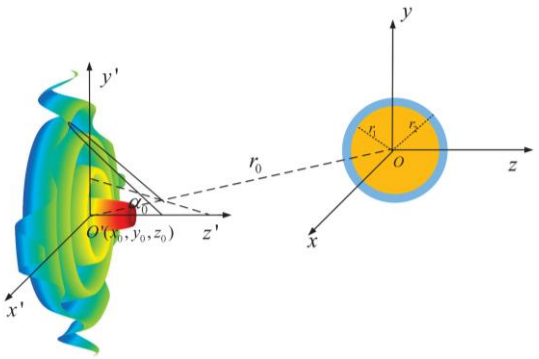

Figure 1 *Geometry of a HOIP coated nanosphere illuminated by a vector Bessel beam*

The core of the particle is a gold nanosphere, whose radius is r_1 and whose dielectric function is given by the Drude–Sommerfeld model [11, 12]:

$$\varepsilon_1(\omega) = \varepsilon_b - \frac{\omega_{Au}^2}{\omega(\omega + i\gamma_{Au})} \tag{1}$$

with

$$\gamma_{Au} = \gamma_{bulk} + A\frac{v_F}{a_{eff}} \tag{2}$$

where ω is the angular frequency, ε_b is the phenomenological parameter, ω_{Au} is the bulk plasmon frequency of gold, γ_{bulk} is the frequency of electron collisions, A is a constant parameter for matching theoretical and experimental results, v_F is the Fermi velocity of the electron, and a_{eff} is the effective radius of the particle. In our calculation, they are $\varepsilon_b = 9.8$, $\omega_{Au} = 9eV$, $\gamma_{bulk} = 0.066eV$, $A = 0.25$, and $v_F = 1.4\times10^6$ m/S. Fig. 3 gives the refractive index of gold. The red solid line is the real part of the refractive index, and the blue dashed line is the imaginary part. The refractive index of HOIP can be obtained from Refractive index database (https://refractiveindex.info/), and Fig. 2 depicts the refractive indices of the HOIP.

The optical force exerted on a particle by a beam is proportional to the net momentum removed from the incident beam, and can be expressed in terms of the surface integration of a Maxwell stress tensor.

$$<\mathbf{F}>=<\oint_S \hat{\mathbf{n}}\cdot\vec{A}dS> \tag{3}$$

where <>represents a time average, $\hat{\mathbf{n}}$ the outward normal unit vector, and S a surface enclosing the particle. The Maxwell stress tensor $\vec{A}$ is given by

$$\vec{A} = \frac{1}{4\pi}\left(\varepsilon\mathbf{EE} + \mathbf{HH} - \frac{1}{2}\left(\varepsilon E^2 + H^2\right)\vec{I}\right) \tag{4}$$

Where, the electromagnetic fields **E** and **H** are the total fields, namely, the sum of the incident and scattered fields. According to GLMT, the optical force can be expressed by

$$\mathbf{F^u(r)} = \frac{2m_3 I_0}{c}\left[\mathbf{e_x}C^u_{pr,x}(\mathbf{r}) + \mathbf{e_y}C^u_{pr,y}(\mathbf{r}) + \mathbf{e_z}C^u_{pr,z}(\mathbf{r})\right] \tag{5}$$

where the longitudinal ($C^u_{pr,z}$) and transverse ($C^u_{pr,x}$ and $C^u_{pr,y}$) radiation pressure cross sections are.

$$\begin{aligned} C^u_{pr,z} = \frac{\lambda^2}{\pi}\sum_{n=1}^{\infty} Re\Big\{ & \frac{1}{n+1}(A_n g^{0,u}_{n,TM} g^{0,u^*}_{n+1,TM} + B_n g^{0,u}_{n,TE} g^{0,u^*}_{n+1,TE}) \\ & + \sum_{m=1}^{n}\Big[\frac{1}{(n+1)^2}\frac{(n+m+1)!}{(n-m)!}\times(A_n g^{m,u}_{n,TM} g^{m,u^*}_{n+1,TM} \\ & + A_n g^{-m,u}_{n,TM} g^{-m,u^*}_{n+1,TM} + B_n g^{m,u}_{n,TE} g^{m,u^*}_{n+1,TE} + B_n g^{-m,u}_{n,TE} g^{-m,u^*}_{n+1,TE}) \\ & + m\frac{2n+1}{n^2(n+1)^2}\frac{(n+m)!}{(n-m)!}C_n(g^{m,u}_{n,TM} g^{m,u^*}_{n,TE} - g^{-m,u}_{n,TM} g^{-m,u^*}_{n,TE})\Big]\Big\} \end{aligned} \tag{6}$$

$$C^u_{pr,x} = \mathrm{Re}(C^u) \qquad C^u_{pr,y} = \mathrm{Im}(C^u) \tag{7}$$

with

$$\begin{aligned} C^u = \frac{\lambda^2}{2\pi}\sum_{n=1}^{\infty}\Big\{ & -\frac{(2n+2)!}{(n+1)^2}F_n^{n+1,u} + \sum_{m=1}^{n}\frac{(n+m)!}{(n-m)!}\frac{1}{(n+1)^2} \\ & \times\Big[F_n^{m+1,u} - \frac{n+m+1}{n-m+1}F_n^{m,u} + \frac{2n+1}{n^2}(C_n g^{m-1,u}_{n,TM} g^{m,u^*}_{n,TE} \\ & - C_n g^{-m,u}_{n,TM} g^{-m+1,u^*}_{n+1,TE} + C_n^* g^{m-1,u}_{n,TE} g^{m,u^*}_{n,TM} - C_n^* g^{-m,u}_{n,TE} g^{-m+1,u^*}_{n,TM})\Big]\Big\} \end{aligned} \tag{8}$$

and

$$\begin{aligned} F_n^{m,u} = & A_n g^{m-1,u}_{n,TM} g^{m,u^*}_{n+1,TM} + B_n g^{m-1,u}_{n,TE} g^{m,u^*}_{n+1,TE} \\ & + A_n^{m^*} g^{-m,u}_{n+1,TM} g^{-m+1,u^*}_{n,TM} + B_n^{m^*} g^{-m,u}_{n+1,TE} g^{-m+1,u^*}_{n,TE} \end{aligned} \tag{9}$$

$$\begin{aligned} A_n &= a_n + a_{n+1}^* - 2a_n a_{n+1}^* \\ B_n &= b_n + b_{n+1}^* - 2b_n b_{n+1}^* \\ C_n &= -i(a_n + b_{n+1}^* - 2a_n b_{n+1}^*) \end{aligned} \tag{10}$$

Note that Eq.(6)–(10) hold for both homogeneous and coated spheres, depending on the use of Mie scattering coefficients. a_n and b_n for a coated sphere is:

$$a_n = \frac{\psi_n(y)\left[\psi_n'(m_2 y) - A_n\chi_n'(m_2 y)\right] - m_2\psi_n'(y)\left[\psi_n(m_2 y) - A_n\chi_n(m_2 y)\right]}{\xi_n(y)\left[\psi_n'(m_2 y) - A_n\chi_n'(m_2 y)\right] - m_2\xi_n'(y)\left[\psi_n(m_2 y) - A_n\chi_n(m_2 y)\right]}$$

$$b_n = \frac{m_2\psi_n(y)\left[\psi_n'(m_2 y) - B_n\chi_n'(m_2 y)\right] - \psi_n'(y)\left[\psi_n(m_2 y) - B_n\chi_n(m_2 y)\right]}{m_2\xi_n(y)\left[\psi_n'(m_2 y) - B_n\chi_n'(m_2 y)\right] - \xi_n'(y)\left[\psi_n(m_2 y) - B_n\chi_n(m_2 y)\right]}$$

$$A_n = \frac{m_2\psi_n(m_2 x)\psi_n'(m_1 x) - m_1\psi_n'(m_2 x)\psi_n(m_1 x)}{m_2\chi_n(\tilde{n}_2 x)\psi_n'(m_1 x) - m_1\chi_n'(m_2 x)\psi_n(m_1 x)}$$

$$B_n = \frac{m_2\psi_n(m_1 x)\psi_n'(m_2 x) - m_1\psi_n'(m_1 x)\psi_n(m_2 x)}{m_2\chi_n'(m_2 x)\psi_n(m_1 x) - m_1\chi_n(m_2 x)\psi_n'(m_1 x)} \tag{11-14}$$

where $\psi_n(x) = xj_n(x)$, $\chi_n(x) = -xy_n(x)$, $\xi_n(x) = xh_n^{(1)}(x)$ are Ricatti–Bessel functions. $x = kr_1$, and $y = kr_2$ are the dimensionless size parameters of the core and coating, respectively. In Eq.(6)–(10), $g^n_{m,TE}$ and $g^n_{m,TM}$ are beam shape coefficients (BSCs)[3].

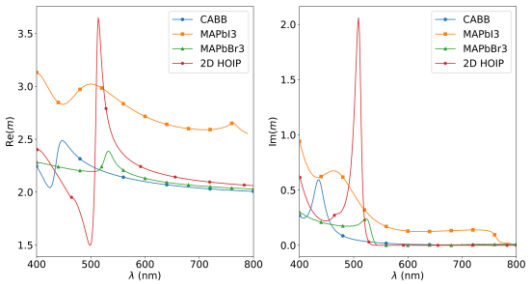

Figure 2 Refractive index of HOIP

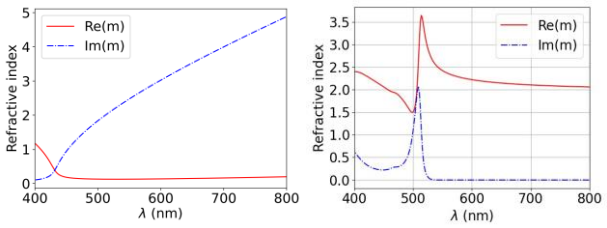

Figure 3 *Refractive index of HOIP and gold respectively*

3 Numerical Results

The optical force of polarized Bessel beam on HOIP-coated gold nanospheres is calculated using the theory developed in the previous section. The effects of beam order *l*, polarization, half-cone angle α_0, and thickness of perovskite coating on optical F_z are discussed. In the calculation, the wavelength of the incident beam ranges from 400 to 800 nm, and the half-cone angle α_0 ranges from 0 to 90◦. Each figure consists of six sub-figures, corresponding to different polarizations. In the figure, xp, yp, rc, lc, rp, and ap represent x, y, right circular, left circular, radial and azimuthal polarizations, respectively.

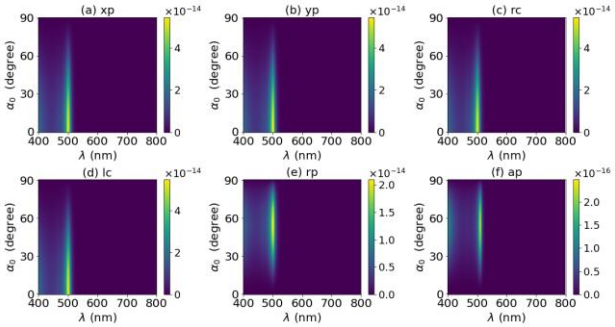

Figure 4 *Optical force on a HOIP-coated gold nanosphere by a zeroth-order Bessel beam. The radius of the core is 10 nm, and that of the coating is 1 nm.*

First, the optical force on a 2D HOIP-coated gold nanosphere is investigated. Fig. 4 depicts the optical force on a gold nanosphere by a zeroth-order (l = 0) Bessel beam. The radius of the sphere is a = 10nm. Caused by localized surface plasmon resonance (LSPR), we can see an island with broad band peaks in each subfigure. The central wavelength of the island for all polarizations (except for the azimuthal polarization) is same. This means that polarization of the incident beam will not change the central wavelength. Fig. 4 depicts the light force on HOIP-coated gold nanospheres under zero-order (l = 0) Bessel beam irradiation. In calculation, the HOIP coating thickness τp = 1nm. In general, HOIP coatings affect the location and shape of the island. The results show that the 2D HOIP coating results find two islands for all polarizations except azimuthal polarization. The first is located at a smaller wavelength and a wider location, while the second is located at a larger wavelength and a narrower location.

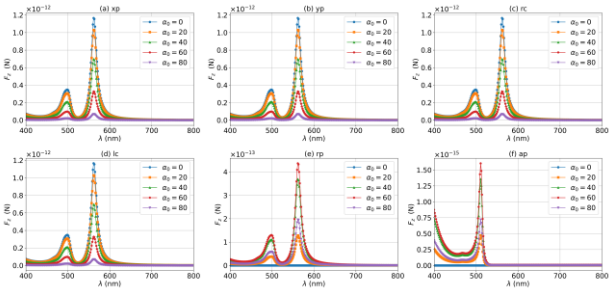

Figure 5 *Optical force on a HOIP-coated gold nanosphere illuminated by zeroth-order Bessel beams with various α_0*

In order to further investigate the effect of HOIP coating on the optical force, we consider the effect of half-cone angle, the optical forces on a HOIP-coated gold nanosphere illuminated by zeroth-order Bessel beam with various α_0 are calculated and depicted in Fig. 5. In the figure, the curves for α_0 = 0, 20◦, 40◦, 60◦ and 80◦ are given. the optical force versus α_0 for wavelength λ = 548 nm, In the calculation, the thickness of the coating is 5nm. We calculated the optical force on gold nanospheres with different coatings. In our calculation, the thickness of the coating τp is 0,2,4,6,8 nm. Fig. 6 shows the result of a HOIP-coated gold nanosphere illuminated by a zero-order Bessel beam. The results show that when the coating is 2D HOIP and the thickness increases from 0nm to 8nm, we can see two peaks, and both peaks move towards larger wavelengths as the coating thickness increases. However, we can find that the right island (with a larger central wavelength) is more sensitive to coating thickness. If the incident beam is a first-order Bessel beam, the effect of coating thickness is very similar to that of zero-order beam incidence.

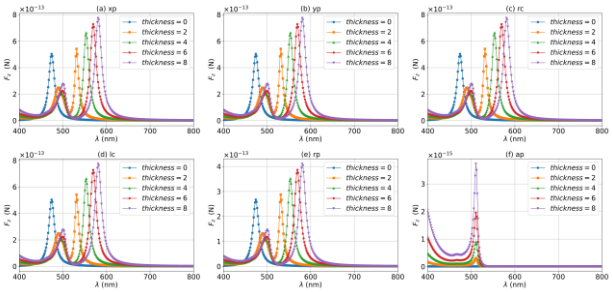

Figure 6 *Optical force on a gold nanosphere coated by HOIP with various thicknesses by a zeroth-order Bessel beam, α_0=40◦.*

4 Conclusion

The optical properties of HOIP-coated gold nanospheres have been studied in this paper. The effects of beam parameters (order, half-cone angle, wavelength, polarization) and particle parameters (coating thickness) on optical properties are analyzed and discussed. The numerical results show that LSPR caused by gold core will

form an island. A HOIP-coating would move the island toward a larger wavelength. If the coating is 2D HOIP, two islands can be observed. One is wider and located at a smaller wavelength, and the other is narrower and located at a larger wavelength. Increasing the thickness of the HOIP coating will make the central peak shift to a larger wavelength, and the optical force corresponding to linear polarization and circular polarization will decrease with the increase of the half-cone angle. In summary, the results of this study hold great promise for the development of advanced optical trapping and manipulation techniques, as well as the creation of novel optical tweezers and metamaterials.

5 Acknowledgement

This work was supported by the basic strengthening program key basic research projects.

6 References

[1] A. Ashkin, J. M. Dziedzic, J. E. Bjorkholm, and S. Chu, "Observation of a single-beam gradient force optical trap for dielectric particles," Opt. Lett. 11, 288–290 (1986).

[2] S. Hu, J.-y. Ye, Y. Zhao, and C.-l. Zhu, "Advanced optical tweezers on cell manipulation and analysis," The Eur. Phys. J. Plus 137, 1024 (2022).

[3] B. Yan, X. Ling, R. Li, et al., "Optical force and torque on a graphene-coated gold nanosphere by a vector Bessel beam," Micromachines 13, 456 (2022)

[4] Y. Zhang, C. Min, X. Dou, et al., "Plasmonic tweezers: for nanoscale optical trapping and beyond," Light. Sci. & 281 Appl. 10, 59 (2021).

[5] C.-H. Huang, T. Kudo, R. Bresolí-Obach, et al., "Surface plasmon resonance effect on laser trapping and swarming 283 of gold nanoparticles at an interface," Opt. Express 28, 27727–27735 (2020).

[6] Y. Ren, Q. Chen, M. He, et al., "Plasmonic optical tweezers for particle manipulation: principles, methods, and applications," ACS nano 15, 6105–6128 (2021).

[7] J. Durnin, "Exact solutions for nondiffracting beams. i. the scalar theory," J. Opt. Soc. Am. A 4, 651–654 (1987).

[8] C. Vetter, R. Steinkopf, K. Bergner, et al., "Realization of free-space long-distance self-healing bessel beams," Laser & Photonics Rev. 13, 1900103 (2019).

[9] S. N. Khonina, N. L. Kazanskiy, S. V. Karpeev, and M. A. Butt, "Bessel beam: Significance and applications—a progressive review," Micromachines 11, 997 (2020).

[10] R. Li, P. Li, J. Zhang, et al., "Optical bessel tractor polarized beams on a charged sphere of arbitrary size," J. Quant. Spectrosc. Radiat. Transf. 219, 186–198 (2018).

[11] A. Pinchuk, U. Kreibig, and A. Hilger, "Optical properties of metallic nanoparticles: influence of interface effects and interband transitions," Surf. science 557, 269–280 (2004).

[12] M. Farokhnezhad and M. Esmaeilzadeh, "Graphene coated gold nanoparticles: an emerging class of nanoagents for photothermal therapy applications," Phys. Chem. Chem. Phys. 21, 18352–18362 (2019).

The 14th International Conference on
Laser-light and Interactions with Particles (LIP2024)
September 18-22nd, 2024, Xi'an, Shaanxi, China

ANALYSIS OF PHOTONIC NANOJET BASED ON FINITE DIFFERENCE FREQUENCY DOMAIN

Yuexiao JIAO[1], Renxian LI [1,*], Huan TANG [1], Li XIAO [1], Bing WEI[1], Shuhong GONG[1]
[1] School of Physics, Xidian University, Xi'an 710071, China
Corresponding author:rxli@mail.xidian.edu.cn

Abstract

Photonic nanojet (PNJ) is a common optical phenomenon, which is generally generated by dielectric microcylinders or dielectric microspheres illuminated by a plane wave. Due to the convergence effect of this phenomenon on the incident wave, the intensity of the electric fields is greatly enhanced, and it is now widely used in optical imaging [1-4], optical tweezers [5-7], nanolithography [8-9], and optical switching [10]. Since the propagation direction of photonic jets always follows the axial direction, it is relatively difficult to manipulate off-axis particles in three-dimensional space. In order to solve this problem, Minins proposed a curved photon nano-jet called photonic hook (PH) [11], which can be excited by asymmetric systems, such as rotating particles or particles with inhomogeneous refractive indices etc. Therefore, in this paper, the influence of the refractive index distribution of the scattering objects on the photonic hook morphology is discussed based on the finite difference frequency domain method (FDFD). It has some application prospects in the design of optical devices.

1 Inrtoduction

With the progress of science, mankind's exploration of the microscopic world has become more and more in-depth, and the connection between optics and the microscopic world has become more and more intense. There have also been many advances in the study of light scattering by microscopic particles.

Photonic nanojets are generated when a light beam is incident on a dielectric cylinder or dielectric sphere. The photonic nanojet is influenced by the incident wave parameters and particle parameters. The incident wave parameters include polarization state, wavelength, amplitude, etc. Particle parameters include particle size and dielectric constant, etc. Because of this, we can generate our desired PNJ by changing the parameters above.The photonic hook (PH) is known as a special PNJ. The morphology of the photonic hook as a curved photonic jet is determined by the effective length L_{eff}, the deviation angle, and the tilt angle, as shown in Fig. 1.

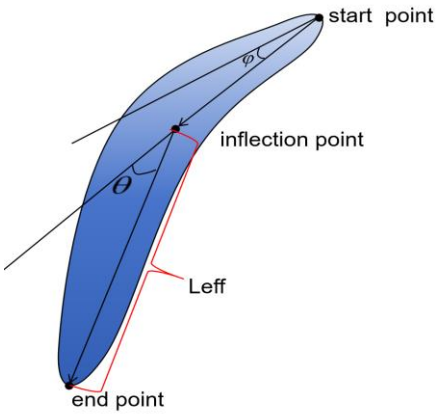

Figure 1 *Schematic of a curved photonic nanojet (PNJ)*

2 Method

2.1 Two-dimensional FDFD algorithm

We obtain the distribution of the field using computational electromagnetism by adjusting the parameters of the dielectric particles. The finite difference frequency domain (FDFD) method is derived from Maxwell's equations. Add a suitable UPML (uniaxial perfectly matched layer) to the initial set of frequency domain Maxwell's equations:

$$\begin{cases}\nabla\times\mathbf{E}=-j\omega[S][\mu]\mathbf{H}\\ \nabla\times\mathbf{H}=+j\omega[S][\varepsilon]\mathbf{E}\end{cases} \tag{1}$$

Where, S is the tensor of the UPML. For a two-dimensional environment, S_z equals to 1

$$\left[\varepsilon_{r,UPML}\right]=\left[\mu_{r,UPML}\right]=[S]=\begin{bmatrix}1/s_x & 0 & 0\\ 0 & s_x & 0\\ 0 & 0 & s_x\end{bmatrix}\begin{bmatrix}s_y & 0 & 0\\ 0 & 1/s_y & 0\\ 0 & 0 & s_y\end{bmatrix}\begin{bmatrix}s_z & 0 & 0\\ 0 & s_z & 0\\ 0 & 0 & 1/s_z\end{bmatrix} \tag{2}$$

$$=\begin{bmatrix}s_y s_z/s_x & 0 & 0\\ 0 & s_x s_z/s_y & 0\\ 0 & 0 & s_x s_y/s_z\end{bmatrix}$$

The vector Maxwell's equations (Eq. (1)) can be written as six scalar equations as:

$$\begin{cases} \dfrac{\partial E_z}{\partial y}-\dfrac{\partial E_y}{\partial z}=k_0\mu_{xx}\tilde{H}_x \\ \dfrac{\partial E_x}{\partial z}-\dfrac{\partial E_z}{\partial x}=k_0\mu_{yy}\tilde{H}_y \\ \dfrac{\partial E_y}{\partial x}-\dfrac{\partial E_x}{\partial y}=k_0\mu_{zz}\tilde{H}_z \\ \dfrac{\partial \tilde{H}_z}{\partial y}-\dfrac{\partial \tilde{H}_y}{\partial z}=k_0\varepsilon_{xx}E_x \\ \dfrac{\partial \tilde{H}_x}{\partial z}-\dfrac{\partial \tilde{H}_z}{\partial x}=k_0\varepsilon_{yy}E_y \\ \dfrac{\partial \tilde{H}_y}{\partial x}-\dfrac{\partial \tilde{H}_x}{\partial y}=k_0\varepsilon_{zz}E_z \end{cases} \tag{3}$$

Where, $\tilde{H}_x$, $\tilde{H}_y$, and $\tilde{H}_z$ are normalized magnetic fields, and are defined as the component of the magnetic field strength along each coordinate axis. $k_0 = 2\pi/\lambda$ is the wavenumber in vacuum, with λ being the wavelength in vacuum.

The first, second and sixth equations of Eq. (3) correspond to TM mode, and can be written as differiental form:

$$\begin{cases} \dfrac{E_z|_{i,j+1}-E_z|_{i,j}}{\Delta y'}=\mu_{xx}|_{i,j}\,\tilde{H}_x|_{i,j} \\ -\dfrac{E_z|_{i+1,j}-E_z|_{i,j}}{\Delta x'}=\mu_{yy}|_{i,j}\,\tilde{H}_y|_{i,j} \\ \dfrac{\tilde{H}_y|_{i,j}-\tilde{H}_y|_{i-1,j}}{\Delta x'}-\dfrac{\tilde{H}_x|_{i,j}-\tilde{H}_x|_{i,j-1}}{\Delta y'}=\varepsilon_{zz}|_{i,j}\,E_z|_{i,j} \end{cases} \tag{4}$$

After considering all cells, Eq. (4) can be written as a matrix equation:

$$\begin{cases} \mathbf{D}_{y'}^{e}\mathbf{e}_z=\boldsymbol{\mu}_{xx}\tilde{\mathbf{h}}_x \\ -\mathbf{D}_{x'}^{e}\mathbf{e}_z=\boldsymbol{\mu}_{yy}\tilde{\mathbf{h}}_y \\ \mathbf{D}_{x'}^{h}\tilde{\mathbf{h}}_y-\mathbf{D}_{y'}^{h}\tilde{\mathbf{h}}_x=\boldsymbol{\varepsilon}_{zz}\mathbf{e}_z \end{cases} \tag{5}$$

Where D is the derivative matrix and the relationship between them is:

$$\mathbf{D}_x^h=-\left(\mathbf{D}_x^e\right)^{\mathbf{H}},\quad \mathbf{D}_y^h=-\left(\mathbf{D}_y^e\right)^{\mathbf{H}} \tag{6}$$

After solving for the derivative matrix, we can solve for the wave matrix. According to the TF/SF technique, the SF masking matrix Q is set to identify the scattered field, which divides the scattered field and the total field region. Therefore, the source field, which can be derived by the QAAQ technique, can be added on the boundary of the region, and the field can be obtained by finding the product of the source vector and the inverse of the wave matrix. Above is the general flow of the 2D FDFD algorithm.

Photonic nanojet, as the name suggests, refers to the propagation of a beam of light, photons converge together to form a photonic nanojet with an intensity far exceeding that of the incident wave. And by changing the beam or the particles, it is possible to obtain a different photonic nanojet. There are many ways to generate this phenomenon, mostly starting with beams and particles, and obtaining different degrees of intensity enhancement. For example, in Fig. 2., the computational domain is $[-4\lambda, 4\lambda]$ in the x and y directions, the radius of the infinitely long cylinder is 2λ twice the wavelength The refractive indices for Fig. 2(a) and (b) are 1.3 and 1.4, respectively.

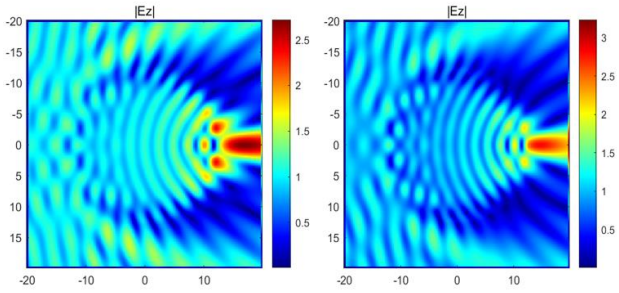

(a) m=1.3 (b) m=1.4

Figure 2 Photonic nanojet for different refractive index m

We can clearly see that the cylinders with higher refractive indices converge more strongly. The next part of this paper will proceed to introduce the effect of the change of the dielectric cylinder on the formation of PNJ.

It has already been said that the direction of the photonic jet along the axis. When we want to apply to optical tweezers and other scenarios, it is difficult to operate for off-axis particles. In order to solve this problem, we need to bend the photonic jet, also known as the photonic hook (PH) Recently, based on the Magnus effect of optics, researchers have proposed a new approach to the use of the rotation of particles (do not change the target and the structure of the incident beam) to design a photonic hook. Such an approach requires high control of the rotational angular velocity of the particles, but we can realize the generation of photonic hooks by building a non-uniform refractive index column.

2.2 Scattering from a non-uniform dielectric sphere

An infinitely long microcylinder is placed parallel to the z-axis in the xy-plane cross-section, and is illuminated by a TM polarized plane wave propagating along the x-axis . The environment is a vacuum (μ_0, ε_0). The electric and magnetic fields of the incident wave are:

$$\begin{cases} \mathbf{E}_{inc}=E_0e^{jkx}\mathbf{e}_z \\ \mathbf{H}_{inc}=\dfrac{E_0}{\eta_0}e^{jkx}\mathbf{e}_y \end{cases} \tag{7}$$

with

$$\eta_0 = \sqrt{\frac{\mu_0}{\varepsilon_0}} = 120\pi \tag{8}$$

Eq. (8)represents the vacuum wave impedance. The time factor is $e^{+j\omega t}$. The computational domain is $x \in (-12\pi, 12\pi), y \in (-12\pi, 12\pi)$, the thickness of the PML layer is one-tenth of the periphery of the computational domain. The entire computational domain is surrounded by the PML layer.The wavelength is 632.8nm. The values of amplitude and relative permeability are both 1. Microcylindrical radius is $a = 2\lambda$. Its refractive index partition is parallel to the x-axis direction and in the center of the y-axis of the computational domain. Setting the refractive index n_high=1.3317 (water) for the upper part and n_low for the lower part as 1.35, 1.40, 1.45, 1.50, 1.55, 1.60, 1.65, 1.70. The epsilon modeling data obtained when the refractive index of the upper part is 1.3317 and that of the lower part is 1.35, the result is shown in Fig. 3. We move the scattering object to the left to better observe the morphology of the photonic nanojet.

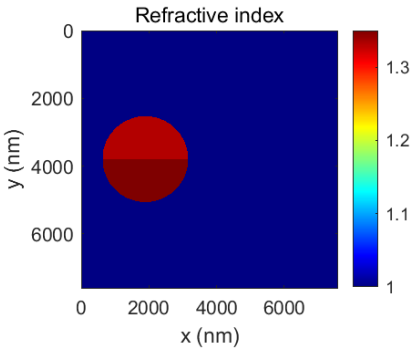

Figure 3 *Schematic of the interface of the established scattering model*

Since the incident wave is a TM mode and the electric field component is only present in Ez, we plot the modal value of Ez with the PML layer removed:

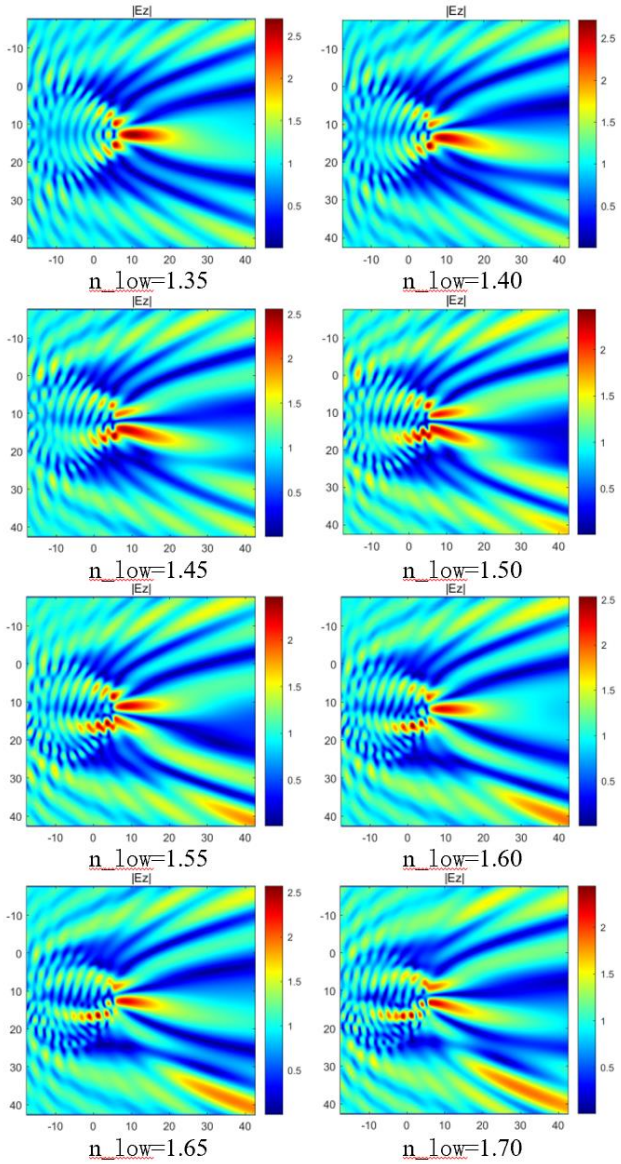

Figure 4 *Modal value plots for the removal of the PML layer*

At this point we can see that the enhancement to the amplitude-normalized field reaches a maximum at the main flap, which is more than twice as large as the incident field, the direction of the photonic jet is no longer along the axial direction, and the intensity distributions of the main flap and the secondary flap are changing. It is noteworthy that at n_low equal to 1.50, two jets of essentially equal strength appear in the figure.

3 Discussion and conclusion

In the work of this paper, a preliminary study has been done on the generation of photon jets and photon hooks, which can be used to generate curved photon jets with different morphologies using an asymmetric system while the particles are at rest, laying the groundwork for the design of an optical device for the manipulation of off-axis particles using optical tweezers.

4 References

[1] CHEN Z, TAFLOVE A, BACKMAN V. Photonic nanojet enhancement of backscattering of light by nanoparticles: a potential novel visible-light ultramicroscopy technique[J]. Optics Express, 2004, 12(7): 1214-1220.

[2] BENINCASA D S, BARBER P W, ZHANG J Z, et al. Spatial distribution of the internal and near-field intensities of large cylindrical and spherical scatterers[J]. Applied Optics, 1987, 26(7): 1348-1356.

[3] MININ I, MININ O. Photonics of mesoscale nonspherical and non axysimmetrical dielectric particles and application to cuboid-chain with air-gaps waveguide based on periodic terajet-induced modes[C]//2015 17th International Conference on Transparent Optical Networks (ICTON). IEEE, 2015: 1-5.

[4] LUK'YANCHUK B S, PANIAGUA-DOMÍNGUEZ R, MININ I, et al. Refractive index less than two: photonic nanojets yesterday, today and tomorrow[J]. Optical Materials Express, 2017, 7(6):1820-1847.

[5] KOVROV A, NOVITSKY A, KARABCHEVSKY A, et al. A photonic nanojet as tunable and polarization-sensitive optical tweezers[J]. Annalen der Physik, 2018, 530(9): 1800129.

[6] NEVES A A R. Photonic nanojets in optical tweezers[J]. Journal of Quantitative Spectroscopy and Radiative Transfer, 2015, 162: 122-132.

[7] LI Y, XIN H, LIU X, et al. Trapping and detection of nanoparticles and cells using a parallel photonic nanojet array[J]. ACS nano, 2016, 10(6): 5800-5808.

[8] JACASSI A, TANTUSSI F, DIPALO M, et al. Scanning probe photonic nanojet lithography[J].ACS applied materials & interfaces, 2017, 9(37): 32386-32393.

[9] ZHENG H, ZHOU Y, UGWU C F, et al. Large-scale metasurfaces based on grayscale nanosphere lithography[J]. ACS Photonics, 2021, 8(6): 1824-1831.

[10] BORN B, KRUPA J D A, GEOFFROY-GAGNON S, et al. Integration of photonic nanojets and semiconductor nanoparticles for enhanced all-optical switching[J]. Nature Communications, 2015,6(1): 1-9.

[11] O. V. Minin and I. V. Minin, Diffractive Optics and Nanophotonics: Resolution Below the Diffraction Limit (Springer,2016).

The 14th International Conference on
Laser-light and Interactions with Particles (LIP2024)
September 18-22nd, 2024, Xi'an, Shaanxi, China

THE INTERNAL-FIELD DISTRIBUTIONS OF CHIRAL PARTICLE BY DUAL HERMITE-GAUSSIAN BEAMS

Jing Bai[1*], Wen-Hao Ma[1], Cheng-Xian Ge[2], Zhen-Sen Wu [3], Tong Xu[1]

[1] School of Electronic Engineering, Xi'an University of Posts & Telecommunications, Xi'an, Shaanxi, 710121, China
[2] The 39th Research Institute of China Electronics Technology Corporation, Xi'an, Shaanxi, 710065, China
[3] School of Physics and Optoelectronic Engineering, Xidian University, Xi'an, Shaanxi, 710071, China *
jbaiyoudian@163.com
Corresponding author: jbaiyoudian@163.com

Abstract

With the continuous development of laser technology, the study of particle-beam interactions has become a hot topic, finding broad applications in biomedical , polymer science , aerosol detection , and other fields. Within the framework of the generalized Lorenz-Mie theory, expressions for the spherical vector wave functions of arbitrary incident dual Hermite-Gaussian beams are obtained using the complex source-point method and coordinate rotation theory. Analytical solutions for the scattering of dual Hermite-Gaussian beams by chiral particles are derived based on the boundary continuity conditions of the electromagnetic field. A comparative analysis is conducted between the research findings and simulated results reported in existing literature, validating the theoretical propositions and methods proposed in this paper. Detailed analyses are provided on the influences of beam mode order, incident angle, particle size, waist radius, polarization angle, chirality parameter, and beam center position on the numerical results of near-field and far-field scattering.

1 Introduction

Since the introduction of GLMT [1], Kim utilized the complex source-point method to expand higher-order Hermite-Gaussian beams into the form of spherical vector wave functions (SVWFs), investigating the scattering characteristics of high-order Hermite-Gaussian beams on isotropic homogeneous spheres [2]. Yokota further studied the scattering characteristics of two-dimensional and three-dimensional Hermite-Gaussian beams in parallel cylinders, deriving the relationship between real-parameter Hermite-Gaussian beam modes and the complex-source multipole excitation field, and found that the scattering field of beam modes can be represented by a finite number of multipole scattering fields [3]. In 2009, Li expanded Hermite-Gaussian beams using SVWFs within the framework of GLMT. By employing the complex source-point method, Li represented the beam field of high-order Hermite-Gaussian beams incident on multilayered spheres and obtained the scattering coefficients using electromagnetic field boundary conditions [4]. In 2012, Qu utilized the derivatives of higher-order Gaussian beams and Davis's first-order approximation of slowly varying functions to describe the intensity distribution patterns of high-order Hermite-Gaussian beams. This work focused on studying the scattering characteristics of high-order off-axis Hermite-Gaussian beams [5]. Building on this, Qu used the complex source-point method and coordinate rotation theory to derive the spherical vector wave function expansion of arbitrary incident Hermite-Gaussian beams. They provided expressions for the internal and far-field scattering of Hermite-Gaussian beams on anisotropic spheres [6]. In 2017, Huang conducted a study on the scattering and polarization characteristics of Hermite-Gaussian beams on aerosol particles based on GLMT and the complex source-point method [7].

However, the above-mentioned literature primarily investigates the scattering characteristics of single Hermite-Gaussian beams. In recent years, with the advancement of light scattering research, the study of particle scattering by dual beams has gradually emerged. Compared to single-beam scattering, dual-beam scattering can reconstruct the spatial structure of targets by simultaneously collecting multiple scattering signals, thereby enhancing spatial resolution and accurately determining the position and shape of targets. Additionally, dual-beam scattering can simultaneously acquire scattering characteristics of targets at different angles, providing more information about the targets, such as shape and surface structure, which helps to comprehensively understand the properties of the targets. These advantages have led to widespread applications of dual-beam scattering in fields such as optical measurements, antenna design, and seismic detection. Considering the study of the scattering characteristics of high-order dual Hermite-Gaussian beams remains an area that requires further exploration. The findings of such research provide crucial theoretical support and practical recommendations for the advancement of dual-beam optical manipulation techniques and chiral particle identification and classification technologies.

2 Theoretical background

This chapter introduces the expansion of dual Hermite-Gaussian beams in terms of spherical vector wave functions and the scattering theory of chiral spheres. The scattering of chiral particles by single Hermite-Gaussian beams is extended to the scattering of chiral particles by dual Hermite-Gaussian beams. Figure 1 depicts a schematic diagram of chiral particles illuminated by dual Hermite-Gaussian beams.

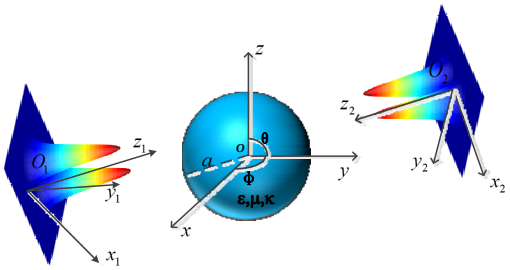

Figure1 *Schematic diagram of the irradiation of a chiral particle by dual Hermite-Gaussian beams*

Based on the conclusions drawn by Siegman, electromagnetic multipole fields located at complex source points can be utilized to generate higher-order complex beam fields. Therefore, for a Hermite-Gaussian beam of order uv, its vector potential can be expressed as:

$$A_H^{u,v} = \hat{x}\psi_H^{u,v} = \hat{x}C\frac{\partial^{u+v}}{\partial x^u \partial y^v}\frac{\exp(ikR)}{ikR} \tag{1}$$

In Eq. (1), C is the optical normalization parameter, $\hat{x}$ denotes the unit vector of the polarization direction, $R=[(x+x_0)^2+(y+y_0)^2+(z+z_0-ib)^2]^{1/2}$ denotes the distance between the complex source point $Q(-x_0,-y_0,-z_0+ib)$ and the observation point $P(x,y,z)$, $b=kw_0^2/2$, k is the free-space wave number, and w_0 is the beam center.

To represent higher-order beams using spherical vector wave functions, according to the theory proposed by Watson, the higher-order beam can be expanded using spherical scalar functions as:

$$\psi_H^{u,v} = \sum_{n=0}^{\infty}\sum_{m=-n}^{n} H_{u,v}^{(1)}(n,m) f_{mn}^{(1)} \quad |r| < \left|r_0 e^{\pm i\Delta}\right| \tag{2}$$

In Eq. (2), $f_{nm}^{(1)} = j_n(k_0 r)P_n^{|m|}(\cos\theta)e^{im\phi}$ is the concatenated Legendre function, $r_0=\left[x_0^2+y_0^2+(z-ib)^2\right]^{1/2}$, $\phi_0=\tan^{-1}y_0/x_0$.

Following the conclusions of Kim, in the form of expansion using spherical vector wave functions, the vector potential of the Hermite-Gaussian beam is set as:

$$A_H^{u,v} = C\sum_{n=1}^{\infty}\sum_{m=-n}^{n}\left[\alpha^{(1)}(u,v,n,m)\mathrm{M}_{mn}^{(1)}(r,k)+\beta^{(1)}(u,v,n,m)\mathrm{N}_{mn}^{(1)}(r,k)\right] \tag{3}$$

In Eq. (3), $\mathrm{M}_{mn}^{(1)}$, $\mathrm{N}_{mn}^{(1)}$ are the spherical vector wave functions. $\alpha^{(1)}(u,v,n,m)$ and $\beta^{(1)}(u,v,n,m)$ are beam expansion coefficients.

By calculating this we can get:

$$\alpha^{(1)}(u,v,n,m) = \frac{1}{2n(n+1)}\left[H_{u,v}^{(1)}(n,m-1)+(n-m)(n+m+1)H_{u,v}^{(1)}(n,m+1)\right] \tag{4}$$

$$\beta^{(1)}(u,v,n,m) = \left\{\frac{(n+1)}{(2n-1)}\left[H_{u,v}^{(1)}(n-1,m-1)-(n-m)(n-m-1)H_{u,v}^{(1)}(n-1,m+1)\right] - \frac{n}{(2n+3)}\left[H_{u,v}^{(1)}(n+1,m-1)-(n+m+2)(n+m+1)H_{u,v}^{(1)}(n+1,m+1)\right]\right\} \tag{5}$$

the electromagnetic and magnetic fields of the incident Hermite-Gaussian beam in the form of the spherical vector wave function expansion can be obtained:

$$E_H^{inc} = i\omega C\sum_{n=1}^{\infty}\sum_{m=-n}^{n}\left[\alpha^{1(1)}(u,v,n,m)\mathrm{M}_{mn}^{(1)}(r,k)+\beta^{1(1)}(u,v,n,m)\mathrm{N}_{mn}^{(1)}(r,k)\right] \tag{6}$$

$$H_H^{inc} = i\omega C\frac{k}{i\omega\mu_0}\sum_{n=1}^{\infty}\sum_{m=-n}^{n}\left[\beta^{1(1)}(u,v,n,m)\mathrm{M}_{mn}^{(1)}(r,k)+\alpha^{1(1)}(u,v,n,m)\mathrm{N}_{mn}^{(1)}(r,k)\right] \tag{7}$$

The rotation coefficients are:

$$\rho(m,s,n) = (-1)^{s+m}\left[\frac{(n+m)!(n-s)!}{(n-m)!(n+s)!}\right]^{1/2} u_{sm}^{(n)}(-\alpha) \tag{8}$$

By substituting the rotation coefficients, the spherical vector wave function expansion of the Hermite-Gaussian beam in the particle coordinate system is given by:

$$E_H^{inc} = i\omega C\sum_{n=1}^{\infty}\sum_{m=-n}^{n}\sum_{s=-n}^{n}\rho(s,m,n)\left[\alpha^{1(1)}(u,v,n,s)\mathrm{M}_{mn}^{(1)}(r_{10},k)+\beta^{1(1)}(u,v,n,s)\mathrm{N}_{mn}^{(1)}(r_{10},k)\right] \tag{9}$$

$$H_H^{inc} = i\omega C\frac{k}{i\omega\mu_0}\sum_{n=1}^{\infty}\sum_{m=-n}^{n}\sum_{s=-n}^{n}\rho(s,m,n)\left[\beta^{1(1)}(u,v,n,s)\mathrm{M}_{mn}^{(1)}(r_{10},k)+\alpha^{1(1)}(u,v,n,s)\mathrm{N}_{mn}^{(1)}(r_{10},k)\right] \tag{10}$$

Based on previous results, the following expression for the expansion of the spherical vector wave function of the chiral dielectric spherical scattering field can be obtained:

$$E^S = \sum_{n=1}^{\infty}\sum_{m=-n}^{n}\left[A_{mn}^S\mathrm{M}_{mn}^{(3)}(r,k)+B_{mn}^S\mathrm{N}_{mn}^{(3)}(r,k)\right] \tag{11}$$

$$H^S = \frac{k_0}{i\omega\mu_0}\sum_{n=1}^{\infty}\sum_{m=-n}^{n}\left[A_{mn}^S\mathrm{N}_{mn}^{(3)}(r,k)+B_{mn}^S\mathrm{M}_{mn}^{(3)}(r,k)\right] \tag{12}$$

Figure 2 plots the internal electric field strength of the second beam of incident angle $0°$, $180°$ respectively. It can be observed that total field appears to have a very small value in both forward and backward directions and the extremely large values are mainly distributed in the lateral position and show a symmetric flap-like distribution.

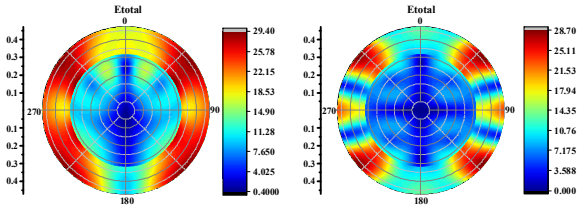

Fig. 2. *The internal-field distributions of chiral spheres under the illumination of dual-beam HG12 at different incident angles.*

In this paper, the authors further investigate the more complex dual Hermite-Gaussian wave opponent particle scattering.

3 Acknowledgement

The authors wish to acknowledge the National Natural Science Foundation of China for its support of Grant no. 62001377, the Natural Science Foundation of Shaanxi Province under Grant nos. 2023-JC-QN-0657, 2023-JC-QN-0774, 2022KJXX-95. Xi'an Science and Technology Association Youth Talent Nurturing Program under Grant no 959202313013.

4 References

[1] Ren K F, Gouesbet G, Gréhan G. Integral localized approximation in generalized Lorenz–Mie theory[J]. Applied optics, 1998, 37(19): 4218-4225.

[2] Kim J S, Lee S S. Scattering of laser beams and the optical potential well for a homogeneous sphere[J]. Josa, 1983, 73(3): 303-312.

[3] Yokota M, Takenaka T, Fukumitsu O. Scattering of a Hermite–Gaussian beam mode by parallel dielectric circular cylinders[J]. JOSA A, 1986, 3(4): 580-586.

[4] Hai-Ying L, Zhen-Sen W, Zheng-Jun L. Scattering from a multi-layered sphere located in a high-order Hermite-Gaussian beam[J]. Chinese Physics Letters, 2009, 26(10): 104203.

[5] Qu T, Wu Z S, Li H Y, et al. Scattering Properties of the Higher-Order Hermite Gaussian Beam[J]. Advanced Materials Research, 2012, 571: 357-361.

[6] Qu T, Wu Z, Shang Q, et al. Scattering of an anisotropic sphere by an arbitrarily incident Hermite–Gaussian beam[J]. Journal of Quantitative Spectroscopy and Radiative Transfer, 2016, 170: 117-130.

[7] Huang Q, Cheng M, Guo L, et al. Scattering of aerosol particles by a Hermite–Gaussian beam in marine atmosphere[J]. Applied Optics, 2017, 56(19): 5329-5335.

The 14th International Conference on
Laser-light and Interactions with Particles (LIP2024)
September 18-22nd, 2024, Xi'an, Shaanxi, China

SCATTERING BY A PLASMA ANISOTROPIC COATED SPHERE LOCATED IN AN OFF-AXIS ZERO-ORDER BESSEL BEAM

Zheng Jun Li[1], Yu Feng Zhou[1,*], Qing Chao Shang[1], Hai Ying Li[1], Zhen Sen Wu[1]

1. School of Physics, Xidian University, Xi'an, 710071, P. R. China.

Corresponding author: lizj@xidian.edu.cn

Abstract

Based on the Generalized Lorenz–Mie theory (GLMT), electromagnetic scattering of a plasma anisotropic coated sphere illuminated by an off-axis Zero-order Bessel beam (ZOBB) is investigated. The expansion expressions of the ZOBB are given in terms of the spherical vector wave functions (SVWFs) and the expansion coefficients are derived using the orthogonality of associated Legendre function and exponential function. By introducing the Fourier transform, the electromagnetic (EM) fields in the plasma anisotropic layer are expressed as the addition of the first and the second SVWFs. The scattering coefficients are analytically derived by applying the continuous tangential boundary conditions to each interface among the internal isotropic dielectric or conductor sphere, the anisotropic shell, and the free space. The accuracy of the theory and codes are verified by comparing the numerical results reduced to the special cases of a plane wave incidence and a plasma anisotropic sphere with results from references. The effects of the conical angle, the beam center position, coating thickness and dielectric parameters on the Radar cross section (RCS) are analyzed. The applications of this theoretical development in the fields of target shielding, and anti-radar coating are numerically discussed.

1 Introduction

The EM scattering of a plane wave by a coated spherical particle has been extensively discussed in many areas such as combustion, biomedicine, chemical engineering, remote sensing and so on. Within a theoretical framework similar to the classic Lorenz-Mie theory [1], rigorous formulations were first developed for scattering using two concentric spheres by Aden and Kerker [2]. This general solution was subsequently specialized for a lossless or lossy dielectric-coated conductor sphere. Wu presented numerical results for EM scattering by a multilayered sphere [3]. A concentric sphere Mie scattering model is employed to describe light scattering by pulmonary alveoli and airway surface liquid by Durkee et al. [4]. EM scattering by a coated sphere with arbitrary amount of surface charges is studied by Gao et al. [5].

Due to wide applications in optical signal processing, radar cross section (RCS) controlling, microwave device fabrication, etc., a great interest in the interaction between EM wave and anisotropic media is being grown. As a typical anisotropic medium, research on EM scattering of plasma anisotropic spheres is of special importance in the target shielding field and properties in the space environment. In addition to, studies on the homogeneous plasma anisotropic sphere [6-9] and plasma anisotropic cylinder [10-12]. Numerous investigations have focused on the interaction between a plane wave and a plasma anisotropic coated sphere. However, almost all excitation sources in all these studies are limited to a plane wave.

Nevertheless, the EM scattering of a Bessel beam by plasma anisotropic particles has not yet been reported. In fact, Bessel beam has attracted widespread attention in various fields, such as optical trapping and manipulation, particle sizing since its naissance by Durnin [13], because of its non-diffraction and self-reconstruction properties. Using representation of EM fields, the scattering problem of a Bessel beam by spherical particles has been investigated by several scholars. Ma and Li [14] investigated unpolarized Bessel beam scattering by a dielectric sphere. Ambrosio et al. [15] provided an expansion coefficient in terms of SVWFs by applying an integral localized approximation. Mishra [16] derived a vector wave theory to describe the Bessel beam for an arbitrary half-conical angle. Using this vector description, Mitri investigated the scattering of a ZOBB [17] by a dielectric sphere. Using an analytical method, the scattering of a ZOBB by a concentric sphere was investigated by Chen et al. [18], but this ZOBB was assumed to present on-axis incidence only. Utilizing GLMT [19, 20], the polarization-sensitive photonic jet of a dielectric sphere excited by a ZOBB is studied [21]. Despite the wealth of knowledge obtained from these works, however, the scattering particle in all of these previous studies is limited to isotropic medium.

However, the EM scattering of a ZOBB by a plasma anisotropic coated sphere has not yet been studied. Beam propagation and scattering in inhomogeneous plasma anisotropic media are complex, making analysis difficult. Moreover, the expansion terms m are not only equivalent zero for off-axis ZOBB scattering, which also enhances the difficulty of the solution and numerical calculations of the plasma anisotropic particle scattered from an off-axis beam. This paper aims to develop a precise solution to the general case of an off-axis ZOBB scattering by a plasma anisotropic coated isotropic dielectric or conductor sphere, study the role of the anisotropy and beam center positioning in far-field scattering diagrams, and understand the mechanism of wave-medium interaction.

2 Theoritical treatements

Consider a plasma anisotropic coated isotropic sphere or conductor sphere center-located in a spherical coordinate system $Oxyz$. As shown in Fig. 1, the outer and inner radii are a_1 and a_2, respectively. The inner sphere is coated with a plasma anisotropic material characterized by the permittivity tensor $\overline{\overline{\varepsilon}}_1$ and permeability tensor $\overline{\overline{\mu}}_1$ with the coating thickness d ($d = a_1 - a_2$) in its primary system $Oxyz$. The inner medium may be vacuum, isotropic medium or metal. Three distinct regions are thus defined, namely, region 0 for the free space with ε_0 and μ_0, region 1 for the plasma anisotropic medium, and region 2 for the isotropic sphere, metal or cavity with ε_2 and μ_2. The particle is illuminated by an off-axis ZOBB that propagates in the z-axis direction and the center O' of the ZOBB is located at (x_0, y_0, z_0) in $Oxyz$. The beam coordinate system $O'x'y'z'$ is parallel to particle system $Oxyz$.

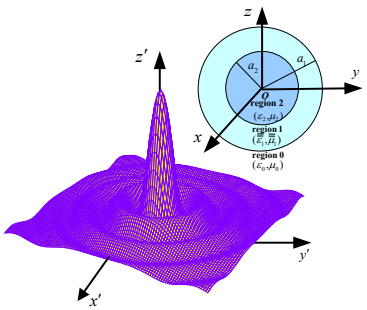

Fig. 1. Plasma anisotropic coated isotropic or metal sphere illuminated by an off-axis ZOBB with α=5°

The EM field components of the ZOBB propagating along z'-axis in $O'x'y'z'$ can be derived [16, 17]:

$$\begin{aligned}\mathbf{E}' = \frac{1}{2}E_0 e^{ik_{z'}z'}\Bigg\{&\Bigg[\left((1+\frac{k_{z'}}{k_0}-\frac{k_{R'}^2x'^2}{k_0^2R'^2})\right)J_0(k_{R'}R')\\&-J_1(k_{R'}R')\frac{k_{R'}(y'^2-x'^2)}{k_0^2R'^3}\Bigg]\hat{e}_{x'}\\&+x'y'\left[J_1(k_{R'}R')\frac{2k_{R'}}{k_0^2R'^3}-\frac{k_{R'}^2}{k_0^2R'^2}J_0(k_{R'}R')\right]\hat{e}_{y'}\\&+\frac{x'}{ik_0R'}(1+\frac{k_{z'}}{k_0})k_{R'}J_1(k_{R'}R')\hat{e}_{z'}\Bigg\}\end{aligned} \tag{1}$$

$$\begin{aligned}\mathbf{H}' = \frac{E_0}{2}\sqrt{\frac{\varepsilon_0}{\mu_0}}e^{ik_{z'}z'}\Bigg\{&x'y'\left[\frac{2k_{R'}J_1(k_{R'}R')}{k_0^2R'^3}-\frac{k_{R'}^2J_0(k_{R'}R')}{k_0^2R'^2}\right]\hat{e}_{x'}\\&-\left[J_1(k_{R'}R')k_{R'}\frac{x'^2-y'^2}{k_0^2R'^3}-(1+\frac{k_{z'}}{k_0}-\frac{y'^2k_{R'}^2}{k_0^2R'^2})J_0(k_{R'}R')\right]\hat{e}_{y'}\\&+\frac{k_{R'}y'}{ik_0R'}(1+\frac{k_{z'}}{k_0})J_1(k_{R'}R')\hat{e}_{z'}\Bigg\}\end{aligned} \tag{2}$$

where $J_0(k_{R'}R')$ is the cylindrical Bessel function of the first kind of the zero order, E_0 is the characteristic amplitude, $k_{R'} = k_0 \sin\alpha$ is transverse wave number, $k_{z'} = k_0 \cos\alpha$ is longitudinal wave number, α is so-called conical angle of the ZOBB, $R' = \sqrt{x'^2 + y'^2}$, and k_0 is wave number in the medium, respectively. $\hat{e}_{x'}$, $\hat{e}_{y'}$ and $\hat{e}_{z'}$ are the unite vector in $O'x'y'z'$.

The EM fields can be transformed to the particle coordinate system $Oxyz$. Since the vector description of the ZOBB in Eq. (1) and (2) stemming forms Maxwell equations, the ZOBB can be expanded in terms of SVWFs in $Oxyz$ as:

$$\begin{aligned}\mathbf{E}^i &= \sum_{n=1}^{\infty}\sum_{m=-n}^{n}\left[a_{mn}^i\mathbf{M}_{mn}^{(1)}(\mathbf{r},k_0)+b_{mn}^i\mathbf{N}_{mn}^{(1)}(\mathbf{r},k_0)\right]\\ \mathbf{H}^i &= \frac{k_0}{i\omega\mu_0}\sum_{n=1}^{\infty}\sum_{m=-n}^{n}\left[a_{mn}^i\mathbf{N}_{mn}^{(1)}(\mathbf{r},k_0)+b_{mn}^i\mathbf{M}_{mn}^{(1)}(\mathbf{r},k_0)\right]\end{aligned} \tag{3}$$

where $\mathbf{r}$ is the position vector from particle center O, the superscript "i" indicates the relative parameters of the incident fields. a_{mn}^i and b_{mn}^i are the expansion coefficients of the incident fields. $\mathbf{M}_{mn}^{(l)}(\mathbf{r},k_0)$ and $\mathbf{N}_{mn}^{(l)}(\mathbf{r},k_0)$ are the SVWFs, and l=1, 2, 3, or 4 represents four kinds of spherical Bessel functions in the SVWFs [22].The expansion coefficients of the incident fields are derived as [23, 24]:

$$\begin{aligned}\begin{pmatrix}a_{mn}^i\\ b_{mn}^i\end{pmatrix} &= \begin{pmatrix}\sqrt{\mu_0/\varepsilon_0}\\ 1\end{pmatrix}\frac{2n+1(k_0a_1)^2}{E_0\,4\pi n(n+1)\psi_n(k_0a_1)}\frac{(n-m)!}{(n+m)!}\\&\times\int_0^{2\pi}\int_0^{\pi}\begin{pmatrix}iH_{r=a_1}^i\\ E_{r=a_1}^i\end{pmatrix}P_n^m(\cos\theta)e^{-im\phi}\sin\theta d\theta d\phi\end{aligned} \tag{4}$$

where $\psi_n(k_0a_1)$ is the spherical Riccati-Bessel function of the first kind, and $P_n^m(\cos\theta)$ is the associated Legendre function of the first kind. E_r^i and H_r^i are the radial electromagnetic fields of the original ZOBB in particle coordinate system which can be obtained from Eqs. (1) and (2) by utilizing the transformation relationship : $\hat{e}_r = \sin\theta\cos\phi\hat{e}_x + \sin\theta\sin\phi\hat{e}_y + \cos\theta\hat{e}_z$.

The scattered fields of the particle can be expanded in terms of SVWFs in $Oxyz$ as:

$$\begin{aligned}\mathbf{E}^s &= \sum_{n=1}^{\infty}\sum_{m=-n}^{n}\left[a_{mn}^s\mathbf{M}_{mn}^{(3)}(\mathbf{r},k_0)+b_{mn}^s\mathbf{N}_{mn}^{(3)}(\mathbf{r},k_0)\right]\\ \mathbf{H}^s &= \frac{k_0}{i\omega\mu_0}\sum_{n=1}^{\infty}\sum_{m=-n}^{n}\left[a_{mn}^s\mathbf{N}_{mn}^{(3)}(\mathbf{r},k_0)+b_{mn}^s\mathbf{M}_{mn}^{(3)}(\mathbf{r},k_0)\right]\end{aligned} \tag{5}$$

where the superscript "s" indicates the relative parameters of the scattered fields, and a_{mn}^s and b_{mn}^s are the scattering coefficients. For plasma anisotropic medium shown in Fig. 1, the permittivity and permeability are characterized by tensors $\overline{\overline{\varepsilon}}_1$ and $\overline{\overline{\mu}}_1$, expressed as:

$$\overline{\overline{\varepsilon}}_1 = \begin{bmatrix}\varepsilon_{1xx} & \varepsilon_{1xy} & 0\\ \varepsilon_{1yx} & \varepsilon_{1yy} & 0\\ 0 & 0 & \varepsilon_{1zz}\end{bmatrix}\varepsilon_0, \qquad \overline{\overline{\mu}}_1 = \mu_0\overline{\overline{I}} \tag{6}$$

Using the Fourier transform method, the fields on coated plasma anisotropic medium in region 1 ($a_2 \le r \le a_1$, designated by the superscript 1) can be expanded as [25-27],

$$\mathbf{E}_1^I = \sum_{l=1}^{2}\sum_{q=1}^{2}\sum_{n=1}^{\infty}\sum_{m=-n}^{n}\sum_{n'=1}^{\infty} 2\pi F_{mn'q}^{(l)} \int_0^{\pi} \Big[A_{mnq}^{e}\mathbf{M}_{mn}^{(1)}(\mathbf{r},k_q) + B_{mnq}^{e}\mathbf{N}_{mn}^{(1)}(\mathbf{r},k_q) + C_{mnq}^{e}\mathbf{L}_{mn}^{(1)}(\mathbf{r},k_q)\Big] P_{n'}^{m}(\cos\theta_k) k_q^2 \sin\theta_k d\theta_k$$

$$\mathbf{H}_1^I = \sum_{l=1}^{2}\sum_{q=1}^{2}\sum_{n=1}^{\infty}\sum_{m=-n}^{n}\sum_{n'=1}^{\infty} 2\pi F_{mn'q}^{(l)} \int_0^{\pi} \Big[A_{mnq}^{h}\mathbf{M}_{mn}^{(1)}(\mathbf{r},k_q) + B_{mnq}^{h}\mathbf{N}_{mn}^{(1)}(\mathbf{r},k_q) + C_{mnq}^{h}\mathbf{L}_{mn}^{(1)}(\mathbf{r},k_q)\Big] P_{n'}^{m}(\cos\theta_k) k_q^2 \sin\theta_k d\theta_k \quad (7)$$

where the superscript "I" indicates the relative parameters of the internal fields; $k_q\,(q=1,2)$ is the wavenumber of the EM wave in the plasma anisotropic medium. Due to the existence of the extraordinary wave, the EM field in the plasma anisotropic sphere must be expanded in terms of the whole SVWFs M, N, and L. In Eq. (8), the six expansion coefficients $A_{mnq}^{e}, B_{mnq}^{e}, C_{mnq}^{e}, A_{mnq}^{h}, B_{mnq}^{h}$ and C_{mnq}^{h} can be obtained through the orthogonality of the SVWFs and their expressions are found in [7].

Because the EM fields are finite at the origin, the internal fields of the isotropic sphere or conductor sphere in region 2 ($r \le a_2$) can be expanded as:

$$\mathbf{E}_2^I = \begin{cases} \sum_{mn}\Big[a_{mn}''\mathbf{M}_{mn}^{(1)}(\mathbf{r},k'') + b_{mn}''\mathbf{N}_{mn}^{(1)}(\mathbf{r},k'')\Big], & k'' \neq 0 \\ 0, & k'' \to \infty \end{cases} \quad (8)$$

$$\mathbf{H}_2^I = \begin{cases} \dfrac{k''}{i\omega\mu''}\sum_{mn}\Big[a_{mn}''\mathbf{N}_{mn}^{(1)}(\mathbf{r},k'') + b_{mn}''\mathbf{M}_{mn}^{(1)}(\mathbf{r},k'')\Big], & k'' \neq 0 \\ 0, & k'' \to \infty \end{cases} \quad (9)$$

where $k'' = \omega\sqrt{\mu_2\varepsilon_2}$ is the wave number in region 2, and $\varepsilon_2 \to \infty$ denotes a conductor sphere. a_{mn}'' and b_{mn}'' are the unknown expansion coefficients of the EM fields in region 2.

Applying the spherical boundary at $r = a_1$ and $r = a_2$, the scattering coefficients a_{mn}^{s} and b_{mn}^{s} can be derived:

$$a_{mn}^{s} = \frac{1}{h_n^{(1)}(k_0 a_1)}\Bigg\{ \sum_{l=1}^{2}\sum_{q=1}^{2}\sum_{n'=1}^{\infty} 2\pi F_{mn'q}^{(l)} \int_0^{\pi} A_{mnq}^{e} z_n^{(l)}(k_q a_1) \cdot P_{n'}^{m}(\cos\theta_k) k_q^2 \sin\theta_k d\theta_k - a_{mn}^{i} j_n(k_0 a_1)\Bigg\} \quad (10)$$

$$b_{mn}^{s} = \frac{1}{h_n^{(1)}(k_0 a_1)}\Bigg\{ \frac{i\omega\mu_0}{k_0}\sum_{l=1}^{2}\sum_{q=1}^{2}\sum_{n'=1}^{\infty} 2\pi F_{mn'q}^{(l)} \int_0^{\pi} A_{mnq}^{h} z_n^{(l)}(k_q a_1) \cdot P_{n'}^{m}(\cos\theta_k) k_q^2 \sin\theta_k d\theta_k - b_{mn}^{i} j_n(k_0 a_1)\Bigg\} \quad (11)$$

Taking E_0 ($E_0 = 1$) as the amplitude of the incident electric field, the RCS for the far-region scattered field can be calculated as:

$$\sigma = \lim_{r\to\infty}\left(4\pi r^2 \left|\mathbf{E}^{s}\right|^2 / \left|\mathbf{E}^{i}\right|^2 \right) = \frac{4\pi}{k_0^2}\Bigg\{ \left| \sum_{n=1}^{\infty}\sum_{m=-n}^{n} (-i)^n e^{im\phi}\left[m a_{mn}^{s}\pi_{mn} + b_{mn}^{s}\tau_{mn}\right]\right|^2 + \left| \sum_{n=1}^{\infty}\sum_{m=-n}^{n} (-i)^{n+1} e^{im\phi}\left[a_{mn}^{s}\tau_{mn} + m b_{mn}^{s}\pi_{mn}\right]\right|^2 \Bigg\} \quad (12)$$

During programming calculation, the angular functions $\pi_{mn} = P_n^m(\cos\theta)/\sin\theta$, $\tau_{mn} = dP_n^m(\cos\theta)/d\theta$ are introduced.

3 Numerical results and disscussion

To verify the accuracy of our theory, two comparisons are made. As shown in Fig. 2, the results obtained from our codes reduced to a plane wave incidence for a plasma coated spherical shell are coincident with the results given in [28].

When $\alpha = 0^\circ$, the ZOBB will degenerate into a plane wave. As shown in Fig. 2 the angular distribution of the RCS of a plasma anisotropic sphere shell illuminated by an on-axis ZOBB when the conical angle is equal to zero is calculated. It is in good agreement with those given in [28], which verifies the correctness of the procedure and results in this paper. Figure 2 also shows the angular distributions of the RCS when the conical angle of the incident ZOBB is different. It can be seen that the RCS decreases as a whole with the increase of conical angle. The maximum value of the RCS appears in the direction of cone angle. For example, when $\alpha = 60^\circ$, the maximum value of RCS appear in the direction of scattering angle of about 60°.

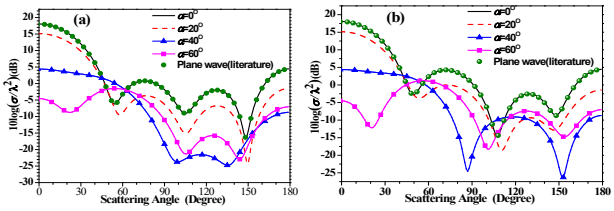

Fig. 2 Results reduced to the case of a plasma anisotropic shell illuminated by a plane wave compared with those results in [2]: (a) E-Plane, (b) H-Plane. ($a_1 = 0.6\lambda$, $a_2 = 0.3\lambda$, $\varepsilon_{1xx} = \varepsilon_{1yy} = 2.5\varepsilon_0$, $\varepsilon_{1zz} = 1.5\varepsilon_0$, $\varepsilon_{1yx} = -\varepsilon_{1xy} = \mathrm{i}\varepsilon_0$, $\overline{\overline{\mu}}_1 = \mu_0\overline{\overline{I}}$, $\varepsilon_2 = \varepsilon_0$, $\mu_2 = \mu_0$, $(x_0, y_0, z_0) = (0,0,0)\lambda$.)

4 Conclusion and perspectives

In conclusion, we have demonstrated the interactions of an off-axis ZOBB with a plasma anisotropic coated shell, isotropic and metal sphere by rigorously solving Maxwell equations in the spherical coordinate system. The accuracy of the theory is verified by comparing the numerical results reduced to the special cases of a plane wave incidence and the case of a plasma anisotropic sphere with those results from references. The complete expansion coefficients of a plasma anisotropic sphere are given through the orthogonality of the SVWFs.. The effects of the conical angle of the ZOBB, the beam center positioning, the size parameters of the coated spherical structure, the imaginary part of dielectric parameters on the angular distribution of the RCS are discussed in detail. The conical angle of the ZOBB considerably influences the intensity of the RCS, but has little effect on the angular distribution. When the conical angle is large, the maximum value of the

RCS will appear at the position where the scattering angle is equal to the conical angle but not at the forward scattering position. The position offset of the beam center along x- or y-axis weakens the scattering intensity and deflects the scattering angle corresponding to the largest RCS. Especially, the shortcoming that the forward and backward scattering intensity is not calculated in previous literatures is solved by introducing the recursion relation of angular functions. The application of the coating thickness of conductor sphere coated with plasma anisotropic medium in target stealth is discussed through numerical calculation: the increase of the coating thickness of the plasma anisotropic coating layer enhances the scattering intensity in the forward and backward regions, and creates a blind area at a specific coating thickness and scattering angle. This characteristic may be of great value in radar target stealth. The results presented in this paper are hopeful to provide an effective calibration for research on the scattering properties of multilayered anisotropic targets.

5 Acknowledgement

The authors acknowledge the support by the Fundamental Research Funds for the Central Universities (ZYTS24114).

6 References

[1] G. Mie, "Beitrage zur Optik truber Medien speziell kolloidaler Metallosungen," Ann. Phys. **25**: 377-455 (1908).
[2] A. L. Aden, and M. Kerker, "Scattering of electromagnetic Waves from two concentric Spheres," J. Appl. Phys. **22**: 1242-1246 (1951).
[3] Z. S. Wu, and Y. P. Wang, "Electromagnetic scattering for multilayered sphere-recursive algorithms," Radio Sci. **26**: 1393-1401 (1991).
[4] M. S. Durkee, G. K. Fletcher, C. Carlson, K. Matheson, and K. C. Maitland, "Light scattering by pulmonary alveoli and airway surface liquid using a concentric sphere model," Opt. Lett. **43**: 5001 (2018).
[5] C. X. Gao, B. Q. Sun, and Y. J. Zhang, "Electromagnetic wave scattering by charged coated spheres," J. Quant. Spect. and Rad. Trans **272**: 107757 (2021).
[6] W. Ren, "Contributions to the electromagnetic wave theory of bounded homogeneous anisotropic media," Phys. Rev. E **47**: 664-673 (1993).
[7] Y. L. Geng, X. B. Wu, and L. W. Li, "Analysis of electromagnetic scattering by a plasma anisotropic sphere," Radio Sci. **38**: 1104 (2003).
[8] Z. F. Lin, and S. T. Chui, "Electromagnetic scattering by optically anisotropic magnetic particle," Phys. Rev. E **69**: 056614 (2004).
[9] R. J. Tarento, K. H. Bennemann, and P. Joyes, "Mie scattering of magnetic spheres," Phys. Rev. E **69**: 026606 (2004).
[10] J. C. Monzon, "TWO-Dimensional Scattering by a Homegeneous Anisotropic Rod," IEEE Trans. Antennas Propagat. **AP-34**: 1243-1249 (1986).
[11] B. Beker, K. R. Umashankar, and A. Taflove, "Numerical analysis and validation of the combined electromagnetic scattering by arbitrary shaped two-dimensional anisotropic objects," IEEE Trans. Antennas Propagat. **37**: 1573-1581 (1989).
[12] X. B. Wu, and K. Yasumoto, "Three-dimensional scattering by an infinite homogeneous anisotropic circular cylinder: an analytical solution," J. Appl. Phys. **82**: 1996-2003 (1997).
[13] J. Durnin, "Exact solutions for nondiffracting beams. I. The scalar theory," J. Opt. Soc. Am. A **4**: 651-654 (1987).
[14] X. B. Ma, and E. B. Li, "Scattering of an unpolarized Bessel beam by spheres," Chin. Opt. Lett. **8**: 1195-1198 (2010).
[15] L. A. Ambrosio, and H. E. H. Figueroa, "Integral localized approximation description of ordinary Bessel beams and application to optical trapping forces," Biomed Opt Express **2**: 1893-1906 (2011).
[16] S. R. Mishra, "A vector vave analysis of a Bessel beam," Opt. Commun. **85**: 159-161 (1991).
[17] F. G. Mitri, "Arbitrary scattering of an electromagnetic zero-order Bessel beam by a dielectric sphere," Opt. Lett. **36**: 766-768 (2011).
[18] Z. Y. Chen, Y. P. Han, Z. W. Cui, and X. W. Shi, "Scattering of a zero-order Bessel beam by a concentric sphere," J. Opt. **16**: 055701 (2014).
[19] J. A. Lock, and G. Gouesbet, "Rigorous justification of the localized approximation to the beam-shape coefficients in generalized Lorenz-Mie theory.I. On-axis beams," J. Opt. Soc. Am. A **11**: 2503-2515 (1994).
[20] G. Gouesbet, and J. A. Lock, "Rigorous justification of the localized approximation to the beam-shape coefficients in generalized Lorenz-Mie theory. II. off-axis beams," J. Opt. Soc. Am. A **11**: 2516-2525 (1994).
[21] F. P. Wu, J. J. Wang, Z. C. Cui, S. Aihoon, P. Briard, and Y. P. Han, "Polarization-sensitive photonic jet of a dielectric sphere excited by a zero-order Bessel beam," J. Quant. Spect. and Rad. Trans **280**: 108093 (2022).
[22] D. Sarkar, and N. J. Halas, "General vector basis function solution of Maxwell's equations," Phys. Rev. E **56**: 1102-1112 (1997).
[23] G. Gouesbet, B. Maheu, and G. Grehan, "Light Scattering from a sphere arbitrarily located in a Gaussian beam, using a Bromwich formulation," J. Opt. Soc. Am. A **5**: 1427-1443 (1988).
[24] Z. J. Li, Z. S. Wu, T. Qu, Q. C. Shang, and L. Bai, "Multiple scattering of a zero-order Bessel beam with arbitrary incidence by an aggregate of uniaxial anisotropic spheres," J. Quant. Spectrosc. Radiat. Transfer. **169**: 1-13 (2016).
[25] Y. L. Geng, X. B. Wu, and L. W. Li, "Characterization of Electromagnetic Scattering by a Plasma Anisotropic Spherical Shell," IEEE Trans. Antennas Propagat. **3**: 100-103 (2004).
[26] Y. L. Geng, C. W. Qiu, and N. Yuan, "Exact solution to electromagnetic scattering by an impedance sphere coated with a uniaxial anisotropic layer," IEEE Trans. Antennas Propagat. **57**: 572-576 (2009).
[27] Z. J. Li, Z. S. Wu, T. Qu, H. Y. Li, L. Bai, and L. Gong, "Light scattering of a non-diffracting zero-order Bessel beam by uniaxial anisotropic bispheres," J. Quant. Spectrosc. Radiat. Transfer. **162**: 56-65 (2015).
[28] Z. S. Wu, Z. J. Li, H. Li, Q. K. Yuan, and H. Y. Li, "Off-axis Gaussian beam scattering by an anisotropic coated sphere," IEEE Trans. Antennas Propagat. **59**: 4740-4748 (2011).

The 14th International Conference on
Laser-light and Interactions with Particles (LIP2024)
September 18-22nd, 2024, Xi'an, Shaanxi, China

TUNABLE TERAJETS FORMED BY MICROSPHERE COMPOUND LENSES

Haojie Wang, Xikang Zhou , Ping Li and Yiping Han*

School of Physics, Xidian University, Xi'an, 710071, China

Corresponding author: hanyp@mail.xidian.edu.cn

Abstract

Terajets, recognized as powerful tools within the terahertz spectrum, have shown extensive potential for applications in high-resolution terahertz imaging. This study introduces the use of compound microsphere lenses to generate tunable terajets. By adjusting the size, refractive indices, and gap between the two microspheres in the lens setup, we have successfully produced terajets with diverse characteristics. These advancements thereby broaden the practical applications of this technology.

1 Introduction

Terahertz (THz) imaging has emerged as a significant technology with the potential to revolutionize applications ranging from security screenings to medical diagnostics due to its ability to penetrate opaque materials and produce clear images without harmful radiation [1, 2]. Despite its advantages, the broader adoption of THz imaging has been limited by its inherently lower resolution, primarily due to the longer wavelengths used compared to visible light [3]. Addressing this limitation is crucial for expanding the utility of THz imaging in high-resolution applications[4-8].

Recent advancements have highlighted the potential of terajets — intensely focused THz beams generated through microscale dielectric structures — as a solution to overcome the resolution barriers in traditional THz imaging methods[9-15]. Terajets exploit the unique properties of the THz spectrum to achieve super-resolution capabilities beyond the diffraction limit, offering a new horizon for THz imaging techniques[16].

In this study, we explore an innovative approach to enhance the flexibility and functionality of THz imaging through the use of compound microsphere lenses. These lenses, comprised of two microspheres with adjustable parameters, are designed to generate tunable terajets. By carefully modifying the size, refractive indices, and gap between the microspheres within the lens setup, we have been able to produce terajets with a range of characteristics tailored to specific imaging needs.

2 Methodology

To investigate the potential of microsphere compound lenses for producing narrowly focused terajets, we conducted numerical simulations to explore the propagation of terahertz radiation through these lenses. Utilizing the finite-difference time-domain (FDTD) method, the interaction of terahertz waves with a dual-sphere configuration is studied. This configuration features a leading sphere with a radius r_1 and a refractive index n_1, followed by a second sphere with a radius r_2 and a refractive index n_2, as illustrated in **Figure 1**. The entire lens structure was exposed to a y-polarized plane wave advancing along the positive z-axis, characterized by a wavelength of 3 mm (equivalent to a frequency of 0.1 THz).

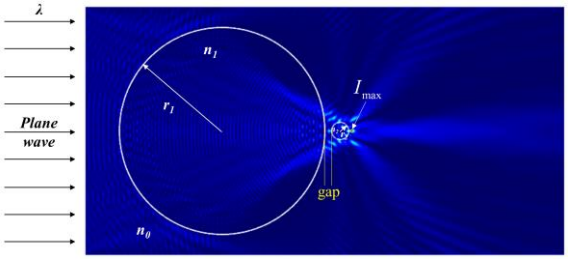

Figure 1 *A schematic diagram of the terajet generated by a microsphere compound lens.*

To elucidate the optical phenomena underlying microsphere compound lenses with the specified parameters, a geometric optical analysis was undertaken. The structural parameters of these lenses mirrored those utilized in our preceding numerical simulations, as shown in Figure 1. This analysis elucidates the light propagation trajectories when a microsphere compound lens, positioned in the x-z plane, is illuminated, as depicted in **Figure 2**.

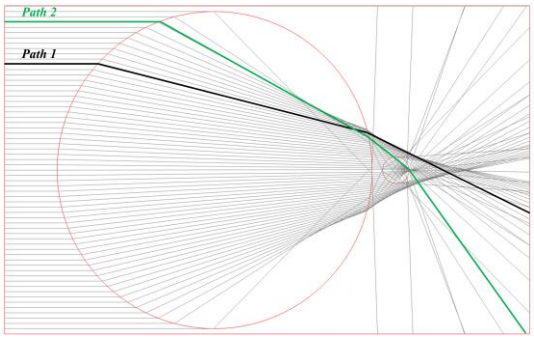

Figure 2 *Main light paths of illumination pass through the microsphere compound lens.*

The propagation pathway of the light through the lens system is segmented into two principal trajectories: Path 1, where light traverses only through the front sphere, and Path 2, which includes passage through both the front and the subsequent sphere. Light traveling along these paths converges on different regions on the shadowed side of the lens, contributing to distinct optical effects. Notably, Path 1

results in light converging due to the front sphere's influence, while Path 2 demonstrates accelerated convergence influenced by the higher refractive index of the latter sphere. This results in a tightly focused beam closer to the lens structure, forming a compact region of high energy concentration. This analysis helps explain the formation of a smaller focal point and the emergence of an elongated terajet as observed in **Figure 1**.

According to the geometric optics theory, under the paraxial approximation, the focal length f of a microsphere can be determined by the following formula[17]:

$$f = \frac{nr}{2(n-n_0)} \quad (1)$$

When two microspheres are spaced by a distance g, the combined focal length of the lens system can be computed using the lens group formula:

$$\frac{1}{f_{total}} = \frac{1}{f_1} + \frac{1}{f_2} - \frac{g}{f_1 f_2} \quad (2)$$

where f_1 and f_2 represent the focal lengths of the front and secondary microsphere lenses, respectively. These values can be derived from Eq.(1).

3 Results and discussion

After conducting a series of simulation studies, we have chosen to focus on adjusting the distance gg between two microspheres while fixing r_1=10λ, n_1=1.43, r_2=0.83λ, and n_2 =1.49 to investigate its influence on terajets. Specifically, we varied g in increments of λ, ranging from 0 to 10λ. We found that altering the distance between the two microspheres significantly influences the properties of the terajets, including the maximum intensity (I_{max}), the focal length (f), the working distance (WD), and the full width at half maximum ($FWHM$), as shown in **Table 1**.

Characteristics of Terajets	Min level	Max level
I_{max} (V^2/m^2)	16.1	46.9
f (λ)	0	3.7
WD (λ)	0.6	7.0
$FWHM$ (λ)	0.25	0.88

Table 1 *The variation range of characteristics in terajets formed by microsphere compound lenses.*

As illustrated in **Table 1**, the configuration of the microsphere compound lenses effectively confines the FWHM of the formed terajets to a narrow range. This demonstrates the considerable potential of this setup for applications in high-resolution terahertz imaging.

4 Conclusions

This study highlights the use of compound microsphere lenses to generate tunable terajets within the terahertz spectrum, demonstrating their potential for high-resolution imaging applications. By adjusting the size, refractive indices, and spacing between two microspheres, we successfully tailored the properties of the terajets. Our findings show that precise control over these parameters can significantly influence key characteristics such as maximum intensity, focal length, working distance, and $FWHM$. The ability to confine the $FWHM$ to a narrow range, as evidenced by our simulations, underscores the substantial potential of microsphere compound lenses for enhancing terahertz imaging technology.

5 References

[1] Chan WL, Deibel J, Mittleman DM. Imaging with terahertz radiation. Rep Prog Phys. 2007;70:1325.

[2] Yu C, Fan S, Sun Y, Pickwell-MacPherson E. The potential of terahertz imaging for cancer diagnosis: A review of investigations to date. Quantitative imaging in medicine and surgery. 2012;2:33.

[3] Zhao J, Chu W, Guo L, Wang Z, Yang J, Liu W, et al. Terahertz imaging with sub-wavelength resolution by femtosecond laser filament in air. Sci Rep. 2014;4:3880.

[4] Adam AJL. Review of near-field terahertz measurement methods and their applications: how to achieve sub-wavelength resolution at THz frequencies. Journal of Infrared, Millimeter, and Terahertz Waves. 2011;32:976-1019.

[5] Llombart N, Cooper KB, Dengler RJ, Bryllert T, Siegel PH. Confocal ellipsoidal reflector system for a mechanically scanned active terahertz imager. IEEE Trans Antennas Propag. 2010;58:1834-41.

[6] Xu Y, Zhang X, Tian Z, Gu J, Ouyang C, Li Y, et al. Mapping the near-field propagation of surface plasmons on terahertz metasurfaces. Appl Phys Lett. 2015;107.

[7] Tuniz A, Kuhlmey BT. Subwavelength terahertz imaging via virtual superlensing in the radiating near field. arXiv preprint arXiv:221111205. 2022.

[8] Balbekin NS, Kulya MS, Belashov AV, Gorodetsky A, Petrov NV. Increasing the resolution of the reconstructed image in terahertz pulse time-domain holography. Sci Rep. 2019;9:180.

[9] Pacheco-Peña V, Beruete M, Minin IV, Minin OV. Terajets produced by dielectric cuboids. Appl Phys Lett. 2014;105.

[10] Pacheco-Peña V, Beruete M, Minin IV, Minin OV. Multifrequency focusing and wide angular scanning of terajets. Opt Lett. 2015;40:245-8.

[11] Nguyen Pham HH, Hisatake S, Minin OV, Nagatsuma T, Minin IV. Enhancement of spatial resolution of terahertz imaging systems based on terajet generation by dielectric cube. Apl Photonics. 2017;2.

[12] Minin IV, Minin OV, Kharitoshin NA. Localized high field enhancements from hemispherical 3D mesoscale dielectric particles in the refection mode. 2015 16th International Conference of Young Specialists on Micro/Nanotechnologies and Electron Devices: IEEE; 2015. p. 331-3.

[13] Minin IV, Minin OV, Pacheco-Peña V, Beruete M. All-dielectric periodic terajet waveguide using an array of coupled cuboids. Appl Phys Lett. 2015;106.

[14] Calvo-Gallego J, Delgado-Notario JA, Minin OV, Abidi EH, Ferrando-Bataller M, Fobelets K, et al. Enhancing resolution of terahertz imaging systems below the diffraction limit. Optics & Laser Technology. 2023;164:109540.

[15] Paddubskaya A, Valynets N, Novitsky A, Minin O, Minin I. Terajet-assisted time-domain super-resolution imaging. J Phys D: Appl Phys. 2024;57:145104.
[16] Xiaoming M, Zaichao J, Qingshan Q, Bin C, Zhenwei Z, Yuping Y. Research advances of high-resolution THz imaging based on terajet effect. Opto-Electronic Engineering. 2020;47:190590-1--10.
[17] Born M, Wolf E. Principles of optics: electromagnetic theory of propagation, interference and diffraction of light: Elsevier; 2013.

The 14th International Conference on
Laser-light and Interactions with Particles (LIP2024)
September 18-22nd, 2024, Xi'an, Shaanxi, China

SCATTERING OF GAUSSIAN BEAMS BY A ROTATING DIELECTRIC CYLINDER

Zhuoyuan SHI[1], Renxian LI[1,*], Huan TANG[1], Yuan ZHANG[1], Bing WEI, Shuhong GONG, Igor V. Minin[2,3] and Oleg V. Minin[2]

[1] School of Physics, Xidian University, Xi'an 710071, China
[2] Siberian State University of Geosystems and Technologies, Novosibirsk, 630108, Russia
[3] Novosibirsk Branch of Rzhanov Institute of Semiconductor Physics SBRAS "Technological Design Institute of Applied microelectronics", Novosibirsk, 630090

Corresponding author: rxli@mail.xidian.edu.cn

Abstract

In our previous work [1], we investigated the scattering phenomenon of plane waves on a rotating cylinder by changing the rotational dimensionless parameter of the cylinder, and found the critical values of PNJ and resonance phenomena of the particle, and concluded that the rotation of the particle can cause or destroy the resonance scattering. This article extends the beam to a Gaussian beam, which can be regarded as a superposition of individual plane waves with different propagation directions, amplitudes, and polarizations, and uses the vector angular spectral decomposition method (VASDM) and the multilevel expansion method (MEM) to obtain an arbitrary expression of the structured beam. Considering the continuity conditions inside and outside the rotating cylinder, the relationship between the scattering coefficients and the beam factors (BSCs) of the incident beam is established, and the scattering of a Gaussian beam on a rotating cylinder is investigated.

In this paper, based on Minkowski theory and "instantaneous rest-frame" theory, the total electric field strength is numerically calculated and discussed. Then the effect of resonance on PNJ is analyzed. The resonance scattering of rotating dielectric columns under the action of structured beams provides a new direction for the research of PNJ and whispering gallery mode (WGM) as well as the design and application of ultra-sensitive sensors and resonators.

1 Inrtoduction

When a beam incident on a dielectric cylinder, the photonic nanojet is generated. The photonic nanojets are determined by the incident wave parameters (including wavelength and polarization state) and particle parameters (including particle size and refractive index). The rich and varied characteristics of photonic jets make them potentially valuable in the fields of breaking diffraction limit imaging, capture and manipulation of biological cells [2], and nanoparticle detection [3]. In the process of research, scientists have found an interesting phenomenon, that is, resonance scattering will occur under certain conditions. This is due to the total internal reflection of light, where electromagnetic waves are strongly confined to microcavities with circular symmetry, a phenomenon also known as whispering gallery mode (WGM). Due to its high sensitivity [4], high resolution [5] and modulability [6], WGM resonator has attracted wide attention in optical sensing [7,8], biomedical molecules [9,10], environmental media/heat sensing [11], chemical analysis [12,13] and other fields.

With the development of human society, human beings have explored the microcosmic world more and more deeply, and the limitations of technical means for research are becoming more and more obvious in this process. The invention of optical tweezers makes human research on the microscopic world from passive cognition to active control, which has played a great role in many research fields. For example, physics [14-16], colloid science [17-18], single molecule biology [19-20], cell biology [21] and other disciplines have applied optical tweezers technology to varying degrees. Optical tweezers are especially widely used in the study of biological cells because of their subcontact or even non-contact manipulation and trapping of micro and nanoparticles.

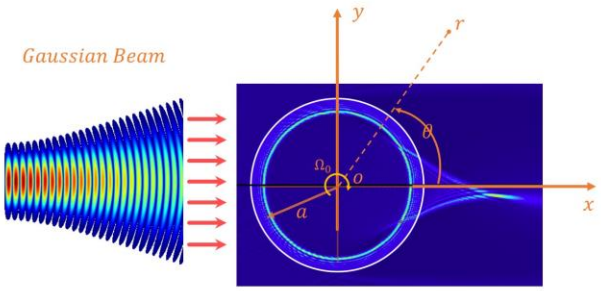

Figure 1 *Schematic diagram of the resonance phenomenon produced by a Gaussian beam acting on a rotating dielectric cylinder.*

Structured beams have some special shapes and characteristics, such as Gaussian beams and Bessel beams. Compared with plane waves, Gaussian beams are characterized by their intensity distribution following the Gaussian function law, while Bessel beams have self-reconstructing [24] and non-diffracting properties [23], and the main flap of the beams has high intensity and long propagation distance, which is of high application value. People can use Bessel beam not only to improve the beam modulability of photonic water jet, but also to meet the requirements of practical applications, such as making the

photonic jet break through the diffraction limit, which can be applied to photolithography and optical tweezers and other fields.

In summary, the study of scattering of plane waves and structured beams by rotating dielectric columns is of particular importance. Therefore, based on the theory of Minkowski and "instantaneous rest-frame", the scattering characteristics of particles when plane waves and Gaussian beams are applied to dielectric micro-columns are calculated in the article, and the effects of the incidence of structured beams with different beam parameters and polarization states are discussed, and the effects of the parameters of the particles of rotating dielectric cylinders on the scattering are also discussed. The effect of the rotating medium cylinder particle parameters on scattering is also explored. This study is of some significance for further research and development in particle manipulation, medicine, and atmospheric physics.

2 Method

2.1 Derivation of electromagnetic field expressions

The multipole expansion of the incident field is shown below:

$$\mathbf{E}_{inc}=\sum_{n=-\infty}^{\infty}E_n\left[A_n\mathbf{M}_n^{(1)}(kr)+B_n\mathbf{N}_n^{(1)}(kr)\right] \tag{1}$$

where A_n and B_n are the incidence coefficients.

The multipole expansion of the internal and scattered fields are:

$$\mathbf{E}_{sca}=-\sum_{n=-\infty}^{\infty}E_n\left[a_n\mathbf{M}_n^{(3)}(kr)+b_n\mathbf{N}_n^{(3)}(kr)\right] \tag{2}$$

$$\mathbf{E}_{\text{int}}=\sum_{n=-\infty}^{\infty}E_n\left[c_n\mathbf{M}_n^{(1)}(\kappa_n r)+d_n\mathbf{N}_n^{(1)}(\kappa_n r)\right] \tag{3}$$

where $\mathbf{M}_n^{(\cdots)}$ and $\mathbf{N}_n^{(\cdots)}$ are vector cylinder harmonic functions expressed as follows:

$$\begin{aligned}\mathbf{M}_n&=\left(in\frac{Z_n(\rho)}{\rho}\hat{r}-Z_n'(\rho)\phi\right)e^{in\phi}\\ \mathbf{N}_n&=Z_n(\rho)\hat{z}e^{in\phi}\end{aligned} \tag{4}$$

within a particle, $\rho=\kappa_n r$, and $\kappa_n=\sqrt{m^2k^2+2n\beta\left(m^2-1\right)(k/a)}$. Externally to a particle, $\rho=kr$. Where m is the particle refractive index and n is the partial-wave index. $\beta=(\Omega_0 a/c)$ is the rotational dimensionless parameter, Ω_0 is the rotational angular velocity of the particle, a is the radius of the particle, k is the wave number outside the particle, and κ_n is the wave number inside the particle. For $\mathbf{M}_n^{(1)}$ and $\mathbf{N}_n^{(1)}$, Z_n is represented by the first Bessel function J_n. For $\mathbf{M}_n^{(3)}$ and $\mathbf{N}_n^{(3)}$, Z_n is represented by the first kind of Hankel function H_n.

Substituting Eq.(4) into equations Eqs.(1) , (2) and (3) gives:

$$\begin{aligned}\mathbf{E}_{inc}&=\sum_{n=-\infty}^{\infty}E_n\left[A_n\left(in\frac{J_n(kr)}{kr}\hat{r}-J_n'(kr)\phi\right)+B_nJ_n(kr)\hat{z}\right]e^{in\phi}\\ \mathbf{E}_{sca}&=-\sum_{n=-\infty}^{\infty}E_n\left[a_n\left(in\frac{H_n(kr)}{kr}\hat{r}-H_n'(kr)\phi\right)+b_nH_n(kr)\hat{z}\right]e^{in\phi}\\ \mathbf{E}_{\text{int}}&=\sum_{n=-\infty}^{\infty}E_n\left[c_n\left(in\frac{J_n(\kappa_n r)}{\kappa_n r}\hat{r}-J_n'(\kappa_n r)\phi\right)+d_nJ_n(\kappa_n r)\hat{z}\right]e^{in\phi}\end{aligned} \tag{5}$$

Using the continuity condition $r=a$ at the boundary:

$$\begin{cases}E_\phi^{\text{int}}=E_\phi^{inc}+E_\phi^{sca}\\ E_z^{\text{int}}=E_z^{inc}+E_z^{sca}\\ H_\phi^{\text{int}}=H_\phi^{inc}+H_\phi^{sca}\\ H_z^{\text{int}}=H_z^{inc}+H_z^{sca}\end{cases} \tag{6}$$

Thus the internal field coefficients and scattering coefficients can be obtained as follows:

$$\begin{aligned}a_n&=A_n\frac{J_n'(kr)\left[\frac{\kappa_n}{\omega\mu_0}J_n(\kappa_n r)+(\varepsilon_1-\varepsilon_0)\Omega rn\frac{J_n(\kappa_n r)}{\kappa_n r}\right]-\frac{k}{\omega\mu_0}J_n'(\kappa_n r)J_n(kr)}{H_n'(kr)\left[\frac{\kappa_n}{\omega\mu_0}J_n(\kappa_n r)+(\varepsilon_1-\varepsilon_0)\Omega rn\frac{J_n(\kappa_n r)}{\kappa_n r}\right]-\frac{k}{\omega\mu_0}J_n'(\kappa_n r)H_n(kr)}\\ c_n&=A_n\frac{\frac{k}{\omega\mu_0}J_n'(kr)H_n(kr)-\frac{k}{\omega\mu_0}H_n'(kr)J_n(kr)}{\frac{k}{\omega\mu_0}J_n'(\kappa_n r)H_n(kr)-H_n'(kr)\left[\frac{\kappa_n}{\omega\mu_0}J_n(\kappa_n r)+(\varepsilon_1-\varepsilon_0)\Omega rn\frac{J_n(\kappa_n r)}{\kappa_n r}\right]}\\ b_n&=B_n\frac{\kappa_nJ_n(kr)J_n'(\kappa_n r)-kJ_n(\kappa_n r)J_n'(kr)}{\kappa_nH_n(kr)J_n'(\kappa_n r)-kJ_n(\kappa_n r)H_n'(kr)}\\ d_n&=B_n\frac{kH_n(kr)J_n'(kr)-kJ_n(kr)H_n'(kr)}{\kappa_nH_n(kr)J_n'(\kappa_n r)-kJ_n(\kappa_n r)H_n'(kr)}\end{aligned} \tag{7}$$

By substituting the Eq. (7) into the expression of the electromagnetic field, the electromagnetic field expression of an arbitrary beam incident on a rotating dielectric cylinder can be derived. The expressions of beam factors A_n and B_n should be derived for beams with different structures.

2.2 Derivation of beam factors for Gaussian beams

The electric field component can be expanded in the cylindrical coordinate system as:

$$\begin{aligned}E_z(\rho,\varphi,z)&=\frac{E_0\sqrt{\pi}W_0}{\lambda}\sum_{n=-\infty}^{\infty}i^nJ_n(k\rho)e^{in\varphi}\\ &\times\int_{-\infty}^{\infty}\exp\left[-\frac{1}{4}k^2W_0^2q^2+ikpx_0-ikqy_0-in\gamma\right]dq\end{aligned} \tag{8}$$

where $p^2+q^2=1$ and $k=2\pi/\lambda$ is the propagating wave number.

The analogy between the above equation and Eq. (5) yields:

$$B_n=\frac{\sqrt{\pi}W_0}{\lambda}\int_{-\infty}^{\infty}\exp\left[-\frac{1}{4}k^2W_0^2q^2+ikpx_0-ikqy_0-in\gamma\right]dq \tag{9}$$

The Gaussian beam incident wave factor is approximated:

$$B_{n1}=\left[1+\left(\frac{n}{6}\right)\left(s\sqrt{2iQ_0}\right)^3\left(z^3-3z\right)\right]B_{n0} \tag{10}$$

where, $B_{n0}=e^{ikx_0}\sqrt{iQ_0}\exp\left[-iQ_0\left(ky_0+n\right)^2/W_0^2\right]$, $l=kW_0^2$, $z=s\sqrt{2iQ_0}\left(n+ky_0\right)$ and $s=1/\left(kW_0\right)$. The electric field

representation of the incident field can be obtained by substituting Eq. (11) into Eq. (5).

3 Discussion and conclusion

In this work, the numerical discussion can be divided into two parts, the first part is the effect of the parameters of the rotating cylinder on the scattering characteristics, the variation of both the Mie size parameter ka of the particles and the rotational dimensionless parameter β affect the generation of the scattered field at all times, by varying the parameters of the particles we find the case of the resonance rings generated by the particles at different radii and at specific rotational speeds and analyze it numerically. The second part is the effect of the parameters of the Gaussian beam on the scattering characteristics. The parameters of Gaussian beam are wavelength λ and beam waist half longitude W_0. Similarly, we find the case of resonance rings produced by particles at different wavelengths and beam waist half longitudes and try to find out the pattern and analyze it. This study is of some significance for further research and development in particle manipulation, medicine, and atmospheric physics.

4 Acknowledgement

This work was supported by the National Natural Science Foundation of China (62001345, 62201411, 62371378).

5 References

[1] Tang H, Li R, Gong S, et al. Curved photonic nanojet generated by a rotating cylinder[J]. Optics Express, 2023, 31(2): 986-996.

[2] Grigorenko A N, Roberts N W, Dickinson M R, et al. Nanometric optical tweezers based on nanostructured substrates[J]. Nature Photonics, 2008, 2(6): 365-370.

[3] Xixi C, Tian W, Yonggong Z, et al. Subwavelength imaging and detection using adjustable and movable droplet microlenses[J]. Photonics Research. 2020,8(3):225-234.

[4] J. Zhu, S. K. Ozdemir, Y.-F. Xiao, L. Li, L. He, D.-R. Chen, and L. Yang, "On-chip single nanoparticle detection and sizing by mode splitting in an ultrahigh-q microresonator," Nat. photonics 4, 46–49 (2010).

[5] T. Birks, J. Knight, and T. Dimmick, "High-resolution measurement of the fiber diameter variations using whispering gallery modes and no optical alignment," IEEE Photonics Technol. Lett. 12, 182–183 (2000).

[6] K. Ge, B. Niu, F. Liu, J. Ruan, Z. Xu, D. Guo, X. Wang, L. Lv, and T. Zhai, "Electrically tunable wgm lasing in a metal-dielectric core–shell hybrid microcavity," Appl. Phys. Lett. 120 (2022).

[7] G. Palma, M. Falconi, F. Starecki, V. Nazabal, T. Yano, T. Kishi, T. Kumagai, and F. Prudenzano, "Novel double step approach for optical sensing via microsphere wgm resonance," Opt. Express 24, 26956–26971 (2016).

[8] X. Jiang, A. J. Qavi, S. H. Huang, and L. Yang, "Whispering-gallery sensors," Matter 3, 371–392 (2020).

[9] F. Shu, X. Jiang, G. Zhao, and L. Yang, "A scatterer-assisted whispering-gallery-mode microprobe," Nanophotonics 7, 1455–1460 (2018).

[10] Y. Wang, S. Zeng, G. Humbert, and H.-P. Ho, "Microfluidic whispering gallery mode optical sensors for biological applications," Laser & Photonics Rev. 14, 2000135 (2020).

[11] A. Schweinsberg, S. Hocdé, N. N. Lepeshkin, R. W. Boyd, C. Chase, and J. E. Fajardo, "An environmental sensor based on an integrated optical whispering gallery mode disk resonator," Sensors Actuators B: Chem. 123, 727–732(2007).

[12] Y. Sun and X. Fan, "Analysis of ring resonators for chemical vapor sensor development," Opt. Express 16, 10254–10268 (2008).

[13] Y.-n. Zhang, T. Zhou, B. Han, A. Zhang, and Y. Zhao, "Optical bio-chemical sensors based on whispering gallery mode resonators," Nanoscale 10, 13832–13856 (2018).

[14] Kheifets, S., Simha, A., Melin, K., Li, T., Raizen, M.G.. Observation of brownian motion in liquids at short times: instantaneous velocity and memory loss. Science 2014; 343(6178):1493–1496.

[15] Ohlinger, A., Deak, A., Lutich, A.A., Feldmann, J.. Optically trapped gold nanoparticle enables listening at the microscale. Physical review letters 2012;108(1):018101.

[16] Li, T., Kheifets, S., Medellin, D., Raizen, M.G.. Measurement of the instantaneous velocity of a brownian particle. Science 2010; 328(5986): 1673–1675.

[17] Crocker, J.C., Grier, D.G.. When like charges attract: the effects of geometrical confinement on long-range colloidal interactions. Physical review letters 1996;77(9):1897–1900.

[18] Sun, Z., Xu, S., Dai, G., Li, Y., Lou, L., Liu, Q., Zhu, R.. A microscopic approach to studying colloidal stability.The Journal of chemical physics 2003; 119(4):2399–2405.

[19] Wang, H., Liu, X., Li, Y., Han, B., Lou, L., Wang, K.. Optical technic of isolation a single chromosome. Shengwu Wuli Xuebao 2004;20(1):50–56.

[20] Wang, H., Liu, X., Li, Y., Han, B., Lou, L., Wang, K.. Isolation of a single rice chromosome by optical micromanipulation. Journal of Optics A: Pure and Applied Optics 2003;6(1):89–93.

[21] Svoboda, K., Schmidt, C.F., Schnapp, B.J., Block, S.M.. Direct observation of kinesin stepping by optical trapping interferometry. Nature 1993;365(6448):721–727

[22] Wei, M.T., Zaorski, A., Yalcin, H.C., Wang, J., Hallow, M., Ghadiali, S.N., Chiou, A., Ou-Yang, H.D.. A comparative study of living cell micromechanical properties by oscillatory optical tweezers. Optics express 2008;16(12):8594–8603.

[23] Berry, M.V., Balazs, N.L.. Non spreading wave packets. American Journal of Physics 1979; 47(3):264–267.

[24] Durmin, J.. Exact solutions for nondiracting beams. J Opt Soc Am A 1987;4:651–654.

The 14th International Conference on
Laser-light and Interactions with Particles (LIP2024)
September 18-22nd, 2024, Xi'an, Shaanxi, China

COMBINATION OF VECTORIAL COMPLEX RAY MODEL AND EQUIVALENT CURRENT METHOD FOR THE SCATTERING FIELD NEAR RAINBOW CAUSTICS

Yuchen YIN [1], Jiaqi LENG [1], Xiang'e HAN [1], Kuanfang REN [1,2] and Qingwei DUAN [1,*]

[1] School of Physics, Xidian University, Xi'an 710071, China
[2] CORIA-UMR 6614, Normandie Université, CNRS, Saint-Etienne du Rouvray 76801, France
Corresponding author: qwduan@xidian.edu.cn

Abstract

For the light scattering by nonspherical particles of size much larger than the wavelength of incident wave, the vectorial complex ray model (VCRM) has been proposed more than 10 years. Compared to traditional ray methods, VCRM integrates the wavefront curvature as an intrinsic property of a light ray, thereby making it possible to calculate the amplitude and phase of each ray easily and rigorously in the sense of ray model. However, VCRM had been subjected to the shackle as a ray model: the light intensity near caustics (rainbow caustic for instance) tends to infinity. Until recently, Zhang and Ren et al. combined the VCRM with physical optics to correct this defect [Opt. Lett. 47, 2149-2152 (2022)]. In this communication, we present a hybrid method which combines the VCRM with the equivalent current method (ECM) to calculate the scattered intensity near caustics. The results for the primary rainbows of spherical droplets are compared with those obtained by an analytical model, and the agreements are excellent.

1 Introduction

The study on the light scattering by particles has found wide applications in atmospheric optics, bio-optical imaging and materials science etc. So far, various methods and models have been developed, while each of them has its specific domain of application. The analytical models such as the Mie theory [1] are limited to particles of very simple shape such as spheres or infinite circular cylinders. For particles of the other shapes, the solutions can be roughly divided into two categories: the numerical methods and the approximate methods. The numerical methods [2], though exact, are severely limited by the particle size. For nonspherical particles of size much greater than the wavelength, high-frequency approximation methods such as the geometrical optics approximation (GOA) are usually preferred. However, the conventional GOA methods encounter difficulties in dealing with particles of curved surface where the refracted and reflected wavefronts are converged or diverged.

In this context, the vectorial complex ray model (VCRM) has been proposed and developed [3-5]. In VCRM, the wavefront curvature is introduced as an intrinsic property of rays, by which the divergence factor and the phase shift due to focal lines can then be deduced directly. It is thus very suitable for the light scattering by a large nonspherical particle of smooth surface such as falling droplets, pendent droplets and raindrops etc. However, VCRM had been subjected to the shackle as a ray model: the light intensity near caustics (rainbow caustic for instance) tends to infinity.

To correct this defect, in 2022 Zhang and Ren et al. combined the VCRM with physical optics (PO) [6], and the results for the intensity near rainbow caustics agreed well with the rigorous Debye series expansion (DSE). In their method, the amplitude and phase of the scattered rays on a virtual line (v-line) which is orthogonal to the rainbow ray were calculated by VCRM, then the scattered intensity in far field was computed by diffraction integral using the PO method. Instead of the combination with PO, in this communication, we propose a hybrid method which combines the VCRM with the equivalent current method (ECM) used by Ping Yang et al. [7]. In this hybrid method (VCRM+ECM), the electric and magnetic fields on the v-line are calculated by VCRM, while the scattered intensity in far field was computed by diffraction integral using the equivalent currents and magnetic currents.

The body of the paper is organized as follows: Section 2 presents a brief introduction to VCRM, then in Section 3 the method ECM to calculate the equivalent electric/magnetic currents and the scattering intensity in far field are given. The simulated results for the scattering field near rainbow caustics are compared with DSE in Section 4. The final part is the conclusion.

2 Brief introduction to VCRM

In the framework of VCRM, the incident light wave is described by bundles of rays, and each ray possesses the properties of direction, polarization, phase, amplitude and a crucial one -- the curvature of wavefront [3, 5, 6].

The electric field of a light ray can be written as

$$E_{X,p} = A_{X,p} \exp\left(\mathrm{j}\Phi_{X,p}\right) \tag{1}$$

where $X = \parallel$ or $\perp$, representing parallel or perpendicular polarization, and p is the order of emergent ray. As shown in Figure 1, $p = 0$ stands for the externally reflected rays

and $p \geq 1$ for the emergent rays undergone $p-1$ internal reflections. The amplitude $A_{X,p}$ is described as

$$A_{X,p} = \sqrt{D_p}\left|\varepsilon_{X,p} E_0^i\right| \tag{2}$$

where E_0^i is the initial incident field, D_p is the divergence factor which describes the convergence or divergence of wavefront, and $\varepsilon_{X,p}$ describes the effects of reflection and transmission. For a sphere considered here,

$$\varepsilon_{X,p} = \begin{cases} r_X & , p = 0 \\ (1-r_X^2)(-r_X)^{p-1} & , p \geq 1 \end{cases} \tag{3}$$

where r_X is the reflection coefficients. The divergence factor D_p is given as

$$D_p = \left|\prod_{i=1}^{p} \frac{R'_{1,i} R'_{2,i}}{R_{1,i+1} R_{2,i+1}}\right| \left|\frac{R'_{1,p+1} R'_{2,p+1}}{\left(R'_{1,p+1}+d\right)\left(R'_{2,p+1}+d\right)}\right| \tag{4}$$

where $R_{1,i}$ and $R_{2,i}$ are the principal curvature radii of the incident wavefront at the i-th interaction point, while $R'_{1,i}$ and $R'_{2,i}$ are those of the refracted or reflected wavefront. d is the distance from the point of emergence to the point of observation.

The phase of a ray is calculated by

$$\Phi_{X,p} = \Phi_0 + \Phi_f + \Phi_P + \Phi_r \tag{5}$$

where Φ_0 is the initial phase of incident ray, Φ_P the phase due to optical path, Φ_f the phase shift due to the focal lines, and Φ_r the phase shift due to reflection.

For the scattered rays of order $p = 2$, there is an extreme angle θ_R along which the scattered ray is called the rainbow ray. As did in [6], a v-line orthogonal to the rainbow ray is set, on which the amplitude and phase of the scattered rays are calculated by VCRM as shown in Figure 1. The amplitude and phase of a light ray on the v-line can be deduced through simple geometric relation [6].

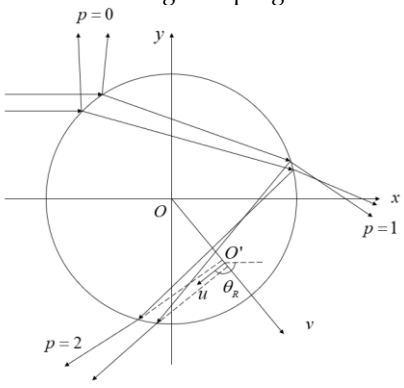

***Figure 1**. Schema of the virtual v-line on which the electric and magnetic field are calculated by VCRM.*

3 Combination with ECM

After the electric field on the v-line is calculated as described above, the corresponding magnetic field can be deduced directly by $\mathbf{H} = \hat{k} \times \mathbf{E}$. It is worth noticing that the impedance is omitted in order to unify the magnitudes of the equivalent electric current and magnetic current [7] described in the following. Then, the scattered light intensity in the far-field region is computed by the integration of the equivalent currents and magnetic currents. Suppose the wave propagates in the xy-plane. In this communication, we focus on the perpendicular polarization (TM wave), i.e. the electric field is along the z-axis.

By means of the boundary integral of Green's formula, the scattering field in direction of $\hat{r}$ is given by [7]

$$\begin{aligned} E_{TM}(\hat{r}) = & \sqrt{\frac{2}{\pi kr}} \exp\left[\mathrm{j}\left(kr + \frac{3\pi}{4}\right)\right] \frac{\mathrm{j}}{4} \\ & \times \int_v \left[\mathrm{j}k\left(\hat{u}\cdot\hat{r}\right)E(v) + \frac{\partial E(v)}{\partial u}\right] \exp\left(-\mathrm{j}k\hat{r}\cdot\mathbf{v}\right) dv \end{aligned} \tag{6}$$

The subscript TM indicates perpendicular polarization, and $\hat{u}$ is the unit vector normal to the v-line, as shown in the Figure 1. In such a 2D case, the TM element of scattering matrix is obtained by the equivalent currents [7]

$$\begin{aligned} F_{TM}(\hat{r}) = & \int_v \left[J_z(v) - s_x M_y(v) + s_y M_x(v)\right] \\ & \times \exp\left(-\mathrm{j}k\hat{r}\cdot\mathbf{v}\right) dv \end{aligned} \tag{7}$$

where J_z, M_x and M_y are the components of the equivalent currents $\mathbf{J}$ and magnetic currents $\mathbf{M}$ which have the same magnitude due to the previous unifying operation and are related to the magnetic and electric fields on v-line by

$$\mathbf{J}(v) = \hat{u} \times \mathbf{H}(v) \tag{8}$$

$$\mathbf{M}(v) = -\hat{u} \times \mathbf{E}(v) \tag{9}$$

Then Eq. (7) can be rewritten as

$$\begin{aligned} F_{TM}(\hat{r}) = & \int_v \left[u_x H_y(v) - u_y H_x(v) - \left(\hat{u}\cdot\hat{r}\right)E_z(v)\right] \\ & \times \exp\left(-\mathrm{j}k\hat{r}\cdot\mathbf{v}\right) dv \end{aligned} \tag{10}$$

And the scattering field is obtained by

$$E_{TM}(\hat{r}) = \sqrt{\frac{2}{\pi kr}} \exp\left[\mathrm{j}\left(kr + \frac{3\pi}{4}\right) - \mathrm{j}ku\right] \frac{k}{4} F_{TM}(\hat{r}) \tag{11}$$

As a convention, the factor kr is omitted in calculating the far-field intensity.

4 Results

The following part shows the results of the proposed hybrid method VCRM+ECM, and the comparison with the rigorous DSE. The region of observation is near the rainbow caustics formed by the scattered rays of order $p = 2$. The wavelength of incident light is 632.8 nm, and the relative index of refraction is 1.333. The number of incident rays is set as 4000, and the time cost for one scattering diagram is less than 1 second on personal computer (intel i9-13900KS). To assess the effectiveness and validity of the proposed method, the comparisons for

three spherical droplets of radii 100 μm , 500 μm and 1000 μm are shown in Figure 2(a), (b) and (c), respectively.

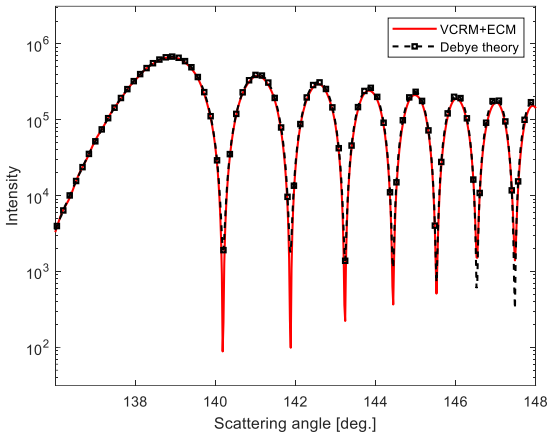

(a) $a = 100$ μm

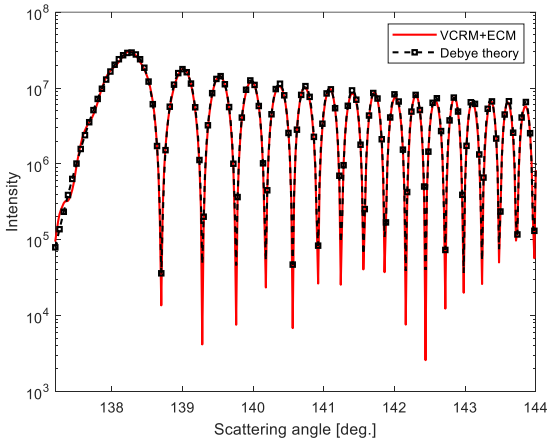

(b) $a = 500$ μm

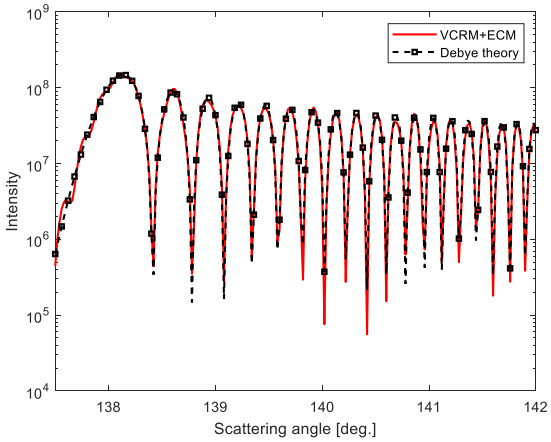

(c) $a = 1000$ μm

Figure 2 *Comparison of the hybrid method VCRM+ECM with the rigorous DSE for the scattering field near rainbow caustics formed by three droplets of different radii a.*

From Figure 2, we can see that the agreement of VCRM+ECM with the rigorous DSE is excellent for the electric field in the perpendicular polarization. This consistency confirms the effectiveness and accuracy of the hybrid method VCRM+ECM proposed in current paper.

5 Conclusion

In this work, we proposed a hybrid method VCRM+ECM to calculate the scattering field near caustics. It combines the merits of the VCRM and ECM: the former is flexible in dealing with the scattering by large particles of any shape of smooth surface, while the latter correct the defect of a ray method near caustics. The application to the parallel polarization case is under study. The extension of the proposed method VCRM+ECM to the scattering by large non-spherical particle in three-dimensional space needs more efforts and is in progress.

6 Funding

National Natural Science Foundation of China (62205262); Overseas Expertise Introduction Project for Discipline Innovation (B17035).

7 References

[1] H. C. van de Hulst, *Light scattering by small particles* (Dover Publications, 1981).

[2] M. I. Mishchenko, J. W. Hovenier, and L. D. Travis, eds., *Light Scattering by Nonspherical Particles: Theory, Measurements, and Applications* (Academic Press, 2000).

[3] K. F. Ren, F. Onofri, C. Rozé, and T. Girasole, *Vectorial complex ray model and application to two-dimensional scattering of plane wave by a spheroidal particle*, Optics Letters 36(3), 370–372 (2011).

[4] F. R. Onofri, K. F. Ren, M. Sentis, Q. Gaubert, and C. Pelcé, *Experimental validation of the vectorial complex ray model on the inter-caustics scattering of oblate droplets*, Optics Express 23(12), 15768–15773 (2015).

[5] Q. Duan, F. R. Onofri, XE Han, and K. F. Ren, *Numerical implementation of three-dimensional vectorial complex ray model and application to rainbow scattering of spheroidal drops*, Optics Express 31, 34980-35002 (2023).

[6] C. Zhang, C. Rozé, and K. F. Ren, *Airy theory revisited with the method combining vectorial complex ray model and physical optics*, Optics Letters 47(9), 2149–2152 (2022).

[7] P. Yang and K. N. Liou, *Light scattering by hexagonal ice crystals: comparison of finite-difference time domain and geometric optics models*, J. Opt. Soc. Am. A 12, 162-176 (1995).

The 14th International Conference on
Laser-light and Interactions with Particles (LIP2024)
September 18-22nd, 2024, Xi'an, Shaanxi, China

RESEARCH ON HOLOGRAPHIC FOCUSING SCHLIEREN IMAGING FOR THREE-DIMENSIONAL INHOMOGENEOUS FLOW FIELD VISUALIZATION

Yiqin LI [1], Zhiming LIN [1], Kaihui LIU [1], Qiwen JIN [1], Yingchun WU [1], Xuecheng WU [1,*]

[1] State Key Laboratory of Clean Energy Utilization, Zhejiang University, Hangzhou, China, 310027

**Corresponding author: wuxch@zju.edu.cn*

Abstract

Flow field visualization and measurement techniques are important measurement tools, which use the propagation law of beams in the flow field with non-uniform density to measure the flow field qualitatively and quantitatively. Existing flow field measurement techniques, such as schlieren and shadowgraphy, have been developed and widely used, but they can only perform two-dimensional measurements and the imaging has an integral effect. In this paper, we present a new technique, holographic focusing schlieren imaging (HFSI), which introduces a coherent reference wave to interfere with the wavefront generated by the traditional focusing schlieren method to form a hologram of focusing schlieren image. Therefore, it can realize the visualization and quantitative measurement of the three-dimensional flow field with non-uniform density. Meanwhile, a holographic focusing schlieren imaging system is constructed. The intertwined jets spatially separated by a certain distance are used as the experimental objects to capture the out-of-focus holograms and reconstruct the focusing schlieren images of different jets in the depth-of-field direction. The proof-of-concept experiments validate the feasibility of the HFSI method.

1 Introduction

Flow field display and measurement technology [1] is one of the important contents of the research of fluid mechanics, which obtains the structure of the flow field and related data without changing the physical and chemical properties of the fluid. Then it can analyze the two-dimensional or three-dimensional information of the flow field. Fluid temperature, pressure, Mach number and other state parameters have a definite functional relationship with density. Meanwhile, the optical refractive index of the fluid is a function of its density, thus depending on the refractive index change, the flow field can be displayed. At present, the flow field display and measurement technology mainly includes shadowgraphy, schlieren technology, interference technology and holographic imaging technology.

Conventional schlieren technology [2-4] uses the knife edge to block the deflected light. The spatial filtering of this knife edge filters out the spectral information of the light source. Therefore, the characteristic structure caused by the change in the density of the flow field is more obvious on the imaging screen. However, the measurement results of conventional schlieren technology have the problem of integration effect.

Focusing schlieren technology is proposed [5] and has some advantages over conventional schlieren technology. It limits the imaging depth of field of the system through the introduction of the source grid and cutoff grid. To a certain extent, it can rule out the interference of the imaging integral effect. The single image recorded is the flow field information of a certain cross-section location of the spatial field, so as to make it have a certain analysis capability of calculating the density field [6,7]. However, it is just applicable to two-dimensional measurements, and the construction of three-dimensional flow field information needs to be realized by shooting different focusing planes several times, which is difficult to be applied to transient scenes.

For three-dimensional field measurements, there are currently chromatographic imaging [8], spectroscopic imaging [9], optical field imaging [10] and other technologies. They can realize three-dimensional flow field reconstruction by means of multi-view or multi-section, but there are limitations such as having multi-window requirements for the structure of the area under test, difficulty in completely repeating the actual test condition, difficulty in operation, and low resolution.

To sum up, in this paper, we propose to combine digital holography and focusing schlieren technology to develop holographic focusing schlieren imaging (HFSI) technology, which utilizes a single-camera configuration to achieves three-dimensional flow visualization through a single recording in single field of view (FOV).

2 HFSI system

Figure 1 shows the HFSI system. In the system, a pulsed laser with a pulse width of 0.5 ns and a wavelength of 532 nm is used as the light source. The laser beam is divided into two beams with an intensity ratio of 9:1 as the object light and the reference light. The object light is modulated by a source grid, a focusing lens and a cutoff grid, in which the source grid has an opaque stripe width of 1 mm and a transparent stripe width of 1 mm, and the cutoff grid has an opaque stripe width of 1 mm and a transparent stripe width of 1 mm. The cutoff grid is located in the conjugate image of the source grid. And the focusing lens has a diameter of 60 mm and a focal length of 250 mm. The reference light is modulated by a spatial filter and a collimated lens. In order

to ensure the interference of the two beams, a delay path consisting of two prisms is set up in the light path of the two beams. Finally, the two beams of light interfered and merged into the CCD plane for image recording, and the image information of the other cross sections was reconstructed using the holographic reconstruction algorithm. Then the focusing schlieren image can be obtained at different depths, thus reflecting the structure of the 3D flow field.

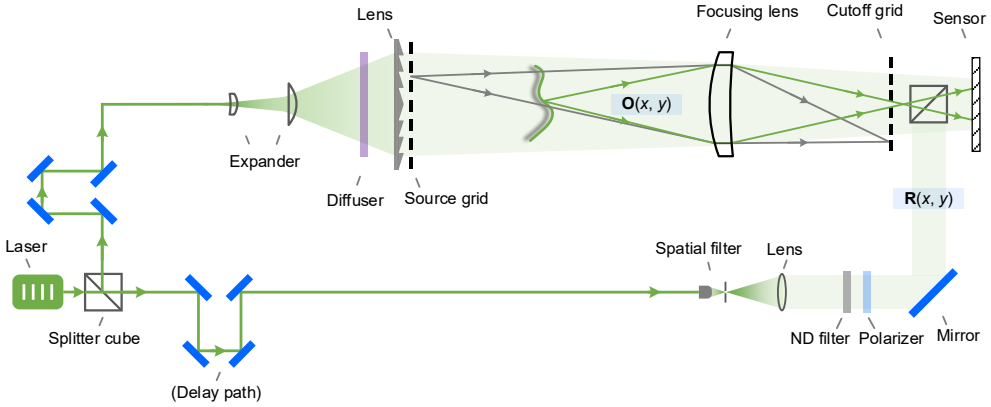

Figure 1 *Optical configuration of HFSI. O(x, y) represents the object wave. R(x, y) denotes the reference wave.*

3 Proof-of-concept experiment

A compressed air jet was chosen for the experiment, which can produce the small-scale supersonic flow. The two beams of jets were placed crosswise with a distance of 30 mm between them and the diameter of the jet nozzle outlet was 1.5 mm. The compressed air jet transitioned into the turbulent flow at the nozzle outlet. Figure 2 shows the imaging of the two jets at their respective focusing positions, including the focusing schlieren images with LED and laser as the light source as well as the reconstructed images obtained by using HFSI technology. The focusing schlieren images are used as a reference to compare the reconstruction effect of the HFSI technology more intuitively.

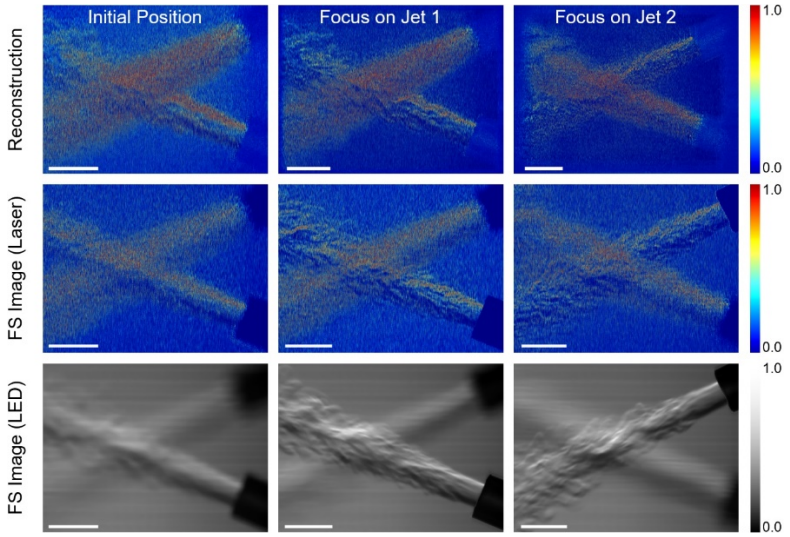

Figure 2 *Reconstruction results of HFSI. From up to bottom, each row represents HFSI's reconstruction, FS image using laser illumination, and FS image using LED illumination. (Scale bar: 3 mm)*

Among them, the focusing schlieren images are obtained by placing the two jets at the corresponding focusing positions respectively; the HFSI images are obtained by taking the out-of-focus image at a fixed position and then reconstructing them to the focusing position respectively by using reconstruction techniques to obtain the corresponding focusing image. The images have been processed with background reduction and contrast enhancement to significantly enhance the recognizability of the jet. Comparison of the obtained images shows that the outer contour of the jets can be well distinguished in the reconstructed images of HFSI, which proves that HFSI has certain three-dimensional imaging characteristics.

4 Conclusions

This work presents a new flow field measurement technology named holographic focusing schlieren imaging (HFSI). HFSI takes only a single-camera and single-lens configuration to achieve three-dimensional flow visualization in single FOV. And the reconstruction of HFSI image enables 3D flow visualization along the test volume with adjustable intervals, breaking the limitation of single section imaging. Overall, HFSI holds significant practical value in the scenarios, where multiple optical windows for 3D analysis are not equipped, such as in a wind tunnel and combustion chamber.

5 Acknowledgements

This work was supported by the National Natural Science Foundation of China (No. 52276167) and the Fundamental Research Funds for the Central Universities (2022ZFJH004).

6 References

[1] YUSOFF Y A, MOHAMAD F, SUNAR M S, et al. Flow visualization techniques: A review; proceedings of the Trends in Applied Knowledge-Based Systems and Data Science: 29th International Conference on Industrial Engineering and Other Applications of Applied Intelligent Systems, IEA/AIE 2016, Morioka, Japan, August 2-4, 2016, Proceedings 29, F, 2016 [C]. Springer.

[2] SETTLES G S. Schlieren and shadowgraph techniques: visualizing phenomena in transparent media [M]. Springer Science & Business Media, 2001.

[3] PORNEALA C, WILLIS D A J A P L. Observation of nanosecond laser-induced phase explosion in aluminum [J]. 2006, 89(21).

[4] ITSARIYAPINYO P J P O F. Visualization of the flow behind a backward-facing step using a schlieren technique and tetrafluoroethane [J]. 2022, 34(11).

[5] BURTON R A J J. A modified schlieren apparatus for large areas of field [J]. 1949, 39(11): 907-8.

[6] LAGUARDA L, SANTIAGO PATTERSON J, SCHRIJER F, et al. Experimental investigation of shock–shock interactions with variable inflow Mach number [J]. 2021, 31(5): 457-68.

[7] VANDERCREEK C, SMITH M, YU K. Focused schlieren and deflectometry at AEDC hypervelocity wind tunnel No. 9; proceedings of the 27th AIAA Aerodynamic Measurement Technology and Ground Testing Conference, F, 2010 [C].

[8] WATANABE M, ABE A, CASEY R, TAKAYAMA K. Holographic interferometric observation of shock wave phenomena[C]. Laser Interferometry IV: Computer-Aided Interferometry, 1992. SPIE.

[9] MARTíNEZ-GONZáLEZ A, MORENO-HERNáNDEZ D, GUERRERO-VIRAMONTES J, ZAMARRIPA-RAMíREZ J, CARRILLO-DELGADO C. Multiplane temperature measurement of fluid flows using a color focusing schlieren system [J]. Optics & Laser Technology, 2021, 142: 107256.

[10] KERTH P, HERMANN T, MCGILVRAY M. Three-dimensional focusing schlieren using a plenoptic camera[C]. International Conference on Flight Vehicles, Aerothermodynamics, Re-entry Missions and Engineering, 2019. ESA Conference Bureau.

The 14th International Conference on
Laser-light and Interactions with Particles (LIP2024)
September 18-22nd, 2024, Xi'an, Shaanxi, China

ACCURACY OF THE ANOMALOUS DIFFRACTION APPROXIMATION IN MODELLING SCATTERING PATTERNS OF BIOLOGICAL CELLS

Nadia E. ÁLVAREZ-CHÁVEZ [1], Anays ACEVEDO-BARRERA [1], Roberto MÁRQUEZ-ISLAS [2], Jose C. PERALES [3] and Augusto GARCÍA-VALENZUELA [1,*]

[1] Instituto de Ciencias Aplicadas y Tecnología (ICAT), Universidad Nacional Autónoma de México, Ciudad de México, 04510, Mexico
[2] Unidad de Investigación y Desarrollo Tecnológico (UIDT), Hospital General de México "Dr. Eduardo Liceaga", Ciudad de México, 06726, Mexico
[3] Laboratorio de Biofísica y Metabolismo, Facultad de Medicina, Universidad de Barcelona, Barcelona, 08907, España

Corresponding author: augusto.garcia@icat.unam.mx

Abstract

We aim to delineate regions of validity of the Anomalous Diffraction Approximation (ADA) in calculating the scattering patterns of biological cells. To this end, here we compare exact solutions given by Mie theory for the scattering pattern of a homogeneous spherical particles with the corresponding calculation using the ADA. First, as a reference, we compare the extinction cross sections calculated with each method and compute the relative error of ADA. We obtain the domain of validity of ADA in the space of the size parameter and the refractive index contrast, and we establish the limits by defining an acceptable maximum value for the relative error. Then, we compare scattering patterns and identify the range of angles of scattering for which ADA predicts with sufficient accuracy the scattering pattern obtained with Mie's theory for different particles of optical characteristics similar to biological cells.

1 Introduction

The Anomalous Diffraction Approximation (ADA) is a widely used approximation for estimating the scattering and absorption cross sections of particles of arbitrary shape. ADA accurately describes the scattering of light by soft particles with a small relative complex refractive index (low contrast, $|m-1| \ll 1$, with $m = n_p/n_m$) and large size parameter ($\chi \gg 1$, with $\chi = k_m a$ for a spherical particle of radius a with k_m being the wave number in the medium surrounding the particle) [1,2]. ADA considers only the phase delay suffered by the incident wave as it traverses the particle. The phase delay is proportional to the geometrical path travelled through the particle (see Figure 1) and Refractive Index (RI) contrast. ADA is simple and makes the study of light scattering by large particles of arbitrary geometry straightforward [3,4]. Thus, ADA is a useful tool to simulate the light scattering by biological cells.

Measuring the scattering pattern by biological cells is not difficult. One advantageous way is to fix cells on a transparent glass slide, forming a disordered monolayer of cells and transmitting light perpendicularly to the plane of the cell's monolayer [4]. The transmitted light is then projected on a screen some distance away from the monolayer, displaying the average of the scattering patterns of the illuminated cells. ADA can be used advantageously to model the scattering patterns of biological cells and retrieve averaged microstructural information from the measured scattering patterns. However, even if biological cells have a large size parameter in the visible spectrum, they usually contain smaller particles inside, such as organelles (nucleus, mitochondria, etc) [4]. Therefore, it is necessary to know the limits of ADA in predicting accurately the scattering patterns by not too large particles. This is our main goal in this work.

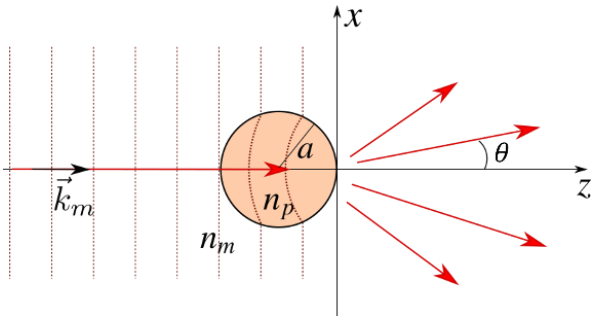

Figure 1 *Scattering by a spherical particle when ADA is valid.*

We estimate ADA's validity limits by comparing its predictions for spherical particles with exact solutions provided by Mie theory [5-7].

2 Theory

In this section, we present the ADA formulae for extinction cross section σ_{ext} and the elements, $S_1(\theta)$ and $S_2(\theta)$, of the amplitude scattering matrix as defined in the book by C. Bohren and D. Huffman [5]. Also, we define the relative error of σ_{ext} using Mie theory as the reference.

2.1 Extinction cross-section

The extinction cross section is described by the optical theorem $\sigma_{ext} = (4\pi/k_m^2)Re\{S(0)\}$ where $S(0)$ is the forward scattering amplitude [$S(0) = S_1(0) = S_2(0)$]. Within the ADA and substituting the scattering amplitude in the forward direction, $S(0)$, yields:

$$\sigma_{ext} = -2Re\left\{\int_{-\infty}^{\infty}\left(e^{i\Delta x} - 1\right)dxdy\right\}, \quad (1)$$

Where $\Delta x = 2\left(k_0[n_p - n_m]\mathrm{Re}\left(\sqrt{a^2 - x^2 - y^2}\right)\right)$ is the phase delay of the wave transmitted through the spherical along the z-axis. n_p is the particle refractive index, n_m is the matrix refractive index and a the particles radius.

2.2 Scattering amplitude

The scattering amplitude function $S_1(\theta)$ within the ADA is given by:

$$S_1(\theta) = \frac{k_m^2 \cos\theta}{2\pi}\int_{-\infty}^{\infty}(e^{i\Delta x} - 1)e^{-ik_x - ik_y}dxdy\,, \quad (2)$$

and the scattering amplitude function $S_2(\theta)$ within the ADA is given by:

$$S_2(\theta) = \frac{k_m^2 \cos\theta}{2\pi}\sqrt{1 + \frac{\sin^2\theta}{\cos^2\theta}}\int_{-\infty}^{\infty}(e^{i\Delta x} - 1)e^{-ik_x - ik_y}dxdy\,, \quad (3)$$

With the expressions given in Eqs (1), (2), and (3) we calculate the relative error maps of ADA as a function of the relative complex RI and the size parameter. The relative complex refractive index is defined as $m = (\mathrm{Re}\{n_p\} - n_m)/n_m$ and the size parameter as $\chi = k_m a$.

The relative error (e) for any of the quantities in Eqs (1), (2) or (3) for spherical particles can be defined as:

$$e = \frac{(e_{ADA} - e_{Mie})}{e_{Mie}}\,, \quad (4)$$

where e_{ADA} and e_{Mie} represent the extinction cross section or either of the scattering amplitude elements calculated with ADA and Mie theory respectively.

3 Results

In this section we show the calculations of the relative error of ADA in calculating σ_{ext} and compare the scattering pattern calculated with ADA and Mie some examples of spherical particles with size and RI close to those of biological cells. We performed all calculations at a wavelength of $\lambda = 532$ nm.

3.1 Relative error of ADA in the extinction cross-section

In Figs. 2(a)-2(b), we show theoretical maps of the relative error in the extinction cross-section, for spherical particles of radius from 0 to 10 μm RI contrast ranging from 0 to 0.5. The RI of the medium surrounding the particles was taken to be 1.3331. Part (a) of the figure represents the error map of σ_{ext} for a particle without absorption, and part (b) represents the error map of σ_{ext} assuming there is optical absorption inside the particle. We used a complex RI for the particle with an imaginary part of $n_p'' = 0.1$.

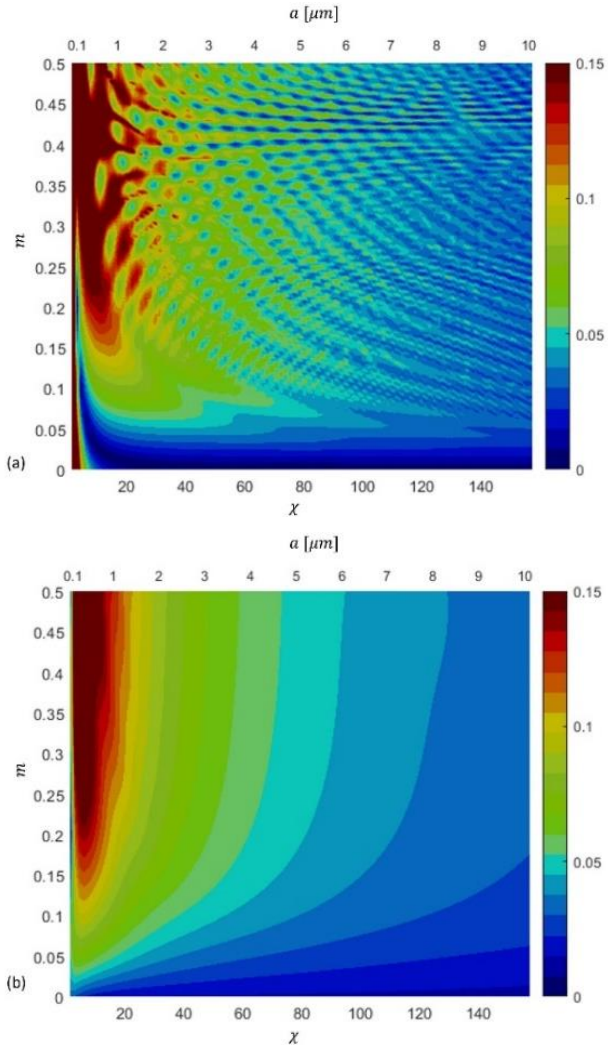

Figure 2 *Relative error map of the extinction cross section σ_{ext} as a function of the particle size parameter and RI contrast, considering a particle (a) without absorption and (b) with absorption.*

3.2 The scattering amplitude of non-polarized light as a function of the scattering angle: ADA versus Mie.

In Figs. 3(a)-3(b), we plot the average of the squared modulus of the scattering amplitude elements, $S_{prom} = (|S_1(\theta)|^2 + |S_2(\theta)|^2)/2$, calculated with ADA and Mie theory as a function of the scattering angle.

This is proportional to the scattered intensity for unpolarized light. Part (a) was calculated for a sphere of radius $a = 1$ μm and two values of the RI contrast: A low contrast m_1 with $n_p = 1.38$ and a high contrast m_2 with $n_p = 1.7$; in both cases, we used $n_m = 1.33$. In part (b) we chose a sphere of radius $a = 6$ μm, a low contrast m_1 with $n_p = 1.38$ and a high contrast m_2 with $n_p = 1.8$. Again, in both cases $n_m = 1.33$.

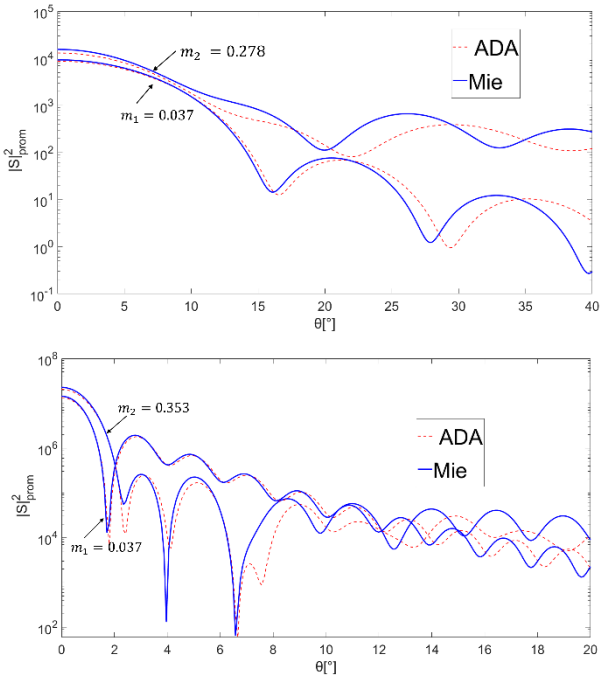

Figure 3 *Average scattering amplitude* $|S|^2$. *(a) sphere of radius* $a = 1\ \mu m$. *(b) sphere of radius* $a = 6\ \mu m$.

Fig. 3 shows that ADA provides a good approximation for the scattering pattern for particles of a radius of 1 μm and of 6 μm with low RI contrast (0.0353) up to about $\theta = 10^o$-15^o. Even for somewhat smaller particles of radius close to one wavelength, ADA offers good accuracy for angle up to 10^o. For larger contrasts, the range of scattering angles for which ADA gives a good approximation reduces. This range of angles and RI contrast for which ADA is applicable to calculate with reasonable precision the scattering patterns of biological cells with organelles, such as mitochondria and nucleus for scattering angles of about 10^o.

3.1 2D scattering patterns from a spherical cell without and with a spherical organelle using ADA

In Figs. 4(a)-4(b), we show a theoretical scattering pattern of cells without and with an organelle. The x and y axes are the corresponding distance in arbitrary units on a screen placed far away from the cell. Calculations were performed assuming linearly polarized light along the x axis.

Part (a) corresponds to a homogeneous spherical cell radius $a = 2$ μm and a cytoplasm of RI $n_p = 1.37$. The RI of the surrounding medium (extracellular medium) was taken to be $n_m = 1.35$. Part (b) is for a cell of radius $a = 2$ μm (cell) and RI $n_p = 1.37$ (citoplasm) with an organelle inside it of radius $a_o = 0.8$ μm (e.g. nucleus) and RI $n_{po} = 1.40$ (nucleus). The RI of the extracellular medium in both cases was taken to be $n_m = 1.35$. For part (b) of Fig. 4, the organelle was placed off centre as shown in the upper-left inset.

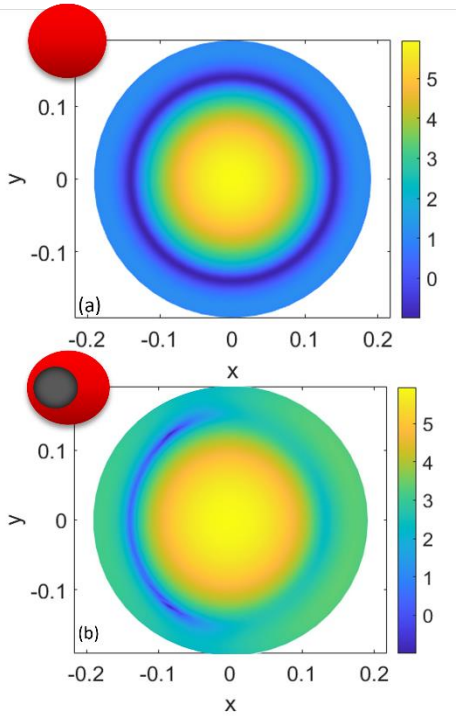

Figure 4. *Scattering patterns of a cell without an organelle (a) and with a spherical, off-centre, organelle (b).*

4 Conclusions

We are in the process of evaluating the precision of ADA in calculating the scattering pattern of biological cells considering the main organelles inside them. The objective is to provide a mathematical tool to evaluate and retrieve information of the physical state of some of the organelles within cells from scattering patterns. The results obtained so far are encouraging.

5 References

[1] Liu, C. (1998). Validity of anomalous diffraction approximation in m−χ domain. Atmospheric Research, 49(1), 81-86.

[2] Howie, A., & Basinski, Z. S. (1968). Approximations of the dynamical theory of diffraction contrast. Philosophical Magazine, 17(149), 1039-1063.

[3] Farone, W. A., & Robinson, M. J. (1968). The Range of Validity of the Anomalous Diffraction Approximation to Electromagnetic Scattering by a Sphere. Applied Optics, 7(4), 643.

[4] Morris, V. J., & Jennings, B. R. (1977). Anomalous diffraction approximation to the low-angle scattering from coated spheres: a model for biological cells. Biophysical Journal, 17(1), 95-101.

[5] C.F. Bohren, and D.R. Huffman, *Absorption and scattering of light by small particles* (Wiley, New-York, 1983).

[6] Videen, G., & Chýlek, P. (1998). Anomalous diffraction approximation limits. Atmospheric Research, 49(1), 77-80.

[7] Thomas, M. E. (2018). Improved-anomalous diffraction approximation for accurate extinction, scatter, and absorption efficiency calculations. SPIE.

The 14th International Conference on
Laser-light and Interactions with Particles (LIP2024)
September 18-22nd, 2024, Xi'an, Shaanxi, China

MAGNETIC RESONANCE GENERATED BY A ROTATING DIELECTRIC CYLINDER

Huan TANG[1], Renxian LI[1,*], Zhuoyuan SHI[1], Yuan ZHANG[1], Bing WEI[1], Shuhong GONG[1], Igor V. MININ[2,3], and Oleg V. MININ[2]

[1] School of Physics, Xidian University, Xi'an 710071, China
[2] Siberian State University of Geosystems and Technologies, Novosibirsk, 630108, Russia
[3] Novosibirsk Branch of Rzhanov Institute of Semiconductor Physics SBRAS "Technological Design Institute of Applied microelectronics", Novosibirsk, 630090, Russia

Corresponding author: rxli@mail.xidian.edu.cn

Abstract

The magnetic resonance of a rotating dielectric cylinder scattering a plane wave is studied based on Minkowski's theory and the "instantaneous rest-frame" hypothesis. The reason and characteristics of the magnetic resonance generated by a rotation dielectric cylinder are numerically explored. Numerical results show that the magnetic resonance generated by rotation is a whispering gallery mode (WGM)-like type sensitive to the rotation dimensionless parameter β. β determines the intensity and distribution of resonance inside the particle and provides a new degree of freedom for modulating resonances. The results provide a novel idea for the design of ultra-sensitive sensors and resonators, which have promising application prospects in optical communication, optical microscopy, and optical signal processing.

1 Introduction

It is widely known that the photonic nanojet (PNJ) [1] appears on the shadow side when a plane wave is incident on a mesoscale dielectric particle. Abundant research has been carried out on PNJ for its unique features, which have shown promising application prospects in particle manipulation, nanoparticle detection, and photoetching. As another extraordinary phenomenon in mesotronics [2], the WGM resonance [3] generated due to the total internal reflection of light is also widely used in microlaser optics, optical microscopy, and optical signal processing.

As early as 1908 [4], Mie theoretically investigated the WGM in a spherical cavity indirectly through scattering spectra. During 1910-1912 [5], Lord Rayleigh discovered the WGM resonance in studying the acoustic wave propagation phenomena in the dome of St Paul's Cathedral. The early experimental study of WGM was mainly in the microwave region, with the development of laser spectroscopy technology. Until the 1970s [6], the study of WGM resonance was extended to the optical band. The radiation pressure enhancement effect caused by the WGM resonance was first observed in optical tweezers manipulating tiny spherical water droplets. With the deepening of research, the theoretical achievements of the WGM resonance extend to engineering. Many materials for WGM resonators have been discovered and synthesized in this process, including glass, crystals, polymers, semiconductors, and liquids. Various structures of WGM resonators are designed at the mesoscale: spheres, cylinders, rings, bubbles, etc. The optical resonator structure of the WGM resonance is a centrally symmetric circular structure, which can effectively confine the light field in a limited space to form a resonance distribution, thus there are small internal losses in the WGM resonator. For the high sensitivity, high resolution, and tunability characteristics of WGM resonators [7], it has received widespread attention in many fields such as optical sensing, biomedical molecules, environmental media/thermal sensing, and chemical analysis.

While current studies on WGM have focused solely on stationary dielectric particles, the existence of resonance within a moving mesoscale particle remains uncertain. To address this, a model has been established for scattering plane waves by rotating dielectric cylinders [8-9]. The studies found that resonance scattering occurs when a plane wave illuminates a dielectric cylinder rotating at a specific angular velocity. Due to the rotation, a new optical path difference is created within the particle, resulting in additional fields and the emergence of resonance. However, while these studies only discuss the electric field resonance caused by rotation, the impact of rotation on the magnetic field remains unexplored. Does rotation also create magnetic resonance within the particle? What is the relationship between electric and magnetic resonance within the particle? These questions hold significant importance for resonator design.

We construct a scattering theoretical framework based on the " instantaneous rest-frame" hypothesis and Minkowski's theory [10] to study the magnetic resonance caused by rotating cylinders. We focus on a new degree of freedom defined as the rotation dimensionless parameter β. The impact of β on the magnetic resonance is highlighted, and the reason and characteristics of the magnetic resonance generated by β are revealed and discussed. The relevant results have promising application prospects in the design of ultra-sensitive sensors and resonators.

2 Method

Figure 1 gives the diagram of a magnetic resonance when a plane wave illuminates a spinning mesoscale dielectric cylinder. The plane wave propagating in x direction. The cylinder rotates with angular velocity Ω, with radius a and centre O, located in a coordinate system (r,θ,φ). Based on the "instantaneous rest-frame" theory, the angular velocity satisfies $\Omega \ll c/a$, and c is the speed of light in free space.

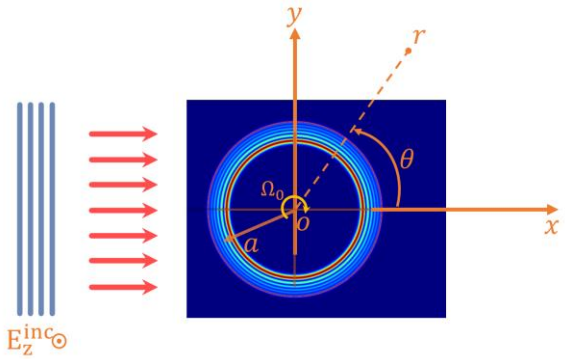

Figure 1 *Schematic diagram of the magnetic resonance generated between a plane wave and a rotation dielectric cylinder.*

When a plane wave illuminates to a stationary cylinder, the electromagnetic field satisfies the classical Maxwell equations as follows

$$\begin{aligned}\nabla\times\mathbf{E}&=-\frac{\partial}{\partial t}\mu_0\mathbf{H}\\ \nabla\times\mathbf{H}&=\frac{\partial}{\partial t}\varepsilon\mathbf{E}\end{aligned}\tag{1}$$

If the cylinder is spinning, the electromagnetic field inside the cylinder satisfies the Minkowski Maxwell equations as follows

$$\begin{aligned}\nabla\times\mathbf{E}&=-\frac{\partial}{\partial t}(\mu_0\mathbf{H}-\mathbf{\Lambda}\times\mathbf{E})\\ \nabla\times\mathbf{H}&=\frac{\partial}{\partial t}(\varepsilon\mathbf{E}+\mathbf{\Lambda}\times\mathbf{H})\end{aligned}\tag{2}$$

Where $\mathbf{\Lambda}=(\varepsilon_1\mu_0-\varepsilon_0\mu_0)\mathbf{v}$, $\mathbf{v}=\Omega r\phi$. μ_0 is permeability, ε_0 and ε_1 are the dielectric constants outside and inside the particle, respectively. Consider the time-harmonic factor is $e^{-\mathrm{j}\omega t}$, the expressions of electric fields defined in the form of the multipole expansion and vector wave functions are as follows,

$$\begin{aligned}\mathbf{E}_{inc}&=\sum_{n=-\infty}^{\infty}E_n\left[A_n\mathbf{M}_n^{(1)}(kr)+B_n\mathbf{N}_n^{(1)}(kr)\right]\\ \mathbf{E}_{sca}&=-\sum_{n=-\infty}^{\infty}E_n\left[a_n\mathbf{M}_n^{(3)}(kr)+b_n\mathbf{N}_n^{(3)}(kr)\right]\\ \mathbf{E}_{\mathrm{int}}&=\sum_{n=-\infty}^{\infty}E_n\left[c_n\mathbf{M}_n^{(1)}(\kappa_n r)+d_n\mathbf{N}_n^{(1)}(\kappa_n r)\right]\end{aligned}\tag{3}$$

$A_n=i\cos(\alpha)$ and $B_n=\sin(\alpha)$ are the beam shape coefficients of the incident beam. α is the polarization angle which determines the polarization state of incident wave. $\alpha=0$ and $\alpha=\pi/2$ correspond to TM and TE polarization, respectively. $\mathbf{M}_n^{(\cdots)}$ and $\mathbf{N}_n^{(\cdots)}$ are vector cylinder functions, whose expressions are given as follows

$$\begin{aligned}\mathbf{M}_n&=\left(in\frac{Z_n(\rho)}{\rho}\hat{r}-Z_n'(\rho)\phi\right)e^{in\phi}\\ \mathbf{N}_n&=Z_n(\rho)\hat{z}e^{in\phi}\end{aligned}\tag{4}$$

a_n,b_n,c_n, and d_n are the scattering coefficients. Inside and outside the cylinder, $\rho=\kappa_n r$ and $\rho=kr$, respectively. κ_n and k are the wave number inside and outside the cylinder, where $\kappa_n=\sqrt{m^2k^2+2n\beta(m^2-1)}(k/a)$. m and n are the relative refractive index of particle and partial-wave index, respectively. $\beta=\Omega a/c$ is the rotation dimensionless parameter. $Z_n^{(\cdots)}(\rho)$ corresponds to the spherical Bessel and Hankel functions of the first kind when the superscript is 1 and 3. The expression of ρ inside and outside the particle is kr and $\kappa_n r$ with $r=\sqrt{x^2+y^2+z^2}$, respectively.

Substitute Eq. (3) into Eq. (1)-(2) respectively, the magnetic fields are expressed as follows

$$\begin{aligned}\mathbf{H}_{inc}(r)&=-i\frac{k}{\omega\mu_0}\sum_{n=1}^{\infty}E_n\left[A_n\mathbf{N}_n^{(1)}(kr)+B_n\mathbf{M}_n^{(1)}(kr)\right]\\ \mathbf{H}_{sca}(r)&=i\frac{k}{\omega\mu_0}\sum_{n=-\infty}^{\infty}E_n\left[a_n\mathbf{N}_n^{(1)}(kr)+b_n\mathbf{M}_n^{(1)}(kr)\right]\\ \mathbf{H}_{\mathrm{int}}(r)&=-i\frac{\kappa_n}{\omega\mu_0}\sum_{n=-\infty}^{\infty}E_n\left[c_n\mathbf{N}_n^{(1)}(kr)+d_n\mathbf{M}_n^{(1)}(kr)\right]\\ &+(\varepsilon_1-\varepsilon_0)\Omega r\sum_{n=-\infty}^{\infty}E_n\left\{d_nJ_n(\kappa_n r)\hat{r}-c_nin\frac{J_n(\kappa_n r)}{\kappa_n r}\hat{z}\right\}e^{in\varphi}\end{aligned}\tag{5}$$

The continuity condition at the boundary $(r=a)$ of a rotating medium cylinder is considered as follows

$$\begin{cases}E_\phi^{\mathrm{int}}=E_\phi^{inc}+E_\phi^{sca},E_z^{\mathrm{int}}=E_z^{inc}+E_z^{sca}\\ H_\phi^{\mathrm{int}}=H_\phi^{inc}+H_\phi^{sca},H_z^{\mathrm{int}}=H_z^{inc}+H_z^{sca}\end{cases}\tag{6}$$

Substitute Eq. (1) and Eq. (5) into Eq. (6), the scattering coefficients are attained as

$$\begin{aligned}a_n&=A_n\frac{C_nJ_n(\kappa_n a)J_n'(ka)-kJ_n(ka)J_n'(\kappa_n a)}{C_nJ_n(\kappa_n a)H_n'(ka)-kH_n(ka)J_n'(\kappa_n a)}\\ b_n&=B_n\frac{\kappa_nJ_n(ka)J_n'(\kappa_n a)-kJ_n(\kappa_n a)J_n'(ka)}{\kappa_nH_n(ka)J_n'(\kappa_n a)-kJ_n(\kappa_n a)H_n'(ka)}\\ c_n&=A_n\frac{kJ_n(ka)H_n'(ka)-kH_n(ka)J_n'(ka)}{C_nJ_n(\kappa_n a)H_n'(ka)-kH_n(ka)J_n'(\kappa_n a)}\\ d_n&=B_n\frac{kJ_n(ka)H_n'(ka)-kH_n(ka)J_n'(ka)}{kJ_n(\kappa_n a)H_n'(ka)-\kappa_nH_n(ka)J_n'(\kappa_n a)}\end{aligned}\tag{7}$$

Where $C_n=\left[\kappa_n+\omega\mu_0n(\varepsilon_1-\varepsilon_0)\Omega/\kappa_n\right]$.

3 Discussion and conclusion

The magnetic resonance generated by the interaction between a spinning mesoscale dielectric cylinder and a TM plane wave is calculated as Figure 2. Where (a) and (b) correspond to the case that $\beta=1.94879\times10^{-2}$ and $\beta=2.31455\times10^{-2}$. In the calculation, wavelength λ is set as 632.8nm. The relative refractive index and size parameter of a rotating cylinder are $m=1.57$ and $ka=100$ (the corresponding radius is a=10.0713μm). The amplitude of the electric field is $E_0=1\mathrm{V}$.

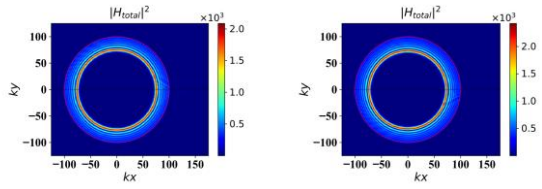

(*a*) $\beta = 1.94879\times10^{-2}$ (*b*) $\beta = 2.31455\times10^{-2}$

Figure 2 *The magnetic resonance generated by a spinning mesoscale dielectric cylinder. (a) and (b) correspond to cases where* β *is* $\beta = 1.94879\times10^{-2}$ *and* 2.31455×10^{-2} *, respectively.*

In Figure 2, it can be seen that the intensity of the magnetic field is confined in resonance rings, which are evenly distributed on the corresponding resonance ring. Under the resonance condition, the plane wave is continuously reflected inside the particle, and should have formed a series of standing waves. However, due to the additional field introduced into the particle by rotation, the resonant point arrays distributed in the resonance ring will shift along the direction of particle rotation and fuse into a resonance ring with uniform intensity distribution. This is the reason why the resonance caused by rotation is a WGM-like type. In addition, the resonance inside the particle is composed of multiple resonance rings with uniform intensity distribution, and the intensity is different between adjacent resonance rings. And the intensity and number of resonant rings are also different at different rotation speeds. A conclusion is proposed that the rotation can be used to generate magnetic resonance, which is sensitive to rotation dimensionless parameter β .

This magnetic resonance with uniform intensity distribution rings is unique, which provides a new design method for a resonator with better stability, uniformity, and applicability. Besides, the research can be extended to magnetic resonance caused by rotating spheres [11-13] based on the framework proposed by this manuscript, which will expand the application field of optical resonators.

4 Acknowledgement

This work was supported by the National Natural Science Foundation of China (62001345, 62201411, 62371378).

5 References

[1] Z. Chen, A. Taffove, and V. Backman, "Photonic nanojet enhancement of backscattering of light by nanoparticles: a potential novel visible-light ultramicroscopy technique," Opt. Express 12(7), 1214–1220 (2004).

[2] Minin I V, Minin O V. Mesotronics: some new, unusual optical effects[C]//Photonics. MDPI, 2022, 9(10): 762.

[3] Owen J F, Chang R K, Barber P W. Internal electric field distributions of a dielectric cylinder at resonance wavelengths[J]. Optics Letters, 1981, 6(11): 540-542.

[4] Mie G. Beiträge zur Optik trüber Medien, speziell kolloidaler Metallösungen[J]. Annalen der physik, 1908, 330(3): 377-445.

[5] Rayleigh L. The problem of the whispering gallery[J]. Scientific papers, 1912, 5: 617-620.

[6] Ashkin A, Dziedzic J M. Observation of resonances in the radiation pressure on dielectric spheres[J]. Physical Review Letters, 1977, 38(23): 1351.

[7] Labrador-Páez L, Soler-Carracedo K, Hernández-Rodríguez M, et al. Liquid whispering-gallery-mode resonator as a humidity sensor[J]. Optics express, 2017, 25(2): 1165-1172.

[8] Tang H, Li R, Gong S, et al. Curved photonic nanojet generated by a rotating cylinder[J]. Optics Express, 2023, 31(2): 986-996.

[9] Shi Z, Tang H, Zhang Y, et al. Resonance scattering by a rotating cylinder[C]//AOPC 2023: Nanophotonics. SPIE, 2023, 12961: 35-41.

[10] Tai C T. Two scattering problems involving moving media[J]. The Ohio State University Antenna Laboratory Report, 1964: 1691-7.

[11] Tang H, Shi Z, Zhang Y, et al. Unusual optical phenomena inside and near a rotating sphere: the photonic hook and resonance[J]. Optics Express, 2024, 32(7): 12950-12966.

[12] Tang H, Shi Z, Zhang Y, et al. Optical magnus effect of spinning dielectric sphere[C]//AOPC 2023: Nanophotonics. SPIE, 2023, 12961: 42-48.

[13] Zhang Y, Tang H, Shi Z, et al. Photonic hooks generated by a rotating dielectric sphere[C]//AOPC 2023: Nanophotonics. SPIE, 2023, 12961: 49-57.

The 14th International Conference on
Laser-light and Interactions with Particles (LIP2024)
September 18-22nd, 2024, Xi'an, Shaanxi, China

A THEORETICAL SCATTERING MODEL OF THE RAIN–WIND–SEA WAVE INTERACTIONS AT HIGH WINDS

Yu DU[1], Xiaoxiao ZHAGN [1,*], Xiang SU [2] , Zhensen WU [3] and Xiaoyu LIU [1]

[1] School of Electronic Engineering, Xi'an University of Posts & Telecommunications, Xi'an, 710121, China
[2] China Academy of Space Technology, Xi'an, 710100, China
[3] School of physics, Xidian University Xi'an, 710126, China

**Corresponding author: zhangxiao_0708@126.com*

Abstract

High-resolution SAR (Synthetic Aperture Radar) is a potential powerful tool for atmospheric and oceanic remote sensing. There is at present insufficient theoretical scattering modelling of the rain–wind–wave interactions for SAR data interpreting in raining areas, especially at high winds. We develop a theoretical rain-wind backscatter model with different backscatter mechanisms including volume scattering and attenuation in the atmosphere caused by raindrops, rain altered wind wave model (ring wave) as well as breaking waves and foam at high winds in the air-sea boundary layer. High-resolution scattering coefficient distribution for rainfall over the sea surface is presented, which lays the foundation for high-resolution SAR interpreting.

1 Introduction

The study of the electromagnetic scattering mechanism from sea surface is of great significance in remote sensing [1]. Rainfall is sometimes inevitable under high sea conditions and is the main factor affecting the circulation of heat and humidity on the sea. The multiple scattering due to rain may have some influence on the quality of signal received [2]. Its impact on radar echo is mainly manifested in two aspects: (1) volume scattering caused by raindrops and attenuation effect in the atmosphere. (2) The annular spectrum of raindrops on the sea surface under the disturbance of rainfall affects the roughness of the sea surface, and then affects the radar scattering echo. Therefore, it is of great significance to establish a rainfall sea surface scattering model for the study of weather and climate above the sea surface.

The paper is organized as follows: a three particle layers model including rainfall in the atmosphere, secondary droplets and foam layers for rainfall over the ocean surface is proposed in Section 2. Subsequently, the rain volume scattering in the atmosphere and the volume-facet scattering in the air-sea interface is established for backscattering simulation from rainy sea surfaces. High-resolution scattering coefficient distribution for rainfall over a rough sea surface is presented in Section 3. Finally, Section 4 provides a summary.

2 Methods

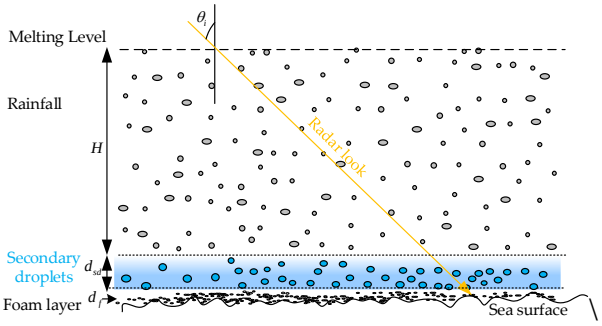

Figure 1. *Sketch map for rainfall over the ocean surface including three different particle layers: rainfall in the atmosphere, secondary droplets and foam layer*

We assume the rainfall over the ocean surface forms three different particle layers (shown as Fig.1): rainfall in the atmosphere with a cloud height of H (usually a few kms), a dense cloud of seawater droplets generated by raindrop impinging on the ocean surface with a thickness of *dsd* (a height estimated by visual observation of about 0.5 m), and foam layer generated by wave breaking at high winds with a thickness of df (0-20cm height corresponds to different wind speed). The lower two layers forms the air-sea boundary layer, including sea waves (with breaking waves and foam at high winds), ring waves, stalks, crowns, and secondary drops. Hence the air-sea boundary layer is a dense cloud of seawater droplets, which is a high conductivity medium and a strong absorber of the radar waves compared with that the raindrops attenuation in the atmosphere. Next, we will analyze the scattering and attenuation characteristics of the above three layers respectively.

2.1 Rain volume scattering in the atmosphere

As most raindrop size is less than 3 mm, we have modelled the raindrop scatterers as spherical Rayleigh particles. Following [3], the scattering coefficient caused by raindrops can be written as

$$\sigma_{pp} = 4\pi n_0 k^4 \left|\frac{\varepsilon_{rain}-1}{\varepsilon_{rain}+2}\right| \frac{H}{\tan\theta}\left\langle \tau_p^2 \right\rangle + \sigma_{pp}^{\text{air-sea}} \alpha_{pp} \quad (1)$$

Where ε_{rain} denotes complex relative permittivity of the raindrops, $n_0 = \int_0^\infty N(D)dD$ is the number of raindrops per unit volume, θ is the incident angle, H is the cloud height. The second term in equation (4) is the rainfall penetration attenuation applied to sea surface scattering, where $\sigma_{pp}^{\text{air-sea}}$ represents scattering in the air-sea interface, which will be discussed in Section 2.2, and the attenuation α_{pp} is expressed as

$$\alpha_{pp} = \exp(-2H\sec\theta \frac{4n_0\pi}{k}\text{Im}\left\langle S_{pp}^f \right\rangle) \quad (2)$$

In equation (1) and (2), $\left\langle \tau_p^2 \right\rangle$ and $\left\langle S_{pp}^f \right\rangle$ are the element of the phase matrix and scattering matrix, respectively, where the bracket denotes ensemble average. The expression for τ_p^2 and $\left\langle S_{pp}^f \right\rangle$ are as follows:

$$\begin{aligned}
&\tau_v = \frac{a^3}{3}\left[\frac{1}{g_a} + (\frac{1}{g_c} - \frac{1}{g_a})\sin^2\theta\right], \quad \tau_h = \frac{a^3}{3g_a} \\
&\tau'^2_v = \frac{a^3}{9}\left[\frac{1}{g_a^2} + (\frac{1}{g_c^2} - \frac{1}{g_a^2})\sin^2\theta\right] \\
&\text{Im}\left\langle S_{vv}^f \right\rangle \approx 3k^2 \frac{\text{Im}(\varepsilon_{rain})}{\left|\varepsilon_{rain}+2\right|^2}\left\langle \tau_v \right\rangle + \frac{2k^5}{3}\left|\frac{\varepsilon_{rain}-1}{\varepsilon_{rain}+2}\right|\left\langle \tau'^2_v \right\rangle \\
&\text{Im}\left\langle S_{hh}^f \right\rangle = 3k^2 \frac{\text{Im}(\varepsilon_{rain})}{\left|\varepsilon_{rain}+2\right|^2}\left\langle \tau_h \right\rangle + \frac{2k^5}{3}\left|\frac{\varepsilon_{rain}-1}{\varepsilon_{rain}+2}\right|\left\langle \tau_h^2 \right\rangle
\end{aligned} \quad (3)$$

where g_a and g_c are the geometric parameters of a Rayleigh scattering particle, a denotes the equivalent raindrop radius.

2.2 volume-facet scattering in the Air-sea interface

As mentioned, the air-sea boundary layer includes sea waves (with breaking waves and foam at high winds), ring waves, and splash products such as stalks, crowns, and secondary drops. The contribution of each of these splash products to the backscattering varies with incidence angle and polarization. Among the splash products, only secondary drops were considered in this paper because the thickness of stalk and crown was is only about 2 cm, which is far less than the thickness of secondary raindrops layer (with a dense population of secondary drops extends a height estimated by visual observation of about 0.5 m. (50cm), and it is generally believed that stalks and crowns would become dominant only at low grazing angles, which is beyond the scope of this article.

The total scattering coefficients of the sea surface can be expressed by combining the KA and SPM contributions:

$$\begin{aligned}
&\sigma_{pq}^{sea}(\boldsymbol{k}_i, \boldsymbol{k}_s) = \sigma_{pq}^{KA}(\boldsymbol{k}_i, \boldsymbol{k}_s) + \sigma_{pq}^{SPM}(\boldsymbol{k}_i, \boldsymbol{k}_s) \\
&= \pi k^2 q^2 \left|\mathbb{U}_{pq}\right|^2 P(z_x^{\tan}, z_y^{\tan})/q_z^4 \\
&+ \pi k^4 \left|\varepsilon_{sea}-1\right|^2 \left|\mathbb{F}_{pq}\right|^2 S_\zeta(\boldsymbol{q}_l)
\end{aligned} \quad (4)$$

Where $\mathbb{U}_{pq}$ and $\mathbb{F}_{pq}$ is the polarmetric coefficient for KA and SPM components respectively. $P(z_x^{\tan}, z_y^{\tan})$ is probability distribution function of the surface slope, and $q = \left|\boldsymbol{q}\right| = \left|k(\hat{k}_s - \hat{k}_i)\right|$. ε_{sea} is the permittivity of the surface. The spatial power spectrum $S_\zeta(\boldsymbol{q}_l)$ expressed in terms of the capillary spectrum is $S_\zeta(\boldsymbol{q}_l) = \psi_{sea}(\boldsymbol{k})/\boldsymbol{q}_l$, where $\boldsymbol{q}_l$ is the projection of vector $\boldsymbol{q}$ onto the plane tangent. The surface roughness in the raining areas will be altered, thus we should take the ring wave the into account for the SPM contribution.

According to ring wave model proposed in [4], the surface variance spectrum can be expressed as a function of rain rate (RR) and the terminal fall velocity of the drops:

$$\begin{aligned}
\Psi(k, RR) = &\left\{\frac{64}{9}\frac{\omega^2}{g^2k^4}\int_0^\infty N(D)W^3(D)D^2\left[J_2\left(\frac{kD}{2}\right)\right]^2 dD\right\} \\
&\cdot\left\{\frac{1}{8v_r k^2}\left(e^{-\alpha t_0} - e^{-\alpha\tau}\right)\right\}
\end{aligned} \quad (5)$$

Where ω and wavenumber k are related by the dispersion relation for surface waves: $\omega = \left[gk\left(1 + \frac{Tk^2}{\rho_w g}\right)\right]^{1/2}$. T is the surface tension ($T = 7.9\times10^{-2}\,\text{N}\cdot\text{m}^{-1}$) and ρ_w, the density of water.

In equation (6), $J_2(kR)$ is the second order Bessel functions of the first kind. The damping rate α and the kinematic viscosity v_0 are related by $\alpha = 4k^2 v_0\left[\left(1 - e^{-2kd_{\text{mix}}}\right)\frac{v_e}{v_0} + e^{-2kd_{\text{mix}}}\right]$. d_{mix} is the depth of the turbulent upper layer, and v_e is the eddy viscosity.

The spatial power spectrum $S_\zeta(\boldsymbol{q}_l)$ in equation (4) expressed in terms of the capillary spectrum is modified as $S_\zeta(\boldsymbol{q}_l) = \left[\psi_{sea}(\boldsymbol{k}) + \psi_{ring}(\boldsymbol{k})\right]/\boldsymbol{q}_l$.

The volume-facet scattering of the sea surface and particle layers was obtained by the vector radiative transfer (VRT) theory. The zero-order and first-order solution of the VRT equation are used in this paper with the following expression.

$$\sigma_{pq}^{air-sea-0}(\theta_i)=\sigma_{pq}^{sea}(\theta_i)e^{-2\kappa_e d_{sd}\sec\theta_i}$$

$$\sigma_{hh}^{air-sea-1}(\theta_i)=\frac{3}{4}\cos\theta_i\frac{\kappa_s}{\kappa_e}(1-\mathrm{e}^{-2\kappa_e d\sec\theta_i})$$

$$\cdot(1+\left|R_{h0}\right|^4\times\mathrm{e}^{-2\kappa_e d_{sd}\sec\theta_i})+3\mathrm{d}\kappa_s\left|R_{h0}\right|^2\mathrm{e}^{-2k_e d_{sd}\sec\theta_i} \quad (6)$$

$$\sigma_{vv}^{air-sea-1}(\theta_i)=\frac{3}{4}\cos\theta_i\frac{\kappa_s}{\kappa_e}(1-\mathrm{e}^{-2\kappa_e d_{sd}\sec\theta_i})$$

$$\cdot(1+\left|R_{v0}\right|^2\mathrm{e}^{-2\kappa_e d_{sd}\sec\theta_i})+3\mathrm{d}\kappa_s\left|R_{v0}\right|^2\mathrm{e}^{-2\kappa_e d_{sd}\sec\theta_i}\cos^2(2\theta_i)$$

The first term indicated as $\sigma_{pq}^{air-sea-0}$ represents scattering of the local facet from the bottom surface. The second term $\sigma_{hh}^{air-sea-1}$ and $\sigma_{vv}^{air-sea-1}$ represent volume–surface interaction of the secondary droplets and the sea surface for HH and VV polarizations respectively. R_{h0} and R_{v0} are the Fresnel coefficients of the local facet, and θ_i is the local incident angle. κ_s and κ_e are the scattering and extinction coefficients of the secondary droplets:

3 Results and Discussions

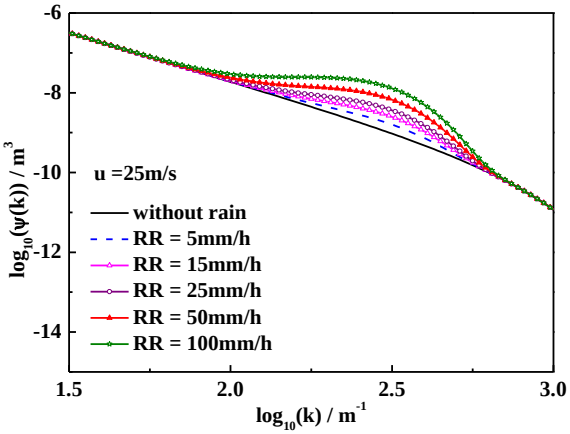

Figure 2. *Elfouhaily spectra with different rain rate*

The shape of the Elfouhaily spectrum altered by the ring wave spectrum model is depicted in figure 1 with different rain rate. It is observed from figure 1 that the effect of rain-induced turbulence is to enhance surface waves spectrum. The dominant energy is from ring-waves with wavenumbers from about 50 m-1 to 500 m-1 and the peak is at about 0.02 wavelength. From figure 1 we can conclude that the ring wave spectrum enhancements increases with the rain rate.

Figure 3 shows the results of scattering coefficients with for VV polarizations of the sea surface with the rainfall rate of 5mm/h. From the graph, it can be seen that the scattering effect of raindrops on the sea surface leads to an enhancement of the sea surface scattering coefficient.

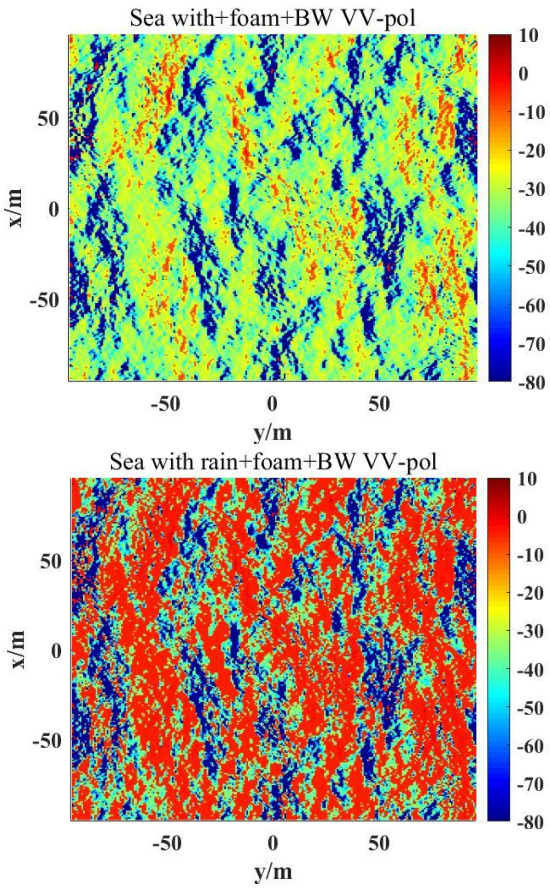

Figure 3. *Scattering coefficient distribution of a deterministic sea surface and sea surface with rain for VV polarization*

4 References

[1] Yaël Demarty, Laetitia Thirion-Lefevre, Vincent Gobin, Modelling of the electromagnetic scattering by sea surfaces at grazing incidence. Application to HF surface wave radars, Comptes Rendus Physique, 11(1):87-95 (2010)

[2] Moses Oludare Ajewole, Tomohiro Oguchi, Attenuation and depolarization of millimeter waves due to incoherent scattering in tropical rainfall, Journal of Quantitative Spectroscopy and Radiative Transfer, 83(2): 149-158 (2004)

[3] F. Xu, X. Li, P. Wang, J. Yang, W. G. Pichel, Y. Q. Jin.. A Backscattering Model of Rainfall Over Rough Sea Surface for Synthetic Aperture Radar. IEEE Transactions on Geoscience and Remote Sensing 53(6): 3042-3054 (2015)

[4] Bliven, L. F. Sobieski, P. W. Craeye, C. Rain generated ring-waves: Measurements and modelling for remote sensing. International Journal of Remote Sensing 18(1): 221-228 (1997).

The 14th International Conference on
Laser-light and Interactions with Particles (LIP2024)
September 18-22nd, 2024, Xi'an, Shaanxi, China

REFLECTION AND REFRACTION OF GAUSSIAN BEAM BY A BIAXIAL ANISOTROPIC SLAB

Bing Yan[1*], Huanyong Zhang[2] and Chenhua Liu[3]

[1] Shool of Information and Communication Engineering, North University of China, Taiyuan 030051, China;
[2]Shool of Electronics and Information Engineering, Anhui University, Anhui 230039, China;
[3]Application Science Institute, Taiyuan University of Science and Technology, Taiyuan 030024, China;
*Corresponding author: yanbing122530@126.com

Abstract

An exact analytical solution is obtained to the reflection and refraction of a Gaussian beam by a biaxial anisotropic slab. The electromagnetic waves in different regions are expanded in terms of rectangular vector wave functions or represented as superposition of eigen plane waves, and the unknown expansion coefficients or angular spectrum amplitudes are determined by virtue of the boundary conditions. For a localized beam model, the normalized field intensity distributions are calculated, and the propagation characteristics are discussed briefly.

Formulation

Considerable theoretical and experimental investigations have been carried out about the electromagnetic (EM) properties of anisotropic media. Undoubtedly, it is one canonical problem to analyze the reflection and refraction of EM waves at a plane interface between isotropic and anisotropic media. The reflection and transmission of an EM plane wave normally incident on a stratified bianisotropic slab have been examined by He *et al* [1], and on a uniaxially bianisotropic slab by Semchenko *et al* [2]. A number of studies have been devoted by Stamnes *et al* to the analysis of the transmission of a Gaussian beam into a uniaxial or biaxial crystal [3-6]. Graham *et al* considered the reflection and transmission of an EM plane wave from biaxially anisotropic– isotropic interfaces [7]. In recent works, we have discussed the propagation characteristics of a Gaussian beam or an arbitrary EM beam through a uniaxial anisotropic slab, by applying the cylindrical or rectangular vector wave functions (VWFs) expansions [8-10]. The Davis-Barton first-order corrected model of the Gaussian beam (localized beam model) as [11-14] is used.

As illustrated in Fig.1, an incident Gaussian beam, described in the Cartesian coordinate system $O'x'y'z'$ (beam coordinate system), propagates from free space towards an infinite biaxial anisotropic slab of thickness d. The axis Oz in the system $Oxyz$ is perpendicular to the interfaces $z=0$ and $z=d$ between free space and the biaxial anisotropic slab. Origin O is on the axis $O'z'$, i.e., at $(0,0,z_0)$ in $O'x'y'z'$, and the propagation direction of the Gaussian beam (axis $O'z'$) has the polar coordinates ζ, η with respect to $Oxyz$. In this paper, an $\exp(-i\omega t)$ time-harmonic convention is assumed for the EM fields.

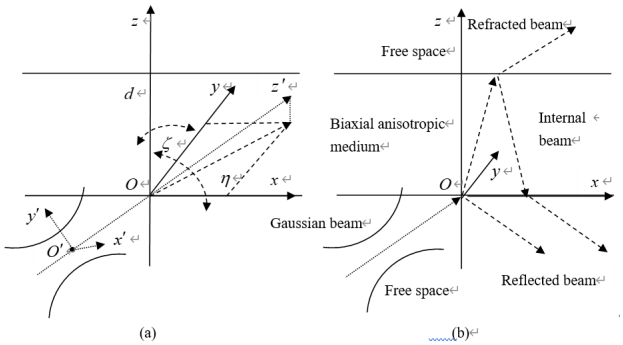

Fig. 1. A Gaussian beam illuminating a biaxial anisotropic slab. (a) The coordinate systems, (b) The configuration.

Figure 2 shows the normalized FIDs in the plane of incidence xOz for a TE and TM polarized Gaussian beam incident on a biaxial anisotropic slab. From Fig. 2 (a) and (b) we can see that at the interface $z=0$ a TM mode Gaussian beam is reflected less than a TE mode Gaussian beam. In addition, the middle of the refracted beam for a TM mode Gaussian beam is at the left of that for a TE mode Gaussian beam, demonstrating that the former is refracted more strongly, which dose not appear for a dielectric slab.

The normalized FIDs are shown in Fig. 3 for the same model as in Fig. 2, but in the plane of incidence yOz. From Fig. 3 (a) and (b) the same propagation phenomena can also be observed for a TM and TE mode Gaussian beam .

A comparison of Fig. 2 (a) and Fig. 3 (a) shows that, even for a TE mode Gaussian beam, the normalized FIDs are different in the planes of incidence xOz and yOz, i.e., the TE mode Gaussian beam has a larger reflection and stronger refraction in the plane yOz than in xOz. However, it is indicated from Fig. 2 (b) and Fig. 3(b) that a TM mode Gaussian beam is reflected less but refracted more strongly in the plane of incidence yOz.

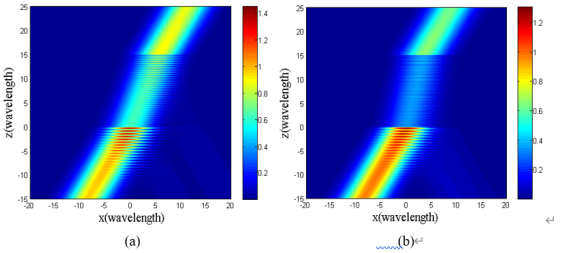

Fig.2. Normalized FIDs in the plane xOz for a biaxial anisotropic slab ($a_x=\sqrt{3}k_0$, $a_y=\sqrt{2}k_0$, $a_z=2k_0$, $d=15\lambda_0$)

respectively illuminated by a (a) TE mode and (b) TM mode Gaussian beam, both with $w_0 = 5\lambda_0$, $z_0 = 0$, $\zeta = \pi/6$ and $\eta = 0$.

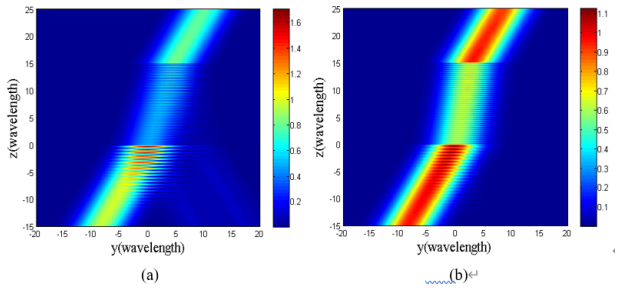

Fig.3. Normalized FIDs in the plane yOz for the same biaxial anisotropic slab as in Fig.2 respectively illuminated by a (a) TE mode and (b) TM mode Gaussian beam, both with $w_0 = 5\lambda_0$, $z_0 = 0$, $\zeta = \pi/6$ and $\eta = \pi/2$.

Conclusion

With the EM field expansions in terms of rectangular VWFs and eigen plane waves, an approach to analyze the propagation of an incident Gaussian beam through a biaxial anisotropic slab is presented. Numerical results of the normalized FIDs show that, in the different planes of incidence, the propagation characteristics of a Gaussian beam are evidently different. It is also demonstrated in the calculations that a TM mode Gaussian beam is refracted more strongly than a TE mode Gaussian beam, in contrast to the well-known case of a dielectric slab. Furthermore, this study can also be extended to other anisotropic slabs in which the eigen plane wave spectrum representations of the EM fields are derived.

References

1. He SL, Hu YD, Ström S. Electromagnetic reflection and transmission for a stratified bianisotropic slab. IEEE Trans Antennas Propag 1994; 42: 856–858.
2. Semchenko IV, Khakhomov SA, Tretyakov SA, Sihvola AH, Fedosenko EA. Reflection and transmission by a uniaxially bi-anisotropic slab under normal incidence of plane waves. J. Phys. D: Appl. Phys 1998; 31: 2458–2464.
3. Sithambaranathan GS, Stamnes JJ. Analytical approach to the transmission of a Gaussian beam into a biaxial crystal. Optics Communications 2002; 209: 55–67.
4. Stamnes JJ, Dhayalan V. Double refraction of a Gaussian beam into a uniaxial crystal. J. Opt. Soc. Am. A 2012; 29: 486-497.
5. Jain M, Lotsberg JK, Stamnes JJ, Ø. Frette, Dhayalan V, Jiang D, Zhao X. Numerical and experimental results for focusing of three-dimensional electromagnetic waves into uniaxial crystals. J. Opt. Soc. Am. A 2009; 26: 691-698.
6. Lotsberg JK, Zhao X, Jain M, Dhayalan V, Sithambaranathan GS, Stamnes JJ, Jiang D. Focusing of electromagnetic waves into a biaxial crystal, experimental results. Optics Communications 2005; 250: 231–240.
7. Graham JW, Lee JK. Reflection and transmission from biaxially anisotropic-isotropic interfaces. Progress In Electromagnetics Research 2013; 136: 681-702.
8. Wang MJ, Zhang HY, Liu GS, Li YL, Dong QF. Reflection and transmission of Gaussian beam by a uniaxial anisotropic slab. Optics Express 2014; 22: 3705-3711.
9. Zhang HY, Zhu D, Wang MJ, Li MQ, Liao TQ. Transmission of electromagnetic beam through a uniaxial anisotropic slab. J. Quant. Spectrosc. Radiat. Transfer 2019; 224: 114–119.
10. Huang ZX, Xu F, Wang BX, Li MQ, Zhang HY. Propagation of Gaussian beam through a uniaxial anisotropic slab. Optics Communications 2016; 380: 336–341.
11. Davis LW. Theory of electromagnetic beam. Phys Rev A 1979; 19: 1177-1179.
12. Barton JP, Alexander DR. Fifth-order corrected electromagnetic field components for a fundamental Gussian beam. J. Appl. Phys 1989; 66: 2800-2802.
13. Gouesbet G. Validity of the localized approximation for arbitrary shaped beam in the generalized Lorenz–Mie theory for spheres. J. Opt. Soc. Am. A 1999; 16: 1641–1650.
14. Gouesbet G, Lock JA, Gréhan G. Generalized Lorenz–Mie theories and description of electromagnetic arbitrary shaped beams: Localized approximations and localized beam models, a review. J. Quant. Spectrosc. Radiat. Transfer 2011; 112: 1–27.
15. Chen ZZ, Zhang HY, Wu XL. Gaussian beam propagation through a biaxial anisotropic circular cylinder. Optik 2020; 223:165650.

The 14th International Conference on
Laser-light and Interactions with Particles (LIP2024)
September 18-22nd, 2024, Xi'an, Shaanxi, China

LIGHT SCATTERING BY A METAL SPHERE USING PHYSICS INFORMED NEURAL NETWORK

Li Xiao[1], Renxian Li[1,*] and Yuan Zhang [1],Yuexiao Jiao[1], Bin Wei[1], Shuhong Gong[1]

[1] 1 School of Physics, Xidian University, Xi'an 710071, China

Corresponding author: rxli@mail.xidian.edu.cn

Abstract

With the increasing abundance of big data and computing resources, the application of physics informed neural network (PINNs) in the field of electromagnetic field computing is gradually expanding its boundaries. By taking full advantage of massive experimental and simulation data to train PINNs models, we can significantly improve their accuracy and efficiency in electromagnetic field calculations. In this paper, the PINNs model is trained using the simulation data generated by the finite-difference frequency-domain (FDFD) to simulate the electromagnetic scattering of three-dimensional metal spheres. The implementation of this method not only demonstrates the potential of PINNs in dealing with complex electromagnetic problems, but also provides new perspectives and tools for electromagnetic scattering research.

1 Introduction

Physics informed neural network (PINNs) is a machine learning model that combines deep learning and physics knowledge. It expresses the physical law in the form of partial differential equation, and approximates the solution of the partial differential equation through neural network, which is equivalent to embedding the physical law into the training process of neural network [1,2]. Compared with traditional physical model-based methods, PINNs has higher flexibility and scalability, and can adaptively learn complex nonlinear dynamic systems and meet the requirements of physical specifications at the same time. In recent years, as a new deep learning technique, , PINNs provides a new way to solve the electromagnetic scattering problem. PINN combines the expressive power of deep learning with the inherent laws of physical problems to solve complex physical problems effectively [3,4].

The principle of traditional electromagnetic scattering methods is mainly based on Maxwell's equations and boundary conditions to solve the scattering field of objects under electromagnetic wave irradiation by analytical or numerical methods [5-7]. Among them, the analytical method is usually suitable for the object with regular shape and simple boundary conditions, which can be solved by the separation of variables method, integral transformation method, Green function method, and other methods. Numerical methods are suitable for objects of any shape, and commonly used numerical methods include finite difference method (FDM), finite element method (FEM), moment method (MoM), etc.

However, the traditional methods for studying electromagnetic scattering also have some limitations. Firstly, for objects with complex shapes, analytical methods are often difficult to apply, while numerical methods require significant computational resources and time. Secondly, traditional methods may encounter difficulties in dealing with problems such as multipath, multiple reflection, and scattering, which require consideration of multiple interactions of electromagnetic waves between objects. In addition, the traditional method also has some limitations in dealing with nonlinear, non-uniform and time-varying problems. With the continuous development of computer technology and numerical methods, PINNs has become a good choice to study electromagnetic scattering problems in recent years, which breaks through the limitations of traditional methods to a certain extent.

The aim of this paper is to solve the Maxwell's equations using a three-dimensional difference matrix, and to calculate the scattered field using the finite-difference frequency-domain (FDFD) as input for training a physical information neural network (PINN) [8]. Subsequently, the trained network is used to calculate the scattered field of a metal sphere, producing a scattering effect consistent with the expected result. Compared with using FDFD method alone, this approach is more efficient and less time-consuming.

2 Method

In the case of three dimensions, assuming a time factor of $\exp(+j\omega t)$, the curl equation of Maxwell's equations is:

$$\begin{cases} \nabla \times \mathbf{E} = -j\omega \mathbf{B} \\ \nabla \times \mathbf{B} = \mathbf{J} + j\omega \mathbf{D} \end{cases} \tag{1}$$

The Maxwell representation of the scattered field form is given by:

$$\begin{cases} \nabla \times \mathbf{E}_{scat} = -j\omega(\mu_0 - \mu)\mathbf{H}_{inc} \\ \nabla \times \mathbf{H}_{sca} = j\omega\varepsilon \mathbf{E}_{scat} - j\omega(\varepsilon - \varepsilon_0)\mathbf{E}_{inc} \end{cases} \tag{2}$$

The above formula of the difference matrix can be expressed in the rectangular coordinate system as follows:

$$\begin{cases} C^e \mathbf{E}_{scat} = -j\omega\mu \mathbf{H}_{sca} + j\omega(\mu_0 - \mu)\mathbf{H}_{inc} \\ C^h \mathbf{H}_{sca} = J + j\omega\varepsilon \mathbf{E}_{scat} + j\omega(\varepsilon - \varepsilon_0)\mathbf{E}_{inc} \end{cases} \tag{3}$$

The difference matrix equation can be simplified to:

$$Ax = b \tag{4}$$

Where A and b are defined as:

$$\begin{cases} A = C^h \mu^{-1} C^e - \omega^2 \varepsilon \\ b = \omega^2 (\varepsilon - \varepsilon_0) E_{inc} \end{cases} \quad (5)$$

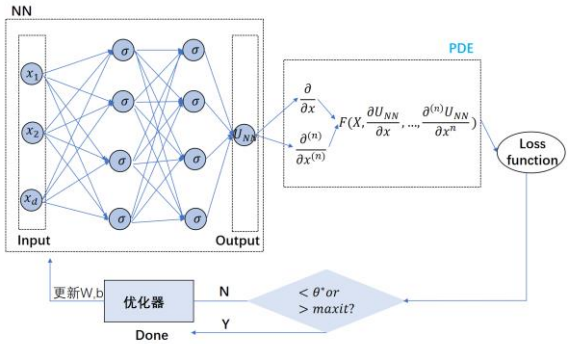

Figure 1 Diagram of PINN's network structure

When PINNs is used to calculate the electromagnetic scattering characteristics of metal spheres, We use the partial differential equation (PDE) based on FDFD as the physical constraint, which eliminates the cumbersome data and boundary condition setting. Our network takes space coordinates (x, y, z) as input parameters and the real and imaginary parts of the electric field (Ex, Ey, Ez) as output. In the calculation process, we use a similar method to FDFD to calculate the values of A and b. Next, we define the following loss function:

$$Loss = AE_{sca}^{PINN} - b \quad (6)$$

This loss function is designed to ensure that PINN's prediction results accurately meet the physical constraints of the FDFD-based partial differential equation PDE, thus obtaining accurate simulation results of the electromagnetic scattering characteristics of the metal sphere. By optimizing this loss function, we can train a neural network model with strong physical perception ability, which provides strong support for the study of electromagnetic scattering problems.

3 Discussion and conclusion

In the process of electromagnetic scattering analysis of metal spheres by PINNs, we creatively combine FDFD difference matrix equation with sparse matrix to realize efficient three-dimensional scattering analysis of metal spheres[9-12]. This combination not only gives full play to the advantages of PINNs in dealing with complex physical problems, but also significantly improves the computational efficiency by optimizing the numerical calculation process, which brings new breakthroughs for the study of electromagnetic scattering problems.

4 Acknowledgement

This work was supported by the National Natural Science Foundation of China (62001345, 62201411, 62371378).

5 References

[1] P. Zhang, Y. Hu, Y. Jin, S. Deng, X. Wu and J. Chen, "A Maxwell's Equations Based Deep Learning Method for Time Domain Electromagnetic Simulations," in IEEE Journal on Multiscale and Multiphysics Computational Techniques, vol. 6, pp. 35-40, 2021, doi: 10.1109/JMMCT.2021.3057793.

[2] Raissi M, Perdikaris P, Karniadakis GE. Physics-informed neural networks: A deep learning framework for solving forward and inverse problems involving nonlinear partial differential equations. Journal of Computational Physics. 2019;378:686-707. doi:10.1016/j.jcp.2018.10.045

[3] B Tarbiyati H, Nemati Saray B. Weight initialization algorithm for physics-informed neural networks using finite differences. Engineering with Computers: An International Journal for Simulation-Based Engineering. August 2023:1-17. doi:10.1007/s00366-023-01883-y.

[4] Choi, S., Jung, I., Kim, H. et al. Physics-informed deep learning for data-driven solutions of computational fluid dynamics. Korean J. Chem. Eng. 39, 515–528 (2022).

[5] Teixeira, F.L., Sarris, C., Zhang, Y. et al. Finite-difference time-domain methods. Nat Rev Methods Primers 3, 75 (2023).

[6] Dmitrenko, A.G., Balashova, O.M. Scattering of an Electromagnetic Wave by a Structure Consisting of Several Perfectly Conducting and Dielectric Finite-Length Thin Cylinders. Radiophys Quantum El 65, 118–129 (2022).

[7] Dmitrenko, A.G., Balashova, O.M. Scattering of an Electromagnetic Wave by a Thin Perfectly Conducting Cylinder Located Inside a Dielectric Body. Radiophys Quantum El 66, 260–269 (2023).

[8] Ren, Q., Wang, Y., Li, Y., Qi, S. (2022). Three-Dimensional Electromagnetic Scattering Solver. In: Sophisticated Electromagnetic Forward Scattering Solver via Deep Learning. Springer, Singapore.

[9] Kissel, M., Diepold, K. Structured Matrices and Their Application in Neural Networks: A Survey. New Gener. Comput. 41, 697–722 (2023).

[10] Bell, N., Garland, M.: Efficient sparse matrix-vector multiplication on cuda. Nvidia Technical Report NVR-2008-004 2(5) (2008)

[11] Dettmers, T., Zettlemoyer, L.: Sparse networks from scratch: faster training without losing performance. arXiv preprint arXiv:1907.04840 (2019)

[12] Atashgahi, Z., Pieterse, J., Liu, S. et al. A brain-inspired algorithm for training highly sparse neural networks. Mach Learn 111, 4411–4452 (2022).

The 14th International Conference on
Laser-light and Interactions with Particles (LIP2024)
September 18-22nd, 2024, Xi'an, Shaanxi, China

THE OPTICAL FIBER COUPLING EFFICIENCY

IN THE NEAR-SEA ATMOSPHERE IS OPTIMIZED BY USING A FOCUSING MIRROR

Xuan GAO[1,*], Yiping HAN[1], Jiajie WANG[1], Yunqin ZHOU[1], Xikang ZHOU[1], Chen YAN[1]

[1]School of Physics, Xidian University, Xi 'an 710071, China

Corresponding author: 20051110203@stu.xidian.edu.cn

Abstract

This paper utilizes a focusing mirror system to enhance the fiber coupling efficiency for long-distance transmission in space optical communication. We derived an expression for the coupling efficiency of single-mode fibers based on the power spectrum of a marine atmospheric turbulence with anisotropy and the theory of annular beams. Our research indicates that the use of a focusing mirror can improve the fiber coupling efficiency, and an annular beams exhibit better coupling efficiency compared to Gaussian beams. Furthermore, the study demonstrates that compared to the atmospheric environment, a marine atmosphere is more complex, leading to a more severe impact on fiber coupling efficiency. The research in this paper contributes to improving fiber coupling efficiency in complex environments and holds practical application value in free-space optics.

1 Introduction

The efficiency of random light coupling into fibers is also crucial for the design of optical communication link receivers. In practical free-space communication links, the impact of turbulence in the environment on the fiber when coupling the light beam into it is inevitable[1, 2]. The marine atmosphere is an important environmental factor in the research of free-space optical communication [3].

Numerous researchers have extensively studied the coupling efficiency of single-mode fibers in the ocean [4] and atmospheric turbulence[5]. Hanson et al. conducted experiments under ideal conditions to investigate how to improve fiber coupling efficiency in underwater turbulence [6]. Researchers have discussed the impact of source coherence on improving fiber coupling efficiency[4]. Others have examined the maximum fiber coupling efficiency and optimal beam size for random angular jitter in free-space laser systems and their applications[7]. Despite the multifaceted analysis in the above studies to enhance fiber coupling efficiency, addressing practical application issues remains insufficient. Some researchers have indicated that using a focusing mirror system can improve the transmission quality of beams in turbulence[8]. Therefore, building upon this, we investigate the fiber coupling efficiency of annular beams in a marine atmospheric turbulence using a focusing mirror system and compare it with factors such as atmospheric turbulence and Gaussian beams.

2 Physical theoretical model

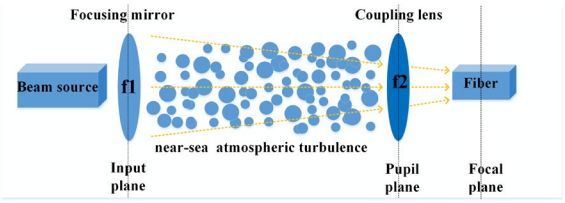

Figure1. *Schematic of the annular beam passing through the focusing mirror system and then coupled into the fiber in a marine turbulence atmosphere*

The fiber-coupling efficiency in Sea-surface environment is defined as the ratio of the average power coupled into the fiber, $\langle P_c \rangle$, to the average power in the receiver aperture plane, $\langle P_a \rangle$, considering the back-propagated fiber-mode profile. The fiber coupling efficiency is then given by[2]

$$\eta = \frac{\langle P_c \rangle}{\langle P_a \rangle} = \frac{\iint_A F_A^*(\rho_1) F_A(\rho_2) W(\rho_1, \rho_2, z) d\rho_1 d\rho_2}{\iint_A |E_A(\rho)|^2 d\rho}, \quad (1)$$

where $E_A(\rho)$ is described as the incident optical field at the receiver aperture plane, $W(\rho_1, \rho_2, z)$ is the mutual coherence function of the spatial beam in turbulence, $F_A(\rho)$ is the back-propagated fiber mode for single-mode fiber at the front surface of the coupling lens, the asterisk denotes the complex conjugation. The expression is as follows:

$$F_A(\rho) = \sqrt{\frac{2}{\pi S^2}} \exp\left(-\frac{\rho^2}{S^2}\right), \quad (2)$$

where λ is the laser wavelength, d is the fiber-mode field radius and f_2 is the focal length of the coupling lens.

An annular beam profile in the source plane can be expressed as[8, 9]:

$$E(r,\theta,0) = \exp\left(-\frac{iC_0}{\omega_0^2} r^2 + im_0\theta\right) \sum_{u=1}^{N} \frac{(-1)^{u-1}}{N} \binom{N}{u} \left[\exp\left(-\frac{ur^2}{\omega_0^2}\right) - \exp\left(-\frac{ur^2}{\varepsilon\omega_0^2}\right)\right], \quad (3)$$

where $C_0 = k\omega_0^2/2f_1$ is the initial beam pre-focusing parameter, ω_0 is beam waist size, f_1 is focal length of the focusing mirror, The constant C_0 occurring in Eq.(3) shows the existence of a mirror. m_0 is the initial quantum number, $\binom{N}{u}$ is the binomial coefficient, N is the beam order, u is a positive integer, ε represents the obscure ratio of the annular beam and satisfy the constraint $0 < \varepsilon < 1$ .For an annular beam, after tedious calculation and simplify, we can obtain the average power $\langle P_a \rangle$ in the receiver aperture plane and the average power coupled into the fiber, $\langle P_c \rangle$ as follows:

$$
\begin{aligned}
P_a &= \iint_A \left| E_A(\rho,\varphi,z) \right|^2 d\rho \\
&= \int_0^R \frac{k^4\rho^3\pi}{64z^4} \times \sum_{u=1}^{N} \frac{(-1)^{u-1}}{N} \binom{N}{u} \times \sum_{u=1}^{N} \frac{(-1)^{u-1}}{N} \binom{N}{u} \\
&\times \left\{ \begin{array}{l} \frac{1}{a_1^{1.5}} \exp\left(-\frac{k^2\rho^2}{8a_1z^2}\right) \times \left[I_{\frac{m_0-1}{2}}\left(\frac{k^2\rho^2}{8a_1z^2}\right) - I_{\frac{m_0+1}{2}}\left(\frac{k^2\rho^2}{8a_1z^2}\right) \right] \\ -\frac{1}{a_2^{1.5}} \exp\left(-\frac{k^2\rho^2}{8a_2z^2}\right) \times \left[I_{\frac{m_0-1}{2}}\left(\frac{k^2\rho^2}{8a_2z^2}\right) - I_{\frac{m_0+1}{2}}\left(\frac{k^2\rho^2}{8a_2z^2}\right) \right] \end{array} \right\}, \quad (4) \\
&\times \left\{ \begin{array}{l} \frac{1}{b_1^{1.5}} \exp\left(-\frac{k^2\rho^2}{8b_1z^2}\right) \times \left[I_{\frac{m_0-1}{2}}\left(\frac{k^2\rho^2}{8b_1z^2}\right) - I_{\frac{m_0+1}{2}}\left(\frac{k^2\rho^2}{8b_1z^2}\right) \right] \\ -\frac{1}{b_2^{1.5}} \exp\left(-\frac{k^2\rho^2}{8b_2z^2}\right) \times \left[I_{\frac{m_0-1}{2}}\left(\frac{k^2\rho^2}{8b_2z^2}\right) - I_{\frac{m_0+1}{2}}\left(\frac{k^2\rho^2}{8b_2z^2}\right) \right] \end{array} \right\} d\rho
\end{aligned}
$$

and

$$
\begin{aligned}
P_c &= \int_0^R \int_0^R \int_0^{2\pi} \int_0^{2\pi} F_{A_1}^*(\rho_1) F_{A_1}(\rho_2) W(\rho_1,\rho_2,z) \rho_1\rho_2 d\rho_1 d\rho_2 d\theta_1 d\theta_2 \\
&= \frac{\pi^2 k^4}{8z^4 S^2} \rho_1\rho_2 \exp\left[\frac{ik}{2z}\left(\rho_1^2 - \rho_2^2\right) - \frac{\rho_1^2+\rho_2^2}{\rho_0^2} - \frac{\rho_1^2+\rho_2^2}{M_1^2} \right] \\
&I_{m_0}\left(\frac{2\rho_1\rho_2}{\rho_0^2}\right) \sum_{u=1}^{N} \frac{(-1)^{u-1}}{N} \binom{N}{u} \sum_{u=1}^{N} \frac{(-1)^{u-1}}{N} \binom{N}{u} \\
&\times \left\{ \begin{array}{l} \frac{1}{a_1^{1.5}} \exp\left(-\frac{k^2}{8z^2a_1}\rho_1^2\right) \left[I_{\frac{m_0-1}{2}}\left(\frac{k^2}{8z^2a_1}\rho_1^2\right) - I_{\frac{m_0+1}{2}}\left(\frac{k^2}{8z^2a_1}\rho_1^2\right) \right] - \\ \frac{1}{a_2^{1.5}} \exp\left(-\frac{k^2}{8z^2a_2}\rho_1^2\right) \left[I_{\frac{m_0-1}{2}}\left(\frac{k^2}{8z^2a_2}\rho_1^2\right) - I_{\frac{m_0+1}{2}}\left(\frac{k^2}{8z^2a_2}\rho_1^2\right) \right] \end{array} \right\}, \quad (5) \\
&\times \left\{ \begin{array}{l} \frac{1}{b_1^{1.5}} \exp\left(-\frac{k^2}{8z^2b_1}\rho_2^2\right) \left[I_{\frac{m_0-1}{2}}\left(\frac{k^2}{8z^2b_1}\rho_2^2\right) - I_{\frac{m_0+1}{2}}\left(\frac{k^2}{8z^2b_1}\rho_2^2\right) \right] - \\ \frac{1}{b_2^{1.5}} \exp\left(-\frac{k^2}{8z^2b_2}\rho_2^2\right) \left[I_{\frac{m_0-1}{2}}\left(\frac{k^2}{8z^2b_2}\rho_2^2\right) - I_{\frac{m_0+1}{2}}\left(\frac{k^2}{8z^2b_2}\rho_2^2\right) \right] \end{array} \right\} d\rho_1 d\rho_2
\end{aligned}
$$

with

$$
\begin{aligned}
a_1 &= \frac{iC_0}{\omega_0^2} - \frac{ik}{2z} + \frac{u}{\omega_0^2}, a_2 = \frac{iC_0}{\varepsilon\omega_0^2} - \frac{ik}{2z} + \frac{u}{\omega_0^2} \\
b_1 &= \frac{u}{\omega_0^2} - \frac{iC_0}{\omega_0^2} + \frac{ik}{2z}, b_2 = \frac{u}{\varepsilon\omega_0^2} - \frac{iC_0}{\omega_0^2} + \frac{ik}{2z}
\end{aligned}, \quad (6)
$$

where R is the radius of the receiving aperture. where ρ_0 is the coherence length in marine turbulent atmosphere, and it can be written as

$$
\begin{aligned}
\rho_0^{-2} &= \frac{\pi^2 k^2 z}{6} A(\alpha) \tilde{C}_n^2 \varsigma^{-2} \\
&\left[\begin{array}{l} \kappa_0^{4-\alpha} \frac{\Gamma(\alpha/2-2)}{\Gamma(\alpha/2)} + \Gamma\left(2-\frac{\alpha}{2}\right) \kappa_H^{4-\alpha} - \frac{0.061}{\kappa_H} \kappa_0^{5-\alpha} \frac{\Gamma(5/2)\Gamma((\alpha-5)/2)}{\Gamma(\alpha/2)} \\ -0.061\Gamma\left(\frac{5-\alpha}{2}\right) \kappa_H^{4-\alpha} + 2.836 \frac{\kappa_0^{7-3\alpha/2}}{\kappa_H^{3-\alpha/2}} \frac{\Gamma(7/2-\alpha/4)\Gamma(3\alpha/4-7/2)}{\Gamma(\alpha/2)} \\ +2.836\Gamma\left(\frac{7}{2}-\frac{3\alpha}{4}\right) \kappa_H^{4-\alpha} \end{array} \right]. \quad (7)
\end{aligned}
$$

where , $A(\alpha) = 0.0333$, $\alpha = 11/3$, C_n^2 is the generalized refractive index structure constant, $k_H = 3.41/li, k_0 = 2\pi/L_0$. l_i is the turbulence inner scale. L_0 is the Turbulence outer scale. $\kappa_\varsigma = \sqrt{\varsigma^2\left(\kappa_x^2 + \kappa_y^2\right)\kappa_z^2}$, ς represents the anisotropy factor.

3 Numerical simulation and analysis

Based on the theoretical analysis of fiber coupling efficiency for annular beams transmitted in anisotropic marine atmospheric turbulence, we investigated the effects of focusing mirror, initial size parameters of annular beam, marine atmosphere turbulence intensity, and anisotropy parameter on the coupling efficiency of annular beams. In the simulation, the parameters are set as follows: $R = 0.2m, \omega_0 = 0.02m, d = 5um$, $L_0 = 4\text{m}$, $l_i = 0.001\text{m}$, $\lambda = 1064nm$, $C_n^2 = 10^{-15} m^{-2/3}$, $\varsigma = 3$ $m = m_0 = 0$, $z = 500\text{m}$. If not specified otherwise, the parameters remain unchanged.

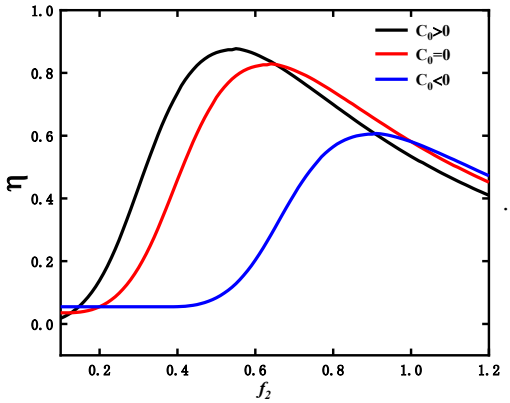

Figure2. *The influence of focusing mirror on the fiber coupling efficiency under different focal lengths of coupling lenses.*

Figure.2 discusses the effects of focusing mirror ($C_0 > 0$), without mirror ($C_0 = 0$), and diverging mirror ($C_0 < 0$) on the coupling efficiency of single-mode fibers. We found that using a focusing mirror can enhance the fiber coupling efficiency, while a diverging mirror suppresses it. Secondly, with the increase in the focal length of the coupling lens, the fiber coupling efficiency shows a trend of first increasing and then decreasing. Figure.3 examines the impact of initial beam size. It can be observed that as the initial beam size increase, the coupling efficiency of annular beams sharply increases, while Gaussian beams exhibit a slower increase. This further indicates the superior turbulence suppression capability of annular beams compared to Gaussian beams, resulting in a significant improvement in fiber coupling efficiency.

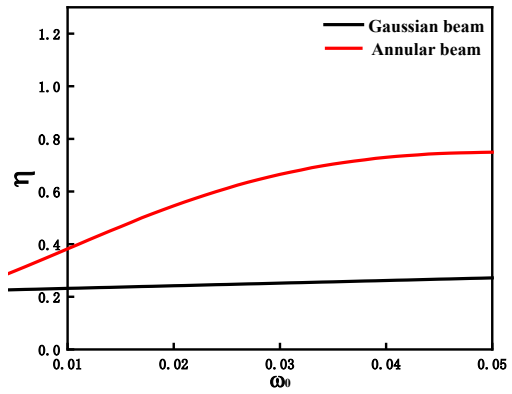

Figure 3. *The difference between Gaussian beam and annular beam is compared*

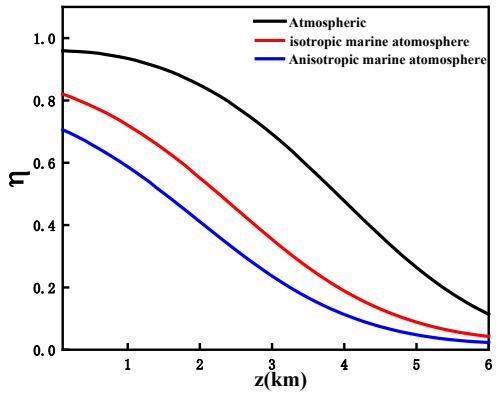

Figure 4. *The fiber coupling efficiency in different sea surface environments*

Figure.4 primarily discusses the influence of atmospheric turbulence, isotropic marine atmospheric turbulence, and anisotropic marine atmospheric turbulence on the coupling efficiency of annular beams at different transmission distances. From Figure 4, it can be observed that as the transmission distance increases, the coupling efficiency of single-mode fibers for annular beams gradually decreases. The impact of isotropic marine atmospheric turbulence on fiber coupling is more serious, and the marine atmosphere environment is more complex compared to the general atmospheric environment.

4 Conclusion

This paper investigates the coupling efficiency of single-mode fibers for annular beams with a focusing mirror system in anisotropic marine turbulence. Our research indicates: The focusing mirror system can enhance the coupling efficiency at specific transmission distances. Control over the focal length of the focusing mirror and the coupling lens can improve the coupling efficiency under different intensities of marine atmospheric turbulence. Annular beams exhibit better turbulence suppression compared to Gaussian beams. Additionally, our research highlights the complexity of the marine atmospheric that requires further investigation. The research findings can serve as a reference for the design of optical communication links for marine atmospheric turbulence fiber sensors.

5 References

1. M. C. Gökçe, Y. Baykal, and Y. Ata, "Coupling efficiency of multimode beam to fiber in atmospheric turbulence," J.Quant.Spectrosc.Radia.Transf **303**(2023).
2. B. Hu, H. Shi, and Y. Zhang, "Fiber-coupling efficiency of Gaussian–Schell model beams through an ocean to fiber optical communication link," Opt.Commun **417**, 14-18 (2018).
3. K. J. Grayshan, F. S. Vetelino, and C. Y. Young, "A marine atmospheric spectrum for laser propagation," Waves in Random and Complex Media **18**, 173-184 (2008).
4. B. Hu, Y. Zhang, and Y. Zhu, "New model of the fiber coupling efficiency of a partially coherent Gaussian beam in an ocean to fiber link," Opt. Express **26**(2018).
5. H. Takenaka, M. Toyoshima, and Y. Takayama, "Experimental verification of fiber-coupling efficiency for satellite-to-ground atmospheric laser downlinks," Opt. Express **20**(2012).
6. F. Hanson and M. Lasher, "Effects of underwater turbulence on laser beam propagation and coupling into single-mode optical fiber," Appl.Opt **49**(2010).
7. M. Toyoshima, "Maximum fiber coupling efficiency and optimum beam size in the presence of random angularjitter for free-space laser systems and their applications," J. Opt. Soc. Am. A **23**(2006).
8. M. Zhou, Y. Zhou, G. Wu, and Y. Cai, "Reducing the cross-talk among different orbital angular momentum modes in turbulent atmosphere by using a focusing mirror," Opt. Express **27**(2019).
9. Z. R. Mei and D. M. Zhao, "Controllable dark-hollow beams and their propagation characteristics," J. Opt. Soc. Am. A **22**(2005).

The 14th International Conference on
Laser-light and Interactions with Particles (LIP2024)
September 18-22nd, 2024, Xi'an, Shaanxi, China

ON-AXIS AVERAGE INTENSITY OF RADIALLY POLARIZED ANUMALOUS VORTEX BEAMS IN MARITIEM TURBULENT ATMOSPHERE

Hassan T. Al-Ahsab[1,2,*], Mingjian Cheng[1] and Lixin Guo[1]

[1] School of Physics, Xidian University, Xi'an, China
[2] Physics Department, Faculty of Applied Science, Thamar University, Thamar, Yemen,
Corresponding author: lxguo@xidian.edu.cn.

Abstract

Based on the Huygens–Fresnel integral formula, an analytical expression for the on-axis intensity of radially polarized anomalous vortex beam (RPAVB) propagating through maritime atmospheric turbulence is derived. The impact of the incident RPAVB and the turbulence parameters on the on-axis intensity has been investigated. Numerical results illustrate that the RPAVB loses its dark hollow form when its on-axis intensity reaches a certain limit at a specific propagation distance which then decreases for longer propagation distance. RPAVB with a short wave length or wide beam width, which results in an increase in the beam order, topological charge or initial beam width, loses its dark hollow form faster. An increase in the strength of maritime atmospheric turbulence with high refractive index structure constant values or a decrease in the size of inner–scales and the non-Kolmogorov parameter causes faster fall in the on-axis intensity and its peak moving toward the source. These findings can be utilized in the design of optical wireless communication links for maritime atmospheric turbulence.

1 Introduction

Vector vortex beams or spirally polarized beams which combine the properties of vortex beams, a doughnut-shaped intensity form with a spiral phase, and vector beams have gained an increasing interest due to their increasing applications in different fields such as manipulation and trapping particles, remote sensing and free space optics communication [1-3] However, random media significantly challenges the use of vector vortex beams in free-space optical communication [1, 3]. Fluctuations in atmospheric refractive index affect the beams' phase and intensity, causing issues like intensity scintillation [4], beam wander [5], beam spreading [6], and OAM mode crosstalk [7]. To overcome this limitation, researchers have created various models of vortex beams designed to enhance their efficiency and usefulness [8, 9]. An example of such a model is the anomalous vortex beams (AVBs) which have unique characteristics compared to traditional vortex beams such as a unique phase structure, self-focusing property, maintain beam size in strongly nonlocal nonlinear media, and transformation into Laguerre-Gaussian beams in free space [10-14].

AVBs have shown great potential in trapping and manipulation particles and optics communication with power retention, high information-carrying capacity and OAM detection probability in certine circumstances [12-14]. Despite their potential, there is a lack of studies on the intensity distribution of vector AVBs in maritime turbulent atmospheres, highlighting an important area for future research. To the best of our knowledge, there are no studies on how source and marine turbulence parameters affect the on-axis intensity variations of vector AVBs in maritime turbulent atmosphere. This study aims to understand how these factors influence on-axis intensity fluctuations. We analyse the on-axis normalized intensity distribution characteristics of RPAVB propagating through maritime turbulent atmosphere.

2 Theoretical model

In cylindrical coordinate system, the vector electric field of a radially polarized anomalous vortex beam at the source plane (i.e., z = 0) can be described as in):

$$\mathbf{E}(\rho_0,\varphi_0,0)=E_0\left(\frac{\rho_0}{w_0}\right)^{2n+|s|}\exp\left(-\frac{\rho_0^2}{w_0^2}\right)\begin{bmatrix}\cos(s\varphi_0+\Phi)\\ \sin(s\varphi_0+\Phi)\end{bmatrix}, \quad (1)$$

where ρ_0 and φ_0 denotes the cylindrical coordinates at the source plane; n and s refer to the beam order and topological charge of the beam, respectively; Φ indicates initial phase angle that determines the polarization of the beam, resulting in azimuthal polarization for $\Phi=\pi/2$ and radial polarization for $\Phi=0$.

Within the framework of the paraxial approximation, the second-order statistical properties of the RPAVB are characterized by the beam coherence-polarization matrix [Gori1998]

$$W(\boldsymbol{\rho}_1,\boldsymbol{\rho}_2,z)=\begin{pmatrix}W_{xx}(\boldsymbol{\rho}_1,\boldsymbol{\rho}_2,z) & W_{xy}(\boldsymbol{\rho}_1,\boldsymbol{\rho}_2,z)\\ W_{yx}(\boldsymbol{\rho}_1,\boldsymbol{\rho}_2,z) & W_{yy}(\boldsymbol{\rho}_1,\boldsymbol{\rho}_2,z)\end{pmatrix}, \quad (2)$$

where

$$W_{\alpha\beta}(\boldsymbol{\rho}_1,\boldsymbol{\rho}_2,z)=\left\langle E_\alpha(\boldsymbol{\rho}_1,\boldsymbol{\rho}_2,z)E_\beta^*(\boldsymbol{\rho}_1,\boldsymbol{\rho}_2,z)\right\rangle(\alpha,\beta=x,y), \quad (3)$$

with $\boldsymbol{\rho}_1,\boldsymbol{\rho}_2=(\rho_1,\varphi_1),(\rho_2,\varphi_2)$ are two arbitrary position vectors at plane z = constant, $E_\alpha(\boldsymbol{\rho}_1,\boldsymbol{\rho}_2,z)E_\beta^*(\boldsymbol{\rho}_1,\boldsymbol{\rho}_2,z)$ indicate the components of electric field along x-axis and y-axis, respectively, $\langle\ \rangle$ refers to an ensemble average over the medium statistics, (*) indicates the complex conjugate operator. At the source plane z = 0 the coherence-polarization matrix of RPAVB can be written as

$$W(\boldsymbol{\rho}_1,\boldsymbol{\rho}_2,z=0)=E_0\left(\frac{\rho_0}{w_0}\right)^{2n+|s|}\exp\left(-\frac{\rho_0^2}{w_0^2}\right)\times\begin{pmatrix}\cos(s\varphi_1)\cos(s\varphi_2) & \cos(s\varphi_1)\sin(s\varphi_2)\\ \sin(s\varphi_1)\cos(s\varphi_2) & \sin(s\varphi_1)\sin(s\varphi_2)\end{pmatrix}, \tag{4}$$

Based on the extended Huygens–Fresnel integral, supposing $\boldsymbol{\rho}_1=\boldsymbol{\rho}_2=\boldsymbol{\rho}$, the coherence-polarization matrix elements at the receiver plane can be given as [16]

$$W_{\alpha\beta}(\boldsymbol{\rho},\boldsymbol{\rho},z)=\left(\frac{k}{2\pi z}\right)\iint W_{\alpha\beta}(\rho_0,\varphi_0,0)\exp\left[-\frac{ik}{2z}(\boldsymbol{\rho}_{01}-\boldsymbol{\rho})^2+\frac{ik}{2z}(\boldsymbol{\rho}_{02}-\boldsymbol{\rho})^2+\frac{(\boldsymbol{\rho}_{01}-\boldsymbol{\rho}_{02})^2}{\rho_0^2(z)}\right]d\boldsymbol{\rho}_1 d\boldsymbol{\rho}_2 \tag{5}$$

where ρ_0 is the coherence length of a spherical wave propagation in maritime atmospheric turbulence that is expressed as [12]

$$\rho_0=\frac{\pi^2}{6}A(\alpha)\tilde{C}_n^2k^2z\left[\kappa_0^{4-\alpha}U\left(2;\frac{6-\alpha}{2};\frac{\kappa_0^2}{\kappa_H^2}\right)-0.061\frac{\kappa_0^{5-\alpha}}{\kappa_H}\times U\left(\frac{5}{2};\frac{7-\alpha}{2};\frac{\kappa_0^2}{\kappa_H^2}\right)+2.836\frac{\kappa_0^{(14-3\alpha)/2}}{\kappa_H^{(6-\alpha)/2}}\Gamma\left(\frac{14-\alpha}{4}\right)\times U\left(\frac{14-\alpha}{4};\frac{18-3\alpha}{4};\frac{\kappa_0^2}{\kappa_H^2}\right)\right], \tag{6}$$

where $A(\alpha)=\Gamma(\alpha-1)\cos(\pi\alpha/2)/(4\pi^2)$, $\Gamma(*)$ refers to the Gamma function, α indicates the parameter of non-Kolmogorov turbulence, $\tilde{C}_n^2$ is the generalized refractive index structure constant in units of $m^{3-\alpha}$, $\kappa_0=2\pi/L_0$ with the outer scale of turbulence, $\kappa_H=c(\alpha)/l_0$ with inner scale of turbulence l_0 and $c(\alpha)$ given by

$$c(\alpha)=\left(\pi A(\alpha)\left[\Gamma\left(\frac{3-\alpha}{2}\right)\left(\frac{3-\alpha}{3}\right)-0.061\Gamma\left(\frac{4-\alpha}{2}\right)\left(\frac{4-\alpha}{3}\right)+2.836\Gamma\left(\frac{12-3\alpha}{4}\right)\left(\frac{4-\alpha}{2}\right)\right]\right)^{1/(\alpha-5)}.$$

By substituting Eq. (4) into Eq. (5) with $\rho=0$ for on-axis intensity, one can obtain

$$I(0,z)=\frac{k^2E_0^2}{z^2w_0^{4n+2|s|}}\frac{\Gamma(n+|s|+1)^2}{4(Q_1Q_2)^{n+|s|+1}\Gamma(|s|+1)}\left(\frac{1}{\rho_0^2}\right)^{|s|}\times{}_2F_1\left[n+|s|+1;n+|s|+1;|s|+1;-\frac{1}{(\rho_0^2)^2Q_1Q_2}\right], \tag{7}$$

where

$$Q_1=\frac{1}{\rho_{0,M}^2(z)}+\frac{1}{w_0^2}+\frac{ik}{2z},Q_2=\frac{1}{\rho_{0,M}^2(z)}+\frac{1}{w_0^2}-\frac{ik}{2z}, \tag{8}$$

and ${}_qF_p[*;*;*]$ refers to the confluent hypergeometric function. In the preceding integration the following formulas have been used [17]

$$\int_0^{2\pi}\cos(s\phi)\exp[\eta\cos(\varphi_1-s\phi)]d\phi=2\pi\cos(s\varphi)J_s(i\eta), \tag{9}$$

$$\int_0^{2\pi}\sin(s\phi)\exp[\eta\cos(\varphi_1-s\phi)]d\phi=2\pi\sin(s\varphi)J_s(i\eta),$$

$$\int_0^{\infty}x^ne^{-\beta x^2}J_\nu(\gamma x)dx=\frac{\Gamma[(\nu+n+1)/2]}{2^{\nu+1}\beta^{(\nu+n+1)/2}\Gamma[(\nu+1)]}\beta^\nu\times{}_1F_1\left[(\nu+n+1)/2;\nu+1;-\frac{(\gamma\gamma^*)}{4\beta}\right], \tag{10}$$

$$\int_0^{\infty}x^{\nu-1}e^{-\eta x}{}_pF_q\left[\beta_1,\beta_2,...,\beta_n;\gamma_1,\gamma_2,...,\gamma_n;\mu x\right]dx=\Gamma(\nu)\beta^{-\nu}{}_{p+1}F_q\left[\beta_1,\beta_2,...,\beta_n,\sigma;\gamma_1,\gamma_2,...,\gamma_n;\frac{\mu}{\eta}\right] \tag{11}$$

3 Numerical results and discusions

In this section, we conduct a numerical investigation into the on-axis intensity distribution of RPAVB through marine atmospheric turbulence. To gain insights into the on-axis intensity evolution during propagation, as described by Eq. 7. Throughout our numerical analysis and simulation, we maintain the following parameters as constants unless otherwise specified: $E_0=1$, $n=3$, $s=2$, $\lambda=632\,nm$, $w_0=0.02m$, $L_0=10m$, $l_0=5\times10^{-3}m$, $\alpha=11/3$ and $\tilde{C}_n^2=5\times10^{-15}m^{(3-\alpha)/2}$. Figure 1 illustrates the on--axis normalized intensity distribution for different initial beam parameters. Figs. 1 (A) and (B) show that as the beam order n and topological charge s increase, the peak value of the on-axis intensity distribution moves away from the source. This phenomenon is caused by the increasing radius of the hollow centre of the beam, resulting in more diffraction and a shift in the self-focusing point away from the source. In addition, Fig. 1 (C) demonstrates the variation of the on--axis normalized intensity distribution along the propagation distance for different beam waist w_0. It is evident that increasing the beam waist w_0 leads to the peak value of the intensity also moving away, accompanied by a widening of the curve. Furthermore, the wavelength λ of the incident RPAVB also has an effect, as shown in Fig. 1 (D). As the wavelength λ increases, the peak shifting of the on-axis intensity is towards the source. This suggests that RPAVB with longer wavelengths loses its dark hollow faster, potentially contributing to the shifting of the focus point towards the source of the beam.

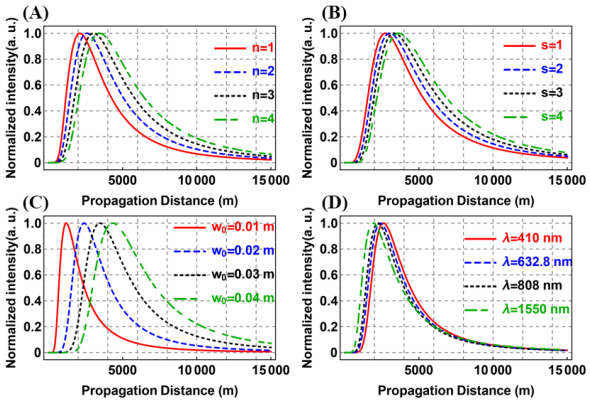

Figure 1 On-axis normalized intensity distribution of MAVB for different beam order n (A), topological charge s (B), beam waist width w_0 (C) and wavelength λ versus the propagation distance.

The normalized on--axis normalized intensity distribution of the RPAVB is shown in Fig. 2 for different

maritime atmospheric turbulence parameters as a function of propagation distance. The figure highlights the significant impact of the refractive index structure constant on the on--axis intensity of the RPVAV. As the turbulence strength increases, the peak of the on-axis intensity moves towards the source and falls to zero faster. This behavior is also observed with a decrease in the non-Kolmogorov parameter, indicating that the marine atmosphere is more affected as α approaches 3.1 [12] and less affected as α approaches 4. Temperature and humidity also play critical roles in the strength of turbulence, with increasing humidity resulting in stronger turbulence. A decrease in the size of inner-scales causes an abundance of them, leading to a faster fall in the on-axis intensity and its peak moving towards the source. On the other hand, the effect of outer-scale on the on-axis intensity is insignificant compared to other parameters of maritime atmospheric turbulence. The figure indicates a small shift of the on-axis beam peak towards the source when the outer-scale increases, confirming that the intensity distribution is affected by more turbulence due to an increase in the outer-scale.

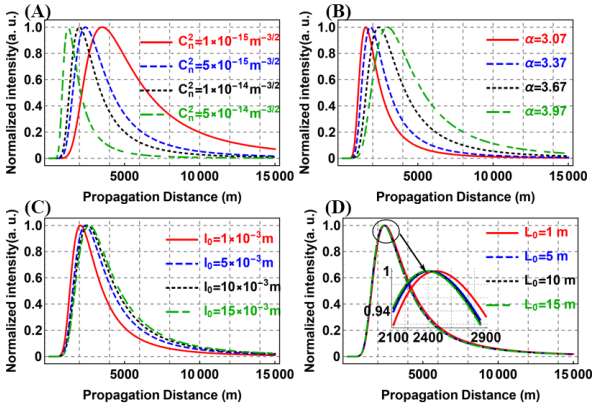

Figure 2 On-axis normalized intensity distribution of MAVB for different refractive index structure constant C_n^2 (A), non-Kolmogrov parameter α (B), inner--scale l_0 (C) and outer-scale of turbulence L_0 versus the propagation distance.

4 Conclusions

In conclusion, on-axis intensity distribution of radially polarized anomalous vortex beam (RPAVB) is investigated based on the Huygens–Fresnel integral formula. Numerical results reveal that the on-axis intensity of RPAVB is arrived to maximum at a faster rate in maritime atmosphere as the beam order, topological charge, or beam waist decreases, or the wavelength increases. These findings confirm that the beam parameters at the source play a critical role in determining the distance at which the beam loses its dark hollow form in turbulent media. Further, increasing the strength of maritime atmospheric turbulence by increasing the refractive index structure constant and decreasing the inner–scale size results in a quicker shift of the peak value of the on–axis intensity towards the source, followed by a faster decline to zero.

5 References

[1] Rosales-Guzmán C., Ndagano B., Forbes A., A review of complex vector light fields and their applications, J. Opt. 20:123001 (2018).

[2] Zhan Q., Cylindrical vector beams: from mathematical concepts to applications, Adv. Opt. Photonics 1:1–57 (2009).

[3] Ndagano B., Nape I., Cox M. A., Rosales-Guzman C. Forbes A, Creation and detection of vector vortex modes for classical and quantum communication, J. Light. Technol. 36(2):292–301 (2017).

[4] Wiedemann J., Nelson C., and Avramov-Zamurovic S., Scintillation of laser beams carrying orbital angular momentum propagating in a near-maritime environment, Opt. Commun. 458:124836 (2020).

[5] Cheng M., Guo L., Li J., Yan X., Sun R., You Y. Effects of asymmetry atmospheric eddies on spreading and wander of Bessel-Gaussian beams in anisotropic turbulence, IEEE Photonics J. 10(4): 1–10 (2018).

[6] Young C. Y., Gilchrest Y. V., Macon B. R., Turbulence induced beam spreading of higher order mode optical waves, Opt. Eng. 41(5):1097–1103 (2002).

[7] Li Y., Zhang Y., OAM mode of the Hankel–Bessel vortex beam in weak to strong turbulent link of marine-atmosphere, Laser Phys. 27:045201 (2017).

[8] Shen Y., Wang X.,.Xie Z, Min C., Fu X., Liu Q., Gong M., Yuan X., Optical vortices 30 years on: OAM manipulation from topological charge to multiple singularities, Light. Sci. & Appl. 8:1–29 (2019).

[9] Kotlyar V. V., Kovalev A. A., Porfirev A. P., *Vortex laser beams* (CRC Press, New-York, 2018).

[10] Yang Y., Dong Y., Zhao C., Cai Y., Generation and propagation of an anomalous vortex beam, Opt. Lett. 38:5418–5421 (2013).

[11] Dai Z., Yang Z., Zhang S., Pang Z., You K.., Propagation dynamics of modified hollow gaussian beams in strongly nonlocal nonlinear media, Laser Phys. 25:025401 (2014).

[12] Al-Ahsab H. T., Cheng M., Guo L., Cao Y. Wang S.., Propagation behavior of orbital angular momentum in vector anomalous vortex beams under maritime atmospheric turbulence, Front. Phys. 11:1238101 (2023).

[13] Dong M., Jiang D., Luo N., Yang Y., Trapping two types of Rayleigh particles using a focused partially coherent anomalous vortex beam, Appl. Phys. B 125:1–8 (2019).

[14] Li F., Lui H., Ou J., Spiral spectrum of anomalous vortex beams propagating in a weakly turbulent atmosphere, J. Mod. Opt. 67:501–506 (2020).

[15] Andrews L. C., Phillips R. L., *Laser beam propagation through random media, Laser Beam Propagation Through Random Media* (SPIE Press, Washington, 2005).

[16] Gradshteyn I. S., Ryzhik I. M., *Table of integrals, series, and products* (Academic press, USA, 2014).

The 14th International Conference on
Laser-light and Interactions with Particles (LIP2024)
September 18-22nd, 2024, Xi'an, Shaanxi, China

LIGHT SCATTERING BY ANISOTROPIC OBJECTS USING PHYSICS-INFORMED NEURAL NETWORK

Yuan Zhang[1], Renxian Li[1,*], Huan Tang[1], Zhuoyuan Shi[1], Bing Wei[1], Shuhong Gong[1]

[1] School of Physics, Xidian University, Xi'an 710071, China

**Corresponding author: rxli@mail.xidian.edu.cn*

Abstract

Prediction of scattered electromagnetic (EM) fields from anisotropic objects provides insight into the interaction between electromagnetic waves with materials with directional properties. To overcome the disadvantage of computationally expensive and time-consuming of traditional computational methods, deep learning technique has been successfully used to rapidly and accurately predict the scattered field. However, in practice, it is very difficult to construct large training datasets for complex targets. By taking physical constraints into consideration, physics informed neural networks (PINNs) can solve partial differential equations (PDEs) with small (or sometimes even no) datasets, and provide physical explanations. In this paper, we use Maxwell's equations as physical constraints to solve the plane wave scattering a two-dimensional anisotropic object using PINNs. In the simulations, the PINNs results for the electromagnetic field at different anisotropy coefficients κ are mainly discussed in terms of objects such as infinitely long cylinders. The results are of great significance in many fields such as advanced material design and biomedical imaging.

Introduction

Electromagnetic waves are scattered, absorbed or propagated in different ways when they encounter the surface of an object. The study of electromagnetic scattering aims to understand the mechanisms by which electromagnetic waves interact with objects and how these mechanisms can be used to solve a variety of practical problems. It is important in the fields of communication, remote sensing and medical imaging [1,2,3,4]. Electromagnetic propagation in anisotropic media differs from simple isotropic materials, and its electromagnetic properties change with direction. The use of analytical methods requires unusually complex mathematical models to describe the solution. The use of common numerical methods, such as the finite element method (FEM) [5], the frequency-domain finite-difference method (FDFD) [6], and the time-domain finite-difference method (FDTD) [7,8], can also present significant challenges in terms of mesh delineation and the setting of boundary conditions. The above traditional electromagnetic solving methods require tedious mathematical derivations and calculations, which can consume a lot of time and resources, and the results are usually unsatisfactory.

Meanwhile, with the rapid development of artificial intelligence (AI) technology, researchers have applied neural networks to computational electromagnetics in an attempt to predict scattered fields instead of traditional electromagnetic solvers. Deep Learning (DL) methods such as convolutional neural networks (CNNs), recurrent neural networks (RNNs) and generative adversarial networks (GANs) have made amazing advances in the field of computational physics for modelling physical learning agents [9]. Deep learning techniques can be used to identify hidden rules of control system behaviour by creating function mappings between input and output data [10]. Models can be extended from limited training data to unknown scenarios. Trained on a different set of boundary conditions, the model can then accurately predict the electromagnetic field under new boundary conditions outside of the training dataset. This generalisation capability greatly improves the accuracy of the simulation. Traditional deep learning methods rely on a large dataset for training. However, it is difficult to obtain large training datasets for complex scatterers in practical applications, and some a priori knowledge is often implicit in the training data (e.g., the electric field data satisfies Maxwell's equations), which is ignored by purely data-driven deep learning methods.

As a result, PINNs have emerged. Lagaris [11] et al pioneered the use of physics informed neural networks (PINNs) for solving Maxwell's equations for scattering problems. In 2019, Raissi [12] classified the model equations as physical constrains into regularisation terms and encoded them into a neural network by adding the loss of the control equations, the loss of the boundary conditions and the loss of the initial conditions to the loss function. Using PINNs we can obtain a more generalised neural network model with small datasets that learns both the distributional and physical laws underlying the data samples. This greatly alleviates the data dependency of traditional neural networks. In summary, PINNs are important in the field of computational electromagnetism.

In this paper, we encode the set of Maxwell's equations satisfied by anisotropic scatterers as physical constraints into a neural network, train the constructed fully-connected network with an infinitely long cylinder as an example, and study the scattered electric field of anisotropic targets. Meanwhile, we compare the prediction results with those obtained by the FDFD results to verify the accuracy and feasibility of our proposed method.

Method

In this paper, we propose a deep learning method for solving Maxwell's equations. According to the electromagnetic uniqueness theorem [13], we can transform the electromagnetic orthogonal problem into an optimisation process and use the powerful optimisation capability of deep learning to solve the frequency domain electromagnetic field.

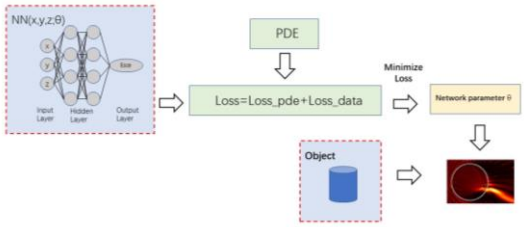

Figure 1 Schematic diagram of the PINNs network

Figure 1 shows a diagram of the forward PINNs. We first define a network NN with θ as the network parameter. When using the frequency-domain approach, the inputs to the network are spatial coordinates without time information and the outputs are the real and imaginary parts of the scattered magnetic field. The loss function in this paper consists of two parts:

$$\text{Loss} = \text{Loss}_{\text{pde}} + \text{Loss}_{\text{data}} \tag{1}$$

Where

$$\begin{cases} \text{Loss}_{data} = \dfrac{1}{N_d}\sum_{i=1}^{N_d}\left(\left|E_i^P\right| - \left|E_i^T\right|\right) \\ \text{Loss}_{pde} = \dfrac{1}{N_s}\sum_{i=1}^{N_s}\left(\left|f_1^{\,2}\right| + \left|f_2^{\,2}\right| + \left|f_3^{\,2}\right|\right) \end{cases} \tag{2}$$

where Loss_pde and Loss_data correspond to PDE constraints and data constraints, respectively. E_i^P and E_i^T denote the predicted and true values.

Next we derive the expressions for f_1, f_2, and f_3 in Eq (2). A scatterer in free space is known to satisfy Maxwell's equations in the frequency-domain:

$$\nabla\times\bar{E} = -j\omega\bar{B}, \nabla\times\bar{H} = j\omega\bar{D} \tag{3}$$

Where ω is the angular frequency. The formulation developed in this paper is based on the pure scattered field formulation in which the total field is the sum of the known incident and the unknown scattered fields, and the incident field satisfies:

$$\nabla\times\bar{E}_{inc} = -j\omega\mu_0\bar{H}_{inc}, \nabla\times\bar{H}_{inc} = j\omega\varepsilon_0\bar{E}_{inc} \tag{4}$$

Then

$$\begin{cases} \nabla\times\bar{E}_{sca} + j\omega\mu\bar{H}_{sca} - \dfrac{\omega\kappa_h}{c}\bar{E}_{sca} = \left(j\omega\mu_0 - \mu\right)\bar{H}_{inc} + \dfrac{\omega\kappa_h}{c}\bar{E}_{inc} \\ \nabla\times\bar{H}_{sca} - j\omega\varepsilon\bar{E}_{sca} - \dfrac{\omega\kappa_e}{c}\bar{H}_{sca} = \left(j\omega\varepsilon - \varepsilon_0\right)\bar{E}_{inc} + \dfrac{\omega\kappa_e}{c}\bar{H}_{inc} \end{cases} \tag{5}$$

In the above equation, ε is the dielectric constant, μ is the magnetic permeability, and κ_h and κ_e are the anisotropy coefficients of the electric and magnetic fields, respectively. The vector Eq (5) is expanded into scalar equations in a Cartesian coordinate system (in this paper we use TM waves as an example). In the meantime, to prevent waves from reflecting off the boundary and re-entering the simulation domain, it is assumed that the object is surrounded by perfectly matched layers (PML), in this paper we use stretched coordinate PML (SC-PML). Magnetic field is normalized using: $\tilde{H} = -j\eta_0\bar{H}$. Ultimately, the functions f_1, f_2, and f_3 in Eq (2) satisfied by the computational domain are:

$$\begin{cases} f_1 = \dfrac{1}{s_y}\dfrac{\partial E_{sca,z}}{\partial y'} - \dfrac{1}{s_z}\dfrac{\partial E_{sca,y}}{\partial z'} - -\kappa_{hx}E_{sca,x} - \mu_{r,x}\tilde{H}_{sca,x} - \left(\mu_{r,x}-1\right)\tilde{H}_{inc,x} - \kappa_{hx}E_{inc,x} \\ f_2 = \dfrac{1}{s_z}\dfrac{\partial E_{sca,x}}{\partial z} - \dfrac{1}{s_x}\dfrac{\partial E_{sca,z}}{\partial x} - \kappa_{hy}E_{sca,y} - \mu_{r,y}\tilde{H}_{sca,y} - \left(\mu_{r,y}-1\right)\tilde{H}_{inc,y} - \kappa_{hy}E_{inc,y} \\ f_3 = \dfrac{1}{s_x}\dfrac{\partial \tilde{H}_{sca,y}}{\partial x} - \dfrac{1}{s_y}\dfrac{\partial \tilde{H}_{sca,x}}{\partial y} - \kappa_{ez}\tilde{H}_{sca,z} - \varepsilon_{r,z}E_{sca,z} - \left(\varepsilon_{r,z}-1\right)E_{inc,z} - \kappa_{ez}\tilde{H}_{inc,z} \end{cases} \tag{6}$$

with

$$\begin{cases} \kappa_{hx} = \kappa_{hy} = \kappa_{ez} = 0, PMLregion \\ \kappa_{hx} = \kappa_{hy} = \kappa_{ez} = \kappa, Non-PMLregion \end{cases} \tag{7}$$

Finally, the network NN is trained to find the best network parameters by minimizing the total loss defined in Eq. (2) through gradient optimizers such as Adam and L-BFGS .

Conclusion

In this paper, we use PINNs to solve the scattering of plane waves by two-dimensional anisotropic objects. The scattered electric fields are successfully predicted in the case of data-free. The effects of anisotropy coefficients κ on the scattered field and the total field are discussed. This research has promising applications in many fields such as advanced material design and biomedical imaging.

Acknowledgement

The authors acknowledge the support from the National Natural Science Foundation of China [61901324 ,62001345].

References

[1] M. S. Zhdanov, Geophysical inverse theory and regularization problems, vol. 36, Elsevier, 2002.

[2] A. Abubakar, P. M. Van den Berg, and J. J. Mallorqui, "Imaging of biomedical data using a multiplicative regularized contrast source inversion method," IEEE Transactions on Microwave Theory and Techniques, vol. 50, no. 7, pp. 1761–1771, 2002.

[3] X. Wang, T. Qin, R. S. Witte, and H. Xin, "Computational Feasibility Study of Contrast Enhanced Thermoacoustic Imaging for Breast Cancer Detection Using Realistic Numerical Breast Phantoms," IEEE Transactions on Microwave Theory and Techniques, vol. 63, no. 5, pp. 1489–1501, 2015.

[4] C. A. Balanis, Antenna theory: analysis and design, John wiley & sons, 2016.

[5] J.-M. Jin, The finite element method in electromagnetics, John Wiley & Sons, 2015.

[6] R. C. Rumpf, "Simple implementation of arbitrarily shaped total-field/scattered-field regions in finite-difference frequency-domain," Progress In Electromagnetics Research B, vol. 36, pp. 221–248, 2012.

[7] A. Taflove, S. C. Hagness, and M. Piket-May, "Computational electromagnetics: the finite-difference time-domain method," The Electrical Engineering Handbook, vol. 3, pp. 629–670, 2005.

[8] K. Yee, "Numerical solution of initial boundary value problems involving Maxwell's equations in isotropic media," IEEE Transactions on antennas and propagation, vol. 14, no. 3, pp. 302–307, 1966.

[9] A. Massa, D. Marcantonio, X. Chen, M. Li, and M. Salucci, "DNNs as applied to electromagnetics, antennas, and propagation—A review," IEEE Antennas and Wireless Propagation Letters, vol. 18, no. 11, pp. 2225–2229, 2019.

[10] Y. Li, Y. Wang, S. Qi, Q. Ren, L. Kang, S. D. Campbell, P. L. Werner, and D. H. Werner, "Predicting Scattering From Complex NanoStructures via Deep Learning," IEEE Access, vol. 8, pp. 139983–139993, 2020.

[11] I. E. Lagaris, A. Likas, and D. I. Fotiadis, "Artificial neural networks for solving ordinary and partial differential equations," IEEE transactions on neural networks, vol. 9, no. 5, pp. 987– 1000, 1998.

[12] M. Raissi, P. Perdikaris, and G. E. Karniadakis, "Physics-informed neural networks: A deep learning framework for solving forward and inverse problems involving nonlinear partial differential equations," Journal of Computational physics, vol. 378, pp. 686–707, 2019.

[13] L. D. Landau, The classical theory of fields, vol. 2, Elsevier, 2013.

The 14th International Conference on
Laser-light and Interactions with Particles (LIP2024)
September 18-22nd, 2024, Xi'an, Shaanxi, China

A LINE-BY-LINE CALCULATION MODEL OF THE RADIATION CHARACTERISTICS OF HIGH-TEMPERATURE GASES

ZHAO Yansi[1], HAN Yiping[1,*]

[1] Laboratory for Electromagnetic Scattering and Optoelectronic Characteristics of Targets, XIDIAN University, Xi'an, 710071, China

*Corresponding author: yphan@xidian.edu.cn

Abstract This paper presents a high-temperature gas temperature correction model and a high-resolution line-by-line calculation program for accurate determination of gas absorption coefficients and other spectral parameters that vary with temperature. The model uses the HITRAN molecular line database to correct molecular partition functions and line intensities based on temperature, considering Doppler and pressure broadening mechanisms and utilizing the Voigt line shape function. The program calculates absorption coefficients and transmittance for two gases at different high temperatures. Experimental results confirm increased absorption coefficients and transmittance with higher temperatures. The proposed temperature correction model agrees excellently with experimental data, showing its accuracy for studying high-temperature gas radiation transfer properties.

1 Introduction

In the process of hypervelocity collision of space vehicles, the extreme critical conditions of high temperature and high pressure will lead to the vaporization of hypervelocity impact products and the chemical reaction of energetic materials (such as the detonation of warhead charges and fuel leakage and combustion) after reaching a certain critical point. The gasification products of hypervelocity impact are the main radiation sources of the hypervelocity impact process, and most of the energy of gas radiation is concentrated in the near-infrared spectrum, and its main radiation mechanisms are vibration and rotational transition[1], and the thermal radiation characteristics of different gases are very different, which is related to their internal molecular structure. It is one of the key technologies to study the radiation mechanism and calculation of ultra-high-velocity impact gasification products. With the deepening of research and the increasing demand for evaluation models, the importance and application value of radiation from impact gasification products have been continuously recognized. However, due to the strong selectivity of the thermal radiation properties of gases[2], it is challenging to study the thermal radiation properties of gases and their radiation analysis.

2 Quantum Theory of Gas Radiation

The quantum theory of gas radiation is the basic theory that studies the radiation produced by gases at high temperatures. According to quantum theory, the electronic state inside a gas at high temperatures can be thermally excited, causing the gas to radiate energy to the outside world in the form of absorbing and emitting photons, a process called gas radiation. At high temperatures, the radiation process of the gas mainly involves intramolecular vibrations and rotational transitions.

The radiation of hypervelocity impact gaseous clouds mainly comes from the thermal excitation caused by the thermal motion of the components and a series of related processes. Therefore, the study of the quantum theory of gas radiation is essential to understand the mechanism of gas radiation behavior at high temperatures. In this paper, a temperature correction model for high-temperature gases is established by studying this theory, so as to carry out the study of the radiation characteristics of high-temperature gases.

3 Correction Model of High Temperature Gas Temperature

3.1 Principle of Line-by-Line Calculation

The line-by-line calculation method is to utilize the quantum mechanical principles and formulas of atomic molecules to establish the relationship between spectral parameters and parameters of gas radiation properties. The line-by-line method, supported by a library of molecular spectral line parameters, can be used to obtain the spectral absorption coefficient of a gas that varies dramatically with the wavenumber η, where the spectral absorption coefficient is equal to the sum of the line absorption coefficients $\kappa_{\eta i}$ of the overlapping spectral lines.

$$\kappa_\eta = \sum_i \kappa_{\eta i} = \sum_i S_i F(\eta - \eta_i) \tag{1}$$

Where $\kappa_{\eta i}$ is the absorption coefficient of the i spectral line at wavenumber η, S_i is the spectral intensity of the i line, $F(\eta - \eta_i)$ is the line shape function of the i line, η_i is the wavenumber η at the center of the i line.

3.2 Temperature Correction

The expression for the intensity of the spectral lines at standard temperature[3] is:

$$S_{ij} = I_a \frac{A_{ij}}{8\pi c \nu_{ij}^2} \frac{g' \exp\left(-c_2 E''/T\right)\left(1-\exp\left(-c_2\nu_{ij}/T\right)\right)}{Q(T)} \quad (2)$$

Where i and j denote the low-energy and high-energy states, I_a is the isotopic abundance weighting, A_{ij} is the Einstein coefficient of spontaneous radiation, g' is the statistical weighting of the high-energy state, $E'' = E_i$ is the low-energy state energy, c_2 is the second radiative constant, υ_{ij} is the number of spectral line-leap waves, T denotes the temperature, and $Q(T)$ is the total internal partition function, with the following expressions:

$$Q(T) = \sum_k g_k \exp\left(-\frac{c_2 E_k}{T}\right) \quad (3)$$

Where g_k denotes the k isotopic weighting factor of the molecule and E_k denotes the corresponding energy level.

In order to facilitate the program implementation, the reference temperature $T_{\text{ref}} = 296K$ is selected, and the spectral line intensity $S_{ij}(T_{\text{ref}})$ at the standard temperature is used to obtain the spectral line intensity of a single molecule at any temperature T is obtained as:

$$S_{ij}(T) = S_{ij}(T_{\text{ref}}) \frac{Q(T_{\text{ref}})}{Q(T)} \frac{\exp\left(-c_2 E''/T\right)}{\exp\left(-c_2 E''/T_{\text{ref}}\right)} \frac{\left[1-\exp\left(-c_2\nu_{ij}/T\right)\right]}{\left[1-\exp\left(-c_2\nu_{ij}/T_{\text{ref}}\right)\right]} \quad (4)$$

The line-by-line method also requires the selection of a suitable spectral line. The shape of the spectral line is determined by the spectral line broadening mechanism, which mainly includes natural, collision and Doppler broadening. In this paper, the effects of pressure and Doppler broadening are considered, and the Voigt line function, which is a convolution form of the Gaussian (Doppler broadening) spectral line function and the Lorentzian (pressure broadening) spectral line function, is used for high temperature cases [4].

The spectral line widths are also very temperature dependent. The half-width of a spectral line represents half the distance between two points halfway between the peaks on the spectral line profile, and the half-height width of the Doppler broadening is given by the following equation:

$$\alpha_D(T) = \frac{\nu_{ij}}{c}\sqrt{\frac{2N_A kT\ln 2}{M}} \quad (5)$$

Where υ_{ij} is the spectral line jump center wave number, c is the speed of light, k is Boltzmann's constant, M is the molecular molar mass, and N_A is Avogadro's constant.

The Lorentz spectral line function is given by the following equation:

$$f_L\left(\nu;\nu_{ij},T,p\right) = \frac{1}{\pi}\frac{\gamma(p,T)}{\gamma(p,T)^2 + \left[\nu - \left(\nu_{ij} + \delta\left(p_{\text{ref}}\right)p\right)\right]^2} \quad (6)$$

The Lorentzian half-width of a gas with temperature T and pressure P is given by the following equation:

$$\gamma(p,T) = \left(\frac{T_{\text{ref}}}{T}\right)^{n_{\text{air}}}\left(\gamma_{\text{air}}\left(p_{\text{ref}},T_{\text{ref}}\right)\left(p-p_{\text{self}}\right) + \gamma_{\text{self}}\left(p_{\text{ref}},T_{\text{ref}}\right)p_{\text{self}}\right) \quad (7)$$

Where n_{air} is the temperature dependence coefficient of the air-broadened half-width in the standard state, γ_{air} is the air-broadened half-width in the standard state, and γ_{self} is the self-broadened half-width in the standard state, which were obtained from the molecular database.

Note that the spectral line positions are subject to pressure offset correction, as shown in Figure 1. The dashed lines refer to the conversion and negative pressure offset at zero pressure.

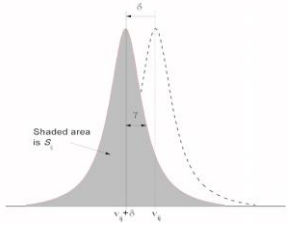

Figure 1 *Schematic of fundamental spectroscopic parameters of a line transition*

The shift in spectral line position due to the pressure shift in the number of jump wavenumber can be expressed as:

$$\nu_{ij}^* = \nu_{ij} + \delta\left(p_{\text{ref}}\right)p \quad (8)$$

4 Calculation results and validation

Based on the temperature correction model of high temperature gas established above, the high resolution line-by-line calculation method was used to develop the line-by-line calculation program for high temperature gas on the basis of HITRAN molecular spectral line database. Among them, the wavenumber sampling interval is 0.01, the equal wavenumber truncation method[15] is used, and the number of truncated waves is twenty, which means that only the contribution of the spectral lines located in the twenty range of the sampling point to the sampling point is considered. The spectral line shape function is selected according to section 3.2, and is obtained by convolving the Gaussian and Lorentzian spectral line functions. The absorption coefficients and transmittances of the gases at high temperatures are calculated as follows.

4.1 Absorption Coefficient

The absorption coefficients of CO_2 at concentration $X_{CO_2} = 0.1$, temperature $T = 296K$, pressure $P = 1atm$, and wavenumber range 2300-2305 cm^{-1} were calculated by this temperature-corrected model. As shown in Figure 2, the absorption coefficients calculated by the model in this paper are slightly lower than the numerical results in the literature at the peak value by comparing with the literature[5]. However, the overall basic match verifies the accuracy of the computational model in this paper.

The absorption coefficients of CO_2 before and after temperature correction are calculated in Figure 3 for a concentration $X_{CO_2} = 0.1$, temperature $T = 296K$, pressure $P = 1atm$, and wavenumber range of 2300-2305 cm^{-1}. It can

be seen that the difference in correction at 296K is very small and almost matches.

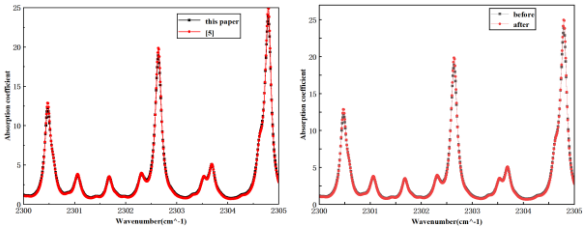

Figure 2 *Comparison of absorption coefficients at low temperature.* ***Figure 3*** *Comparison chart of temperature correction at low temperature*

The relationship curve of absorption coefficient with wave number change for CO_2 at $T=5000K$ and wavenumber range 660-680 cm^{-1} is calculated in Figure 4, which proves the accuracy of the temperature-corrected model of high-temperature gas in this paper. In Figure 5, the relationship curve of absorption coefficient with wavenumber change before and after temperature correction for CO_2 at $T=3500K$, wavenumber range 2300-2305 cm^{-1} is calculated. It can be seen that the temperature-corrected absorption coefficient is more in line with the actual situation of high temperature.

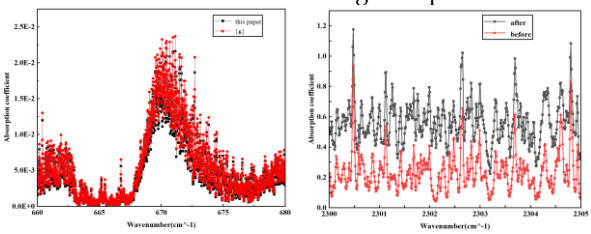

Figure 4 *Comparison of absorption coefficients at high temperature.* ***Figure 5*** *Comparison chart of temperature correction at high temperature*

4.2 Transmittance

This subsection calculates another high temperature gas radiation characterization parameter, transmittance, which is based on the high temperature gas absorption coefficients calculated in section 4.1. The formulae are given below:

$$\tau_a(\nu)=\exp\left(-\int_0^L K_\nu dx\right) \tag{9}$$

Where K_ν is the gas absorption coefficient and L is the optical path length. The typical gases CO_2 and H_2O , which appear most in engineering applications, are shown in Figures 6, 7 and 8 as examples.

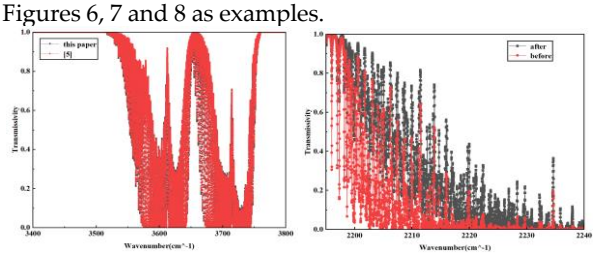

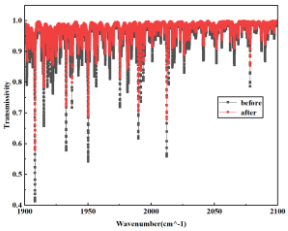

Figure 6 *Comparison of transmittance at low temperature.*
Figure 7 *Comparison of temperature correction at low temperature.* ***Figure 8*** *Comparison of temperature correction at high temperature*

In Figure 6, 7,and 8, the transmittance curves of CO_2 at $T=300K$, $1000K$, and $3500K$, with a concentration of $X_{CO_2}=0.5$ and an optical path length of 10 cm , as well as the transmittance with wave number for different wave number ranges are calculated. From Figure 8 and 9, it can be seen that the transmittance after temperature correction is higher than that before temperature correction, and the maximum difference is about 0.2, which is more in line with the actual situation of high temperature after temperature correction.

5 Conclusion

In this paper, a temperature-corrected model for high-temperature gases is developed. Then the high-resolution absorption coefficients and transmittance spectra of CO_2 and H_2O gas molecules at different high temperatures under certain pressures, concentrations and path lengths were calculated by using the high-resolution line-by-line method and a calculation program was developed.

This paper focuses the research on the temperature correction of gas radiation characteristics, compared to other existing research results at this stage. The effect of high temperature on gas radiation characteristics is explored. The proposed high temperature gas correction model is more accurate.

6 References

[1] St WU Yonghong, XIA Dehong. The study of the mechanism of thermal radiation of gases and the calculation of thermal radiation characteristics[J]. Thermal Science and Technology, 2003, 2(4): 342-346.
[2] YIN Xuemei, WANG Chen, Wang Lei, et al. Comparison of accuracy of broadband k distribution model and other gas radiation characteristic calculation models[J]. Thermal and Power Engineering, 2020, 35(6): 164-169.
[3] GORDON I E, ROTHMAN L S, HARGREAVES R J, et al. The HITRAN2020 molecular spectroscopic database[J]. Journal of Quantitative Spectroscopy and Radiative Transfer, 2022, 277(3): 107-949.
[4] TENNYSON D, JONATHAN R, NERNATH T E, et al. Recommended isolated-line profile for representing high-resolution spectroscopic transitions (IUPAC Technical Report), Pure and Applied Chemistry, 2014, 86(4): 1931-1943.
[5] MEI Fei, JIANG Yong, CHEN Shiguo, et al. A line-by-line computational model of gas absorption and its experimental verification[J]. Acta Optica Sinica, 2012, 32(03): 314-321.
[6] TASHKUN S, PEREVALOV V I. CDSD-4000: High-resolution, high-temperature carbon dioxide spectroscopic databank. Journal of Quantitative Spectroscopy and Radiative Transfer, 2011, 112(9): 1403-1410.

Xidian University

Directly under the Ministry of Education, Xidian University (XDU) is a national key university featuring electronic and information science. XDU dedicates primarily to the electronics and information research and education, with an integration of a wide range of academic subjects covering engineering, science, humanities and social sciences.

It is one of the universities funded by Project 211 and Project 985 Innovation Platform for Superiority Subject, one of the first 35 universities having the model School of Software and one of the first 9 universities having the model School of Microelectronics. It is an essential base of IT talents fostering and high level scientific research innovation in China.

XDU has over 37,000 students including over 12,000 graduates. The university consists of 28 colleges. XDU is one of the pioneer universities which establish the majors of information theory, information systems engineering, radar, microwave antenna, electronic machinery. In the fields of electronics and information, XDU possesses distinctive advantages and features in cultivation and scientific research. There are 15 doctorate disciplines, 27 master disciplines, 15 centers for post-doctoral studies and 66 undergraduate programs. In the Fourth National Assessment of First-level Disciplines, electronics ranks first, information and telecommunications engineering ranks third and computer science and technology ranks seventh in China.

XDU has established cooperative relationships with 188 universities and institutions in more than 42 countries and regions. 67 joint laboratories have been founded with multinational corporations, including Microsoft, IBM, Intel, SAP, TI, ADI, etc.

Since its establishment in 1931, XDU has cultivated more than 340,000 graduates in the fields of electronics and engineering. XDU has been making great efforts to upgrade itself into a world first-class university featured in electronics and information science. Today, Xidian's mission is to attract and foster global talents making technology serve people better. Our vision is to lead China's western region to connect with the rest of the world. Our core values are open, embrace, cooperate and share.

Xi’an City

Xi’an, the eternal city, records the great changes of the Chinese nation just like a living history book. Called Chang’an in ancient times, Xi’an is one of the birthplaces of the ancient civilization in the Yellow River Basin area of the country. During Xi’an’s 3,100 year development, 13 dynasties such as *Zhou*, *Qin*, *Han* and *Tang* placed their capitals here. So far, Xi’an enjoys equal fame with Athens, Cairo, and Rome as one of the four major ancient civilization capitals.

Xi’an is the capital of Shaanxi province, located in the southern part of the *Guanzhong* Plain. With the *Qinling* Mountains to the north and the *Weihe* River to the south, it is in a favorable geographical location surrounded by water and hills. It has a semi-moist monsoon climate and there is a clear distinction between the four seasons. Except the colder winter, any season is relatively suitable for traveling.

The cultural and historical significance of the area, as well as the abundant relics and sites, help Xi’an enjoy the laudatory title of “Natural History Museum”. The Museum of *Terra Cotta Warriors and Horses* is praised as “the eighth major miracle of the world”, Mausoleum of Emperor *Qin Shi Huang* is listed on the World Heritage List, and the City Wall of the Ming Dynasty is the largest and most intact Ming Dynasty castle in the world. In the city, there is the 3000 year old *Banpo* Village Remains from the Neolithic Age, and the Forest of Stone Steles that holds 3,000 stone steles of different periods from the *Han* Dynasty to the *Qing* Dynasty. Around Xi’an, the *Famen* Temple enjoys the reputation of being the “forefather of pagodas and temples in Central Shaanxi”, because it holds the finger bones of *Sakyamuni*—the founder of Buddhism. The natural landscape around Xi’an is also marvelous. Mt. *Huashan*, as one of the five best-known mountains in China, is famous for its breath-taking cliffs and its unique characteristics.

Xi’an is the most important city in northwest China. Praised as “the capital of table delicacies”, Xi’an has been rich in the delicious Shaanxi snack, delicate Guangdong Cuisine, various kinds of fashionable foreign delicacies, and popular Sichuan Cuisine such as the hot pot. Among all the delicacies, the most famous and popular one is the Muslim Snack Street. There are a lot of shopping outlets for locals and tourists alike. The night life in Xi’an has a unique glamour. Traditional ways include enjoying the night scenery around the Bell Tower, taking part in a Tang Dynasty Dinner Show, strolling on the ancient Big Wild Goose Pagoda Square and watching the music fountain performance. More modern and fashionable ways include singing in the KTV, hanging out in a bar, or dancing in a Disco. All in all, any experience in this ancient city will bring you fun and possibly a little surprise!

Xi’an Attractions

Terra Cotta Warriors and Horses Museum

The well-known Terra-cotta Museum is located east of Emperor Qin’s Mausoleum, which covers a total area of 20 hectares. The museum is decorated with verdant trees, blooming flowers and carpets of green grass. The scenery in the museum looks quite elegant and delightful. Three main buildings of the museum, which were named Pit 1, Pit 2, Pit 3, were constructed on their original sites in different periods of time. Emperor Qin’s Terra-cotta Museum is not only a treasure house where the tourists can learn history, culture and human civilization, but also a main scenic spot of Xi’an city. It can receive about 1.5 million tourists annually. Approximately 40 million visitors from home and abroad have visited the Museum within the last 20 years. Today “the eighth Wonder of the world” has almost become synonym of the Terra-cotta Warriors and Horses in 1987, the Emperor Qin’s Mausoleum was put on the list of the UNESCO as a world-class cultural heritage site. Now the Museum is well-known widely as a huge modern on-site museum and it is going to be one of the best in the world.

City Wall

When Zhu Yuanzhang, the first Emperor of the Ming Dynasty (1368-1644), captured Huizhou, a hermit named Zhu Sheng admonished him that he should 'built high walls, store abundant food supplies and take time to be an Emperor,' so that he could fortify the city and unify the other states. After the establishment of the Ming dynasty, Zhu Yuanzhang followed his advice and began to enlarge the wall built initially during the old Tang dynasty (618 -907), creating the modern Xi'an City Wall. It's the most complete city wall that has survived in China, as well being one of the largest ancient military defensive systems in the world.

After the extension, the wall now stands 12 meters (40 feet) tall, 12-14 meters (40-46 feet) wide at the top and 15-18 meters (50-60 feet) thick at the bottom. It covers 13.7 kilometers (8.5 miles) in length with a deep moat surrounding it. Every 120 meters, there is a rampart which extends out from the main wall. All together, there are 98 ramparts on the wall, which were built to defend against the enemy climbing up the wall. Each rampart has a sentry building, in which the soldiers could protect the entire wall without exposing themselves to the enemy. Besides, the distance between every two ramparts is just within the range of an arrow shot from either side, so that they could shoot the enemy, who wanted to attack the city, from the side. On the outer side of the city wall, there are 5948 crenellations, namely battlements. The soldiers can outlook and shoot at the enemy. On the inner side, parapets were built to protect the soldiers from falling off.

Since the ancient weapons did not have the power to break through a wall and the only way for an enemy to enter the city was by attacking the gate of the city wall. This is why complicated gate structures were built within the wall. In Xian, the city wall includes four gates and they are respectively named as Changle (meaning eternal joy) in the east, Anding (harmony peace) in the west, Yongning (eternal peace) in the south and Anyuan (forever harmony) in the north. The south gate, Yongning, is the most

beautifully decorated one. It is very near to the Bell Tower, center of the city. Important greeting ceremonies organized by the Provincial Government are usually held in the south gate square.

Each city gate has three gate towers: Zhenglou, Jianlou and Zhalou. The most outside is Zhalou, which stands away from the City Wall and is opposite to Zhenglou. It was used to raise and lower the suspension bridge. Jianlou with small windows in the front and flanks was used as a defensive outpost. Zhenglou, in the inner, is the main entrance to the city. The wall connects Jianlou and Zhenglou Towers. The area between them within the wall was called “Wong Cheng”, in which the soldiers stationed. From Wong Cheng, there are sloped horse passages leading to the top of the city wall.

Initially, the wall was built with layers of dirt, with the base layer including also lime and glutinous rice extract. Throughout the time Xi’an City Wall has been restored three times. In 1568, Zhang Zhi (the government officer of that period) was in charge to rebuild the wall with bricks. In 1781, another officer, Bi Yuan, refitted the city wall and the gate towers. More recently (since 1983) the Shaanxi Provincial Government restored the city wall again. A circular park has been built along the high wall and the deep moat. The thriving trees and flowers decorate the classical Chinese architecture of the wall, adding additional beauty to Xi’an City.

Big Wild Goose Pagoda

As the symbol of the old-line Xian, Big Wild Goose Pagoda is a well-preserved ancient building and a holy place for Buddhists. It is located in the southern suburb of Xian City, about 4 kilometers (2.49 miles) from the downtown of the city. Standing in the Da Ci'en Temple complex, it attracts numerous visitors for its fame in the Buddhist religion, its simple but appealing style of construction, and its new square in front of the temple. It is rated as a National Key Cultural Relic Preserve as well as an AAAA Tourist Attraction.

This attraction can be divided into three parts: the Big Wild Goose Pagoda, the Da Ci'en Temple, and the North Square of Big Wild Goose Pagoda.

Big Wild Goose Pagoda Originally built in 652 during the reign of Emperor Gaozong of the Tang Dynasty (618-907), it functioned to collect Buddhist materials that were taken from India by the hierarch Xuanzang.

Xuanzang started off from Chang'an (the ancient Xian), along the Silk Road and through deserts, finally arriving in India, the cradle of Buddhism. Enduring 17 years and traversing 100 countries, he obtained Buddha figures, 657 kinds of sutras, and

several Buddha relics. Having gotten the permission of Emperor Gaozong (628-683), Xuanzang, as the first abbot of Da Ci'en Temple, supervised the building of a pagoda inside it. With the support of royalty, he asked 50 hierarchs into the temple to translate Sanskrit in sutras into Chinese, totaling 1,335 volumes, which heralded a new era in the history of translation. Based on the journey to India, he also wrote a book entitled 'Pilgrimage to the West' in the Tang Dynasty, to which scholars attached great importance.

First built to a height of 60 meters (197 feet) with five stories, it is now 64.5 meters (211.6 feet) high with an additional two stories. It was said that after that addition came the saying-'Saving a life exceeds building a seven-storied pagoda'. Externally it looks like a square cone, simple but grand and it is a masterpiece of Buddhist construction. Built of brick, its structure is very firm. Inside the pagoda, stairs twist up so that visitors can climb and overlook the panorama of Xian City from the arch-shaped doors on four sides of each storey. On the walls are engraved fine statues of Buddha by the renowned artist Yan Liben of the Tang Dynasty. Steles by noted calligraphers also grace the pagoda.

Shaanxi History Museum

Shaanxi History Museum, which located in the northwest of the Dayan Pagoda of ancient city Xi'an, is the first huge state museum with modern facilities in China, and given the reputation of “bright pearl of ancient city, treasure house of China”.

Conformed to last wish of former Primer Minister Zhou Enlai, Shaanxi History Museum was built from 1983, and was finished on June 20th, 1991 and open to the public. The museum has a collection of 370000 pieces of relics. The museum is an architecture of Tang style, “Hall in center, storied buildings in corners”, elegant and dignified, magnificent scale, combination of traditional architecture and modern

science, which completely embodied folk tradition, local feature, and epoch spirit.

Shaanxi is the imperial capital since ancient times, and more than 13 feudal dynasties built their capitals there in history including Zhou, Qin, Han, and Tang. The province is rich in cultural relics. With the completion of Shaanxi History Museum, it collected over 370,000 precious relics which were unearthed in Shaanxi Province, large quantities, full categories, high grade. The bronze wares, pottery figures, and mural paintings in Tang tombs and so on, are all wonderful artistic treasures.

Since the open of the museum, it held on the rules of combination of collecting, conservation, propagandizing, education, and scientific research, exerted the advantage of many historical relics, and conducted relic displays of various styles. Those all posted the rich meaning of relics from different degrees, and displayed the rich cultural achievements of China. Simultaneously, the relics were exhibited over-seas in the cities of Japan, France, United States, United Kingdom, Germany and other countries and regions.

With best display, excellent order, high quality service, elegant surrounding, and special charm, the museum attracted tourists home and abroad. After the opening, the museum accepted thousands of tourists and became the important window to propagandize Chinese excellent culture, carry out patriotism instruction, and international exchange.

Along with the marching step of times, Shaanxi History Museum met the 21st century, with newer visage, vitality and energy, make greater achievements for constructions of socialist material and spiritual civilization.